SCHOLARLY PUBLICATIONS

A CURRENT AWARENESS BULLETIN
OF RESEARCH OUTPUT

@DTU

(75th Edition)

MARCH, 2018

BY: CENTRAL LIBRARY

DELHI TECHNOLOGICAL UNIVERSITY
(FORMERLY *DELHI COLLEGE OF ENGINEERING)*
GOVT. OF N.C.T. OF DELHI
SHAHBAD DAULATPUR, MAIN BAWANA ROAD
DELHI 110042

PREFACE

This is the **Seventy Fifth** Issue of Current Awareness Bulletin started by Delhi Technological University, Central Library. The aim of the bulletin is to compile, preserve and disseminate information published by the faculty, students and alumni for mutual benefits. The bulletin also aims to propagate the intellectual contribution of Delhi Technological University (DTU) as a whole to the academia.

The bulletin contains information resources available in the internet in the form of articles, reports, presentations published in international journals, websites, etc. by the faculty and students of DTU. The publications of faculty and student which are not covered in this bulletin may be because of the reason that the full text either was not accessible or could not be searched by the search engine used by the library for this purpose.

The learned faculty and students are requested to provide their uncovered publications to the library either through email or in CD, etc. to make the bulletin more comprehensive.

This issue contains the information published during **March, 2018**. The arrangement of the contents is alphabetical. The full text of the article which is either subscribed by the university or available in the web is provided in this bulletin.

Central Library

CONTENTS

1. A Grey Wolf Optimization Approach for Improving the Performance of Wireless Sensor Networks, ***6.Ajay Kaushik[1]***, ***3.S. Indu[2]*** and ***3.Daya Gupta[1]***, [1]Computer Science and [2]Electronics and Communication, DTU

2. A Hybrid Framework for Action Recognition in Low-Quality Video Sequences, ***6.Tej Singh***[1] and ***3.Dinesh Kumar Vishwakarma***[2], [1]Ece and [2]IT, DTU

3. A Novel Low power and Swing Restoration SRAM Logic Circuit Technique, ***3.Ram Murti Rawat***, CSE, DTU

4. A Novel Solution to Prevent Diesel Pilferage at Telecom Tower Site, ***8.1.Abhishek Grover*** and ***7.1.Brejesh Lall***, Electronics and Communications, DTU

5. A Robust Framework for Abnormal Human Action Recognition using $\mathcal{R}$-Transform and Zernike Moments in Depth Videos, ***6.Chhavi Dhiman*** and ***3.Dinesh Kumar Vishwakarma***, Electronics and IT, DTU

6. AMMONIA PRODUCTION FROM A NON-GRID CONNECTED FLOATING OFFSHORE WIND-FARM: A SYSTEM-LEVEL TECHNO-ECONOMIC REVIEW, ***8.VISMAY V. PARMAR***, DTU

7. AN EXPLORATORY FACTOR ANALYSIS FOR DEVELOPING A SCALE OF ETHICS, A KNOWLEDGE MANAGEMENT PERSPECTIVE, ***6.Nishant Gaur*** and ***3.Vikas Gupta***, DSM, DTU

8. Conceptualization of the Balanced Scorecard for Organizational Performance Measurement, ***3.Vikas Gupta*** and ***6.Meenu Chopra***, DSM, DTU

9. Design and Development of an Electronic Level Transmitter using Inter Digital Capacitor, ***7.1.Sayyed Faizan Ali*** and Nirupama Mandal, Electronics and Communications, DTU

10. Effect of rotational speed in friction stir processing on the microstructural and mechanical characteristics of cast AS21A magnesium alloy, ***6.Sumit Joshi*** , ***3.Ramesh Chandra Singh*** and ***3.Rajiv Chaudhary***, Mechanical, DTU

11. Fabrication and sliding wear behavior of some lead-free bearing materials, ***3.Ramesh Chandra Singh***, ***3.Rajiv Chaudhary*** and ***3.Vipin Kumar Sharma***, Mechanical, DTU

12. Fuzzy assessment of the risk factors causing cost overrun in construction industry, Savita Sharma and ***3.Pradeep K. Goyal***, Civil, DTU

13. Green Computing in Sensors-Enabled Internet of Things: Neuro Fuzzy Logic-Based Load Balancing, Pankaj Kumar Kashyap , Sushil Kumar , Upasana Dohare , ***3.Vinod Kumar*** and Rupak Kharel, Computer, DTU

14. L,M&A: An Algorithm for Music Lyrics Mining and Sentiment Analysis, ***6.Vasu Saluja***, ***3.Minni Jain*** and ***6.Prakarsh Yadav***, Computer. DTU

15. Meta-analyses of associations of obesity with risk of melanoma and acne based on case-control studies, ***8.Avni Mehta*** and ***3.Yasha Hasija***, Biotechnology, DTU

16. New sinusoidal oscillator configurations using operational transresistance amplifier, ***6.Gurumurthy Komanapalli***, ***3.Rajeshwari*** Pandey and ***3.Neeta Pandey***, Electronics and Communication, DTU

17. Recent developments in bandwidth improvement of dielectric resonator antennas, Sounik Kiran Kumar Dash and ***6.1.Taimoor Khan***, Electronics and Communications, DTU

18. Sarcasm Detection Using Soft Attention-Based Bidirectional Long Short-Term Memory Model With Convolution Network, LE HOANG SON, ***3.AKSHI KUMAR***, ***6.SAURABH RAJ SANGWAN***, ***7.ANSHIKA ARORA***, ANAND NAYYAR AND MOHAMED ABDEL-BASSET, Computer Science, DTU

19. Sentiment analysis of multimodal twitter data, ***3.Akshi Kumar*** & ***3.Geetanjali Garg***, Computer Science, DTU

20. Spatial shape feature descriptors in classification of engineered objects using high spatial resolution remote sensing data, ***6.Rubeena Vohra*** and ***3.K. C. Tiwari***, Civil, DTU

21. The impact of knowledge management system on student performance : A case study of the University of Delhi, ***6.Namita Jain*** and ***3.Vikas Gupta***, DSM, DTU

22. Thermodynamic performances using energy-exergy analysis of NH3H2O vapor absorption refrigeration system cascaded with vapor compression refrigeration systems using ecofriendly refrigerants, ***3.R.S. Mishra***, Mechanical and Production Industrial and Automobiles, DTU

23. Strength enhancement of the subgrade soil of unpaved road with geosynthetic reinforcement layers, ***6.Meenakshi Singh***, ***3.Ashutosh Trivedi*** and Sanjay Kumar Shukla, Civil, DTU

24. Zero-index metamaterial based all-dielectric nanoantenna, ***6.Nishant Shankhwar***, ***3.Yogita Kalra***, Qiang Li and ***3.Ravindra Kumar Sinha***, Applied Physics, DTU

1. *Chancellor*

2. *Pro Vice Chancellor*	***2.1.*** *Ex Pro Vice Chancellor*
3. *Faculty*	***3.1.*** *Ex Faculty*
4. *Teaching-cum-Research Fellow*	***4.1.****Asst. Librarian*
5. *Alumni*	
6. *Research Scholar*	***6.1.*** *Ex Research Scholar*
7. *PG Scholar*	***7.1.*** *Ex PG Scholar*
8. *Undergraduate Student*	***8.1.*** *Ex Undergraduate Student*

Wireless Personal Communications
https://doi.org/10.1007/s11277-019-06223-2

A Grey Wolf Optimization Approach for Improving the Performance of Wireless Sensor Networks

Ajay Kaushik[1] · **S. Indu**[2] · **Daya Gupta**[1]

© Springer Science+Business Media, LLC, part of Springer Nature 2019

Abstract

Optimizing the energy consumption of sensor nodes have been a big design issue in wireless sensor networks (WSNs). Energy efficient WSN usually compromise with network stability which is a crucial factor in ensuring full, lasting and reliable coverage of the network. Connected dominating set (CDS) based virtual backbone and traditional cluster based approach are two most commonly used data delivery protocols in a WSN. The paper proposes a distance based stable connected dominating set methodology using a meta-heuristic algorithm grey wolf optimization (DBSCDS-GWO) for achieving a stable, balanced and energy efficient CDS based WSN. We also propose a distance based stable clustering algorithm using GWO (DBSC-GWO) for improving the performance of cluster based WSN. DBSCDS-GWO performs better than RMCDS-GA and SAECDS-GA by 70.5% and 67.7% respectively and DBSC-GWO performs better than LEACH and DRESEP by 74.7% and 50.6% respectively in terms of both network stability and energy efficiency. Performance of the proposed algorithm is validated using Matlab simulation and Netsim Emulator.

Keywords Connected dominating set · Dominator · Dominatee · WSN · Cluster head · Network stability · Energy dissipation

Abbreviations

SN	Sensor node
WSN	Wireless sensor network
CDS	Connected dominating set
GWO	Grey wolf optimization
DBSCDS-GWO	Distance based stable connected dominating set methodology using GWO

✉ Ajay Kaushik
ajaykaushik777@gmail.com

S. Indu
s.indu@dce.ac.in

Daya Gupta
dgupta@dce.ac.in

[1] Department of Computer Science and Engineering, Delhi Technological University, Delhi, India

[2] Department of Electronics and Communication Engineering, Delhi Technological University, Delhi, India

Published online: 11 March 2019

DBSC-GWO	Distance based stable clustering algorithm using GWO
RMCDS-GA	Reliable minimum CDS using Genetic algorithm
SAECDS-GA	Stability aware evolutionary CDS using GA
LEACH	Low energy adaptive clustering hierarchy
VB	Virtual backbone
DS	Dominating set
G (V, E)	Graph (vertices, edges)
CH	Cluster head
mCDS	Minimum size CDS
ACO	Ant colony optimization
LBCDS-GA	Load-balanced CDS construction using GA
LEACH-C	LEACH-Centralized
IPI	Inheritance population initialization
FDN, HDN, LDN	First, half and last dead node
IoT	Internet of Things
IoE	Internet of Everything

1 Introduction

WSNs have proved their utility in medical field, defense domain, weather forecasting and several other industrial and commercial applications. A large number of SNs are used for above mentioned applications to ensure adequate coverage and guard against any possible node failure. However, in a densely populated network following concerns may arise: (1) many nodes interfering with each other: (2) multiple data transmission routes: (3) individual nodes communicating with distant nodes and unnecessarily dissipate their energy: (4) a new routing path devised for every small topological change. These challenges can be countered by using some nodes in the network as virtual backbone (VB).

A dominating set (DS) is often used as a VB. For any graph G (V,E) having V vertices and E edges, DS is a subset of V such that V is in DS or is adjacent to a node in DS. A DS has many applications in WSN. For the sake of structure of WSN, DS has to be connected [1] known as CDS. The CDS backbone structure (Fig. 1a) minimizes the

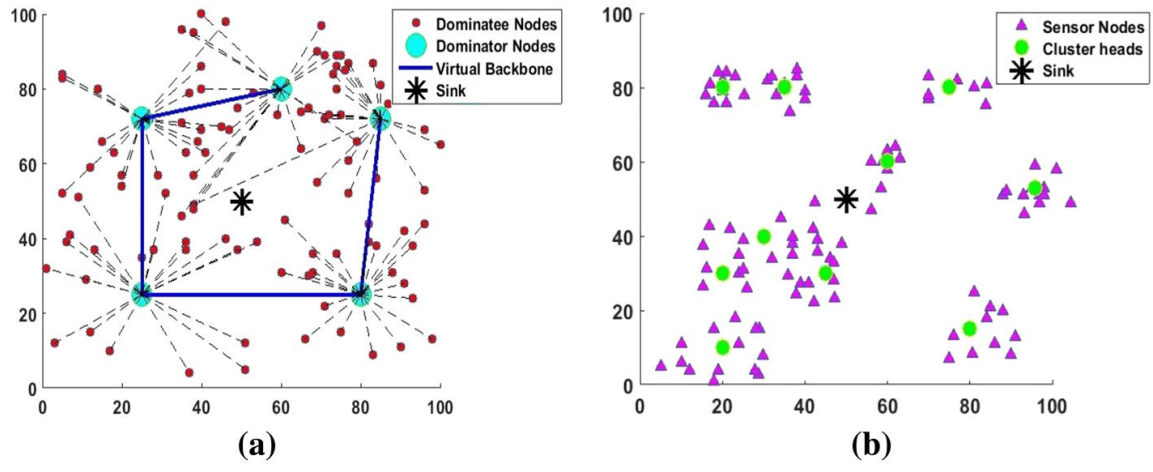


Fig. 1 **a** A virtual backbone based CDS network containing dominator nodes and dominatee nodes. **b** A cluster based traditional WSN scenario

communication load of SNs, optimizes bandwidth, reduces the total network energy dissipation and increases the network lifetime [2–4]. Load balancing and energy efficiency of the CDS nodes are crucial parameters to obtain a stable and long lasting network. A CDS based network can be made energy efficient by minimizing the CDS size. However, if CDS size is too small, some useful features of original CDS may be compromised [5] which outline the need of some novel protocols to achieve energy efficiency and load balancing in a CDS WSN.

Virtual backbone based CDS is used for efficient data delivery protocol for very large WSNs whereas cluster based traditional WSN (e.g. Low Energy Adaptive Clustering Hierarchy, LEACH) is used for optimum data transmission in smaller networks. Cluster based WSN forms clusters of SNs for energy efficient data transfer to the sink (Fig. 1b). In very large networks, each SN is assigned to a cluster head (CH) but improper load distribution among the SNs in a cluster may lead to early death of SNs, resulting in loss of information covered by those nodes. Therefore, behavior of WSN becomes unstable after the death of first node. The time period (in terms of rounds) from the start of network operation until the death of the first SN is called stability period. Instability period is the time interval from the death of the first SN until the death of the last SN. Hence, load balancing and minimizing the energy dissipation of CHs are crucial factors in a stable and energy efficient cluster formation [6].

We propose a novel distance-based energy efficient and load balancing method, using meta heuristic algorithm GWO [7] which gives a commendable improvement in performance of both CDS WSN and cluster based WSN. DBSCDS-GWO and DBSC-GWO optimize the transmission distance and balance the network load to generate energy efficient and stable sensor network. The article is divided into 6 sections. Literature review is presented in Sect. 2. Problem formulation is presented in Sect. 3. Implementation of GWO in CDS WSN and cluster based WSN is presented in Sect. 4. Results are discussed in Sect. 5. Conclusion and future work is discussed in Sect. 6.

2 Literature Review

Ever since the mapping of CDS to WSN has been introduced, numerous attempts have been made to obtain a mCDS (minimum size CDS) by pruning the CDS size using mathematical concepts [8]. Most of the algorithms in the past aimed at first building a CDS and then pruning the CDS size based on some rules while some other proposed algorithms include first constructing a minimum independent set of nodes and then connecting them to form a CDS. Guha et al. [9] implemented many algorithms for minimum CDS construction. The greedy algorithm presented in [9] is still considered to be one of the best algorithms to construct a mCDS. An algorithm for unit disk graphs is presented in [10] that form mCDS using a spanning tree. CDS pruning is done by sequentially removing the dominator nodes, but the algorithm is lengthy as well as trivial. In [11] a genetic algorithm based methodology (RMCDS-GA) is presented that addresses the reliability issues in CDS. Authors in [12] propose a CDS routing protocol based on energy and connectivity of the nodes. The algorithm in [12] aims to minimize duplicate transmission of packets. In [13] an ACO based technique for constructing a mCDS set is presented. Authors provided an efficient algorithm that takes into account weight of the vertex being covered. In [14] authors construct CDS on the basis of time and message complexity, CDS thus formed takes care of all the routing tasks in a WSN.

Authors in [15] used GA to build an LBCDS and simultaneously perform load balanced allocation of dominatees to dominator nodes. In [4] a three phase algorithm is presented for first constructing a dominating set and then pruning it to achieve stability.

Among all the previously proposed methods very limited studies have been conducted to achieve an energy efficient and load balanced CDS WSN. Though the problem of energy efficiency has been addressed in [16, 17] by minimizing the total energy dissipation in the network but they did not consider load balancing. Furthermore, use of GA in [16, 17] results in slow convergence rate, increased memory usage and excessive network overhead. In [10] and [4] authors tried to prune the CDS size to reduce the network cost, but they also did not focus on balancing the network load. A few researchers have proposed load balancing in CDS [18, 19] but they did not emphasize on minimizing the energy dissipation by the dominator nodes and in the entire network.

In cluster based WSN algorithms, LEACH [20] makes a random CH selection which may choose a CH from the nodes that already have a low residual energy. LEACH achieves energy efficient network but in the process, it makes the network unstable due to random CH selection and load imbalance in the network. Many variations to of LEACH have been proposed over the years to improve the performance of a cluster based WSN. LEACH-C proposed in [21] is a centralized algorithm in which cluster formation and CH selection is done by the sink. Clusters are formed in such a way that SNs dissipate minimum energy during data transmission. A hybrid energy efficient distributed (HEED) algorithm [22] was proposed as an extension of LEACH. HEED focus on remaining CH energy during cluster formation and minimize the intra CH communication cost in the network. For balanced clustering in WSN, a weight based clustering approach was proposed in [23] which not only minimizes the intra CH distance but also ensure that a SN with maximum remaining energy is elected as a CH to achieve an energy efficient network. In [6] DRESEP was introduced to increase the network lifetime. DRESEP extends the network lifetime but similar to LEACH, it also does not achieve network stability. In DRSEP a dual hop communication is used. SN is chosen as CH on the basis of number of rounds for which it is not CH. This is a random criterion of CH selection and a low energy node which is not CH for a long time may become CH.

Proposed work makes a WSN more stable and energy efficient in the following ways.

- DBSCDS-GWO selects a set of dominator nodes deterministically and finds the optimum location of the dominator nodes with respect to the sink and the dominatee nodes using the meta-heuristic approach GWO.
- In a CDS WSN, the main criterion to achieve a stable network is to balance the load and delay the death of the first dominator. For measuring relative energy of sensor nodes, we propose a parameter Dominator Lifetime Index (DLI) for each dominator $\mathrm{Dom_i}$ as shown in Eq. 1.

$$DLI_i = \frac{(D_{energy}(i) - E_{diss}(i))}{(E_{diss}(i))} \tag{1}$$

where $D_{energy}(i)$ is the initial energy of Dom_i, $E_{diss}(i)$ is the energy dissipated by Dom_i per round, DLI_i is a measure of approximate lifetime (rounds) of each dominator node. The algorithmic framework minimizes the Inter Quartile Range (*IQR*)/variation among the *DLIs* of all the dominator nodes resulting in equal lifetime and equal load allocation of dominator nodes.

Similarlly, DBSC-GWO uses CH Lifetime Index (*CLI*), which is similar to *DLI* and minimize the *IQR* among the *CLI* of all the CHs resulting in a WSN with balanced load. Hence all the above factors favor high stability period of a WSN with increased network lifetime.

- The major source of energy dissipation in a WSN is the data transmission distance. The energy dissipation is proportional to transmission distance. Therefore we propose a parameter Effective Transmission Distance (*ETD*) as given in Eq. 2 and minimize it.

$$ETD = \Phi \; or \; \eta \quad (whichever \; is \; shorter) \tag{2}$$

For all dominators D in CDS WSN, Φ is the sum of (1) transmission distance between a dominator node and the sink and (2) transmission distance between a dominatee node and a dominator node and η is the transmission distance between a dominatee node and the sink.

For all CHs in a cluster based WSN, Φ is the sum of (1) transmission distance between a CH and the sink and (2) transmission distance between a SN and a CH, η is the transmission distance between a SN and the sink.

Life of a SN is governed by its energy consumption patterns and transmission distance of data sent by the node. Therefore we propose the parameters *DLI* (Eq. 1) as an indication of energy consumption and *ETD* (Eq. 2) as an indication of data transmission distance. Further, the algorithm tries to keep the value of *DLI* uniform for all nodes, which balances the load of each node.

3 Problem Formulation

We know that energy conservation is very important in WSN. The network can be made energy efficient by pruning the number of dominator nodes in a CDS, but with the expense of reduced lifetime of dominator nodes due to increased load as shown in Eqs. 3 and 4 respectively.

$$N_{diss} \, \alpha \, D \tag{3}$$

$$D_{Load} \, \frac{1}{\alpha} \, D \tag{4}$$

where N_{diss} is the energy dissipated by entire network, D denotes all dominator nodes in the network and D_{Load} is the load on a dominator node. Above equations show that energy consumption in the network increases with an increase in D. Also, pruning of dominator size will result in increase in dominator load. Hence, just minimizing the dominator nodes in CDS will not improve network lifetime. We know that

$$E_{diss} \, \alpha \, \Phi \tag{5}$$

$$E_{diss} \, \alpha \, \eta \tag{6}$$

$$E_{diss} \, \alpha \, D_{Load} \tag{7}$$

where E_{diss} is the energy dissipated by the dominator node. Equations 5–7 show that the energy dissipated by the dominator node increases with an increase in Φ, η, and D_{Load}. Hence we can maximize the lifetime and stability of the dominator nodes, by minimizing Φ, η and by ensuring equal load distribution among all the dominators.

Let $V_{i,j}$ be a decision variable (Eq. 8) which assigns every dominatee node to a dominator node.

$$V_{i,j} = \begin{cases} 1 \ \textit{if node } S_i \textit{ is assigned to dominator } D_j, \\ 0 \ 1 < i, \quad j < N \end{cases} \tag{8}$$

For all dominators in $DBSCDS - GWO$, we minimize the objective function X given in Eq. 9.

$$X = E_{diss} + D + ETD + IQR(DLI) \tag{9}$$

where $IQR(DLI)$ is the variance in the lifetime of all the all dominators in a CDS WSN. For all CHs in $DBSCS - GWO$, we minimize the objective function Z given in Eq. 10.

$$Z = CH_{diss} + ETD + IQR(CLI) \tag{10}$$

where CH_{diss} is the energy dissipated by the CHs and $IQR(CLI)$ denotes the variance in the lifetime of all CHs in a cluster based WSN.

Subject to constraint

$$V_{i,j} \in \{0, 1\} 1 < i, j < N \tag{11}$$

The objective function (Eqs. 9, 10) optimizes the energy consumption in a WSN.

3.1 Energy Model

The energy model (Fig. 2) and the communication overhead involved for transmitting $k-bit$ data over a distance d are given in Eqs. 12 and 13 respectively. Here E_{tr} denotes the energy dissipated in sending an k-bit message. E_{amp} denotes the amplification factor. E_{el} denoted energy in electronics and K_{diss} denotes the dissipation constant.

When the distance (d) < threshold value (d_0), free space (fs) model is used. When $(d \geq d_0)$, multi path (mp) fading model is used.

$$E_{tr}(k, d) = E_{el} * K_{diss} + E_{amp(fs)} * d^2 \quad for \ d < d_0 \tag{12}$$

$$E_{tr} = E_{el} * K_{diss} + E_{amp(mp)} * d^4 \quad for \ d \geq d_0 \tag{13}$$

$$E_{rec} = E_{el} * K_{diss} \tag{14}$$

Equation 14 represents the energy dissipated to receive (E_{rec}) a k-bit message.

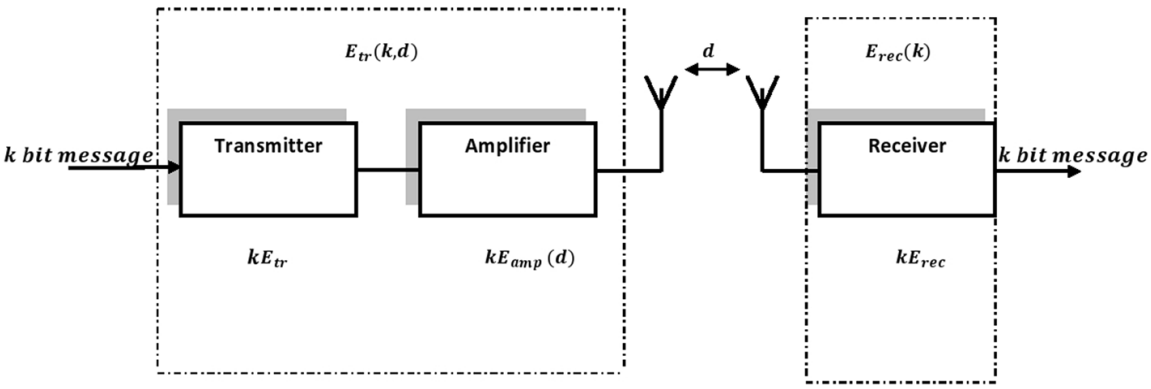


Fig. 2 Energy model used in the communication process

4 Proposed Methodology

4.1 DBSCDS-GWO

Selecting a load balanced CDS structure with minimum *ETD* can attain stability and optimum energy utilization in the network. We propose Gray Wolf Optimization based DBSCDS-GWO for achieving the same. The algorithm is initialized by defining WSN parameters such as number of dominators, deployment region size, packet size, initial energy of the nodes, radio model, control packets etc.

4.1.1 Mapping of DBSCDS-GWO

Once initialized, various CDS structures are obtained using mCDS algorithm [9] and inheritance population initialization (IPI) mechanism [24]. Let a CDS network is represented by S_N number of nodes having D dominators and P dominatees. Each wolf $(W_i, 1 < i < n)$ can be represented by a binary vector of length S_N. Each gene (g) in the vector is 1 for dominator node and 0 for dominatee node as given in Eq. 15.

$$W_i(g) = \begin{cases} 1, & \textit{if } g \textit{ is a dominator} \\ 0, & \textit{if } g \textit{ is a dominatee} \end{cases} \tag{15}$$

$$Wolf W_i \;\; 0\;0\;0\;1\;0\;0\;0\;0\;1\;0\;0\;1\;..\;S_N$$

For mapping the problem to GWO we use two terms *DLI* and *ETD* for each vector.

Dominator lifetime index DLI_i(Eq. 1) indicates the approximate lifetime (rounds) of each dominator Dom_i(where $i = 1$to D) in a CDS WSN. We obtain a vector containing the *DLI* value for each dominator node in a CDS. An optimally balanced CDS structure will have minimum *IQR (DLI)*.

$$\textit{DLI vector for a CDS WSN} \;\; \mathrm{DLI_i}\;\; \mathrm{DLI_{i+1}}\;\; \mathrm{DLI_{i+2}}\;\; \mathrm{DLI_{i+3}}\;\; ..\;\; \mathrm{DLI_{D-1}}\;\; \mathrm{DLI_D}$$

Effective transmission distance ETD is evaluated in Eq. 2. An energy efficient CDS structure will have minimum *ETD*.

4.1.2 GWO Implementation

GWO starts its search process by a set of wolves (solutions) randomly scattered in search space looking for the prey (optimum solution) [7]. Position of each grey wolf is denoted by a vector as shown in Eq. 16 where n is the size of the search space.

$$\overrightarrow{\mathrm{X}} = \{x[1], x[2], x[3] \ldots x[n]\} \tag{16}$$

During the hunting (optimization) process of GWO, the fitness of each wolf is calculated using Eq. 17. The fitness function for the proposed DBSCDS-GWO is defined such that it minimizes *IQR*(*DLI*) and *ETD* in a network and optimizes D to obtain a stable, energy efficient and optimum size CDS WSN. The fitness $F_{DBSCDS-GWO}$ for each wolf is minimized using GWO.

$$F_{DBSCDS-GWO} = ETD + (IQR(DLI)) + D \tag{17}$$

Wolves having the top 3 fitness values are saved as α, β, and δ respectively and the remaining wolves (ω) in the population update their position according to α, β, and δ. For searching the optimum solution (prey), GWO operates in 2 steps i.e. encircling the prey and hunting.

Encircling the prey The wolf encircles the prey in order to stop their movement. This could be mathematically formulated in Eqs. 18 and 19.

$$\vec{D} = \left|\vec{C}.\vec{X}_p(t) - \vec{X}(t)\right| \tag{18}$$

$$\vec{X}(t+1) = \vec{X}_p(t) - \vec{A} \cdot \vec{D} \tag{19}$$

where t shows the present iteration, $\vec{X}_p$ is prey's position vector and $\vec{X}$ is wolf's position vector. The vectors $\vec{A}$ and $\vec{C}$ are the coefficient vectors obtained from Eqs. 20 and 21 respectively.

$$\vec{A} = 2\vec{a}.\vec{r}_1 - \vec{a} \tag{20}$$

$$\vec{C} = 2\vec{r}_2 \tag{21}$$

$\vec{a}$ is linearly reduced from 2 to 0 over the iterations. Here $\vec{r}_1$ and $\vec{r}_2$ are the random vectors in the interval [0,1].

Hunting The position of the prey (optimum solution) is best known by α, β, and δ. Therefore we calculate and save the updated position of α, β, and δ in Eqs. 22-24.

$$D_\alpha = \left|C_1.X_\alpha - X_{W_i}\right| \tag{22}$$

$$D_\beta = \left|C_2.X_\beta - X_{W_i}\right|, \tag{23}$$

$$D_\delta = \left|C_3.X_\delta - X_{W_i}\right|, \tag{24}$$

In Eqs. 22–24, X_{W_i} denotes the position of wolf W_i, $\vec{X}_\alpha$ is α wolf's position and $\vec{D}_\alpha$ is updated α position. Similarly, $\vec{X}_\beta$ is β wolf's position and $\vec{D}_\beta$ is the updated β position. $\vec{X}_\delta is\delta$ wolf's position and $\vec{D}_\delta$ denote the updated δ position.$C_{1,}C_2, C_3$ are calculated as per Eq. 21. The final positions ($\vec{X}_1$, $\vec{X}_2$, $\vec{X}_3$) of a wolf for the current iterations are evaluated as per Eqs. 25–27 [7].

$$X_1 = X_\alpha - A_1 \cdot D_\alpha \tag{25}$$

$$X_2 = X_\beta - A_2 \cdot D_\beta \tag{26}$$

$$X_3 = X_\delta - A_3 \cdot D_\delta \tag{27}$$

$A_{1,}A_2, A_3$ are calculated as per Eq. 21. The wolf finally updates its position according to the best solutions α, β and δ (Eq. 28).

$$\vec{X}(t+1) = (\vec{X}_1 + \vec{X}_2 + \vec{X}_3)/3 \tag{28}$$

4.1.3 New Population

A new population is generated after the updating process. A check is made on the new population and only those solutions which form a CDS are retained. Each ω wolf in the new population is again modified according to new α, β and δ. The above process is repeated until either maximum iterations or optimum solution is reached.

4.1.4 Convergence of GWO

There will be abrupt changes in the movement of the wolves in the initial steps of the optimization. These changes minimize as the algorithm approaches optimization which corresponds to minimization in the difference between fitness values of α, β, δ and ω wolves in every iteration [7].

After obtaining the optimum solution, the dominatee nodes sense data from its surroundings and transfer this data to the sink using *ETD*. The process is repeated till the network remains stable. The pseudo code for DBSCDS-GWO is explained below.

1. Initialize the population Size Pi. Initialize the max numbers of iteration I_{max}.
2. **while** $I < I_{max}$ **for each** iteration **do**
3. **for each** wolf W_i **do**
4. Clone the **CDS** to W_i.
5. Compute the fitness function ($F_{DBSCDS-GWO}$) of each wolf using equation 17.
6. Update leader wolves X_α, X_β, X_δ. - three best wolves.
7. Use Eq 20 and Eq. 21 to calculate the coefficient vectors.
8. Update the wolves' position using Eq. 28.
9. **end**
10. **end**
11. Optimum CDS based WSN is obtained after final iteration/convergence.

4.2 DBSC-GWO

In the Distance based Stable Clustering algorithm, the primary emphasis is on minimizing the energy dissipation by CHs and SNs along with balancing the CH load. Initially, every SN and CH is assigned a unique ID and a wolf comprises of a combination of SNs and CHs. Many such wolves are obtained in each iteration to produce an initial population. For each CH in the population, CH Lifetime Index (*CLI*) is calculated similar to *DLI* (Eq. 1). *ETD* is calculated in Eq. 2. The fitness value $F_{DBSC-GWO}$ (Eq. 29) for each wolf is minimized using GWO.

$$F_{DBSC-GWO} = ETD + (IQR(CLI)) \tag{29}$$

Based on the fitness of each wolf, GWO is implemented as per Sect. 4.2. Each SN senses the data from its surroundings and transfers this data to the sink using *ETD*. The pseudo code for DBSC-GWO is given below.

Initialize the population Size Pi. Initialize the max numbers of iteration I_{max}.
while $I < I_{max}$ **for each** iteration **do**
  for each wolf W_i **do**
    Clone the **WSN** to W_i.
    Compute the fitness function (F_{DBSC_GWO}) of each wolf using equation 29.
    Update leader wolves X_α, X_β, X_δ. - three best wolves.
    Use Eq. 20 and Eq. 21 to calculate the coefficient vectors.
    Update the wolves' position using Eq. 28.
  end
end
Optimum cluster based WSN is obtained after final iteration/convergence.

5 Experimental Results

The proposed methodology is validated using Matlab and Netsim Emulator. In experiment 1, DBSCDS-GWO is compared with the existing CDS based algorithms RMCDS-GA [11] and SAECDS-GA [16]. In experiment 2, DBSC-GWO is compared with traditional WSN algorithms LEACH [20] and DRESEP [6]. Matlab is used to implement and validate the energy efficiency and stability of the proposed algorithms but Matlab doesn't have a GUI based network simulator. Therefore, we use Netsim to simulate a better visual picture of the sensor network and energy dissipation pattern of each sensor node. Simulation parameters for DBSCDS-GWO are demonstrated in Table 1.

5.1 Experiment 1

Comparison of DBSCDS-GWO with RMCDS-GA [11] and SAECDS-GA [16] in terms of variation in D (dominator nodes) with respect to communication range, variation in E_{diss} (energy dissipated by dominator nodes) with respect to total number of nodes in the network, variation in N_{diss} (energy dissipated by the network) with respect to total number of nodes in the network and variation in network instability period with respect to the network size is presented in Figs. 3,4a, b and 5 respectively. The network becomes unstable with the death of first node and if first node dies at a later stage then the time gap between the expiry of first and last node will be minimized. We measure this time gap as network

Table 1 Parameters for DBSCDS-GWO simulation

Parameter	Value taken
Range (r)	20–40 m
Area (M)	40×40 to 100×100
S_N	100–160
Initial energy of S_N	1.5 J
E_{DA}	5 nj/bit
E_{elec}	50 nj/bit
E_{amp}	100 pJ/bit/m^2
Radio amplifier energy	.0013 pj/bit/m^4

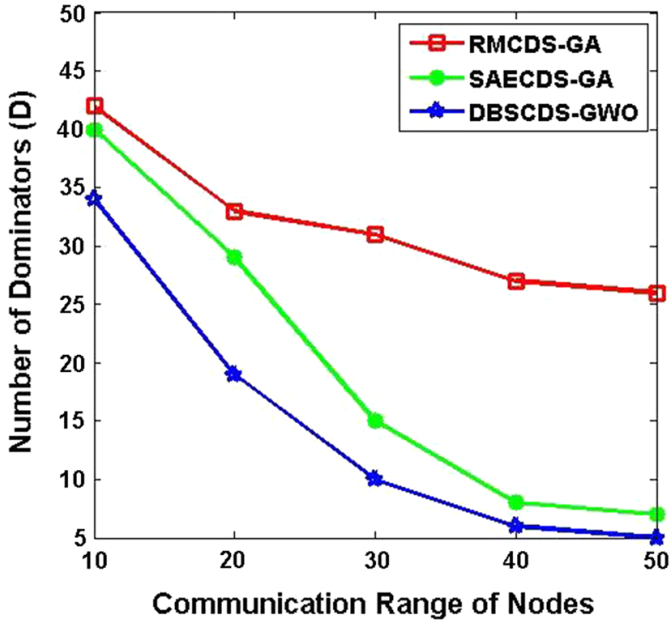


Fig. 3 Comparison of DBSCDS-GWO with existing algorithms in terms of variation in D with respect to communication range of the nodes

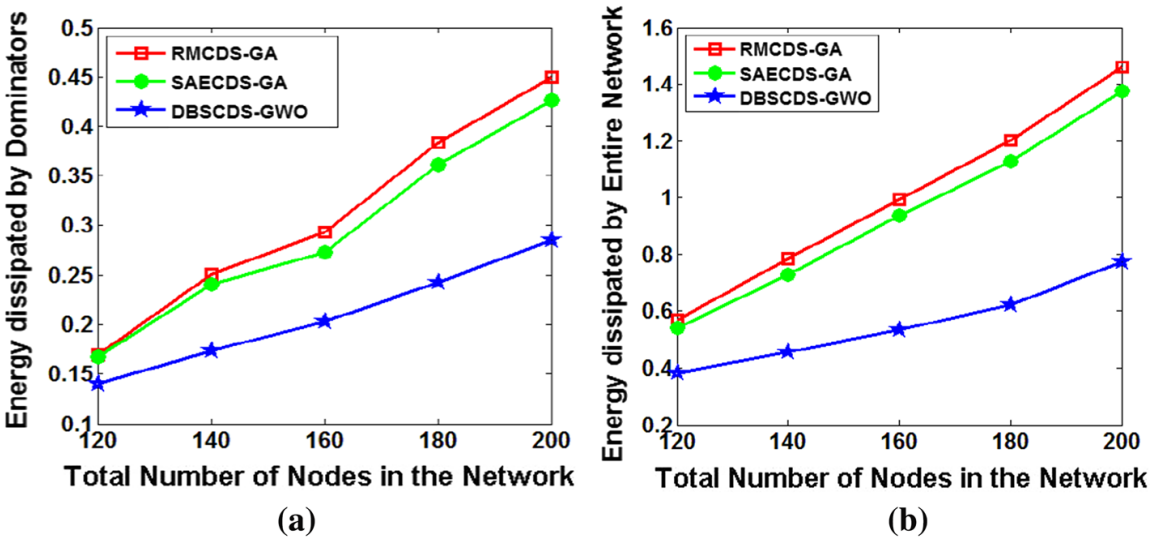


Fig. 4 Comparison of DBSCDS-GWO with existing algorithms in terms of variation in **a** E_{diss} with respect to total nodes in the network and **b** N_{diss} with respect to total nodes in the network

instability period and represent it in terms of rounds. The instability period of a network decreases with increase in network size as shown in Fig. 5. The performance improvement of DBSCDS-GWO over existing algorithms for various parameters is presented in Table 2. DBSCDS-GWO reduces E_{diss} and N_{diss} and improves network stability due to minimization of *ETD* and balanced dominator load.

Table 3 presents the performance of DBSCDS-GWO in terms of 3 parameters, namely communication range (r), deployment area (M) and number of nodes (S_N). Results are compared considering 3 cases (1) M and S_N are constant and output for varying r is obtained; (2) S_N and r are constant and output is obtained for varying M; (3) M and r are constant and the output is taken for varying S_N. In case 1, 2 and 3, DBSCDS-GWO minimizes both N_{diss} and E_{diss} more effectively than the exisiting algorithms. This is due to the reason that DBSCDS-GWO reduces the dominator size in a CDS and also finds optimum location of

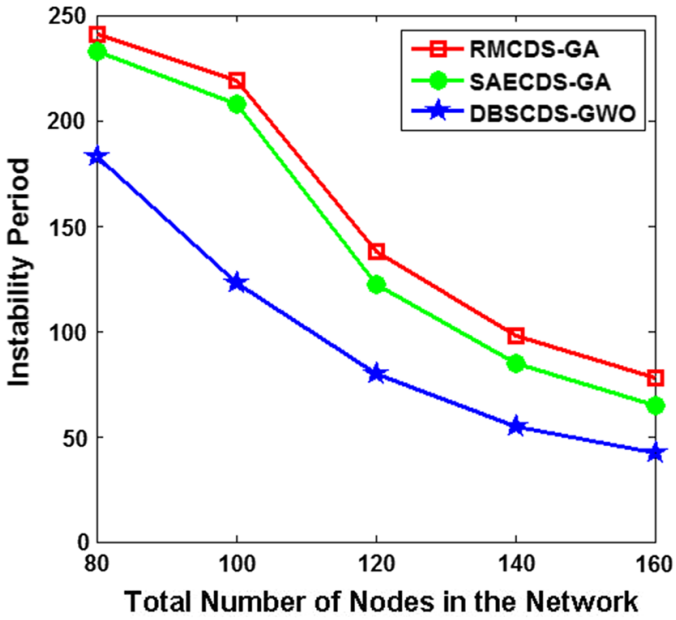


Fig. 5 Comparison of DBSCDS-GWO with existing algorithms in terms of instability period with respect to total nodes in the network

the dominatee nodes with respect to dominators and the sink which in turn minimize *ETD*. Results from case 3 show that E_{diss} and N_{diss} increases with increasing S_N. This is because a dominator node becomes more loaded with increase in S_N which results in increase of E_{diss} and N_{diss}.

Figure 6 shows that DBSCDS-GWO minimizes the fitness function more effectively and converges 33.2% faster than SAECDS-GA due to better convergance rate of GWO in comparison to GA [7].

5.2 Experiment 2

For DBSC-GWO we take initial energy of the nodes as .1 J, area as 100*100, sink at (50, 50), E_{elec} as 50 nj/bit and E_{amp} as 100 pJ/bit/m2. Comparison of DBSC-GWO with LEACH [20], and DRESEP [6] in terms of energy efficient stability, alive nodes in the network, and load balancing is presented in Figs. 7, 8 and 9 respectively. We measure the performance of DBSC-GWO in terms of first, half and last dead node represented by FDN, HDN and LDN respectively. Number of rounds from the initial time to the FDN is called the stability period or the FDN of the WSN. Number of rounds from the initial time to the half dead nodes and when there is no alive node present are called as HDN and LDN respectively. Figure 7 shows the rounds elapsed for FDN, HDN, and LDN of a network. DBSC-GWO outperforms LEACH, and DRESEP in terms of FDN, HDN and stability period due to balanced load in DBSC-GWO. Figure 8 shows that the nodes in DBSC-GWO are alive for a longer period of time as compared to the existing works. The performance gain of DBSC-GWO over existing algorithms is presented in Table 4.

The energy bar graph (Fig. 9) and energy stem curve (Fig. 10) are plotted corresponding to the rounds when average network energy reduces to 75, 50 and 25% respectively. The energy bar plot in Fig. 9 shows that energy dissipation of CH nodes in the network is uniform and stable in DBSC-GWO as compared to the past algorithms for 75, 50 and 25% network energy. The uniform dissipation of CH energy is due to balanced load in DBSC-GWO. Similarly, we represent the energy of alive CH nodes and dead CH nodes in the network using a energy stem curve as shown in Fig. 10. Alive and dead CH nodes are represented by pink and thick blue dots respectively. It is seen in energy stem curve that

Table 2 Performance improvement of DBSCDS-GWO over existing algorithms

Algorithms	Parameters							
	D (dominator nodes)		E_{diss} (energy dissipated by D)		N_{diss} (energy dissipated by network)		Instability period	
	Dominator nodes	GWO improvement (%)	Value (Joules)	GWO improvement (%)	Value (Joules)	GWO improvement (%)	Number (rounds)	GWO improvement (%)
RMCDS-GA	34	70.5	.252	30.9	.784	41.5	219	43.8
SAECDS	31	67.7	.241	27.8	.728	37	208	40.8
DBSCDS-GWO	10	–	.174	–	.458	–	123	–

Table 3 Comparison of DBSCDS-GWO with SAECDS-GA, and RMCDS-GA in terms of dominator energy dissipation and network energy dissipation

	r = 20			r = 25			r = 35			r = 40		
	D	E_{diss}	N_{diss}	D	E_{diss}	N_{diss}	D	E_{diss}	N_{diss}	D	E_{diss}	N_{diss}
Case 1: $S_N = 100$, M = 100 × 100, r = 20–40												
RMCDS-GA	52	.167	.432	37	.156	.398	31	.134	.453	24	.099	.401
SAECDS-GA	49	.155	.413	34	.128	.388	27	.109	.432	21	.085	.381
DBSCDS-GWO	24	.104	.290	17	.078	.246	6	.029	.120	5	.023	.104
	M = 40 × 40			M = 60 × 60			M = 80 × 80			M = 100 × 100		
	D	E_{diss}	N_{diss}	D	E_{diss}	N_{diss}	D	E_{diss}	N_{diss}	D	E_{diss}	N_{diss}
Case 2: S_N = 100, M = 40 × 40 − 100 × 100, r = 20												
RMCDS-GA	24	.084	.179	26	1.2	.276	34	.135	.362	46	.178	1.651
SAECDS-GA	21	.060	.166	22	.80	.222	31	.111	.311	44	.149	1.402
DBSCDS-GWO	3	.010	.029	7	.30	.082	14	.059	.172	24	.103	1.284
	$S_N = 100$			$S_N = 120$			$S_N = 140$			$S_N = 160$		
	D	E_{diss}	N_{diss}	D	E_{diss}	N_{diss}	D	E_{diss}	N_{diss}	D	E_{diss}	N_{diss}
Case 3: S_N = 100 – 160, M = 100 × 100, r = 20												
RMCDS-GA	48	.176	.463	49	.215	.563	52	.293	.734	53	.312	.924
SAECDS-GA	45	.149	.406	46	.194	.536	48	.241	.677	50	.296	.848
DBSCDS-GWO	25	.108	.301	25	.131	.375	26	.138	.439	28	.196	.569

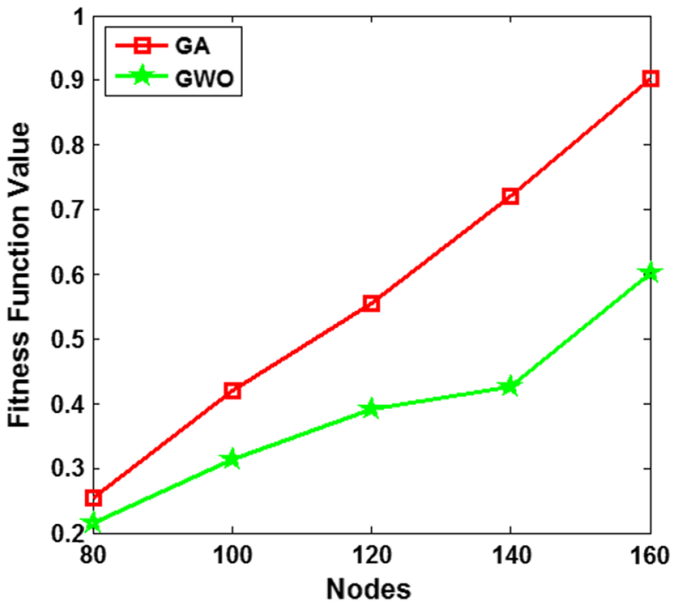


Fig. 6 Convergence rate comparison of GWO with GA in terms of fitness function minimization

remaining energy of nodes in DBSC-GWO is uniform as compared to remaining energies of LEACH and DRESEP. In case of LEACH and DRESEP, some node dies (denoted by blue dots) when network energy reduces very low to 25%. However, due to the balanced

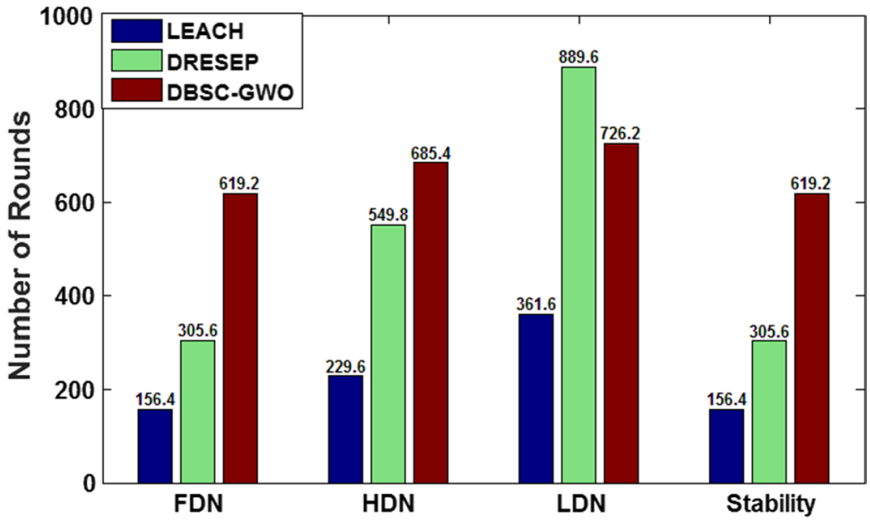


Fig. 7 Comparison of of DBSC-GWO with LEACH and DRESEP in terms of FDN, HDN, LDN and stability period

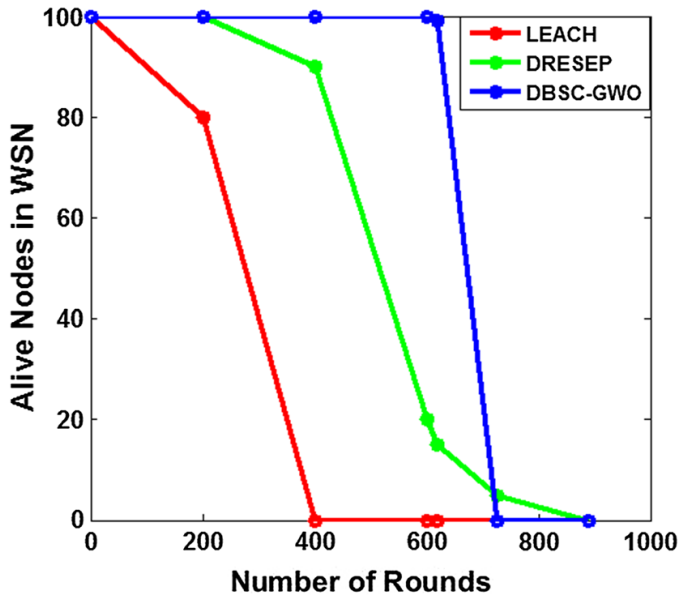


Fig. 8 Comparison of DBSC-GWO with LEACH and DRESEP in terms of alive nodes in a WSN

load in proposed algorithm, nodes remain alive even when the network remaining energy reduces to 25%.

5.3 Energy Dissipation Pattern

Energy dissipation pattern of each SN can be visualized by using a GUI. We have simulated the same using Netsim. The sensor network we consider has 100 SNs distributed in $100 \times 100\ m^2$ area. Each SN has an initial energy of 1 J (or 1000 mill joule), sink is located

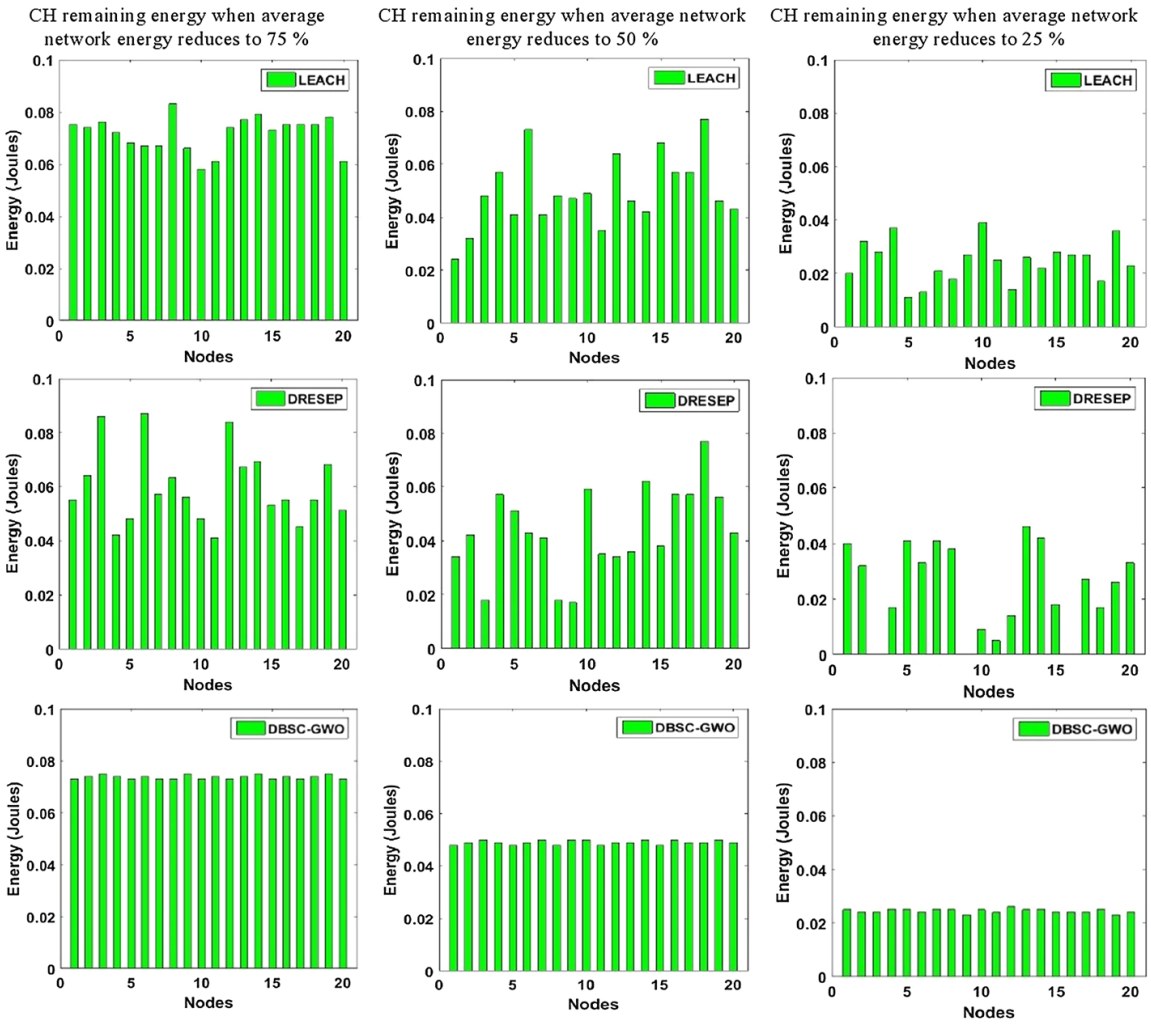


Fig. 9 Energy bar plot for comparison of the DBSC-GWO with LEACH and DRESEP

Table 4 Performance gain of DBSC-GWO over past algorithms

Algorithm	Parameter					
	Stablility period		Alive nodes (after 600 rounds)		Dead nodes (after 650 rounds)	
	Number (rounds)	GWO improvement (%)	Nodes	GWO improvement (%)	Nodes	GWO improvement (%)
LEACH	156.4	74.7	0	100	100	82
DRESEP	305.6	50.6	18	82	90	80
DBSC-GWO	619.2	–	100	–	18	–

at (50, 50), E_{elec} is 50 nj/bit and E_{amp} is 100 pJ/bit/m2. The network is shown in Fig. 11 with SNs, CHs and the sink. Link denoted by green line in Fig. 11 represents the packet flow from CH to the sink.

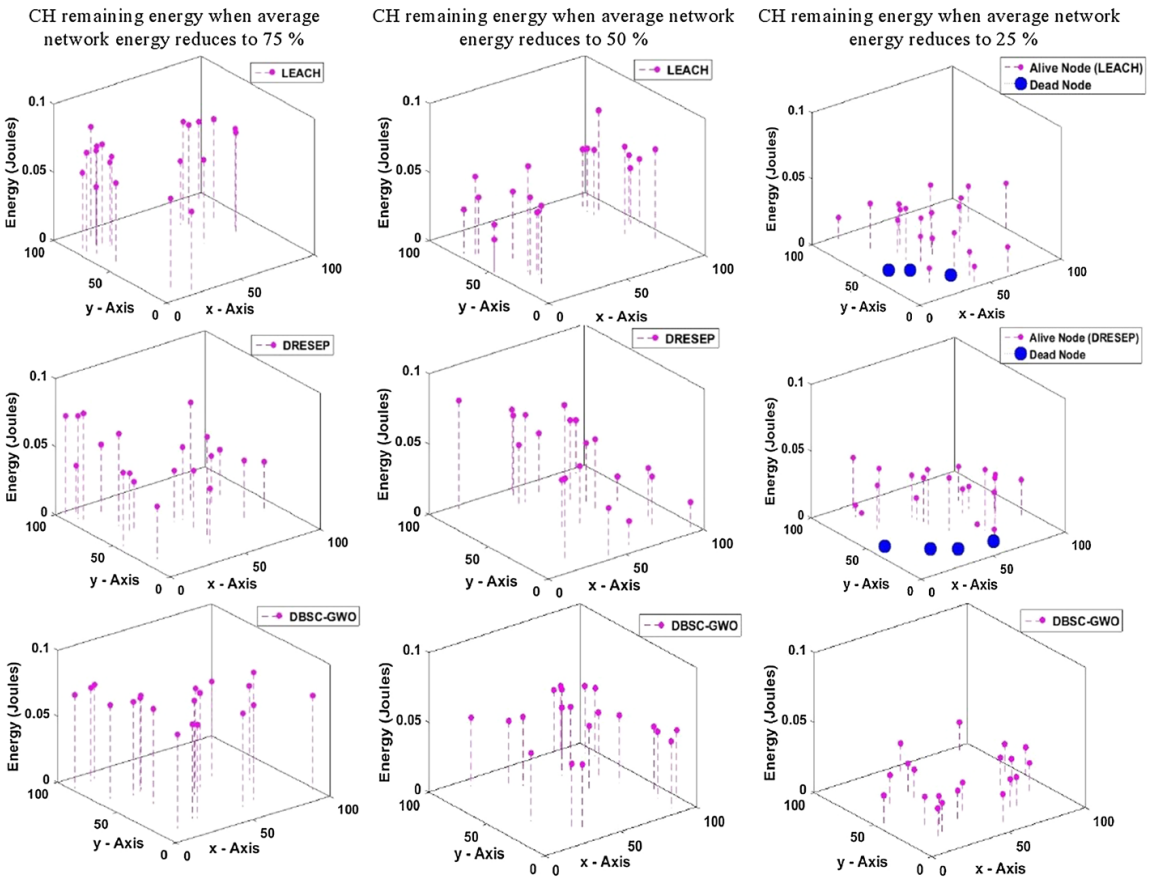


Fig. 10 Energy stem plot for comparison of the DBSC-GWO with LEACH and DRESEP

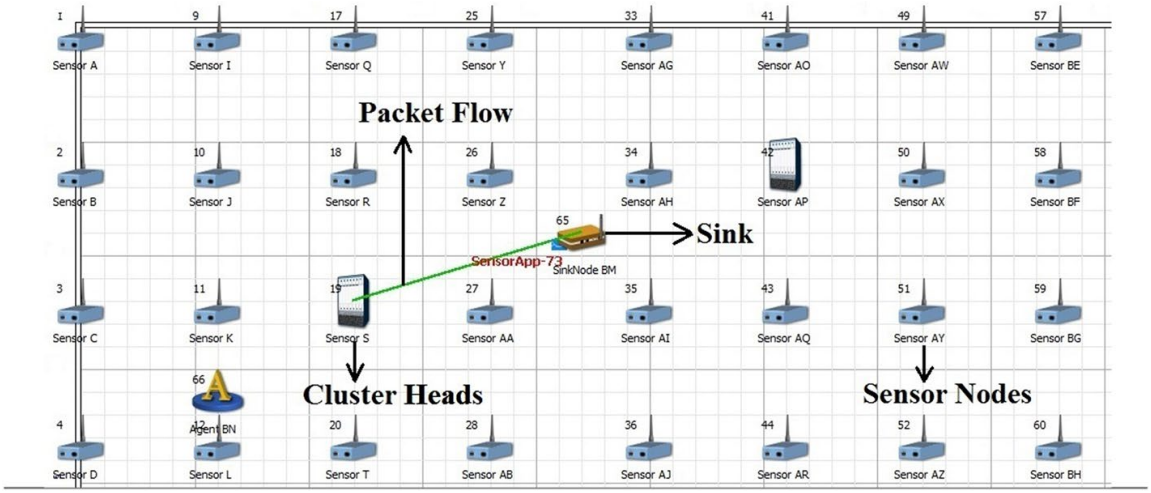


Fig. 11 Packet transmission in Netsim. Cluster Head sending the information to the sink (green link). (Color figure online)

The energy dissipation pattern of the nodes of sensor network shown in Fig. 11 is plotted in Fig. 12a, b. The X and Y axis corresponds to the X and Y coordinates of SNs and Z axis corresponds to the energy consumed by the nodes. The peaks in Fig. 12a represent the non-uniform energy dissipation of the nodes in the network, before applying

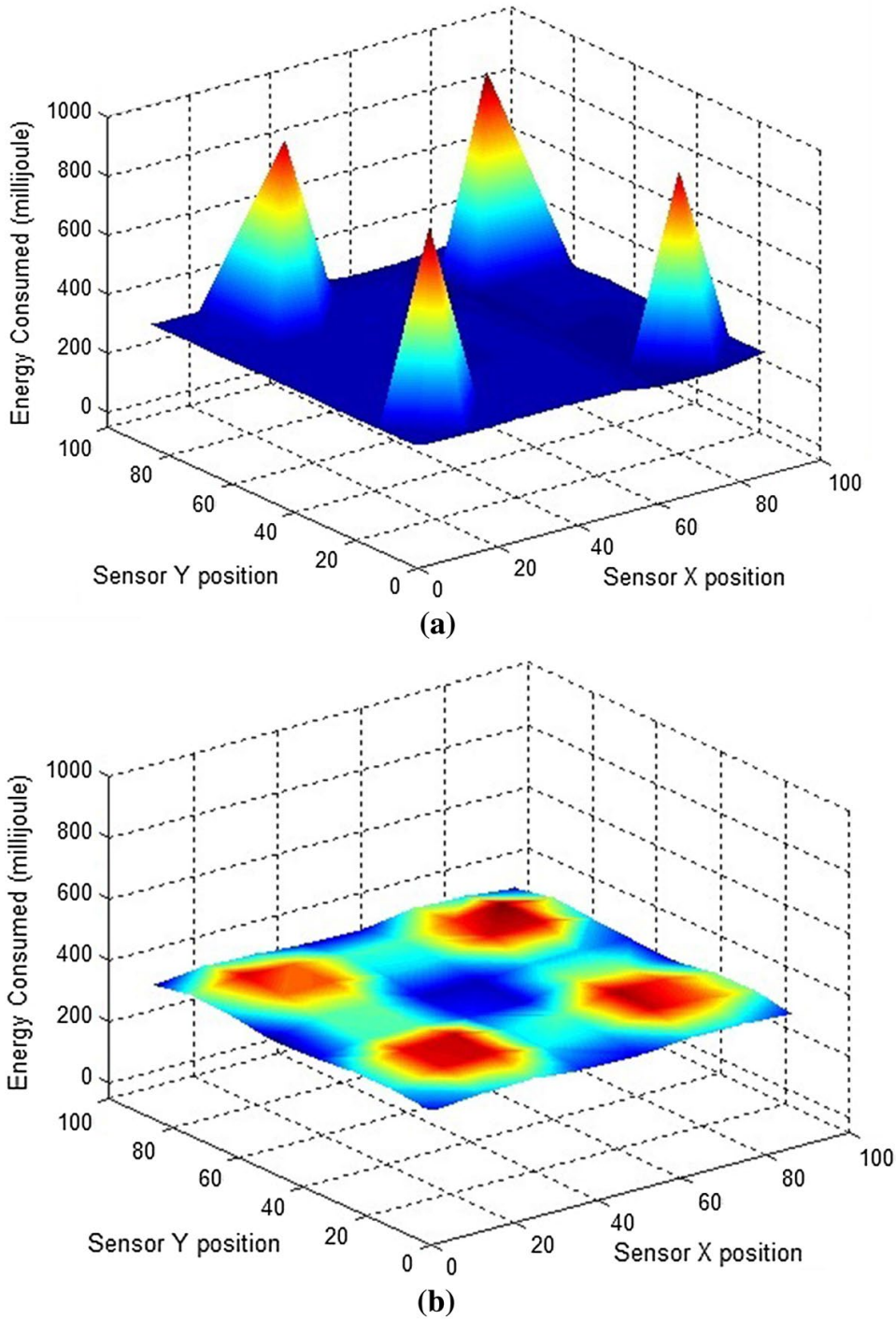


Fig. 12 **a** Non uniform dissipation of node energy (denoted by peaks) before applying the proposed algorithm. **b** Uniform dissipation of node energy (flat curve) after applying the proposed algorithm

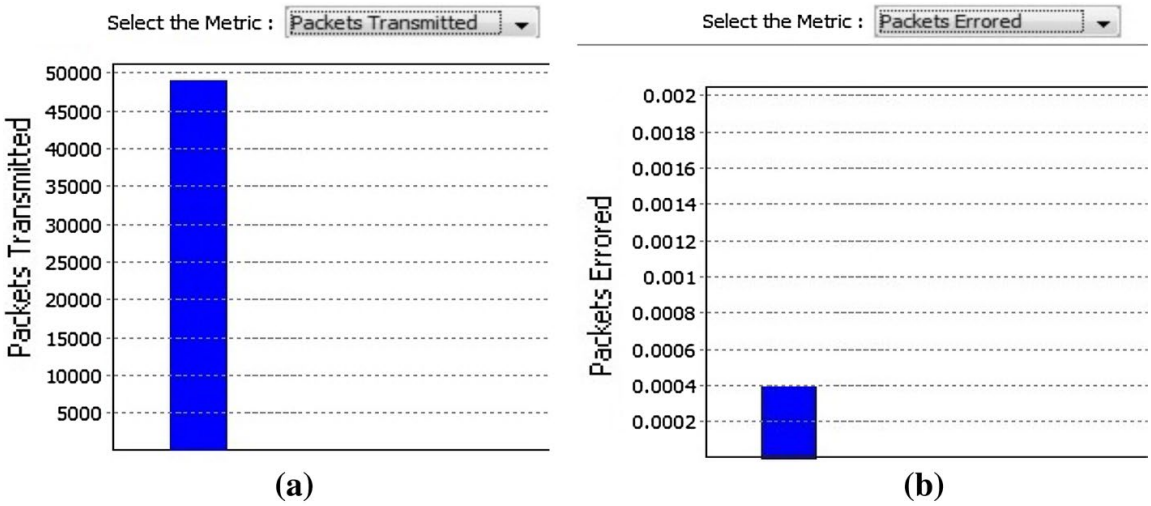


Fig. 13 Performance of WSN designed in Netsim for **a** Packets transmitted to the sink. **b** Packet error

the proposed algorithm. The flat graph shown in Fig. 12b represents uniform energy dissipation of the nodes after applying proposed algorithm.

An important parameter of WSN performance is its packet delivery rate and packet drop ratio. The output graphs of packets transmitted to the sink and packet error are shown in Fig. 13a, b respectively. It can be seen from Fig. 13a, b that proposed algorithm efficiently transmits packets to the sink and improves the WSN performance with minimal error.

6 Conclusions and Future work

A major design issue in WSN is energy efficiency and load balanced clustering so that available network lifetime can be efficiently utilized. The paper presents two algorithms DBSCDS-GWO and DBSC-GWO for CDS WSN and cluster based WSN respectively to achieve a stable and energy efficient network. Both algorithms ensure deterministic dominator/CH selection, minimize the effective transmission distance involved in the transmission of sensed data to the sink and balance the network load. DBSCDS-GWO performs better than RMCDS-GA and SAECDS-GA by 70.5%, 67.7% respectively in terms of energy efficiency and network stability. On the other hand DBSC-GWO performs better than LEACH and DRESEP by 74.7% and 50.6% respectively in terms of energy efficient network and stability. The proposed approach can be extended for new emerging technologies like IoT (Internet of Things) and IoE (Internet of Everything), where the network size is huge and there is a need to optimize the energy consumption by SNs. Therefore, proposed algorithm can be used to minimize the energy consumption by SNs, which makes it useful for IoT and IoE applications.

Acknowledgements We acknowledge the contribution of undergraduate student Gayatri K.V.R in this work.

References

1. Ramar, R., & Shanmugasundaram, R. (2015). Connected k-coverage topology control for area monitoring in WSNs. *Wireless Personal Communication, 84,* 1051. https://doi.org/10.1007/s11277-015-2675-9.
2. Butenko, S., Cheng, X., Du, D. Z., & Pardolos, P. M. (2002). On the construction of virtual backbone for Ad Hoc WSN. *Cooperative Control: Models, Applications, and Algorithms, 1,* 43–54.
3. Golden Julie, E., & Tamilselvi, S. (2016). CDS-fuzzy opportunistic routing protocol for WSNs. *Wireless Personal Communication, 90,* 903. https://doi.org/10.1007/s11277-016-3250-8.
4. Rai, M., Verma, S., & Tapasvi, S. (2009). A power aware minimum CDS for WSNs. *Journal of Networks, 4*(6), 511–519.
5. Du, H., Wu, W., Ye, Q., et al. (2013). CDS-Based virtual backbone construction with guaranteed routing cost in WSNs. *IEEE Transactions on Parallel and Distributed Systems, 24*(4), 652–661.
6. Mittal, N., & Singh, U. (2015). Distance-based residual energy efficient stable election protocol for WSNs. *Arabian Journal for Science and Engineering, 40,* 1637–1646.
7. Mirjalili, S., Mirjalili, S. M., & Lewis, A. (2014). Grey wolf optimizer. *Advances in Engineering Software, 69,* 46–61.
8. Haynes, T. W., Stephen, T., & Slater, P. J. (1998). *Fundamentals of domination in graphs*. New York: Marcel Dekker Inc.
9. Guha, S., & Khuller, S. (1998). Approximation algorithms for CDSs. *Algorithmica, 20,* 374–387.
10. Lu, G., Zhou, M. G., Tang, Y., Zhou, M. Y., Niu, X. Z., & She, K. (2009). Approximation algorithms for CDS problem in unit disk graphs. *Journal of Electronic Science and Technology of China, 3*(7), 214–222.
11. He, J., Cai, Z., Ji, S., Beyah, R., & Pan, Y. (2011). A GA for constructing a reliable MCDS in probabilistic wireless networks. *Wireless algorithms, systems, and applications, WASA, 2011,* 96–107.
12. Kies, A., Maaza, Z. M., Belbachir, R., Boumedjout, A., & Mekki, R. (2015). Routing protocol based on CDSE virtual topology in Ad Hoc Network. *Wireless Personal Communication, 80,* 923. https://doi.org/10.1007/s11277-014-2063-x.
13. Jovanovic, R., & Tuba, M. (2013). ACO algorithm with pheromone correction strategy for the minimum CDS problem. *Computer Science and Information Systems, 8*(3), 133–149.
14. Razieh, A. et al. (2011). CDS problem and its application to WSN. In *First international conference on advanced communications and computation*.
15. He, J., Ji, S., Yan, M., Pan, Y., & Li, Y. (2012). Load-balanced CDS construction in WSNs via GA. *International Journal of Sensor Networks, Inderscience, 11*(3), 166–178.
16. Khalil, E. A., Ozdemir, S. (2015). Prolonging stability period of CDS Based WSNs. In: *IEEE international wireless communication and mobile computing conference* (pp. 776–781).
17. Khalil, E. A., & Ozdemir, S. (2017). Reliable and energy efficient topology control in probabilistic WSNs via multi-objective optimization. *The Journal of Supercomputing, 73,* 2632–2656.
18. Jing, He, Ji, S., Pan, Y., & Li, Y. (2014). Greedy construction of load-balanced virtual backbones in WSNs. *Wireless Communications and Mobile Computing, 14,* 673–688.
19. He, J., Ji, S., Yan, M., Pan, Y., Li, Y. (2011). GA based construction of load-balanced CDSs in WSNs. In: *IEEE military communications conference* (pp. 667–672).
20. Heinzelman, W. R., Chandrakasan, A., Balakrishnan, H. (2000). Energy efficient communication protocol for wireless micro sensor networks. In: *33rd International conference on system sciences* (pp. 3005–3014).
21. Heinzelman, W. R., Chandrakasan, A., & Balakrishnan, H. (2002). An application-specific protocol architecture for wireless micro sensor networks. *IEEE Transactions on Wireless Communications, 1*(4), 660–670.
22. Younis, O., & Fahmy, S. (2004). HEED approach for WSN. *IEEE Transactions on Mobile Computing, 3*(4), 366–379.
23. Soussi, M., Meddeb, A. (2016). Minimum Energy Multi-Objective Clustering Model for WSNs. In: *Paper presented in wireless communications and mobile computing* (pp. 769–773).
24. Mohanty, J. P., Mandal, C. (2014) A distributed greedy algorithm for construction of mCDS in WSN. In: *Paper presented in AIMoC* (pp. 104–110).

Publisher's Note Springer Nature remains neutral with regard to jurisdictional claims in published maps and institutional affiliations.



Ajay Kaushik is a senior research fellow (Ph.D. research scholar) in the Department of Computer Science and Engineering at Delhi Technological University (DTU), Delhi, India. His areas of interest are wireless sensor networks and nature inspired algorithms. He did his M.Tech. (Master of Technology), post B.Tech. in Computer Science and Engineering. He qualified UGC NET-JRF with a percentage of 70.8% in year 2013. He has always been among the top rank-holders of the university in these courses. He has published several research papers in international journals and conferences in wireless sensor networks and nature inspired algorithms.



S. Indu is a Professor in the Department of Electronics and communication Engineering, Delhi Technological University, Delhi, and is currently the head of the department there. She has done Ph.D. in Computer Engineering from University of Delhi and M.Tech, Post B. Tech. from University of Kerala, Kerala. She was awarded the Best Branch Counselor award 2013 IEEE USA. Her research interests are in the field of Computer Vision, Image Processing, and wireless sensor network. She has 3 completed sponsored research projects. She published several research papers in international journals and conferences.



Daya Gupta is a Professor in the Department of Computer Engineering, Delhi Technological University, Delhi. She has done Ph.D. in Computer Engineering from University of Delhi and M.Sc. (Maths), Post M.Sc. Diploma (Computers Sc.) from IIT, Delhi. She is a senior member of IEEE and a life member of CSI. Her research interests are in the field of requirement engineering, network security, ad hoc networks and image classification in remote sensing. She has published several research papers in international journals and conferences and has chaired sessions and delivered invited talks at many national and international conferences.

A Hybrid Framework for Action Recognition in Low-Quality Video Sequences

Tej Singh[1], Dinesh Kumar Vishwakarma[2]

[1]Department of Electronics and Communication Engineering, [2]Department of Information Technology, Delhi Technological University, Bawana Road, Delhi

[1]ttomar07@gmail.com, [2]dvishwakarma@gmail.com

Abstract: Vision-based activity recognition is essential for security, monitoring and surveillance applications. Further, real-time analysis having low-quality video and contain less information about surrounding due to poor illumination, and occlusions. Therefore, it needs a more robust and integrated model for low quality and night security operations. In this context, we proposed a hybrid model for illumination invariant human activity recognition based on sub-image histogram equalization enhancement and k-key pose human silhouettes. This feature vector gives good average recognition accuracy on three low exposure video sequences subset of original actions video datasets. Finally, the performance of the proposed approach is tested over three manually downgraded low qualities Weizmann action, KTH, and Ballet Movement dataset. This model outperformed on low exposure videos over existing technique and achieved comparable classification accuracy to similar state-of-the-art methods.

Keywords: Human Activity Recognition (HAR); Histogram Equalization (HE); Grids and Cells; Low-Quality Videos.

1 Introduction

Today human activity recognition in videos become a trendy area in computer vision community due to its wide range of applications such as video surveillance, robotics, patients monitoring, online gaming, sports, terrorist activities, content-based video analysis, and gait analysis [1] [2] [3] [4]. The major challenges in activity recognition in the video are varying illumination conditions, view variation, camera jitters, low resolution and cluttered background. At present most of the activity recognition solutions focused on high definition (HD) videos, but this is not suitable for low-quality video and many real-time video applications. That is why activity classification in low-contrast frames is one of the unexplored areas till now. It is difficult to extract the moving person from a dark background in a low contrast video [5] [6]. Further, it is necessary to enhance the quality of low contrast videos received for real-life applications. The video enhancement techniques aim to provide better visual appearance from an input of low exposure video to high exposure video for automated video processing, object detection, segmentation and human activity recognition [7]. It can be observed that many approaches toward action recognition in videos have been developed on different benchmark but very few on low-resolution videos. Further, it is challenging task to

enhance the low-quality videos for specific applications due to low contrast, high ISO as compared to signal to noise ratio (SNR), acquiring source, environmental artefacts, inter-frames coherence and storage limitations. Therefore, a robust Human Activity Recognition (HAR) model need to developed to overcome the challenges present in low contrast videos and to recognise action classes in videos. With the objective to investigate and provide a unique solution to this problem, we propose a joint utilisation of histogram equalization image enhancement technique and spatiotemporal key poses feature representation model for action recognition in low qualities video sequences. In our model first, we enhanced the quality of manually degraded video frames by utilized work presented in [8] and recognised the action classes in such improved video frame. This hybrid approach represents a robust model for illumination invariant activity recognition.

2 Related Work

Based on existing literature survey there are two type video enhancement techniques: Spatial and Frequency transform domain video enhancement. In spatial based approaches image, pixels are directly manipulated while frequency based working on transform image obtained from the spatial spectrum. Till now various approaches [9] [10] [11] for video enhancement are proposed, but there is no unified solution which can apply for design criteria. The spatial domain based approaches are easy to implement with fewer time complexities and suitable for real-time applications. Further, these techniques high sensitive to camera jitters, and background changes [12] [10]. The video enhancement technique based on the transform domain operate on coefficients of images, e.g. Fourier transform [13] [11] [14]. These approaches have less computational complexities but difficult to synchronised the enhancement procedure on images simultaneously. Singh and Kapoor [8] proposed the low exposure enhancement technique, (ESIHE) based on sub-image histogram equalisation that improves the appearance quality of the image. The enhancement technique for low luminance images outperforms over other spatial histogram equalization technique. It is easy to extract the local and global texture features from an enhancement image so that images enhancement techniques have been useful for low-quality video frames.

The shape and motion feature descriptors methods are used to recognised human activity in video sequences. The shape feature is extracted from human body silhouettes while the motion feature relies on the optical flow of body motion. The shape descriptor is more useful as compared to motion because the motion feature is not so robust when the object is moving at different speeds. In work [15] proposed a silhouette based approach Motion History Images (MHI) and Motion Energy Images (MEI) template to recognised human activity. Chaaraoui et al. [16] introduced the human silhouettes based feature extraction approach and optimised these parameters for activity recognition. Thurau and Hlavac [17] introduced a Histogram of the Gradient-based approach using binary silhouettes to represent human action in video frames. Vishwakarma and Kapoor [18] proposed a hybrid classifier model for HAR system using key pose silhouettes. The key-frames are selected using maximum entropy energy frames compare with higher energy frames. See and Rheman [19] proposed a spatiotemporal based approach to recognise the action in low-quality videos. They test existing approached on down-sampled video of the original dataset to reduce the quality of videos. Similar methods were

introduced in [20] [21] [22] on down-sampled video of low quality. The key ingredient of proposed work as follows:

- Low-quality input video sequences are enhanced using sub-histogram equalization technique.
- A robust spatiotemporal representation feature vector is obtained using key pose segmented human body silhouettes.
- A hybrid cascaded approach is developed through enhancement and representation of low-quality video sequences which is robust to illumination.
- Performance of the cascaded model is evaluated on three downsampled low exposure human action videos datasets, the recognition accuracy achieved on these dataset is compared with similar state-of-the-art methods and achieved superior performance.

The organisation of the proposed work as follows: Related work are discussed in section 2. Section 3 consists of a block diagram of the proposed model for human activity recognition. In section 4 the experimental setup and results are discussed on video dataset. The work is concluded in last section 5.

3 Proposed Framework of Activity Recognition

Our HAR model is based on the selection of k- key poses from enhancing output obtained from low-quality input video sequences using a low exposure refinement sub histogram equalization technique [8]. Human body silhouette is extracted from these equalization frames using segmentation GLCM segmentation technique [23] and normalised to into fixed cells. Further, the PCA technique [24] is used for dimension reduction, and classification of action classes is done through SVM linear classifier is used for action recognition. The Fig.1 depicts the proposed framework of our model.

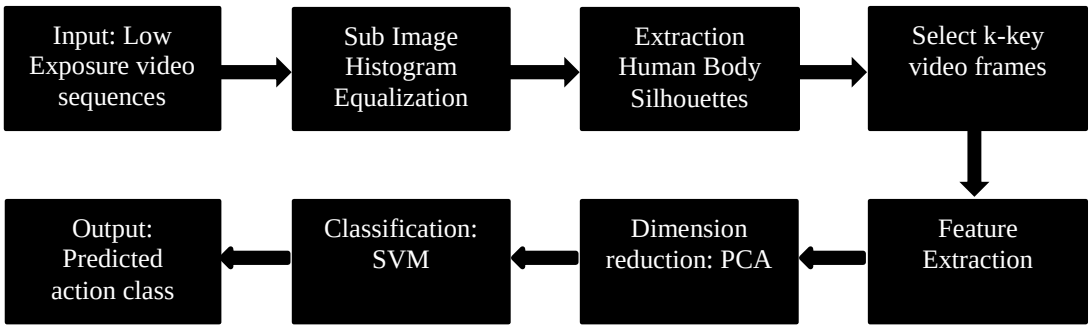


Fig. 1. Proposed framework for activity recognition.

3.1 Low contrast sampling of video sequences

It is a challenging task to track the object in low-quality videos due to less brightness, contrast and gamma factors. The brightness is one of the essential factors which discriminates the object from a background in video frames for better visual perception. A good contrast level distinguishes the one object from another in the video image and helps to track it. Similarly,

the gamma factor is used to uniform linear contrast functions between the images and easy to recognized activity in videos.

In this work, the original video sequences downsampled into low-quality video frames, i.e. low contrast frames because of no such dataset available publically till now. In the video conversion process, no additional compress technique is used for output videos and retaining the original frames rate. The original video frames converted into subset of low quality frames which are having different combination of brightness and contrast such as: S1 (Brightness =-20%, Contrast = -20%), S2 (Brightness =-40%, Contrast = -40%), and S3 (Brightness =-50%, Contrast = -50%). These low-quality videos subsets represent meaningful feature extraction for action recognition. The Weizmann [25], KTH [26] and Ballet Movement [27] datasets were converted into low-quality video subsets for evaluation of our algorithm.

Steps	**Algorithm**
1	Input: human actioned video sequences
2	Convert the original video sequences into low-quality sub-set S1, S2, and S3 video frames.
3	Compute the histogram of each subset frames.
4	Calculate the thresholding and exposing parameters.
5	Compute the clipping threshold histogram parameter.
6	Calculate sub image histogram from clipped based on threshold parameter.
7	Compute equalisation technique on all sub histograms.
8	Add the all subframes into a single frame for activity analysis.
9	Compute entropy images for each video sequences.
10	Apply a grey level 9×9 co-occurrence matrix to extract binary human silhouettes from entropy images.
11	Select the k-keyframes having significant energy compared to highest energy frames.
12	Divide the key frames into grid and cells.
13	Count the intensity value in each cells and put into feature vector
14	Output: Predicted Activity



Original video frame **(a)**

Brightness =-20% Contrast = -20% Set (S1) **(b)**

Brightness =-40% Contrast = -40% Set (S2) **(c)**

Brightness =-50% Contrast = -50% Set (S3) **(d)**

Fig. 2 Low contrast video frames (b), (c), and (d) from original video frames (a).

3.2 Sub-Image Histogram Equalization Technique

The spatial domain image enhancement technique, based on sub-image histogram equalisation (ESIHE) showed effective performance on low exposure greyscale images while preserving the enhanced rate and entropy of the original images. Also, this approach provides a good enhancement rate for low-quality video frames.

This image enhancement technique is having mainly three steps, threshold calculation for exposure, histogram clipping, and subdivision equalisation.

Exposure threshold parameter is used to measure the intensity of the image or frame, and it can be defined as:

$$\mathcal{E}_t = \frac{1}{\mathrm{L}} \frac{\sum_{k=1}^{\mathrm{L}} h(k)k}{\sum_{k=1}^{\mathrm{L}} h(k)} \tag{1}$$

here $h(k)$ is a histogram of the image and L shows the grey level in input frames.
To divide the image into under and the overexposure region a parameter $\mathfrak{L}_a$ and it gives exposure value less or greater than L/2 for an image frame having dynamic value (0 to L) defined as:

$$\mathfrak{L}_a = \mathrm{L}(1 - \mathcal{E}_t) \tag{2}$$

To control the histogram enhancement rate histogram clipping is required which is calculated as:

$$\mathrm{T}_c = \frac{1}{\mathrm{L}} \sum_{k=1}^{\mathrm{L}} h(k) \tag{3}$$

$$h_c(k) = \mathrm{T}_c \qquad for\ h(k) \geq \mathrm{T}_c \tag{4}$$

where $h(k)$ and $h_c(k)$ are the original and clipped histogram respectively.
The sub-image histogram equalization process consists of sub-images ranging from grey level (0 to L-1). If $\mathcal{P}_{\mathrm{L}}(k)$ and $\mathcal{P}_U(k)$ are the probability density function (PDF) of these sub-images frames defined as:

$$\mathcal{P}_{\mathrm{L}}(k) = \frac{h_c(k)}{\mathcal{N}_{\mathrm{L}}} \qquad for\ 0 \leq k \leq \mathfrak{L}_a \tag{5}$$

$$\mathcal{P}_U(k) = \frac{h_c(k)}{\mathcal{N}_U} \qquad for\ \mathfrak{L}_a + 1 \leq k \leq \mathrm{L} - 1 \tag{6}$$

where $\mathcal{N}_{\mathrm{L}}$ and $\mathcal{N}_U$ are total number of pixels in sub-images.
The cumulative distribution function (CDFs) of these sub-images given,

$$\mathcal{C}_{\mathrm{L}}(k) = \sum_{k=1}^{\mathfrak{L}_a} \mathcal{P}_{\mathrm{L}}(k) \tag{7}$$

$$\mathcal{C}_U(k) = \sum_{k=\mathfrak{L}_a+1}^{\mathrm{L}-1} \mathcal{P}_U(k) \tag{8}$$

The transfer function for histogram equalization is obtained from Eq.1 to Eq.6 defined as

$$\mathcal{F}_{\mathrm{L}} = \mathfrak{L}_a \times \mathcal{C}_{\mathrm{L}} \tag{9}$$

$$\mathcal{F}_U = (\mathfrak{L}_a + 1) + (\mathrm{L} - \mathfrak{L}_a + 1)\mathcal{C}_U \tag{10}$$

Where $\mathcal{F}_{\mathrm{L}}$ and $\mathcal{F}_{U}$ are the transfer function used for the sub-image histogram equalization respectively. The final output obtained from a combination of both transfer function of these sub-images into one complete image frame.

3.3 Extraction of Silhouette from texture information

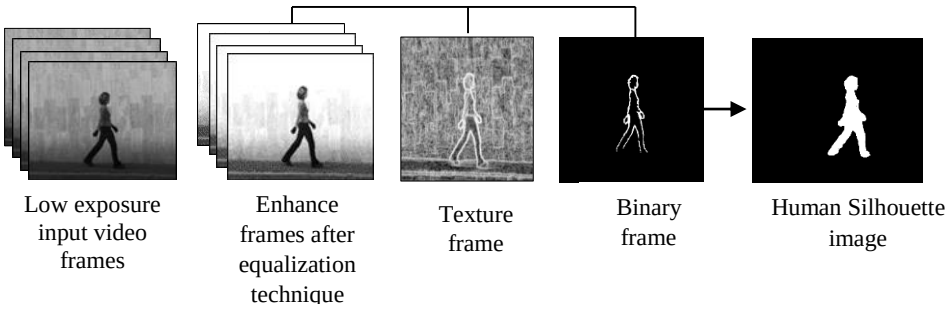


Fig. 3. Human silhouettes extraction using GLCM method [23] from enhance video sequences after enhancement.

Background subtraction is a fundamental step to recognized human activity from video sequences. We extracted human silhouette using grey level co-occurrence matrix (GLCM) method, which gives efficient results for video representation. The entropy of an image is the most critical parameter for classification of texture information in images. If entropy is higher than the details in the image is complex. It can be calculated as:

$$E = \sum_m \sum_n p(m,n) \log(p(m,n)) \tag{11}$$

Where $p(m,n) = \frac{\mathcal{M}(m,n)}{\sum_{m,n} \mathcal{M}(m,n)}$ is PDF and m, n are indices to the co-occurrence matrix $\mathcal{M}$.

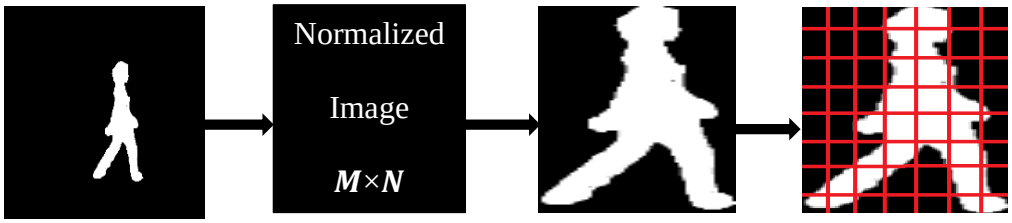


Fig 4. Cell formation from key frames

The different textural information in the image is represented using an entropy-based 9×9 neighbourhood filter. This filter matrix is converted into binary form with some thresholding and yields image with a white spot at different pixel locations. By comparing the contours, that having the largest area is considered as a human blob and is selected as a human silhouette.

3.4 Feature Extraction using k-key pose frames

3.4.1 Extractions of k-key pose frames

The robust features extraction is main objective of video sequences analysis that should be invariant to illumination, background changes, noise, and body poses etc. It can be observed that not all video frames consist of meaningful information about the object. Due to this, keyframes are extracted which contains maximum information as compared to other frames.

These keyframes are processed for feature extraction. The higher energy of k- key pose frames calculated as:

$$\mathcal{U}_t = \sum_i^M \sum_j^N \|\mathcal{I}_t(i,j)\|^2 \quad (12)$$

Such keyframes are arranged in time interval manner concerning higher energy frames. These frames are robust and invariant for discriminating various human actions. Further, these frames are divided into cells grids for calculating white pixel used in the feature extraction task.

3.4.2 Feature computation and representation

The total number of cells T_c in the key frames given by

$$\mathrm{C}_1, \mathrm{C}_{2,}\mathrm{C}_3 \dots\dots\dots\dots\dots\dots\dots\dots \mathrm{C}_{\mathrm{T}_c} \quad (13)$$

The number of white pixels ρ_i in the binary silhouettes frames are counted as:

$$\mathrm{w}_i = count\{\mathrm{C}_i(x,y)\}, \;\; where\; i = 0,1,2,\dots\dots\dots\dots\dots \mathrm{T}_c \quad (14)$$

The final feature matrix for video dataset having, number of videos of all action classes can be demonstrated as:

$$\mathcal{F}_{\mathcal{V}} = \begin{pmatrix} \mathcal{F}_1 = \mathrm{w}_1,\mathrm{w}_2,\mathrm{w}_{3,}\dots\dots\mathrm{w}_{\mathrm{T}_c}, \; \mathrm{w}_1,\mathrm{w}_2,\mathrm{w}_{3,}\dots\dots\dots\mathrm{w}_1,\mathrm{w}_2,\mathrm{w}_{3,}\dots\mathrm{w}_{\mathrm{T}_c} \\ \mathcal{F}_1 = \mathrm{w}_1,\mathrm{w}_2,\mathrm{w}_{3,}\dots\dots\mathrm{w}_{\mathrm{T}_c}, \; \mathrm{w}_1,\mathrm{w}_2,\mathrm{w}_{3,}\dots\dots\dots\mathrm{w}_1,\mathrm{w}_2,\mathrm{w}_{3,}\dots\mathrm{w}_{\mathrm{T}_c} \\ \vdots \\ \mathcal{F}_{\mathbb{V}_T} = \mathrm{w}_1,\mathrm{w}_2,\mathrm{w}_{3,}\dots\dots\mathrm{w}_{\mathrm{T}_c}, \mathrm{w}_1,\mathrm{w}_2,\mathrm{w}_{3,}\dots\dots\dots\mathrm{w}_1,\mathrm{w}_2,\mathrm{w}_{3,}\dots\mathrm{w}_{\mathrm{T}_c} \end{pmatrix} \quad (15)$$

Where, $\mathcal{F}_i = [\mathrm{w}_1, \mathrm{w}_2, \mathrm{w}_{3,} \dots\dots \mathrm{w}_{\mathrm{T}_c}, \mathrm{w}_1, \mathrm{w}_2, \mathrm{w}_{3,} \dots\dots \mathrm{w}_1, \mathrm{w}_2, \mathrm{w}_{3,} \dots \mathrm{w}_{\mathrm{T}_c}]$ feature vector for a single video of activity.

The dimension of the final feature vector is calculated as:

$$\mathcal{F}_{\mathcal{V}} = \mathbb{V}_T \times \mathrm{T}_c \quad (16)$$

For speedy classification rate, the dimension of a final feature vector or $\mathcal{F}_{\mathcal{V}}$ is further reduced by popular dimension reduction technique Principle Component Analysis (PCA) [24]. Finally, the lower dimension feature set is classified by most famous machine learning technique Support Vector Machine (SVM) [28].

4 Experimental Result and Analysis

We evaluated our experiments on three well known standard action datasets Weizmann [25], KTH [26] and Ballet Movement [27]. These datasets are recorded with uniform background and controlled environment conditions.

4.1 Weizmann Action Dataset

This was the first human activity dataset recorded by Gorelick et al. [25] in 2005. It was very simple and most familiar dataset for action recognition. The videos are recorded with a fixed camera in a static background and fixed illumination environmental conditions. It consists of total 90 videos in which nine subjects are doing ten action classes: “jumping jack”, “running”,

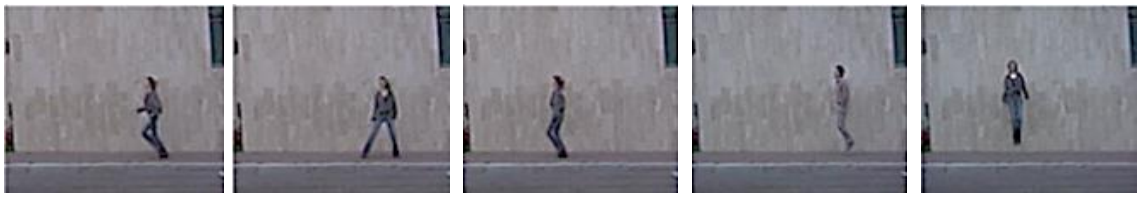


Fig. 5. Example frames of Weizmann action dataset [25]

“jumping”, “walking”, “bending”, “forward jump with both legs”, “jumping forward with one leg”, “one hand waving”, “two hands waving”, “sideways jumping”, and “jumping at the same place”. This dataset is recorded with low spatial frame resolution with 144×180 at a frame rate of 15fps. The video samples frames of this dataset are depicted in Fig.5.

4.2 KTH Action Dataset

KTH action [26] is found to be more difficult dataset than as compared to the Weizmann action due to changing environmental conditions. It is most frequently used dataset for human activity recognition in indoor as well as outdoor in changing illumination environment. It contains twenty-five subjects acting pre-defined six action classes: “jumping”, “hand-clapping”, “jogging”, “running”, “hand-waving”, and “walking” in four different scenarios. All video sequences are recorded at the frame rate of 25 fps with a spatial resolution of 160x120 pixels. The sample frames from a video of KTH action dataset is depicted in Fig.6.

4.3 Ballet Movement Dataset



Fig. 6. Example frames of KTH action dataset [26]

The Ballet movement dataset [27] contains 8 ballet dancing activities performed by 3 dancers such as “standing hand opening”, “standing still”, “turning”, “left-to-right hand opening”, “leg swinging”, “jumping”, “hopping”, and right-to-left hand opening. This dataset consists of 44 labelled video sequences. There are 3 actors, one woman and two men in which only one actor is performing in each video at a particular time. This dataset is challenging due to intra-class dissimilarity and inter-class similarity between different activities performed by dancers speed, apparels, spatial and temporal scales. The example sequences from video of Ballet dataset are shown in Fig.7.

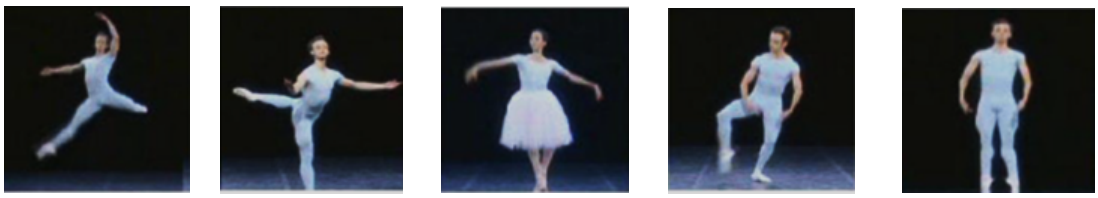


Fig. 7. Example frames of Ballet movement action dataset [27]

4.4 Classification Results and Comparison

The performance accuracy of our feature extractor is measured in terms of mean average precision (mAP), which is determined through action classification of datasets by SVM classifier in leave-one-out cross-validation (LOOCV) manner. The current implementation of the algorithm is run on an Intel® Core™ i5 3.2GHz processor with 8 GB memory card. The

average recognition rate (ARR) is calculated using Eq. 17.

$$\text{Accuracy} = \frac{\text{TP+TN}}{\text{TP+TN+FP+FP}} \times 100\% \quad (17)$$

where, TN, TP, FN, and FP are defined as true negative, true positive, false negative, and false positive respectively.

Table 1 shows the results of average recognition accuracy on three low-quality video sub-sets of standard action dataset. Further, the performance of these hybrid feature representations is comparable with our previous work [18] on original datasets. Tables 2, 3, and 4 depicted comparisons among the state-of-the-art approaches on these datasets.

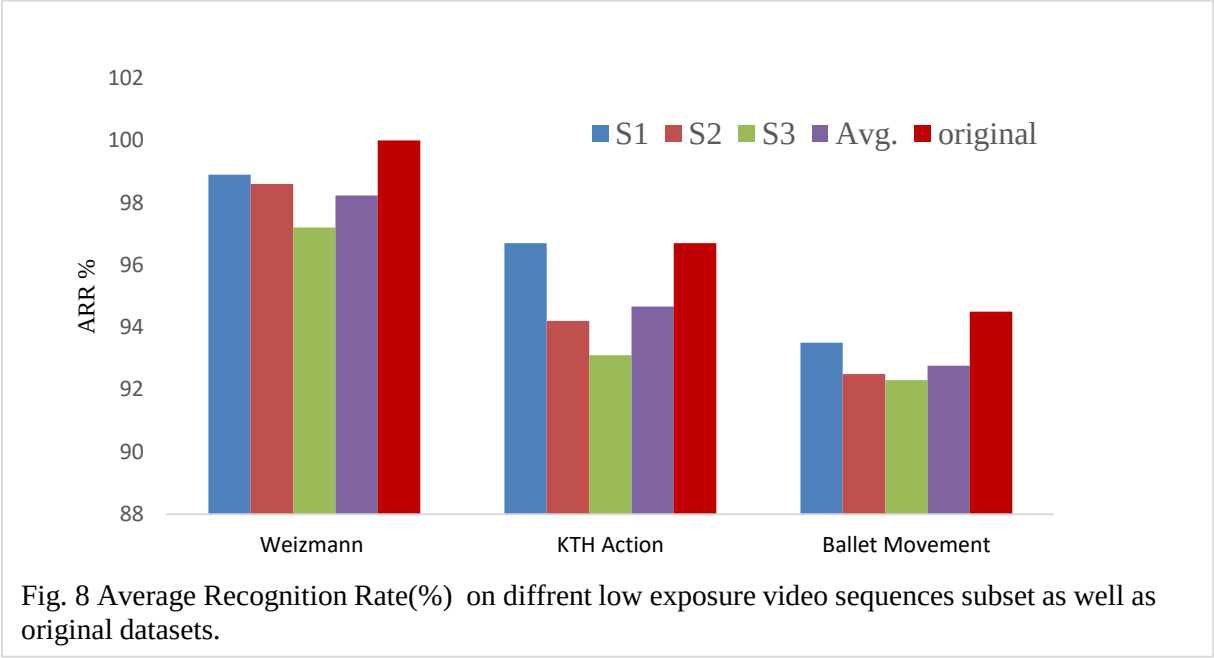


Fig. 8 Average Recognition Rate(%) on diffrent low exposure video sequences subset as well as original datasets.

Table 1. ARR of Low-Quality Video Sequences of Standard Action Dataset

Methods	Weizmann			KTH Action			Ballet Movement		
	S1	S2	S3	S1	S2	S3	S1	S2	S3
Proposed Method	98.9	98.6	97.2	96.7	94.2	93.1	93.5	92.5	92.3
ARA (%)	**98.23**			**94.66**			**92.76**		

Table 2 shows the comparable accuracy of our model on low-quality video sequences as compared with similar approaches to Weizmann dataset.

Table 2. Result comparison on Weizmann action dataset

Methods	Gorelick et al. [25]	Chaaraoui et al. [16]	Melfi et al. [29]	**Our method**
ARA (%)	97.50	92.80	99.02	**97.66**

Table 1 shows the ARR of Weizmann dataset and cross-validation results of different actions. There are present challenges because of the high interclass similarity in key poses of running,

walking, and jumping but our model outperforms in such kind of actions and each action discriminated with 97.66 % average recognition accuracy on three low-quality video sequences subset of the original dataset. There is slightly less confusion in the case of ‘jack hand’ and ‘wave-2’due to similar activities.

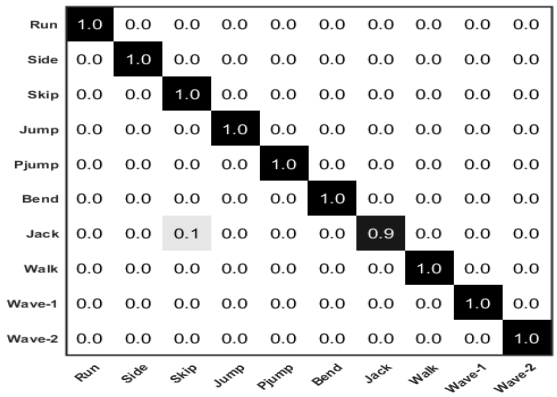


Fig. 9 (a)

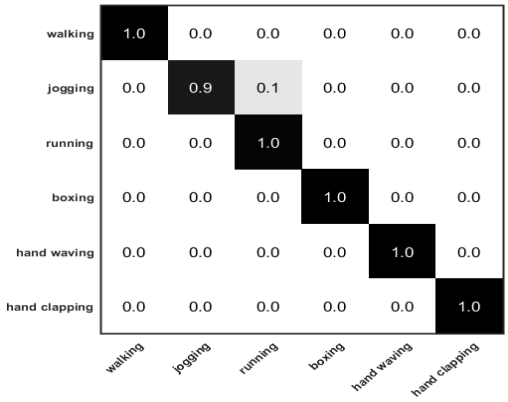


Fig.9 (b)

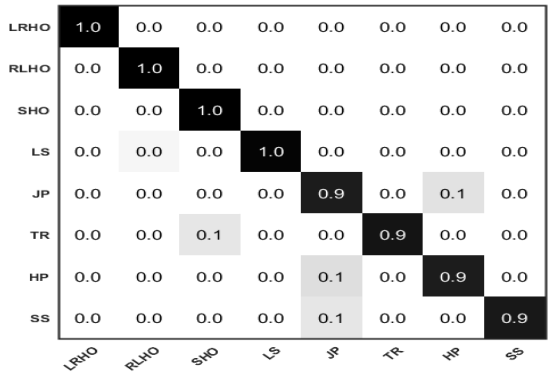


Fig.9 (c)

Fig. 9 Confusion matrix on (a) Weizmann (b) KTH (c) Ballet datasets.

Fig. 9 (a) shows the confusion matrix of Weizmann dataset and cross-validation results of different actions. There are present challenges because of the high interclass similarity in key poses of running, walking, and jumping but our model outperforms in such kind of actions and each action discriminated with 100 % recognition accuracy. There is slightly less confusion in the actions such as ‘jack hand’ and ‘wave-2’ due to similar activities.

Table 3. Result comparison on KTH dataset

Methods	Saghafi and Rajan [30]	Melfi et al. [29]	Zheng et al. [31]	See and Rehman [19]	**Our method**
ARA (%)	92.60	95.60	94.58	90.28	**94.50**

From Table 1, KTH dataset shows much satisfactorily results with average recognition accuracy 94.50 % on three low-quality video sequences subset of original dataset and much lesser misclassification is found only three classes: ‘running’, ’walking’, and ‘jogging’ due to similar action. In Fig. 9 (b) the confusion matrix for KTH dataset shows much satisfactorily

results with average recognition accuracy 98.70 %. Table 3 shows the best accuracy of our model on low-quality video sequences as compared with similar approaches to KTH dataset.

Table 4. Result comparison on Ballet dataset

Methods	Fathi & Mori [27]	Wang and Mori [32]	Iosifidis et al. [33]	**Our Method**
ARA (%)	51	91.30	91.10	**92.36**

The average recognition accuracy on three low-quality video sequences subset of an original dataset of 92.75 % computed through our method on Ballet dataset is shown in Table 1. The action recognition in this dataset is complicated due to clothing, gender, and size variations. Our feature extractor is insensitive to these variations and complexity of actions. It can be observed from the confusion matrix Fig. 9 (c) that there is little bit confused about of action pair such as 'hopping' and' jumping', 'leg swing' and 'Right to left-hand opening', 'turning right' and 'stand hand opening', and 'jumping and standing still' besides this our model outperform in comparison with the existing state-of-the-art methods.

5 Conclusion

In this work, we proposed a novel hybrid classification model based on the sub-image histogram equalisation technique which is more effective for enhancement on low exposure greylevel images. We have utilized the idea of such that a good quality enhances frames has higher entropy as well as high textural information as compared to low exposure frames. The human body silhouettes are extracted from these improve video frames for activity recognition. The key poses frames represent the spatiotemporal variations of human shapes. A robust feature vector is obtained from the grid and cells from these binary silhouettes and classified through a supervised machine learning technique, Support Vector Machine (SVM). In future, we can optimize the model for complex interaction and low-quality video surveillance applications.

References

[1] T. Singh and D. Vishwakarma, "Video benchmarks of human action datasets: a review," *Artificial Intelligence Review,* vol. 150, pp. 1-48, 2018.

[2] C. Dhiman and D. K. Vishwakarma, "A review of state-of-the-art techniques for abnormal human activity recognition," *Engineering Applications of Artificial Intelligence,* vol. 77, pp. 21-45, 2018.

[3] J. K. Aggarwal and M. S. Ryoo, "Human activity analysis: A review," *ACM Computing Survey,* vol. 43, no. 3, pp. 1-43, 2011.

[4] H. Aggarwal and D. K. Vishwakarma, "Covariate conscious approach for Gait recognition based upon Zernike moment invariants," *IEEE Transactions on Cognitive and Development Systems,* vol. 99, pp. 1-1, 2016.

[5] Y. Rao, W. Lin and L. T. Chen, "Image-based fusion for video enhancement of nighttime surveillance," *Optical Engineering Letters,* vol. 49, no. 2, pp. 1-3, 2010.

[6] A. Ilie, R. Raskar and J. Yu, "Gradient domain context enhancement for fixed cameras," *International Journal of Pattern Recognition and Artificial Intelligence,* vol. 19, no. 4, pp. 533-549, 2005.

[7] Y. Rao and L. Chen, "A Survey of Video Enhancement Techniques," *Journal of Information Hiding and Multimedia Signal Processing,* vol. 3, no. 1, pp. 71-99, 2012.

[8] K. Singh and R. Kapoor, "Image enhancement using Exposure based Sub Image Histogram Equalization," *Pattern Recognition Letters,* vol. 36, pp. 10-14, 2014.

[9] J. Li, Y. Tao, P. Quan and Y. Cheng, "Combining scene model and fusion for night video enhancement," *Journal of Electronics,* vol. 26, no. 1, pp. 88-93, 2009.

[10] Y. Rao and L. Chen, "An efficient contourlet transform-based algorithm for video enhancement," *Journal of Information Hiding and Multimedia Signal Processing,* vol. 2, no. 3, pp. 282-293, 2011.

[11] S. Lee, "An efficient content-based image enhancement in the compressed domain using Retinex theory," *IEEE Trans. Circuits and Systems for Video Technology,* vol. 17, no. 2, pp. 199-213, 2007.

[12] E. P. Bennett and L. McMillan, "Video enhancement using per-pixel virtual exposures," *ACM Trans. Graphics,* vol. 24, no. 3, pp. 845-852, 2005.

[13] S. S. Agaian, S. Blair and K. A. Panetta, "Transform coefficient histogram-based image enhancement algorithms using contrast entropy," *IEEE Trans. Image Processing,* vol. 16, no. 3, pp. 741-758, 2007.

[14] Y. Rao, Z. Chen, M.-T. Sun, Y.-F. Hsu and Z. Zhang, "An effective night video enhancement algorithm," in *Visual Communications and Image Processing (VCIP),* Tainan, 2011.

[15] A. F. Bobick and J. W. Davis, "The recognition of human movement using temporal templates," *IEEE Transactions on Pattern Analysis and Machine Intelligence,* vol. 23, no. 3, pp. 257-267, 2001.

[16] A. A. Chaaraoui, P. C. Pérez and F. F. Revuelta, "Sihouette-based human action recognition using sequences of key poses," *Pattern Recognition Letters ,* vol. 34, no. 15, pp. 1799-1807, 2013.

[17] C. Thurau and V. Hlavac, "Pose primitive based human action recognition in videos or still images," in *Computer Vision and Pattern Recognition,* Anchorage, 2008.

[18] D. K. Vishwakarma and R. Kapoor, "Hybrid classifier based human action recognition using silhouettes and cells," *Expert Systems with Applications,* vol. 42, no. 20, pp. 6957-6965, 2015.

[19] J. See and S. Rahman, "On the effects of low video quality in human action recognition," in *Int. Conf. on Digital Image Computing: Techniques and Applications (DICTA),* Adelaide, 2015.

[20] S. Rahman and J. See, "Spatio-temporal mid-level feature bank for action recognition in low quality video," in *IEEE Int. Conf. on Acoustics, Speech and Signal Processing (ICASSP),* Shanghai, 2016.

[21] S. Rahman, J. See and C. Ho, "Action recognition in low quality videos by jointly using shape, motion and texture features," in *IEEE Int. Conf. on Signal and Image Processing Applications (ICSIPA),* Kuala Lumpur , 2015.

[22] S. Rahman, J. See and C. Ho, "Deep CNN object features for improved action recognition in low quality videos," in *Int. Conf. on Computational Science and Engineering (ICCSE),* Shandong, 2016.

[23] R. Haralick, K. Shanmugam and I. Dinstein, "Textural feature for image Classification," *IEEE Transactions on System Man, and Cybernetics,* vol. 6, pp. 610-621, 1973.

[24] I. Jolliffe, "Principal Component Analysis and Factor Analysis," in *Principal Component Analysis,* New York, Springer, 1986, pp. 115-128.

[25] L. Gorelick, M. Blank, E. Shechtman, M. Irani and R. Basri, "Actions as Space-Time Shapes," in *The Tenth IEEE International Conference on Computer Vision (ICCV'05),* 2005.

[26] C. Schuldt, I. Laptev and B. Caputo, "Recognizing human actions: a local SVM approach," in *17th International Conference on Pattern Recognition,* 2004.

[27] A. Fathi and G. Mori, "Action recognition by learning mid-level motion features," in *IEEE conference on Computer Vision and Pattern Recognition,* Anchorage, AK, USA, 2008.

[28] C. Cortes and V. Vapnik, "Support-vector networks," *Machine Learning,* vol. 20, no. 3, p. 273–297, 1995.

[29] R. Melfi, S. Kondra and A. Petrosino, "Human Activity modelling by spatio temporal textural appearance," *Pattern Recognition Letters,* vol. 34, pp. 1990-1994, 2013.

[30] B. Saghafi and D. Rajan, “Human action recognition using Pose-based discriminant embedding,” *Signal Processing: Image Communication,* vol. 27, pp. 96-111, 2012.

[31] Y. Zheng, H. Yao, X. Sun, S. Zhao and F. Porikli, “Distinctive action sketch for human action recognition,” *Signal Processing* , vol. 144, p. 323–332, 2018.

[32] Y. Wang and G. Mori, “Human Action Recognition Using Semi-Latent Topic Model,” *IEEE Transactions on Pattern Analysis and Machine Intelligence,* vol. 31, no. 10, pp. 1762-1764, 2009.

[33] A. Iosifidis, A. Tefas and I. Pitas, “Discriminant bag of words based representation for human action recognition,” *Pattern Recognition Letters,* vol. 49, pp. 185-192, 2014.

ResearchGate

See discussions, stats, and author profiles for this publication at: https://www.researchgate.net/publication/323871458

A Novel Low power and Swing Restoration SRAM Logic Circuit Technique

Article *in* International Journal of Engineering and Technical Research · March 2018

DOI: 10.17577/IJERTV7IS020174

CITATIONS
0

READS
39

1 author:



Ram Murti Rawat
Delhi Technological University
3 PUBLICATIONS **0** CITATIONS

SEE PROFILE

Some of the authors of this publication are also working on these related projects:

A Novel Low power and Swing Restoration SRAM Logic Circuit Technique View project

All content following this page was uploaded by Ram Murti Rawat on 09 July 2018.

The user has requested enhancement of the downloaded file.

Published by :
http://www.ijert.org

International Journal of Engineering Research & Technology (IJERT)
ISSN: 2278-0181
Vol. 7 Issue 02, February-2018

A Novel Low power and Swing Restoration SRAM Logic Circuit Technique

Ram Murti Rawat
Assistant Professor, Dept. of CSE
Delhi Technological University,
Delhi, India

***Abstract*- Design and Analysis of Static RandomAccess memories (SRAMs) which focus on optimizing Read and Write operation of 8T SRAM cell which is better than 6T SRAM cell Using Swing Restoration Dual Node Voltage. The read and Write time and improve Stability. PMOS Transistor with less width reduces the power consumption. In this paper Comparative Analysis of 6T and 8T SRAM Cells is done for 180nm Technology with Cadence Virtuoso schematics Tool.**

Keywords- Swing Restoration Logic, Dual Voltage, Delay, Stability, Read and Write access time, Low Power and Power dissipation.

I. INTRODUCTION

Low power SRAMs have become a critical component of many VLSI chips. This is especially true for microprocessors, where the on-chip cache sizes are growing with each generation to bridge the increasing divergence in the speeds of the processors and the main memory [P. Barnes 2010, S. Hesley, et.al, 2009]. This Paper is organized as follows: the characteristics of 6T SRAM cell are described are represented in section II. In section III, Proposed 8T SRAM cell is described. Section IV includes the simulation results which give comparison of different parameters of 6T and 8T SRAM cells and section V conclusion the work.

II. SIX TRANSISTOR (6T) SRAM CELL

In a conventional 6T SRAM cell, the data storage nodes are directly accessed through the bit-line access transistors during read operations, as shown in Fig.1. While reading, the storage node voltages are disturbed between cross-coupled inverter pair and bit lines. The BL and BLB are the bit lines and WL is the word line. The access transistors are controlled by WL (word line) to perform the operation of read and write operation. Bit lines act as input and output nodes. During a read operation, bit lines transfer the data from SRAM cells to a sense amplifier. Based on the technology the minimum length of the transistors is 180nm [1].

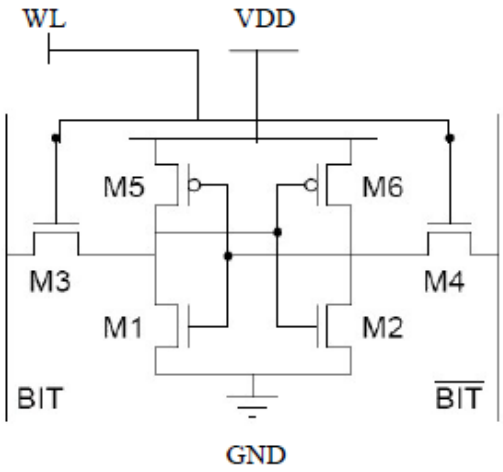


Fig.1. 6T SRAM Cell

III. PROPOSED EIGHT TRANSISTOR (8T) SRAM CELL

In this proposed SRAM, Dual Voltage with Swing Restoration Logic Perform node voltage in Hold, read and write operation and other parameters like Delay, Stability, are used. Comparison between Low power design 6T and proposed 8T SRAM Cell design is done. The comparison result revels that read, write and hold mode operation for 8T SRAM cell is better than 6T SRAM cell. This is because higher noise margin are obtained which ensure good write ability for the bit-cell.

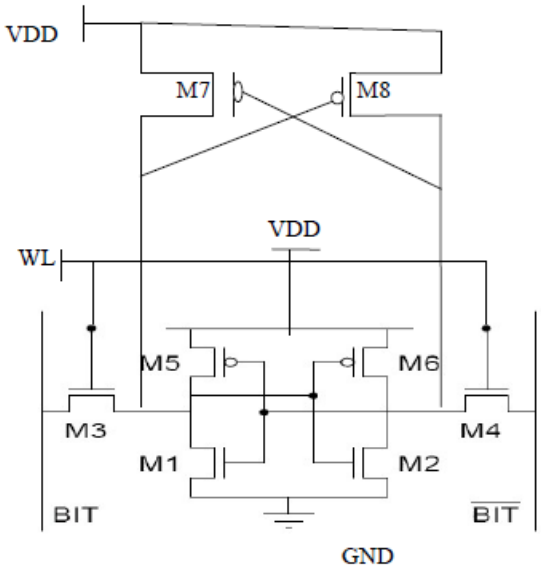


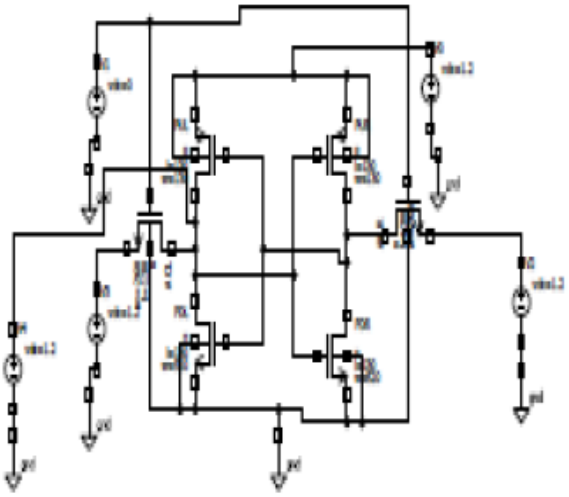
Fig.2. Proposed 8T SRAM Cell

(This work is licensed under a Creative Commons Attribution 4.0 International License.)

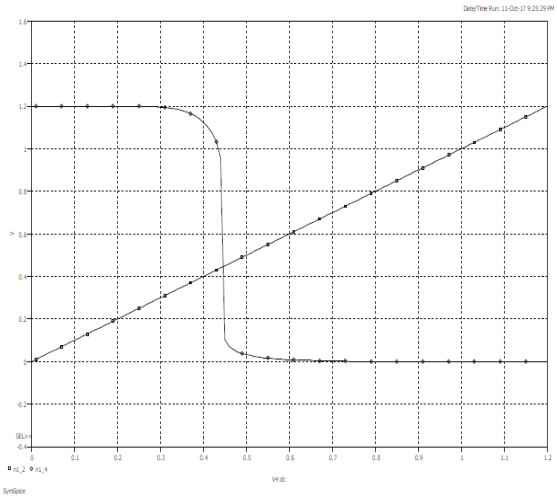
International Journal of Engineering Research & Technology (IJERT)
ISSN: 2278-0181
Vol. 7 Issue 02, February-2018

IV. SIMULATION RESULTS AND DC ANALYSIS

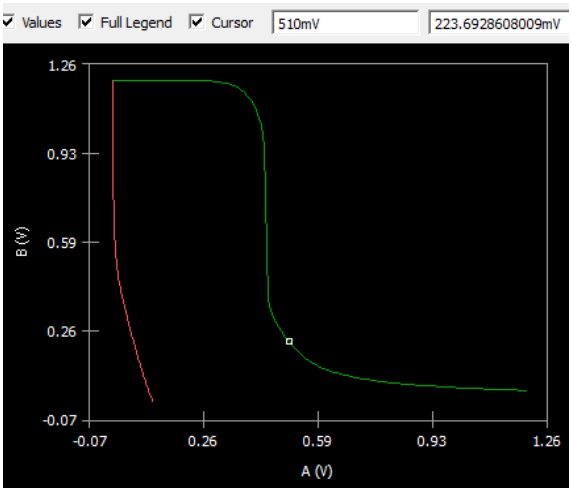
A. 6T SRAM cell output



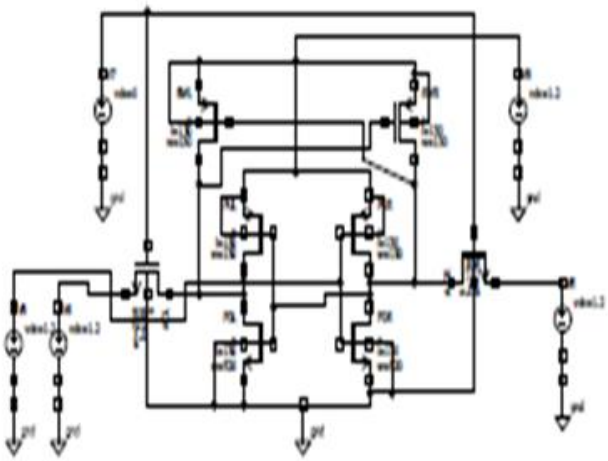
B. 6T SRAM cell DC analysis



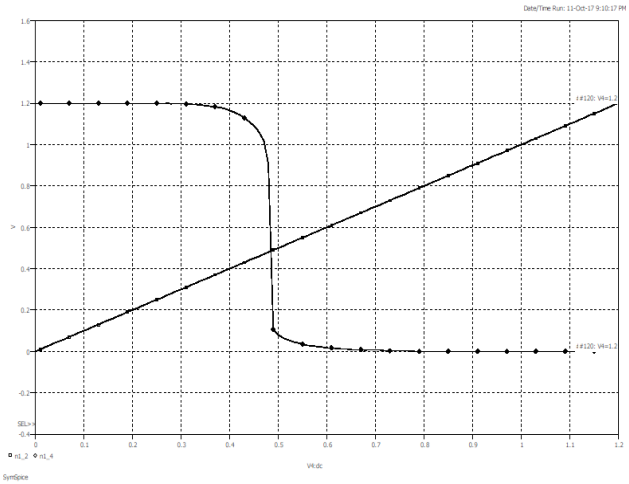
E. 6T SRAM CELL WRITE NOISE MARGIN



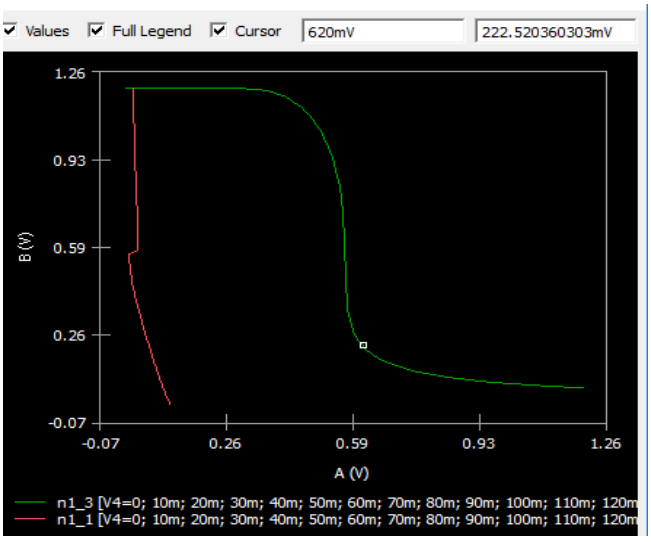
C. PROPOSED 8T SRAM CELL OUTPUT



D. PROPOSED 8T SRAM CELL DC ANALYSIS



F. PROPOSED 8T SRAM CELL WRITE NOISE MARGIN



(This work is licensed under a Creative Commons Attribution 4.0 International License.)

International Journal of Engineering Research & Technology (IJERT)
ISSN: 2278-0181
Vol. 7 Issue 02, February-2018

V. CONCLUSION

A low power and swing node restoration SRAM logic circuit technique is presented in the paper. In this paper comparative analysis of 6T and 8T SRAM cells in 180nm Technology is also presented.

In the proposed SRAM cell and Dual node voltage with Swing Restoration logic perform D.C. analysis Hold mode operation. D.C. analysis HOLD operation good noise margin 8T SRAM cell is better than 6T. This conclusion is good for power consumption is low. Then 8T SRAM Cell Write mode is power analysis is better Then 6T SRAM Cell. Then speed is higher for proposed 8T SRAM Cell.

REFERENCES

[1] Seevinck, "Static-Noise Margin Analysis of MOS SRAM Cells,"IEEE Journal of Solid-State Circuits, SC-22,5 (Oct. 1987),748-754.

[2] H.L. yeger et al, "Domino circuit Topology", U.S. Patent 6784695, Aug. 31,2004.

[3] A.S. Sedra and K.C. Smith Microelectronic circuits, Fourth Edition, new York: oxford,1988.

[4] S.M. Kang and Leblebici, CMOS Digital Integrated circuits, Analysis and Design, Second Edition, Mc Graw-Hill,1999.

(This work is licensed under a Creative Commons Attribution 4.0 International License.)

IJERT

ISSN : 2278 - 0181

Call for Papers 2018

OPEN ACCESS

Click Here for more details

International Journal of Engineering Research & Technology

☑ Fast, Easy, Transparent Publication

☑ More than 50000 Satisfied Authors

☑ Free Hard Copies of Certificates & Paper

Publication of Paper : Immediately after Online Peer Review

Why publish in IJERT ?

✓ Broad Scope : high standards

✓ Fully Open Access: high visibility, high impact

✓ High quality: rigorous online peer review

✓ International readership

✓ Retain copyright of your article

✓ No Space constraints (any no. of pages)

Submit your Article

www.ijert.org

View publication stats

This article has been accepted for inclusion in a future issue of this journal. Content is final as presented, with the exception of pagination.

A Novel Solution to Prevent Diesel Pilferage at Telecom Tower Site

Abhishek Grover and Brejesh Lall

***Abstract*— Monitoring of energy consumption is a critical application at a telecom tower site. This paper presents a novel power monitoring application. In addition to power consumption measurement, power monitoring could be useful in preventing the pilferage of diesel used to run generators at a tower site. The problem of diesel pilferage has been analyzed, and a concealed power monitoring solution has been presented. The monitoring algorithm can be integrated with the pulse width modulation controller used in switch-mode power supply rectifier. The measurement philosophy has been validated, designed, and experimentally tested. Simulink models of power supply at a tower site have been used for validation. A prototype for the above-mentioned system has been designed using MATLAB and a microcontroller. The combination of these two tools emulates a power quality analyzer. Power quality analysis is the central theme of this solution. The difference in power quality and the impact of load on the power source have been used to construct features for this solution. The proposed solution has been experimentally tested by recording input power waveforms of an ac-to-dc converter.**

***Index Terms*— Energy measurement, load monitoring, power quality, rectifier, sensorless control, tower site.**

I. Introduction

TOWER sites are an integral component of telecom infrastructure. An exponential increase in the number of users and required services over the last 15 years had led to an increase in the number of tower sites in all parts of the world. With this increase, telecom operators had to bear increased operating expenses (OPEXs) related to the maintenance of equipment and power requirements. The primary power source at a tower site is AC grid supply and secondary sources such as diesel generator (DG) and valve regulated lead acid batteries are used when grid supply is not available [1]. DG is the primary source of power in remote areas where grid connectivity is not available. Equipment at tower site has to be regularly checked and maintained to ensure that the site is running efficiently. Regular oiling of the DG, refiling of diesel tanks, maintenance of air conditioning and electrical equipment used for lightening and power conversion, regular check-up of communication equipment, reporting of power consumption metrics, and securing of the site against theft of diesel or ancillaries such as batteries, solar cells, inverters, etc., are some of the housekeeping stuff required at the tower site. For telecom operators, it would be difficult to solely monitor and provide services to tower sites spread throughout the country, so they usually hire service providing agencies and give them charge of maintaining sites within a specific region. Therefore, the hired agency and its deployed men become the single point of contact to telecom operators for operating expenses of tower site.

One of the significant recurring expenses is diesel procurement for DGs. As per a study conducted [2] for the petroleum ministry of India, mobile towers consume 1.54% of the total diesel sold in India which amounts to more than one million tons of diesel consumption annually. A technician, guard, landowner, and local people man the tower sites. They are responsible for management operations at a tower site. Such a sizable recurring expenditure and a contractual agency as its guardian lead to mushrooming of diesel mafia in the telecom infrastructure service industry. Sensing and metering strategies were rare at tower sites in the early 2000s, so a primary method of pilfering diesel was through incorrect reporting of diesel consumption and selling the excess diesel. As the number of tower sites grew, pilferage activities increased, and more local people got involved in it, and slowly these activities started to be considered as a norm in the industry. A report [3] suggests that telecom operators in India are losing around Rs. 2200 crore annually due to the diesel pilferage. Telecom operators tried to curb this menace with sophisticated technologies. Various companies [4], [5] have been offering various measurement and monitoring solutions. One of the solutions extensively adapted is the use of two separate meters for grid and diesel energy consumption. Another consists of using a level sensor and viscosity sensor inside diesel tanks to measure an abrupt change in fuel level or its quality to counter against the mixing of water, other liquids, and stones in diesel tanks which is rampant at tower sites. At various sites, monitoring using CCTV cameras has also been employed. The solutions developed also consist of a communication link such as global system for mobile communication (GSM) controller for relaying the measured data directly to the network center. The monitoring philosophy presently being used has been explained in Fig. 1. At many sites, the local people had found methods to make these devices redundant. They repeatedly remove the monitoring instruments or break their connection. In some places, the grid connections for power equipment

Manuscript received August 17, 2018; revised December 8, 2018; January 8, 2019. The Associate Editor coordinating the review process was He Wen. *(Corresponding author: Abhishek Grover.)*

The authors are with the Bharti School of Telecommunication Technology and Management, Indian Institute of Technology Delhi, New Delhi 110016, India (e-mail: abhishekgrover13@gmail.com; brejesh@ee.iitd.ac.in).

Color versions of one or more of the figures in this paper are available online at http://ieeexplore.ieee.org.

Digital Object Identifier 10.1109/TIM.2019.2895485

0018-9456 © 2019 IEEE. Personal use is permitted, but republication/redistribution requires IEEE permission.
See http://www.ieee.org/publications_standards/publications/rights/index.html for more information.

This article has been accepted for inclusion in a future issue of this journal. Content is final as presented, with the exception of pagination.

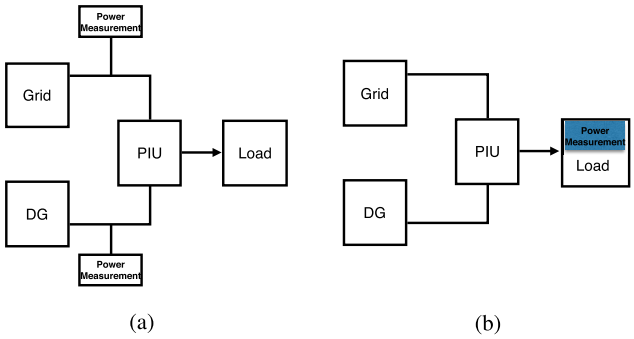


Fig. 1. Schematic comparison between the present and the proposed monitoring philosophies. (a) Present solution. (b) Proposed solution.

were routed through the DG meter, i.e., even when the grid is supplying power, DG meter records consumption. Some sophisticated methods had also been used such as applying a DC voltage across level sensor so that it records a filled tank even when the tank is empty. The viscosity of diesel and the mixture of diesel and kerosine is almost the same, and locals use this technique for the pilferage of diesel. It has been observed in most of these methods that the involvement of local technician, visibility, and accessibility of the monitoring device has led to the ineffectiveness of remedial solutions.

Any solution which does not fall under the service purview of the local technician, which is invisible from outside and is integrated inside the essential components of the telecom tower site can be useful in reporting correct and legal consumption of diesel. This paper presents a novel solution with such merits. In any electrical system point of common coupling (PCC) of source and load contains essential information about the type of elements connected to it. Nonintrusive monitoring [6] is a well-established technique for identifying the appliances operating in a residential apartment at a particular instant using the power waveforms obtained from the ac utility meter. In the present scope of application, the load is same, i.e., base transceiver station (BTS), air conditioning system, and lightening system, it is the source (grid, DG, or battery) which can vary based on availability. A power interface unit (PIU) is used at tower sites as an interface between power sources and electrical loads. The proposed solution aims to identify the source based on the power quality of the waveform at PCC. The node used for power waveform acquisition will be at the input of switch-mode power supply (SMPS) rectifier which is used to convert 220 V ac to -48 V dc. SMPS-based converter introduces a significant amount of nonlinearities in the current waveform due to their nonlinear action. The grid is an infinite source as compared to the load at a tower site, so these variations are minimally reflected in voltage waveform. DG capacity is usually decided based on specific load requirements thus these variations are reflected in large magnitude on the voltage waveform when DG is operating. This distinction in power quality has been utilized to identify the source by the acquisition device connected on the load side. Thus, a single acquisition device integrated inside the rectifier can be used to identify and measure the energy consumption from the source currently powering the load. The power consumption information needs to be communicated to the network center. GSM-based solutions have been used in many telemonitoring applications [7] but have been ineffective at tower sites as the controller is repeatedly removed with the help of a local technician. A better solution is to convey this information using the available backhaul communication link. Fig. 1 shows the comparison of the present solutions with the proposed solution.

The utilization of voltage and current waveforms at the PCC of source and load has been presented as a solution to the problem of diesel pilferage at a tower site. Such an approach could be used for health monitoring of electrical loads. Fault detection applications in smart grid can also make use of the proposed algorithms. Many of the sensorless measurement applications such as speed detection of motors [26], [27] and electrical load parameter estimation can employ the methods used in this paper. Nonintrusive load monitoring (NILM) applications [25] can make use of the statistical evaluation suggested in this paper. Simulink models for power management circuitry at a telecom tower site have been presented. Such models could be efficaciously used in testing applications of load monitoring and power quality data analytics (PQDA). A prototype for the above-mentioned objective has been designed and tested. It is a low-cost prototype intended for acquiring power waveforms. The acquired waveforms can be used for power quality analysis in MATLAB. A parameter for quantifying diesel quality based on voltage waveform at the output of DG has also been proposed. The proposed algorithms can be easily implemented on the computing platform available at a tower site.

The organization of this paper is as follows. Section I is an introduction, Section II is preliminaries, Section III is the proposed solution, Section IV is simulation models, Section V is experimental setup, Section VI is results and discussion, and Section VII is conclusion.

II. Preliminaries

The voltage and current waveforms at input power node of load are dependent on the quality of the source and consumption pattern of the load. For a fixed source, these waveforms can be used to quantify the behavior of loads connected, and for a fixed load, it can be used to comment on the power drawn from the source. The voltage and current variations introduced at PCC are thus dependent on the equipment used at a tower site. In power transmission systems, quantifying variations based on power quality standards have been widely studied [8], [9]. The effects on voltage and current waveforms due to changing pattern of loads connected have been extensively utilized in the field of NILM. This section gives an overview of the equipment at a tower site. Various studies related to cause of variations and their analysis in the field of power quality and load monitoring have been explored to give an overview of the origin of variations and their utilization for various applications.

A. Telecom Tower Site

The telecom network infrastructure can be divided into three types as follows.

1) Passive infrastructure, which consists of power supply, DG, air conditioning unit, and earthing.

This article has been accepted for inclusion in a future issue of this journal. Content is final as presented, with the exception of pagination.

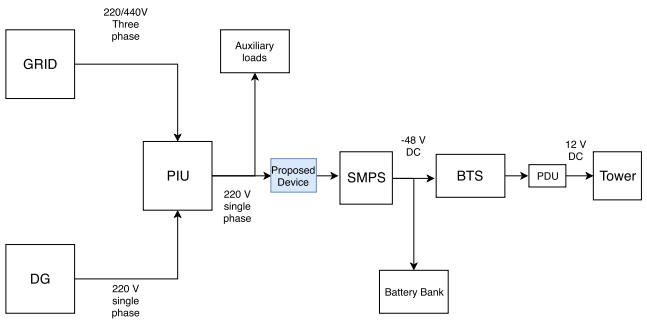


Fig. 2. Schematic of the power supply at a tower site.

2) Backhaul, which consists of intermediate links between base station controller (BSC) and towers, BSC and mobile services switching center.
3) Active infrastructure, which consists of the spectrum, BTS, microwave radio, switches, antenna, and the other transmission related equipment.

The schematic of the power supply at a tower site can be understood as shown in Fig. 2. BTS runs on −48 V dc and is powered using three sources: ac grid, DG, and battery bank. SMPS-based converters are used to convert 220 V single-phase ac supply to −48 V dc. The power demand at a tower site ranges from 1 to 8.5 kW where more than 80% of configurations have demand less than 3.5 kW [10]. At most sites, tower owners install DGs of 10–15 kVA capacity and supplement it with battery banks of 300–900 AH capacities. When grid supply is interrupted, PIU sends a trigger signal to DG and power is available within minutes of this initiation [11]. During transition, battery bank supplies power to telecommunication equipment. The exact manner of utilization of battery bank depends on the operator. The battery bank is connected in float working mode on dc power line. As the rectifier output is interrupted, battery bank starts supplying current. It depends on operator's transition procedure whether he runs DG when battery bank is depleted or shortly after interruption of grid supply. Auxiliary loads consist of illumination equipment and air conditioning unit. At some sites, an integrated power management system (IPMS) is used. An IPMS consists of PIU and SMPS in the same enclosure. The −48 V power line in BTS is converted to 12 or 24 V supply using a power distribution unit [10] for supplying power to equipment mounted on the tower. Over the years telecom operators and equipment manufacturers have incorporated various monitoring solutions. A telemanagement integrated system [12] has been implemented to monitor and manage power units, air conditioning unit, and network alarms with aggregated reports available on the web. PIU manufacturers have included various additional functions such as site condition monitoring, raising alarms for mains fail, door open/intruder, low fuel, smoke/fire, shelter high temperature, and rectifier fail [13]. The above-mentioned implementations consist of individual connections to various devices. The proposed solution with a single connection on the power line on load side can be easily incorporated in such implementations and would prove more useful.

B. Power Quality

Power quality is used to quantify power waveform parameters in electricity generation and transmission. Power quality is the combination of voltage quality and current quality [14], where the voltage quality is concerned with deviations of the actual voltage from the ideal sinusoidal voltage with a constant nominal amplitude and frequency, and the current quality is the equivalent definition for current. All disturbances such as impulses, sags, swells, harmonics, and notches can be described under power quality. The process of extracting information from raw power quality measurement is known as PQDA [15], [16]. It has been efficaciously used in smart grid applications such as fault location in the grid [17], load parameter estimation [18], and home appliance monitoring [19]. The disturbances introduced on the power line at tower site are mainly due to the rectifier and switching converters used for ac-to-dc conversion. Rectifier loads generate distorted line current [20], [21] due to their nonlinear action which leads to voltage distortion. Switching converters introduce harmonics on the power line which is a growing concern due to increase in usage of power electronic devices. Zhuo *et al.* [22] have proposed a method to determine voltage harmonic emission caused by a major nonlinear load based on the fact that harmonics at PCC are majorly due to current consumed by the load. de Andrade *et al.* [29] have proposed a method for estimating harmonic contribution at PCC by utility and consumer. In systems powered by a DG, the power quality at PCC also depends on the quality of fuel used in tanks. Low-calorie content of fuel leads to misfirings in engine unit, thus causing a sudden decrease in torque applied to the rotor of a generator which leads to voltage variations in the output of the generator [23].

C. Load Monitoring

The variations observed at the acquisition node could be due to system dynamics on the supply side or the load side. For source identification and fuel quality quantification as suggested in this paper, it is of interest to distinguish between variations introduced due to source and those due to load. The operation of a load is classified into transient and steady states. The variations introduced are different for each state. In the present field of applications, we are mostly interested in the steady-state operation of loads. The magnitude variations introduced in the current waveform, active power, reactive power, and admittance are significantly due to loads [24], [25]. Frequency variations on the power line are mostly attributed to load dynamics [26], [27]. The change in current consumption of BTS also introduces variations on current waveform [28]. Thus, it can be concluded that the current waveform related parameters contain information related to load behavior. The effect of current variations on the voltage waveform depends on the type of source powering the load. Thus, voltage waveforms will play a crucial role in source identification algorithm as suggested in this paper.

III. Proposed Solution

The proposed device would be monitoring voltage and current waveform at the input node of rectifier used to convert

This article has been accepted for inclusion in a future issue of this journal. Content is final as presented, with the exception of pagination.

ac voltage to dc voltage. Fig. 2 shows the location of the proposed device in the schematic of the power supply.

The device senses the power signal on the power line and identifies the power source currently powering the system. This information is sent to the telecom operator, and the operator should pay for diesel consumption based on the electricity consumption during DG run time. The device would indicate poor fuel quality if the waveform quality is not maintained in this duration. The onus of maintaining fuel quality and DG lies on infrastructure providing agency, and it should be penalized by telecom operators if the voltage quality is not maintained. The specific equipment such as PIU and rectifier are serviced only by their companies representative technician, and the local technician has no role in servicing of these type of equipment. A conventional deterrence for the local people against tampering with such equipment is that any misconnection can bring the site down which is detrimental to their vital source of income. One may contemplate on the location of the node selected for data acquisition (DAQ). For example, at many sites, PIU is handling most of the power consumption metric tasks, but the physical connections to the sources can be easily tampered with leading to incorrect readings. The source identification philosophy presented in this paper can be effectual with the power management equipment presently being used at a tower site. The signal acquisition and processing can be integrated with the microcontroller in PIU or the pulse width modulation (PWM) controller in SMPS rectifier. The solution presented is used to envisage an effective monitoring location that not only can be used to report real energy consumption but can also be used to identify other parameters related to the system. Parameters such as the quality of diesel used, the health of equipment, and legal loads connected to the power supply can be deduced with such nonintrusive monitoring approach. It is to be noted that identifying legal loads is an essential application since illegal connections of ac supply are quite rampant at tower sites.

Two parameters have been identified by which power sources can be distinguished through power line monitoring. A parameter for estimating fuel quality based on voltage variations has also been suggested. Power quality standard EN50160 suggests 200 ms rms values and a 10-min interval for statistical quantification of very short variations [14]. A similar approach has been utilized to quantize voltage variations for source identification. The proposed algorithm consists of data aggregation and data processing. The sampling rate used for DAQ is 2 kHz, thus 200 ms waveform consists of 400 samples. Such sets of 400 samples are collected recursively and information is aggregated to one total harmonic distortion (THD) value and one voltage rms value and current rms value for 200 ms interval. The 10-min interval information is stored in N THD values (a_k) and N normalized rms values (v_k, i_k) as shown in Fig. 3, where N is equal to 3000 for a 10-min interval. The power source is classified as DG if the mean THD value is greater than t_1 and the parameter p is greater than t_2. The threshold values t_1 and t_2 are calculated based on on-site data as discussed in Section VI.

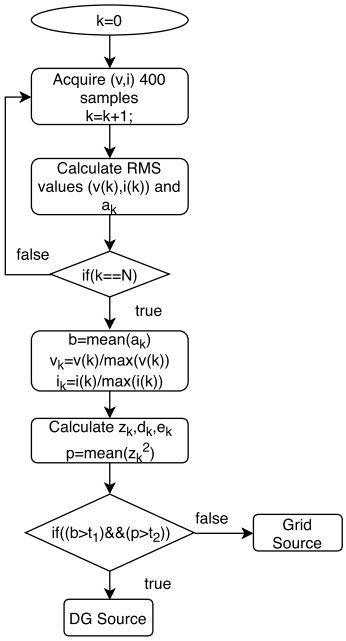


Fig. 3. Algorithm for data aggregation and data processing.

A. Total Harmonic Distortion

The magnitude of harmonics introduced in voltage (v) due to current (i) is directly proportional to source impedance (z_s). The source impedance of synchronous generator is much higher than that of utility transformer. Thus, the THD value of the voltage waveform when DG is operating is more substantial than the case when ac grid is supplying power. THD value is calculated based on the magnitude of discrete Fourier transform (DFT) values of the voltage sequence as given in the following equation:

$$a_k = \frac{\sqrt{f_{2n}^2 + f_{3n}^2 + f_{4n}^2 + f_{5n}^2}}{f_n} \tag{1}$$

where f_n denotes the absolute DFT value of the fundamental frequency, f_{2n}, f_{3n}, and f_{4n} are absolute DFT values of second, third, and fourth harmonics, respectively. The mean value of a_k is used to determine the source

$$b = \frac{\sum_{j=1}^{N} a_j}{N}. \tag{2}$$

DFT values can be calculated using fast Fourier transform (FFT), Goertzel algorithm, and sine fitting approximation methods [30]. The accuracy achieved using these algorithms is acceptable for the application at hand. The primary criteria for selecting one of these are the computation burden we would like to give to our measurement device. We would be using the Goertzel algorithm [31] as its simple linear filtering approach of DFT calculation requires low computation and can be easily implemented on low-cost microcontrollers usually used in energy measurement applications.

Another simple technique for THD calculation uses a sine-wave generator whose output frequency is locked to the fundamental frequency of input ac signal [32]. The rms voltage, fundamental frequency rms, and THD are calculated as given

This article has been accepted for inclusion in a future issue of this journal. Content is final as presented, with the exception of pagination.

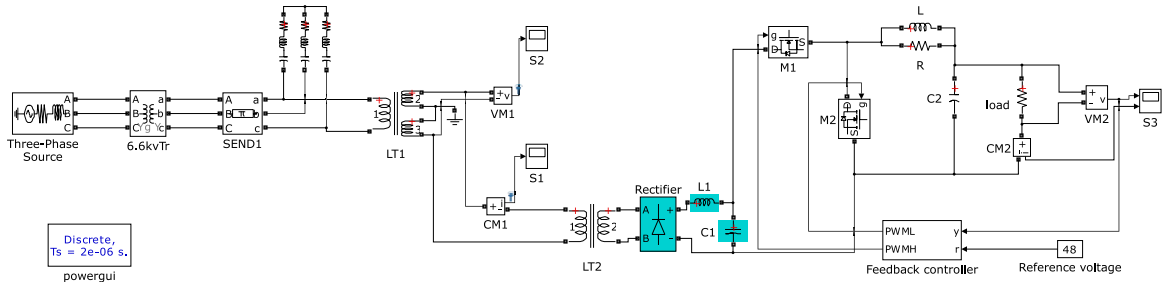


Fig. 4. Simulation model of the power supply when grid power is active.

in the following equations:

$$v_{\text{rms}} = \frac{\sqrt{\sum_{n=1}^{N} v(n)_{\text{ph}} * v(n)_{\text{ph}}}}{N} \tag{3}$$

$$v_{\text{fund}} = \frac{\sqrt{\sum_{n=1}^{N} v(n)_{\text{pure,ph}} * v(n)_{\text{ph}}}}{N} \tag{4}$$

$$a_k = \frac{\sqrt{v_{\text{rms}}^2 - v_{\text{fund}}^2}}{v_{\text{rms}}} \tag{5}$$

where $(v(n)_{\text{ph}})$ is the input voltage sample, and $(v(n)_{\text{pure,ph}})$ is the generated voltage sample.

The above-mentioned method does include the measurement noise as well in THD calculation, but it is the best method if low computation is a requirement. In this application, we would be calculating THD values (a_k) after every 200 ms and then at the end of the 10-min interval, a decision has to be taken about source identification based on the mean of calculated THD values. The mean in case of DG power would be much higher than in the case of grid power.

B. Voltage Magnitude Variations With Respect to Current Magnitude Variations

When a load draws current from a source, there is a voltage drop across the source impedance. The current consumption of BTS is always varying, and this leads to variations in voltage magnitude across the load. These variations are more significant in DG voltage magnitude than in grid voltage magnitude

$$z_k = \frac{v_{k+1} - v_k}{i_{k+1} - i_k}. \tag{6}$$

where v_k and i_k are normalized rms values as described in algorithm in Fig. 3

$$p = \frac{\sum_{j=1}^{N} z_j^2}{N}. \tag{7}$$

The parameter z_k is used to capture variation in voltage with respect to current variations and the parameter p is useful in quantifying these variations over a 10-min interval. The values of p are much higher in DG waveform than in grid waveform.

C. Low Fuel Quality

Misfirings in engine unit lead to a sharp dip in amplitude followed by a sharp increase in amplitude. The sharp dip is due to the drop in torque output of engine unit, and the sharp rise is due to the increase in torque value in the next engine cycle and due to voltage regulation of DG. This sharp increase and decrease are reflected in 200-ms rms values as well. The first step in this algorithm consists of normalizing the rms values with respect to the maximum obtained rms value in the 10-min interval. Then the difference between each consecutive value is calculated

$$d_k = v_{k+1} - v_k. \tag{8}$$

The sequence d_k consists of a high positive value followed by a negative value at the temporal location of misfiring. The difference between these two values indicates the amount of misalignment in firing instants of cylinders in the engine, which, in turn, is related to the quality of fuel used. Thus, we define e_k to measure this difference as

$$e_k = d_{k+1} - d_k. \tag{9}$$

The sequence e_k has a substantial negative value in the event of misfiring in an engine. The fuel quality algorithm detects and counts such events using thresholding. The threshold has been decided based on the fact that only those misfirings that cause the torque to drop to such a low value which causes a 5% change in the second-order difference of normalized rms values are considered as a misfiring event. The total number of misfirings in the 10-min interval can be used to quantify the quality of fuel used in diesel tanks.

IV. Simulation Models

Before field tests, it is essential to validate the suggested algorithms in a simulation environment. Simulink-based models have been quite useful in analyzing microgrid and smart grid applications [33], [34]. A simulink model of the power supply at telecom tower site has been designed to analyze variations observed on a power line and evaluate the efficacy of source distinguishing algorithm. The designed model gives a clearer picture of the environment in which the proposed solution will be implemented.

Grid supply shown in Fig. 4 has been modeled as a 66 kV three-phase power source with an X/R ratio of 7 to model the source impedance of utility supply. The power source block is followed by a three-phase step down transformer with star connected windings to step down the voltage to 6.6 KV. A pi section has been used to model a 1-km transmission line between source and load. Three loads L1(P: 100 kW, Ql: 100 VAR, Qc: -100 VAR), L2 (P: 10 kW, Ql: 100 VAR,

This article has been accepted for inclusion in a future issue of this journal. Content is final as presented, with the exception of pagination.

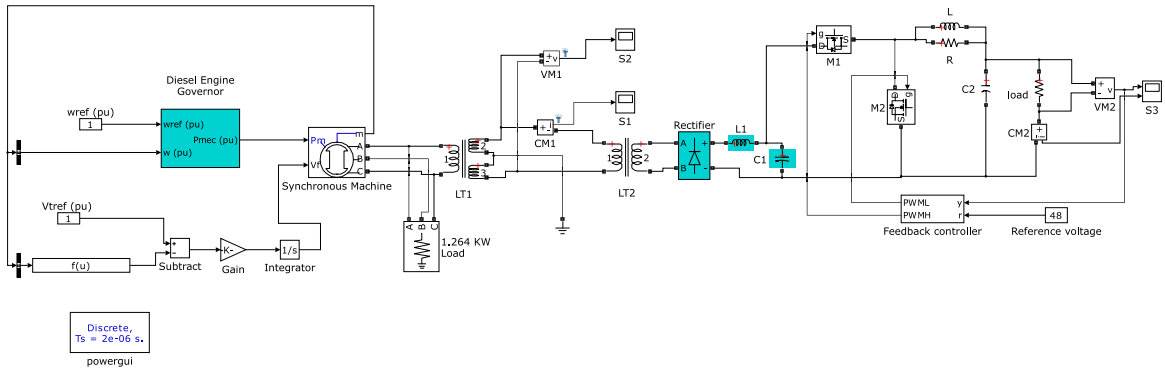


Fig. 5. Simulation model of the power supply when DG power is active.

Qc: −100 VAR), and L3(P: 10 kW, Ql: 100 VAR, Qc: −100 VAR) where P is the active power, Ql is the inductive reactive power, and Qc is the capacitive reactive power have been used to model various other loads connected to grid supply. A linear transformer has been used to convert the three-phase 6.6 kV supply to 200 V single-phase supply available at tower sites. At some sites, three phase supply is available, and the PIU selects the best phase which is then given as input to the rectifier. Fig. 5 shows the simulation model of power supply at tower site when DG is active. The governor consists of an engine unit and a control loop for output voltage frequency. The torque output of governor is adjusted based on the difference of the required frequency and the actual output voltage frequency. The field voltage of the synchronous generator is controlled using an excitation transformer, which generates field voltages based on the stator voltages. The frequency control loop in diesel engine governor unit has been modeled as a second-order control system with a zero at $s = -4$ and poles at $s = -111.11, -28.73$ [35]. The parameters for all the blocks have been configured in per unit system in which nominal frequency is 60 Hz, and nominal line-to-line voltage is 460 V. The synchronous machine block in simulink has abstracted all the essential measurements such as stator current and voltages, field voltages, and rotor speed in the form of a bus. This bus essentially models an excitation transformer of DG. The control loop for field voltage consists of a PI controller with gain factor $K = 40$. Simulink models the synchronous generator as a current source. The 1.264-kW load shown in Fig. 6 has been connected to model the source impedance of a current source.

SMPS block shown in Fig. 2 consists of a Bridge rectifier and a buck converter as shown in Figs. 4 and 5. The rectifier is used to convert 220 V ac to 140 V dc. The Synchronous buck converter is used to convert 140 V dc to 48 V dc. The gate voltage of high side (M1) and low side (M2) MOSFETs is controlled using a PWM controller [36]. The output voltage of buck converter is regulated at 48 ± 0.3 V. BTS is modeled as a resistive load (load) with an approximate power consumption of 1.15 kW which is similar to average power consumption at a tower site. VM1 and VM3 are simulink voltage measurement units. CM1 is the simulink current measurement unit. S1, S2, and S3 are simulink scope blocks.

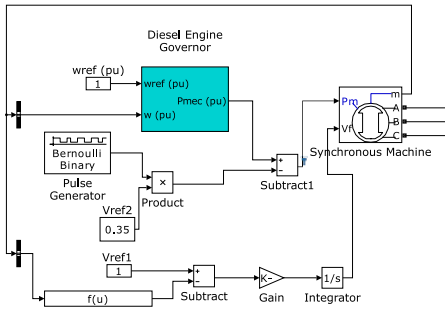


Fig. 6. Simulation model for introducing effect of engine misfire in synchronous generator.

Diesel quality quantization algorithm can also be validated using simulation models by introducing disturbance torque combinations suggested by Anderson and Mirheydar [23]. Fig. 6 shows a method of introducing drop in output torque of diesel engine governor based on high or low logic values of Bernoulli binary generator. A drop in torque value is introduced for logic "1" value. The probability of logic "1" controls the total number of misfiring events that will be introduced in the simulation runtime interval. A probabilty of 0.07 for logic "1" with a sample time of 0.133 s was selected for the Bernoulli binary generator shown in Fig. 6.

It is to be noted that there are many other loads such as the air conditioning equipment and lightening equipment at a tower site. In the simulation model, only the effect of the SMPS converter on the power supply has been modeled. The SMPS converter, supplying power to the BTS, is a major nonlinear load at a tower site. The power consumption of other devices is much less in comparison to BTS. The amount of nonlinearity introduced by such devices is low. Thus, modeling the effect of BTS on the power source suffices for the application at hand.

V. Experimental Setup

The experiment consists of testing the proposed solution in a laboratory environment using the two power sources, ac-to-dc converter and an electrical load as shown in Fig. 7. An experimental setup was developed as shown in Fig. 7(a) in the I.C. Engine lab at IIT Delhi to validate the proposed

This article has been accepted for inclusion in a future issue of this journal. Content is final as presented, with the exception of pagination.

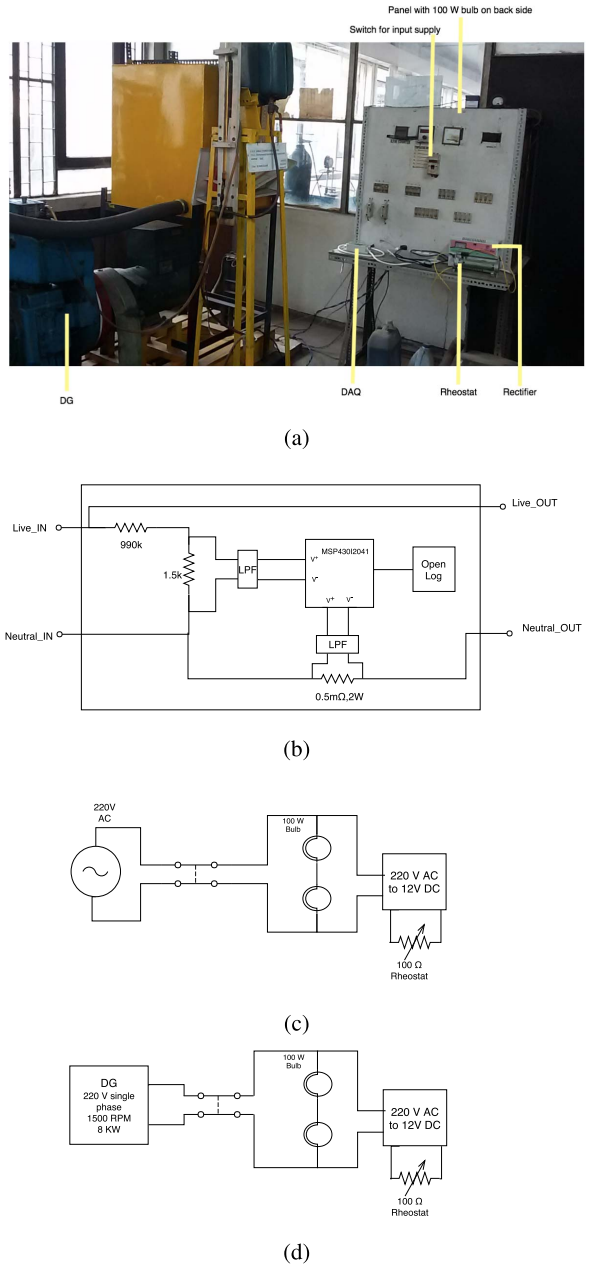


Fig. 7. Experimental setup for two power sources. (a) Experimental setup connections with DG as power source. (b) Sensing configuration for the DAQ system. (c) grid supply setup. (d) DG supply setup.

solution. An electrical load panel consisting of 100 W bulbs and switches was used as a load for the two power sources. A nonlinear load in the form of an ac-to-dc converter was also connected on the panel. The two power sources are 220 V grid supply and a 8 kW, 1500 rpm, 220 V single-phase DG. The connections of the input switch are changed to select a particular power source. A DAQ unit has been designed to record voltage and current waveforms on a single-phase power line. The schematic of the system has been depicted in Fig. 7(b). The connections Live_IN and Neutral_IN are connections on the source side of PCC and the connections Live_OUT and Neutral_OUT are connections on the load side of PCC. EVM430I2040 [37] from Texas Instruments was used to design the DAQ system. The output data are stored on a microSD card for further processing using OpenLog [38]. Each power supply was turned on for a particular duration and current and voltage waveforms were recorded in each case. Fig. 7(c) depicts the schematic for the setup when grid supply is active, and Fig. 7(d) depicts the schematic for the setup when DG is active. The effect of a small nonlinear load on the voltage and current quality of the power source has been used to demonstrate that power quality data can be used for source identification.

It is to be noted that in the DAQ system, only a simple low-pass filter with a bandwidth of 10 kHz, as available on EVM430I2040, has been used to filter out high-frequency noise. No other noise or variations injected into the power waveforms is being filtered. The reason for this is that most of the analysis steps embedded in the proposed algorithm are based on the established power quality standards. The variations on the power line would differ a lot between various intervals. The variations may be due to noise injected from the environment, load variations, dip in power quality of the source, and various other factors. These cannot be accounted for in a short interval. In a long interval, we can deduce some vital information from power quality variations. For example, in our case, there can be huge variations in each 200-ms interval, but the final decision is evaluated only at the end of a 10-min interval. In a 10-min interval, we can be sure that the harmonics count would be much greater in case of DG supply than in the case of grid supply. In a 10-min interval, one can be sure that the variations in voltage supply will be much less in the case of grid supply than in DG. Thus, the statistical evaluation is playing the role of filtering operation subtly.

VI. Results and Discussion

The algorithms proposed in Section III were applied to waveforms generated in simulation models presented in Section IV. The voltage measurement block v1 in Fig. 5 records the voltage samples across the input side of SMPS rectifier, and the current measurement block c1 in the figure records the input current. These two measurement units indicate the location of the proposed device at a tower site. The simulation model was executed for a duration of 20 s and data were stored in.mat format for further processing. The sampling time for simulation model was 2e-06s. The data were downsampled to 2 kHz for the calculation of parameters. Fig. 8 shows the comparison of the voltage and current waveforms for a duration of 50 ms. Variations in current are present in waveforms of both models, but their effects on voltage waveform are more prominent in the case of DG. The DG voltage waveform has more distortion than the grid voltage waveform. Applying FFT to the voltage waveform results in the frequency spectra depicted in Fig. 9. The presence of harmonics is apparent in the DG waveform.

A duration of 20 s consists of hundred 200 ms intervals. Each 200 ms interval leads to one a_k value. At the end of 20 s, there would be 100 a_k values. These values have been given in form of a bargraph in Fig. 10 for the two cases. The x-axis denotes the value and the y-axis denotes the number of total

This article has been accepted for inclusion in a future issue of this journal. Content is final as presented, with the exception of pagination.

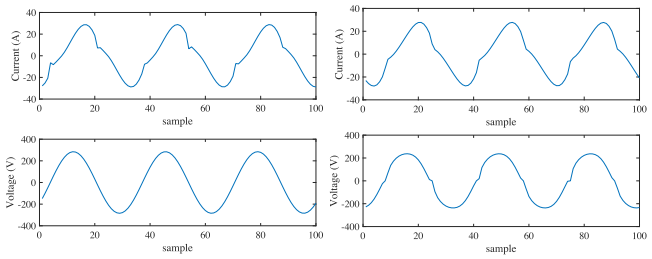


Fig. 8. Comparison between voltage and current waveforms of (a) grid supply and (b) DG supply.

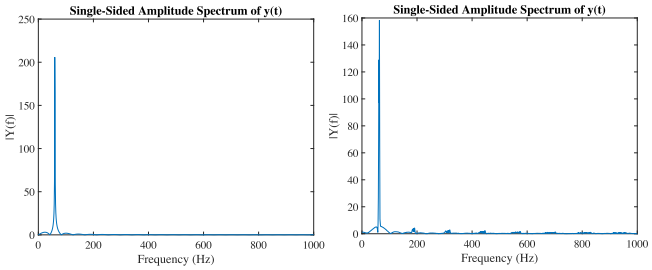


Fig. 9. Comparison between voltage spectrum of (a) grid supply and (b) DG supply.

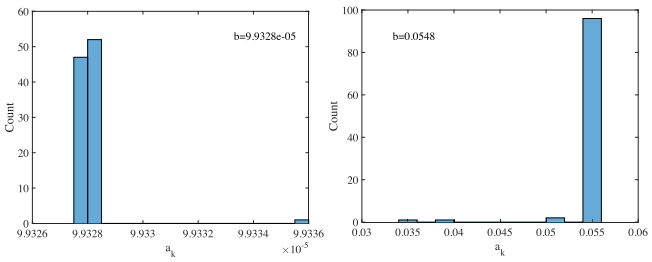


Fig. 10. Comparison between a_k values. (a) Grid supply. (b) DG supply.

a_k values lying in that range during the 20 s interval. It could be seen in the bargraph that there is a big difference in the range of parameter values for the two cases. The range of a_k values in grid supply is lying between 9.9327e-05 and 9.9336e-05. The range of a_k values in DG supply is lying between 0.035 and 0.055. The value of b for the grid in simulation results was 9.9328e-05 and for DG was 0.0548. The huge difference in values indicates that a thresholding technique would prove useful in distinguishing source based on parameter b. The threshold value for parameter b should be selected only using the on-site data for a specific location. The voltage and current waveforms should be acquired at a specific site for 1–2 days. The selected duration must include active intervals for each power source. The value of b should be selected based on 95% significance value. The actual values obtained using on-site data may differ a lot considering the variations that may occur due to various loads and power quality of source at the tower site. Calculation of parameter p involves the calculation of z_k. Fig. 11 shows a bargraph of z_k values of grid and DG for 20-s interval. The x-axis denotes

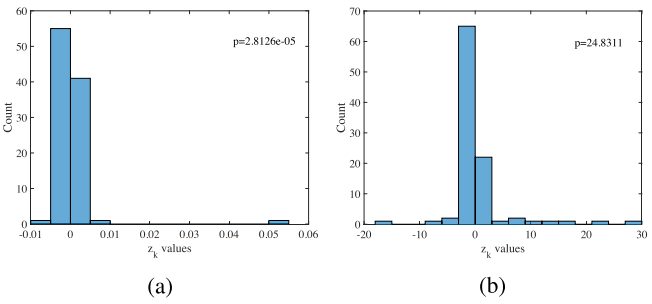


Fig. 11. Comparison between z_k values. (a) Grid supply. (b) DG supply.

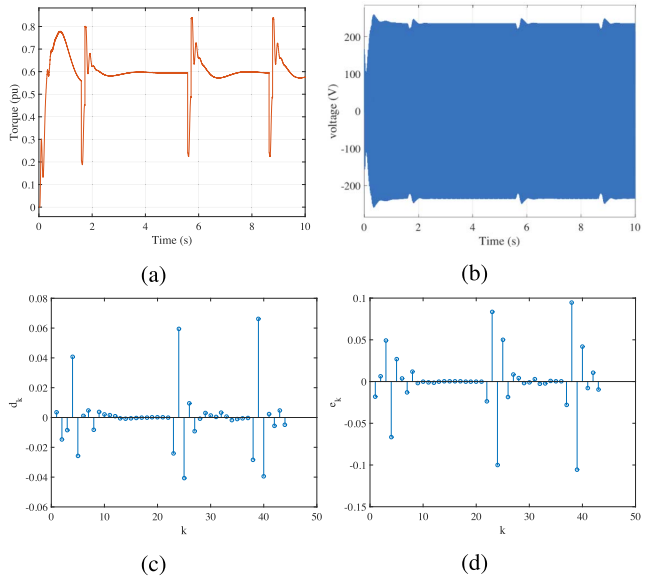


Fig. 12. (a) Drop in torque values when an engine misfires. (b) Corresponding voltage fluctuations in output of synchronous generator. (c) d_k values. (d) e_k values.

the value and the y-axis denotes the number of total z_k values lying in that range during the 20-s interval. Comparison of the two figures shows that the values of z_k are much smaller in grid voltage waveforms. The range of z_k values in grid supply is lying between -0.01 and 0.06. The range of z_k values in DG supply is lying between -20 and 30. The values of p for grid and DG are 2.8126e-05 and 24.8311, respectively. The difference in two values indicates that the parameters z_k and p are practical tools in distinguishing two available sources. The threshold for p should be decided based on the on-site data. It is to be noted that the results obtained are an outcome of the persistent variations due to the power supply which is the most significant load at a tower site. Therefore, they are valid in all situations irrespective of other load connections.

The detection of fuel quality is an added advantage of our source monitoring approach. The quality of fuel is inversely related to the number of misfirings in the engine unit. The total number of misfirings in the 10-min interval indicates the fuel quality. The results for 10-s simulation run of the DG model with engine misfirings have been presented in Fig. 12. Fig. 12(a) shows the drop in torque values when an engine misfires. The corresponding variations in voltage waveform have been depicted in Fig. 12(b). The voltage variations start

This article has been accepted for inclusion in a future issue of this journal. Content is final as presented, with the exception of pagination.

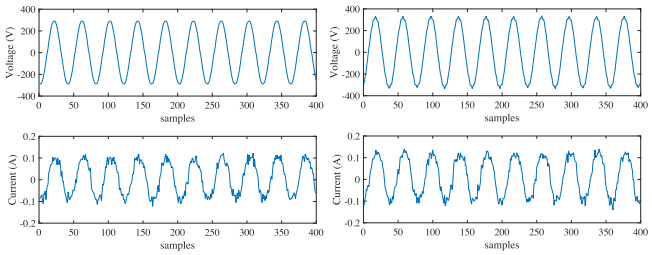


Fig. 13. Comparison between voltage and current waveforms in experimental setup. (a) Grid supply. (b) DG supply.

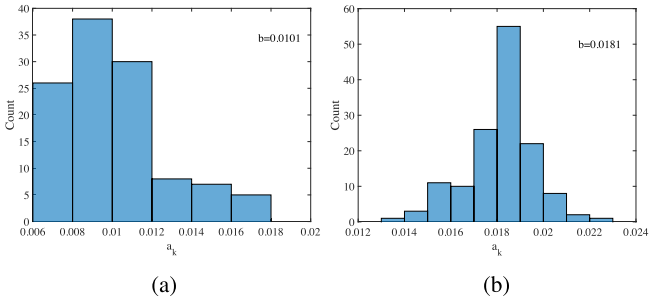


Fig. 14. Comparison between a_k values in experimental setup. (a) Grid supply. (b) DG supply.

after a slight delay. This is due to the delay between the input torque signal and the output voltage of a synchronous generator. This physical phenomenon is modeled as a delay element in the diesel engine governor block shown in Fig. 5. A dip in voltage and then a rapid increase is a characteristic of source dynamics and is independent of load. This variation is also reflected in 200-ms rms values. As suggested in fuel quality algorithm, parameter d_k is calculated based on the difference of such rms values. Fig. 12(c) shows d_k values for the three misfiring events. The parameter e_k is calculated as the difference of two consecutive d_k values. A large negative value in e_k indicates the location of misfirings. Detection and counting of such misfirings are used for quantizing the fuel quality.

Besides the simulation, we have also constructed an experimental setup to validate our algorithms. First, the grid supply was connected to the load panel for a period of approximately 114 s, and then the DG was connected to the load panel for a period of approximately 140 s. The DAQ unit was connected in series between the load and source. The data set for grid supply consisted of 114 200-ms intervals and the data set for DG supply consisted of 139 200-ms interval. Fig.13 shows the voltage and current waveforms in experimental setup for a duration of 200 ms. The effect of nonlinear current is more pronounced in DG supply voltage than in grid supply. Fig. 14 shows a_k values for the two cases. The range of a_k values in grid supply is lying between 0.06 and 0.18. The range of a_k values in DG supply is lying between 0.013 and 0.023. The value of b in this particular experiment was 0.0101 for grid supply and 0.0181 for DG supply. The difference may appear small but it would be large in practical cases as voltage distortion is highly correlated with the magnitude of current

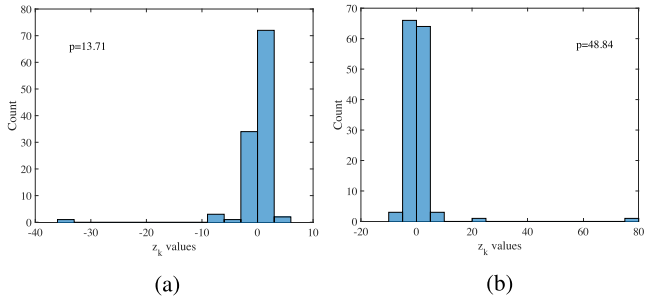


Fig. 15. Comparison between z_k values in experimental setup. (a) Grid supply. (b) DG supply.

drawn by the nonlinear load [22]. Fig. 15 shows the z_k values for the two cases and the result is as expected. The range of z_k values in grid supply is mostly lying between -5 and 5. The range of z_k values in grid supply is mostly lying between -10 and 10. The value of p in this particular experiment was 13.71 for grid supply and 48.84 for DG supply.

The results show that the proposed algorithm works in real-world scenario as well. It can easily be adapted for power measurement applications at a tower site. A real tower site data might have been best to depict the effectiveness of the solution, but it is difficult to get approval for such experiments on a tower site. The reason for not getting approval was the proposed series configuration of the measurement unit. As proposed in the solution, the measurement unit has to be connected in series between the PIU and the rectifier unit. The series configuration was preferred to parallel connections due to two reasons. First, it ensures a perfect integration of the measurement device with the circuitry. It is much easier to tamper with a parallel connection than with a series connection. Second, parallel connections utilize electric and magnetic field for DAQ. The ambient electric and magnetic field are very high at a tower site, and that would have introduced noise in the parameters measured in this solution. However, it is difficult to convince equipment manufacturers and operators for an experimental setup with a series connected device. Their primary concern is that any malfunction in a series connected device may affect their devices and lead to an interruption in site's working. We want to emphasize the fact that, even without the onsite data, this paper proves the applicability of the solution. We have used only a single nonlinear load in our simulation models to stress the fact that a single nonlinear load can have a pronounced effect on a smaller power source. The underlying concept, grid being an infinite source, is also a generally accepted notion. In the experimental setup, the normal grid supply available at our institute was used for the readings. The load used was a minimal load as compared to the sources that have been used. The loads at a tower site are much higher, and their effect on power source would be much higher. In spite of the modest nonlinearities and load values used to emulate a tower site, the results indicate that nonlinear loads introduce a characteristic variation on the power line and such variations can be used for source identification. Power management unit manufacturers can effectively use this method for power measurement applications at a tower site and in similar applications.

This article has been accepted for inclusion in a future issue of this journal. Content is final as presented, with the exception of pagination.

VII. Conclusion

It can be concluded that the power quality data can be used to measure the power consumption of a source from a measurement unit integrated inside the load. This arrangement helps us in concealing the measurement unit, thus preventing any tampering with its connections or readings. No additional hardware is required at the tower site as the algorithm can be implemented in the PWM controller used in rectifiers at the tower site. Simulink models for power management circuitry at a telecom tower site have been presented. Simulation models and experimental setup have been used to present a novel application of power quality and load monitoring. Such applications always deal with high-power electrical devices and getting access to a real data set is a bit difficult. The random physical phenomenon associated with such applications cannot be easily quantified. In such cases, validating an application using simulation and experimental setup is of utmost importance as we can easily change scenarios, clearly highlight the proposed connections, and use various kinds of load to validate our hypothesis. We have been able to clearly show the methods in which power quality and load monitoring applications can be validated. A low-cost prototype for acquiring power waveforms has been designed and tested. A parameter for quantifying the diesel quality based on power quality output of DG has been proposed.

The single point concealed monitoring approach presented in this paper would prove useful in many applications related to energy monitoring and theft prevention. Data centers, construction sites, and manufacturing units also employ secondary sources for their power requirements. Hybrid energy systems consist of a number of energy sources. Usually, the cost of energy generation is different for each source. Thus, monitoring of energy consumption will require individual measuring units for all sources. The energy consumption can be monitored with a single measurement unit in such systems using the approach mentioned in this paper. Fuel quality detection gives a glimpse of applications in which users can quantize the quality of power supplied by the source. Thus, a number of applications can make judicious use of the proposed algorithms and monitoring philosophy.

References

[1] M. Peterson and R. Winstead, "Evaluating the efficiency of hybrid power systems at telecom cell sites: Using system-level metrics for accurately determining tower energy efficiency," in *Proc. 35th Int. Telecommun. Energy Conf. Smart Power Efficiency (INTELEC)*, Oct. 2013, pp. 1–6.

[2] Petroleum Planning and Analysis Cell. *All India Study on Sectoral Demand of Diesel & Petrol*. Accessed: Jun. 2, 2018. [Online]. Available: http://ppac.org.in/WriteReadData/Reports/201411110329450069740AllIndiaStudyonSectoralDemandofDiesel.pdf

[3] DNAIndia.com. (Nov. 3, 2014). *Telecom Tower Companies Fight a Losing War Against 'Diesel Mafia'*. Accessed: Jun. 2, 2018. [Online]. Available: http://www.dnaindia.com/india/report-telecom-tower-companies-fight-a-losing-war-against-diesel-mafia-2031509

[4] *IFMS: IOT & Cloud Based Solution*. Accessed: Jun. 2, 2018. [Online]. Available: http://www.loudcell.com/iot-cloud-solution.htm

[5] *Telecom and IOT Overview*. Accessed: Jun. 2, 2018. [Online]. Available: http://www.6thenergy.com/#/telecom#telecom

[6] J. Alcalá, J. Ureña, Á. Hernández and D. Gualda, "Event-based energy disaggregation algorithm for activity monitoring from a single-point sensor," *IEEE Trans. Instrum. Meas.*, vol. 66, no. 10, pp. 2615–2626, Oct. 2017.

[7] A. Flammini, D. Marioli, E. Sisinni, and A. Taroni, "Environmental telemonitoring: A flexible GSM-DECT-based solution," *IEEE Trans. Instrum. Meas.*, vol. 56, no. 5, pp. 1688–1693, Oct. 2007.

[8] I. Urbina-Salas, J. R. Razo-Hernandez, D. Granados-Lieberman, M. Valtierra-Rodriguez, and J. E. Torres-Fernandez, "Instantaneous power quality indices based on single-sideband modulation and wavelet packet-Hilbert transform," *IEEE Trans. Instrum. Meas.*, vol. 66, no. 5, pp. 1021–1031, May 2017.

[9] J. Li, Z. Teng, Q. Tang, and J. Song, "Detection and classification of power quality disturbances using double resolution S-transform and DAG-SVMs," *IEEE Trans. Instrum. Meas.*, vol. 65, no. 10, pp. 2302–2312, Oct. 2016.

[10] *The True Cost of Providing Energy to Telecom Towers in India*, Energy, Intelligent, 2012.

[11] V. Karthigeyan, M. Aswin, L. Priyanka, K. N. D. Sailesh, and K. Palanisamy, "A comparative study of lithium ion (LFP) to lead acid (VRLA) battery for use in telecom power system," in *Proc. Int. Conf. Comput. Power, Energy Inf. Commun. (ICCPEIC)*, Mar. 2017, pp. 742–748.

[12] P. Fabio, M. Antonetti, and M. Grossoni, "Power and conditioning telemanagement integrated system," in *Proc. 27th Int. Telecommun. Conf. (INTELEC)*, Sep. 2005, pp. 83–88.

[13] *Power Interface Unit (PIU)*. Accessed: Jun. 2, 2018. [Online]. Available: http://acmecleantech.in/productdocument/1082422654_Power%20Interface%20Unit.pdf

[14] M. H. J. Bollen and I. Y. H. Gu, *Signal Processing of Power Quality Disturbances*, vol. 30. Hoboken, NJ, USA: Wiley, 2006.

[15] S. Santoso and D. D. Sabin, "Power quality data analytics: Tracking, interpreting, and predicting performance," in *Proc. IEEE Power Energy Soc. Gen. Meeting*, Jul. 2012, pp. 1–7.

[16] T. Atalik *et al.*, "Multipurpose platform for power system monitoring and analysis with sample grid applications," *IEEE Trans. Instrum. Meas.*, vol. 63, no. 3, pp. 566–582, Mar. 2014.

[17] A. Cataliotti, V. Cosentino, D. Di Cara, and G. Tinè, "LV measurement device placement for load flow analysis in MV smart grids," *IEEE Trans. Instrum. Meas.*, vol. 65, no. 5, pp. 999–1006, May 2016.

[18] B. Dehkordi, M. Moallem, and A. Parsapour, "Predicting foaming slag quality in electric arc furnace using power quality indices and fuzzy method," *IEEE Trans. Instrum. Meas.*, vol. 60, no. 12, pp. 3845–3852, Dec. 2011.

[19] M. Šíra and V. N. Zachovalová, "System for calibration of nonintrusive load meters with load identification ability," *IEEE Trans. Instrum. Meas.*, vol. 64, no. 6, pp. 1350–1354, Jun. 2015.

[20] R. Redl and A. S. Kislovski, "Telecom power supplies and power quality," in *Proc. 17th Int. Telecommun. Energy Conf. (INTELEC)*, Oct./Nov. 1995, pp. 13–21.

[21] J. Barros, R. I. Diego, and M. de Apraíz, "A discussion of new requirements for measurement of harmonic distortion in modern power supply systems," *IEEE Trans. Instrum. Meas.*, vol. 62, no. 8, pp. 2129–2139, Aug. 2013.

[22] Y. Zhuo, J. Wu, G. Tang, F. Hu, and Y. Yu, "Power monitoring device with quantitative harmonic source identification," in *Proc. Asia-Pacific Power Energy Eng. Conf. (APPEEC)*, Mar. 2010, pp. 1–4.

[23] P. M. Anderson and M. Mirheydar, "Analysis of a diesel-engine driven generating unit and the possibility for voltage flicker," *IEEE Trans. Energy Convers.*, vol. 10, no. 1, pp. 37–47, Mar. 1995.

[24] D. F. Teshome, T. D. Huang, and K.-L. Lian, "Distinctive load feature extraction based on Fryze's time-domain power theory," *IEEE Power Energy Technol. Syst. J.*, vol. 3, no. 2, pp. 60–70, Jun. 2016.

[25] Y.-H. Lin and M.-S. Tsai, "Development of an improved time–frequency analysis-based nonintrusive load monitor for load demand identification," *IEEE Trans. Instrum. Meas.*, vol. 63, no. 6, pp. 1470–1483, Jun. 2014.

[26] K. D. Hurst and T. G. Habetler, "A comparison of spectrum estimation techniques for sensorless speed detection in induction machines," *IEEE Trans. Ind. Appl.*, vol. 33, no. 4, pp. 898–905, Jul. 1997.

[27] D. Shi, P. J. Unsworth, and R. X. Gao, "Sensorless speed measurement of induction motor using Hilbert transform and interpolated fast Fourier transform," *IEEE Trans. Instrum. Meas.*, vol. 55, no. 1, pp. 290–299, Feb. 2006.

[28] J. Lorincz, T. Garma, and G. Petrovic, "Measurements and modelling of base station power consumption under real traffic loads," *Sensors*, vol. 12, no. 4, pp. 4281–4310, Mar. 2012.

This article has been accepted for inclusion in a future issue of this journal. Content is final as presented, with the exception of pagination.

[29] G. V. de Andrade, S. R. Naidu, M. G. G. Neri, and E. G. da Costa, "Estimation of the utility's and consumer's contribution to harmonic distortion," *IEEE Trans. Instrum. Meas.*, vol. 58, no. 11, pp. 3817–3823, Nov. 2009.
[30] P. M. Ramos, M. F. da Silva, R. C. Martins, and A. M. C. Serra, "Simulation and experimental results of multiharmonic least-squares fitting algorithms applied to periodic signals," *IEEE Trans. Instrum. Meas.*, vol. 55, no. 2, pp. 646–651, Apr. 2006.
[31] J. G. Proakis and D. G. Manolakis, *Digital Signal Processing: Principles, Algorithms, and Applications*. London, U.K.: Pearson, 2001.
[32] M. Mesganaw. *Quantifying Harmonic Distortion: Estimating THD Without Performing a Full FFT Operation*. Accessed: Jun. 2, 2018. [Online]. Available: https://e2e.ti.com/blogs_/archives/b/smartgrid/archive/2016/09/26/quantifyingharmonic-distortionestimatingthdwithout-performingafullfftoperation
[33] D. Yubing, G. Yulei, L. Qingmin, and W. Hui, "Modelling and simulation of the microsources within a microgrid," in *Proc. Int. Conf. Elect. Mach. Syst. (ICEMS)*, Oct. 2008, pp. 2667–2671.
[34] A. Karabiber, C. Keles, A. Kaygusuz, B. B. Alagoz, and M. Akcin, "Power converters modeling in MATLAB/Simulink for microgrid simulations," in *Proc. 4th Int. Istanbul Smart Grid Congr. Fair (ICSG)*, Apr. 2016, pp. 1–5.
[35] G. Sybille and T. Zabaiou. *Emergency Diesel-Generator and Asynchronous Motor*. Accessed: Jun. 2, 2018. [Online]. Available: https://in.mathworks.com/help/physmod/sps/examples/emergency-diesel-generator-and-asynchronous-motor.html
[36] P. Giroux. *Synchronous Buck Converter*. Accessed: Jun. 2, 2018. [Online]. Available: https://in.mathworks.com/help/physmod/sps/examples/synchronous-buck-converter.html
[37] *MSP430i2040 Sub Metering EVM*. Accessed: Jun. 2, 2018. [Online]. Available: http://www.ti.com/tool/evm430-i2040s
[38] *OpenLog Hookup Guide*. Accessed: Jun. 2, 2018. https://learn.sparkfun.com/tutorials/openlog-hookup-guide



Abhishek Grover received the B.Tech. degree in electronics and communication engineering from Delhi Technological University, New Delhi, India, in 2015, and the M.S. (Research) degree from the Bharti School of Telecommunication Technology and Management, IIT Delhi, New Delhi, in 2018. He is currently pursuing the Ph.D. degree at IIT Delhi.

His current research interests include embedded systems and signal processing.



Brejesh Lall received the B.Tech. degree in electronics and communication engineering and the master's degree in signal processing from the Delhi College of Engineering, New Delhi, India, in 1991 and 1992, respectively, and the Ph.D. degree in signal processing from IIT Delhi, New Delhi, in 1999.

In 1997, he joined Aricent, Gurgaon, India. In 2005, he joined the Department of Electrical Engineering at IIT Delhi as an Assistant Professor. From 2010 to 2018, he was an Associate Professor. Since 2017, he has been the Head of the Bharti School of Telecommunication Technology and Management, IIT Delhi. He is currently a Professor with the Department of Electrical Engineering, IIT Delhi, and also the Coordinator of the IIT Delhi Ericsson 5G Centre of Excellence. His current research interests include image processing, signal processing, and communication.

This article has been accepted for publication in a future issue of this journal, but has not been fully edited. Content may change prior to final publication. Citation information: DOI 10.1109/JSEN.2019.2903645, IEEE Sensors Journal

A Robust Framework for Abnormal Human Action Recognition using $\mathcal{R}$-Transform and Zernike Moments in Depth Videos

Chhavi Dhiman, Dinesh Kumar Vishwakarma, *IEEE Senior Member*

***Abstract*— The aim of the algorithm is to detect the abnormal actions which are more prone to elderly people in order to make them more independent and improve their quality of life. The framework is structured to construct a robust feature vector by computing R - transform and Zernike moments on Average Energy Silhouette Images (AESIs). The AESIs are generated by the integral sum of the segmented silhouettes obtained from the Microsoft's Kinect sensor v1. The proposed feature descriptor possess scale, translation and rotation invariant properties that is also less sensitive to noise and minimizes data redundancy. It enhances proposed algorithm's robustness and makes the classification process more efficient. The proposed work is validated on a novel abnormal human action (AbHA) dataset and three publically available 3D datasets - UR fall detection dataset, Kinect Activity Recognition Dataset (KARD) and multi-view NUCLA dataset. The proposed framework exhibits superior results from other state-of-the-art methods in terms of Average Recognition Accuracy (ARA). The experimental results demonstrate 96.5%, 96.64%, 95.9% and 86.4% ARA on UR fall detection dataset, KARD dataset, AbHA dataset and multi-view NUCLA dataset, respectively.**

***Index Terms*— Abnormal Human Action and activity recognition, Average Energy Silhouette Images, Zernike moments, R –transform.**

I. INTRODUCTION

SINCE 1980s, human activity recognition has been a growing field in computer vision because of its vast applications in various spheres of life such as surveillance [1-3], healthcare [4], sports [5] and home automation [6]. The concept of automated and intelligent Human Action Recognition (HAR) system has improved the quality of daily living of a common person with the availability of smart surveillance at public places and smart homes. Today, the conception of smart homes has turned out to be a game changer for elderly people to lead an independent and confident life with better healthcare facilities by developing a pervasive, intelligent environment. It provides continuous monitoring and analysis of a person's activities either at atomic level (e.g. walking, bending, drinking) or a higher level (e.g. preparing breakfast, washing hands) backed up by advanced machine learning and vision algorithms [7]. Aggarwal et al. [8], defined high-level human activities as a string of atomic level activities or human actions. Therefore, human activity and human actions are used interchangeably in the paper.

In the previous works [9-11], RGB cameras are used to record action sequences and develop discriminative action descriptors for action analysis. However, RGB based action recognition is sensitive to the lighting conditions and cluttered background. These challenges result in added computational complexity in RGB based HAR solutions. With the innovations in the field of imagery technology, over a period, it has become possible to capture the depth information of the actions in real time and cost-effective manner. Depth values estimation involve infrared radiation. Therefore, they are no more sensitive to lighting conditions or visible light. They make foreground extraction much simpler and faster. Due to these benefits of depth images, the researchers are now inclining towards depth images based action analysis, that has resulted in large set of depth action datasets [12-14] being published capturing indoor actions. Depth images provide fine shape details of the subject in the scene, which improves the understanding of the human shape reducing the effect of self-occlusion [15]. For health monitoring purposes of elderly people, a sudden fall detection is one of the major concerns. Some of the researchers worked out with sensor-based solutions [16] [17], some presented (RGBD) vision based fall detection solution [18] [19]. And it is observed that the sensor-based approaches [20] fail if the individual forgets to wear them due to weak memory or decreased control on their bodies. Some elderly monitory systems also maintain a help button. However, if the individual cannot press the help button due to the sudden nature of the abnormal action, then the purpose is defeated. Therefore, vision-based approaches [21] provide an edge over the sensor-based techniques in terms of its independence from the individual and disturbance to his privacy.

After, looking over all these aspects related with Human Action Recognition (HAR) systems, the proposed work exploits the benefits of depth images to analyse the human action to overcome the potential limitations of RGB and sensor-based approaches, using a real-time and cost-efficient emerging Microsoft's Kinect sensor. The proposed work designs a robust scale, rotation and translation invariant human action recognition framework that is evaluated for publically available UR Fall dataset, KARD dataset, multi-view NUCLA dataset and AbHA dataset to exhibit its robustness for both normal and abnormal action.

Motivation: To develop a real-time human action recognition framework that can distinctly recognise both normal and abnormal types of actions despite of translation, scale and view variations, is a key motivation. More than two-thirds of the accidents suffered by the elderly people are due to fall. It becomes rather difficult to leave the elderly people unattended alone at home. The proposed methodology will reduce the inconvenience caused by wearing sensors on the body, make the elderly people feel independent, and improve their lifestyle. The proposed work is inspired from [22], which analysed elderly person actions

1558-1748 (c) 2018 IEEE. Personal use is permitted, but republication/redistribution requires IEEE permission. See http://www.ieee.org/publications_standards/publications/rights/index.html for more information.

This article has been accepted for publication in a future issue of this journal, but has not been fully edited. Content may change prior to final publication. Citation information: DOI 10.1109/JSEN.2019.2903645, IEEE Sensors Journal

– vomiting, forward fall, backward fall, fainting, chest pain and headache. Therefore, a new dataset is developed to make the proposed framework enriched with understanding of such abnormal actions along with normal actions so that the work can contribute to transform real-life healthcare applications with its real-time and efficient action description ability.

- ***Dataset generation***- Due to the non-availability of the publically available datasets for abnormal actions, a novel dataset is generated using Microsoft Kinect sensor v1. It consists of total 80 samples for five abnormal actions such as 'a headache', 'chest pain', 'fainting', 'backward fall' and 'forward fall'. Eight people repeat each action two times.
- Structural appearance of human pose and its temporal motion content of an action is encrypted as Average Energy Silhouette Images (AESI) by utilising depth images to extract fine binary silhouettes supporting low storage capacity and low computational cost.
- A robust translation, scale and rotation invariant novel action descriptor is developed by unifying the properties of both $\mathcal{R}$ -transform and Zernike moments. Application of Zernike moments develops robust features in respect of rotation invariance, data redundancy, noise resilience and, reconstruction competence. Whereas, $\mathcal{R}$ -transform delivers translation and scale invariance to it.

The rest of this paper is organized as follows: Section 2 provides the glimpses of the earlier state-of-the-arts; Section 3 explains the minutiae of the proposed abnormal human activity recognition framework, which includes the formation of AESI, properties of $\mathcal{R}$ -Transform and Zernike moments and final feature vector construction. Section 4 establishes the experimental details and discussion of results. Section 5 demonstrates conclusion and future work.

II. RELATED WORKS

Computer Vision offers promising solutions to analyse personal behaviour and identify any unusual event. Fall is one of the majorly occurring unusual events [23]. Moreover, a considerable amount of research is done to address fall in recent years using both sensor-based and vision-based approaches. To provide an affordable solution for fall detection Kwolek et al. [12] integrated accelerometric data and depth data. For long-term abnormal behaviour recognition, a hybrid behaviour analysis system LOTAR framework [24] assimilated knowledge-based and data mining based machine-learning techniques for analysis. The hybrid framework depends on different sensing devices such as environmental sensors, magnetic sensors, presence sensors and RFID tags. However, sensors or accelerometer-based approaches restrict the users to keep wearing the accelerometer for the whole day. Instead of using an additional sensor [25] used accelerometer and a tilt sensor built into the smartphone along with real-time tracking using Google'3D mapping to detect occurrence of an emergency situation while travelling in a vehicle. This approach is still limited by the battery capacity of the smartphone. Therefore, it is a big challenge to make a sustainable real time fall detection system.

Shape analysis of the object plays a vital role to understand the action performed. Hence, a big section of researchers [18-22] focused on shape analysis of a person. Rougier et al. [26] analysed the human shape deformations using shape context matching [27] to detect any possible fall using Gaussian mixture model to confirm the safety of elderly individuals at home. Recently, recurrent neural network (RNN) based fall prediction method [28] analysed human biomechanics equilibrium with 91.7% fall prediction. It computed unbalanced posture features using skeleton joints. Yuna et al. [29] utilised $\mathcal{R}$ feature to capture the geometrical statistics of the interest points, which are invariant to geometry transformation and robust to noise. In [30] shape and motion orientation of the object are used as baseline features to define action. The approach utilised spatial edge distribution of gradients and texture based segmentation technique to extract binary silhouette. Whereas, motion orientation is obtained with the help of $\mathcal{R}$ -transform followed by Local Linear Embedding (LLE). Gaglio et al. [13] defined human activity as spatiotemporal evolutions of different body postures. And the recurrent postures are represented by most substantial structures of joint locations. Aggarwal et al. [31] applied Zernike moment invariants (ZMI), a shape descriptor, on Average Energy Silhouette Images (AESI) to detect undesired covariates in the gait sequences such as clothing or carrying bag. In another work [30] integrated Spatial Distribution of Oriented Gradients (SDOGs) and Mean of Directional Pixels (MDPs) method to extract shape features from AESI incorporating ZMI. However, this approach needs to be tested for multi-view gait samples. Sintorn et al. [32] defined Regional Zernike Moments (RZM) that combine zernike moments of the pixels confined in a region to create a suitable measure for texture analysis. In [33], content-based image retrieval complex zernike moments are used for shape feature extraction. A concept of discriminative and informative semantic for human action recognition using mid-level representation based on optical flow method, Hu, and zernike moment together is used in [34] to overcome the problem of non-extraction of abundant visual spatial-temporal information using local and global features. Khan et al. [35] presented an abnormal human activity recognition framework that integrated $\mathcal{R}$ -Transform with Kernel Discriminant Analysis (KDA) to reduce interclass similarity of different activity postures- falling, fainting, vomiting, headache, maintaining individual's privacy. Khan et al. [22] extended the work by developing a hierarchal abnormal human activity recognition framework where activities with high interclass similarities are handled at second hierarchal level that improved the recognition rate from 95.8% to 97.1%. The above-discussed approaches utilised binary silhouettes from RGB images in a closed environment for shape analysis of the object in action. However, in a realistic environment, this binary silhouette generation process [36] is prone to noise and loss of data. To avoid this limitation, the researchers are now targeting over depth images for shape analysis, which simplify the background subtraction process and produces cleaner silhouettes even in complex/dynamic environment. In this direction, Dynamic Motion Maps turned out to be a rich motion descriptor of the action. Chen et al. [37] projected 3D geometry of depth human silhouettes in three different views to develop Depth Motion Maps (DMMs) and witnessed the minute variations of shape during the action. In another work [38] Local Binary Pattern (LBP) of the frontal, side and top view of DMMs are fused to generate compact representation of an action. He further enriched the action descriptor by emphasising temporal structures [39] of the DMMs at level $0, 1$ and 2. Liu et al. [40] defined a multiscale 3-D local steering kernel descriptor to learn local appearances of cuboids around motion-based STIPs and a spatial-temporal vector descriptor to pronounce the spatial-temporal

1558-1748 (c) 2018 IEEE. Personal use is permitted, but republication/redistribution requires IEEE permission. See http://www.ieee.org/publications_standards/publications/rights/index.html for more information.

This article has been accepted for publication in a future issue of this journal, but has not been fully edited. Content may change prior to final publication. Citation information: DOI 10.1109/JSEN.2019.2903645, IEEE Sensors Journal

distributions of shape-based STIPs. Such kind of integration of global and local features definitely improved the discriminative ability of action descriptor despite of view variations and partial occlusion. However, real-time implementation of the work is a major concern. Wang et al. [41] represented the depth sequences of action as Wide Hierarchical Depth Motion Maps (WHDMM) and passed them through view tolerant 3ConvNets.

Real-time acquisition of the action and its recognition [42] with an affordable range is the need of the hour to benefit elderly homecare and healthcare applications in true sense. In the same direction, Munaro et al. [43]presented an open source multi RGB-D camera-based object acquisition, calibration and tracking system in real time. Wei et al. [44] presented a refined convolution pose machine that makes sequential predictions by learning spatial context features i.e human pose. Cai et al. [45] defined 2D human pose by non-parametric representation as Part Affinity Fields (PAFs) to learn and associate body parts with individuals in the multi-person images, which is a remarkable milestone achieved towards human shape analysis.

III. PROPOSED METHODOLOGY

In the proposed work, a robust action descriptor is defined by combining the scale, translation and rotation properties of $\mathcal{R}$ –Transform and Zernike moment. The action is described as a sequence of depth images that is later represented as AESI images encrypted by $\mathcal{R}$ –Transform and Zernike moments. The proposed methodology is as shown in Fig. 1.

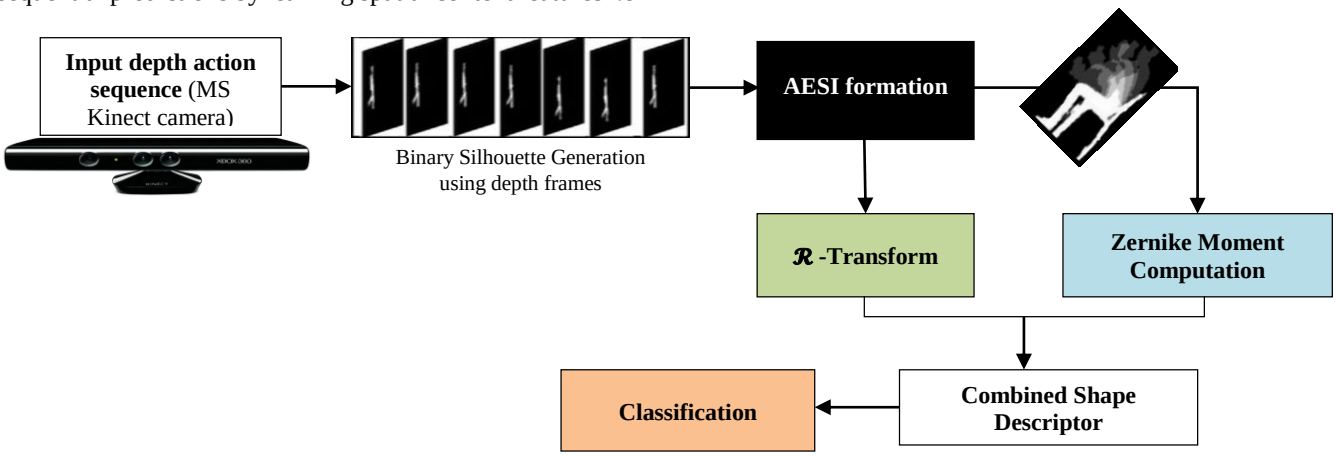


Fig. 1. Flow diagram of the proposed algorithm

A. *Average Energy Silhouette Image*

Initially, fusion of depth action sequences acquired by Microsoft Kinect camera V2, and skeleton joint locations per frame help to locate the person in the frame that makes the fine binary silhouette extraction easier. The entire action video is encrypted as a single image i.e. Average energy Silhouette Image using extracted binary silhouettes. Consider any action with N key frames. Mathematically, AESI of an action is defined as shown in Eq. (1):

$$A(x,y) = \frac{\sum_{t=1}^{N} |I(x,y,t)|^2}{N} \quad (1)$$

where $I(x,y,t)$ represents each binary silhouette frame of the action at time instance$t$. $A(x,y)$ is the final AESI image constructed for one action sequence. The single frame representation of an action sequence as AESI not only removes computational complexity involved in processing entire video but the averaging function of AESI formation smoothens the unwanted noise in the frames. Hence, AESI images are less sensitivity to the noise occurring between the frames also termed as temporal noise.

B. *Shape Descriptor*

Shape of the object possess a meaningful and important information about the action. A strong shape descriptor is a key to a stronger recognition system. AESI is used as a compact representation of the action that hold not only the shape but also the shape variations with time. Combination of $\mathcal{R}$ -transform and Zernike moments is used to define the shape descriptor.

1) $\mathcal{R}$ -transform

$\mathcal{R}$ -transform [30] provides orientation detail of an object which is computed by applying Radon transform, $\mathbb{R}_T$ on AESI images,$A(x,y)$. Radon transform generate directional features as the integral sum of $A(x,y)$, mathematically defined as Eq. (2):

$$\mathbb{R}_T(\sigma,\theta) = \iint_{-\infty}^{\infty} A(x,y)\delta(\sigma - x\cos\theta - y\sin\theta)dxdy \quad (2)$$

where $\theta\epsilon[0,\pi]$, $\delta(.)$is a standard direct delta function which remains zero except at origin and σ is the shortest distance between origin and radon line, given by Eq. (3), graphically illustrated in Fig. 2.

$$\sigma = x\cos\theta + y\sin\theta,\ \ \sigma\epsilon[-\infty,\infty] \quad (3)$$

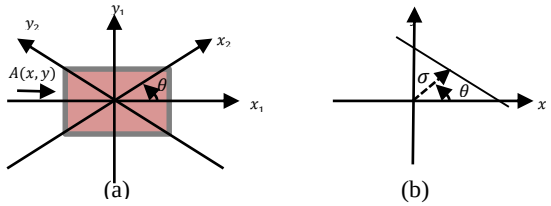


Fig. 2. (a) Projection of lines over 2Dfunction $A(x,y)$ (b) the position of projection line (radon line)

Radon projection, $\mathbb{R}_T$of an image cannot preserve all the parameters of the original geometric transformation-translation, rotation, or scaling the image. Tabbone et al. *[46]* introduced $\mathcal{R}$ -transform that is defined as an integral transform of the squared values of Radon transform, $\mathbb{R}_T$, mathematically defined as in Eq.4.

$$\mathcal{R}(\theta) = \int_{-\infty}^{\infty} \mathbb{R}_T(\sigma,\theta)^2\, \partial\sigma \quad (4)$$

where σ is the radial distance from the centre of the image to the radon line, and θ is the angle. Therefore, Radon transform $\mathbb{R}_T$ generates a 2-D feature representation and $\mathcal{R}$ -transform is a 1-D compact representation of $\mathbb{R}_T$. Normalization of $\mathcal{R}$-transform further improve the similarity measure of the feature vector, mathematically given as Eq. (5).

1558-1748 (c) 2018 IEEE. Personal use is permitted, but republication/redistribution requires IEEE permission. See http://www.ieee.org/publications_standards/publications/rights/index.html for more information.

This article has been accepted for publication in a future issue of this journal, but has not been fully edited. Content may change prior to final publication. Citation information: DOI 10.1109/JSEN.2019.2903645, IEEE Sensors Journal

$$\mathcal{R}_{norm}(\theta) = \frac{\int_{-\infty}^{\infty} \mathcal{R}(\theta) d\theta}{max(\mathcal{R}(\theta))} \quad (5)$$

Properties of $\mathcal{R}$-Transform: The fundamental properties of $\mathcal{R}$ -Transform are illustrated by Tabbone et al. [46] which confirms that it is invariant against the scaling and translation but sensitive against the rotational characteristics. These properties are verified in the work by considering chest pain activity AESI from AbHA dataset as shown in Fig. 3. It is evident from Fig. 4, case 4 that under rotation, there is more deviation in the pixel values corresponding to projection lines resulting, variation in $\mathcal{R}$ -transform signal representation. The $\mathcal{R}$ -transform representation of different abnormal actions – 'chest pain', 'headache', 'fainting', 'falling forward' and 'falling backward', is shown in Fig.4.

2) *Zernike Moment*

Ordinary geometric moments contain a lot of data redundancy. This is not desirable for any feature vector. Whereas Zernike moments reduces data redundancy with the help of complex polynomials called Zernike polynomials which comprise of a complete orthogonal basis set defined on a unit circle. This orthogonality of the polynomials helps to reduce the redundancy, hence producing an enhanced feature. Zernike polynomials were proposed in *[47]* to describe optical irregularities. For Zernike moment's computation, we need to transform the image from cartesian to polar coordinates. Complex Zernike moments can be determined by Eq. (6).

$$Z_{n,m} = \frac{n+1}{\pi} \sum_{(\sigma,\theta)\varepsilon unit\ disc} \sum f(\sigma,\theta) V^*_{n,m}(\sigma,\theta) \quad (6)$$

where, $V_{nm}(\sigma,\theta)$ is the basis function which can be determined by Eq. (7) followed by Eq. (8).

$$V_{nm}(\sigma,\theta) = R_{nm}(\sigma) e^{jm\theta} \quad (7)$$

$$R_{nm}(\sigma) = \sum_{s=0}^{\frac{n-|m|}{2}} \frac{-1^s (n-s)! \sigma^{n-2s}}{s!(\frac{n+|m|}{2}-s)!(\frac{n-|m|}{2}-s)!} \quad (8)$$

where, n is the order of the moment and m is the repetition. There are some constraints on the values of m and n: $n \geq 0, n \geq |m|,\ n - |m|$ is an even number. Since, the moments are calculated on the unit circle, $x^2 + y^2 \leq 1$ holds true. The incentive of Zernike moment is that it is rotation invariant. Table 1 illustrates rotation invariant property of Zernike moment, which is unexploited in $\mathcal{R}$-transform. Lower order zernike moments suggest the static information about the image by giving the basic details. Whereas, higher order moments describe the dynamic information by giving the image detailing. Jin et al. *[48]* established Zernike moments shape description efficacy by detecting heavily occluded targets such as airplane and warship efficiently.

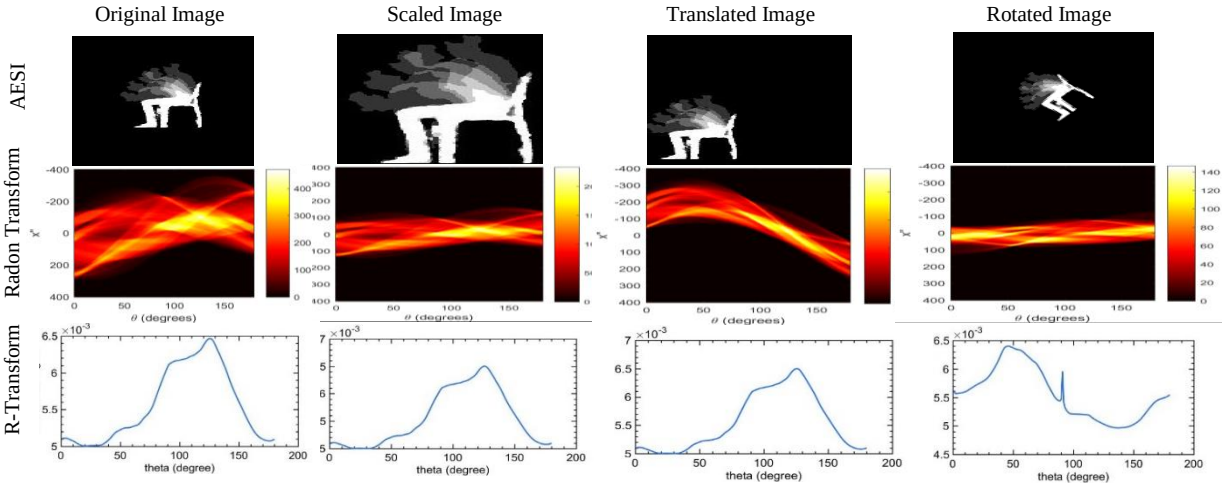
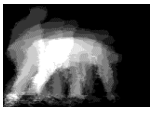
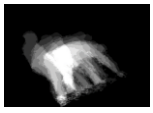
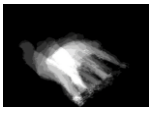
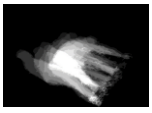
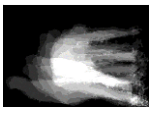
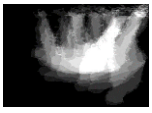


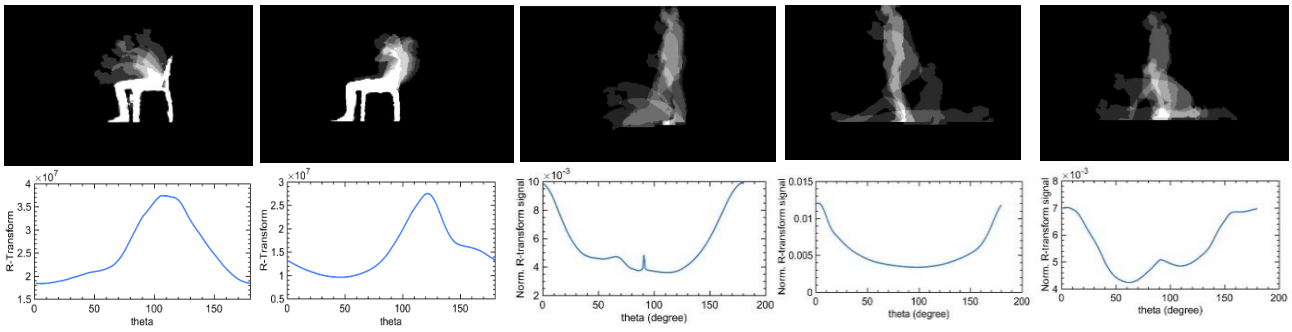
Fig. 3. Illustrates that $\mathcal{R}$-Transform is scale and translation invariant but rotation variant

TABLE I ILLUSTRATES THAT MAGNITUDE OF EACH ZERNIKE MOMENT IS INVARIANT UNDER ROTATION. M_{NM}: MAGNITUDE OF ZERNIKE MOMENT FOR ORDER M AND N.

Angle of Rotation (θ) / **Sample Image UR-ADL Activity (Bending)**	$\theta = 0^0$	$\theta = 30^0$	$\theta = 45^0$	$\theta = 60^0$	$\theta = 90^0$	$\theta = 180^0$
						
M_{20}	**0.572**	**0.552**	**0.518**	0.497	**0.514**	0.368
M_{31}	**0.299**	**0.257**	**0.282**	**0.300**	0.320	**0.230**
M_{33}	**0.115**	**0.130**	**0.134**	**0.129**	0.083	**0.134**
M_{42}	**0.244**	0.137	0.158	**0.188**	**0.205**	**0.269**

1558-1748 (c) 2018 IEEE. Personal use is permitted, but republication/redistribution requires IEEE permission. See http://www.ieee.org/publications_standards/publications/rights/index.html for more information.

This article has been accepted for publication in a future issue of this journal, but has not been fully edited. Content may change prior to final publication. Citation information: DOI 10.1109/JSEN.2019.2903645, IEEE Sensors Journal



(a) Chest Pain (b) Headache (c) Fainting (d) Falling Backward (e) Falling Forward

Fig. 4. Representation of $\mathcal{R}$ Transform for five activitie s- AbHA dataset (a) chest pain (b) Headache (c) fainting (d) falling backward (e) falling forward. Row 1: 130×100 AESI, Row 2: Normalized $\mathcal{R}$-Transform.

C. *Final Feature Vector Formation*

Radon Transform computes a 2D Projection of AESI of size $[480 \times 640]$ along the angle $\in (0^0, 179^0)$. It generates $\mathbb{R}_T$ feature matrix of size $[803 \times 180]$. Application of $\mathcal{R}$ - Transform develops a feature vector of size $[1 \times 180]$ independent of σ by integral transform of the squared values of $\mathbb{R}_T$, Radon transform, as shown in Equation (4) and simultaneously perform dimensionality reduction. Hence, $\mathcal{R}-$Transform produces 1–D projection of $\mathbb{R}_T$ feature matrix given by $F_{\mathcal{R}}$. Zernike moment feature vector F_{zm}, is obtained that includes one magnitude and phase value for every AESI image. Therefore, size of F_{zm} vector is $[1 \times 2]$.

The final feature vector is obtained by concatenation of the $\mathbb{R}$ - transformed feature vector $F_{\mathbb{R}P}$ and Zernike feature vector F_{zm}. Final feature so formed possesses the dimensions as $[1 \times 182]$ per action. By doing so, we are able to inherit the desirable properties of both $F_{\mathbb{R}P}$ and F_{zm} that result in a translation, rotation and scale, invariant feature vector formation.

IV. Experimental Works and Results

In order to assess the performance of the proposed algorithm, experiments are conducted on a novel AbHA dataset and three publically available datasets- UR fall detection dataset, KARD dataset [13] and multi-view NUCLA dataset. The performance of the algorithm is measured in respect of average recognition accuracy. For classification, K-Nearest Neighbour (K-NN) and Support Vector Machine (SVM) are used in the experiments. It is not necessary that features are always linearly separable. Therefore, to handle non-linearly separable action features Radial Basis Function (RBF) kernel based SVM is used for classification. To optimise the performance of the non-linear SVM classifier penalty C, and gamma γ are optimised for each dataset that reduces overfitting. The performance of the proposed framework is measured in terms of Average Recognition Accuracy (ARA), mathematically defined as Eq. (9).

$$\text{ARA} = \frac{\text{TP+TN}}{\text{TP+TN+FP+FN}} \times 100\% \quad (9)$$

where TP, TN, FP, FN are true positive, true negative, false positive and false negative respectively. In order to check the effectiveness of the proposed algorithm, the Average Recognition Accuracy (ARA) is compared with similar state-of-the-arts. The comparisons are relatively limited for UR Fall detection dataset [12] and KARD dataset [12] because few works are reported on these datasets.

A. *UR Fall detection dataset*

The UR fall detection dataset is introduced by Kwolek et al. [12]**.** It comprises of 40 instances of ADL activities and 30 instances for fall. It is organized as a sequence of depth and RGB instances for two viewpoints – front view (parallel to the floor) and top view (ceiling mounted), synchronization data and raw accelerometer data. In this work, only depth instances are chosen from the front view, and AESI are generated for 22 fall and 22 ADL activities for evaluation purpose. Sample images of the RGB/Depth Fall and ADL sequences are shown in Fig. 5.

For UR fall dataset, performance of recognition system is optimised for $'K'$=3, while using K-NN classifier and Leave-One-Out (LOO) cross validation technique is used. For non-linear SVM (C, γ) parameters are set to $(0.4,$ default) while using one-vs-one, and 5-fold cross-validation approach. Where penalty factor C controls the trade-off between the margin maximization and training error. For large value of C the training error will be reduced. However, excessive increase in the value of penalty factor may risk in losing the generalization properties of the classifier. One vs one classification is preferred over one vs all to ensure adequate ratio between testing and training samples for the dataset.

The experimental results are presented in Table II. The obtained ARA for the dataset is compared with other similar state-of-the-art techniques in Table III. From Table II it is clearly evident that integration of Zernike moment and $\mathcal{R}$ - transform improves the recognition ability of the framework, by making it view insensitive. In Table III, some of the state-of-the-arts [12] [20] [49] have achieved higher recognition accuracy than the proposed framework. The main reason behind is that these works have utilised combination of RGB-D and accelerometric data to encrypt the actions. However, the work [12] has achieved only 90% accuracy while utilising only depth maps.

TABLE II ARA of the Proposed Work for UR Fall Detection Dataset

Activities	Action descriptor	Fall	ADL	ARA (%)
SVM (%)	$\mathcal{R}$ -Transform	94.6%	93.2%	93.9%
	$\mathcal{R}$ -Transform + Zernike moments	95.5%	95.5%	**95.5%**
K-NN (%)	$\mathcal{R}$ -Transform	94.7%		**95.99%**
	$\mathcal{R}$ -Transform + Zernike moments	96%	97%	**96.5%**

1558-1748 (c) 2018 IEEE. Personal use is permitted, but republication/redistribution requires IEEE permission. See http://www.ieee.org/publications_standards/publications/rights/index.html for more information.

This article has been accepted for publication in a future issue of this journal, but has not been fully edited. Content may change prior to final publication. Citation information: DOI 10.1109/JSEN.2019.2903645, IEEE Sensors Journal

TABLE III COMPARISON OF ARA WITH SIMILAR STATE-OF-THE-ART FOR UR FALL DETECTION DATASET

Method	Classifier	Input	ARA
Yun et al. [50]	SVM	RGB + v	96.77%
Kwolek et al. [12]	SVM	Depth maps	90%
	SVM	RGB-D + Accelerometer	94.22
	K-NN	RGBD + Accelerometer	95.71
Goudelis et al. [51]	SVM	RGB-D	87.76%
Zerrouki et al. [20]	SVM	RGB + Accelerometer	96.77%
Zerrouki et al. [49]	SVM-HMM	RGB	96.88%
Marcos et al. [52]	CNN	RGB	95%
Proposed Method	K-NN	Depth maps	96.5%

B. *KARD Dataset*

Gaglio et al. [13] introduced Kinect Activity Recognition Dataset (KARD) in 2015. It is composed of eighteen activities as classified in Fig. 5. Ten different individuals perform each activity three times. Therefore, the dataset consists of 540 ($18 \times 3 \times 10$) sequences captured at 640×480 resolution with 30 fps. For activity recognition K-NN ($K = 5$) and SVM with one vs one, 5-fold cross-validation technique is used. Human action recognition results for KARD dataset are provided in Fig. 5 whereas, Table IV compares the performance of the proposed method with other state-of-the-arts exhibiting the generalisability of the proposed approach with superior accuracy. The recognition accuracy achieved by the proposed algorithm is 96.64%, which is 1.74% better than the recent state-of-the-art Cippitelli et al. [53] that achieved 94.9% recognition.

TABLE IV COMPARISON OF ARA WITH SIMILAR STATE-OF-THE-ARTS FOR KARD DATASET

Method	Classifier	Input Data	ARA (%)
Cippitelli et al. [53]	SVM	Skeleton	94.9%
Gaglio et al. [13]	SVM	Skeleton	94.2%
Madany et al. [54]	ConvNet	skeleton	98.5%
Pham et al. [55]	ResNet-44	Skeleton	99.97%
Proposed method	SVM	Depth	96.64%

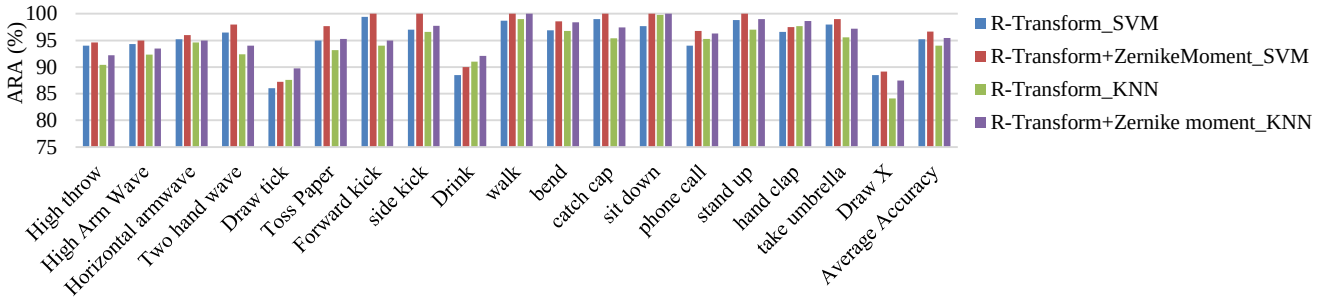
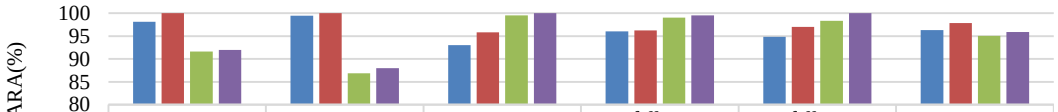


Fig. 5. ARA for KARD dataset using SVM and K-NN



	chest pain	headache	fainting	falling forward	falling backward	overall
R-Transform_SVM	98.1	99.4	93	96	94.8	96.26
R-Transform+Zernike moment_SVM	100	100	95.8	96.2	97	97.8
R-Transform_KNN	91.6	86.9	99.5	99	98.3	95.06
R-Transform+Zernike moment_KNN	92	88	100	99.5	100	95.9

Fig. 6. ARA for AbHA dataset

C. *Abnormal Human Action (AbHA)Dataset*

Abnormal Human Action Dataset (AbHA) [56] includes a novel set of commonly occurring abnormal actions in day-to-day lives of the elderly people such as 'chest pain', 'headache', 'fainting' and 'falling backward' and 'falling forward' as shown in Fig. 7. Due to non-availability of the publicly available dataset for such activities, we generated our own dataset namely AbHA dataset. Which includes five actions, where each action is performed by eight different individuals and repeated two times. Hence, total generated samples are 80 ($8 \times 2 \times 5$). Microsoft's Kinect depth sensor v2 is used to extract fine binary silhouettes by combing both skeleton joint coordinates over depth images. It simplifies the process of background subtraction to obtain binary silhouettes in real time scenario as the Kinect sensor is comparatively insensitive to the noise, clutter and illumination variations. Two third samples are used for training and one third for testing. The classification results on AbHA dataset are presented in Fig. 6. It is clearly observed from Fig. 6 that the recognition rate for a headache and chest pain is 100 % because these actions are highly discriminated while falling forward/fainting/falling backward actions have little less recognition rate due to the substantial resemblance in their postures, which needs to be minimized.

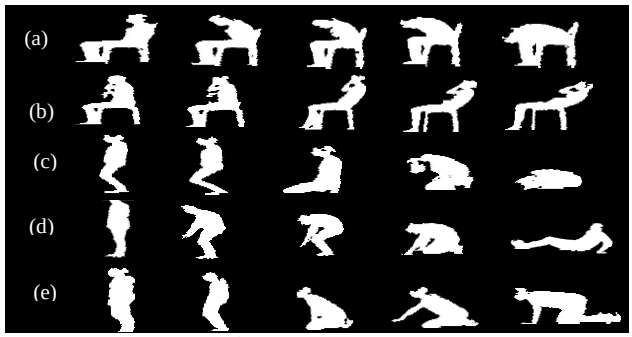


Fig. 7. Binary silhouettes of AbHA dataset (a) chest pain (b) headache (c) fainting (d) falling backward (e) falling forward

D. *NUCLA Multi-view Action dataset*

The NUCLA multi-view action dataset [14] is a collection of RGB-D videos captured from three different

1558-1748 (c) 2018 IEEE. Personal use is permitted, but republication/redistribution requires IEEE permission. See http://www.ieee.org/publications_standards/publications/rights/index.html for more information.

This article has been accepted for publication in a future issue of this journal, but has not been fully edited. Content may change prior to final publication. Citation information: DOI 10.1109/JSEN.2019.2903645, IEEE Sensors Journal

viewpoints: left, front and right, with the Kinect v1 sensor simultaneously. It includes 10 subjects performing 10 actions: pick up with one hand, pick up with two hands, drop trash, walk around, sit down, stand up, donning, doffing, throw, and carry. The three viewpoints are: (a) left, (b) front, and (c) right. The dataset possesses similar actions which makes it very challenging such "pick up with on hand" and "pick up with two hands". For the experiments, two views are used for training and the third view for testing making three possible cross-view combinations.

TABLE V: COMPARISON OF ARA WITH SIMILAR STATE-OF-THE-ARTS ON MULTI-VIEW *NUCLA*

Method	Input	$V^{(3)}$	$V^{(2)}$	$V^{(1)}$	Mean
Li et al. [57]	Depth	58.5	55.2	39.3	51.0
Zhang et al. [58]	Depth	60.6	55.8	39.5	52.0
Rahmani et al. [59]	RGB	75.8	73.3	59.1	69.4
Rahmani et al. [60]	RGB	78.1	-	-	78.1
Liu et al. [61]	RGB-D	91.7	73.0	79.0	81.3
Liu et al. [62]	Skeleton	91.5	85.5	79.2	85.4
Proposed method	$\boldsymbol{\mathcal{R}}$-transfrom_KNN	89	82.4	75	82.13
	Hybrid vector_KNN	91.8	86.1	80.1	86%
	$\boldsymbol{\mathcal{R}}$-transform_SVM	90.6	85.6	79	85.06
	Hybrid vector_SVM	92.0	86.7	80.5	**86.4**

It is observed from the Table V that the view variations of the actions are handled quite well with the integration of Zernike moment with $\boldsymbol{\mathcal{R}}$-transform that improves the performance of the framework by a significant amount 3.87% for K-NN($'K'$=5) and 0.6% for RBF-SVM classifier. Non-linear SVM is optimised for (C, γ) hyper-parameters as (0.99,default) values using one-vs-one, and 5-fold cross-validation. Leave-One-Out (LOO) cross validation technique is used for classification with K-NN classifier.

To verify the real-time performance of the proposed approach the processing time required to generate the feature vector and the time required to test the action sequence is computed and shown in Table VI that shows the processing and testing time involved for action recognition for the proposed framework is superior than [61].

TABLE VI COMPUTATION TIME OF THE PROPOSED FRAMEWORK

Method	Feature vector formation/ action (per video)	Testing time per sample (per video)
Liu et al. [61]	49.1ms	0.68ms
Proposed framework	**0.95ms**	**0.33ms**

V. CONCLUSION

In this paper, a vision based Abnormal Human Action Recognition approach is presented to monitor the daily life actions of elderly people to recognise the abnormal action in order to provide them better services. The proposed framework encrypts an action in terms of AESI image which is rich in the spatio-temporal details and introduce less computational cost. AESI are processed using $\boldsymbol{\mathcal{R}}$-transform and Zernike moments that introduces translational, scale and rotation invariance with appreciable inter-class separation ability. Henceforth, a complete geometrical transformation invariant feature is obtained with less noise sensitivity. The efficacy of the presented approach is validated by using three publically available 3D datasets and our own created dataset. The average recognition accuracy achieved on these datasets are 96.5%, 96.64%, 95.9% and 86.4% on UR fall detection dataset, KARD dataset and new AbHA dataset and multi-view NUCLA dataset, respectively. However, the inter-class similarity between fainting and falling forward needs to be reduced in AbHA dataset.

For future work, the proposed approach can be extended to real-life healthcare applications systems for elderly care at home to improve the quality of life and provide confidence to live an independent life by utilising the stronger action description features of deep architectures.

REFERENCES

[1] G. Tripathi, K. Singh and D. K. Vishwakarma, "Convolutional neural networks for crowd behaviour analysis: a survey," *The Visual Computer*, pp. 1-24, 2018.

[2] J.-W. Hsieh, C.-H. Chuang, S. Alghyaline, H.-F. Chiang and C. H. Chiang, "Abnormal Scene Change Detection From a Moving Camera Using Bag of Patches and Spider Web Map," *IEEE Sensors Journal*, vol. 15, no. 5, pp. 2866-2881, 2015.

[3] W. Sultani, C. Chen and M. Shah, "Real-world Anomaly Detection in Surveillance Videos," in *Conference on Computer Vision and Pattern Recognition*, Long Beach, CA, 2018.

[4] C. Dhiman and D. K. Vishwakarma, "A review of state-of-the-art techniques for abnormal human activity recognition," *Engineering Applications of Artificial Intelligence*, vol. 77, pp. 21-45, 2018.

[5] H.-C. Shih, "A Survey on Content-aware Video Analysis for Sports," *IEEE Transactions on Circuits and Systems for Video Technology*, vol. 28, no. 5, pp. 1212-1231, 2018.

[6] S. Samarah, M. G. A. Zamil, A. F. Aleroud, M. Rawashdeh, M. F. Alhamid and A. Alamri, "An Efficient Activity Recognition Framework: Toward Privacy-Sensitive Health Data Sensing," *IEEE Access*, vol. 5, no. pp, pp. 3848-3859, 2017.

[7] G. Zhu, C. Xu, Q. Huang, Y. Rui, S. Jiang, W. Gao and H. Yao, "Event Tactic Analysis Based on Broadcast Sports Video," *IEEE Transactions on Multimedia*, vol. 11, no. 1, pp. 49-67, 2009.

[8] J. Aggarwal and M. Rayoo, "Human Activity Analysis : A Review," *ACM Computing Surveys*, vol. 43, no. 3, 2011.

[9] L. Wang, Y. Xiong, Z. Wang, Y. Qiao, D. Lin, X. Tang and L. V. Gool, "Temporal Segment Networks: Towards Good Practices for Deep Action Recognition," in *ECCV*, Amsterdam, The Netherlands, 2016.

[10] M. Liua, H. Liua, Q. Suna, T. Zhang and R. Ding, "Salient pairwise spatiotemporal interest points for real-time activity recognition," *CAAI Transactions on Intelligence Technology*, vol. 1, no. 1, pp. 14-29, 2016.

[11] D. K. Vishwakarma and C. Dhiman, "A unifiedmodel for human activity recognition using spatial distribution of gradients and difference of Gaussian kernel," *The Visual Computer*, pp. 1-19, 2018.

[12] B. Kwolek and M. Kepski, "Human fall detection on embedded platform using depth maps and wireless accelerometer," *Computer Methods and Programs in Biomedicine*, vol. 117, no. 3, pp. 489-501, 2014.

[13] S. Gaglio, G. L. Re and M. Morana, "Human Activity Recognition Process Using 3-D Posture Data," *IEEE Transactions on Human-Machine Systems*, vol. 45, no. 5, pp. 586-597, 2015.

[14] J. Wang, B. X. Nie, Y. Xia, Y. Wu and S. C. Zhu, "Cross-view action modeling, learning and recognition," in *CVPR*, Columbus, Ohio, 2014.

[15] X. Yang and Y. Tian, "Super Normal Vector for Human Activity Recognition with Depth Cameras," *Transaction on Pattern Analysis and Machine Intelligence (TPAMI)*, vol. 39, no. 5, pp. 1028-1039, 2017.

[16] S. Gasparrini, E. Cippitelli, E. Gambi, S. Spinsan, J. Wahslen, I. Orhan and T. Lindh, "Proposal and Experimental Evaluation of Fall Detection Solution Based on Wearable and Depth Data Fusion," in *ICT Innovations, Advances in Intelligent Systems and Computing*, Cham, 2015.

[17] Y. Nizam, M. . N. Haji Mohd and M. M. A. Jamil, "A Study on Human Fall Detection Systems: Daily Activity Classification and Sensing Techniques," *International Journal of Integrated Engineering*, vol. 8, no. 1, pp. 35-43, 2016.

1558-1748 (c) 2018 IEEE. Personal use is permitted, but republication/redistribution requires IEEE permission. See http://www.ieee.org/publications_standards/publications/rights/index.html for more information.

This article has been accepted for publication in a future issue of this journal, but has not been fully edited. Content may change prior to final publication. Citation information: DOI 10.1109/JSEN.2019.2903645, IEEE Sensors Journal

[18] Z. Zhang, C. Conly and V. Athitsos, "Evaluating Depth-Based Computer Vision Methods for Fall Detection under Occlusions," in *International Symposium on Visual Computing (ISVC)*, Las Vegas, NV, USA, 2014.

[19] X. Ma, H. Wang, B. Xue, M. Zhou, B. Ji and Y. Li, "Depth-Based Human Fall Detection via Shape Features and Improved Extreme Learning Machine," *IEEE Journal of Biomedical and Health Informatics*, vol. 18, no. 6, pp. 1915-1922, 2014.

[20] N. Zerrouki, F. Harrou, Y. Sun and A. Houacine, "Accelerometer and Camera-Based Strategy for Improved Human Fall Detection," *Journal of Medical Systems*, vol. 40, no. 12, pp. 1-6, 2016.

[21] D. Gafurov, "A survey of biometric gait recognition:Approaches, security and challenges," in *NIK conference*, Oslo, Norway, 2007.

[22] Z. A. Khan and W. Sohn, "A hierarchical abnormal human activity recognition system based on R-transform and kernel discriminant analysis for elderly health care," *Computing*, vol. 95, no. 2, pp. 109-127, 2013.

[23] S. Sadigh, A. Reimers, R. Andersson and L. Laflamme, "Falls and Fall-Related Injuries Among the Elderly: A Survey of Residential-Care Facilities in a Swedish Municipality," *Journal of Community Health*, vol. 29, no. 2, pp. 129-140, 2004.

[24] D. Riboni, G. Civitarese and C. Bettini, "Analysis of Long-term Abnormal Behaviors for Early Detection of Cognitive Decline," in *IEEE International Workshop on Pervasive Technologies and care systems for sustainable Aging-in-place*, Sydney, 2016.

[25] Y. Lee, H. Yeh, K.-H. Kim and O. Choi, "A real-time fall detection system based on the acceleration sensor of smartphone," *International Journal of Engineering Buisness Management*, vol. 10, pp. 1-8, 2018.

[26] C. Rougier, J. Meunier, A. St-Arnaud and J. Rousseau, "Robust Video Surveillance for Fall Detection Based on Human Shape Deformation," *IEEE Transactions on circuits and systems for video technology*, vol. 21, no. 5, pp. 611-622, 2011.

[27] S. Belongie, J. Malik and . J. Puzicha, "Shape Matching and Object Recognition Using Shape Contexts," *IEEE Transactions on Pattern Analysis and Machine Intelligence*, vol. 24, no. 2, pp. 509-522, 2002.

[28] X. Tao and . Z. Yun, "Fall prediction based on biomechanics equilibrium using Kinect," *International Journal of Distributed Sensor Networks*, vol. 13, no. 4, 2017.

[29] C. Yuan, X. Li, W. Hu, H. Ling and S. Maybank, "3D R Transform on Spatio-temporal Interest Points for Action Recognition," in *CVPR*, Portland, OR, USA, 2013.

[30] D. K. Vishwakarma, R. Kapoor and A. Dhiman, "Unified framework for human activity recognition: An approach using spatial edge distribution and R-transform," *AEU-International Journal of Electronics and Communications*, vol. 70, no. 3, pp. 341-353, 2016.

[31] H. Aggarwal and D. K. Vishwakarma, "Covariate conscious approach for Gait recognition based upon Zernike moment invariants," *IEEE Transactions on Cognitive and Developmental Systems*, vol. 10, no. 2, pp. 397-407, 2018.

[32] I. M. Sintorn and G. Kylberg, "Regional Zernike moments for texture recognition," in *International Conference on Pattern Recognition (ICPR2012)*, Tsukuba, 2012.

[33] S. Li, M. C. Lee and C. M. Pun, "Complex Zernike Moments Features for Shape-Based Image Retrieval," *IEEE Transactions on Systems, Man, and Cybernetics - Part A: Systems and Humans*, vol. 39, no. 1, pp. 227-237, 2009.

[34] S. Abdelhedi, A. Wali and A. M. Alimi, "Human activity recognition based on mid-level representations in video surveillance applications," in *International Joint Conference on Neural Networks (IJCNN)*, Vancouver, BC, 2016.

[35] Z. A. Khan and W. Sohn, "Abnormal Human Activity Recognition System based on R-Transform and Kernel Discriminant Technique for Elederly Home Care," *IEEE Transactions on Consumer Electronics*, vol. 57, no. 4, pp. 1843-1850, 2011.

[36] M. Ahmad and S.-W. Lee, "Variable silhouette energy image representations for recognizing human actions," *Image and Vision Computing*, vol. 28, pp. 814-824, 2010.

[37] C. Chen, K. Liu and N. Kehtarnavaz, "Real-time human action recognition based on depth motion maps," *Journal of Real-Time Image Processing*, vol. 12, no. 1, pp. 155-163, 2016.

[38] C. Chen, R. Jafari and N. Kehtarnavaz, "Action Recognition from Depth Sequences Using Depth Motion Maps-based Local Binary Patterns," in *Winter Conference on Applications of Computer Vision*, Hawaii, USA, 2015.

[39] C. Chen, M. Liu, B. Zhang, J. Han, J. Jiang and H. Liu, "3D Action Recognition Using Multi-temporal Depth Motion Maps and Fisher Vector," in *International Joint Conference on Artificial Intelligence*, New York, US, 2016.

[40] M. Liu, H. Liu and C. Chen, "Robust 3D Action Recognition Through Sampling Local Appearances and Global Distributions," *IEEE Transactions on Multimedia*, vol. 20, no. 8, pp. 1932-1947, 2018.

[41] P. Wang, W. Li, Z. Gao, J. Zhang, C. Tang and P. O. Ogunbona, "Action Recognition From Depth Maps Using Deep Convolutional Neural Network," *IEEE Transactions on Human-Machine Systems*, vol. 46, no. 4, pp. 498-509, 2016.

[42] G. Blumrosen, Y. Miron, N. Intrator and M. Plotnik, "Real-Time Kinect Signature-Based Patient Home Monitoring System," *Sensors*, vol. 16, no. 11, pp. 1-21, 2016.

[43] M. Munaro, F. Basso and E. Menega, "OpenPTrack: Open source multi-camera calibration and people tracking for RGB-D camera networks," *Robotics and Autonomous Systems*, vol. 75, pp. 525-538, 2016.

[44] S. E. Wei, V. Ramakrishna, T. Kanade and Y. Sheikh, "Convolutional pose machines," in *CVPR*, Las Vegas, US, 2016.

[45] Z. Cao , T. Simon, S. E. Wei and Y. Sheikh, "Openpose: Real time Multi-Person 2D Pose Estimation Using Part Affinity Fields," in *CVPR*, Hawaii, 2017.

[46] S. Tabbone, L. Wendling and J. -P. Salmon, "A new shape descriptor defined on the Radon transform," *Computer Vision and Image Understanding*, vol. 102, no. 1, pp. 42-51, 2006.

[47] F.Zernike, "Beugungstheorie des schneidenver-fahrens und seiner," in *Physica*, vol. 1, 1934, pp. 689-704.

[48] S. Jin, . S. Li, P. Sun and W. Cai, "Zernike moment based time sensitive targets detection and recognition," in *IEEE Chinese Guidance, Navigation and Control Conference*, Nanjing, 2016.

[49] N. Zerrouki and A. Houacine, "Combined curvelets and hidden Markov models for human fall detection," *Multimedia Tools and Applications*, vol. 77, pp. 6405-6424, 2018.

[50] Y. Yun and I. Y.-H. Gu, "Human fall detection via shape analysis on Riemannian manifolds with applications to elderly care," in *IEEE International Conference on Image Processing*, Quebec City, QC, Canada, 2015.

[51] G. Goudelis, G. Tsatiris, K. Karpouzis and S. Kollias, "Fall detection using History Triple Features," in *Proceedings of the 8th ACM International Conference on Pervasive Technologies Related to Assistive Environments*, Corfu, Greece, 2015.

[52] A. N. Marcos, G. Azkune and I. C. Arganda, "Vision-Based Fall Detection with Convolutional Neural Networks," *Wireless Communications and Mobile Computing*, 2017.

[53] E. Cippitelli, S. Gasparrini, E. Gambi and S. Spinsante, "A Human Activity Recognition System Using Skeleton Data from RGBD Sensors," *Computational Intelligence and Neuroscience*, vol. 3, pp. 1-14, 2016.

[54] N. E. D. E. Madany, Y. He and L. Guan, "Integrating Entropy Skeleton Motion Maps and Convolutional Neural Networks for Human Action Recognition," in *International Conference on Multimedia and Expo* , San Diego, CA, USA, 2018.

[55] H. H. Pham, L. Khoudoura, P. Zegersc and S. A. Velastin, "Exploiting deep residual networks for human action recognition from skeletal data," *Computer Vision and Image Understanding*, 2018.

[56] D. K. Vishwakarma, "Datasets," Delhi Technological University, 2018. [Online]. Available: http://www.dtu.ac.in/Web/Departments/InformationTechnology/faculty/dkvishwakarma.php.

[57] R. Li and . T. Zickler, "Discriminative virtual views for crossview action recognition," in *CVPR*, Providence, 2012.

[58] Z. Zhang, . C. Wang, B. Xiao, . W. Zhou, S. Liu and C. Shi, "Cross-view action recognition via a continuous virtual path," in *CVPR*, 2013.

[59] H. Rahmani and A. Mian, "Learning a non-linear knowledge transfer model for cross-view action recognition," in *CVPR*, 2015.

[60] H. Rahmani, A. Mian and M. Shah, "Learning a deep model for human action recognition from novel viewpoints," *PAMI*, 2017.

[61] J. Liu and A. S. Mian, "Learning Human Pose Models from Synthesized Data for Robust RGB-D Action," *CoRR*, vol. arXiv:1707.00823v2, 2017.

[62] J. Liu, N. Akhtar and . A. Mian, "Skepxels: Spatio-temporal Image Representation of Human Skeleton Joints for Action Recognition," *CoRR*, vol. arXiv:1711.05941v4, 2018.

1558-1748 (c) 2018 IEEE. Personal use is permitted, but republication/redistribution requires IEEE permission. See http://www.ieee.org/publications_standards/publications/rights/index.html for more information.

University of Massachusetts Amherst
ScholarWorks@UMass Amherst

Masters Theses | Dissertations and Theses

2019

Ammonia Production from a Non-Grid Connected Floating Offshore Wind-Farm: A System-Level Techno-Economic Review

Vismay V. Parmar
University of Massachusetts Amherst

Follow this and additional works at: https://scholarworks.umass.edu/masters_theses_2

 Part of the Energy Systems Commons

Recommended Citation
Parmar, Vismay V., "Ammonia Production from a Non-Grid Connected Floating Offshore Wind-Farm: A System-Level Techno-Economic Review" (2019). *Masters Theses*. 750.
https://scholarworks.umass.edu/masters_theses_2/750

This Open Access Thesis is brought to you for free and open access by the Dissertations and Theses at ScholarWorks@UMass Amherst. It has been accepted for inclusion in Masters Theses by an authorized administrator of ScholarWorks@UMass Amherst. For more information, please contact scholarworks@library.umass.edu.

Ammonia Production From A Non-Grid Connected Floating Offshore Wind-Farm: A System-Level Techno-Economic Review

A Thesis Presented

By

VISMAY V. PARMAR

Submitted to the Graduate School of the

University of Massachusetts Amherst in partial fulfillment

of the requirements for the degree

MASTER OF SCIENCE IN MECHANICAL ENGINEERING

February 2019

Mechanical and Industrial Engineering

© Copyright by Vismay V. Parmar 2019

All Rights Reserved

Ammonia Production From A Non-Grid Connected Floating Offshore Wind-Farm: A System-Level Techno-Economic Review

A Thesis Presented

By

VISMAY V. PARMAR

Approved as to style and content by:

Jon G. McGowan, Chair

James F. Manwell, Member

Bernd F. Schliemann, Member

Sundar Krishnamurty, Department Head
Mechanical and Industrial Engineering

DEDICATION

To my parents and my sister
for their love and inspiration

ACKNOWLEDGMENTS

I would like to express my sincere gratitude to Prof. Jon McGowan to give me the opportunity to work on this thesis. It would not have been possible to complete this thesis without his exceptional direction and invaluable insights.

I would also like to thank my committee members Prof. James Manwell and Prof. Bernd Schliemann. They challenged me with intriguing questions which allowed me to explore my research abilities.

I would also like to show my appreciation to my family, for their love and support and their belief in me. Working on this thesis was a great learning experience and I sincerely appreciate all the people who made it possible.

ABSTRACT

AMMONIA PRODUCTION FROM A NON-GRID CONNECTED FLOATING OFFSHORE WIND-FARM:
A SYSTEM-LEVEL TECHNO-ECONOMIC REVIEW

FEBRUARY 2019

VISMAY V. PARMAR

B.Tech, DELHI TECHNOLOGICAL UNIVERSITY, INDIA

M.S.M.E., UNIVERSITY OF MASSACHUSETTS AMHERST

Directed by: Professor Jon G. McGowan

According to U.S. Department of Energy, offshore wind energy has the potential to generate 7,200 TWh of energy annually, which is nearly twice the current annual energy consumption in the United States. With technical advances in the offshore wind industry, particularly in the floating platforms, windfarms are pushing further into the ocean. This creates new engineering challenges for transmission of energy from offshore site to onshore. One possible solution is to convert the energy produced into chemical energy of ammonia, which was investigated by Dr. Eric Morgan. In his doctoral dissertation, he assessed the technical requirements and economics of a 300 tons/day capacity ammonia plant powered by offshore wind. However, in his dissertation, one of the assumptions was connection to the grid which provided auxiliary power to keep the ammonia plant operational and produce at rated capacity. It also allowed selling of excess power to the grid in the scenario of excess power production by wind farm during high winds.

This thesis explores the technical and economical feasibility of a similar system, except that the ammonia plant will be on a plantship and there is no connection to the grid. This creates a challenge as the ammonia synthesis plant must operate between 65-100% loads. Thus, the concept of multiple mini-ammonia plants is used to address the scenario of wind energy production at less than rated power. This will allow operation of one or more mini-ammonia plant (corresponding to the available energy from offshore wind). In the event of wind speed lower than the cutoff wind speed for the turbine, the ammonia plant will use the produced ammonia as fuel, with the help of a gas turbine running on either Brayton

cycle or combined cycle, to keep the plant idling. It will maintain the reaction conditions of the synthesis chamber and will not produce any ammonia. This is an important step as it takes days to reach the reaction conditions to start ammonia production again after shutting down due to unavailability of energy at low winds. Thus, at any windspeed, a mini-ammonia plant would either idle or operate between 65-100% load. This model will be used to simulate the total energy consumption, total energy captured by the wind farm, and the total ammonia produced. This will further help in assessing the final cost of producing, transporting, and consuming ammonia as fuel and thereby provide a better understanding of the feasibility of implementing this technology.

CONTENTS

Page

ACKNOWLEDGMENTS v

ABSTRACT vi

LIST OF TABLES x

LIST OF FIGURES xi

CHAPTER

1 THESIS DESCRIPTION 1

2 BACKGROUND 6
- 2.1 Overview of current technological and cost trends in offshore wind sector in United States 6
- 2.2 Challenges developing in the energy transmission of offshore wind and potential solutions 10
- 2.3 Using ammonia as energy storage medium 11
- 2.4 Combustion of Ammonia 12
- 2.5 Storage of Ammonia 14
- 2.6 Summary 14

3 CALCULATION OF NET AMMONIA PRODUCTION 16
- 3.1 Wind Conditions at the Site 16
- 3.2 Wind Turbine Power Curve 19
- 3.3 Capacity Factor at the Site 20
- 3.4 Size of the Windfarm 22
  - 3.4.1 Number of turbines 22
  - 3.4.2 Arrangement of Wind Turbines 23
- 3.5 Energy Flow from Windfarm to the Ammonia Plant 24
  - 3.5.1 Energy control algorithm 24
  - 3.5.2 Energy extracted from ammonia: 26
- 3.6 Sensitivity Analysis 26
  - 3.6.1 Effect of no of divisions of ammonia plant on annual ammonia production 26
  - 3.6.2 Effect of ammonia gas turbine cycle efficiency 28
- 3.7 Summary 29

4 ECONOMICS OF BASELINE NH_3-OFFSHORE WINDFARM 31
4.1 Capital Costs 31
4.1.1 Offshore Windfarm 32
4.1.2 All-Electric Ammonia Plant 33
4.1.3 Electrolyzer Scaling 35
4.1.4 Total Capital Expenditure of the All-Electric Ammonia Plant 37
4.1.5 Ammonia Powered Gas Turbine Cycle 38
4.1.6 Platform for the All-Electric Ammonia Plant 39
4.2 Operations and Maintenance Costs 40
4.2.1 O & M Costs of he offshore windfarm and the all-electric ammonia plant 40
4.2.2 Transportation Costs 40
4.3 Calculation of Levelized Cost of Ammonia 40
4.3.1 LCOA vs no of divisions of ammonia synthesis loop 42
4.3.2 LCOA vs cost of ammonia powered gas turbine cycle 43
4.3.3 LCOA vs per kW cost of the wind turbine 46

5 RESULTS AND DISCUSSIONS 47

6 FUTURE WORK 49

APPENDICES

APPENDIX A MATLAB MODEL FOR ANNUAL AMMONIA PRODUCTION AND LCOA 50

APPENDIX B MATLAB MODEL FOR CALCULATION OF CAPACITY FACTOR AS A FUNCTION OF AVERAGE WINDSPEED, RATED WINDSPEED AND K = 2.5 58

APPENDIX C MATLAB MODEL FOR CALCULATION OF GRASSROOT COST OF AMMONIA SYNTHESIS LOOP IN 2013 DOLLARS 59

APPENDIX D MATLAB MODEL FOR CALCULATION OF CAPITAL COSTS OF SCALED ELECTROLYZERS SYSTEM 60

BIBLIOGRAPHY 61

LIST OF TABLES

Table Page

4.1 Total Capital Expenditures for the offshore wind turbine with semi-submergible floating structure 32

LIST OF FIGURES

Figure Page

1.1 Flow-chart showing the flow of offshore wind to ammonia production and its utilization . . . 3
1.2 Anhydrous ammonia pipelines . . . 4

2.1 U.S. offshore wind projects . . . 7
2.2 Comparison of rotor diameter and hub height with respect to the production capacity . . . 8
2.3 Offshore wind projects corresponding to different platforms . . . 9
2.4 Water depth along the coast of corresponding states and offshore wind energy potential. . . . 9
2.5 Different methods to utilize anhydrous ammonia. . . . 13

3.1 Offshore wind map of the United States. . . . 17
3.2 Offshore wind map of Massachusetts . . . 18
3.3 Weibull wind distribution for a year . . . 19
3.4 Power Curve comparison btw W2E-151-4.5 and W2E-164-4.5 machines . . . 20
3.5 Capacity Factor as a function of rated windspeed, average windspeed and weibull shape parameter . . . 21
3.6 Capacity Factor trendline with windspeed . . . 21
3.7 Schematic of a windfarm. . . . 24
3.8 Effect of number of divisions of ammonia synthesis loop on the ammonia production curve . . . 27
3.9 Effect of number of divisions of ammonia plant on the annual ammonia production . . . 28
3.10 Effect of efficiency of ammonia powered gas turbine cycle on the annual ammonia production . . . 29

4.1 Cost of ammonia synthesis loop vs Ammonia plant capacity . . . 34
4.2 Cost of ammonia synthesis loop vs No of divisions . . . 35
4.3 Ratio of capital cost of ammonia plant with electrolyzer scaling to the one without scaling vs No of divisions of ammonia synthesis loop . . . 36
4.4 Total capital expenditures based on the ammonia plant capacity . . . 37
4.5 Total capital expenditures of the ammonia plant as a function of ammonia plant capacity . . . 38
4.6 Capacity weighted average costs for major energy sources . . . 39
4.7 Capital cost of the offshore all-electric ammonia production facility vs no of divisions of ammonia synthesis loop . . . 42
4.8 LCOA vs no of divisions of ammonia synthesis loop . . . 43

4.9 LCOA vs Capital Expenditure per kW of the ammonia powered gas turbine cycle 44
4.10 LCOA vs Efficiency of the ammonia powered gas turbine cycle 45
4.11 LCOA vs pew kW capital cost of the turbine 46

CHAPTER 1

THESIS DESCRIPTION

The doctoral thesis by Eric Morgan investigated the technical and economic requirements of ammonia production by 300MW wind farm located near shore in Gulf of Maine [1]. It was connected to the grid in case the wind speed is not high enough to generate any power from the turbines. The wind farm consisted of 100 3MW wind turbines, whose size, diameter, rated speed and hub height were similar to Vestas 3MW and WinWinD 3MW turbine model. However, for this thesis, the turbine model selected will be the latest Wind 2 Energy W2E-151-4.5MW turbine. In addition, there is no auxiliary power support as the only source of energy for the operation of ammonia plant will be the offshore wind farm. In case of low wind speed, a part of stored ammonia will be used in Brayton cycle or combined cycle engine and allow idling of the ammonia plant. Therefore, the question of how much ammonia can be shipped back becomes necessary to answer. The levelized cost of energy was three and half times compared to ammonia produced from natural gas in Morgan's thesis. Using the same methods for calculating ammonia production energy requirements, wind farm energy production, cost scaling, and levelized cost of energy, this thesis aims at a more precise quantitative analysis of the costs and physical dimensions of the ammonia plant powered by wind farm and a more complete and updated picture of the work started by Dr. Eric Morgan.

The United States has a huge offshore wind resource. Utilizing all the resource seems improbable but maximizing it in an engineering sense can possibly be achieved by employing ammonia as an energy storage medium. Why ammonia? Ammonia plants are

already operational at industrial level. It is easy to manufacture, store and transport with modern technologies.

The thesis is divided into several sub-parts parts to get a better understanding of the practicality of the proposed solution for energy transportation.

First, the physical picture of the project is defined. The size of the ammonia plant will be such that it produces at least 300 tons per day. The plant will be constructed on a barge which will be termed as "Ammonia Plantships". This is the same concept used by E.J Francis of Johns Hopkins University/Applied Physics Lab in 1977, to convert the ocean thermal energy to ammonia and ship it back to shore [2]. In a way, this thesis reflects a similar approach, except it encounters higher complexity due to higher relative uncertainty of offshore wind.

According to Transition to Renewable Energy Systems by Detlef Stolten and Viktor Scherer (2013), ammonia synthesis plant can be operated between 65 – 100% load [3]. This means there will be no ammonia production when the energy produced from the offshore wind farm is less than the energy required to run ammonia plant at 65% part-load. This will result in wastage of the power generated from offshore wind if it is not sufficient to produce ammonia.

To address this, the 300 tons/day requirement can be achieved by usage of "n" number of ammonia synthesis plants. For example, 6 plants of 50 tons/day capacity could be used. This will result in lower energy threshold to overcome and thus, ammonia can be produced even at lower power generation from wind turbines.

For example, the 300 tons/day ammonia capacity of plant can be achieved through six 50 tons/day plant. This will lower the threshold energy to overcome to about 24 MW. If the assumed rated speed of the turbine is 11 m/s, then the first 50 tons/day ammonia plant should start producing ammonia at around 6 m/s. This calculation doesn't consider

the capacity factor of the wind turbine.

Secondly, based on weibull statistical distribution of wind, the total energy captured by the wind farm is calculated. Using this energy, the ammonia synthesis plant will manufacture ammonia using state of the art technologies. The electrical energy from wind farm will desalinate sea water and the distilled water produced will run through the electrolyzers which will produce hydrogen gas. To produce nitrogen, air separation method is used. Hydrogen is compressed at around 150 to 250 bars in compressors. The next step is to feed the produced hydrogen and nitrogen in an ammonia synthesis loop, which is a continuous cycle of gases that travel at high temperature and pressure through an adiabatic reactor. A pictorial representation of the above-mentioned process is given in figure 1.1

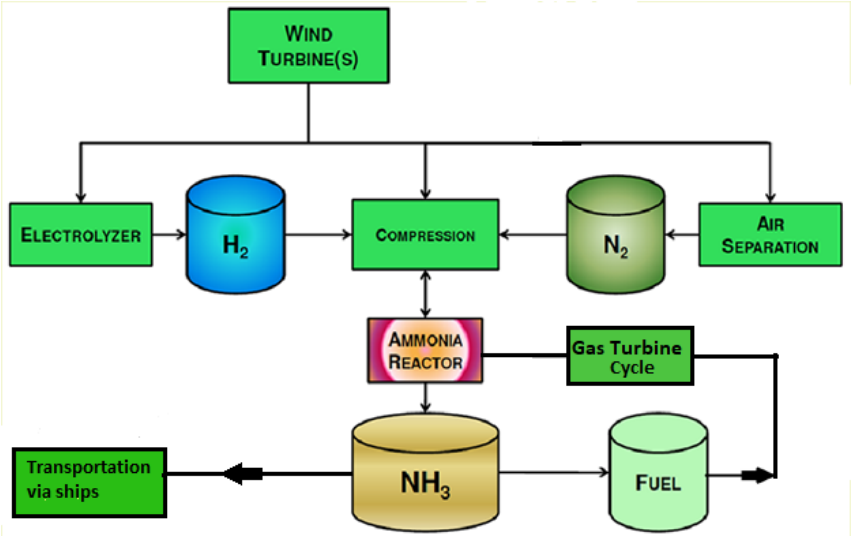


Figure 1.1: Flow-chart showing the flow of offshore wind to ammonia production and its utilization [1]

Once ammonia is produced, it will be stored in pressurized vessels or refrigerated compartments. This will then be transported back to shore via ships or barges. The proposed model incorporates the use of the produced ammonia to keep the plant idling in case of no wind power generation. In this case, idling means there will be no ammonia production, but energy will be supplied from the produced ammonia to maintain of the temperature and pressure of the ammonia synthesis chamber. This step is necessary because it will take days to to restart the plant because of time consumed in regenerating the catalyst used in

the Haber-Bosch process [3], which in turn will make the project less economically viable. Power required for this process will be provided by combusting ammonia through a gas turbine using Brayton/combined cycle. Hence, it is necessary to keep some amount of ammonia on the plant for such scenario.

The next aspect of the thesis is the transportation of the produced ammonia back to shore for its use as either fuel or fertilizer. From the offshore site, ammonia can be brought onshore via ships or barges. Ammonia is regularly transported through ships and the standard transportation cost can be determined [4]. For example, currently, there are 31 barge fleets operational in the United States [4]. Once the ammonia is brought onshore, further delivery can be done through pipelines or, railroads and trucks, in a refrigerated or pressurized tank. There are two pipelines which deliver ammonia as shown in figure 1.2.



Figure 1.2: Anhydrous ammonia pipelines [4]

One is Magellan Ammonia pipeline, extending from Texas to Minnesota and is 1,100 miles long with 20 terminals and delivers 900,000 tons of ammonia per year. Other is the

Kaneb Pipeline, which extends from Louisiana to Nebraska and Indiana with a length of 2,000 miles and delivering 2 million tons per year [4]. Tariffs on the Kaneb pipeline average around $0.026/ton/mile in 2006 dollars. Converting this value to a price of transporting hydrogen, the cost becomes $0.10/kgH2/1000km in 2006 dollars [5].

After delivered, it can be used either as fertilizer or as fuel. However, direct combustion of ammonia in a gas turbine has not been developed at industrial level and that is why, the cost will be quite sensitive to future technologies.

CHAPTER 2

BACKGROUND

2.1 Overview of current technological and cost trends in offshore wind sector in United States

This section is largely summarized by report published by Department of Energy (Office of Energy Efficiency and Renewable Energy) [6] in 2016. The report is aimed at providing information relevant to domestic offshore wind industry market, its challenges and corresponding opportunities. Using this report, the ongoing projects and how the offshore wind market and technology is shaping up can be determined.

According to this report, the global installed capacity of offshore wind is 12,913 MW of commissioned capacity from 111 projects. The 593 ongoing projects indicate that the development capacity of the offshore wind is around 231,000 MW. In the United States, the 28 proposed projects have potential to develop 24,135 MW. Of the 28 projects, developers have full control over the site for 18 sites totaling to 14,785 MW of potential capacity as shown in figure 2.1.

The offshore wind technology is moving towards larger wind turbines and floating wind turbines. For example, the completion of the Burbo Bank Extension project (United Kingdom) in early 2017 was the first commercial project to use a Vestas 164-meter rotor, 8-MW turbine (V164-8 MW) that was first prototyped in 2014. In addition, an upgraded V164 prototype 9.5-MW turbine was debuted in 2017 (Mitsubishi Heavy Industries [MHI]

Vestas Offshore 2017b; Weston 2017a; de Vries 2017). It can be observed from the figure 2.2 that average global wind turbine size in 2015 was 3.4 MW, which increased to 4.7 MW in 2017, and is expected to cross 7 MW by 2021 [6]. The preference is shifting towards larger turbines because it provides provisions for fewer installations and eventually fewer machines to operate and maintain, which can help significantly in lowering wind energy production costs.

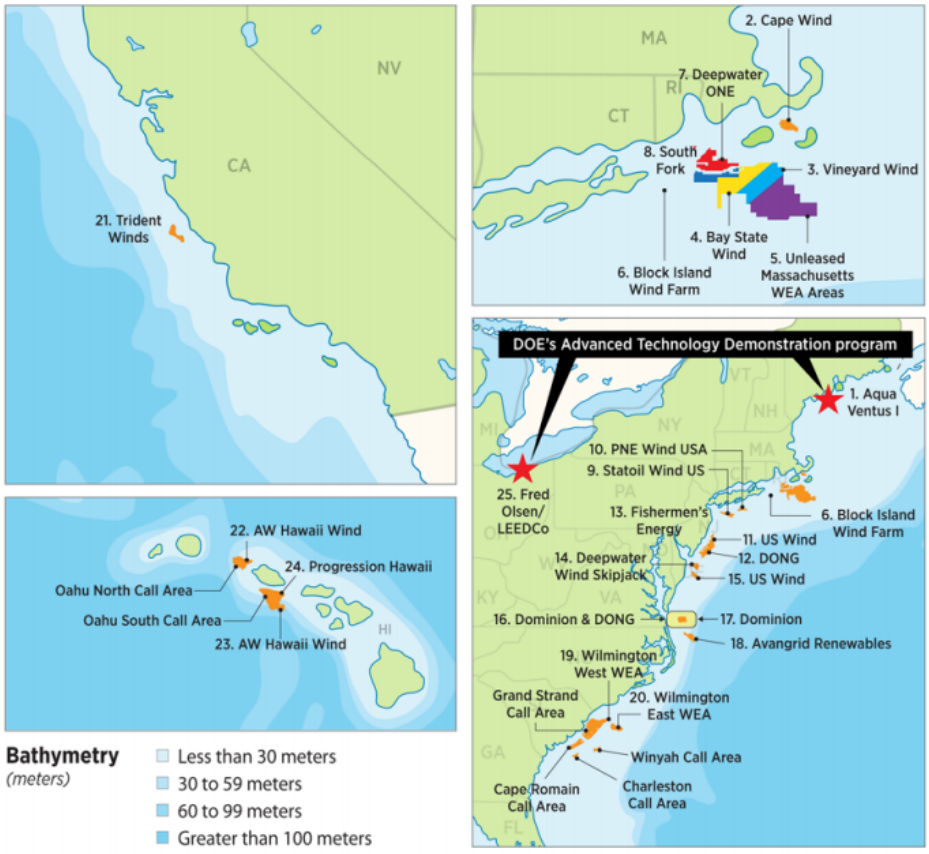


Figure 2.1: U.S. offshore wind projects [6]

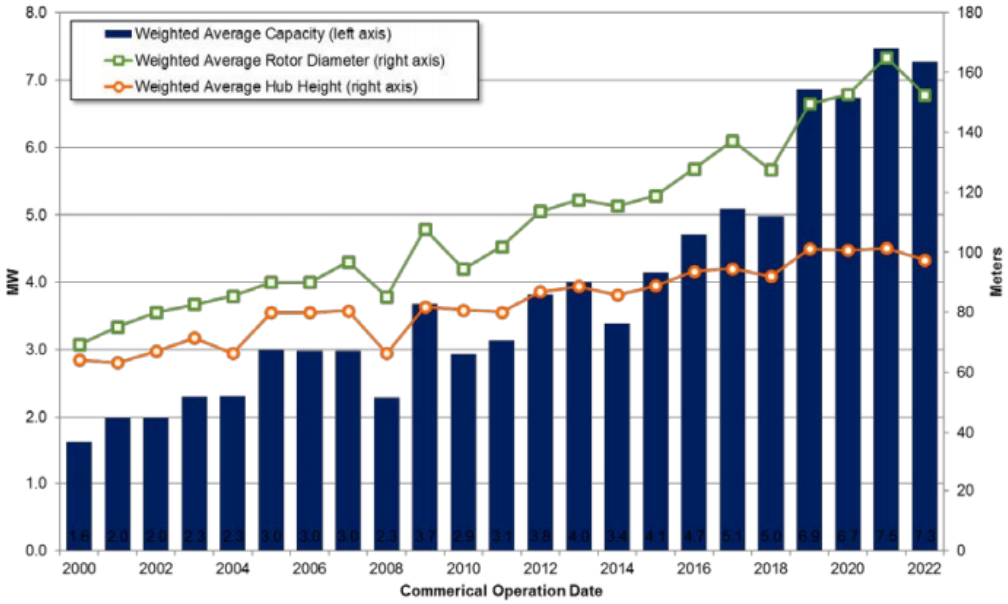


Figure 2.2: Comparison of rotor diameter and hub height with respect to the production capacity. [6]

Another remarkable aspect of this report suggests the shift towards floating wind turbines. The ongoing projects indicate tripling in the installation capacity for floating offshore wind farms to nearly 3000 MW. The global floating offshore wind pipeline has reached 2,905 MW in 2016, with 26 announced projects including 21 demonstration/pilot-scale projects, as well as the five commercial-scale projects in Hawaii, California, and France.

As can be seen from figure 2.4, the offshore wind resource is stronger in areas of deep waters and the use of floating platform wind farms will be pivotal to exploit this resource. There are 11 individual pre-commercial floating projects totaling 229 MW in capacity that have advanced past the planning phase and are either under construction, approved, or have significant resources committed for project development.

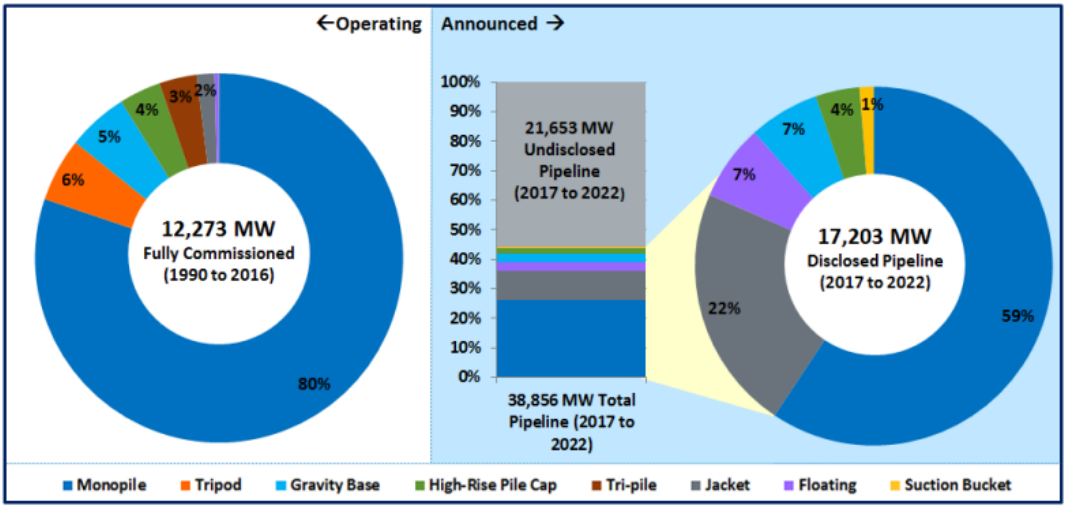


Figure 2.3: Offshore wind projects corresponding to different platforms. [6]

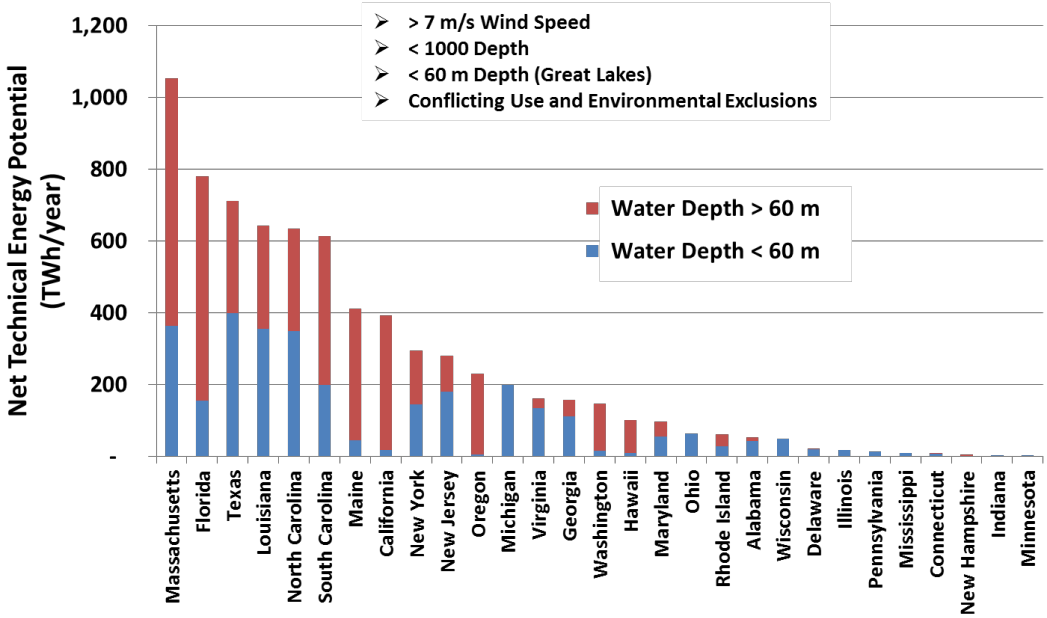


Figure 2.4: Water depth along the coast of corresponding states and offshore wind energy potential. [7]

In summary, it can be derived that there is vast offshore wind resource along the coast of United States. The untapped wind resource is much higher in the deeper waters and further away from the shore. The technology shift in the offshore market indicate that floating platform wind farms will be pivotal in exploiting the offshore wind resource in

regions with deeper water and further away from the shore. It is also a point to note that the design of turbines is shifting to higher power levels.

2.2 Challenges developing in the energy transmission of offshore wind and potential solutions

With distance from the shore increasing, there arise new challenges in transmission. AC electric transmission is no longer economically and efficiency viable owing to large reactive power losses [8]. That paves way to High Voltage Direct Current (HVDC) transmission [9]. But another approach is chemical energy transmission via ammonia, which will be investigated in this thesis. This idea of chemical energy transmission using ammonia is not new and was investigated for OTEC (Ocean Thermal Energy Conversion) in 1977 by E.J Francis and his team in Applied Physics Lab at Johns Hopkins University, where ammonia plant-ships were used to extract thermal energy from oceans and convert to anhydrous ammonia [2].

Other chemicals which can be considered to address energy storage and transmission of offshore wind energy are methanol, hydrogen peroxide, chlorine, sodium hydroxide (caustic soda), and hydrochloric acid. From these, all can be manufactured using electrolysis of sea water except methanol (including other hydrocarbons), because it requires a carbon source [2]. Chlorine, sodium hydroxide, and hydrochloric acid have lower value as energy. They have high production energy demand and would take more number of synthesis plants to saturate existing markets. Hydrogen peroxide production is inefficient and has a low efficiency as combustion booster or energy source [2]. Thus, ammonia and hydrogen can be considered the most promising chemicals to transport the offshore wind to the place of end usage. The physical characteristics of hydrogen, such as low energy density, embrittlement of metals, difficulty in storage and transportation, makes hydrogen a challenging fuel to use. However, with advanced infrastructure already in place to transport ammonia, like pipelines, refrigerated barge, railroads, and trucks, ammonia is chosen

as the suitable chemical for this energy delivery system.

The properties of ammonia which advocate its selection are mentioned below:

- Carbon-free, thus combustion does not produce greenhouse gases [10]
- Ammonia combustion products are pure water and nitrogen [11]
- High energy-density fuel: Properties of ammonia are similar to propane and it can be stored at 17 bars pressure at room temperature. At this pressure it has energy density of 13.77 MJ/L. At the same pressure, that of hydrogen is 0.20 MJ/L. The highest energy-density of hydrogen that can be achieved is 9.98 MJ/L but it is at a temperature of -253 °C [12]
- Currently used as fertilizer to supply nitrogen in plants and is therefore the second most produced chemical in the world [13]

2.3 Using ammonia as energy storage medium

The tecno-economic analysis done in the report "Ocean Thermal Plantships for Production of Ammonia as the Hydrogen Carriers " by C.B. Panchal et. al. conducted by Argonne National Laboratory in 2009 [14], aligns significantly with the design methods to be applied in this thesis. Fundamental difference between that report and this thesis is between the source of energy for the ammonia plant. In Panchal's case, it is ocean thermal energy, whose availability is reliable and almost constant throughout the year. Hence, there will no additional requirement for a backup power source to produce ammonia.

Regardless, this report can be used to determine or extrapolate the physical dimensions of the ammonia plantship proposed for this thesis. The conceptual design of plantship was determined for 265 metric tons per day (MTD) ammonia plant. Considering that the proposed size of ammonia in this thesis is 300 MTD, a reasonable estimate of the dimension of the plant can be scaled. In addition to the dimensions, this literature gives great in-

sight into the day-to-day working of such a plant and recommendations for improving the design with compact aluminum heat exchangers. It also gives directions to implement a commercial scale offshore ammonia plant with capacity of 2600 MTD. And finally, using Department of Energy's H2A model, economic analysis was done to develop itemized cost estimates of for major components and subsystems. This approach, combined with the one given in Morgan's thesis will help in developing cost estimates model for the project. Morgan's cost estimates models were used to develop the economic model for the offshore wind farm and majority of the components of the ammonia plant. However, the underlying approach adopted by CB Panchal in this report will be used to determine costs of the components which were not included in Morgan's model, and achieve an estimate within reasonable accuracy.

In summary, the techno-economical model derived from Morgan(2013) and the plantship design derived from Panchal et. al (2009) form major part of this thesis.

2.4 Combustion of Ammonia

One of the primary reasons behind selecting ammonia as the energy carrier is that the combustion of ammonia yields nitrogen and pure water. This means that in theory, combustion of ammonia is pure and does not produce any greenhouse gases. However, while carrying out the process in actual conditions, some amount of nitrogen oxides production is expected. Combustion of ammonia is also limited in terms of industrial level power production due to the following reasons:

- Low flame speed ($\frac{1}{5^{th}}$ that of methane) [10]
- High ignition temperature 651°C [15]

To address these challenges, Prof. Hideaki Kobayashi of Institute of Fluid Science at Tohoku University in Sendai, Japan, has developed the world's first technology for direct combustion of ammonia in a gas turbine. He applied the use of swirl flow device causing spiral motion of the gases in the combustion chamber. This allowed a better control of the

flow of the ammonia-air mixture. With the help of the device, the swirl flow was created both horizontally and vertically leading to a longer distance of flame stability. Using this concept, his team was able to reach output 41.8 kW using ammonia-methane mixture [10]. Subsequently, they were able to reach the same output using 100% ammonia [10].

However, it is not technologically feasible at this stage in development to scale up from 50 kW to industrial capacity of MW in one step. But with the equipment available to the industries, there is a high probability to use ammonia combustion to generate MWs of power [10].

According to an article published in September 2017 in American Chemical Society by Giddey et. al [16], figure 2.5 can provide a good source of understanding for ammonia utilization at the site of end-use:

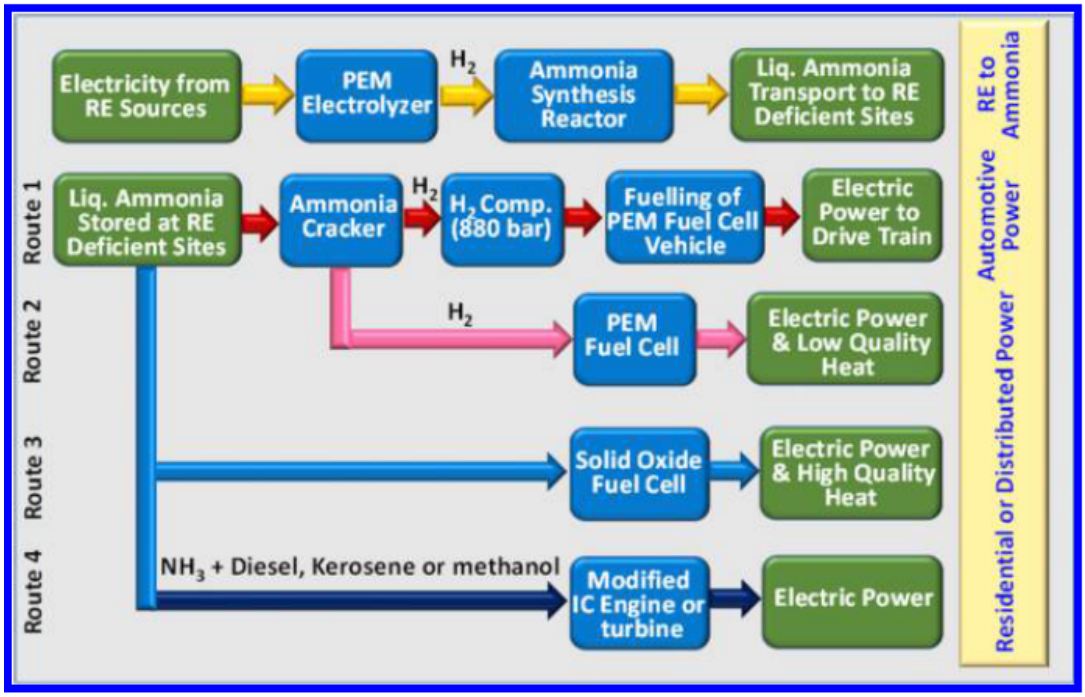


Figure 2.5: Different methods to utilize anhydrous ammonia. [16]

2.5 Storage of Ammonia

The physical properties of ammonia demand high pressure or high refrigeration to store it in a liquid phase. If ammonia is stored in high pressure vessel, it would require nearly 17 bars of pressure to maintain liquid phase and meet minimum safety requirements for storage and transportation. However, full pressure, shop fabricated storage vessels are practical to the size 300 tons [12].

The other method to store ammonia is using refrigerated vessels. They have much higher storage capacity (as high as 66.2 million liters), and do not require high pressure. The temperature requirement for low pressure storage is -33 °C at 1 atm [12]. Depending on the energy requirements to meet these demands and expected storage capacity and costs associated with the system, the decision of whether to use pressurized vessel or refrigerated vessel will be determined.

2.6 Summary

The background can be summarized in the following points:

- Offshore wind farms are moving towards floating platforms allowing the setup distance to be further away from the shore.
- Increased distance from the shore poses challenges for transmission of energy and using anhydrous ammonia as the energy storage and transport medium offers a possible solution.
- Extensive research has been done on how to convert the electrical energy from offshore wind to anhydrous ammonia regarding necessary equipment required and energy associated with the subsystems of the ammonia producing plant.

- There is a wide developed network of ammonia pipelines to transport it long distances at the point of end-use. There are also sophisticated technologies available to store ammonia at high pressure or low temperature.
- Ammonia can be combusted to produce energy (currently not at industrial levels, but much progress has been made to achieve that level) and the combustion process involves significantly lower greenhouse gases emissions compared to the conventional hydrocarbon fuels.

CHAPTER 3

CALCULATION OF NET AMMONIA PRODUCTION

The idea here is to calculate total ammonia produced based on the annual energy production from the offshore wind farm. Using weibull distribution and power curve of the Wind 2 Energy W2E-151-4.5 MW turbine with an upgrade to 164m rotor size, the net annual energy can be determined.

3.1 Wind Conditions at the Site

As mentioned earlier, this thesis utilizes Weibull probability distribution. It gives data on the windspeed and corresponding number of days it affects in a year.

Looking at the offshore wind map at 90m above sea level , the northeast part of United States seem to have strongest winds.

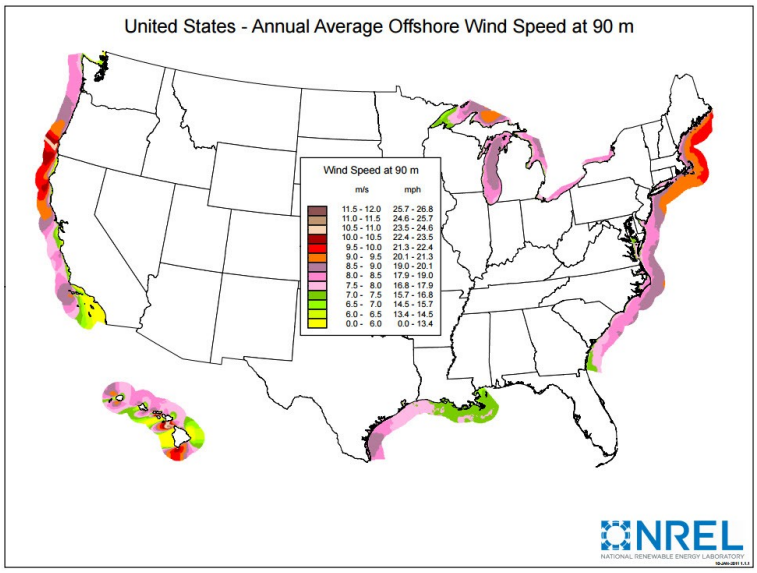


Figure 3.1: Offshore wind map of the United States. Source: NREL

Zooming into the offshore wind map of Massachusetts, the wind at 90m above sea level is 10 m/s at a site which is 50 nautical miles from the shore and has a depth of 60 meters.

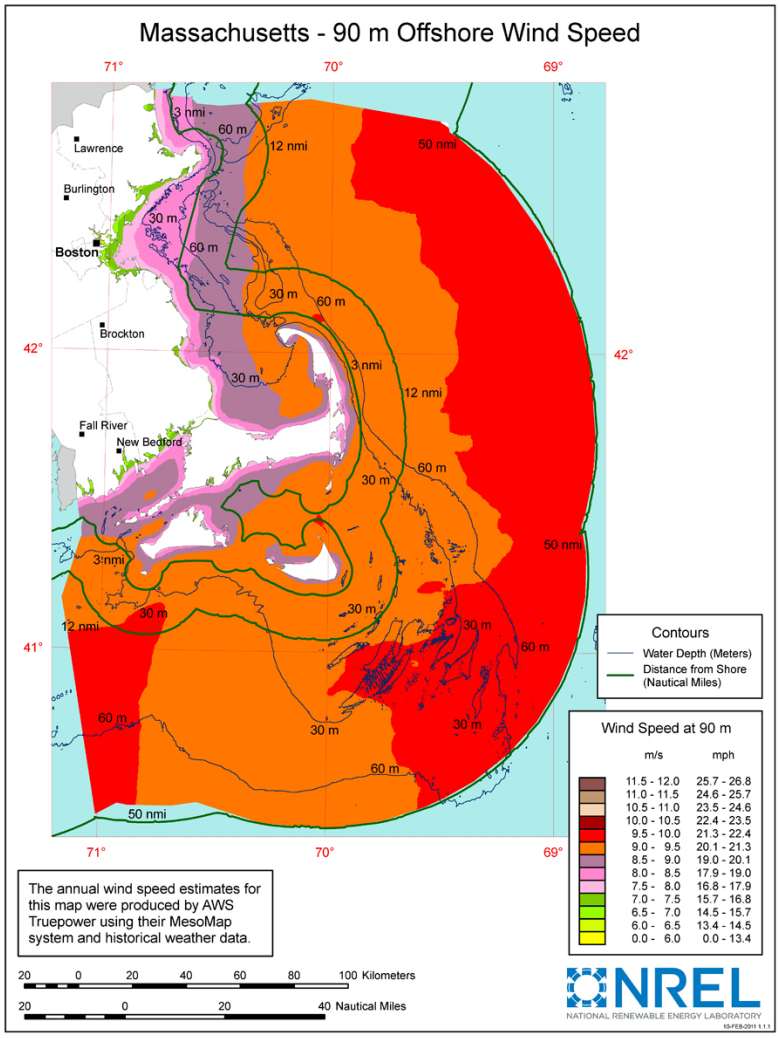


Figure 3.2: Offshore wind map of Massachusetts. Source: NREL

Therefore, the average windspeed $\bar{u}$ at the site is assumed 10 m/s at 90m above sea-level and the Weibull shape parameter (k) is assumed 2.2. Since the hub height of the turbine used for this thesis is 140m, the average windspeed at the hub height can be logarithmically scaled from the formula:

$$u(z_2) = u(z_1)\frac{ln\left(\frac{z_2}{z_0}\right)}{ln\left(\frac{z_1}{z_0}\right)} \tag{3.1}$$

where,

z_1 = 90m,

z_2 = 140m,

$u(z_1)$ = 10 m/s, z_0 = 0.0002 m, surface roughness for calm open sea [17].

This gives average windspeed at 140m hub height as 10.3 m/s. The Weibull scale parameter can be calculated from the formula:

$$c = \bar{u}\left[0.568 + \left(\frac{0.433}{k}\right)\right]^{\left(-\frac{1}{k}\right)} \tag{3.2}$$

$\therefore c = 11.68$ m/s

The Weibull wind distribution is shown in figure 3.3:

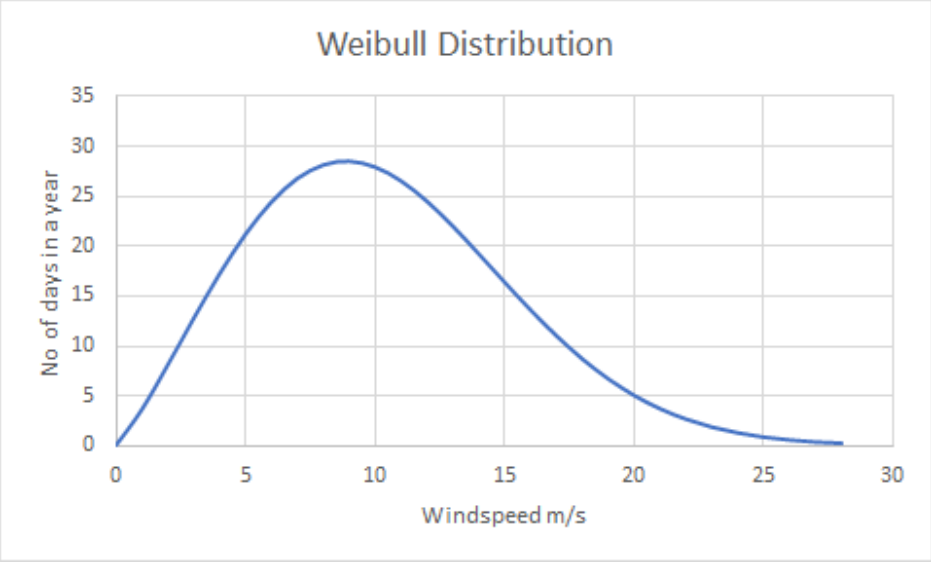


Figure 3.3: Weibull wind distribution for a year

3.2 Wind Turbine Power Curve

The Wind 2 Energy W2E-151-4.5 MW power curve can be obtained from (https://en.wind-turbine-models.com/). However, for the current project, the power curve is adjusted to reflect the power of the same machine but with 164m rotor diameter instead of 151m. The power curve for the turbine is calculated from the formula:

$$P = C_p \frac{1}{2} \rho \pi r^2 \tag{3.3}$$

where ρ is the density of air (1.225 kg/m^3).

Therefore assuming the same C_p, it is scaled by a factor of $\left(\frac{164}{151}\right)^2$, to calculate the power curve for the same machine with 164m rotor diameter. Figure 3.4 shows the comparison between power curves of the original W2E-151-4.5 MW turbine and that with 164 m rotor diameter. The rated windspeed is down to 10 m/s from 12 m/s.

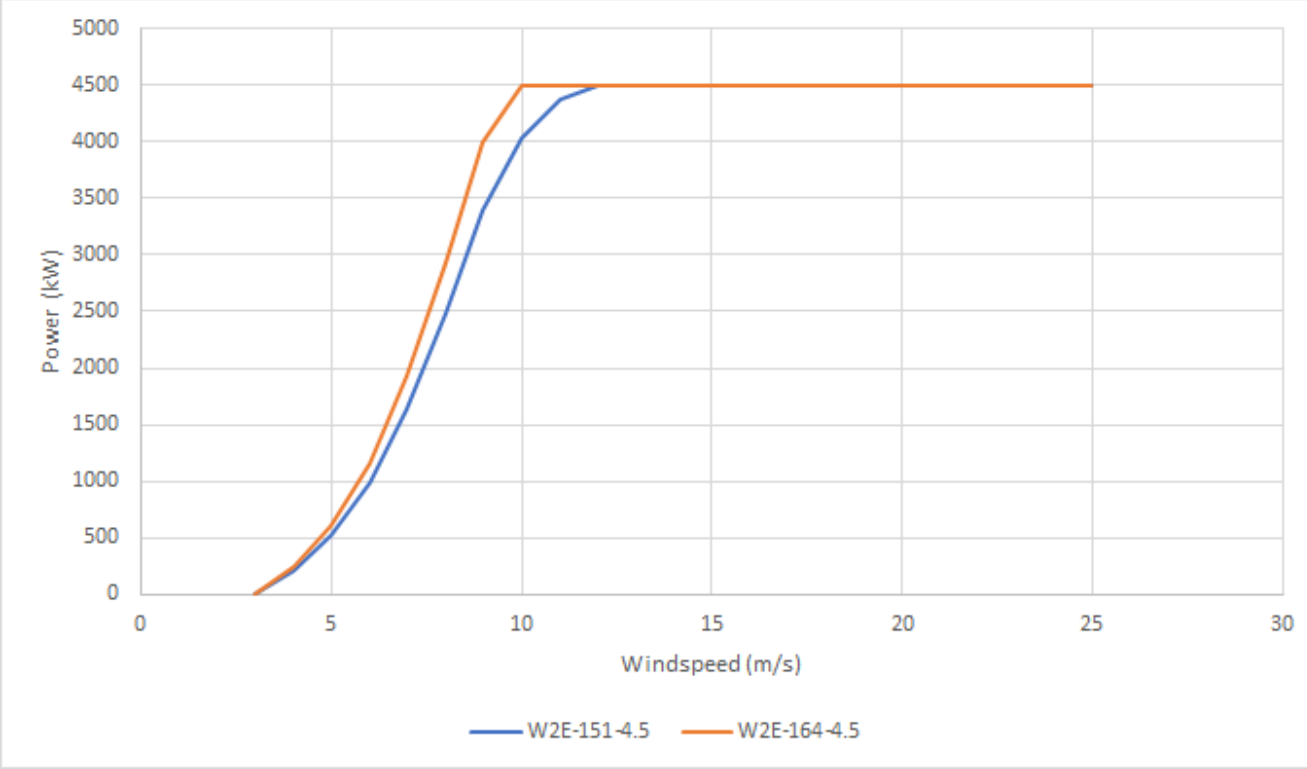


Figure 3.4: Power Curve comparison btw W2E-151-4.5 and W2E-164-4.5 machines

3.3 Capacity Factor at the Site

This factor reflects the ratio between actual energy produced to the energy that could be produced if the wind turbine operated at its rated power in a given period [17]. Since Weibull statistical distribution of wind is used at the site, where the average windspeed at the hub height is 10.3 m/s, the capacity factor at the site can be known [18]. Figure 3.5

shows the value of capacity factor using average windspeed at hub height, rated windspeed of the turbine, and Weibull shape parameter. For this case, the average windspeed is 10.3 m/s, rated windspeed is 10 m/s and weibull shape parameter is 2.5.

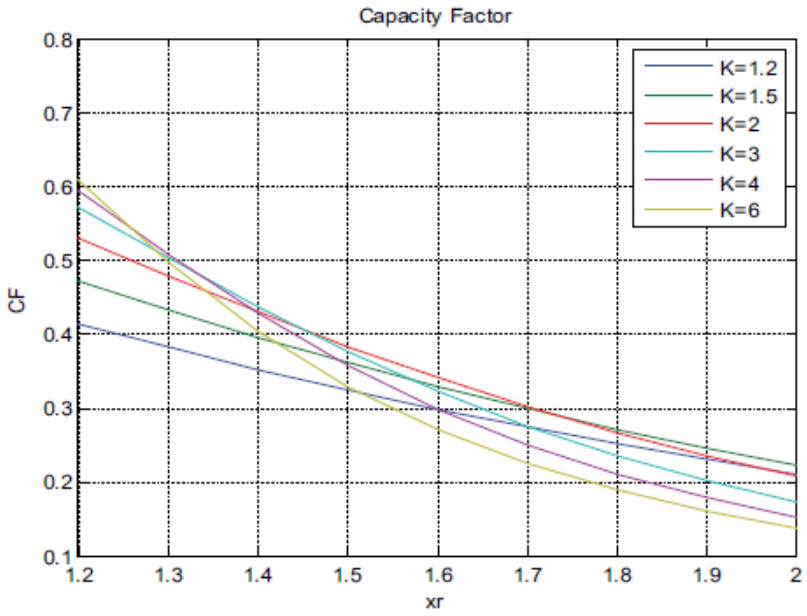


Figure 3.5: Capacity Factor as a function of rated windspeed, average windspeed and weibull shape paramter [18]

Necessary extrapolations were performed using trendline feature in MS Excel to accommodate the parameters used for the current design as shown in figure 3.6.

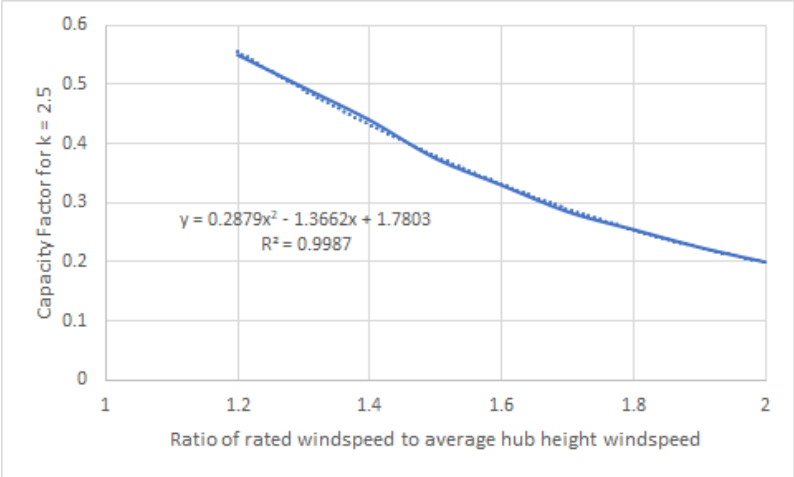


Figure 3.6: Capacity Factor trendline with windspeed

This gave a capacity factor of 0.73. This high capacity factor is due to the fact that average windspeed at the site is 10 m/s which is same as the rated windspeed.

3.4 Size of the Windfarm

According to Morgan(2013), the size of the ammonia plant has a linear relationship with the power required by the ammonia plant [1], given by:

$$P_{NH_3} = 0.482 Size_{NH_3} \tag{3.4}$$

where,

P_{NH_3} = power required by the ammonia plant in MW

$Size_{NH_3}$ = ammonia plant capacity in tons per day

To meet the requirement of ammonia plant capacity of 300 tons/day, the net power required from the offshore wind-farm should be:

$$Size_{NH_3} = 0.482 \times 300MW \tag{3.5}$$

$\therefore Size_{NH_3} = 144.6$ MW

3.4.1 Number of turbines

When the windfarm is connected to the grid, the number of turbines can be estimated by considering three important factors:

- **Array Efficiency:** Wind turbine reduce the wind speed by extracting its kinetic energy causing the downstream turbines will face relatively lower wind speed. Therefore, the total energy captured by a wind farm will be less than the total energy captured by individual turbines. This energy loss is called "Array loss". It is primarily a function of wind turbine downwind and crosswind spacing, wind turbine operat-

ing characteristics, number of wind turbines and size of the wind farm, turbulence intensity, etc. [17]. It is assumed 90% here.

- **Electrical Transmission Efficiency:** This factor reflects the loss in electrical power transmission from the turbine to the plantship. It is assumed as 98% as electrical losses within inter array cables is negligible.

- **Capacity Factor:** It is calculated as 73% for initial analysis.

However, the windfarm considered for this project is non-grid connected. Therefore, any access energy produced from the windfarm will be lost. This means, that the number of wind turbines should be such that the rated power from windfarm should match the power requirement for the ammonia plant operational at rated capacity.

Considering these factors, the number of wind turbines should be:

$$n_{turbine} = \left(\frac{144.6MW}{4.5MW \times 0.9 \times 0.98} \right) \tag{3.6}$$

$\therefore n_{turbine} = 37$

Therefore, 37 turbines will be required to supply power to the ammonia plantship.

3.4.2 Arrangement of Wind Turbines

Array losses are around 10% when the distance between the turbines in downwind direction is 8 to 10 rotor diameter (D), and 5 rotor diameters apart in crosswind direction [19].

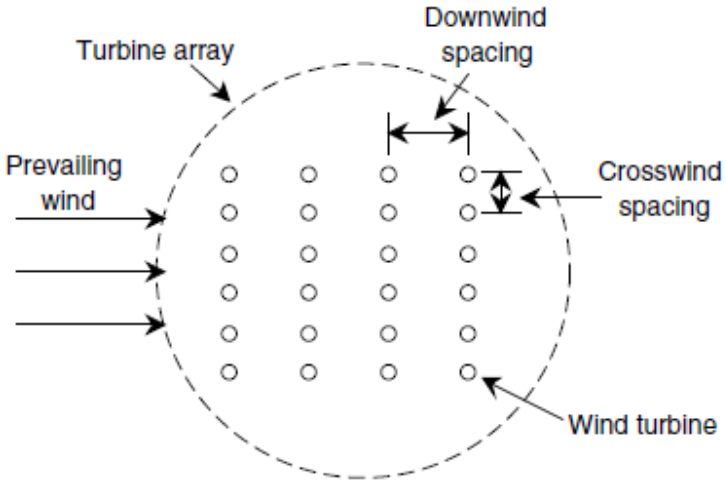


Figure 3.7: Schematic of a windfarm [17].

For this thesis, the downwind spacing will be 10D and crosswind spacing will 5D. And the array efficiency is assumed as 90%. As it is mentioned earlier, the turbines model selected is W2E-151-4.5 MW, which has a rotor diameter of 164m. Therefore, the downwind spacing is 1640 m, while the crosswind spacing is 820 m.

3.5 Energy Flow from Windfarm to the Ammonia Plant

3.5.1 Energy control algorithm

The analytical model of the ammonia production is developed in MATLAB and the code is shown in Appendix A. The 300 tons/day production is divided into ”n” number of ammonia plants. Each plant has 2 energy level: the idling level (I) and the production level (P). As mentioned earlier, ammonia plant can be operational at production level of 65-100%. The idling level I) must be met either by the energy from offshore wind or energy obtained from combustion of ammonia. The production level will be met only from the offshore wind.

From Morgan(2013), the ammonia synthesis chamber requires 8 MW power for a 300 tons/day ammonia production capacity. The 8 MW power here also takes into account the power required to pump the reactants through the pump and into the chamber,along with maintenance of reaction conditions. Therefore, the idling power level for ammonia plant with rated capacity of (300/n) tons/day,

$$I = 8 \left(\frac{\frac{300}{n}}{300} \right) \text{ MW} \tag{3.7}$$

$$\therefore I = 8 \left(\frac{1}{n} \right) \text{ MW}$$

Similarly, the production level can be calculated for each ammonia plant as:

$$P = 0.65 \times 0.482 \times \left(\frac{300}{n} \right) \text{ MW} \tag{3.8}$$

The flow of energy from the windfarm will follow the controlling sequence as:

- For any given wind speed, the term $\left(\frac{\text{Net Energy from the windfarm}}{n} \right)$ will be either less than I, greater than P or between I and P.
- If it less than I, then there is additional requirement of energy from the ammonia gas turbine cycle to keep the plant idling.
- If it is higher than P, then all the ammonia plants will be producing ammonia between 65-100% capacity depending on the amount of energy received to the ammonia plant.
- And if it between I and P, then out of n ammonia plants, the quotient of the value $\left(\frac{\text{Total Energy from Windfarm}}{P} \right)$ will be producing ammonia at 65% capacity. The other wind farms will be idling at power level I. If there is still additional energy available, it will be distributed among the plants which are producing ammonia.

3.5.2 Energy extracted from ammonia:

The energy density of anhydrous ammonia is 11.308 MJ/litres [20]. And the mass density of anhydrous ammonia is 681.82 kg/m^3 [5]. Assuming 40% gas turbine cycle efficiency, the mass of ammonia required to reach idling level can be estimated. (Refer to Appendix A)

3.6 Sensitivity Analysis

This section summarizes the effects of factors like the number of divisions of the ammonia plant, and efficiency of the ammonia-powered gas turbine on the net ammonia production. The ratio of the net annual ammonia production to maximum possible ammonia production is analysed here.The maximum possible ammonia production will be 330×300 tons. On an average, ammonia plant shuts down 5.2 times a year and is operational 330 days in a year [1].

3.6.1 Effect of no of divisions of ammonia plant on annual ammonia production

Figure 3.8 shows the ammonia production curve with the windspeed as well as shows how the addition of division s of the ammonia synthesis plant address the part-load situations.

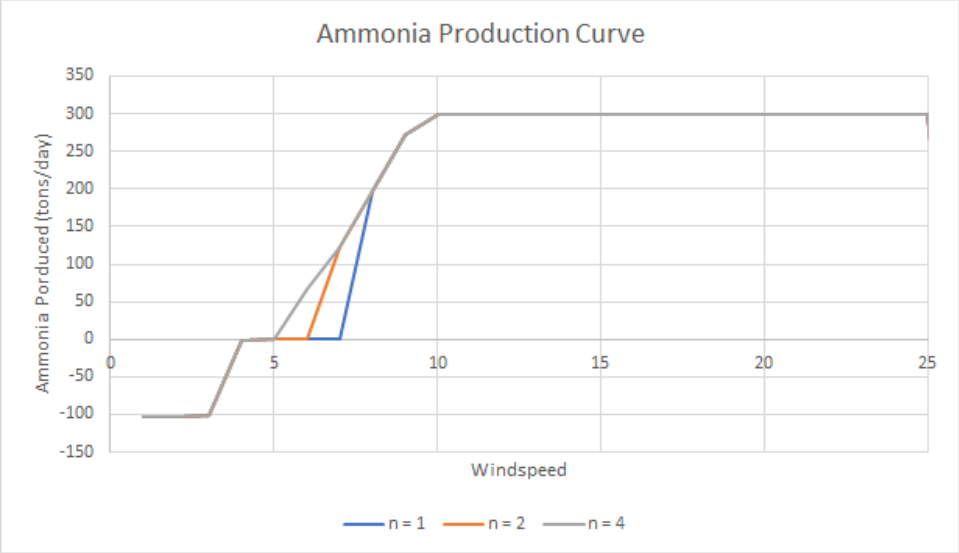


Figure 3.8: Effect of number of divisions of ammonia synthesis loop on the ammonia production curve

Figure 3.9 shows the percent annual ammonia production (capacity factor of ammonia plant) with respect to the number of divisions of ammonia plant.

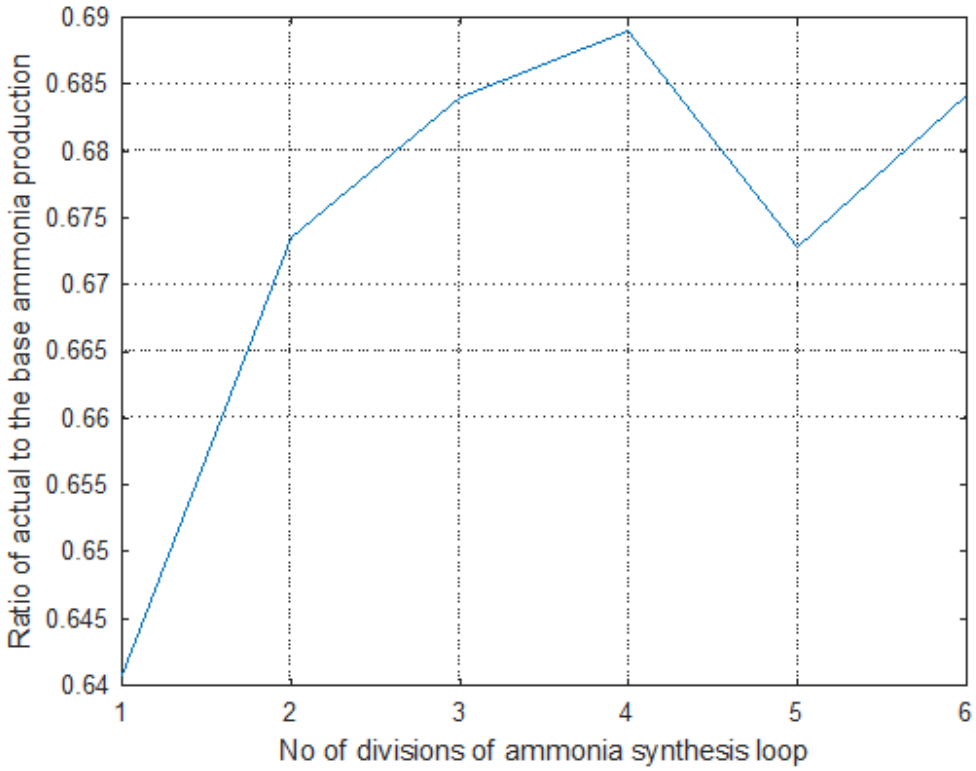


Figure 3.9: Effect of number of divisions of ammonia plant on the annual ammonia production

Having more mini ammonia plants would mean that the threshold energy to produce ammonia at 65% capacity decreases, and so production would start at lower windspeeds. This would increase the annual production. However, it would also utilize more of the produced ammonia to keep it idling during low winds. Therefore, having more number of divisions of ammonia plant does not necessarily mean that it will have higher net annual production, as evident between n = 4 and n = 5 in figure 3.9.

3.6.2 Effect of ammonia gas turbine cycle efficiency

The technology to generate power from ammonia using a gas turbine cycle is not developed at industrial level yet. The review by Valera et. al. covers technologies such as ammonia in cycles either for power, in fuel cells, reciprocating engines, gas turbines and propulsion technologies, and highlightting the challenges with the combustion patterns of

ammonia blends [21]. It is assumed in this thesis, that ammonia can be combusted in a gas turbine at industrial level in megawatts.

Figure 3.10 shows the effects of efficiency of a hypothetical ammonia gas turbine which is used to keep the ammonia synthesis chamber at the reaction temperature and pressure.

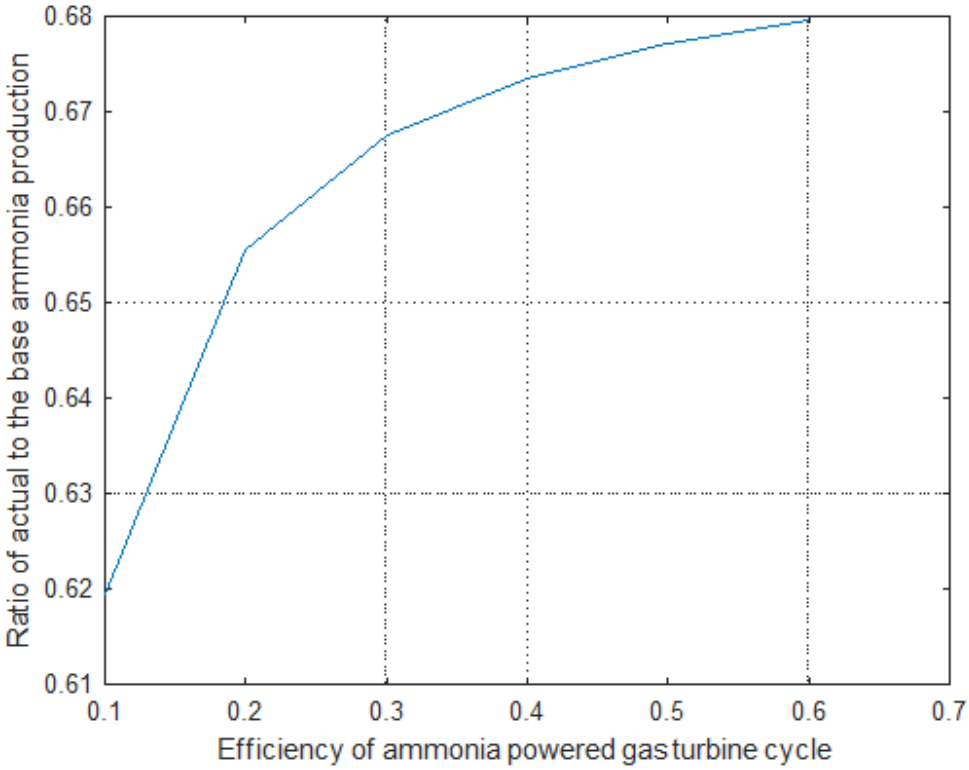


Figure 3.10: Effect of efficiency of ammonia powered gas turbine cycle on the annual ammonia production

It is evident from 3.10 that as the efficiency of the ammonia gas turbine cycle increases, the net ammonia production increases as well because it will take lesser amounts of ammonia from the storage to keep the synthesis chambers idling.

3.7 Summary

In summary, this chapter concludes the system level technological requirements to optimize ammonia production and helps us understand how the parameters govern the net

annual production of ammonia. The emphasis is given only on the net annual production. As the total production increases, it will lower the levelized cost of ammonia (LCOA). But achieving the factors that lead to higher production might increase the overall cost of project. For example, there is more net annual ammonia production when the number of divisions for the synthesis chamber was 4 than that with 2 divisions. However, the LCOA could be higher for 4. This makes way to the next chapter, where the economics of this project are taken into consideration to optimize the design of the project from a techno-economic stand-point.

CHAPTER 4

ECONOMICS OF BASELINE NH_3-OFFSHORE WINDFARM

The economics of the NH_3-Offshore windfarm consists of determining capital costs, operations and management costs (O&M Costs) of the entire project, which is used to determine the Levelized Cost of Ammonia (LCOA). The LCOA in \$/ton is an important cost indicator and helps in assessing how costly is it to produce one ton of ammonia during the entire lifetime of the project. It can be compared with the LCOA for ammonia production using natural gas to give an indication on the economic viability of the offshore wind produced ammonia. The LCOA is basically the ratio of total average lifetime capital costs and operation and maintenance costs over the lifetime ammonia production.

$$LCOA = \left(\frac{\text{Total Lifetime Project Costs}}{\text{Total Lifetime Ammonia Production}} \right) \tag{4.1}$$

Therefore, the first step in calculating LCOA is to determine capital costs of the sub-systems which form the entire project.

4.1 Capital Costs

The major sub-systems whose capital costs need to be determined are:

- Offshore Windfarm
- All-Electric Ammonia Plant
- Ammonia Powered Gas Turbine

- Platform for Ammonia Plant

4.1.1 Offshore Windfarm

The total cost of windfarm is determined from the report *2017 Cost of Wind Energy Review* by Tyler Stehyl et.al. at NREL [22]. A detailed economic overview of a 5.64 MW offshore wind turbine on a floating semi-submersible platform is provided in this report. By using the interdependent ratios between capital costs, balance of system, finances, the capital costs for the turbine used for this project W2E-164-4.5 MW can be scaled as well.

	5.64 MW offshore turbine	**Vestas V164-9.5 MW**	**W2E-4.5-164**
	($/kW)	**($/kW)**	**($/kW)**
Turbine Capital Costs	**1521**	**1200**	**2533**
Development Costs	190	150	316
Engnieering Management	96	76	160
Substructure and foundation	1653	1304	2753
Site access, staging, and port	67	53	112
Electrical Infrastructure	1175	232	490
Assembly and Installation	137	334	704
Balance of Plant	**3318**	**2148**	**4535**
Insurance during construction	51	40	85
Decommissioning bond	22	17	37
Construction financing	352	278	586
Contingency	290	229	483
Plant commissioning	51	40	85
Financial Costs	**766**	**604**	**1276**
Total CapEx	**5605**	**3953**	**8344**

Table 4.1: Total Capital Expenditures for the offshore wind turbine with semi-submergible floating structure

The costs for the 5.64 MW semi-submergible floating offshore wind turbine were obtained from the NREL's report on 2017 Cost of Wind Energy Review [22]

The cost of W2E-164-4.5 MW turbine in $/kW is derived from Vestas V164-9.5 MW turbine cost, which is hypothesized from the 5.64 MW machine costs given in 2017 Cost of Wind Energy Review [22]. The idea here is that the capital cost of the 4.5 MW turbine

is almost the same as that of 9.5 MW turbine, because it can be imagined as the derated version of 9.5 MW turbine. This will save some costs in the generator. But going with a conservative assumption, the cost of 4.5 MW turbine is considered same as the 9.5 MW turbine. Therefore, the cost of each item on the 4.5 MW turbine can be obtained by scaling the cost of that item in the 5.64 MW column by $\left(\frac{1200}{1521} \times \frac{9500}{4500}\right) = 1.67$.

One notable increase is the cost for assembly and installation. This is because the the cost for 5.64 MW turbine was estimated for a site which was 30km from the shore. The 4.5 MW turbine site is 50 nautical miles from the shore (almost 93 km). Applying linear relationship between assembly and installation cost with the distance from the shore, the cost came around 704 $/kW for the 4.5 MW machine.

Another notable aspect of the comparison is the cost for electrical transmission. This project is not connected to the grid. Therefore, it saves the cost for export cables. However, there still needs to be electrical infrastructure required for inter array connection through cables. The cost of inter array cable in 2014 was €190k/km [23]. Using Purchase Price Index (PPI) of 0.737 €/$ for 2014 (data from Organisation for Economic Co-operation and Development) and then inflating the cost for 2018 with a factor of 1.0682 (from Bureau of Labor Statistics), the cost of inter array cables is $ 275384/km. For a 300 MW, the expected length of the inter array cables is typically 75 km [24].

The cost of offshore substation in 2014 is €18.6 millions for a 500 MW windfarm and €28.5 for 1000 MW windfarm with floating foundation [23]. This can be used to extrapolate the cost of substation for the current windfarm using the same method mentioned above. This results in the total offshore electrical infrastructure as 490$/kW.

From this data, the total capital expenditure is 8344$/kW. For a 4.5 MW turbine, the total CapEx is estimated as 37.6 million dollars.
The CapEx of the windfarm will be 37.6 $\times$ no of turbines required.

4.1.2 All-Electric Ammonia Plant

The all-electric ammonia plant uses the same design as defined in Morgan's dissertation except for 2 changes. There are multiple ammonia synthesis chambers and also the

addition of ammonia powered gas turbines to keep the plant idling. The cost estimates can be easily obtained using the CEPCI indexes for 2018 and 2010 and scaling the data available from Morgan's dissertation. However, there is a difference in the synthesis loop calculation. He had used a synthesis loop for 300 tons/day capacity. But for this thesis, multiple synthesis loop are utilized. This will add the necessary complexity to address part-load operations at windpseeds lower than rated for the turbines.

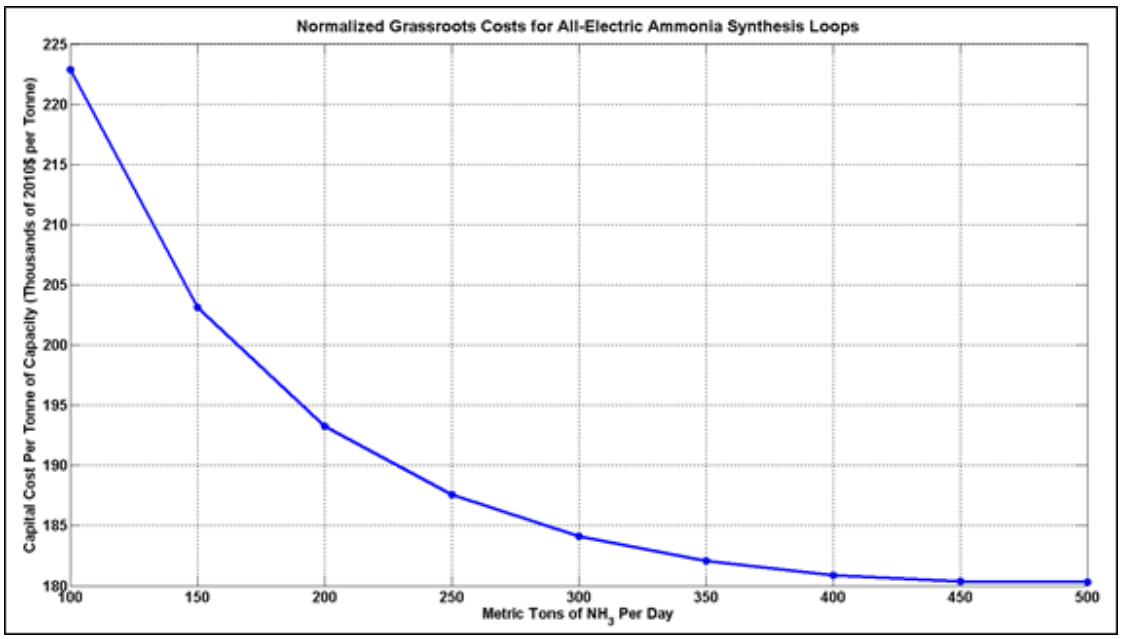


Figure 4.1: Cost of ammonia synthesis loop vs Ammonia plant capacity [1]

Figure 4.1 can be converted into cost of ammonia synthesis loop vs no of divisions of 300 tons/day capacity as shown in figure 4.2 and a trendline can be added to obtain an equation governing the cost of ammonia synthesis loop in 2013 dollars. This can be scaled to 2018 dollars using CEPCI indexes.

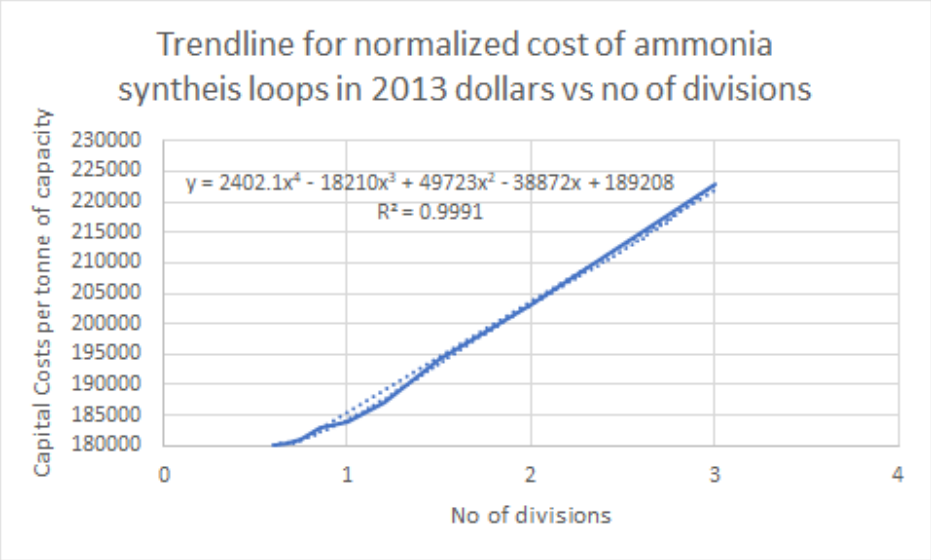


Figure 4.2: Cost of ammonia synthesis loop vs No of divisions

As it can be seen from the figure 4.2, as the number of divisions increase, the capital cost of synthesis loop increase significantly. The only reason to increase the divisions will be to get more ammonia production at part-load conditions. It will be shown in the next chapter how the increase in the number of divisions increase the total ammonia production and how it affects the levelized cost of ammonia. Increasing the number of divisions above a certain number can also be disadvantageous as more ammonia will be combusted to keep all the synthesis loops under idling condition.

4.1.3 Electrolyzer Scaling

The idea here is to scale up the chemical processing equipment common to each electrolzer. This provides opportunity to reduce the overall capital cost of the electrolyzer system [1]. This same concept was used for electrolyzer system in the dissertation by Morgan (2013). However, for this thesis, electrolyzer scaling needs to consider that the minimum load on the electrolyzer system should be 20% under operation [1]. This creates a challenge to the concept of using multiple ammonia synthesis loops. For example, there are 4 ammonia synthesis loops of 75 tons/day rated output and one of the loop is producing ammonia while the other three are idling. Therefore, the electrolyzers system must oper-

ate to match the hydrogen requirements of the synthesis loop under operation. It might be lower than 20% load if the whole electrolyzer system for 300 tons/day rated ammonia output is scaled.

Therefore, the number of electrolyzers scaled are depend on the number of divisions of the ammonia synthesis loop. For example, the 300 tons/day rated ammonia output requires nearly 126 electrolyzers. If the synthesis loop has 3 divisions of 100 tons/day rated output, then a total of $\frac{126}{3} = 42$ electrolyzers will be scaled together. The capital cost in thousands of 2010 dollars of the scaled electrolyzer system can be obtained from equation given in [1].

$$C_{scaledelectrolyzer} = 786X + 712X^{0.7} + 148X^{0.5} + 368X^{0.75} + 442X^{0.8} \tag{4.2}$$

where, X is the number of electrolyzers to be scaled.

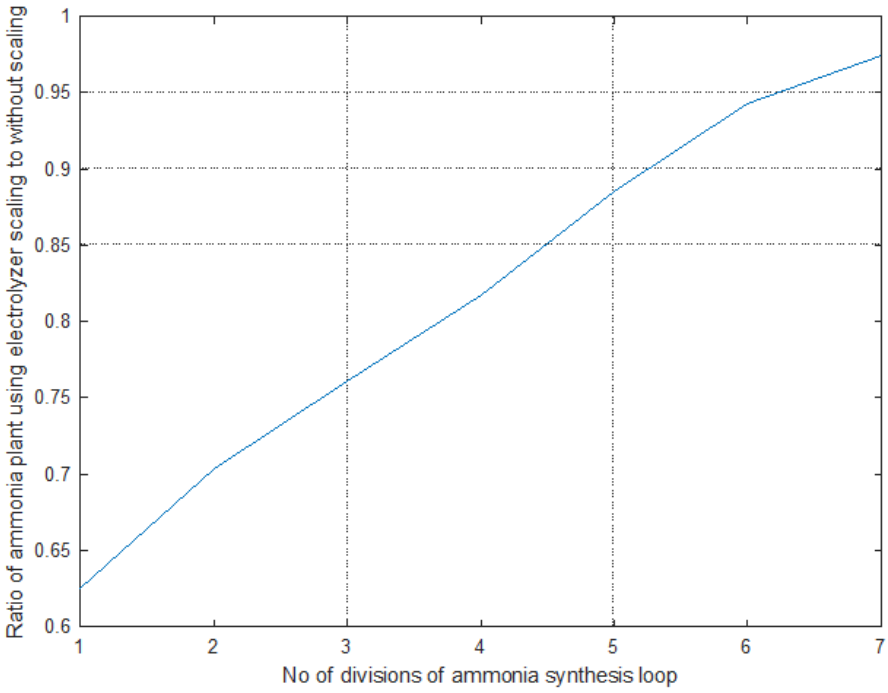


Figure 4.3: Ratio of capital cost of ammonia plant with electrolyzer scaling to the one without scaling vs No of divisions of ammonia synthesis loop

As shown in figure 4.3, using the electrolyzer scaling, the capital cost of the all-electric ammonia is almost 70 to 82% as the number of divisions of ammonia synthesis loop is between 2 and 4 compared to those without electrolyzer scaling. Therefore, to reduce the capital cost of the all-electric ammonia plant, the electrolyzer scaling concept is used based on the number of divisions of ammonia synthesis loop.

4.1.4 Total Capital Expenditure of the All-Electric Ammonia Plant

Figure 4.4 shows the overall capital costs of the all-elctric ammonia plant in 2010$. The costs are considered for the scaled electrolyzer. This makes sense as when there are 3 ammonia synthesis loops of 100 tons/day capacity, then the total capital expenditures of the ammonia plant would be 3 $\times$ (the cost associated with the 100 tons/day plant. This method also makes sure the there are 3 systems of electroylzer scaled corresponding to each ammonia synthesis loop. It also makes sure that other equipments, like air separation unit (ASU), mechanical vapor compression (MVC), are scaled according to their requirements.

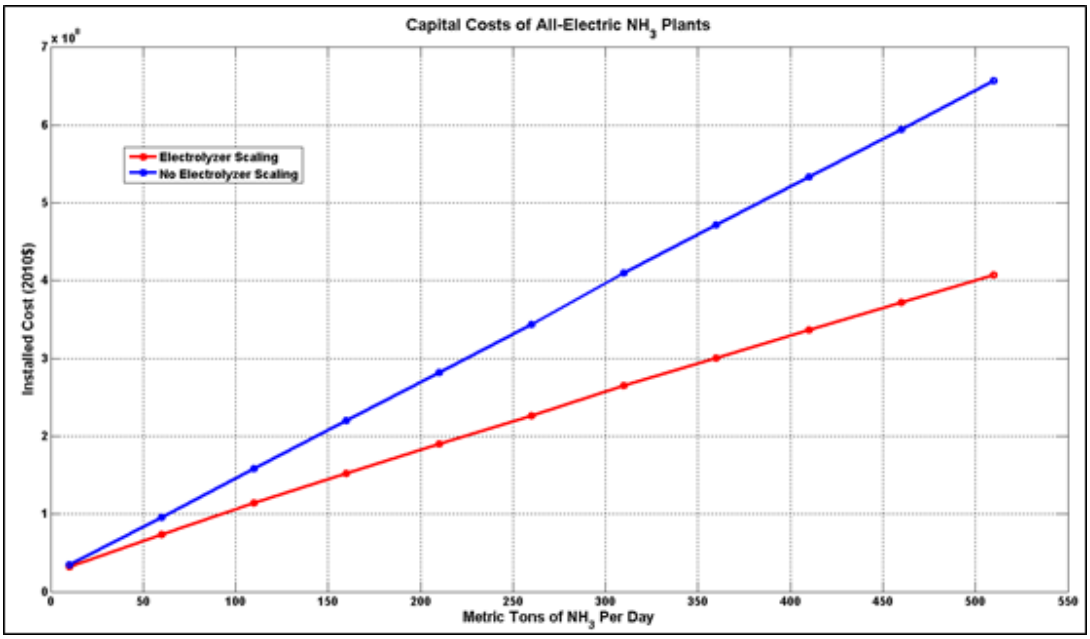


Figure 4.4: Total capital expenditures based on the ammonia plant capacity [1]

It is scaled by a factor of $\left(\frac{\text{CEPCI value of 2018}}{\text{CEPCI value of 2010}}\right)$ to get the overall cost of the ammonia plant in 2018 dollars. Using trendline feature in MS Excel, the equation for the cost as a function of ammonia plant capacity is given in figure 4.5

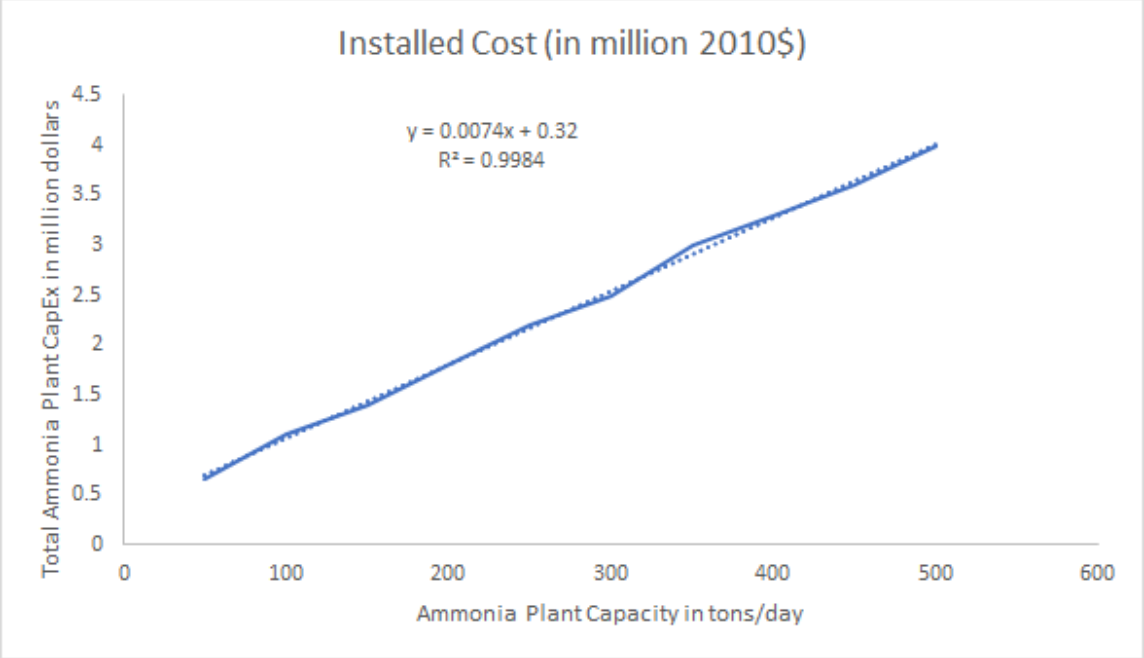


Figure 4.5: Total capital expenditures of the ammonia plant as a function of ammonia plant capacity

4.1.5 Ammonia Powered Gas Turbine Cycle

Ammonia powered gas turbine cycle is essential to keep the ammonia synthesis chamber at reaction conditions. It is evident that ammonia can be combusted in gas turbines to generate electricity. However, the technology is not sophisticated enough yet to produce electricity at industrial level. Valera-Medina et. al. at Cardiff University are using a 2MW gas turbine to conduct research on using ammonia as fuel [25].

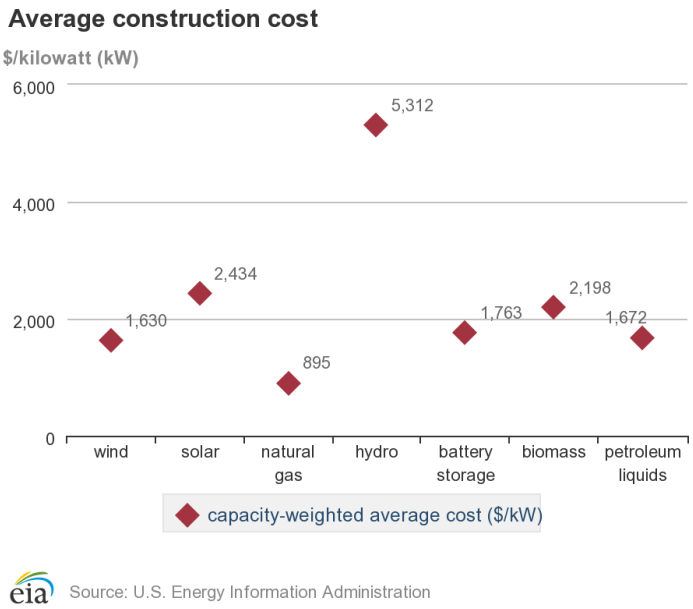


Figure 4.6: Capacity weighted average costs for major energy sources. Source: U.S. Energy Information Administration

Since it unknown at this point how much the cost of ammonia-combustion generator would be, it is assumed at 5000 $/kW. However, there will be sensitivity analysis conducted in the next chapter to determine how much is LCOA dependent on the capital cost of ammonia powered gas turbine cycle.

4.1.6 Platform for the All-Electric Ammonia Plant

The platform or plantship design is derived from the study conducted by Panchal et. al. [14] in 2009. They designed the plantship for a capacity of 265 metric tons of ammonia per day using Ocean Thermal Energy Conversion (OTEC). However, the major subsytems are quite similar to the one in the project. Therefore, the size and cost of the plantship can be scaled for a 300 tons/day plant in 2018 using inflation rate from 2009 to 2018 (17.87%) and multiplying by a factor of $\left(\frac{300}{265}\right)$. This comes out to 95.81 million dollars in 2018.

4.2 Operations and Maintenance Costs

4.2.1 O & M Costs of he offshore windfarm and the all-electric ammonia plant

The O& M costs of wind turbine can be obtained by scaling them from the report *2017 Cost of Wind Energy Review* by Tyler Stehyl et.al. at NREL [22]. This was estimated as 21.3 millions dollars per year.

The O& M costs for the ammonia plant can be assumed as 3% of the total capital expenditures of the ammonia plant with the ammonia powered gas turbine and the plantship. In the dissertation by Morgan, it was also assumed 3% of the CapEx of all-electric ammonia plant for estimation of its O& M cost.

4.2.2 Transportation Costs

The other aspect to add in the estimation of O & M cost is considering transportation costs of produced ammonia from offshore manufacturing facility to an onshore facility.

The offshore windfarm is almost 50 nautical miles away from the shore. A reasonable assumption regarding the shipping costs can be derived from the 1977 paper "Alternative form of energy transmission from OTEC plants" by Konopka et. al [26]. The cost was given in dollars per million BTU, which was converted in dollars per ton in 1977 dollars and then using inflation converted to 2018 dollars as 54$/ton for 100 miles. Another source which verifies this cost is the article in 2013 by Dr. Duncan Seddon called "Ammonia Production Cost", where it is stated that the shipping cost of ammonia is in the range of 50$/ton [27].

Therefore, for this project, the cost of ammonia shipping is considered 55$/ton.

4.3 Calculation of Levelized Cost of Ammonia

The LCOA can be derived from the equations 4.3 and 4.4 using the following parameters:

$$LCOA = \frac{P_d + P_a \left(\frac{\left(\frac{1}{1+r}\right) - \left(\frac{1}{1+r}\right)^{(n_{loan}+1)}}{1 - \left(\frac{1}{1+r}\right)} \right) + (Wind_{O\&M} + NH_{3_{O\&M}}) \left(\frac{\left(\frac{1+i}{1+r}\right) - \left(\frac{1+i}{1+r}\right)^{(n_{life}+1)}}{1 - \left(\frac{1+i}{1+r}\right)} \right)}{\text{Total Lifetime } NH_3 \text{ Production}} \tag{4.3}$$

Where,

P_d = Down Payment on the entire project = 10% of the total CapEx C_c

$Wind_{O\&M}$ = Annual Operations and Mangement Cost of the windfarm

$NH_{3_{O\&M}}$ = Annual Operations and Mangement Cost of the ammonia plant

i = Inflation rate = 3%

r = Nominal Discount Rate = 7%

n_{loan} = duration of the loan = 15 years

n_{life} = project lifetime = 20 years

The down payment and the annual payment on the loan are dependent on the capital cost of the entire project. The operations and maintenance costs are already considered as a percentage of the capital costs. The down payment for the loan is assumed 10% of the entire capital cost, while the annual payment P_a can be calculated from the formula as:

$$P_a = (C_c - P_d) \left[\frac{b}{1 - (1+b)^{-n_{loan}}} \right] \tag{4.4}$$

where,

b = rate of interest on the loan = 4%

4.3.1 LCOA vs no of divisions of ammonia synthesis loop

As the number of divisions increase, the total CapEx of the ammonia plant increases significantly as shown in figure 4.7. The figure 4.7 shows only the total CapEx of the offshore ammonia facility and not that of the project. It is sum of capital expenditure of the ammonia plant, the ammonia powered gas turbine cycle, and the supporting plantship.

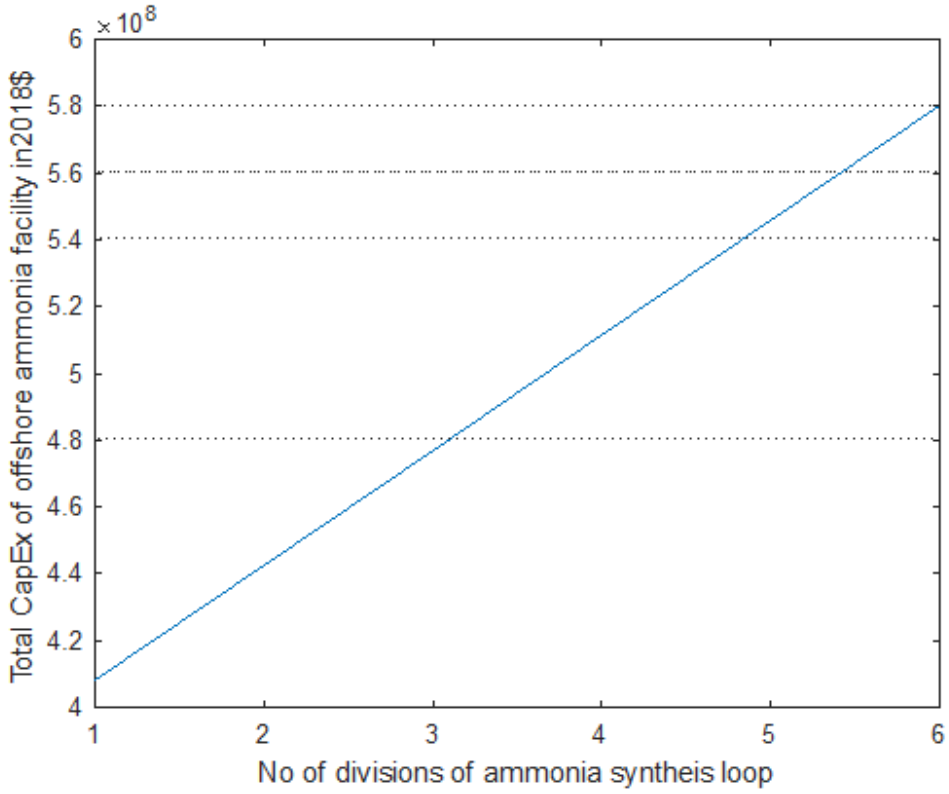


Figure 4.7: Capital cost of the offshore all-electric ammonia production facility vs no of divisions of ammonia synthesis loop

But as shown in figure 3.9, the net ammonia production also increases upto a point. Therefore, it is essential to identify optimum number of divisions to account for both - total production as well as economy of the plant.The LCOA of the plant with respect to the number of divisions is represented in the figure 4.8:

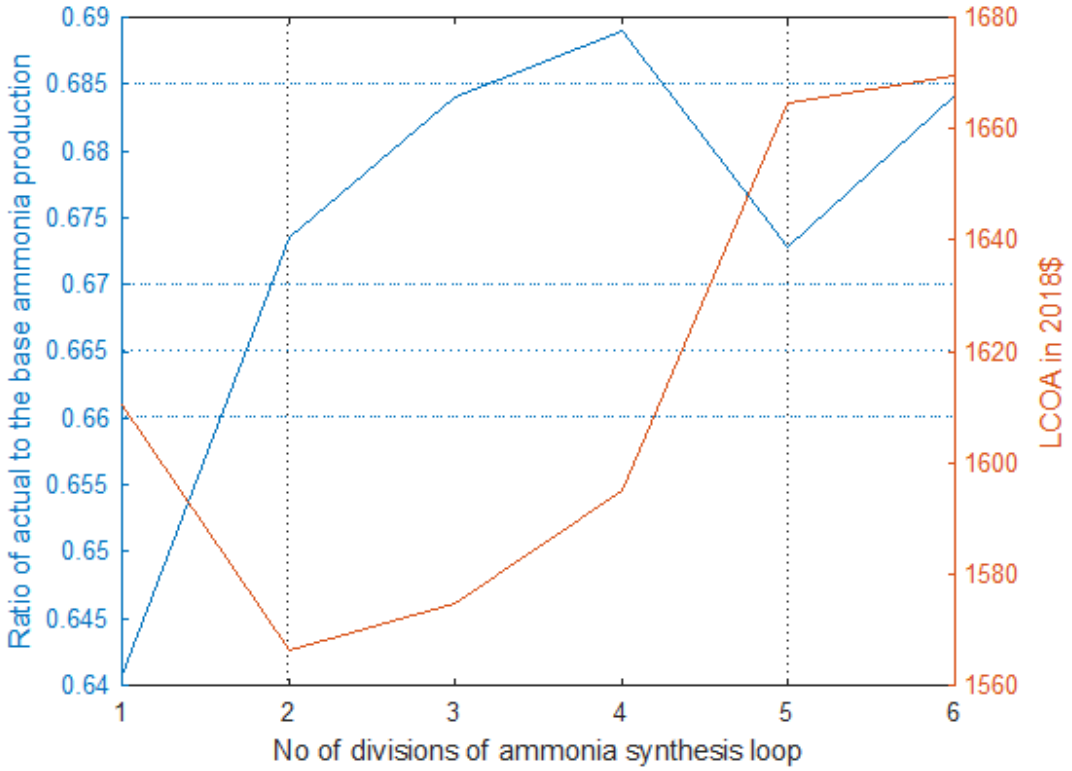


Figure 4.8: LCOA vs no of divisions of ammonia synthesis loop

As expected, the divisions certainly help to increase the net annual production but with considerable increase in the LCOA as well. It can be seen that the LCOA is lowest at almost (\$1566/ton of NH_3) when there are only 2 divisions i.e. 2 synthesis loops of 150 tons/day capacity. The difference between net annual production between that obtained with 2 divisions and 4 divisions is also not big. Therefore, dividing the synthesis loop into 2 parts would be optimum and is established as the baseline parameter.

4.3.2 LCOA vs cost of ammonia powered gas turbine cycle

Utility scaled ammonia powered gas turbines are still in the development phase and it is challenging to get a good estimate of how costly the technology would be when it is available. Therefore, using the weighted average costs of the power cycle for different energy sources, the baseline capital expenditure was estimated as \$5000/kW. This value

falls on the high end of spectrum of the capital expenditure for gas turbines cycles as shown in figure 4.6.

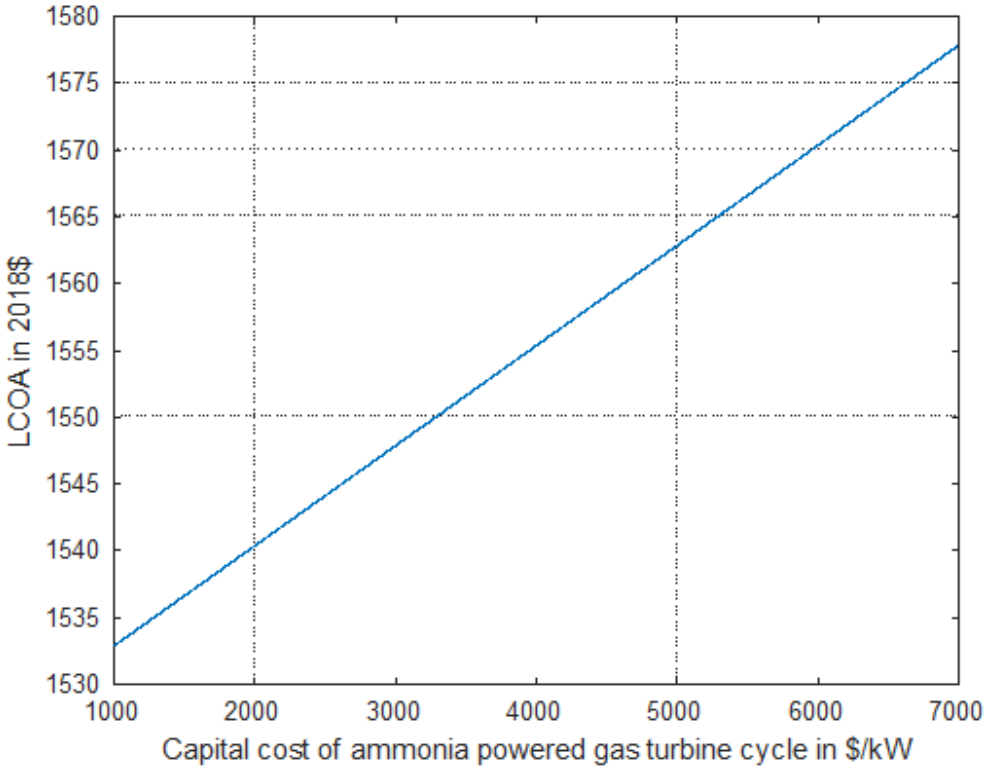


Figure 4.9: LCOA vs Capital Expenditure per kW of the ammonia powered gas turbine cycle

The LCOA certainly increases when the capital cost the ammonia powered gas turbine is higher. However, on a variation of 1000$/kW to 7000$/kW, the LCOA only increases by $40/ton. This is because the total capital expenditure of the gas turbine cycles is relatively small compared to other sub-systems like the windfarm and the ammonia plant. The sensitivity of the efficiency of the gas turbine cycle on the LCOA is shown in figure 4.10:

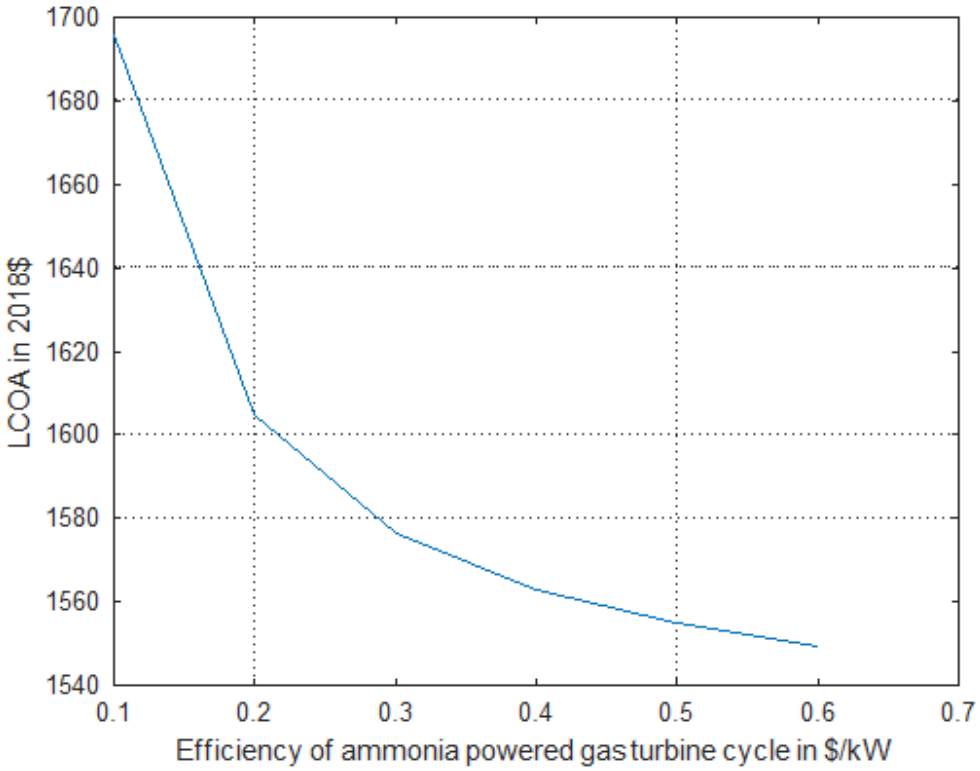


Figure 4.10: LCOA vs Efficiency of the ammonia powered gas turbine cycle

In the context of this project, the future research on developing the ammonia powered gas turbine cycle should be focused more on higher efficiency compared to the cost.

4.3.3 LCOA vs per kW cost of the wind turbine

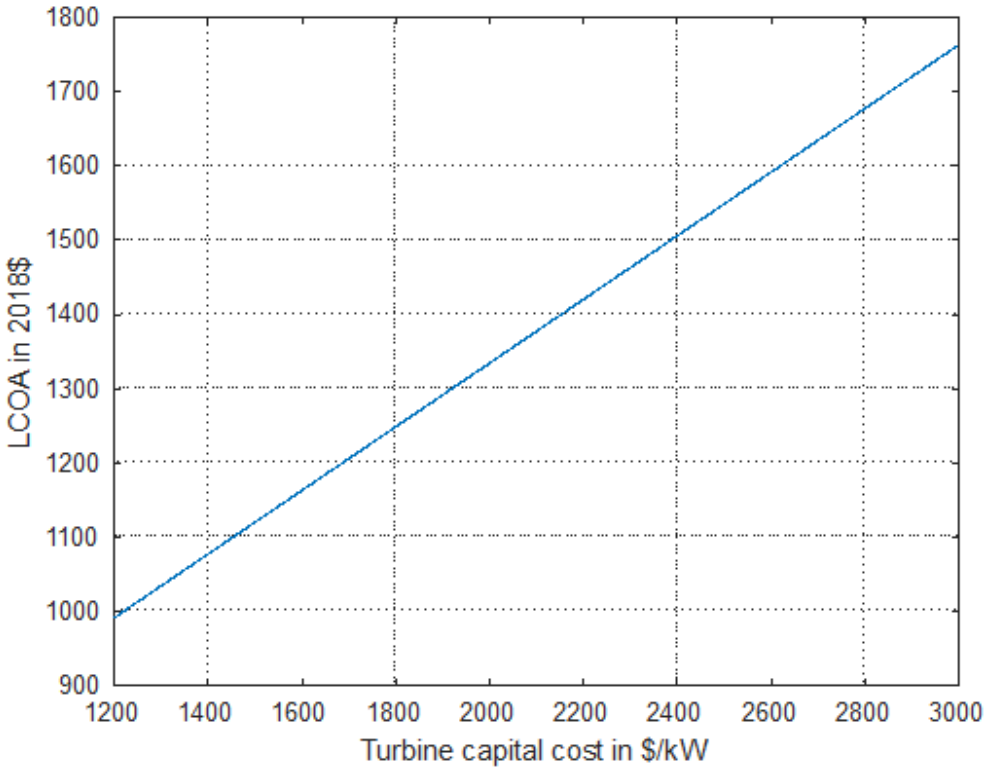


Figure 4.11: LCOA vs pew kW capital cost of the turbine

As shown in figure 4.11, the LCOA linearly increases with increase in per kW cost of the turbine. Since 2008, wind turbine prices per kW have steeply declined, despite increases in size. These price reductions, coupled with improved turbine technology, have exerted downward pressure on project costs and wind power prices [28]. Therefore, it can be expected that with decrease in per kW price of the turbine, the LCOA will also linearly decrease within acceptable range.

CHAPTER 5

RESULTS AND DISCUSSIONS

The Levelized Cost of Ammonia for the current project is almost 350$/ton higher than that calculated by Morgan (2013). There are many reasons to get this higher cost:

- There is no connection to the grid. Therefore, it is not possible to run the plant at a constant rate of 300 tons/day due to variable power output from the offshore wind-farm.
- Other reason is that with connection to the grid, the excess electricity from the wind farm can be sold into the grid. Here, the control system does not allow the turbines to produce more than the required power.
- Multiple ammonia synthesis loops to allow production of ammonia at part-loads. The capital cost increases quite remarkably as the number of divisions of synthesis loop increases.
- Addition of ammonia powered gas turbine means use of ammonia from storage to keep the plant idling. This means that there is a decrease in net ammonia production.
- The ammonia plant is supported by a plantship and it adds around 96 million dollars in the total capital expenditures.
- The LCOA is dependent heavily on the per kW cost of the wind turbine. For this project, a turbine with 164m is used with semi-submersible floating support structure. The estimated capital cost of this turbine was much higher than that calculated

in Morgan's thesis. But with technological advances and steep price reduction since 2008, the LCOA can get lower in the future.

- Although the cost of ammonia powered gas turbine does not affect the LCOA in a significant way, its efficiency plays an important role on how much of the produced ammonia will be consumed and thereby affect the net annual ammonia production.

Another aspect that stands out in this thesis was how the net annual ammonia production is affected by the number of divisions of the ammonia synthesis loop. It seemed that with higher number of divisions, the threshold energy to start ammonia production could be lower and production could be started at lower windspeeds as well. However, the increase in divisions of synthesis loop also demanded certain power to keep them idling which had to be met through the produced ammonia. Therefore, there it was necessary to reach an optimum number of division from production as well as economic standpoint. In this project, that number was 2. But at different site, with different capacity factor, the optimum number of divisions might be affected.

Overall, it was observed that ammonia was produced at much lower capacity (around 65% of the base ammonia production). And it costs around 350$/ton more than that calculated by Morgan (2013). Therefore, there is a significant requirement of further research to lower overall plant capital expenditure. This project warranted the use of turbine with large rotor size and its higher cost was one of the driving factor behind the higher LCOA. Therefore, using ammonia as a possible solution to energy storage medium for far offshore plant to be feasible will require huge reductions in capital costs of wind turbines with larger rotor sizes, along with a matured and efficient ammonia powered gas turbine cycle.

CHAPTER 6

FUTURE WORK

This thesis is a system-level analysis to understand the feasibility of ammonia production from a non-grid connected floating offshore wind farm. It uses Weibull statistical distribution to estimate the wind distribution in a year. Because of this, this model fails to consider the ramp up and down time of sub-system components like Air Separation Unit (ASU), Electrolysers,etc. If a 10 min data point analysis is considered, it will add more complexity to the control algorithm for the flow of energy. However, this will also open opportunities to create a more robust model where the flow of energy at every second can be directed by factoring in the dynamics of the components. Also with higher accuracy of wind forecast for the next few days, reasonable decisions could be made if one or more of the synthesis loops could be shut down, thereby allowing it to preserve the produced ammonia rather than combusting it to keep it idling. Other advantage of performing this analysis with 10 min wind data is the prediction of systematic schedule of the plant using wind forecast. It will be possible to maintain one of the synthesis loops while others are under operation, thereby allowing continuous operation throughout the year. This will certainly increase the net annual ammonia production.

Another aspect which needs to be researched is the estimation of accurate wind turbine prices. As the thesis shows, any reductions or additions in the capital expenditure of wind turbine prices will have an amplified effect on the LCOA. The future update on this work will also require a more accurate estimation of the efficiency and capital expenditure of the ammonia powered gas turbine cycle.

APPENDIX A

MATLAB MODEL FOR ANNUAL AMMONIA PRODUCTION AND LCOA

```
%%Define Initial Paramters
ammonia_plant_cap = 300; %tons/day
wind_farm_size = ammonia_plant_cap*0.482; %MW
Avg_wind = 10; %m/s at 90m above sea-level
Avg_wind = Avg_wind*(log(140/0.0002)/log(90/0.0002)); %Scaling
    windspeed at hub height 140m
n = 2; %no of divisions of the ammonia synthesis loop
capacity_factor = cf(Avg_wind);
array_eff = 0.9;
electrical_eff = 0.98;
no_of_turbines = ceil(wind_farm_size/(capacity_factor*9.5*
    array_eff*electrical_eff));
op_days = 330; %number of days in a year for ammonia plant
    operation
k = 2.2; %Weibul Shape Parameter
c = Avg_wind*((0.568)+((0.433/k)))^(-1/k); %Weibul Scale
    Parameter
Energy_Density_Ammonia = 11.308; %MJ/litre
Mass_Density_Ammonia = 681.82; %kg/m^3;
```

```
Specific_Density_Ammonia = Energy_Density_Ammonia/(
    Mass_Density_Ammonia/1000); %MJ/kg
Ammonia_turbine_eff = 0.4; %Efficiency of ammonia gas turbine
Idling_Usage = 8*(ammonia_plant_cap/300); %MW
I = Idling_Usage/n ; % I = Idling power required per ammonia
    plant
Min_P = 0.65; %Min percentage for part-load ammonia plant
    operation
P = (Min_P*wind_farm_size)/n; %Min power required per ammonia
    plant to operate at min part load
Base_Annual_Ammonia_Produced = op_days*ammonia_plant_cap;

%%Power_curve and wind_distribution
u_wind = ones(30,1);
for i = 1:1:30
    u_wind(i) = i;
end

no_of_days = zeros(30,1);
for i = 1:1:30
    no_of_days(i) = op_days*(k/c)*((u_wind(i)/c)^(k-1))*exp(-(
        u_wind(i)/c)^k); %Weibull probabilitic distribution
end

power_per_turbine=[0.0; 0.0; 0.0; 154.38; 593.75; 1246.88;
    2137.50; 3289.38; 4750.00; 6531.25; 8312.50; 9381.25; 9500.0;
    9500; 9500; 9500; 9500; 9500; 9500; 9500; 9500; 9500; 9500;
    9500; 9500; 0; 0; 0; 0; 0 ]; %kW
power_wind_farm = zeros(30,1);
```

```
for i = 1:1:30
    if power_per_turbine(i)*electrical_eff*array_eff*0.001*
       no_of_turbines > wind_farm_size
        power_wind_farm(i) = wind_farm_size;
    else
        power_wind_farm(i) = power_per_turbine(i)*electrical_eff*
           array_eff*0.001*no_of_turbines;
    end
end
%%End of power curve and weibull distribution
%% Controlling the wind energy flow to the ammonia plants
 Power_Idling = zeros(30,n);          %Additional power from
    ammonia to idle
 Ammonia_Idle = zeros(30,n);          %Additional ammonia in tons
    to idle
 Net_Ammonia_Used = zeros(30,1);
 Ammonia_synthesized = zeros(30,n);
 Net_Ammonia_Produced = zeros(30,1);
 x = zeros(30,1);
 for i = 1:1:30
     if power_wind_farm(i)/n < I
         Power_Idling(i,1:n) = I - (power_wind_farm(i)/n);
         Ammonia_Idle(i,1:n) = (0.001*Power_Idling(i,1:n)
            *24*3600)/(Ammonia_turbine_eff*
            Specific_Density_Ammonia);
         Net_Ammonia_Used(i) = sum(Ammonia_Idle(i,:));
         Ammonia_synthesized(i,:) = 0;
         Net_Ammonia_Produced(i) = sum(Ammonia_synthesized(i,:))
            - (Net_Ammonia_Used(i));
```

```
end

if power_wind_farm(i)/n > P
    Ammonia_synthesized(i,:) = (power_wind_farm(i)/n)/0.482;
    Net_Ammonia_Produced(i) = sum(Ammonia_synthesized(i,:) -
        Net_Ammonia_Used(i));
end

if ((power_wind_farm(i)/n) > I) && ((power_wind_farm(i)/n) <
    P)
x(i) = floor(power_wind_farm(i)/P);
y = power_wind_farm(i) - (x(i)*P);
if y > (I*(n-x(i)))
    Ammonia_synthesized(i,1:x(i)) = (P + ((y - (I*(n-x(i))))
        /x(i)))/0.482;
    Net_Ammonia_Produced(i) = sum(Ammonia_synthesized(i,:))
        - Net_Ammonia_Used(i);
end

if y < (I*(n-x(i)))
 Net_Ammonia_Used(i) = (((I*(n-x(i))) - y)*0.001*24*3600)/(
    Ammonia_turbine_eff*Specific_Density_Ammonia);
 Ammonia_synthesized(i,1:x(i)) = (Min_P*(wind_farm_size/n))
    /0.482;
 Ammonia_synthesized(i,x(i)+1:n) = 0;
 Net_Ammonia_Produced(i) = sum(Ammonia_synthesized(i,1:n)) -
     (Net_Ammonia_Used(i));
end
```

```
    end
    Net_Annual_Ammonia_synthesized = zeros(30,1);
    for i = 1:1:30
        Net_Annual_Ammonia_synthesized(i) = Net_Ammonia_Produced(i
            )*no_of_days(i);
    end
    sum_net_ammonia_produced = sum(Net_Annual_Ammonia_synthesized
        (:));
    ratio = sum_net_ammonia_produced/Base_Annual_Ammonia_Produced;

   %%%Net Capital Costs
%%Estimating the windfarm capital costs
capital_cost_per_turbine = 1200; %$/kW
net_Capital_cost_per_turbine = capital_cost_per_turbine*9500; %
    rated power is 9500kW
balance_of_system_turbine = 9500*(capital_cost_per_turbine/1521)
    *(3318-1175+140+(-137+(137*(92.6/30)))); %ratio estmiated from
     ref [X] and subtracting electrical costs
financial_cost_turbine = 9500*(capital_cost_per_turbine/1521)
    *766;
total_CapEx_turbine = net_Capital_cost_per_turbine +
    balance_of_system_turbine + financial_cost_turbine;
total_CapEx_windfarm = total_CapEx_turbine*no_of_turbines;

%%Estimating the capital cost of all electric ammonia plant
CEPCI_2010 = 550.8;
CEPCI_2018 = 591.3;
plant_capital_cost_2010 = 4*(10^8); %dollars for 300 tons/day
    capacity plant
```

```
synthesis_chamber_2010 = plant_capital_cost_2010*0.14;
grassroot_cost_300 = 184000; %dollars for a 300 tons per day
    capacity ammonia plant
grassroot_cost_n = grassroot_2018(n); %dollars for a 300 tons per
     day capacity ammonia plant
synthesis_chamber_2018 = synthesis_chamber_2010*((n*
    grassroot_cost_n)/grassroot_cost_300);
plant_capaital_cost_2018_no_scaling = (CEPCI_2018/CEPCI_2010)*(
    plant_capital_cost_2010 - synthesis_chamber_2010 +
    synthesis_chamber_2018);
plant_CapEx_scaled_2018 = (CEPCI_2018/CEPCI_2010)*(
    cap_elec_scaled(n)- synthesis_chamber_2010 +
    synthesis_chamber_2018);
ratio_plant_scaled_nonscaled = plant_CapEx_scaled_2018/
    plant_capaital_cost_2018_no_scaling;

%%Estimating capital cost of the ammonia plantship
panchal_platform_cost_2009 = 71800000; %dollars for 265 tons per
    day
panchal_capacity = 265; %tons per day
platform_cost_2018 = panchal_platform_cost_2009*(300/
    panchal_capacity)*1.1787;

%%Estimating capital cost for ammonia powered turbine for idling
    usage
average_construction_cost = 5000; %dollars per kilowatt
net_generator_capital_cost = n*I*average_construction_cost*1000;
    %dollars
```

```
%%Estimating total capital expenditure of offshore ammonia
    facility
offshore_ammonia_capex = plant_CapEx_scaled_2018+
    platform_cost_2018+net_generator_capital_cost;

%%Estimating total capital expediture of the whole system
capital_cost_system_2018_non_scaled = total_CapEx_windfarm +
    plant_capaital_cost_2018_no_scaling + platform_cost_2018 +
    net_generator_capital_cost;
capital_cost_system_2018_scaled = total_CapEx_windfarm +
    plant_CapEx_scaled_2018 + platform_cost_2018 +
    net_generator_capital_cost;

%%%Net Operation Costs
%%Operational Costs for windfarms
windfarm_operational_costs = 9500*no_of_turbines*93*(
    capital_cost_per_turbine/1505); %scaling from capital cost
    used in the ref to the used in this thesis

%%Operational Costs for all electric ammonia plant
NH3_OM_scaled = 0.03*(offshore_ammonia_capex);
NH3_transportation = 3000000; %2018 dollars
Net_OM_scaled = windfarm_operational_costs + NH3_OM_scaled +
    NH3_transportation;
%%Economic Analysis
r = 0.07;   %Nominal Discount Rate
i = 0.03;   %Inflation Rate
n_loan = 15; %loan period
n_life = 20; %lifetime of project
```

```
Pd = 0.1*capital_cost_system_2018_non_scaled; %Total down payment
Pa = (capital_cost_system_2018_non_scaled - Pd)
    *(0.04/(1-((1+0.04)^-n_loan))); %Annual Payment
LCOA_scaled = (Pd + (Pa*(((1/(1+r))-((1/(1+r))^(n_loan+1)))
    /(1-(1/(1+r))))) + (Net_OM_scaled*((((1+i)/(1+r))-(((1+i)/(1+r
    ))^(n_life+1)))/(1-((1+i)/(1+r)))))))/(n_life*
    sum_net_ammonia_produced);
end
```

APPENDIX B

MATLAB MODEL FOR CALCULATION OF CAPACITY FACTOR AS A FUNCTION OF AVERAGE WINDSPEED, RATED WINDSPEED AND K = 2.5

```
function y = cf(u_wind,rated_windspeed)
xr_cf = rated_windspeed/u_wind;
y = (0.2879*(xr_cf^2)) - (1.3662*xr_cf) + 1.7803; %equation
    obtained from using trendline feature in MS Excel
end
```

APPENDIX C

MATLAB MODEL FOR CALCULATION OF GRASSROOT COST OF AMMONIA SYNTHESIS LOOP IN 2013 DOLLARS

```
function y = grassroot_2018(n)
y = (2.4021*(n^4)) - (18.21*(n^3)) + (49.723*(n^2)) - (38.872*n)
    + 189.21; %equation obtained from using trendline feature in
    MS Excel
y = y*1000;
end
```

APPENDIX D

MATLAB MODEL FOR CALCULATION OF CAPITAL COSTS OF SCALED ELECTROLYZERS SYSTEM

```
function plant_CapEx_sclaed_2010 = cap_elec_scaled(n)
CapEx_no_elec_sclaed = 4*(10^8)*0.77; %total cost of
    electrolysers without scaling
CapEx_per_elec = 2456000; %capital cost per electrolyzer
X = CapEx_no_elec_sclaed/CapEx_per_elec; %Total no of
    electrolyzer required for 300 tons per day ammonia plant
Xn = X/n; %no of electrolyzers required to operate 1 synthesis
    loop out of n
Scaled_cost_2010_Xn = n*((786*Xn)+(712*(Xn^0.7))+(148*(Xn^0.5))
    +(368*(Xn^0.75))+(442*(Xn^0.8)))*1000; %total cost of scaled
    electrolyzer for n divisions of synthesis loop
plant_CapEx_sclaed_2010 = (2.5*(10^8))-(((786*X)+(712*(X^0.7))
    +(148*(X^0.5))+(368*(X^0.75))+(442*(X^0.8)))*1000) +
    Scaled_cost_2010_Xn; %plant capital cost with scaling in 2010$
end
```

BIBLIOGRAPHY

[1] E. Morgan, "Techno-economic feasibility study of ammonia plants powered by offshore wind," Open Access Dissertations. 697, University of Massachusetts Amherst, 2013.

[2] E. Francis, "Investment in commercial development of ocean thermal energy conversion (otec) plant-ships. final report, september 1976–august 1977," 1977.

[3] J. Fuhrmann, M. Hülsebrock, and U. Krewer, "Energy storage based on electrochemical conversion of ammonia," *Transition to Renewable Energy Systems*, pp. 691–706, 2013.

[4] R. Hattenbach, "Transportation and delivery of anhydrous ammonia," *2006 Annual NH3 Fuel Conference, Golden, CO (United States)*, 2006.

[5] G. Thomas and G. Parks, "Potential roles of ammonia in a hydrogen economy: a study of issues related to the use of ammonia for onboard vehicular hydrogen storage," *US Department of Energy, Washington, DC*, 2006.

[6] W. Musial, P. Beiter, P. Schwabe, T. Tian, T. Stehly, P. Spitsen, A. Robertson, and V. Gevorgian, "2016 offshore wind technologies market report," *National Renewable Energy Laboratory (NREL), Golden, CO (United States)*, 2017.

[7] O. of Energy Efficiency & Renewable Energy, "Computing america's offshore wind energy potential," 2016. [Online]. Available: https://www.energy.gov/eere/articles/computing-america-s-offshore-wind-energy-potential,Date_accessed:2018-07-21

[8] C. Rocco, "Offshore wind farms: too much energy is lost in cables," 2018. [Online]. Available: http://www.youris.com/energy/energy-grid/offshore-wind-farms-too-much-energy-is-lost-in-cables.kl,Date_accessed:2018-08-30

[9] A. Williams, "Hvdc vs. hvac cables for offshore wind," 2011. [Online]. Available: http://newenergyupdate.com/wind-energy-update/hvdc-vs-hvac-cables-offshore-wind,Date_accessed:2018-07-30

[10] "Ammonia-fueled gas turbine power generation," 2017. [Online]. Available: http://www.ammoniaenergy.org/ammonia-fueled-gas-turbine-power-generation/

[11] "Dutch gas plants made fossil free?" 2016. [Online]. Available: https://news.vattenfall.com/en/article/dutch-gas-plants-made-fossil-free,Date_accessed:2018-08-25

[12] J. R. Bartels, "A feasibility study of implementing an ammonia economy," *Digital Repository@ Iowa State University*, 2008.

[13] J. Brightling, "Ammonia and the fertiliser industry: The development of ammonia at billingham," *Johnson Matthey Technology Review*, vol. 62, no. 1, pp. 32–47, 2018.

[14] C. Panchal, P. Pandolfini, W. Kumm *et al.*, "Ocean thermal plantships for production of ammonia as the hydrogen carrier," *Argonne National Laboratory*, 2009.

[15] "Development of an ammonia-burning gas turbine engine," *Solar Division of International Harvester Company*, 1968.

[16] S. Giddey, S. Badwal, C. Munnings, and M. Dolan, "Ammonia as a renewable energy transportation media," *ACS Sustainable Chemistry & Engineering*, vol. 5, no. 11, pp. 10 231–10 239, 2017.

[17] J. F. Manwell, J. G. McGowan, and A. L. Rogers, *Wind energy explained: theory, design and application*. John Wiley & Sons, 2010.

[18] A. L. de Medeiros, A. M. Araújo, O. D. de Oliveira Filho, and J. Rohatgi, "Defining capacity factor by weibull shape parameter and mean wind speed," *Wind Engineering*, vol. 39, no. 3, pp. 253–260, 2015.

[19] P. Lissaman, A. Zaday, and G. Gyatt, "Critical issues in the design and assessment of wind turbine arrays," in *Proc. 4th International Symposium on Wind Energy Systems, Stockholm*, 1982.

[20] S. Sasaki and J. Sarlashkar, "Internal combustion engine with ammonia fuel," May 1 2012, uS Patent 8,166,926.

[21] A. Valera-Medina, H. Xiao, M. Owen-Jones, W. David, and P. Bowen, "Ammonia for power," *Progress in Energy and Combustion Science*, vol. 69, pp. 63–102, 2018.

[22] T. J. Stehly, P. C. Beiter, D. M. Heimiller, and G. N. Scott, "2017 cost of wind energy review," National Renewable Energy Lab.(NREL), Golden, CO (United States), Tech. Rep., 2018.

[23] A. Myhr, C. Bjerkseter, A. Ågotnes, and T. A. Nygaard, "Levelised cost of energy for offshore floating wind turbines in a life cycle perspective," *Renewable Energy*, vol. 66, pp. 714–728, 2014.

[24] M. J. Kaiser and B. Snyder, "Offshore wind energy installation and decommissioning cost estimation in the us outer continental shelf," *US Bureau of Ocean Energy Management, Enforcement and Regulation*, 2010.

[25] S. Crolius, "Report from the european conference: Ammonia-fueled gas turbines, year = 2017, url = http://www.ammoniaenergy.org/report-from-the-european-conference-ammonia-fueled-gas-turbines/, urldate = 2018-11-30."

[26] A. Talib, A. Konopka, N. Biederman, C. Blazek, and B. Yudow, "Alternative forms of energy transmission from otec plants," in *Sun: Mankind's Future Source of Energy*. Elsevier, 1978, pp. 1744–1755.

[27] D. Seddon, "Ammonia production cost," 2013. [Online]. Available: http://www.duncanseddon.com/docs/pdf/ammonia-production-costs.pdf/ Date_Accessed:2018-12-10

[28] R. Wiser and M. Bolinger, "2017 wind technologies market report," *Office of Energy Efficiency and Renewable Energy*, 2018.

Delhi Business Review ✠ Vol. 19, No. 2 (July - December 2018)

AN EXPLORATORY FACTOR ANALYSIS FOR DEVELOPING A SCALE OF ETHICS

A KNOWLEDGE MANAGEMENT PERSPECTIVE

Nishant Gaur*
Vikas Gupta**

PURPOSE
ETHICS has been broadly analyzed and explored from work-place perspective. However, research on ethics from knowledge management (KM) perspective is weak; very few empirical studies have been done in this regard. The paper aims to create scale for ethics to fill the gap. The scale which has been developed by the author(s) is aimed to be used for testing the relationship between ethics and KM in future.

Design/Methodology/Approach: *In this study, the existing literature was examined and it was then administered and investigated to 278 employees in different organizations. Exploratory Factor Analysis (EFA) was employed to determine the scale and further reliability of factors.*

Findings: *Five factors of ethics have been identified. These factors are: F1: Organizational Values and Ethical Climate; F2: Commitment, Responsibility, and Team Working Morale; F3: Intellectual Capital and Trusteeship; F4: Ethical Issues, and F5: Obstacles to Ethical Behavior.*

Research Limitations/Implications: *The scale is perceptual to assess and evaluate ethical dimensions, which may or may not be authentic indicator of ethical dimensions existing in the organization.*

Practical Implications: *The scale can be used as an instrument for investigating the effectiveness in KM process, KM ownership, and KM practices.*

Originality/Value: *The scale is a valid and reliable measure of ethical constructs. It is a credible tool to investigate ethical behavior and framework that the employees feel, think, and believe exists within their organization.*

Key Words: *Knowledge Management (KM), Ethics.*

Introduction

Ethics, in simple words, is all about right and wrong. As a field of study, there are two schools of thoughts that have emerged, teleological and deontological. Teleological perspective (Hume, 1750; Smith, 2002) refers to the consequence of an action as indicator of good or bad and deontology perspective (Kant, 1991) refers to the action as an ethical indicator. The other perspective to ethics is individual's behavior as ethical (Crisp, 2011).

In this era of knowledge based competition, organizations use unique, creative, and innovative techniques

* *Research Scholar, Delhi School of Management, Delhi Technological University, Delhi, India.*

** *Assistant Professor, Delhi School of Management, Delhi Technological University, Delhi, India.*

to improve their structure and enhance their performance (Michael, Mckeen, & Singh, 2009). In this endeavor to become successful, these organizations overlook the ethical issues. It has been noted that knowledge of ethics is derived more from employees' experience as compared to academic knowledge (Lee, 2010). With globalization and rapid technological changes, there is a need to address ethical issues, as the world is experiencing compromise on ethics like knowledge hoarding, manipulation, and misappropriation. Personal ethics, interpersonal behavior in moral ecology, and articulation and dissemination of ethical standards plays pivot role in addressing ethical concerns. There are various socio economical, technological, and legalistic issues which are obstacles for sustaining ethical culture in an organization. The ethics provide the organization with guiding principles for KM and facilitate effective implementation and execution of KM practices resulting in a win-win situation for all the stakeholders. The ethics is the independent variable which impacts the dependent variable KM. The available literature is limited for ethics impacting KM. The current study focuses on developing and testing research questionnaire for ethics from KM perspective.

Literature Review

Ethics

Ethics are behavioral codes which are recognized as right and good at individual level as well as societal level. Ethics provide a guideline for individual practice as well as collective practice in community (Tseng & Fan, 2011). The understanding of ethics in a community is dependent on value system of that particular community (Macintyre, 1985). Individuals being a member of organization as well as community are guided to respect ethical norms of organization and society to which they belong (Tseng & Fan, 2011). The ethics can be referred to as ideals embedded in a group or community of people and are reflected through their culture (Akhavan, Ramezan, & Moghaddam, 2013). Collective ethics of society or nation are referred to as ethos. Ethics are referred to good and bad attributes, conducts, intentions or moral duties, and commitments towards organization or society. Akhavan et al. (2013) has listed four dimensions of ethical principles: organizational value and justice; team working morale; intellectual ownership and trusteeship; and commitment and responsibility. Organizational values and justice is the most vital aspect of ethical principles constituting collective trust and organizational trust; fair, honest, and humble behavior of employees; criticism taking, and perseverance in works. Team working morale refers to ethical conduct while working in a team which involves cooperation, empathy, self-awareness, self-control, affability, and council with others. Intellectual ownership and trusteeship refers to obeying intellectual property rights, maintaining confidentiality, and trusteeship. Other ethical dimension includes responsibility, commitment, and loyalty towards organization. It also includes working conscience and being foresighted at work.

PRIMES model is explained by Huff (2010) as "a model comprising of several ethical parameters from individual and surrounding perspective. It constitutes personality, integration of morality, moral ecology, and skills" (p. 19). "Personality depicts work that people prefer and the path they choose to accomplish it" (John & Srivastava, 1999, p. 102). Integration of morality refers to moral commitment of individuals and gives direction to individual action in diverse situations. Moral ecology is the surrounding environment of an individual which influences and dominates individual action in diverse situation. Moral skills and knowledge is awareness that individual possess about different moral actions and content.

Obstacles to ethical behavior depict that behavior which individual persists to restrain share of knowledge and also includes manipulation of knowledge for individual interest or personal gain. Different obstacles to ethical behavior are knowledge hoarding, plagiarism, manipulation, misappropriation, and property and privacy right conflict. Sharing of tacit knowledge, that is, personal knowledge in form of ideas and experiences is dependent on owner's willingness to share as it serves as economic means to the employee. When employee hesitates in knowledge sharing

with organization, it leads to knowledge hoarding. The knowledge is sometimes modified, altered, suppressed, amplified, and omitted for some personal interests or individual gain leading to manipulation and misappropriation of knowledge. There is also conflict among employee and organization over knowledge ownership. The former consider knowledge as a phenomenon carried in the mind of individuals whereas, the latter view knowledge as an asset created by providing the employees resources both financial & technological, infrastructure, and reward. Ethical issues comprise of technical issue, socio economic issue, and legalistic issue. Technical team responsible for designing and implementing of KM system come across a number of unethical aspects. In these situations, technical staff can act as a whistleblower to make management aware about the unethical aspects. Also, there is a hidden agenda for implementation of KM in an organization that accounts for socio economic issue in ethical practices. The underlying motivation to implement KM system is to capture employee's knowledge to reduce human resource cost by carrying out retrenchment in the organization (Bryant, 2006). Legalistic aspect in KM based organization is concerned with conflict over knowledge ownership right between employees and organization (Baskervile & Dullipovici, 2006) (as shown in table no. 1).

Linking Ethics and KM

It is necessary to have ethical framework or collaborative ethical tool for KM system constituting several ethical parameters and constructs, as KM system might adopt unethical path to accomplish objectives and goals for profit and wealth maximization (Glisby & Holden, 2003). "Ethical approach to KM is built on trust, fairness, and justice as they stimulate individuals to participate in KM process. Trust prevents employees from knowledge hoarding" (Delong & Fahey, 2000, p. 113). "Trust facilitates sharing and creation of knowledge" (Burchell & Cook, 2008, p. 36). Trustworthiness among individuals in a group impacts the extent to which knowledge is shared. Where there is trust in an organization, individual can depend on organization to care for them. Trust enables colleagues and managers to freely share knowledge instead of hiding or protecting that knowledge. Patel & Ragsdell (2011) highlighted the need for a fair and ethical behavior.

Tseng & Fan (2011) highlighted the significance of an ethical organizational climate for facilitating knowledge processes. "The ethical approach to KM supports an organization to engage individuals in knowledge process and also to build database acquiring and retaining individual knowledge and experience" (Liebowitz, 1999, p. 37). Fair KM practices rewards individuals for their knowledge contributions (Baskerville & Dullipovici, 2006). According to Sen (1993), the organizations are rewarded for treating its employees in fair and equitable manner. "Organizations rewarding individuals with incentives for knowledge contribution encourages fairness" (Bock & Kim, 2002, p. 16). As suggested by Wang & Noe (2010), "knowledge processing behavior can prove to be motivational when it provides the benefits of recognition, promotion, and salary hike to the employees and also contributes in expanding their expertise and knowledge base" (p. 115). Also, "KM practices need to be fair and unbiased. The knowledge which individual possesses is an intellectual capital of the individual and organizations may refrain from controlling it" (Chen & Choi, 2005, p. 107; Gorman, 2004). According to Da Costa, Prior, & Rogerson, (2010), "atmosphere of fairness and equality can be seen where individuals feel driven to share, create, and process knowledge" (p. 580). On the basis of above discussion, it is proposed to link ethics and KM.

There are various Indian research studies on knowledge (Tomblin & Maheshwari, 2004), Leadership (Singh & Kumar, 2013), Organizational Culture (Kumar, 2012), Technology (Kumar, 2012), knowledge management (Singh, 2001; Grover & Banerjee, 2005; Sharma, 2005; Sharma, 2008; Singh & Sharma, 2008a; Singh & Sharma, 2008b; Singh & Sharma, 2008c; Singh & Sharma, 2008d; Kumar, 2014) per se and the factors affecting knowledge management, for example, technology (Kumar, 2012), Organizational Culture (Sharma, 2005; Singh & Sharma, 2011a; Singh & Sharma, 2011b; Kumar, 2014), leadership (Kumar, 2013), knowledge manager (Dutt, 2006), and how knowledge management results into higher employees satisfaction (Singh & Sharma, 2011b).

Table No. 1: Ethics Dimensions and Respective Indicators

S. No.	Dimensions	Indicators/Areas	Sources
1.	Organizational Value and Justice	Collective trust	Suhonen, Stolt, Katajisto, Charalambous, & Olson (2015), Akhavan et al. (2013), Azmi (2010a), Khenifer & Moghimi (2009), Ali (2008), Raps (2005), Inkpen & Tsang (2005), Hutchings & Michailova (2004), Galford & Drapeau (2003)
		Organizational trust	
		Honesty	
		Fair behaiviour	
		Humility	
		Criticism taking	
		Perseverance in works	
2.	Commitment and Responsibility	Responsibility	Suhonen et al. (2015), Akhavan et al. (2013), Bove & Jhonson (2012), Calof & Smith (2012), Michie & Johnston (2012), Jordan & Troth (2011), Azmi (2010b), Huysmans & Wit (2004), Chua (2002), Nahapiet & Ghosal (1998)
		Working conscience	
		Commitment	
		Loyalty	
		Foresight	
3.	Intellectual Ownership and Trusteeship	Secrecy	Sayce (2012), Azmi (2010b), Khenifer & Moghimi (2009), Akhavan et al. (2013)
		Intellectual property right	
		Trusteeship	
		Care in authenticity	
		Council with others	
4.	Team Working Morale	Helping and empathy with others	Akhavan, et al. (2013), Azmi (2010b), Meng-Hsiang & Fang-Yang (2003), Ferris (2008), Huysmans & Wit (2004), Chua (2002)
		Affability	
		Self-control	
		Self-control	
5.	PRIMES (Ethical Action Model)	Personality	Huff (2010)
		Integration of morality	
		Moral ecology	
		Skills & knowledge	
6.	Ethical Issues	Socio economic issue	Suhonen et al. (2015), Bryant (2006)
		Technical issue	
		Legalistic issue	
7.	Obstacles to Ethical Behaviour	Knowledge hoarding	Zyngier & Nagpal (2015)
		Manipulation	
		Misappropriation	
		Plagiarism	
		Property & privacy right conflict	
		Autonomy in knowledge sharing	

Conceptual Model

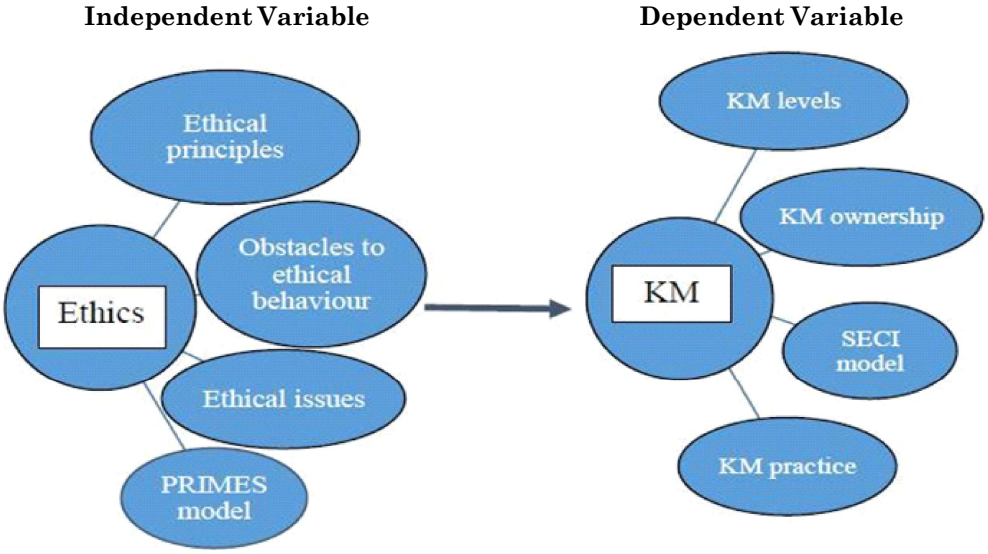


Figure No.1: Ethics impacting KM System

Source: Compiled by authors

Research Methodology

Study Design

An exploratory factor analysis was carried out with the primary objective of reducing the number of items and investigating that the factors/constructs stated in the literature are appropriate according to the present scenario. Also, grouping provided by the literature needed to be reviewed or regrouped. Initially, the process of Factor Analysis was considered to be used for identifying the ethical dimensions outlined in the literature. Subsequently, Exploratory Factor Analysis was used because of the possibility of identification of other meaningful factors involving combination of items. The factors resulted from the EFA were then tested for the reliability.

Research Instrument

The preliminary section of questionnaire demanded respondents to fill demographic details like age, gender, qualification, and work experience. The research instrument with 36 questions was created covering variables grouped under the constructs discussed in literature which includes organizational values and justice, commitment and responsibility, intellectual ownership and trusteeship, team working morale, ethical issues, obstacles to ethical behavior, individual ethics, and moral ecology. The variables so derived at the end were used after approval from various experts in the field of ethics, human resource, and compliance.

Participants

A convenience method of sampling was employed. The questionnaire was sent to 300 participants. There were 278 respondents to the questionnaire. All participants were assured of anonymity and confidentiality.

Analysis

The demographic details of the respondents are shown in table no. 2.

Table No. 2: Demographic Details

Sample Characteristics	Frequency (n=278)	Percentage
Gender		
Male	186	67%
Female	92	33%
Age		
18-25	85	30%
26-35	119	43%
35-59	69	25%
60 and above	5	2%
Education		
Graduate	129	46%
Post Graduate	133	48%
Doctorate	16	6%
Experience		
Freshers	18	6%
1-5 years	120	43%
6-10 years	50	18%
10-20 years	72	26%
Above 20 years	18	7%

The Exploratory Factor Analysis (Principle Component Analysis) employed a rotated component matrix to identify and reduce the number of factors and to make interpretation of analysis easier. Minimum factor loadings were set at 0.40 (Nunnally, 1978).

Principal-Axis Factor Analysis was employed using SPSS 22 to examine the dimensions of the constructs. The rotation method used in the paper is varimax rotation. The goal of varimax rotation is to simplify and clarify the data structure. The main goal of EFA is to extract the smallest number of interpretable factors contributing to the correlation among of variables. The items that are grouped together after applying EFA are said to measure the same underlying construct (Kerlinger, 1986). EFA is helpful when the researchers are trying to understand the dimensions of a construct. It also helps in identifying the variables which do not have any contribution in the construct.

EFA is the first step to identify and extract important variables which could be further tested using Confirmatory Factor Analysis. The 33 scale items loaded on to 5 factors accounts for 60.61% of the explained variance (as shown in table no. 3).

Extraction Method: Principal Component Analysis

The Kaiser-Meyer Olkin measure (Cerny & Kaiser, 1977; Kaiser, 1970) of sampling adequacy was 0.910 as shown in table no. 4. The 'p' value is less than 0.01, so it could be construed that EFA is an appropriate strategy. Further, the Bartlett's Test of Sphericity (Bartlett, 1950, 1951) yielded a Chi-Square value of 4851.993, with 528 df.

Table No. 3: Total Variance Explained

Component	Initial Eigen Values			Extraction Sums of Squared Loadings			Rotation Sums of Squared Loadings		
	Total Variance	% of Variance	Cumulative %	Total Variance	% of Variance	Cumulative %	Total Variance	% of Variance	Cumulative %
1.	10.72	32.47	32.47	10.72	32.47	32.47	8.05	24.40	24.40
2.	4.38	13.28	45.76	4.38	13.28	45.76	4.75	14.40	38.80
3.	2.07	6.27	52.03	2.07	6.27	52.03	3.03	9.18	47.98
4.	1.66	5.02	57.04	1.66	5.02	57.04	2.51	7.61	55.59
5.	1.18	3.57	60.61	1.18	3.57	60.61	1.66	5.02	60.61
6.	0.97	2.94	63.55						
7.	0.89	2.70	66.25						
8.	0.83	2.53	68.78						
9.	0.77	2.33	71.11						
10.	0.75	2.27	73.38						
11.	0.67	2.03	75.41						
12.	0.62	1.88	77.29						
13.	0.60	1.81	79.10						
14.	0.58	1.75	80.85						
15.	0.56	1.71	82.56						
16.	0.55	1.66	84.22						
17.	0.47	1.41	85.63						
18.	0.46	1.38	87.01						
19.	0.41	1.25	88.26						
20.	0.41	1.24	89.51						
21.	0.38	1.15	90.65						
22.	0.37	1.14	91.79						
23.	0.36	1.11	92.89						
24.	0.33	1.01	93.90						
25.	0.30	0.92	94.82						
26.	0.28	0.83	95.65						
27.	0.26	0.80	96.45						
28.	0.25	0.76	97.21						
29.	0.22	0.66	97.88						
30.	0.20	0.61	98.48						
31.	0.19	0.58	99.06						
32.	0.18	0.54	99.60						
33.	0.13	0.40	100.00						

Table No. 4: KMO and Bartlett's Test

Kaiser-Meyer-Olkin Measure of Sampling Adequacy.		0.910
Bartlett's Test of Sphericity	Approx. Chi-Square	4851.993
	Df	528
	Sig.	0.000

Factors were extracted with the Eigen Values more than 1. Items were removed when communalities were less than 0.40 as shown in table no. 5. This resulted in the deletion of 3 items, reducing the total number of items to 33. Communalities displays variance that variable has been accounted for extracted factors. In the communalities 31 variables out of 33 variables displayed more than 0.5 variance.

Table No. 5: Communalities

S. No.	Items/Variables	Initial	Extraction
1.	Employees take social responsibility of their actions.	1.00	0.59
2.	My colleagues are available for counseling at the time of confusion.	1.00	0.60
3.	Employees do not modify or change the information for their personal gain.	1.00	0.59
4.	It is important for employees to have fair and impartial behavior with each other.	1.00	0.66
5.	Employees behave honestly with each other.	1.00	0.71
6.	Consultation with others in tasks and decisions is important for employees.	1.00	0.40
7.	Care in Authenticity (assessing the accuracy of a subject) is important.	1.00	0.62
8.	The behavior of employees in my organization is fair and friendly.	1.00	0.49
9.	Employees have high work consciousness.	1.00	0.68
10.	Employees are responsible and accountable for their tasks.	1.00	0.64
11.	Employees moral actions are influenced by surrounding people in organization	1.00	0.66
12.	Employee's personal characteristics & skills guide their moral actions.	1.00	0.62
13.	Having good manners and openness is admired.	1.00	0.56
14.	Information confidentiality of employees and organization is very important and emphasized.	1.00	0.53
15.	Self-control is important for employees and its emphasized by the organization.	1.00	0.46
16.	Employees do not keep their personal knowledge with themselves rather they share it.	1.00	0.54
17.	Too much autonomy in knowledge sharing is a barrier.	1.00	0.59
18.	Employees trust each other and deal with each other in good faith.	1.00	0.56
19.	Manipulation and misappropriation hinders knowledge sharing.	1.00	0.60

S. No.	Items/Variables	Initial	Extraction
20.	Sharing knowledge and legal issues are inter-related.	1.00	0.57
21.	The boundaries of my knowledge and organizational knowledge are sometimes confusing.	1.00	0.66
22.	Employees feel committed towards organization's goals & mission and their responsibilities.	1.00	0.63
23.	Employees are sympathetic to each other and are willing to help each other.	1.00	0.73
24.	Trusteeship is important and considerable for all members.	1.00	0.76
25.	Employee designing & implementing KMS can act as Whistle-blower.	1.00	0.65
26.	Considers Intellectual Property Right as important and it is emphasized.	1.00	0.63
27.	Employees are loyal to organization and to each other.	1.00	0.71
28.	Employees trust that organizational policies will be done according to given promises.	1.00	0.61
29.	Employees have foresight in their actions and decisions, according to organization's vision.	1.00	0.50
30	Employees and managers trust each other and deal with each other in good faith.	1.00	0.59
31.	Tolerance and perseverance of people in tasks is valuable.	1.00	0.72
32.	Modesty and courtesy is value and virtue.	1.00	0.65
33.	Capturing employees' knowledge into information system leads to downsizing or retrenchment.	1.00	0.50

Table no. 6 has the five factors with the variables and their respective factor loadings. The final 33 items that comprised the independent variable, 'Ethics' are also presented in the same table. The five factors identified are: F1: Organizational Values and Ethical Climate; F2: Commitment, Responsibility, and Team Working Morale; F3: Intellectual Capital and Trusteeship; F4: Ethical Issues, and F5: Obstacles to Ethical Behavior. A factor with fewer than three items is generally weak and unstable; the factors identified have at-least three variables.

In order to estimate reliability, the value of Cronbach Alpha was calculated for each construct (factor) identified through Factor Analysis. As per Nunnally (1978), factors having alpha below 0.70 should be deleted. However, various scholars have also pointed that in exploratory studies alpha less than 0.70 can also be considered, i.e., between 0.50 and 0.70 (Frazier & Rody, 1991; Katabe, 1990; Kohli, 1989; Noordewier, John, & Nevin, 1990). The threshold 0.50 is used in this research (F1-F5). The Cronbach Alpha for all 33 variables is 0.910, that is, above minimum threshold of 0.7 as suggested by Nunnally (1978). There are five constructs and four constructs have been above the minimum threshold of 0.7. The reliability statistics is given in table no. 7.

Discussion and Conclusions

The main objective of the study is to examine that constructs derived from the literature are valid as per the current sample statistics or they need to be reframed by regrouping of the variables according to the obtained statistics. According to the literature, there were seven constructs formed from the

Table No. 6: Factor Loadings

Factor No.	Item No.	Variables/Items	Component				
			1	2	3	4	5
F1	**S16**	Employees do not keep their personal knowledge with themselves rather they share it.	0.696				
F1	**S3**	Employees do not modify or change the information for their personal gain.	0.726				
F1	**S18**	Employees trust each other and deal with each other in good faith.	0.671				
F1	**S28**	Employees trust that organizational policies will be done according to given promises.	0.758				
F1	**S5**	Employees behave honestly with each other.	0.712				
F1	**S4**	It is important for employees to have fair and impartial behaviour with each other.	0.704				
F1	**S32**	Modesty and courtesy is value and virtue.	0.665				
F1	**S31**	Tolerance and perseverance of people in tasks is valuable.	0.842				
F1	**S8**	The behavior of employees in my organization is fair and friendly.	0.840				
F1	**S1**	Employees take social responsibility of their actions.	0.736				
F1	**S30**	Employees and managers trust each other and deal with each other in good faith.	0.762				
F1	**S13**	Having good manners and openness is admired.	0.815				
F1	**S12**	Employee's personal characteristics & skills guide their moral actions.	0.713				
F1	**S11**	Employees moral action are influenced by surrounding people in organization	0.572				
F2	**S10**	Employees are responsible and accountable for their tasks.		0.582			
F2	**S9**	Employees have high work consciousness.		0.581			
F2	**S22**	Employees feel committed towards organization's goals and mission and their responsibilities.		0.813			
F2	**S27**	Employees are loyal to organization and to each other.		0.783			
F2	**S29**	Employees have foresight in their actions and decisions, according to organization's vision.		0.793			
F2	**S6**	Consultation with others in tasks and decisions is important for employees.		0.770			
F2	**S23**	Employees are sympathetic to each other and are willing to help each other.		0.562			

Factor No.	Item No.	Variables/Items	Component				
			1	2	3	4	5
F2	**S15**	Self-control is important for employees and its emphasized by the organization.		0.685			
F2	**S2**	My colleagues are available for counselling at the time of confusion.		0.553			
F3	**S26**	Considers Intellectual Property Right as important and it is emphasized.			0.709		
F3	**S24**	Trusteeship is important and considerable for all members.			0.771		
F3	**S7**	Care in Authenticity (assessing the accuracy of a subject) is important.			0.732		
F3	**S14**	Information confidentiality of employees and organization is very important and emphasized.			0.592		
F4	**S25**	Employee designing & implementing KMS can act as Whistle-blower.				0.748	
F4	**S33**	Capturing employee's knowledge into information system leads to downsizing or retrenchment.				0.818	
F4	**S20**	Sharing knowledge and legal issues are interrelated.				0.727	
F5	**S19**	Manipulation and misappropriation hinders knowledge sharing.					0.662
F5	**S21**	The boundaries of my knowledge and organisational knowledge are sometimes confusing.					0.633
F5	**S17**	Too much autonomy in knowledge sharing is a barrier.					0.575

Table No. 7: Reliability Statistics

Factor No.	Factors/Dimensions	No. of Items	No. of Cases	Cronbach's Alpha
	Overall Reliability	33	278	0.91
F1	Organizational values and ethical climate	14	278	0.95
F2	Commitment, responsibility and team working morale	9	278	0.89
F3	Intellectual capital and trusteeship	4	278	0.81
F4	Ethical issues	3	278	0.75
F5	Obstacles to ethical behavior	3	278	0.53

grouping of different variables. The EFA in the current study resulted in five constructs (factors) comprising of 33 variables. The five factors resulted from EFA are named as, F1: Organizational Values and Ethical Climate; F2: Commitment, Responsibility, and Team Working Morale; F3: Intellectual Capital and Trusteeship; F4: Ethical Issues, and F5: Obstacles to Ethical Behavior.

The study deliberates on ethical constructs specifically from KM perspective. There is deliberation on various obstacles to ethical behavior in KM. These obstacles comprises of knowledge hoarding, manipulation, misappropriation, and privacy rights. The various ethical issues from KM perspective which includes socio economic, legal, and technical issues have also been discussed. The knowledge management in ethical context can be effective in an organization if individual's personality, his environment, commitment towards morality, and moral skills and knowledge are studied in depth. When all these parameters of ethics discussed in the paper would be embedded in the culture of an organization, it will support KM processes, KM practices, and all KM initiatives.

Limitations of the Study

This study does not cover any specific population or profession, neither any specific industry. Thus, this is a generalized research for all professions or industries. The sample of the study constituted 278 respondents from different professions and industries. The sample size could have been larger as larger sample size would have given more appropriate findings. This study has focused on quantitative methodology of data collection and thus, it is restrictive. Moreover, the scale facilitates employees to assess and evaluate ethical dimensions, which may or may not be authentic indicator of ethical dimensions existing in the organization. As it is according to what employee feel, think, and believe about a particular ethical framework that exists within their organization which may or may not be authentic.

Future Research

Research could be conducted to establish the relationship between ethics and KM. The link between ethics and KM may be established for ethical conceptualization of KM. Ethical framework supporting KM initiatives and KM process should be developed and implemented. Further, the impact of ethics on KM processes and activities can be accessed and measured. The scale can be used as an ethical instrument for investigating effectiveness in KM process, KM ownership, and KM practices. For practical implications, managers should understand that adoption of KM processes will not guarantee success until supported by the ethical framework. KM systems can be implemented and executed more successfully in those organizations where there is more emphasis on ethics by the organizations.

The research instrument developed through this study, that is, ethical constructs created using EFA will help to link ethics and KM in future studies. The current research will also add to the literature and knowledge domain in the area of ethics and KM.

References

Akhavan, P., Ramezan, M., & Moghaddam, Y. J. (2013). Examining the role of ethics in knowledge management process case study: An industrial organization. *Journal of Knowledge based Innovation in China, 5*(2), 129-145.

Ali, J. A. (2008). Emiratisation: Drawing UAE nationals into their surging economy. *International Journal of Sociology and Social Policy, 28*(9/10), 365-379.

Azmi, F. T. (2010a). Devolution of HRM and organizational performance: Evidence from India. *International Journal of Commerce and Management, 20*(3), 217-231.

Azmi, I. M. (2010b). Legal and ethical issues in knowledge management in Malaysia. *Computer Law & Security Review*, *26*(1), 61-71.

Bartlett, M. S. (1950). Tests of significance in factor analysis. *British Journal of Statistical Psychology, 3*(2), 77-85.

Bartlett, M. S. (1951). A further note on tests of significance in factor analysis. *British Journal of Statistical Psychology, 4*(1), 1-2.

Baskervile, R., & Dullipovici, A. (2006). *The ethics of knowledge transfers and conversions: Property or privacy rights?* Proceedings of the 39th Annual Hawaii International Conference on System Scien*ces (HICSS'06)*, Kauia, HI, USA. Retrived from http://ieeexplore.ieee.org/stamp/stamp.jsp?tp=&arnumber=1579581&isnumber=33367, Accessed on September 10, 2017.

Bock, G. W., & Kim, Y. G. (2002). Breaking the myths of rewards: An exploratory study of attitudes about knowledge sharing. *Information Resources Management Journal, 15*(2), 14-21.

Bove, L.L., & Johnson, L.W. (2000). A customer-service worker relationship model. *International Journal of Service Industries Management, 11*(5), 491-511.

Bryant, A. (2006). *Knowledge management: The ethics of the Agora or the mechanisms of the market?* Proceedings of the 39th Hawaii International Conference on System Sciences. Retrieved from https://www.researchgate.net/publication/4216331_Knowledge_Management_-_The_Ethics_of_the_Agora_or_the_Mechanisms_of_the_Market, Accessed on July 12, 2017.

Burchell, J., & Cook, J. (2008). Stakeholder dialogue and organizational learning: Changing relationships between companies and NGOs. *Business Ethics: A European Review, 17*(1), 35-46.

Calof, J., & Smith, J. E. (2012). Foresight impacts from around the world: A special issue. *Foresight, 14*(1), 5-14.

Cerny, C. A., & Kaiser, H. F. (1977). A study of a measure of sampling adequacy for factor-analytic correlation matrices. *Multivariate Behavioral Research, 12*(1), 43-47.

Chen, S., & Choi, C. (2005). A social exchange perspective on business ethics: An application to knowledge exchange. *Journal of Business Ethics, 62*(1), 107-128.

Chua, A. (2002). The influence of social interaction on knowledge creation. *Journal of Intellectual Capital, 3*(4), 375-392.

Crisp, R. (2011). *Aristotle: Nicomachean ethics.* Cambridge, UK: Cambridge University Press.

Da Costa, G. J. M., Prior, M., & Rogerson, S. (2010). Organizational knowledge: Ethics and the importance of trust. *Communications in computer and Information Science, 110*(4), 295-304.

Delong, D.W., & Fahey, L. (2000). Diagnosing cultural barriers to knowledge management. *Academy of Management Executive, 14*(4), 113-127.

Dutt, H. (2006). Role of knowledge manager in knowledge product development evidence from the Indian automotive sector. *Delhi Business Review, 7*(1), 59-70.

Ferris, D.L. (2008). The development and validation of the workplace ostracism scale. *Journal of Applied Psychology, 93*(6), 1348-1366.

Frazier, G., & Rody, R. (1991). The use of influence strategies in inter-firm relationships in industrial product channel. *Journal of Marketing, 55*(1), 52-69.

Galford, R. M., & Drapeau, A. S. (2003). Organizational culture: The enemies of Trust. *Harvard Business Review, 81*(2), 88-95.

Glisby, M., & Holden, N. (2003). Contextual constraints in knowledge management theory: The cultural embeddedness of Nonaka's Knowledge-creating company. *Knowledge and Process Management, The Journal of Corporate Transformation, 10*(1), 29-36.

Gorman, G. E. (2004). The uniqueness of knowledge management or the Emperor's New Clothes? *Library Management and Information Services, 19*(1), 17-32.

Grover, D., & Banerjee, S. (2005). Building the business relationship through knowledge management. *Delhi Business Review, 6*(2), 69-74.

Huff, C. (2010). *What does knowledge have to do with ethics*? Retrieved from https://www.researchgate.net/publication/242750758_What_Does_Knowledge_Have_to_do_with_Ethics, Accessed on August 14, 2017.

Hume, D. (1750). Enquiries concerning human understanding and the principles of Morals. Oxford: Clarendon Press.

Hutchings, K., & Michailova, S. (2004). Facilitating knowledge sharing in Russian and Chinese subsidiaries: The role of personal networks and group membership. *Journal of Knowledge Management, 8*(2), 84-94.

Huysman, M., & Wit, D.D. (2004). Practices of managing knowledge sharing: Towards a second wave of knowledge management. *Knowledge and Process Management. The Journal of Corporate Transformation, 11*(2), 81-92.

Inkpen, A. C., & Tsang, E. W. K. (2005). Social capital, network, and knowledge transfer. *The Academy of Management Review, 30*(1), 146-165.

Jordan, P. J., & Troth, A. (2011). Emotional intelligence and leader member exchange: The relationship with employee turnover intentions and job satisfaction. *Leadership & Organization Development Journal, 32*(3), 260-280.

John, O. P., & Srivastava, S. (1999). *The big five trait taxonomy: History, measurement and theoretical perspectives. Handbook of personality: Theory and research.* New York: Guilford.

Kaiser, H. F. (1970). A second generation little jiffy. *Psychometrika, 35*(4), 401-415.

Kant, I. (1991). *Groundwork of the metaphysics of morals*. London: Routledge.

Katabe, M. (1990). Corporate product policy and innovative behavior of European and Japanese multinationals. *Journal of Marketing, 54*(2), 19-33.

Kerlinger, F. N. (1986). *Foundations of behavioral research*. New York : Holt, Rinehart and Winston.

Khenifer, H., & Moghimi, S. M. (2009). Ethics philosophy in organization, case study: Ethical chapters. *QOM University Quarterly, 11*(1), 235-260.

Kohli, A. K. (1989). Effects of supervisory behavior: The role of individual differences among salespeople. *Journal of Marketing, 53*(4), 40-50.

Kumar, M. (2012). *Knowledge management: A study of selected organizations.* Unpublished Doctoral Dissertation, University of Delhi, Delhi, India.

Kumar, M. (2013). Effect of leadership behaviors on knowledge creation in Indian organizations. *Delhi Business Review, 14*(2), 57-82.

Kumar, M. (2014). The relationship of knowledge identification and creation with leadership, culture and technology. *The IUP Journal of Knowledge Management, 11*(2), 7-37.

Lee, S. T. (2010). A knowledge management approach to understanding ethical knowledge in public relations. *Journal of communication management, 16*(2), 1185-203.

Liebowitz, J. (1999). *Knowledge management handbook.* USA: CRC Press.

Macintyre, A. (1985). *After virtue: A study in Moral Theory.* Notre Dame, Indiana: University of Notre Dame Press.

Meng-Hsiang, H., & Feng-Yang, K. (2003). The effect of organization- based self- esteem and deindividuation in protecting personal information privacy. *Journal of Business Ethics, 42*(4), 305-320.

Michael, Z., Mckeen, J., & Singh, S. (2009). Knowledge management and organizational performance: An exploratory analysis. *Journal of Knowledge Management, 13*(6), 392-409.

Michie, S., & Johnston, M. (2012). Theories and techniques of behaviour change: Developing a cumulative science of behaviour change. *Health Psychology Review, 6*(1), 1-6.

Nahapiet, J., & Ghoshal, S. (1998). Social Capital, Intellectual Capital, and the Organizational Advantage. *The Academy of Management Review, 23*(2), 242-266.

Noordewier, T., John, G., & Nevin, J. (1990). Performance outcomes of purchasing arrangements in industrial buyer-vendor relationships. *Journal of Marketing, 54*(4), 80-93.

Nunnally, J. C. (1978). *Psychometric Theory.* New York: McGraw-Hill Book Company.

Patel, M., & Ragsdell, G. (2011). To share or not to share knowledge: An ethical dilemma for UK academics*? Journal of Knowledge Management Practice, 12*(2), 420-427.

Raps, A. (2005). Strategy implementation – An insurmountable obstacle? *Handbook of Business Strategy, 6(*1), 141-146.

Sayce, S. (2012). Being a female pension trustee. *Equality, Diversity and Inclusion: An International Journal, 31*(3), 298-314.

Sen, A. (1993). Does business ethics make economic sense? *Business Ethics Quarterly, 3*(1), 45-54.

Sharma, V. (2005). Knowledge Management- A HR tool to get competitive edge: An empirical study in telecom sector. *Delhi Business Review, 6*(2), 51-60.

Sharma, V. (2008). Knowledge management as a turnaround factor for organisational learning and employee satisfaction: An empirical study in pharmaceutical sector. *Delhi Business Review, 9*(2), 67-78.

Singh, A. K., & Kumar, M. (2013). Organizational leadership in India. In C.S. Sharma & R.K. Singh (Eds.), *Transformational Leadership and Beyond* (pp.53-67). New Delhi, India: Excel India Publishers.

Singh, A. K., & Sharma, V. (2008a). Key attributes of successful knowledge management: An empirical study in telecom

and software sector. *Proceedings of the International Conference on Data Management-2008,* (February 25-26, 2008) at IMT, Ghaziabad (pp. 495-502). Haryana, India: McMillan Publications. ISBN: 10: 0230-63469-9; ISBN: 13: 978-0230-63469-5.

Singh, A.K., & Sharma, V. (2008b). A study on implications of culture driven knowledge management on employee satisfaction in indian telecom sector. In Coskun Can Aktan and OzkanDalbay (Eds.), *Management and Behaviour in Organizations* (Vol. 2, pp. 15-28). Selected Proceedings of the First International Conference on Social Sciences, Organized by Social Sciences Research Society on August 21-22, 2008 at Izmir, Turkey. ISBN: 978-605-5741-16-3.

Singh, A. K., & Sharma, V. (2008c). Knowledge management and organisational learning: An empirical study of its implications on employee satisfaction in telecom sector. *Proceedings of the National Conference on Management- 2007 on Corporate Strategies and Innovations in the Emerging Global Economy* (pp. 302-318) on November, 23-24, 2008 at GGS Indraprastha University, New Delhi. New Delhi: Wisdom Publications.

Singh, A. K., & Sharma, V. (2008d). Antecedents of knowledge management and its impact on employee satisfaction: A study on indian telecom sector. In B.S. Sahay, J. Ranjan, R. R. Thakur, & S. Nicholas (Eds.), *Redefining Business Horizons*. Proceedings of the International Conference on Innovation and Redefining Business (IIRB) -2008 (pp. 570-581) organized at IMT, Ghaziabad, India. Haryana, India: McMillan Publications.

Singh, A. K., & Sharma, V. (2011a). Key attributes of successful knowledge management: An empirical study in telecommunication and software industries. *International Journal Business Information Systems*, *7*(1), 78-92.

Singh, A. K., & Sharma, V. (2011b). Knowledge management antecedents and its impact on employee satisfaction: A study on indian telecommunication industries. *The Learning Organization, Emerald Journal, 18*(2), 115-130. Retrieved from http://www.emeraldinsight.com/10.1108/09696471111103722, Accessed on August 13, 2017.

Singh, V. K. (2001). Knowledge Management: A necessity in new Millennium. *Delhi Business Review, 2*(2), 105-108.

Smith, A. (2002). *The Theory of Moral Sentiments*. Cambridge: Cambridge University Press.

Suhonen, R., Stolt, M., Katajisto, J., Charalambous, A., & Olson, L. L. (2015). Validation of the Hospital Ethical Climate Survey for older people care. *Nursing Ethics, 22*(5), 517-532.

Tomblin, M. S., & Maheshwari, S. K. (2004). Value of knowledge assets: Techniques and problems. *Delhi Business Review, 5*(1), 33-37.

Tseng, F. C., & Fan,Y. J. (2011). Exploring the influence of ethical norms on organizational knowledge management. *Journal of Business Ethics, 101*(2), 325-342.

Wang, S., & Noe, R. A. (2010). Knowledge sharing: A review and direction for future research. *Human Resource Management Review, 20*(2), 115-131.

Zyngier, S., & Nagpal, A. (2015). Knowledge management ethics: Located within the governance framework. *48th Hawaii International Conference on at System Sciences.*

Conceptualization of the Balanced Scorecard for Organizational Performance Measurement

Dr. Vikas Gupta

Asst. Professor, Delhi School of Management,

Delhi Technological University (Formerly Delhi College of Engineering),

DTU (DCE) Campus, Bawana Road, Delhi-110 042, INDIA

Email address: vikasguptadtu@gmail.com

Ms. Meenu Chopra

Research Scholar, Delhi School of Management,

Delhi Technological University (Formerly Delhi College of Engineering),

DTU (DCE) Campus, Bawana Road, Delhi-110 042, INDIA

Email address: mchopra2002@gmail.com

Abstract:

Purpose *– This paper aims to review, analyze and develop a deep understanding of the concept of Balanced Scorecard (BSC) as an organizational performance measurement tool. The BSC was developed to address the problems and limitations of relying solely on traditional financial measures. A detailed analysis on perspectives surrounding the BSC has been carried out*

Design/methodology/approach *– The paper reviews relevant literature on the BSC by focusing on the pertinent issues surrounding the applicability of the BSC model in modern business environment.*

Findings *– It is established that the BSC plays a pivotal role in assisting business executives in making holistic long-term management decisions.*

Practical implications *– It is envisioned that the study should add to the literature on corporate performance measures. The revelations gained through this paper will enable researchers to have an open mind on the way the BSC may be applied for various business environments.*

Originality/value *– The paper clearly points out that the BSC has been successfully implemented in various corporate houses across the world and used to reflect realities of modern business activities better than before, hence making it an effective tool for organizational performance measurement.*
Paper type *Conceptual paper*

Keywords Balanced Scorecard, Organizational Performance.

Biographical Note:
Dr. Vikas Gupta is a Gold Medalist (MBA) and has more than 15 years of experience. He is currently working as an Assistant Professor, Delhi School of Management, Delhi Technological University (Former Delhi College of Engineering). He has many research papers and articles in his credit which are published in International and Indian journals.

His research interests are in the area of knowledge management, innovation, and corporate social responsibility. He has been awarded the Best Faculty Award in the area of management.

Ms. Meenu Chopra is an MBA with more than 12 years of teaching experience. While her tenure at Guru Nanak Institute of Management (affiliated to Guru Gobind Singh IP University), she acted as Coordinator, PGDM managing the entire department. She moved on to teach Bachelor of Business Studies (BBS) at University of Delhi and was worked there for four years. She is currently pursuing Ph.D as Full Time Research Scholar under the DTU Fellowship from Delhi School of Management, Delhi Technological University (Former Delhi College of Engineering).

1. Introduction

Over the last few years, the pressure of reporting corporate performance based on non-financial as well as financial measures has intensified. Generally, it is

believed that the best performance measures are those that link to a business' strategy. Also, performance measures should be concentrated on, and should reward behavior that contributes to business success (see Kaplan and Norton, 1992; 1996a; 1996b; Atkinson and Epstein, 2000). Managers over the years have realized and acknowledged that performance measurement tools applied by an organization should not only be based on financial results but should also focus on non-financial measures which play an important role in the long term success or failure of an organization. After studying the recent developments in the performance measurement literature, it is noticed that more and more executives have begun to adopt the BSC as a tool for analyzing the fit between present day strategy and long term objectives of the firm. There is a growing interest in non-financial measures such as customer satisfaction, employee satisfaction, or innovation, as useful indicators of a firm's future performance. The popularity of the tool has increased manifold in the recent years.

2. Purpose of the Paper

Accordingly, the purpose of the paper is to develop a clear understanding of the various measures adopted by Balanced Scorecard. Also, the paper aims to examine the process, suggested by BSC, of connecting strategy to present day action.

3. What is Balanced Scorecard (BSC)

The balanced scorecard is a strategic planning and management system that is used extensively in business and industry, government, and nonprofit organizations worldwide to align business activities to the vision and strategy of the organization, improve internal and external communications, and monitor organization performance against strategic goals. It was originated by Drs. Robert Kaplan (Harvard Business School) and David Norton as a performance measurement framework that added strategic non-financial performance measures to traditional financial metrics to give managers and executives a more 'balanced' view of organizational performance.

Research suggests that over 50% of large US firms have adopted the BSC. More than half of major companies in the US, Europe and Asia are using balanced scorecard approaches, with use growing in those areas as well as in the Middle East and Africa. A recent global study by Bain & Co listed balanced scorecard fifth on its top ten most widely used management tools around the world, a list that includes closely-related strategic planning at number one. Balanced scorecard has also been selected by the editors of Harvard Business Review as one of the most influential business ideas of the past 75 years.

The balanced scorecard has evolved from its early use as a simple performance measurement framework to a full strategic planning and management system. The “new” balanced scorecard transforms an organization’s strategic plan from an attractive but passive document into the "marching orders" for the organization on a daily basis. It provides a framework that not only provides performance measurements, but helps planners identify what should be done and measured. It enables executives to truly execute their strategies.

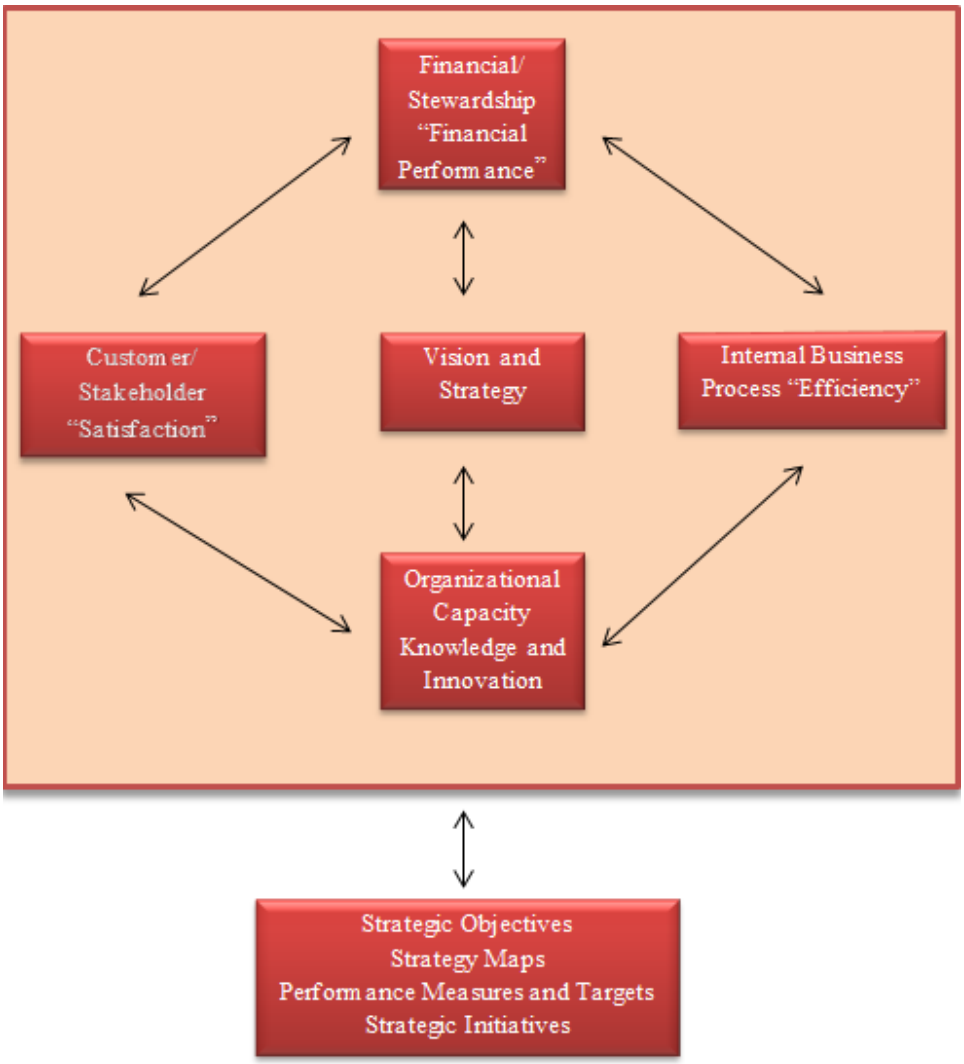
This new approach to strategic management was first detailed in a series of articles and books by Drs. Kaplan and Norton. Recognizing some of the weaknesses and vagueness of previous management approaches, the balanced scorecard approach provides a clear prescription as to what companies should measure in order to 'balance' the financial perspective. The balanced scorecard is a management system (not only a measurement system) that enables organizations to clarify their vision and strategy and translate them into action. It provides feedback around both the internal business processes and external outcomes in order to continuously improve strategic performance and results. When fully deployed, the balanced scorecard transforms strategic planning from an academic exercise into the nerve center of an enterprise. Kaplan and Norton describe the innovation of the balanced scorecard as follows:

"The balanced scorecard retains traditional financial measures. But financial measures tell the story of past events, an adequate story for industrial age

companies for which investments in long-term capabilities and customer relationships were not critical for success. These financial measures are inadequate, however, for guiding and evaluating the journey that information age companies must make to create future value through investment in customers, suppliers, employees, processes, technology and innovation"

Figure 1

Concept of the Scorecard



Source: Adapted from Kaplan R S and Norton D P (1996b), "Using the Balanced Scorecard as a Strategic Management System", Harvard Business Review, Vol. 74, No. 1, pp. 75-85.

4. Perspectives

The balanced scorecard suggests that we view the organization from four perspectives, and to develop metrics, collect data and analyze it relative to each of these perspectives:

4.1 The Learning & Growth Perspective

This perspective includes employee training and corporate cultural attitudes related to both individual and corporate self-improvement. In a knowledge-worker organization, people -- the only repository of knowledge -- are the main resource. In the current climate of rapid technological change, it is becoming necessary for knowledge workers to be in a continuous learning mode. Metrics can be put into place to guide managers in focusing training funds where they can help the most. In any case, learning and growth constitute the essential foundation for success of any knowledge-worker organization.

Kaplan and Norton emphasize that 'learning' is more than 'training'; it also includes things like mentors and tutors within the organization, as well as that ease of communication among workers that allows them to readily get help on a problem when it is needed. It also includes technological tools; what the Baldrige criteria call "high performance work systems."

4.2 The Business Process Perspective

This perspective refers to internal business processes. Metrics based on this perspective allow the managers to know how well their business is running, and whether its products and services conform to customer requirements (the mission). These metrics have to be carefully designed by those who know these processes most intimately; with our unique missions these are not something that can be developed by outside consultants.

4.3 The Customer Perspective

Recent management philosophy has shown an increasing realization of the importance of customer focus and customer satisfaction in any business. These

are leading indicators: if customers are not satisfied, they will eventually find other suppliers that will meet their needs. Poor performance from this perspective is thus a leading indicator of future decline, even though the current financial picture may look good.

In developing metrics for satisfaction, customers should be analyzed in terms of kinds of customers and the kinds of processes for which we are providing a product or service to those customer groups.

4.4 The Financial Perspective

Kaplan and Norton do not disregard the traditional need for financial data. Timely and accurate funding data will always be a priority, and managers will do whatever necessary to provide it. In fact, often there is more than enough handling and processing of financial data. With the implementation of a corporate database, it is hoped that more of the processing can be centralized and automated. But the point is that the current emphasis on financials leads to the "unbalanced" situation with regard to other perspectives. There is perhaps a need to include additional financial-related data, such as risk assessment and cost-benefit data, in this category.

5. The Balanced Scorecard Model

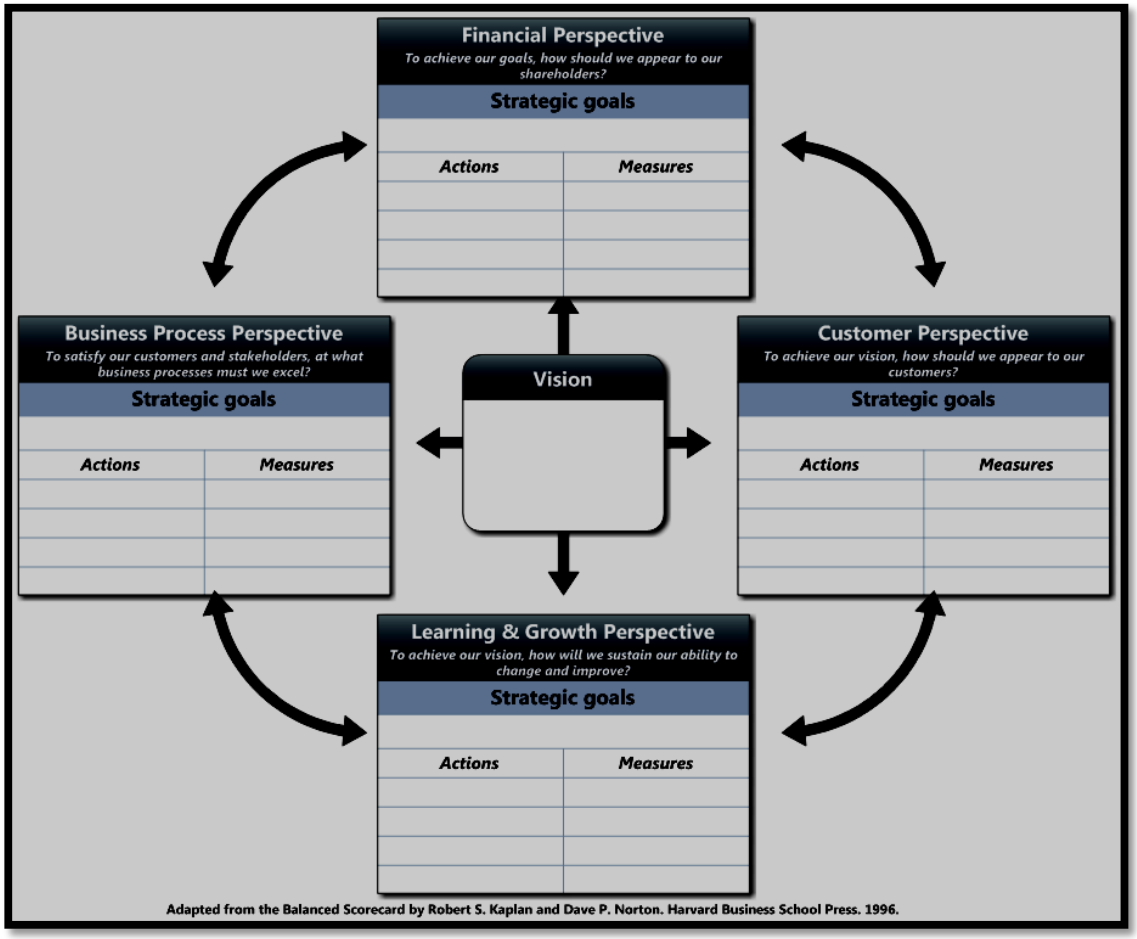
In order to use BSC to its maximum potential, the following points should be diligently followed.

- The major objectives are to be set for each of the perspectives.
- Measures of performance are required to be identified under each of the objectives which would help the organization to realize the goals set under each of the perspectives. These would act as parameters to measure the progress towards the objectives.
- The next important step is the setting of specific targets around each of the identified key areas which would act as a benchmark for performance appraisal.
- The appropriate strategies and the action plans that are to be taken in the various activities should be decided so that it is clear as to how the

organization has decided to pursue the pre-decided goals. Due to this reason, the balanced scorecard is often referred to as a blueprint of the company's strategies.

Figure 2

Perspective and their measurement



Source: *http://www.smartdraw.com/balanced-scorecard/balanced-scorecard-software.htm accessed as on 10.2.16*

6. Implementing a Balanced Scorecard

The balanced scorecard helps everyone in an organization understand and work towards a shared vision. A completed scorecard system aligns the organization's picture of the future (shared vision), with business strategy, desired employee behavior and day-to-day operations. Strategic performance

measures are used to better inform decision-making and show progress toward desired results. The organization can then focus on the most important things that are needed to achieve its vision and satisfy customers, stakeholders, and employees. Other benefits include measuring what matters, identifying more efficient processes focused on customer needs, improving prioritization of initiatives, improving internal and external communications, improving alignment of strategy and day-to-day operations and linking budgeting and cost control processes to strategy.

Figure 3: Process of implementation of the scorecard



Source: Developed by the author

Step one of the scorecard building process starts with an assessment of the

organization's mission and vision, challenges and values. It also includes preparing a change management plan for the organization.

In step two, elements of the organization's strategy, including strategic results, strategic themes and perspectives, are developed to focus attention on customer needs and the organization's value proposition.

In step three, the strategic elements developed in steps one and two are decomposed into strategic objectives, which are the basic building blocks of strategy and define the organization's strategic intent. Objectives are first initiated and categorized on the strategic theme level, categorized by perspective, linked in cause-effect linkages (strategy maps) for each strategic theme and then later merged together to produce one set of strategic objectives for the entire organization.

In step four, the cause and effect linkages between the enterprise-wide strategic objectives are formalized in an enterprise-wide strategy map. The previously constructed theme strategy maps have merged into an overall enterprise-wide strategy map that shows how the organization creates value for its customers and stakeholders.

In step five, performance measures are developed for each of the enterprise-wide strategic objectives. Leading and lagging measures are identified, expected targets and thresholds are established and baseline and benchmarking data is developed.

In step six, strategic initiatives are developed that support the strategic objectives. To build accountability throughout the organization, ownership of performance measures and strategic initiatives is assigned to the appropriate staff and documented in data definition tables.

In step seven, the implementation process begins by applying performance measurement software to get the right performance information to the right people at the right time. Automation adds structure and discipline to implementing the balanced scorecard system, helps transform disparate corporate data into information and knowledge and helps communicate performance information. In short, automation helps people make better

decisions because it offers quick access to actual performance data.

In step eight, the enterprise-level scorecard is cascaded down into business and support unit scorecards, meaning the organizational level scorecard (the first tier) is translated into business unit or support unit scorecards (the second tier) and then later to team and individual scorecards (the third tier). Cascading translates high-level strategy into lower-level objectives, measures and operational details. Cascading is the key to organization alignment around strategy. Team and individual scorecards link day-to-day work with department goals and corporate vision. Performance measures are developed for all objectives at all organizational levels. As the scorecard management system is cascaded down through the organization, objectives become more operational and tactical, as do the performance measures. Accountability follows the objectives and measures, as ownership is defined at each level. An emphasis on results and the strategies needed to produce results is communicated throughout the organization.

In step nine, an evaluation of the completed scorecard is done. During this evaluation, the organization tries to answer questions such as, 'Are our strategies working?', 'Are we measuring the right things?', 'Has our environment changed?' and 'Are we budgeting our money strategically?'

6. Balanced Scorecard Benefits

- Make strategy operational by translating strategy into performance measures and targets.
- Helps focus entire organization on what must be done to create a breakthrough performance.
- Integrates and acts as an umbrella for a variety of often disconnected corporate programs, such as quality, reengineering, process redesign and customer service.
- Breaks down corporate level measures so that local managers, operators and employees can see what they must do well in order to improve organizational effectiveness.

The secret of the balanced scorecard and the reason it has gained such wide acceptance is quite simple. It lets organizations reach their full potential. The breakthrough results of the organizations in the Balanced Scorecard Hall of Fame were created not by new strategies, new people or new processes. Instead, the results were created by focusing the entire organization on the strategy and rewarding people for executing the strategy. The reason behind its popularity is that the organizations have understood the capability this tool has in bringing the desired results to the business by managing the strategies.

Work that was done with a major telecommunications provider is a clear example of the mismatch that is often seen. At the start of the balanced scorecard initiative, the organization was determined that being appreciably superior in customer service was one element of its customer-driven strategy. This strategy was developed before the balanced scorecard was introduced to the organization and banners were hung in call centers throughout the country with slogans such as ‘Customers First’ and ‘Service Matters’; however, customer service levels remained at the same abysmal levels.

Why? This is because the call center employees were measured based on the number of calls that they could process in an hour. This measure drove them to hang up on difficult problems to handle simpler ones, driving customers crazy. After implementing the balanced scorecard, they changed their metric to “percent of problems handled with one call”. This completely changed the atmosphere of the call center and allowed the employees to focus on solving problems—increasing morale, customer satisfaction and eventually profits.

7. Discussion & Conclusion

The balanced scorecard has come a long way after it was first developed by Drs. Kaplan and Norton. The various modifications introduced in balanced scorecard from time to time have made it more apt for measuring and comparing performance to the strategic objectives of an organization. Instead of looking back, organizations can maintain a forward view, since the alignment of strategy with day-to day actions has already been taken care of by

balanced scorecard. This tool has proved to be highly useful and its adoption by various organizations across the globe has proved it.

6. References

Gumbus, A. and Lyons, B. (2002), "The Balanced Scorecard at Philips Electronics", Strategic Finance. California Management Review, Vol. 39, No. 1, pp. 53-79.
http://balancedscorecard.org/Resources/About-the-Balanced-Scorecard assessed on 16.8.2016

Kaplan, R. and Norton, D. (1992), "The Balanced Scorecard – measures that drive performance", Harvard Business Review, January-February, pp. 71-79

Kaplan, R. and Norton, D. (1993), "Putting the Balanced Scorecard to work", Harvard Business Review, September-October, pp. 2-16.

Kaplan, R. and Norton, D. (1996a), "Using the Balanced Scorecard as a strategic management system", Harvard Business Review, January-February, pp. 75-85.

Kaplan, R. and Norton, D. (1996b), "Linking the Balanced Scorecard to strategy", California Management Review, Vol. 39 No. 1, pp. 53-79.

Kaplan, R. and Norton, D. (2000), The Strategy Focused Organisation: How Balanced Scorecard Companies Thrive in the New Business Environment, Harvard Business School Press, Cambridge.

Kaplan, R. and Norton, D. (2001), "Transforming the Balanced Scorecard from performance measurement to strategic management: part 1", Accounting Horizons, Vol. 15 No. 1, pp. 87-104.

Kaplan, R. and Norton, D. (2004a), "Measuring the strategic readiness of intangible assets", Harvard Business Review, Vol. 82 No. 2, pp. 52-63.

Kaplan, R. and Norton, D. (2004b), Strategy Maps: Converting intangible Assets into Tangible Outcomes, Harvard Business School Press, Boston, MA.

Kaplan, R. and Norton, D. (2006), Alignment: Using the Balanced Scorecard to Create Corporate

M. Punniyamoorthy R. Murali, (2008), "Balanced Score for the Balanced Scorecard: a benchmarking tool", Benchmarking: An international Journal, Vol 15 Iss 4 p.p. 420-443

Marr, B. and Schiuma, G. (2003), “Business performance measurement – past, present and future”, Management Decision, Vol. 41 No. 8, pp. 680-687

This article has been accepted for publication in a future issue of this journal, but has not been fully edited. Content may change prior to final publication. Citation information: DOI 10.1109/JSEN.2019.2903296, IEEE Sensors Journal

Design and Development of an Electronic Level Transmitter using Inter Digital Capacitor

Sayyed Faizan Ali, *Member IEEE* and Nirupama Mandal, *Member IEEE*

***Abstract*—A simplified economical liquid level measurement technique has been developed for measuring level of any type of liquid. A fabricated Inter Digital Capacitor (IDC) is used as a primary sensor which transduces the liquid head into corresponding variation in capacitance. This variation in the capacitance changes to an electric signal, using a modified De Sauty bridge circuit. In this paper, different types of water such as mineral water, tap water, distilled water and river water are used as process liquid. This sensor can be relied for detection of the water level, independent of the water type. The theoretical analysis of the work has been illustrated in this paper to describe the working of the proposed transmitter. The proposed sensor has been developed and laboratory tested. It is found that this transmitter exhibited linear characteristics and followed theoretical equations. It has 12.8 mV resolutions for measurement of water level from 0-15 cm range.**

***Index Terms*—Inter Digital Capacitor (IDC), Level transmitter, Modified De-Sauty Bridge, Signal conditioning, Voltage to current converter.**

I. INTRODUCTION

LIQUIDlevel measurement has always been a challenged in harsh and flammable environment in process industries. Liquid level measurement can be done by using various methods [1-3] such as float, differential pressure, magnetostrictive, capacitive method, ultrasonic, optical etc. The conventional float type liquid sensors have simple structure and cheaper but their application is very limited due to their vulnerability to mechanical damage and high maintenance cost. The ultrasonic liquid level sensor is simple in structure and is easy to install. But it is easily susceptible to interference. Different types of new technique have been developed by the researcher in the area of measuring liquid level. J. Terzik *et. al.* [10] have developed a method of measuring fluid level using single ultrasonic sensor and support vector machine. The measurement system is experimented on fuel tank of running vehicle and the result demonstrated that the system has produced most accurate outcome. Canbolta [11] has developed a technique for measuring liquid level using three parallel plate capacitors. The measurement system is capable to reduce the effect of temperature and air dielectric.A novel comb like electrode capacitive sensor for measuring liquid level has been designed and developed [12]. A comb like pattern of electrodes is used to form equivalent capacitance by the electrodes and the liquid within the container which is proportional to the area of the electrodes. The sensor is applicable for non-intrusive monitoring system such as biomedical applications. A non-intrusive method based on lateral displacement for liquid level measurement has been suggested [13]. A material medium having different thickness and refractive index is used in this method so that the light ray passes through this type of medium and the lateral displacement is observed. A simple non-destructive and non-intrusive technique has been developed by Alexander Jahn *et. al.* [14] for measurement of liquid head using two piezoelectric sensor. In this technique, one piezoelectric sensor is used as transmitter whereas another is used as receiver. The measurement of liquid level based on time-domain reflectrometry (TDR) has been presented [15] using two wire probes connected to the outside wall of the tank in which the electromagnetic signal propagates through it. The measurement of liquid level based on the capacitance of the coaxial cylindrical structure for conducting liquid has been proposed by B. Jin *et. al.*[16]. The drawback of this measurement technique is that it is used for conducting liquid only. In flammable and harsh environment, optical signal is chosen in place of electrical signal. B. Jin *et. al.* [17] have designed a technique for intrinsically safe measurement of liquid level with the help of Poly Vinyl Chloride coaxial cable. For detection of water level and temperature, Ameen *et. al.* [18] have designed and developed a liquid level measurement system using Fiber Bragg Grating (FBG) integrated with graphene diaphragm. The graphene diaphragm placed inside the tank gets deformed as the hydrostatic pressure acts on the graphene diaphragm.C. Li *et. al.* [19] have developed a prototype liquid level and temperature sensor based on asymmetrical fiber Mach-Zehnder Interferometer (aFMZI) combined with FBG. The aFMZI is realized by concatenating a fiber tapered and lateral-shifted junction. Liquid level measurement based on no-core fiber (NFC) with temperature compensation using a FBG has been proposed in [20]. Liquid level is measured by integrating FGB with NFC and temperature compensation is done by using temperature sensing property of FBG.

IDC is a multi-finger periodic structure of electrodes on a substrate that could be porous, opaque or transparent [6].

1558-1748 (c) 2018 IEEE. Personal use is permitted, but republication/redistribution requires IEEE permission. See http://www.ieee.org/publications_standards/publications/rights/index.html for more information.

This article has been accepted for publication in a future issue of this journal, but has not been fully edited. Content may change prior to final publication. Citation information: DOI 10.1109/JSEN.2019.2903296, IEEE Sensors Journal

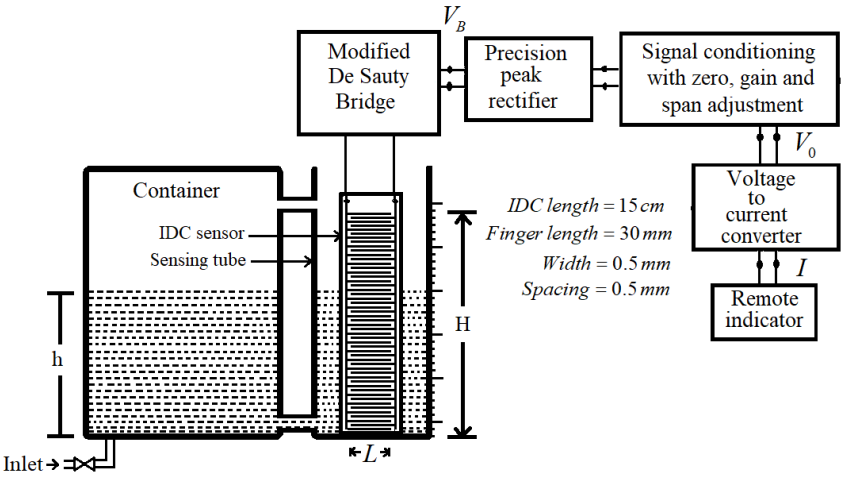


Fig. 1: Schematic diagram of the proposed flow transmitter.

It is a coplanar waveguide developed on the substrate. Each electrode has many fingers. Each finger has width and spacing between two fingers. The structure and capacitance of IDC depend on the width and spacing between two fingers. IDC is used due to its effectiveness to measure the capacitance values. There are various fields in which IDC can be used. It can be used to detect the power cable insulation damage, capacitance of multi layeredstructure, measurement of concrete moisture content etc. R. Igreja *et. al.* [7] have presented an analytical expressions for the capacitance between the two finger electrodes of a periodic inter digital capacitive sensor. It is based on conformal mapping techniques. L. Yonghong *et. al.* [8] have designed a PCB based Inter Digital Capacitor (IDC) sensor for the detection of cross linked polyethylene (XLPE) power cable insulation damage. The structure's parameters of IDC are optimised and the experimental results show that the sensors are capable of detecting different insulation damage effectively. M. N. Alam *et. al.* [9] have designed a meander and circular interdigital capacitive sensor for measurement of moisture content in concrete samples. The experimental result shows good response for increase of moisture content from 0% to 6% for both meander sensor and circular sensor.

In this paper, an IDC is used as a primary sensor which converts the level of the liquid into the corresponding capacitance. A fabricated IDC is placed in the sensing tube as shown in Fig. 1. The sensing tube is connected with the container and a scale is attached outside of the sensing tube as presented in Fig. 1. When the liquid level rises in the container simultaneously the liquid level rises in the sensing tube as well. The variation in liquid head of the sensing tube causes the change in capacitance. This change in capacitance is coupled to one arm of the bridge circuit. A modified De Sauty bridge is used to minimize the stray capacitance effect that acts between the ground and the bridge circuit measuring nodes by maintaining the bridge output nodal points at the same virtual ground potential during the entire process of measurement. A modified De Sauty bridge develops an electrical signal due to the variation of the liquid level in the container. The electrical signal is used for remote transmission.The mathematical equation of the work has been illustrated in this paper to describe the working of the sensor. In the laboratory, the senor has been developed and then tested. The experimental results are reported in this paper.

II. Method of Approach

In this paper, an IDC is used as a primary sensor which converts the level of the liquid in the sensing tube into the corresponding capacitance. The IDC is placed in a sensing tube which is connected at the bottom and top of the storage tank whose level is to be measured.

At zero liquid level i.e. h = 0, the total capacitance C_T is equal to the air capacitance $(C_{air})_H$ and it is given by,

$$C_T = (C_{air})_H = \frac{\varepsilon_o A}{d} \quad (1)$$

where ε_0 is the air permittivity, A is the area of the IDC at no liquid level, d is the spacing between the fingers as well as the thickness of the fingers.

The area of the IDC immersed in the sensing tube at zero liquid level is given by,

$$A = L \times (\mathrm{H} - \mathrm{N\,d}) \quad (2)$$

where H = total height of the IDC, L is the length of the finger, N is the total number of finger.

Equation (1) can be written as,

$$(C_{air})_H = \frac{\varepsilon_o L\,\mathrm{H}}{d} - \varepsilon_o LN \quad (3)$$

Let us assume that the level of process liquid rises at some height 'h' as shown in Fig. 1.Then the total capacitance is the combination of liquid capacitance C_h at height h and the air

1558-1748 (c) 2018 IEEE. Personal use is permitted, but republication/redistribution requires IEEE permission. See http://www.ieee.org/publications_standards/publications/rights/index.html for more information.

This article has been accepted for publication in a future issue of this journal, but has not been fully edited. Content may change prior to final publication. Citation information: DOI 10.1109/JSEN.2019.2903296, IEEE Sensors Journal

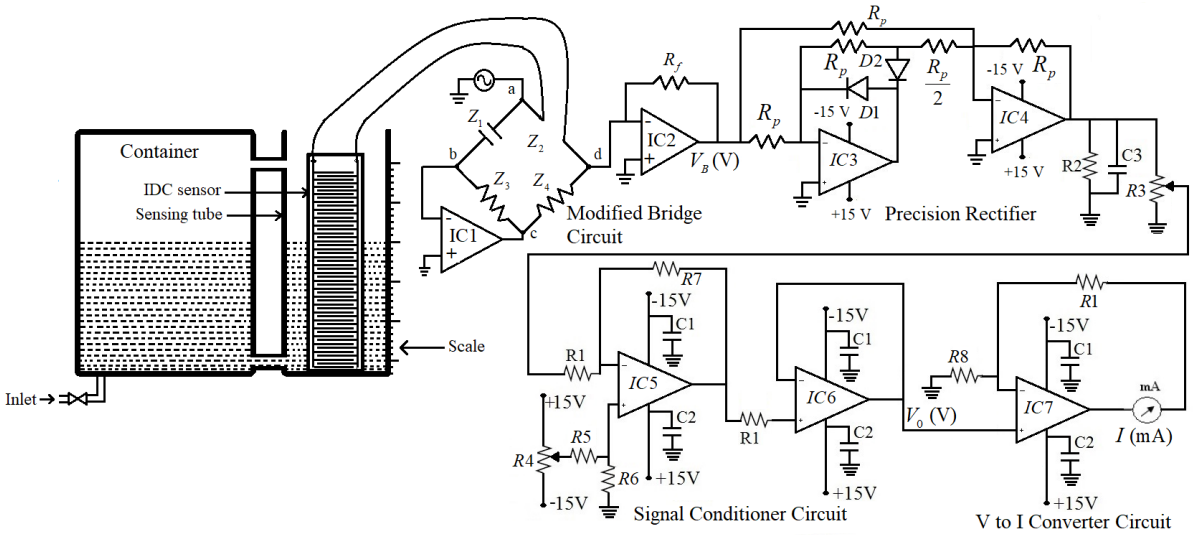


Fig. 2: Proposed level transmitter.

capacitance $(C_{air})_{H-h}$ at height $H-h$ .So, the total capacitance is given by,

$$C_T = C_h + (C_{air})_{H-h} \quad (4)$$

The capacitance C_h due to liquid level at height h is given by,

$$C_h = \frac{\varepsilon_o \varepsilon_r L \times (\mathrm{h} - n\,\mathrm{d})}{d} \quad (5)$$

where n is the number of finger immersed into process liquid. The capacitance $(C_{air})_{H-h}$ due to air at height $H-h$ is given by,

$$(C_{air})_{H-h} = \frac{\varepsilon_o L \times \{\mathrm{H} - h - (\mathrm{N} - \mathrm{n})\,\mathrm{d}\}}{d} \quad (6)$$

On combining equation (5) and (6), we get

$$C_T = \frac{\varepsilon_o(\varepsilon_r - 1)L\,\mathrm{h}}{d} - \varepsilon_o(\varepsilon_r - 1)Ln + \frac{\varepsilon_o L\,\mathrm{H}}{d} - \varepsilon_o LN \quad (7)$$

From the design of IDC sensor, we get

$$nd = \frac{h}{2} \quad (8)$$

Combining equation (8) and (7), we get

$$C_T = \frac{\varepsilon_o(\varepsilon_r - 1)L\,\mathrm{h}}{d} - \frac{\varepsilon_o(\varepsilon_r - 1)L\,\mathrm{h}}{2d} + \frac{\varepsilon_o L\,\mathrm{H}}{d} - \varepsilon_o LN \quad (9)$$

Combining equation (3) and (9), we can write as

$$C_T = K_1 h - \frac{K_1 h}{2} + (C_{air})_H \quad (10)$$

where $K_1 = \frac{\varepsilon_o(\varepsilon_r - 1)L}{d}$ (11)

Equation (10) can be written as,

$$C_T = K_2 h + (C_{air})_H \quad (12)$$

where $K_2 = \frac{K_1}{2}$ (13)

From equation (12), Change in capacitance ΔC can be written as,

$$\Delta C = C_T - (C_{air})_H = K_2 h = \frac{\varepsilon_o(\varepsilon_r - 1)L}{2d} h \quad (14)$$

From equation (14), it can be stated that less width and spacing leads to higher capacitance. Penetration of electric field will be more prominent, with closeness between the electrodes. Elevation in the electric field leads to increase in induced current at the electrode, resulting in an enhanced capacitance. In addition, greater the area covered by the material under test, higher would be the magnitude of capacitance and hence higher measurement sensitivity.

Since the change in capacitance is coupled to one arm of the bridge. The output of the modified bridge circuit is given by,

$$V_B = R_f[j\omega \Delta C]V_{in} \quad (15)$$

where R_f is the feedback resistance, ω is the operating frequency, V_{in} is the supply voltage.

Using equation (14), equation (15) can be written as,

$$V_B = R_f[j\omega K_2 h]V_{in} \quad (16)$$

Here, in equation (16) all the term are constant except the height of the liquid level h .So, equation (16) can be written as,

$$V_B = K_3 h \quad (17)$$

where $K_3 = K_2 R_f \omega V_{in}$ (18)

Since the output voltage of bridge is in AC form so it is rectified with the help of precision rectifier to get the DC voltage. Now, DC output of the precision rectifier is converted into 1-5 V standard signals using a signal conditioning circuit as presented in Fig. 2. The standard voltage signal 1-5 V is to be converted into standard current signal 4-20 mA using Voltage to Current converter circuit for remote transmission.

The output of the signal conditioner is given by,

$$V_0 = K_4 + K_5 V_B \quad (19)$$

where K_4 and K_5 are constant.

Using equation (18) and (19), we get

$$V_0 = K_4 + K_5 K_3 h \quad (20)$$

or, $V_0 = K_4 + K_6 h$ (21)

1558-1748 (c) 2018 IEEE. Personal use is permitted, but republication/redistribution requires IEEE permission. See http://www.ieee.org/publications_standards/publications/rights/index.html for more information.

This article has been accepted for publication in a future issue of this journal, but has not been fully edited. Content may change prior to final publication. Citation information: DOI 10.1109/JSEN.2019.2903296, IEEE Sensors Journal

where $K_6 = K_5 K_3$ (22)

Now, this voltage signal is converted into 4-20 mA current signals using a V to I converter circuit as shown in Fig. 2.

The output of converter is given by,

$$I = K_7 V_0 \quad (23)$$

where K_7 is a constant.

Using equation (21) and (23), we get

$$I = K_7 K_4 + K_7 K_6 h \quad (24)$$

or, $I = \alpha + \beta h$ (25)

where $\alpha = K_7 K_4$ and $\beta = K_7 K_5 \frac{\varepsilon_o(\varepsilon_r - 1)L}{d} R_f \omega V_{in}$ (26)

From equation (21) and equation (25), it clearly indicates that the developed transmitter is linear with respect to the liquid head.

III. Design Methodology

In this work, an IDC is fabricated on FR4 material of dimension 17.5 cm x 4 cm x 1.6 mm with a dielectric constant of 4.4 for measurement of liquid level. The schematic diagram of IDC is presented in Fig. 1.The modified De Sauty Bridge as presented in Fig. 2 has been designed on the bread board. The bridge is excited by stabilized sinusoidal source selected at 5 V and 1000 Hz. A precision rectifier using op-amp 741IC has been designed for rectification of ac to dc signal. This dc signal is converted into 1-5 V standard voltage signal using signal conditioner circuit as shown in Fig. 2. The standard voltage signal is transmitted to the remote place by converting it into standard 4-20 mA current signal using op-amp 741IC based voltage to current converter circuit.

IV. Experimental Results

In this work, the following setup as shown in Fig. 3 is taken for experimental purpose. Here, different type of water like mineral water, tap water, distilled water and river water were used as process liquid at room temperature.



Fig. 3: Photographic view of experimental setup.

The experiment was performed in three steps. Initially, the IDC was placed inside the sensing tube. The liquid level of the container was increased and decreased in steps of 1.5 cm and at each step, the capacitance of the IDC was measured with the help of LCR meter (MECO LCR999A). The maximum liquid level up to which IDC used for experiment was 15 cm. By plotting the graph between the changes in capacitance of different type of water and the liquid head, the characteristic curves of the IDC sensor have been obtained as presented in Fig. 4(a-c). The experiment was done 6 times for both increasing and decreasing modes under the same experimental condition to find out the normalized standard deviation, hysteresis and linearity of the sensor. The standard deviation is normalised by z-score normalization using absolute mean standard deviation technique.

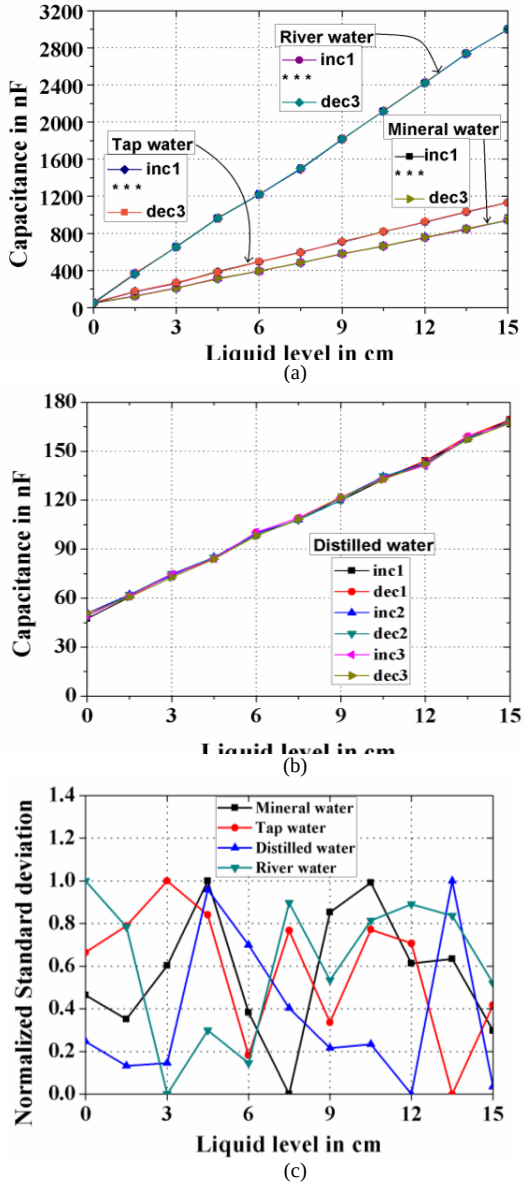


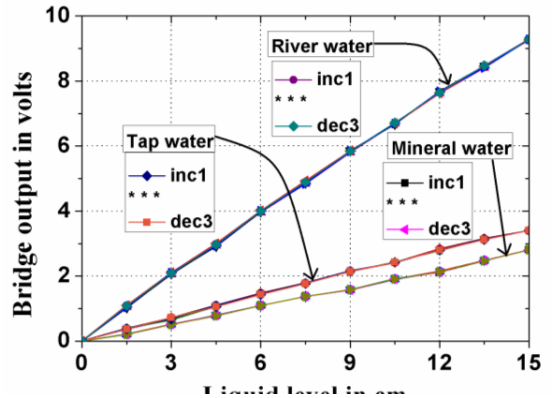
Fig. 4: Static characteristic curve of the IDC sensor for different type of water. (a) Mineral water, Tap water and River water (b) Distilled water (c) Normalized Standard deviation of IDC sensor for different types of water.

In the next step, the two terminals of the capacitance for different type of water were connected to one arm of the modified De Sauty bridge circuit to get the electrical output. The output developed by the bridge circuit for different type of water was measured using digital multimeter. The static characteristic of the bridge output for different type of water are presented in Fig. 5(a-b).The graphs show that the observed

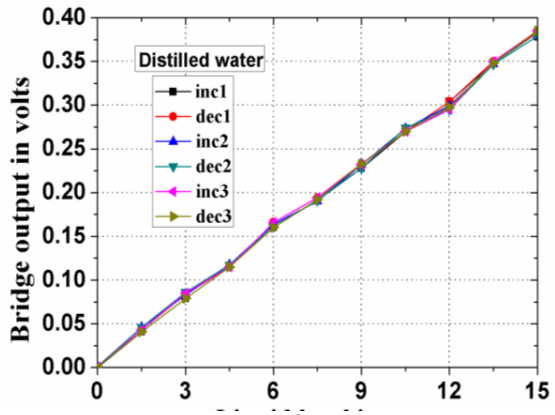
1558-1748 (c) 2018 IEEE. Personal use is permitted, but republication/redistribution requires IEEE permission. See http://www.ieee.org/publications_standards/publications/rights/index.html for more information.

This article has been accepted for publication in a future issue of this journal, but has not been fully edited. Content may change prior to final publication. Citation information: DOI 10.1109/JSEN.2019.2903296, IEEE Sensors Journal

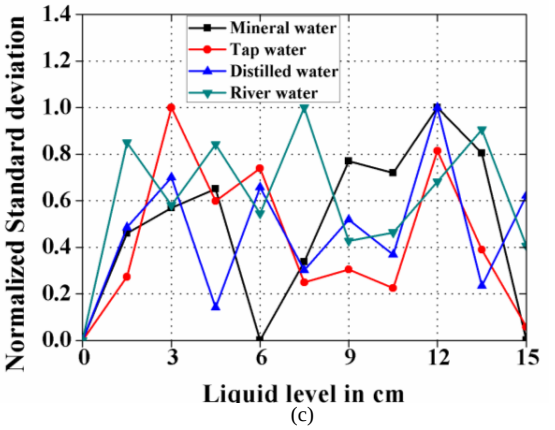
readings are almost linear. The hysteresis and linearity of the sensor was calculated. The normalized standard deviation curve as presented in Fig. 5(c) shows very good repeatability of the transducer.



(a)



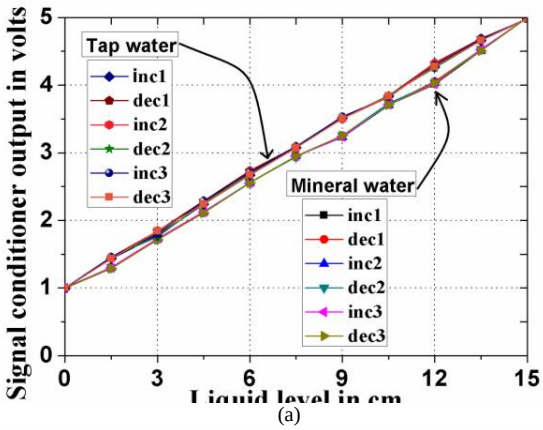
(b)



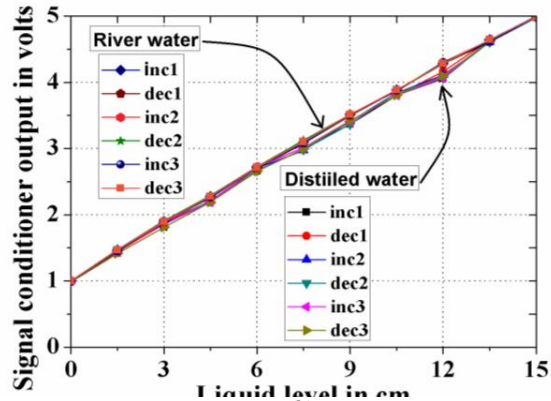
(c)

Fig. 5: Characteristic curve of Bridge output voltage of different type of water (a) Mineral water, Tap water and River water (b) Distilled water (c) Normalized Standard deviation of bridge output for different types of water.

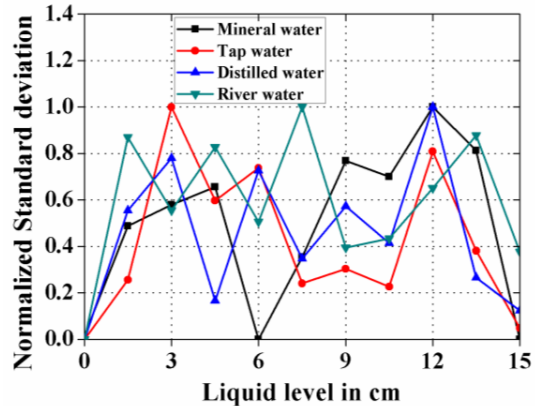
The output of the bridge circuit is an ac voltage signal. So, it is converted to dc voltage signal by precision rectifier. The standard voltage signal of 1-5 V is obtained at the output of the signal conditioner circuit by coupling with the output of the precision rectifier circuit.The static characteristic curve of the signal conditioner for different type of water are shown in Fig. 6(a-b). It shows that the output of the signal conditioner is almost linear. The experiment was repeated for 6 times in both increasing and decreasing modes under the same experimental condition to find the standard deviation, hysteresis and linearity of the sensor. The normalized standard deviation curve as presented in Fig. 6(c) also shows very good repeatability of the system.



(a)



(b)



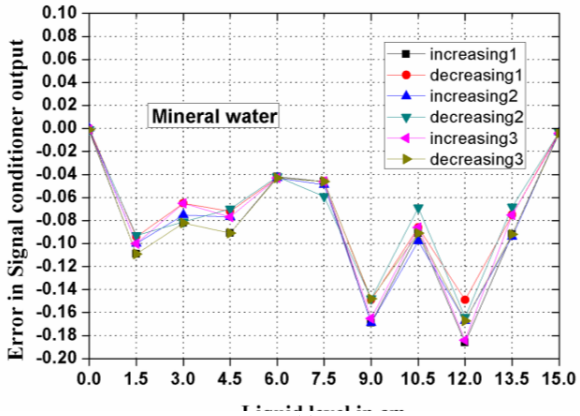
(c)

1558-1748 (c) 2018 IEEE. Personal use is permitted, but republication/redistribution requires IEEE permission. See http://www.ieee.org/publications_standards/publications/rights/index.html for more information.

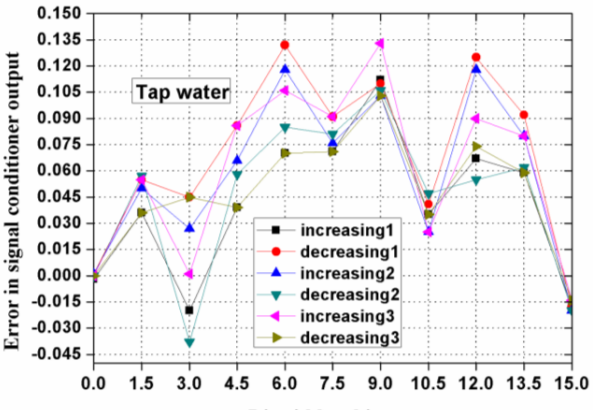
This article has been accepted for publication in a future issue of this journal, but has not been fully edited. Content may change prior to final publication. Citation information: DOI 10.1109/JSEN.2019.2903296, IEEE Sensors Journal

Fig. 6: Characteristic curve of level transducer after signal conditioning of different type of water (a) Mineral water and Tap water (b) Distilled water and River water (c) Normalized Standard deviation of signal conditioner for different types of water.

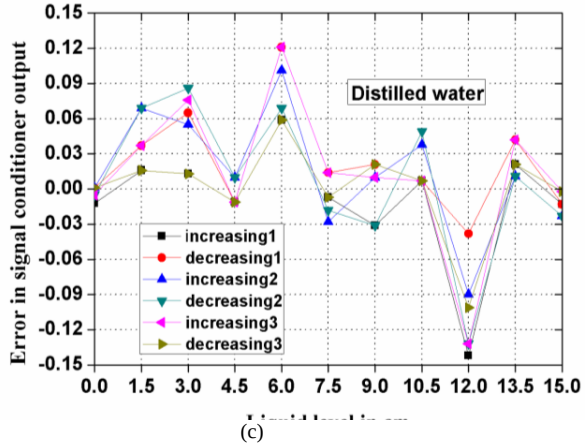
To find out the linearity of the signal conditioner, the errors for different types of liquid were calculated and plotted as shown in Fig. 7(a-d).



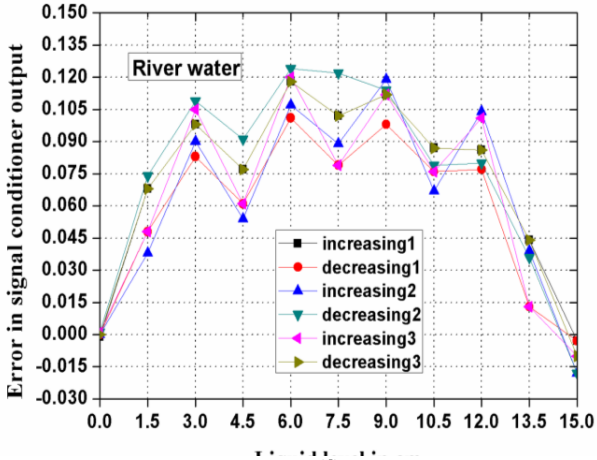
(a)



(b)



(c)



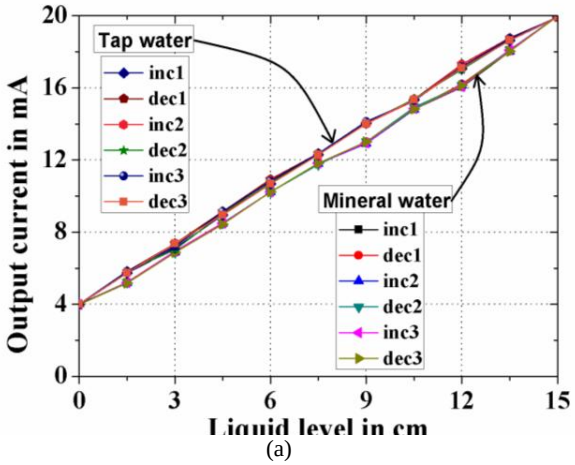
(d)

Fig. 7: Error in signal conditioner output of different types of water (a) Mineral water (b) Tap water (c) Distilled water (d) River water.

In the last step, the standard signal 1-5 V is converted into 4-20 mA using Voltage to Current converter circuit so that the height of liquid level in terms of electrical signal is transmitted to the remote places.The experiment was repeated for six increasing and decreasing modes under the same atmospheric condition. The characteristic curve of the V to I converter for different type of water are presented in Fig. 8(a-b). It shows that the outputs of the converter circuit are almost linear. The standard deviation, hysteresis and linearity of the sensor were calculated. The normalized standard deviation plot in Fig. 8(c) also shows very good repeatability of the proposed level transmitter.

V. Discussion

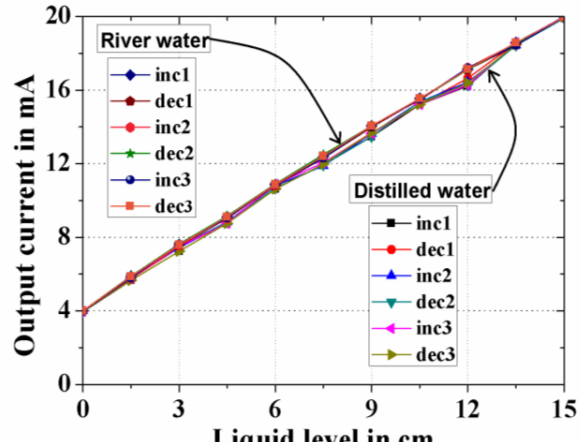
The characteristics graph as shown in Fig. 4 indicates that the proposed level sensor has good linear response. Over the range of 0-15 cm, the change in capacitance of IDC is in nF and the characteristic curve is linear over the entire range of liquid level. The characteristic curve will be linear beyond 15 cm by increasing the height of the IDC.



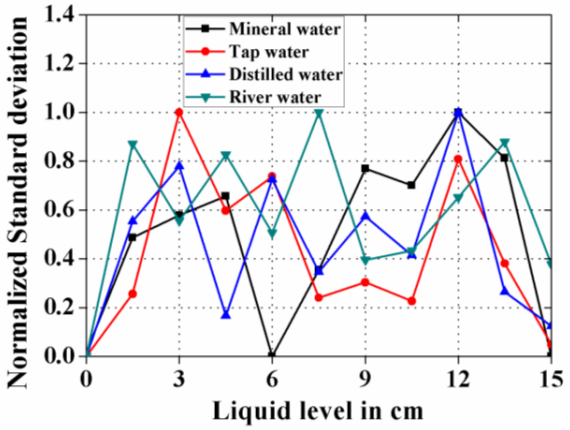
(a)

1558-1748 (c) 2018 IEEE. Personal use is permitted, but republication/redistribution requires IEEE permission. See http://www.ieee.org/publications_standards/publications/rights/index.html for more information.

This article has been accepted for publication in a future issue of this journal, but has not been fully edited. Content may change prior to final publication. Citation information: DOI 10.1109/JSEN.2019.2903296, IEEE Sensors Journal



(b)



(c)

Fig. 8: Characteristic curve of proposed level transmitter of different type of water (a) Mineral water and Tap water (b) Distilled water and River water (c)Normalized Standard deviation of level transmitter for different types of water.

Due to the difference in dielectric constant of different types of water, the capacitance of the IDC varies with the variation of the liquid level in the beaker. The data of the proposed level sensor obtained from the measurement system are shown in Fig. 4(a-b) and the normalized standard deviation of the data set is shown in Fig. 4(c). It is noted that for mineral water the capacitance varies from 47.4 nF to 942.8 nF, for tap water it varies from 47.4 nF to 1133.4 nF, for distilled water it varies from 47.4 nF to 169.3 nF and for river water it varies from 47.4 nF to 3001.6 nF. It is also noted that the sensitivity of mineral water, tap water, distilled water and river water are 59.693 nF/cm, 72.467 nF/cm, 8.131 nF/cm and 197.267 nF/cm respectively**.** From Fig. 4(a-b), the maximum % non-linearity of the proposed sensor in mineral water is -1.91% FSO at 3 cm, in tap water it is 1.67% FSO at 1.5 cm, in distilled water it is 1.85% FSO at 3cm whereas in river water it is 1.04% FSO at 4.5 cm. From Fig. 4(c), it is observed that the standard deviation is almost similar for all types of water into consideration. The maximum standard deviation and maximum hysteresis occurs in distilled water around 2.32 nF and 0.59% of FSO respectively while minimum standard deviation and minimum hysteresis occurs in distilled and river water around 1.04 nF and 0.189% of FSO respectively. The distilled water have maximum percentage deviation of ±2.09 % of FSO whereas river water have minimum percentage deviation of ±1.09 % of FSO. From error graph as presented in Fig. 7(a-d), it is noticed that the maximum error is -0.18 V in mineral water and minimum error is 0.120 V in river water.

VI. Conclusion

An effective IDC sensor for the purpose of water level measurement has been designed and the experiment has been worked out successfully. Liquid level measurement of various type of liquid is possible with the help of this technique. The proposed transducer has 12.8 mV resolutions for measurement of water level from 0-15 cm range at room temperature. There may be slight variation of two to three degree Celsius in temperature of the water but it does not affect the reading of the sensor. Experimental results yield high linearity, sensitivity and besides very less expenditure incurred in the installation. Additionally, the sensor has ability to detect the water level irrespective of the type of water. The overall uncertainty in liquid level measurement using this technique has been studied on short term basis. The temperature variation of the proposed transmitter can be studied further. The variation can be compensated by using different metaheuristic technique like Genetic Algorithm, Artificial Neural Network (ANN) etc. Robustness, lifetime and environmental condition are needed to be further studied to achieve better processing and measuring of higher range of liquid level.

Acknowledgment

The authors would like to thank the Department of Electronics Engineering, Indian Institute of Technology (ISM), Dhanbad (Under MHRD, Government of India) for providing the facilities to carry out this research work.

References

[1] J. P. Bentley, Principles of Measurement Systems, 3rd ed. Singapore: Longman, 1995.

[2] B. G. Lipták, Process Measurement and Analysis, 4th ed. Oxford, U.K.:Butterworth.

[3] D. Patranabis, Principles of Industrial Instrumentation, 3rd ed. New Delhi, India: McGraw-Hill, 2010.

[4] D. M. Considine, process Instrument and Control Hand Book, 2nd ed. New York McGraw-Hill, 1999.

[5] E. Udd, and W. B. Spillman, Jr., Fiber Optic Sensors: An Introduction for Engineers and Scientists, 2nd ed. New York, NY, USA: Wiley, 2011.

[6] A.V. Mamishev, K. S. Rajan, Y. Du, and M. Zahn, "Inter-digital sensors and transducers," *Proc. IEEE*, vol. 92, no. 5, pp. 808–845, May 2004.

[7] R. Igreja, and C. J. Dias, "Analytical evaluation of the inter-digital electrodes capacitance for a multi-layered structure," *Sens. Actuators A Phys.*, vol. 112, no. 2-3, pp. 291–301, May 2004.

[8] L. Yonghong, H. Yunzhi, T. Rui, and W. Beibei, "Application of interdigital capacitive sensors for detecting power cable insulation damage," *IEEE Conference*, pp. 1795-1799, 2015.

[9] Md. N. Alam, R. H. Bhuiyam, R. A. Dougal, and M. Ali, "Concrete moisture content measurement using interdigital near-field sensors," *IEEE Sens. J.*, vol. 10, no. 7, pp. 1243–1248, 2010.

1558-1748 (c) 2018 IEEE. Personal use is permitted, but republication/redistribution requires IEEE permission. See http://www.ieee.org/publications_standards/publications/rights/index.html for more information.

This article has been accepted for publication in a future issue of this journal, but has not been fully edited. Content may change prior to final publication. Citation information: DOI 10.1109/JSEN.2019.2903296, IEEE Sensors Journal

[10] J. Terzic, C. R. Nagarajah, and M. Alamgir, "Fluid level measurement in dynamic environments using a single ultrasonic sensor and Support Vector Machine (SVM)," *Sens. Actuators A Phys.*, vol. 161, pp. 278–287, June 2010.

[11] H. Canbolta, "A novel level measurement technique using three capacitive sensors for liquids," *IEEE Trans. Instrum. Meas.*, vol. 58, no. 10, pp. 3762–3768, Oct. 2009.

[12] C. A. Gong, H. K. Chiu, L. R. Huang, C. H. Lin, Z. D. Hsu and P. H. Tu, "Low-cost comb-electrode capacitive sensing device for liquid-level measurement," *IEEE Sensors J.*, vol. 16, no. 9, pp. 2896-2897, May 2016.

[13] H. K. Singh, N. C. Meitei, S. T. Sarkar, D. Tiwari, andT. Bezboruah, "Truly Nonintrusive Liquid-Level-Sensing Method Based on Lateral Displacement Effect of Light Rays," *IEEE Sensors J.*, vol. 13, no. 2, pp. 801-806, Feb. 2013.

[14] A. Jahn, F. Ehrle, and C. Roppel, "A level sensor for fluids based on hydrostatic deformation with piezoelectric generated sounds in a low frequency range," *IEEE Conference*, pp. 245-249, 2014.

[15] A. Cataldo, E. Piuzzi, E. Benedetto, and G. Cannazza. "Experimental Characterization and Performance Evaluation of Flexible Two-Wire Probes for TDR Monitoring of Liquid Level." *IEEE Trans. Instrum. Meas*, vol. 63, no.12, pp.2779-2788, Dec 2014.

[16] B. Jin, Z. Zhang and H. Zhang, "Structure design and performance analysis of a coaxial cylindrical capacitive sensor for liquid-level measurement," *Sens. Actuators A, Phys*, vol. 223, pp. 84-90, March 2015.

[17] B. Jin, X. Liu, Q. Bai, D. Wang, and Y. Wang, "Design and implementation of an intrinsically safe liquid-level sensor using coaxial cable," *Sensor*, vol.15, pp.12613-12634, May 2015.

[18] O. F. Ameena, M. H. Younus, M. S. Aziz, A. I. Azmi, R. R. Ibrahim and S. K. Ghoshal, "Graphene diaphragm integrated FBG sensors for simultaneous measurement of water level and temperature", *Sens. Actuators A, Phys*, vol. 252, pp. 225-232, Dec. 2016.

[19] C. Li, T. Ning, C. Zhang, X. Wen, J. Li and C. Zhang, "Liquid level and temperature sensor based on an asymmetrical fiber Mach–Zehnder interferometer combined with a fiber Bragg grating," *Else. Optics Communications*, vol. 372, pp. 196-200, April 2016.

[20] C. Li, T. Ning and C. Zhang, "Liquid level measurement based on a no-core fiber with temperature compensation using a fiber Bragg grating," *Sens. Actuators A, Phys*, vol. 245, pp. 49-53, July 2016.



Sayyed Faizan Ali was born in Kanpur, India, in 1989. He received B.Tech. degree in Electronics and Instrumentation Engineering from Uttar Pradesh Technical University, Lucknow, India, in 2011, and M.Tech. degree in Control and InstrumentationEngineering from Delhi Technological University (formerly known as DCE) Delhi, India, in 2015.He is currently pursuing Ph.D. degree with the Department of Electronics Engineering from IIT (ISM) Dhanbad, India. His current research interests include sensor design, controller design and MEMS. He is an active member of Optical Society of America (OSA) and Society of Photo-Optical Instrumentation Engineers (SPIE).



Nirupama Mandal (M'15) was born in India in 1978. She received the B.Sc. (Hons.) degree in physics, the B.Tech. degree in instrumentation engineering, the M.Tech. degree in instrumentation and control engineering, and the Ph.D. (Tech.) degree in instrumentation engineering from the University of Calcutta, Kolkata, India, in 2001, 2004, 2006,and 2012, respectively. She was an Assistant Professor and the Head of the Department of Electronics and Instrumentation Engineering, Asansol Engineering College, Asansol, India, for eight and half years, and joined the Department of Electronics Engineering, IIT(ISM), Dhanbad, India, as an Assistant Professor in 2013. She has authored 37 papers in international journals and 20 papers in international and national conference proceedings. Her current research interests include transducer design, PC based instrumentation, controller design, MEMS and process modeling.

1558-1748 (c) 2018 IEEE. Personal use is permitted, but republication/redistribution requires IEEE permission. See http://www.ieee.org/publications_standards/publications/rights/index.html for more information.

Materials Research Express

PAPER

Effect of rotational speed in friction stir processing on the microstructural and mechanical characteristics of cast AS21A magnesium alloy

To cite this article: Sumit Joshi *et al* 2019 *Mater. Res. Express* **6** 056554

View the article online for updates and enhancements.



IOP ebooks™

Bringing you innovative digital publishing with leading voices to create your essential collection of books in STEM research.

Start exploring the collection - download the first chapter of every title for free.

This content was downloaded from IP address 14.139.251.100 on 06/03/2019 at 04:30

Materials Research Express

PAPER

Effect of rotational speed in friction stir processing on the microstructural and mechanical characteristics of cast AS21A magnesium alloy

RECEIVED
7 December 2018

REVISED
19 January 2019

ACCEPTED FOR PUBLICATION
11 February 2019

PUBLISHED
22 February 2019

Sumit Joshi[1], **Ramesh Chandra Singh and Rajiv Chaudhary**

Department of Mechanical Engineering, Delhi Technological University, Bawana Road, New Delhi-110042, India
[1] Author to whom any correspondence should be addressed.

E-mail: sumitrke1989@gmail.com, rcsingh68@hotmail.com and rch_dce@rediffmail.com

Keywords: Mg-Al-Si, AS21A, magnesium alloy, friction stir processing, Mg_2Si

Abstract

Magnesium-Aluminum-Silicon (Mg-Al-Si) alloys are well recognised for elevated temperature applications as they contain the thermally stable Mg_2Si intermetallic compound. However, the coarse and brittle nature of Mg_2Si deteriorates the mechanical properties; therefore researchers are working on its modification and refinement to enhance the widespread use of heat resistant Mg-Al-Si alloys. In the present work, Mg-Al-Si based AS21A alloy was subjected to Friction Stir Processing (FSP) at three different rotational speeds of 400, 800 and 1200 rpm with a constant travel speed of 50 mm min^{-1}. Microstructural features exhibit the fragmentation of coarse Mg_2Si to fine particles thus creating their homogeneous dispersion and eliminate the casting defects present in the parent material. The morphological structure modification achieved through friction stir processing resulted in the significant enhancement of mechanical properties like strength, ductility etc Further, fracture surface analysis depicted though fractography images proved the brittle nature of cast AS21A alloy and ductile nature of friction stir processed material.

1. Introduction

In the ongoing demand for light weight materials, magnesium alloys are equally comparable to aluminium alloys because of attributes such as high specific strength, low density, high damping capacity and better machinability. Mg-Al-Zn (AZ series) alloy system is the most common commercially employed alloy in automotive and aerospace sectors due to their remarkable features like excellent castability and good mechanical properties [1–3]. However, AZ series alloys exhibit poor mechanical behaviour at high temperature (above 120 °C) due to the presence of low melting point β-$Mg_{17}Al_{12}$ phase (about 460 °C) in the α-Mg matrix [4]. Therefore Mg-Al-Si (AS series) alloys were developed for elevated temperature applications (up to 150 °C) since they contain hard and brittle thermally stable eutectic Mg_2Si intermetallic phase in the matrix. The formation of Mg_2Si is due to very less maximum solid solubility (0.003 at%) of Si in Mg at room temperature thus encouraging the precipitation formation during solidification of casting [5]. Mg_2Si exhibit attributes such as high melting point (1085 °C), low density (1.99×10^3 kg m^{-3}), high elastic modulus (120 GPa), high hardness (460 HV) and low coefficient of thermal expansion (7.5×10^{-6}/K).

Further, Mg_2Si exhibit the pinning effect during grain boundary sliding at elevated temperature thus making the Mg-Al-Si based alloys as heat resistant alloys [6–9]. Volkswagen firm firstly utilised these alloys in the 1970 s for the engine block and powertrain components [10, 11]. However, the major drawback in Mg-Al-Si alloys was their tendency to form undesirable coarse Chinese script Mg_2Si phase, which was attributed to the slow cooling conditions during casting. The coarse and brittle nature of Mg_2Si had a detrimental effect on the mechanical properties and became a major hindrance in the widespread application of Mg-Al-Si series alloys [12, 13]. Therefore researchers have been involved in modification and refinement of Mg_2Si compound to enhance the mechanical properties of Mg-Al-Si based alloys.

© 2019 IOP Publishing Ltd

Table 1. Chemical composition of cast AS21A alloy.

Alloy	Al	Si	Mn	Zn	Cu	Fe	Ni	Mg
Percentage	2.12	1.04	0.221	0.058	0.002	0.003	<0.001	Rest

Various conventional techniques such as grain refiners [14, 15], rapid solidification [16], hot extrusion [17], solution treatment [18] and mechanical alloying [19] were developed for modification/refinement the coarse morphology of Mg_2Si. All these techniques were successful in obtaining the fine Mg_2Si particles and thus enhancing the mechanical strength and ductility of the alloy. However, these techniques display limited grain refinement and also it is difficult to obtain a uniform distribution of Mg_2Si particles. Therefore, researchers have proposed the Severe Plastic Deformation (SPD) techniques such as Equal Channel Angular Pressing (ECAP) [20, 21], Cyclic Extrusion Compression (CEC) [22], Repetitive Upsetting (RU) [23] and Cyclic Closed-Die Forging (CCDF) [24, 25] to overcome the shortcomings of conventional methods through morphological modification of Mg_2Si. SPD techniques impose large strains in the material during deformation which is sufficient in achieving the breakage of Mg_2Si into fine particles and thus attaining their uniform dispersion in the matrix. Wang *et al* [20] reported the breakage of coarse Chinese script Mg_2Si into small particles with uniform dispersion during ECAP of an AZ31-0.5Si alloy which resulted in the significant improvement of ductility. Similarly, Guo *et al* [23] performed CCDF on AZ31-Si composite and attained the fragmentation of Mg_2Si into fine particles that resulted in enhanced yield strength and elongation.

In addition to above SPD techniques, the research is going on a newly emerging technique termed as Friction Stir Processing (FSP). FSP is a very fast and economic SPD approach since the desired microstructure and properties can be attained in a single pass. FSP having its roots related to Friction Stir Welding (FSW) is a solid state method that involves microstructural modification through intense plastic deformation of the material resulting in grain refinement and enhanced mechanical properties [26, 27]. In recent years, numerous studies have been conducted to predict the microstructure and mechanical behaviour of Mg alloys when subjected to FSP. It has been reported that FSP was effective in achieving the significant grain refinement along with the enhanced mechanical properties such as tensile strength and ductility. Further, FSP approach was effectively utilised in modifying the morphology of intermetallic compounds present in the alloy matrix either through their breakup and dissolution ($Mg_{17}Al_{12}$ [28, 29], $Mg_{12}Nd$ [30], Mg_3Zn_2 [31]) or their fragmentation into fine particles (Al_2Ca [32], Al-RE [33]).

It has been concluded from the literature survey that FSP approach employed on Mg alloys was restricted to the Mg-Al-Zn (AZ series), Mg-Al-Mn (AM series), Mg-Zr and Rare Earth (RE) based Mg alloy system. However, it will be more relevant to study the effect of FSP on heat resistant Mg-Al-Si (AS series) alloy system. Therefore in the current study, the effect of FSP on the microstructure and mechanical properties of Mg-Al-Si based AS21A alloy casting has been investigated. The aim was to examine the effect of FSP on the coarse Chinese script morphology of thermally stable Mg_2Si phase present in the AS21A matrix.

2. Experimental details

The present study employed the Mg-Al-Si based AS21A commercial alloy fabricated through gravity die casting. The AS21A casting was further machined in the form of a plate with a dimension of 200 × 80 × 10 mm. The AS21A alloy spectroscopy result performed as per ASTM B94-2013 is presented in table 1.

After the selection and characterisation of the Parent Material (PM), it was subjected to Friction Stir Processing (FSP) technique. In FSP, firstly a non-consumable rotating tool was inserted into the PM plate surface that created severe plastic deformation of the material due to the combined action of stirring and frictional heat. Mechanical stirring was created through tool pin while the frictional heat was generated by the axial force aided penetration of the tool shoulder. After achieving sufficient heat and deformation, the tool pin was in a capacity to direct the material from advancing to retreating side of the plate. Finally, the tool was traversed along the length of the plate to get the desired modified surface. The schematic sketch of the discussed approach is shown in figure 1. An indigenously developed friction stir welding set up (R V machine tools, FSW-4T-HYD) shown in figure 2(a) was utilised for performing the FSP operation.

The following parameters were selected during the entire investigation: three different rotational speeds of 400, 800 and 1200 rpm, the single travel speed of 50 mm min^{-1}, the tilt angle of 2° and plunge depth of 0.1–0.2 mm. Figure 2(b) exhibited the surface appearance of cast alloy plate processed at 400, 800 and 1200 rpm and designated as F1, F2 and F3 respectively. Further, two pass FSP with 100% overlap and the same forward direction was done to accelerate the material mixing and breakage of the hard and brittle eutectic networks present in the AS21A matrix. For FSP operation, the tool having H13 tool steel material and features such as

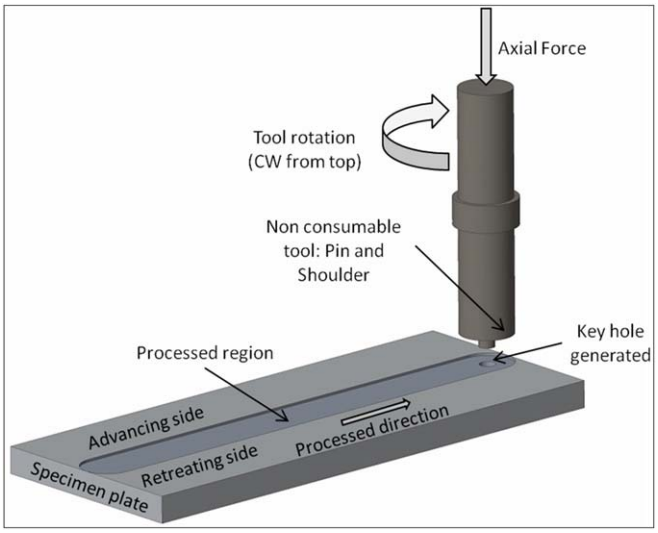


Figure 1. Schematic of Friction Stir Processing (FSP).

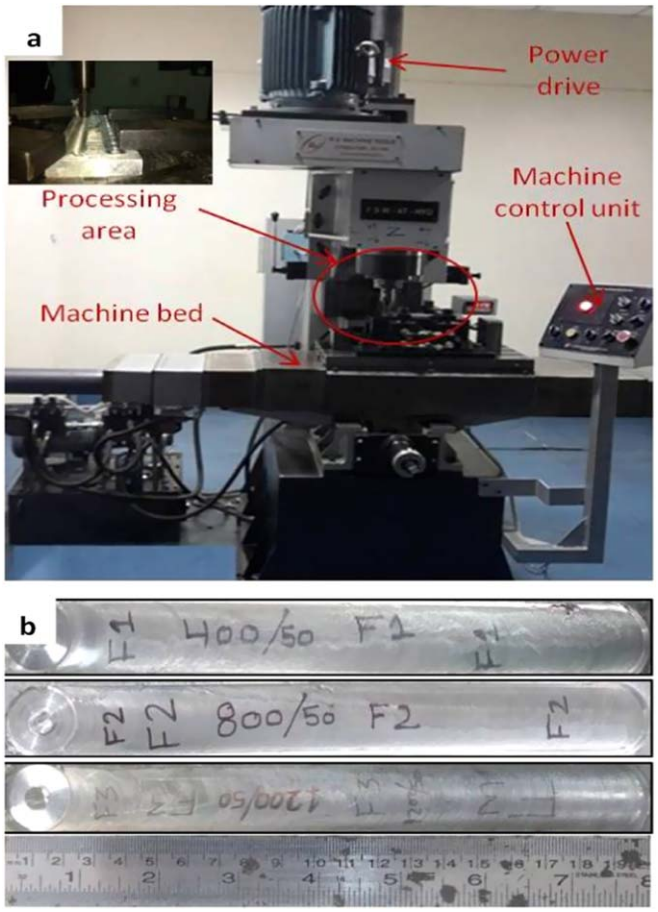


Figure 2. (a) FSW set up; (b) Surface appearance of the processed samples: F1, F2 and F3.

cylindrical threaded pin of 1 mm pitch, pin length of 5 mm, pin diameter of 6 mm and shoulder diameter of 20 mm was employed. The threaded pin was selected to enhance the material flow and mixing from top to bottom. FSP tool employed along with its dimensional features is shown in figure 3. An Infra Red technology based thermal imaging camera (Fluke Ti400) was used for capturing the thermographic images to get an approximation of the peak temperature developed during FSP operation. During the whole experiment, the camera was set up at a fixed distance and angle from the operating region for getting the accurate results. After

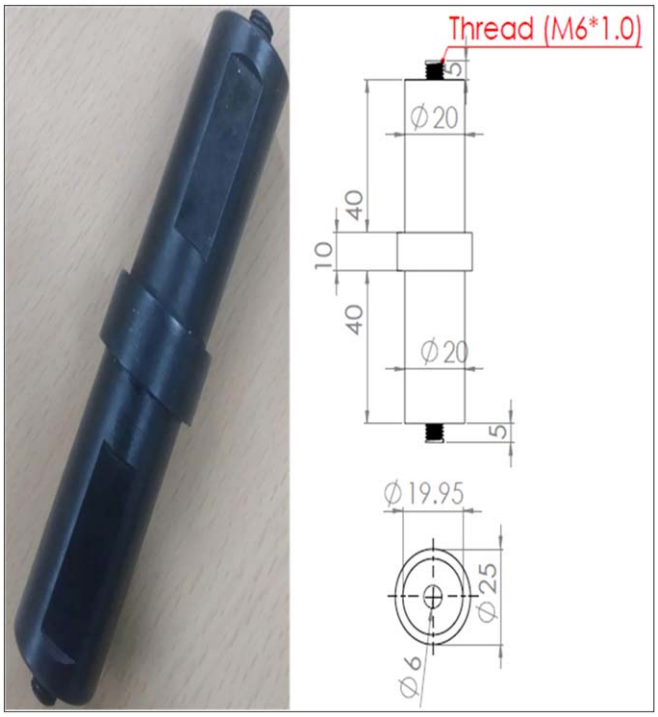


Figure 3. FSP tool with dimensional attributes.

FSP, samples were sliced in the traverse direction from the processed region (figure 2(b)) through wire cut for examining the microstructure and mechanical behaviour. For microstructure characterisation, initially, surfaces orthogonal to processing direction were mechanically polished using different grades of emery paper from coarser to a finer one. Grain structure was revealed by employing acetic picral etchant comprising of ethanol (100 ml), picric acid (6 g), acetic acid (5 ml) and water (10 ml) for 5–10 s. Finally, Optical Microscope (Olympus, model GX 41) was utilised to capture the Optical Microscopic (OM) images of the microstructure. Scanning Electron Microscope (SEM) equipped with EDS facility was utilised for micrographs and elemental analysis. X-ray diffraction analysis was carried out for phase identification through RigaKu x-ray diffractometer having monochromatic Cu-Kα radiation (2θ values: 20°–80°). The microhardness analysis was carried out using a microhardness tester (Model: FM-e7, Future Tech, Japan) attached with Vickers diamond pyramidal indenter (136°) at a load of 100 g and a dwell time of 10 s. Indentations were done along (from left to right) and perpendicular (from top to bottom) in the Stirred Zone (SZ) at an equal interval of 1 mm. The tensile test was performed to determine the mechanical properties using universal Testing Machine (UTM) set up (Tinius Olsen H50KS) at a constant crosshead speed of 2.5 mm min^{-1} and room temperature. Figures 4(a) and (b) depict the tensile specimen before and after fracture respectively. The tensile specimen (figure 4(c)) was prepared as per ASTM B557M-06 standard. SEM micrographs of fractured samples were taken to analyse their fracture behaviour.

3. Results and discussions

3.1. Structural analysis

The OM image of the cast AS21A magnesium alloy is shown in figure 5. It is evident that parent material microstructure was characterised by the α-Mg grains surrounded by the eutectic network of coarse intermetallic compounds distributed at the grain boundaries. The coarse intermetallic morphology appeared as Chinese script which confirmed the presence of hard and brittle thermally stable Mg_2Si phase as depicted in the inset of figure 5. SEM along with EDS spectrum shown in figure 6 confirmed the presence of main alloying elements. Moreover, as shown in figure 7, XRD graph of AS21A alloy justified the presence of Mg_2Si phase in the magnesium matrix. The microstructural findings of AS21A alloy were in good agreement with the literature [34–37] since PM was prepared through the casting route, that's why it was obvious for the evolution of coarse Mg_2Si precipitates in the matrix. Further, casting defects particularly porosity and voids were present in the parent material.

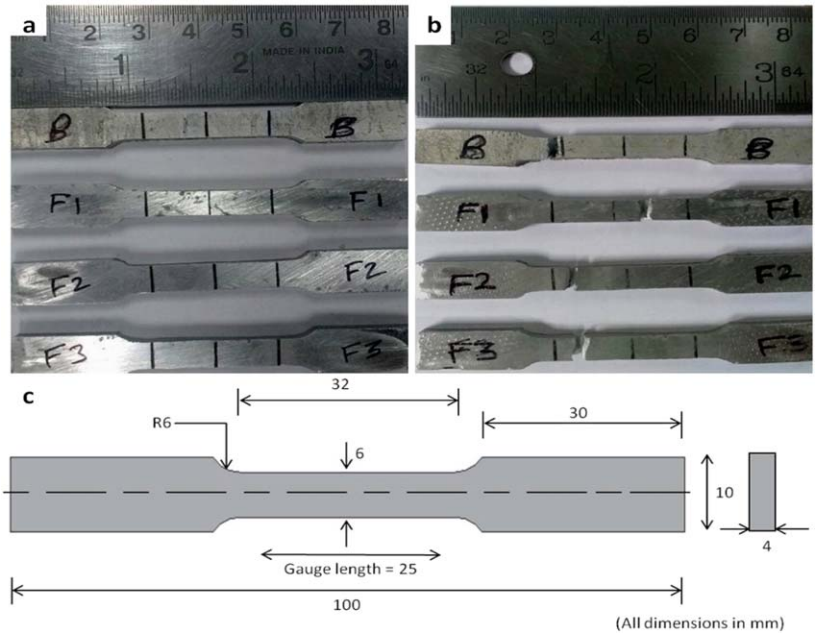


Figure 4. Tensile specimens (a) before fracture, (b) after fracture and (c) prepared as per ASTM B557M-06.

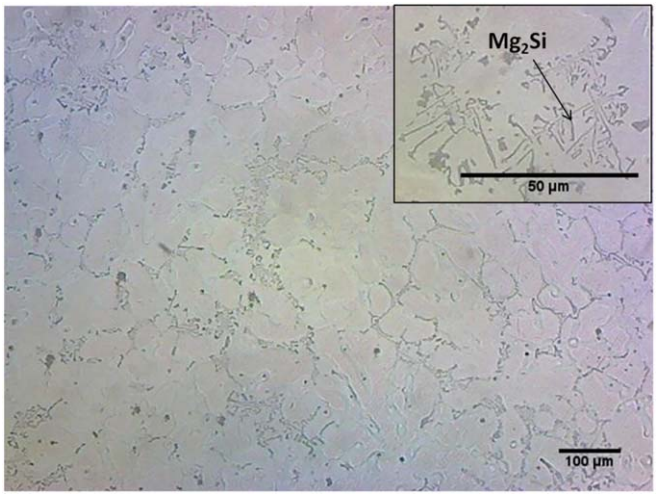


Figure 5. Microstructure of the cast AS21A alloy.

AS21A alloy when subjected to FSP at three different rpm: 400 (F1), 800 (F2) and 1200 (F3), a distinct impression referred as the Stirred Zone (SZ) appeared as shown by the macrograph shown in figure 8. The SZ was sound in all three processing conditions which imply that the intense plastic deformation and material mixing created by FSP was able to diminish the porosity present in the PM. Figure 9 represents the thermal imaging camera with its captured thermographic image of the processed zone. The approximate peak temperature developed was less than 500 °C (380 °C–460 °C), which is very less than the melting point ($T_m \sim 650$ °C) of the Mg alloy, not particularly of AS21A alloy. In other words, FSP produced the temperature in the range 0.7–0.9 T_m which confirmed the absence of parent alloy melting and thus it can be concluded that FSP is a hot working operation.

Figure 10 exhibits the microstructures of the SZ (centre region of the impression in figure 8) developed in the processed samples. On comparing the OM image of parent and processed material, it can be observed that the size and shape of the Mg_2Si phase were modified after FSP. For all three samples, vigorous stirring and forging action produced by the FSP tool pin aided in the fragmentation of coarse eutectic Mg_2Si phase into fine particles and thus attaining their uniform dispersion in the matrix. The microstructure of the transition region shown in figure 11 clearly distinguishes the processed and the unprocessed region. The fragmentation of Mg_2Si was

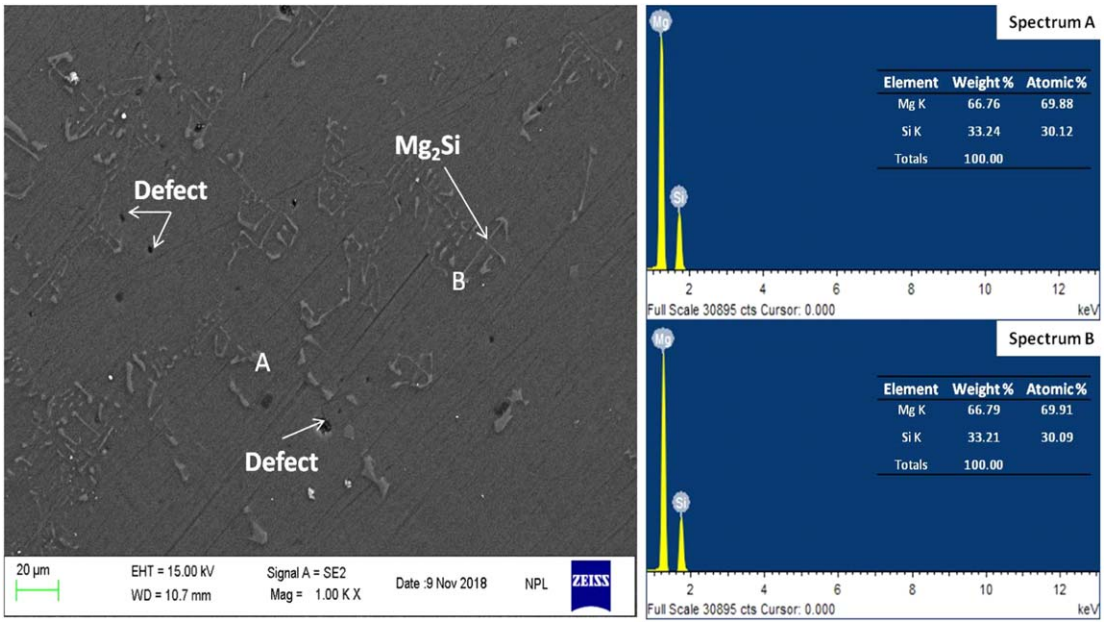


Figure 6. SEM with EDS of cast AS21A alloy.

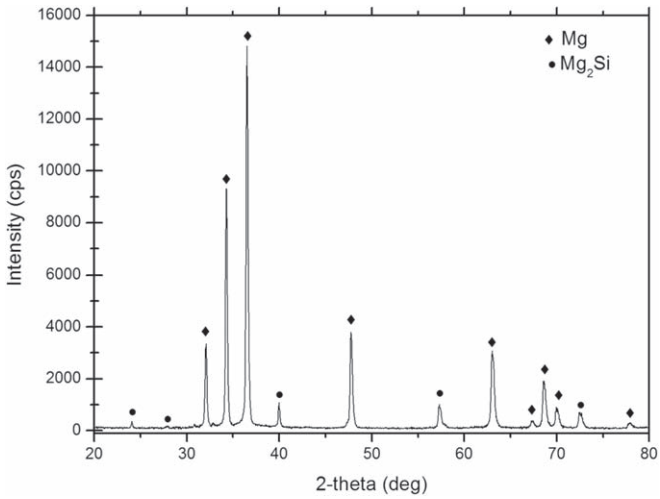


Figure 7. XRD pattern of cast AS21A alloy.

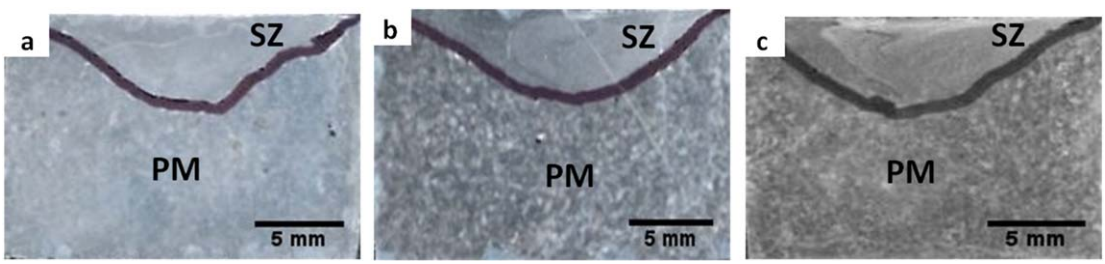


Figure 8. Macrograph of the FSP impression created in samples (a) F1, (b) F2 and (c) F3.

further interpreted from SEM+EDS micrograph as shown in figure 12. The present microstructure findings were in accordance with the study done by Zhang *et al* [16] which states that the FSP of Mg-RE alloy resulted in the mechanical breaking of Al_2Ca intermetallic into fine particles. Arora *et al* [33] concluded that FSP produced a

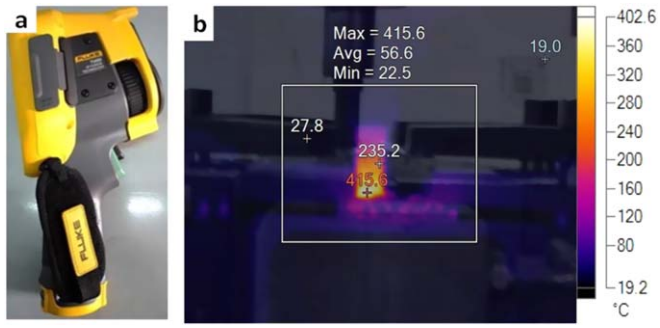


Figure 9. (a) Thermal imaging camera; (b) Thermographic image.

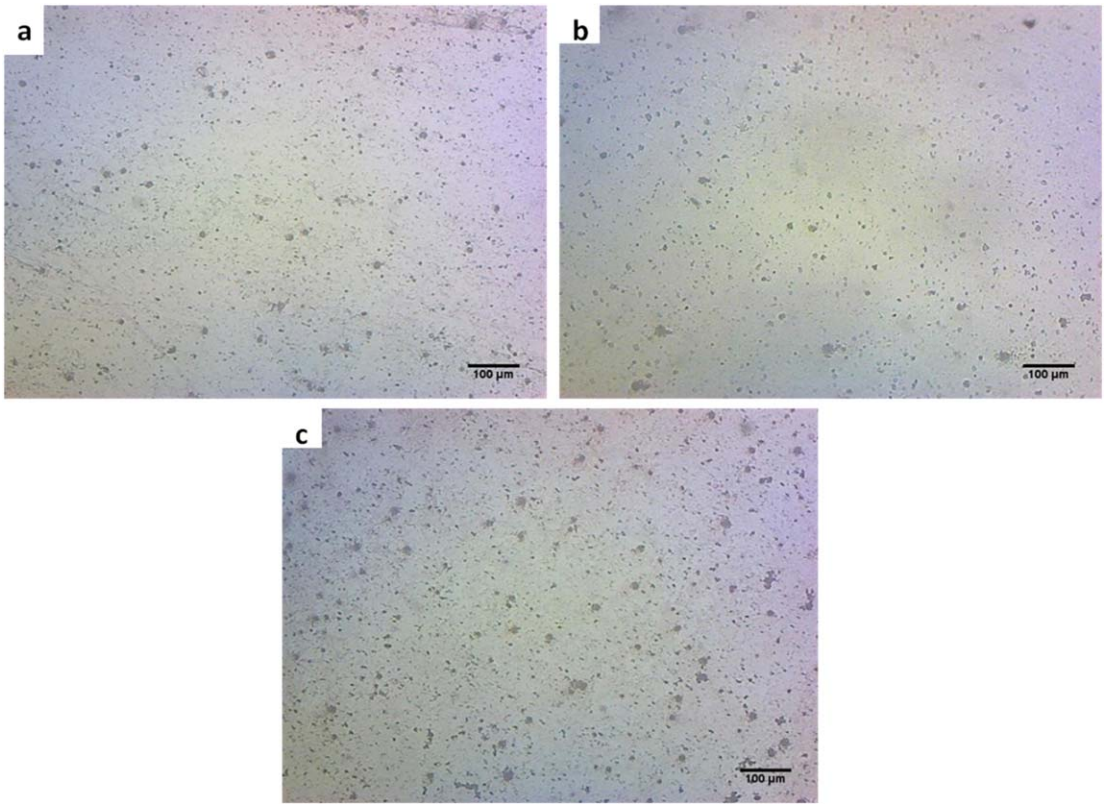


Figure 10. Microstructure of the processed samples: (a) F1, (b) F2 and (c) F3.

homogeneous distribution of fine intermetallics (Al-RE) in the AE42 matrix. Santella *et al* [38] and Ma *et al* [39] observed the uniform dispersion of second phase acicular silicon particles in the aluminium matrix during FSP of A319 and A356 castings. However, FSP of AZ91 and AZ31 alloys resulted in the complete dissolution of β-$Mg_{17}Al_{12}$ as investigated by Wen *et al* [28] and Feng *et al* [29] respectively. It was attributed to the low MP of $Mg_{17}Al_{12}$ (460 °C). In the present work, frictional heat generated the temperature in the range 380 °C–460 °C which was not enough for the dissolution of Mg_2Si due to its very high MP (1085 °C).

The fragmentation of Mg_2Si instead of dissolution was further confirmed by the XRD graph as shown in figure 13. The graph indicates that FSP resulted in a decrease of number and intensity of Mg_2Si peak when compared to the cast sample (figure 6) which confirmed the fragmentation of Mg_2Si into fine particles. Similarly, Cao *et al* [40] performed FSP on Mg-Nd-Y alloy and attained the breakup of $Mg_{12}Nd$ and $Mg_{24}Y_5$ phases into tiny particles that were attributed to the reduction of diffraction peaks.

3.2. Mechanical properties

The mechanical characteristics obtained from UTM and microhardness test are summarised in table 2. The average microhardness of the parent material was 55 HV which was only 20% lower than the specimen

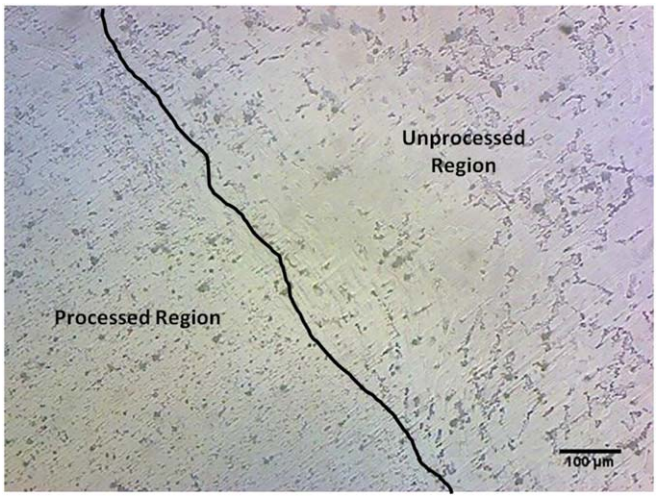


Figure 11. Microstructure of transition zone in the processed sample.

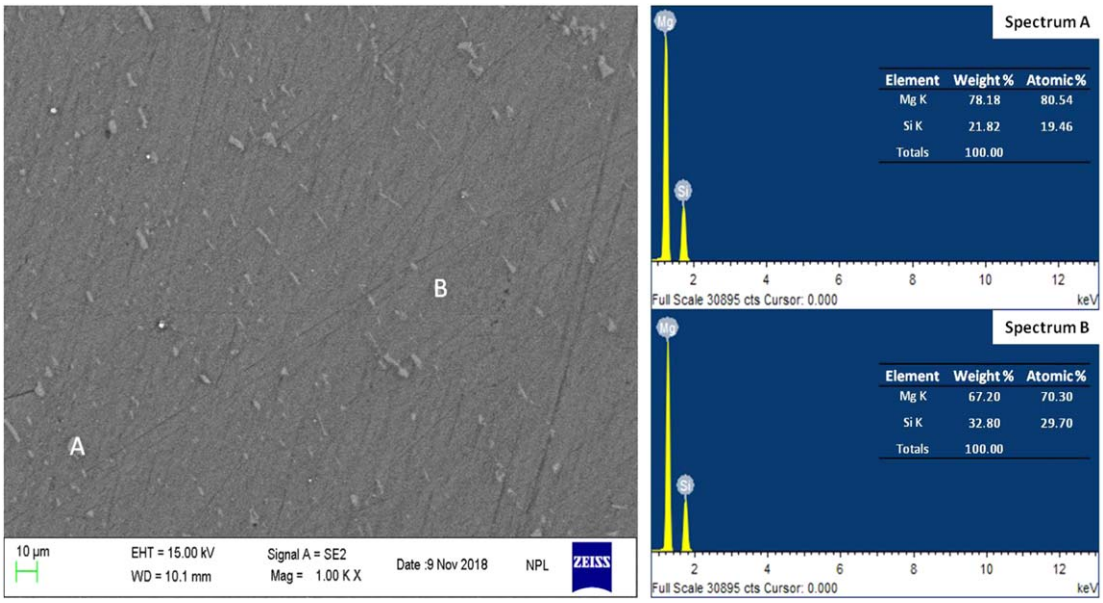


Figure 12. SEM with EDS spectrum of the processed sample.

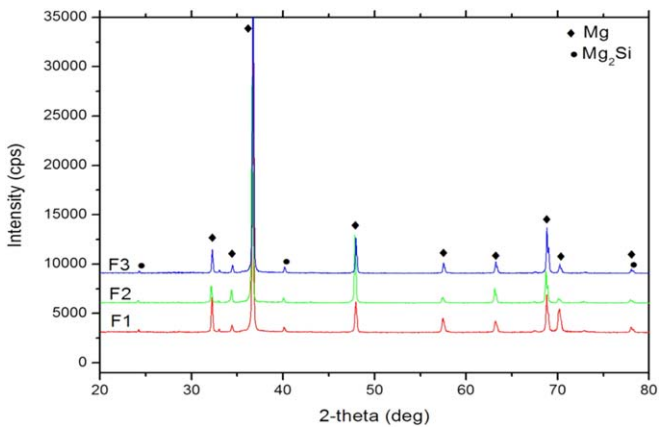


Figure 13. XRD pattern of the FSP samples.

Table 2. Mechanical properties obtained from UTM and microhardness test.

Specimen	Strength (MPa)	% Elongation	Average microhardness (HV)
PM	83.2	3.87	55
F1	91.8	6.72	62[a]
F2	88.6	10.6	66[a]
F3	91.5	7.95	61[a]

[a] Stirred Zone.

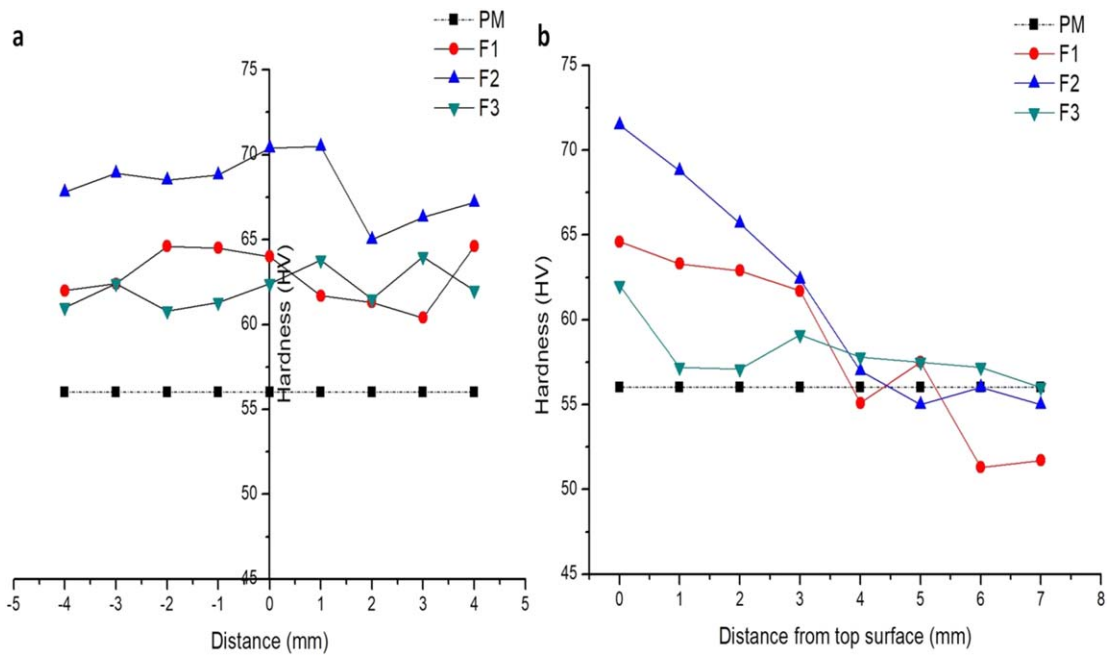


Figure 14. Microhardness variation along the (a) width of SZ and (b) depth of SZ.

processed at 800 rpm (F2). Microhardness variation of the processed samples along the width and depth of SZ is shown in figure 14. The hardness profile clearly shows that the FSP samples exhibited small fluctuation in the microhardness values. The large fluctuation in the PM hardness value can be attributed to the hard Mg_2Si and soft α-Mg networks (figure 5) present in the magnesium matrix. Further, the transformation of the coarse network into small particles due to FSP (figure 10) contributed towards enhancing and homogenising the hardness in the SZ Li *et al* [41] reported a similar trend in respect of microhardness when FSP was performed on the WE43 magnesium alloy.

The rotational speed of 800 was observed as an optimal value for the FSP of AS21A alloy as inferred from table 2. The sample processed at 800 rpm (F2) exhibited highest microhardness (66 HV) compared to F1 (62 HV) and F3 (61 HV) samples. The high hardness of F2 sample can be attributed to the microstructural features obtained after FSP such as breakage and uniform dispersion of Mg_2Si intermetallics (shown in figure 12) in the AS21A matrix. The low rpm in case of F1 sample contributed towards less heat input leading to less material flow thus not in a condition to fully eliminate the casting imperfections present. The following observation was in good agreement with the Mishra *et al* [27] findings which stated that the sufficient amount of heat input is necessary for the formation of the defect-free stirred zone. On the contrary, F3 sample generates a large amount of heat which resulted in the thermal softening of the matrix thus exhibiting lower hardness. Therefore it can be interpreted that the rotational speed in FSP process must be optimized to obtain a defect–free zone which is also reviewed by Sharma *et al* [42]

The stress-strain curve shown in figure 15 explains the tensile behaviour of the cast and FSP treated (F1, F2, F3) specimens. The tensile test results show that the FSP of cast AS21A alloy significantly improved its mechanical properties, especially ductility. The parent material exhibited a little elongation of 4% while the sample processed at 800 rpm (F2) showed the highest elongation of 11%. The coarse and brittle Mg_2Si network attribute of cast AS21A alloy (shown in figure 5) encouraged PM crack formation thus exhibiting the brittle

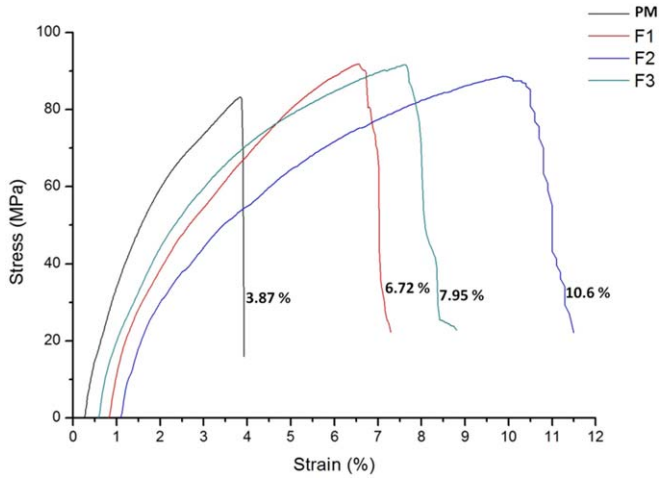


Figure 15. Tensile results obtained from UTM test.

characteristics. After FSP, the significant breakup of the coarse network into small particles (figure 10) encouraged the precipitation strengthening, and there was a significant enhancement in the ductility for all specimens especially the specimen processed at 800 rpm. However, there was a marginal increase in the strength of the samples. Moreover, the casting defects present in the PM were disappeared after FSP, which was also advantageous for the enhancement in ductility of FSP specimens. The high crosshead speed of 2.5 mm min^{-1} can be held responsible for the low strength of the alloy.

The tensile fracture morphologies of the specimens are shown in figure 16. The transverse fractured surface of cast AS21 alloy was characterised by the cleavage facets (point A in figures 16(a) and (b)), wide craters (point B in figure 16(a)) and cracks (point C in figure 16(b)). These typical features indicate the brittle failure of the PM. During tensile deformation of the PM, crack formation was obvious due to the brittle nature of coarse Mg_2Si present at the grain boundary (figure 5) thus exhibiting poor ductility. The FSP sample F1 and F3 transverse fractured surfaces were characterised by the limited and elongated dimples (point A in figures 16(d) and (h)) thus exhibiting the mix ductile and brittle behaviour. Further, FSP sample F2 fractured surface was characterised by the fine and equiaxed dimples as shown in figure 16(f) (point A). The superior ductile behaviour shown by F2 sample justified the appearance of the fractured surface. Cao *et al* [40] also discovered the second phase $Mg_{12}Nd$ as the main factor affecting the mechanical properties particularly ductility of Mg-Nd-Y alloy after FSP.

4. Conclusions

The heat-resistant Mg-Al-Si based AS21A alloy selected as parent material was employed for the current study. The AS21A alloy microstructural features were characterised by the α-Mg grains surrounded by coarse and brittle Mg_2Si Chinese script networks at the grain boundaries. In the present experiment, Friction Stir Processing (FSP) was performed on the parent material followed by its microstructural and mechanical behaviour. Following were the major observations during the entire experiment:

1. FSP technique was able to modify the Chinese script morphology of Mg_2Si intermetallics through its fragmentation into the fine particles in the magnesium matrix, and almost eliminated all the defects present in the parent material.
2. FSP generated the temperature in the range of 380 °C–460 °C which was not sufficient for the dissolution of Mg_2Si in the Mg matrix.
3. The microstructural modifications attained through FSP significantly improved the mechanical properties of AS21A alloy, especially ductility.
4. The specimen processed at 800 rpm (F2) exhibited the highest degree of elongation (11%) compared to the parent material (4%).
5. The fractography results exhibited the brittle and ductile characteristics of the parent material and the processed material respectively.

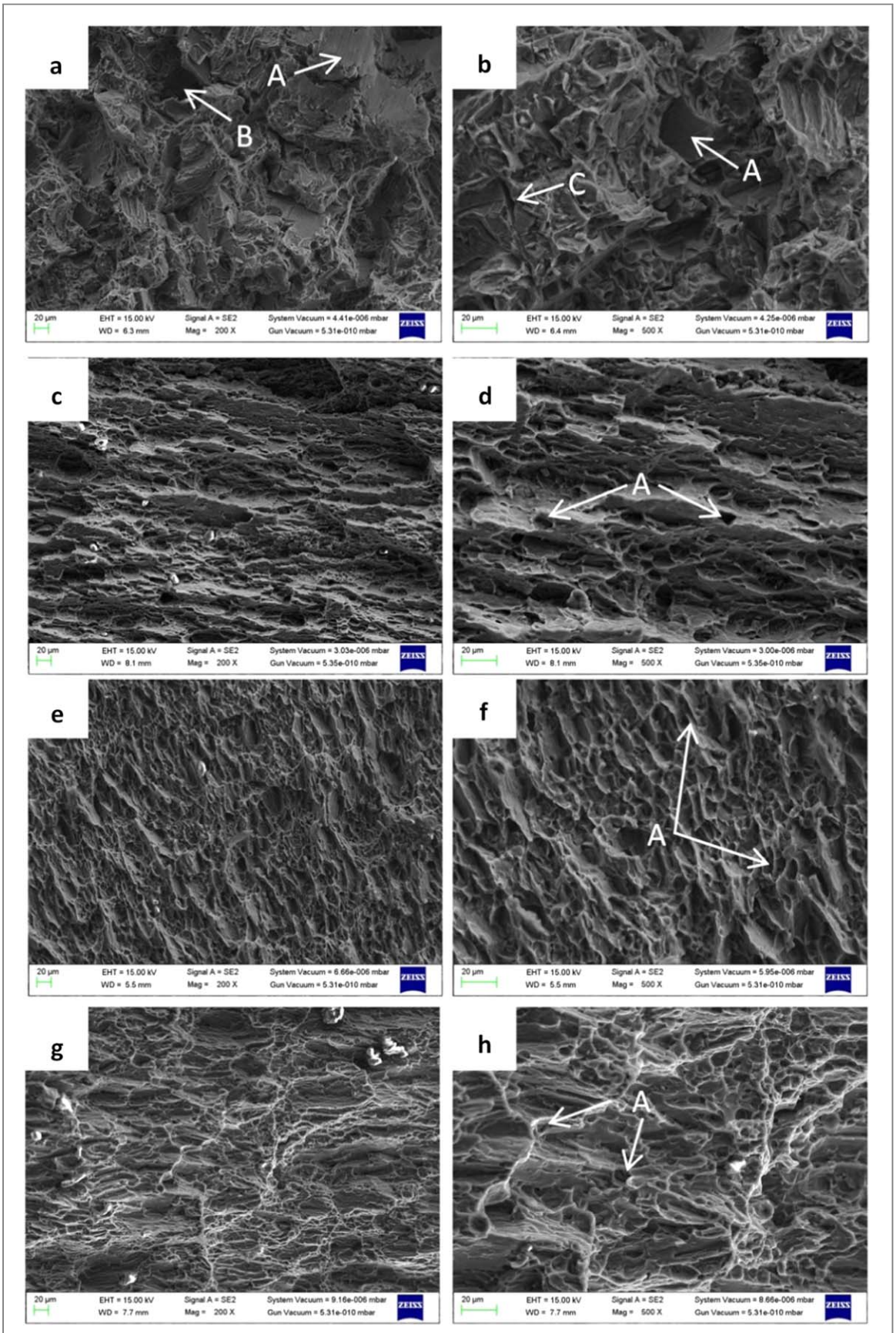


Figure 16. SEM micrographs of the fractured surfaces of (a), (b) parent material; (c), (d) F1; (e), (f) F2; (g), (h) F3 specimens.

Acknowledgments

The authors would like to thank Institute Instrumentation Centre, IIT Roorkee and CSIR-National Physical Laboratory, Delhi for the characterization facility.

Declaration of interest

The authors report no conflicts of interest. The authors alone are responsible for the content and writing of this article.

ORCID iDs

Sumit Joshi https://orcid.org/0000-0001-6932-0510

References

[1] Polmear I, St John D, Nie J F and Qian Ma 2017 *Light Alloys: Metallurgy of Light Metals* 5th edn (Oxford: Butterworth-Heinemann)
[2] Mordike B L and Ebert T 2001 Magnesium properties—applications—potential *Mater Sci Eng* A **302** 37–45
[3] Avedesian M M and Baker H 1999 Magnesium and magnesium alloys *ASM Specialty Handbook* 194–6
[4] Kainer K U 2003 *Magnesium Alloys and Technologies* (Weinheim: Wiley-VCH Verlag GmbH & Co. KGaA)
[5] Brandes E A and Brook G B 2004 *Smithells Light Metals Handbook* (Oxford: Butterworth-Heinemann)
[6] Mabuchi M, Kubota K and Higashi K 1996 Elevated temperature mechanical properties of magnesium alloys containing Mg_2Si *Mater Sci Technol* **12** 35–9
[7] Zhu S, Easton M A, Abbott T B, Nie J F, Dargusch M S, Hort N and Gibson M A 2015 Evaluation of magnesium die-casting alloys for elevated temperature applications: microstructure, tensile properties, and creep resistance *Metall Mater Trans* A **46** 35–43
[8] Luo A and Pekguleryuz M O 1994 Cast magnesium alloys for elevated temperature applications *J Mater Sci* **29** 5259–71
[9] Mabuchi M, Kubota K and Higashi K 1996 Tensile strength, ductility and fracture of magnesium-silicon alloys *J Mater Sci* **31** 1529–35
[10] Luo A A 2013 Applications: aerospace, automotive and other structural applications of magnesium ed M O Pekguleryuz, K U Kainer and A A Kaya *Fundamentals of Magnesium Alloy Metallurgy* (Cambridge: Woodhead Publishing Limited) pp 266–316
[11] Luo A A 2013 Magnesium casting technology for structural applications *Journal of Magnesium and Alloys* **1** 2–22
[12] Badri M, Miresmaeili S M and Nami B 2016 Microstructure and impression creep properties of Ca-Containing AS31 magnesium alloy *Acta Metall Sin (Engl Lett)* **29** 1089–97
[13] Bronfin B, Katsir M and Aghion E 2001 Preparation and solidification features of AS21 magnesium alloy *Mater Sci Eng* A **302** 46–50
[14] Hu J L, Tang C P, Zhang X M and Deng Y L 2013 Modification of Mg_2Si in Mg−Si alloys with neodymium *Trans Nonferrous Met Soc China* **23** 3161–6
[15] Tang S Q, Zhou J X, Tian C W and Yang Y S 2011 Morphology modification of Mg_2Si by Sr addition in Mg−4%Si alloy *Trans Nonferrous Met Soc China* **21** 1932–6
[16] Sheng S D, Chen D and Chen Z H 2009 Effects of Si addition on microstructure and mechanical properties of RS/PM (rapid solidification and powder metallurgy) AZ91 alloy *J Alloys Compd* **470** L17–20
[17] Mabuchi M, Kubota K and Higashi K 1994 Effect of hot extrusion on mechanical properties of a Mg-Si-Al alloy *Mater Lett* **19** 247–50
[18] Cao L J, Ma G R and Tang C C 2012 Effects of isothermal process parameters on semisolid microstructure of Mg−8%Al−1%Si alloy *Trans Nonferrous Met Soc China* **22** 2364–9
[19] Lul J L, Lai M O and Hoe M L 1998 Formaton of nanocrystalline Mg_2Si and Mg_2Si dispersion strengthened Mg−Al alloy by mechanical alloying *Nanostruct Mater* **10** 551–63
[20] Wang Q D, Chen Y J, Zhang L J, Lin J B and Zhai C Q 2006 Microstructure and mechanical properties of AZ31−0.5%Si alloy processed by ECAP *Trans Nonferrous Met Soc China* **16** 1660–3
[21] Gan W M, Wu K, Zheng M Y, Wang X J, Chang H and Brokmeier H G 2009 Microstructure and mechanical property of the ECAPed Mg_2Si/Mg composite *Mater Sci Eng* A **516** 283–9
[22] Zhang Z M, Xu C J, Guo X F and Jia S Z 2008 Reciprocating extrusion of *in situ* Mg_2Si reinforced Mg−Al based composite *Acta Metall Sin (Engl Lett)* **21** 169–77
[23] Guo W, Wang Q D, Ye B, Zhou H and Liu J F 2014 Microstructure and mechanical properties of AZ31−Mg_2Si *in situ* composite fabricated by repetitive upsetting *Trans Nonferrous Met Soc China* **24** 3755–61
[24] Metayer J, Ye B, Guo W, Wang Q, Zhou H and Mollet F 2014 Microstructure and mechanical properties of Mg Si alloys processed by cyclic closed-die forging *Trans Nonferrous Met Soc China* **24** 66–75
[25] Guo W, Wang Q, Ye B and Zhou H 2013 Enhanced microstructure homogeneity and mechanical properties of AZ31–Si composite by cyclic closed-die forging *J Alloys Compd* **552** 409–17
[26] Ma Z Y 2008 Friction stir processing technology: a review *Metall Mater Trans* A **39** 642–58
[27] Mishra R S and Ma Z Y 2005 Friction stir welding and processing *Mater Sci Eng* R **50** 1–78
[28] Wen W, Wang K, Guo Q and Wu N 2012 Effect of friction stir processing on microstructure and mechanical properties of cast AZ31 magnesium alloy *Rare Metal Mat Eng* **41** 1522–6
[29] Feng A H and Ma Z Y 2007 Enhanced mechanical properties of Mg–Al–Zn cast alloy via friction stir processing *Scripta Mater* **56** 397–400
[30] Zheng F Y, Wu Y J, Peng L M, Li X W, Fu P H and Ding W J 2013 Microstructures and mechanical properties of friction stir processed Mg-2.0Nd-0.3Zn-1.0Zr magnesium alloy *Journal of Magnesium and Alloys* **1** 122–7
[31] Ma Z Y, Pilchak A L, Juhasb M C and Williams J C 2008 Microstructural refinement and property enhancement of cast light alloys via friction stir processing *Scripta Mater* **58** 361–6
[32] Zhang D, Suzuki M and Maruyama K 2005 Microstructural evolution of a heat-resistant magnesium alloy due to friction stir welding *Scripta Mater* **52** 899–903

[33] Arora H S, Singh H and Dhindaw B K 2012 Some observations on microstructural changes in a Mg-Based AE42 alloy subjected to friction stir processing *Metall Mater Trans* B **43B** 92–108
[34] Zhang P 2005 Creep behavior of the die-cast Mg–Al alloy AS21 *Scripta Mater* **52** 277–82
[35] Li G H, Gill H S and Varin R A 1993 Magnesium silicide intermetallic alloys *Metall Mater Trans* A **24** 2383–91
[36] Evangelista E, Gariboldi E, Lohne O and Spigarelli S 2004 High-temperature behaviour of as die-cast and heat treated Mg–Al–Si AS21X magnesium alloy *Mater Sci Eng* A **387–389** 41–5
[37] Dargusch M S, Bowles A L, Pettersen K, Bakke P and Dunlop G L 2004 The effect of silicon content on the microstructure and creep behavior in die-cast magnesium AS alloys *Metall Mater Trans* A **35A** 1905–9
[38] Santella M L, Engstrom T, Storjohann D and Pan T Y 2005 Effects of friction stir processing on mechanical properties of the cast aluminum alloys A319 and A356 *Scripta Mater* **53** 201–6
[39] Ma Z Y, Sharma S R, Mishra R S and Mahoney M W 2006 Microstructural modification of As-Cast Al-Si-Mg Alloy by Friction Stir processing *Metall Mater Trans* A **37A** 3323–36
[40] Cao G, Zhang D, Zhang W and Qiu C 2015 Microstructure evolution and mechanical properties of Mg–Nd–Y alloy in different friction stir processing conditions *J Alloys Compd* **636** 12–9
[41] Li J, Zhang D T, Chai F and Zhang W 2014 Microstructures and mechanical properties of WE43 magnesium alloy prepared by friction stir processing *Rare Met* (https://doi.org/10.1007/s12598-014-0306-3)
[42] Sharma V, Prakash U and Kumar B V M 2015 Surface composites by friction stir processing: a review *J. Mater. Process. Technol.* **224** 117–34

Materials Research Express

ACCEPTED MANUSCRIPT

Fabrication and sliding wear behavior of some lead-free bearing materials

To cite this article before publication: Ramesh Chandra Singh *et al* 2019 *Mater. Res. Express* in press https://doi.org/10.1088/2053-1591/ab0be4

Manuscript version: Accepted Manuscript

Accepted Manuscript is "the version of the article accepted for publication including all changes made as a result of the peer review process, and which may also include the addition to the article by IOP Publishing of a header, an article ID, a cover sheet and/or an 'Accepted Manuscript' watermark, but excluding any other editing, typesetting or other changes made by IOP Publishing and/or its licensors"

This Accepted Manuscript is **© 2019 IOP Publishing Ltd**.

During the embargo period (the 12 month period from the publication of the Version of Record of this article), the Accepted Manuscript is fully protected by copyright and cannot be reused or reposted elsewhere.
As the Version of Record of this article is going to be / has been published on a subscription basis, this Accepted Manuscript is available for reuse under a CC BY-NC-ND 3.0 licence after the 12 month embargo period.

After the embargo period, everyone is permitted to use copy and redistribute this article for non-commercial purposes only, provided that they adhere to all the terms of the licence https://creativecommons.org/licences/by-nc-nd/3.0

Although reasonable endeavours have been taken to obtain all necessary permissions from third parties to include their copyrighted content within this article, their full citation and copyright line may not be present in this Accepted Manuscript version. Before using any content from this article, please refer to the Version of Record on IOPscience once published for full citation and copyright details, as permissions will likely be required. All third party content is fully copyright protected, unless specifically stated otherwise in the figure caption in the Version of Record.

View the article online for updates and enhancements.

This content was downloaded from IP address 14.139.251.100 on 08/03/2019 at 04:51

Fabrication and sliding wear behavior of some lead-free bearing materials

Ramesh Chandra Singh[1], Rajiv Chaudhary[1], Vipin Kumar Sharma[1,2,*]

[1]Department of Mechanical Engineering, Delhi Technological University, Bawana Road, Delhi-110042 India.
[2]Department of Mechanical and Automation Engineering, Maharaja Agrasen Institute of Technology, Rohini Sector-22, Delhi-110086, India

Corresponding Author* - vipin.dtu@gmail.com

ORCID ID: https://orcid.org/0000-0002-7356-4590

Abstract

The conventional journal bearing material contains varying amounts of lead (Pb) in it. Pb provides the anti-wear and anti-friction properties. However, Pb has hazardous effects on health and the environment. By considering the environmental aspect in mind, Pb free bearing materials are proposed in this paper. A copper-aluminium-nickel (Cu-NiAl) and copper-phosphorous-aluminium (Cu-PAl) materials were developed using the stir casting method and tribological performance of the developed materials was evaluated using a pin on disc experiments. The experiments were performed in fully flooded, starved and unlubricated conditions at a pressure of 0.31 MPa and 4.39 m/s sliding speed. Optical micrograph, Energy dispersive spectroscopy (EDS) and Scanning electron spectroscopy (SEM) images were obtained to inspect the wear behavior of the developed materials. For the fully flooded lubricating condition, Cu-NiAl resulted with better wear and friction properties as compared to the conventional Pb bronze material. During the starved and unlubricated condition, Cu-PAl material exhibited better tribological properties as compared to Cu-NiAl and Cu-Pb material.

Keywords
Lead-free, bronze, tribology, bearing materials, fully flooded, starved, unlubricated.

1. Introduction

In recent years, issues related to the environment because of the use of hazardous materials have become one of the important considerations in the selection of materials for various applications. In bearing applications, these issues mainly occur because of the presence of lead. The lead present in the bearing come in the environment during the fabrication of the bearings. During this, waste material of the machining process and contaminated lubricant should be disposed of with proper care. Bronzes are the most used material for bearings [1]. The disposal of worn out bearings having lead contents is also a big concern. Lead is added to the bearing materials to improve the anti-frictional properties of it. On the other hand, it results in lowering the strength. So a bearing material without having lead content and with similar properties will help in reducing the harmful effects of lead. As an alternative to the leaded bronze materials, bismuthized bronze, aluminium bronze, and phosphorous bronze have been tested for various properties to be used as the potential bearing materials. Bismuthized bronzes were tested for mechanical and wear properties by Thomson et al. [2]. Bismuthized bronzes were found to have similar performance as compared to leaded bronzes. Thomson et al. uses the casting technique and prepared different samples with different percentages (5 and 10%) of bismuth (Bi) in bronze and compared with a 10% leaded bronze. It is reported that alloy containing 10% Bi have a similar structure to that of lead-containing alloy, but the morphology of lead-bronze bearing is more suitable for bearing applications. It is also found that the variation of friction forces is less in Bi bronze.
Al-bronze materials are also used as the bearing material [3]. Al-Bronze material having 10% Al is used for the casting process and it gives high corrosion resistance and high strength [4]. This alloy (10% Al) also has better comprehensive properties, and it is the widely used alloy in its family (Al-Bronze) [5]. Al-bronze material keeps their strength at high temperature as well. Phosphorous bronze is the potential copper alloy which has good corrosion resistance, wear resistance and machinability. These properties of phosphorous bronze make it suitable for bearing applications. Gebretsadik et al. [6] studied the tribological performance of tin-based plated bearing in boundary as well as mixed lubricating conditions and compared with the conventional lead-based overlay bearing material. Authors used a block on ring test method for the analysis. It is reported that tin-based overlay shows comparable tribological properties for longer test durations. In mixed lubricating condition, tin-based overlay exhibits better wear resistance as compared to lead-based overlay.

In another research article by Gebretsadik et al. [7] Polyamide-lmide overlay with graphite and MoS_2 and Al-Sn materials were tested for tribological properties and compared with lead-based materials. The Polyamide-lmide

Accepted Manuscript

overlay with graphite and MoS_2 resulted in better wear and friction properties as compared to Al-SN and Pb based materials. The Pb based material also resulted in the maximum amount of wear as well. Sharma et al. [8] fabricated copper-aluminium, copper-phosphorous and aluminium-flyash composite materials and evaluated the wear and friction properties using a pin on disc test method. Authors concluded that copper-phosphorus material exhibits better tribological properties as compared to the conventional copper lead bearing material in starved lubricating condition.

For the applications of journal bearings, steel is the most used material for journal (shaft) part of the bearing assembly. So the new journal bearing material should also have better adherence properties concerning steel. It is reported by Li et al. [9] that, materials like Al, Cu, and Zn have very low adherence to steel. It indicates that an alloy of Al-Cu-Zn may be possibly used to make bearings. When the Al bronze alloy is tested against steel material for wear and friction, it reduces the coefficient of friction, however, the wear rate increases [10-11]. During the experimentation, the complex Al-bronze phases got heat-treated and may produce different results. Li et al. developed a Cu-14 Al-X alloy and reported less wear rate and coefficient of friction when tested against 1Cr18Ni9Ti steel [9]. Chmura and Gronostajski mixed the granular aluminium chips and aluminium bronze alloy (8% Al) to develop a composite material for bearings. Authors reported that with the increase of aluminium in bronze the wear intensity tends to decrease [12].

Yan et al. [13] performed the scratch tests using the nano-indentor for evaluating the sliding wear nature of Cu-Al and Cu-Ni nano-twinned metals. The wear and hardness of Cu –Al increases with an increase in Al contents in Cu. Also, the Ni content in Cu improves the wear behavior. Saud et al. [14] investigated the effects of Mn or Ti on the microstrure and corrosion behavior of Cu-Ni-Al alloys. The alloys with 0.7% Mn or Ti resulted with highest strain recovery as compared to other compositions. Panagopopoulos et al. [15] investigated the friction behavior of leaded ($\alpha+\beta$) brass against stainless steel. A pin on disk tribometer was used for the experimentation. Distilled water and NaCl solution was used as the lubricating medium and results were compared with the commercial SAE 80 W lubricant. It is concluded by authors that, aqueous solutions may be used for improving the tribological properties of ($\alpha+\beta$) brass. The aqueous solution helps in making a protective oxide layer which prevents the wearing.

The Cu-Al alloys also behaves excellently to the heat treatment processes. Ding et al. [16] evaluated the stress corrosion cracking susceptibility of the heat treated Cu-Ni-Al alloys. The heat treatment significantly improved the microstructure of the copper alloys. The stress corrosion cracking susceptibility also increases with the heat treatment process. The maximum stress corrosion cracking susceptibility was obtained with annealing heat treatment process. Song et al. [17] reported that, the corrosion behavior of Cu-Ni-Al was closely related to the microstructure. During the tribological testing of material in NaCl solution, it was observed by authors that the finely homogeneous microstructure of the material did not allow the easy penetration of the chloride solution and makes a dense protective film which in result improves the corrosion resistance. The hard faces like β and k phases can be generate by using the heat treatment process. These phases provides the necessary corrosion resistance to the alloy.

Wu et al. [18] observed the improvement in the mechanical and corrosion resistive properties of the Cu-Ni-Al alloys with the heat treatment process. For further improving the surface properties and corrosive resistance of the Cu-Al alloys, Qin et al. [19] used the chromium implantation on the Cu-Al alloys. The chromium content rapidly forms a coating on the Cu-Al surface and enhances the corrosion resistance. Using the similar technique Luo et al. [20] applied the double layers of Ni-Cu and Ni-Al-Cu on copper alloys. The modified Ni-Cu layer on the material improved the corrosion resistance by growing a protective film of $Ni(OH)_2$ and Cu_2O. The comprehensive investigation on the copper alloys is presented in Table 1. From Table 1, it is observed that that Cu-Al alloys are compatible with large number of material elements for the improvement of the tribological properties. Nickel (Ni), Graphite (Gr), Phosphorous (P), Silicon Carbide (SiC), Manganese (Mn) and Chromium (Cr) has been extensively used by researchers for improving the properties of Cu-Al alloys.

Out of all the parameters of characterization, wear is the most critical factor [21]. So it should be handled properly to increase the life of the bearings [22] and sliding is influenced by contacting parts and tribological behavior of the materials [23]. It is reported that abrasive wear is the dominated wear mechanism in case of brass and alloys with magneto fluids [24]. Furthermore, there are several types of wear which occur between the tribo-pairs such as abrasive wear, adhesive wear, diffusion wear and chemical wear. These wear nature involves some complex phenomenon such as transfer of metal, the formation of mechanical alloy and dynamic recrystallization.

Accepted Manuscript

For the prediction of wear properties, pin on disc tribometer has been used by many researchers [25-32]. It consists of a fixed cylindrical pin sliding on a rotating disc. Pressures applied by the pin on the disc and sliding velocity of the disc are the two main parameters of the setup. It consists of friction and wear sensors for the measurement of the wear and friction force.

Table 1: Effects of alloying elements of Cu-Al alloys

Ref. No.	Authors	Material Used	Property Evaluated	Testing Apparatus Used	Processing Method for Material	Effects
[33]	Dang et al.	Ti_3SiC_2/Cu/Al/SiC composites	Wear and Friction	Ball-on-disk	Powder metallurgy	• Al could inhibit the decomposition of Ti_3SiC_2 and enhances the tribological properties.
[34]	Jin et al.	Cu-Al with Cr and Ag	Wear and Friction	Reciprocating friction tester	Powder Metallurgy	• Chromium (Cr) improves the hardness and strength of the Cu-Al composite. • Silver (Ag) present in wear debris increases the plasticity nature of wear debris thereby reduces the three-body abrasion. However, the excess amounts of Cr and Ag are harmful to tribological properties.
[35]	Atapek et al.	CuAl10Ni5Fe4 and CuAl14Fe4Mn2Co	Wear and Friction	Ball on disc	Casting	• Presence of Ni in CuAL10Ni5Fe4 resulted in lower coefficient of friction as compared to CuAl14Fe4Mn2Co. • It also exhibits more corrosion resistance
[36]	Yang et al.	Cu-Al-Ni alloy	Strength, hardness and corrosion resistance		Vacuum Casting	• Role of the Nickel was evaluated for the improvement of mechanical properties and corrosion behavior in NaCl solution. • The increase in Ni element in Cu-Al alloy resulted in more precipitated κ phases, and thus enhances the yield strength and hardness. • Ni content (4.5–10 wt.%) also improved corrosion resistance of the Cu-Al alloy.
[37]	Zhang et al.	ZCuAl9Fe4Ni4Mn2	Wear and Friction	Pin on disc	As casted	• At higher loads the mall loss and friction coefficient increases. • Delamination and abrasive wear were the wear patterns as observed.
[38]	Wang et al.	Cu-9 Ni-Sn	Tribological and Corrosion Properties.	Ball on disc Tribometer	As casted	• Ball on disk experiments were performed in dry, distilled and NaCl solution for the inspection of tribological and corrosion properties. • Friction coefficient was least in NaCl solution as compared to ionized water and dry condition. • Plastic deformation of the material and abrasive wear were the two major wear patters during the dry and ionized water sliding.

Accepted Manuscript

						• Microplowing along with abrasive wear were the wear patterns during the NaCl testing.
[39]	Hassan et al.	Cu-Al-Mg with SiC Particles	Wear and Friction	Pin-on-disk	Slurry casting method.	• Volume losses in wear test of Al–Mg–Cu alloy decrease continuously. • SiC Particles also improves the wear resistance.
[40]	Wen-sheng et al.	Cu-14Al-X and QAl9-4	Wear and Friction	Pin-on-block	Casting	• The wear loss in H_2SO_4 is lower as compared to tribological testing performed in dry or in air.
[41]	Jun et al.	Cu–4Sn–6Zn with carbon fibre (Cf) reinforcement	Wear and Friction	Pin on Plate	Powder Metallurgy	• Wear performance of 9Cf/Cu–4Sn–6Zn was superior to the conventional lead and tin contained bronze. • Adhesive and abrasive, both the wear patterns were observed during the tribo-testing.
[42]	Tan et al.	CuAl10Ni5Fe4	Wear and Friction	PLS-100 rack swing tribometer	-	• Corrosion enhancement enhances the tribological properties of the Cu-Al alloy
[43]	Saarivirta et al.	CuAl10Fe5Ni5	Tribological and Corrosive properties	Pin on disc	Casted ingot	• Experiments were performed in NaCl solution. At low loads the wear induced corrosion is the prime factor at all the considered potentials. • At higher loads abrasive wear was more intense.
[44]	Sláma et al.	CuAl10Ni5Fe4 and CuAl14Fe5	Strength, Hardness	-	Heat Treatment	• The effects of heat treatment were compared for the Cu-Al (9.9 % Aluminium, 5.4 5 Nickel) and Cu-Al (14.5 % Al and 0.12 % Nickel). • The presence of gamma phases in the microstructure of Cu-Al (9.9% Al, 5.4% Ni) alloy impairs the corrosion resistance by imparting high hardness and brittleness. • The presence of beta and gamma phase in Cu-Al (14.5 Al, 0.12 % Ni) made it more brittle and harder.
[45]	Luo et al.	Al 9.85Ni 3.75Fe 3.86Mn1.03	Cavitation erosion tests for mass loss were evaluated	Ultrasonic vibration apparatus	Thermal diffusion process	• Ni-Al-Cu layer was obtained on the Ni-Al-Cu substrate. • There was a reduction of about 6.4 and 5.5 times in mass loss in the cavitation erosion test in distilled water and NaCl solution for the applied coating.
[46]	Qin et al.	81.7Cu, 9.1Al, 4.0Ni, 4.0 Fe, 1.2Mn	Cavitation corrosion rate	Ultrasonically vibratory apparatus	Casting by Vacuum melting	• Annealing, normalizing, quenching and aging methods were used to improve the corrosion rate of the Cu-Al alloy. • The cavitation in corrosion rate reduced by 4.9 times with the quenching technique performed at 450 ºC
[47]	Zhang et al.	Al-Cu-Li alloys	Strength and Toughness	Tensile test and Kahn tear test	As Casted	• Creep aging effects have been observed on the strength and toughness of Al-Cu-Li alloys.

Accepted Manuscript

						• Pre-strain before the artificial aging n improved fracture toughness and strength. • Creep aging increases the nucleation numbers in the matrix which enhances the strength.
[48]	Namboodiri et al.	Cu-Ni-Al	Wear and Strength	Reciprocating sliding tester	Friction Stir Processing	• The FSP improves the strength of the Cu-Al-Ni alloy. • Wear resistance reduces under sea water working condition
[49]	Sundararajan et al.	Cu-Gr-Sic	Mechanical and Tribological Properties	Pin on Disc	Powder Metallurgy	• Graphite and SiC particles were used to fabricate the copper composite. Increasing the SiC contents increases the wear resistance of the copper composite, however coefficient of friction reduces. • Reinforcement increases the hardness of the composite
[50]	Zhai et al.	8.1 Cu 9.5 Al 4.2 Ni 4 Fe 1.2 Mn	Wear and Friction	Tribological and Mechanical	Gas atomization sintering	• Nickel and Aluminium elements in copper matrix, which results in increase in yield strength and the wear resistance • Copper with Ni and Al alloys presents excellent wear properties as the operating sintering temperature increases.
[51]	Lv et al.	Cu-9.5Al-4.2Ni-4Fe-1.2Mn	Effect FSP on grain refinement	Grain refinement and Mechanical Properties	Friction Stir Processing	• FSP increases the hardness of the prepared copper alloy. • The rotational rate of the FSP process also leads to grain refinement.
[52]	Basumatary and Wood	Cu Si Al Mn Fe Ni	Effect of oxide formation			• After immersing the Cu alloys in NaCl solution a layer of Al_2O_3 and Cu_2O oxide is formed on its surface.

By the literature review, it is observed that in the recent past, attempts have been made by researchers to suggest an alternative for the conventional leaded bronze material, however, a detailed tribological study by considering the fully flooded, starved and unlubricated conditions is lacking. Journal bearing generally operates in fully flooded hydrodynamic conditions, however, at higher loading condition and with changes in speed, these bearings do work in starved and in some cases boundary lubricating conditions. So it is important to study the bearing materials in fully flooded, starved and unlubricated condition as well. The main motive of the present work is to study copper-based bearing materials for the wear and friction properties. Based on the experimental investigation an alternative material is proposed which has comparable properties to conventional journal bearing material.

2. Experimental details

2.1 Preparation of test specimens

Powder metallurgy and casting are the two methods which are largely used to fabricate the alloys and composites [53-55]. In the present work, stir casting method was used to fabricate the materials. The schematic presentation of the stir casting setup is shown in Fig. 1. During the casting, the oxidizing conditions were maintained at a temperature of about 1100 °C-1150°C. The aluminium in the melt oxidizes very easily and forms the surface films on the surface of the casting. To prevent this the atmosphere of the casting area was kept free from oxygen by maintaining a closed chamber. After incorporating the alloying elements, the melt was continuously stirred with the help of a steel stirrer. The amounts of Aluminium, Nickel, Tin, and Phosphorous added in the melt were in the account of desired wt% of alloying elements. For Cu-Pb, copper was first melted at 1150 °C and Tin and Lead were added after melting the copper in the crucible. The melt was continuously stirred for the homogenous mixing of the elements. After the complete melting, the melt was superheated to a temperature to 50°C above the pouring temperature. The prepared melts were poured into a preformed dry sand cylindrical mold of length 50 mm and 15 mm diameter. The various specimens for the wear tests were cut from the casted bars. The elemental compositions of Cu-NiAl, Cu-PAl, and Cu-Pb as evaluated by X-ray fluorescence (XRF) spectroscopy is given in Table 2.

Accepted Manuscript

A cast iron disc was used as the counter body for testing the tribological properties of the fabricated material.

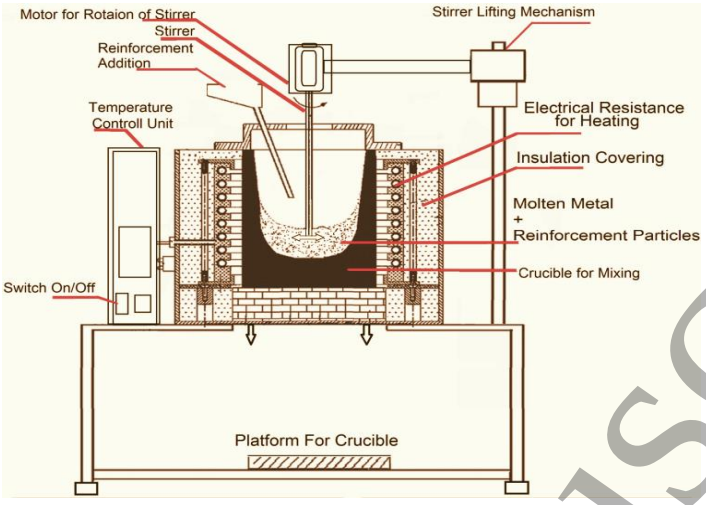


Fig. 1: Schematic presentation of stir casting setup

Table 2: wt % of casted copper alloys

wt. %	Sn	Pb	Si	Al	P	Zn	Mg	Mn	Ni	Cu
Cu-Pb	6.8	1.2	0.0182	-	-	-	0.0001	0.0018	0.29	Bal.
Cu-NiAl	0.0478	-	0.15	9.2	-	-	0.0012	0.3340	4.0	Bal.
Cu-PAl	4.2	0.05	-	0.25	0.30	0.30		-	-	Bal.

For obtaining the optical micrographs of the prepared samples, the specimen surfaces were prepared by polishing. Various grades of silicon carbide papers (400, 600, 800, 1200, 1600 grit sizes) were used, followed by wet polishing with a 0.05 μm alumina powder. The prepared surfaces were etched as per ASTM No. 30. An etching solution with 62.5 ml NH_4OH, 125 ml H_2O_2 (3%), 62.5 ml distilled water is prepared and specimen surfaces were etched. The etched surfaces were observed under an optical microscope at 10X magnification.

2.3 Measurement of Tribological Properties

In the present paper, pin on disc method has been used as per ASTM-G99 standards [56]. In this tribometer, the disc is mounted on a circular chuck with the help of bolts. This circular chuck is further connected with a motor which rotates the chuck and hence the disc at a predetermined speed. The speed of the motor is controlled with the help of a data acquisition system. The pin sample is mounted on one end of bell crank lever. The other end of the lever is used to load the dead weights. The pin remains static during the experimentation. The pin and disc have flat area contact between them. The photographic views of the pin, disc, and tribometer are given in Fig. 2. The bell crank lever has the capability to move laterally which enable the linear variable differential transformer (LVDT) to measure the friction force between the pin and disc. The friction force is used to obtain the coefficient of friction. The wear from the pin samples is calculated by the weight of the pin measured before and after the wear testing by using a precise weighing machine.

Accepted Manuscript

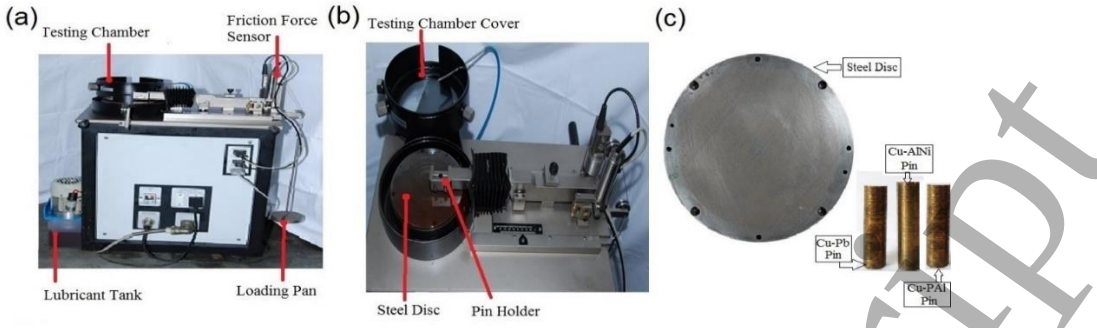


Fig. 2: Schematic diagram of Pin on Disc setup for wear test

2.4 Wear Tests

The prepared disc and pin surfaces were cleaned with acetone solution and dried well before use. A properly cleaned and polished surface provides better contact between the mating parts. It is essential to achieve greater finish for the proper contact. A highly rough surface may lead to interlocking of surface asperities resulting in severe wear. A Telly surf (Taylor Hobson made) surface tester was used to measure the surface roughness for pin and disc specimens. The surface roughness achieved was in the range of 0.2-0.3 µm.

The wear and friction tests were performed in fully flooded, starved and unlubricated conditions. The whole experimentation work was divided into three phases, in the first phase, the fully flooded condition was used. The lubricating oil is continuously supplied with the help of a pumping system at the interface of the pin and disc. The whole chamber of the pin on disc contact was flooded with lubricating oil. Apart from providing lubrication, a lubricant also helps in reducing the wear. Commonly used mono-grade oil does not perform well at high temperatures. Multi-grade oil has significant properties and performs better which helps in preventing the wear between the mating parts. SAE 15W-40 lubricating oil was used for the experiments. A viscometer was used to measure the viscosity and density of the lubricating oil as per ASTM D-445 [57], D-4052 standards [58]. The observed viscosity and density were 106.39 mm^2/s (at 100º C) and 0.83 g/cm^3.

In the second phase, a new disc and pin surface were used for the pin on disc testing and experiment was performed in starved lubrication regime. For this, the disc surface was completely covered with lubricating oil for only once and lubrication supply was cut off. The layer was allowed to settle for some predefined time, after which the experimentation process was started. In the third phase, the freshly prepared pin and disc surfaces were in dry contact and experiments were performed in unlubricated condition.

The normal pressure and sliding distance for the all three experimental phases were kept the same at 0.31 MPa, and 4000 m respectively and three sliding speeds (4.39, 5.18 and 5.97 m/s). The testing variables and conditions were selected on the basis of previous works and aimed at obtaining measurable wear in fully flooded lubricating conditions as well. Table 3 provides the input variables used for this experimental study.

The friction coefficient between the tribopairs was continuously measured for the complete run of the experiments. Mass of every pin was measured before and after the experiment by a weighing balance with 0.0001 g accuracy. From the data of wear loss, wear volume and specific wear coefficient was calculated to assess the wear from the pin samples.

$$K_a = {V_{wear}}/{F_{load} \times S} \quad (1)$$

Where, V_{wear} [m^3] is the measured wear volume, F_{load} [N] is the applied load and S [m] is the sliding distance. All experiments were repeated three times and an average of three observations was used for evaluating the results. The worn pin samples were observed under a scanning electron microscope to study the wear pattern. The energy dispersive X-ray spectroscopy (EDS) was used to inspect the composition of the worn layer on the pin and disc samples.

Accepted Manuscript

Table 3: Input variables used for the experimentation

Test Condition	Values
Sliding Speed	4.39, 5.18, 5.97 m/s
Normal Pressure	0.31 MPa
Pin diameter, Height	10, 30 mm
Disc diameter, height	165, 10 mm
Sliding distance	4000 m
Temperature	22 (°C)
Humidity	50 (%)

3. Results and Discussion

3.1 Material Characterization

The microscopic images of Cu-NiAl, Cu-PAl, and Cu-Pb are shown in Fig. 3. An optical microscope was used to obtain the optical micrographs as 10X magnification. It is seen from Fig. 3 (a) that the Cu-NiAl has copper-rich solid solution α phases and retained β phases throughout the matrix. The overall distribution is uniform and homogeneous. Some areas of very fine precipitates in the α phase are iron-rich and are termed as k_{iv} phase (precipitates of Ni-Fe-Al). The microstructure of Cu-Pb indicates the large evenly distributed lead particles. The lead is practically insoluble in copper, as the mixture freezes, the copper particles freeze first and lead make the globules shape in the copper matrix. In Fig. 3 (c), the δ phase is shown in dark color and lead is seen as light globules. Fig. 3 (b) presents the distribution of alloying elements for Cu-PAl material. Aluminium is seen distributed throughout the matrix of the copper.

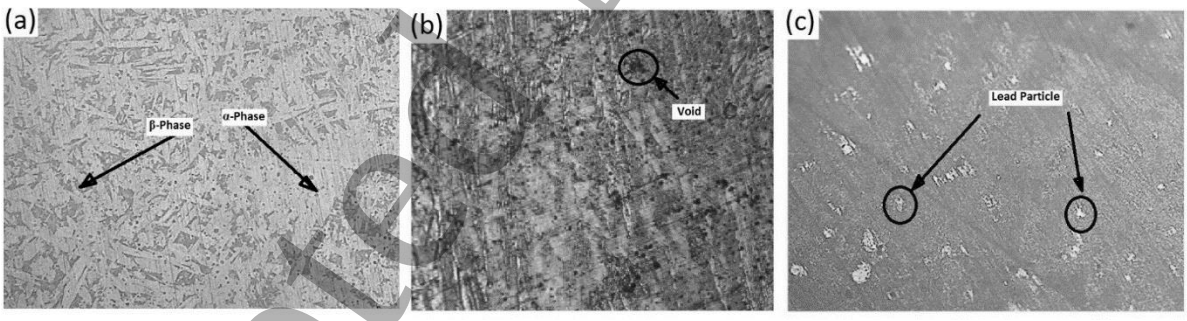


Fig. 3: Optical micrographs for (a) Cu-NiAl (b) Cu-Pb (c) Cu-PAl

Table 4 presents the mechanical properties of the prepared materials. For the evaluation of microhardness of the fabricated materials, a Fischer made microhardness tester was used. The instrument facilitates the digital measurement and control. In its procedure, the head of the system is lowered until the indenter touches the material surface, after this the loading and unloading of the force is carried out. A diamond indenter of square base pyramid shape was used to indent on a cleaned surface of the specimens at a load of 3000 mN for 20 seconds. For each specimen, three hardness values were measured and the average of three was taken for the analysis. The tensile and yield strength were measured by using an INSTRON universal tensile testing machine. Specimens were prepared as ASTM-E8M for the strength testing. The testing was with a tension rate of 1mm/min.

The Cu-NiAl has the maximum hardness value as 243.6. The precipitation of the α phase into the β phase helped in achieving the higher hardness value. The soft globules of lead particles limited the hardness of Cu-Pb material

Accepted Manuscript

to 116.6 HV. The Cu-NiAl had a maximum tensile strength of 610 MPa and yield strength of 430 MPa. The presence of high amount of Al and Ni provides the strength to the copper matrix.

Table 4: Mechanical properties of fabricated materials

Property/Material	Tensile Strength(MPa)	Yield Strength(MPa)	Vicker Hardness (Hv)
Cu-NiAl	610	430	243.6
Cu-PAl	550	450	212.9
Cu-Pb	269	207	116.6

3.2 Wear and Friction Properties

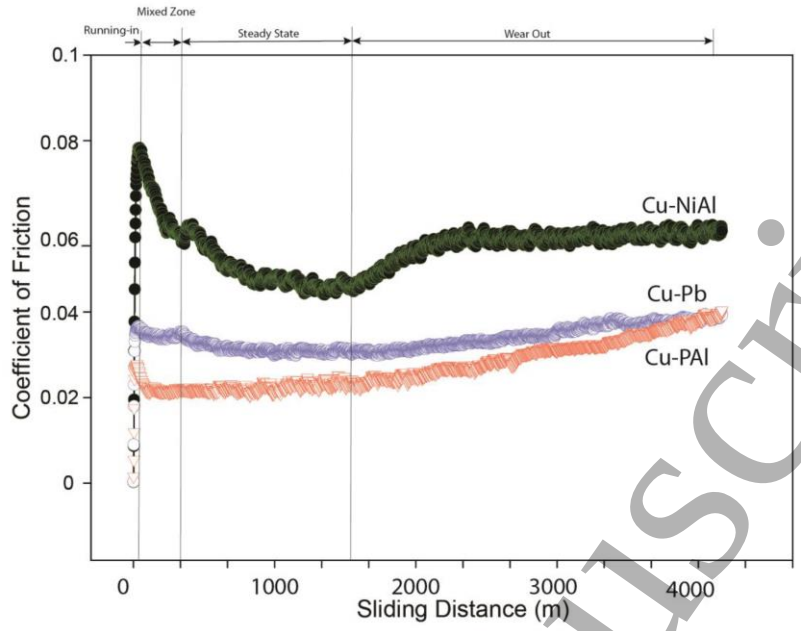
The friction sensor installed on a pin on disc machine measures the friction force between the pin and disc samples. The measured friction force from the sensors is used to calculate the coefficient of friction. The friction sensor records the friction force for complete run of the sliding distance (4000 m). These continuous measurements were analyzed and average COF values were calculated and plotted against the sliding speed in Fig. 4 (b-d). The coefficient of friction contains three basic parts as 'running in', 'steady state', and 'wear out'. For explaining these three parts, Fig. 4 (a) presents the COF with sliding distance at 0.31 MPa pressure and 4.39 m/s sliding speed values under starved lubrication regime. At the beginning of the running in stage, the surface asperities of the mating parts generate the substantial friction. The coefficient of friction increases and reaches a maximum value. In the running-in stage, the surface asperities get removed from the mating surfaces and the surfaces become smooth at the steady-state stage. An intermediate stage of the mixed zone is also observed during the testing. This mixed zone represents the transition of the coefficient of friction from running in stage to the steady-state region. During the steady state, the coefficient of friction is nearly constant and minimum. It is desirable for the mating parts to run in the steady-state region. This helps in increasing the life of the components. The wear out stage, starts after the steady-state region. In this the coefficient of friction again starts increasing, indicating the massive wear between the mating parts.

The frictional behavior of the three materials is presented in Fig. 4 (b-d), which shows the variation of COF as a Stribeck curve obtained from the experimental data. For the Stribeck curve the experiments were performed at three sliding speed values and COF is plotted against the sliding speed. For low sliding speed values the COF values are maximum in all the lubrication regimes, and with increase in sliding speed, the COF starts reducing. It is seen from Fig. 4 (b) that the average coefficient of friction in fully flooded condition reaches to 0.02 for Cu-Pb, 0.016 for Cu-NiAl and 0.015 for the Cu-PAl material at 4.39 m/s sliding speed value. With further increase in the sliding speed the COF reduces for all the three considered materials. The Cu-PAl material resulted in least amount of coefficient of friction. The range of COF (0.009-0.020) indicates that the contacts were in hydrodynamic lubrication regime. The presence of aluminium in the copper matrix for Cu-NiAl and Cu-PAl helps in maintain the low values of COF. The oxygen in SAE 15W-40 lubricating oil combines with aluminium and makes a layer of Al_2O_3 which protects the material from wearing and reduces the COF. This Al_2O_3 oxide layer is also reported by [52] in NaCl solution.

Fig. 4 (c) presents the average COF values for the starved lubrication condition. In starved condition, a single layer of oil was applied on the disc surface and experiments were performed. In this, the lubricating oil prevents the metal to metal contact for some-time after which, a heavy amount of wearing was observed during the experimentation. This leads to higher COF for all three materials. Cu-NiAl resulted in the maximum amount of COF and Cu-PAl performs slightly better than the Cu-Pb material at all bearing characteristic number values. However, for a particular material the COF values reduces considerably at higher bearing characteristic numbers. The soft phases of lead and phosphorous help in reducing the COF for Cu-PAl and Cu-Pb materials. The soft phases in the Cu-PAl and Cu-Pb detached themselves from the copper matrix and leave behind microvoids. These microvoids act as the lubricant reservoir and provide the lubricant oil in case of scarcity of lubricating oil.
The dry sliding results for COF with varying bearing characteristic number are presented in Fig. 4 (d). The presence of lead and phosphorous in Cu-Pb and Cu-PAl helps in reducing the COF values. Fig. 5 (a-c) shows a transfer of metal layer on the disc surface, which prevents the wear of the pin and disc surfaces and hence the two surfaces remain smooth and resulted in low COF values.

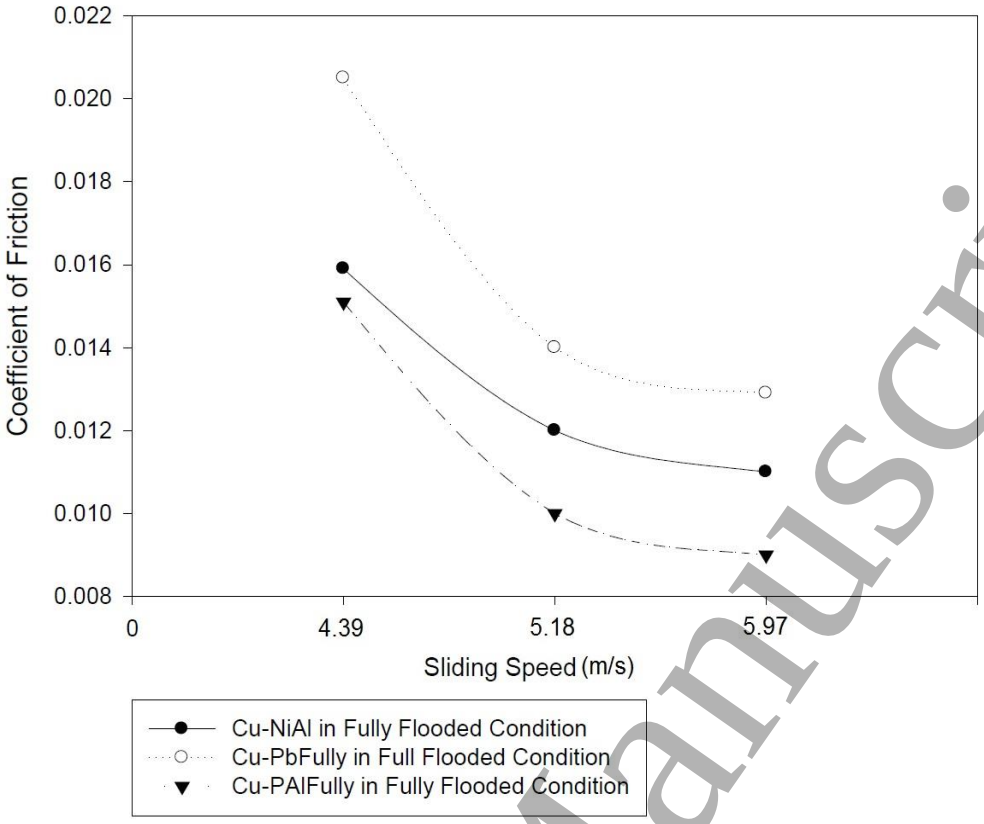
Accepted Manuscript

(a)

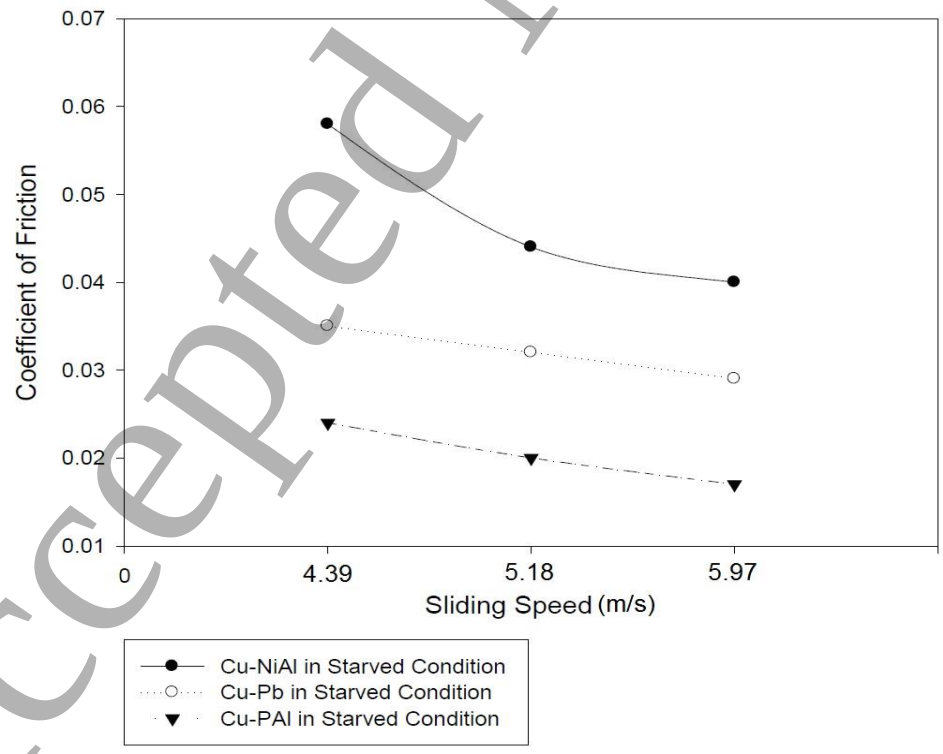


Accepted Manuscript

(b)



(c)



Accepted Manuscript

(d)

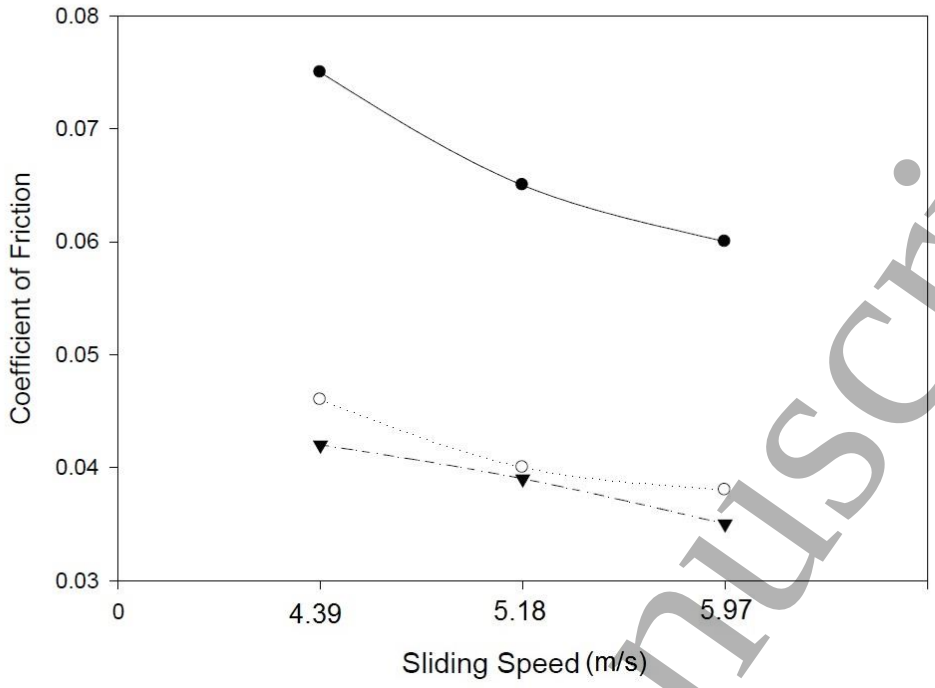


Fig. 4: (a) Variation of the coefficient of friction at 0.31 Pa and 4.29 m/s in starved condition (b) COF with sliding speed in fully flooded lubrication condition (c) COF with sliding speed in Starved lubrication condition (d) COF with sliding speed in unlubricated condition

During the testing of the wear, the change in weight of the pin samples was recorded to evaluate the specific wear rate. Equation (1) was used to calculate it. It is seen from Fig. 7 (a,b,c) that, in case of fully flooded condition the Cu-NiAl resulted in low specific wear rate as compared to Cu-Pb and Cu-PAl for all the considered sliding speed values. Formation of the aluminium oxide layer due to the presence of oxygen in lubricating oil on the surface of the material could be a reason for this improvement in wear properties [59, 60]. The oxide film formed on the Al bronze materials consists of alumina-rich inner layer and copper oxide film as an outer layer. During the initial sliding of the pin on disc specimen, the alumina oxide layer transfers and adheres itself to the steel disc. This phenomenon forms a stable layer on the steel disc surface and a stable copper-rich oxide layer remain on the pin surface. This stable combination of two oxide layers on the disc and pin provides the excellent wear resistance to the Cu-NiAl. The oxygen present in the lubricant oil helps in maintaining the continuous formation of this oxide layer [61]. Since aluminium oxide is a very hard compound, so it works as a load carrying phase. The presence of zinc in the material also forms an oxide as zinc oxide which helps the material in lubrication [62].

In the case of starved and unlubricated conditions, Cu-NiAl resulted in the maximum amount of SWR. In the absence of lubricating oil, the lead and phosphorous in Cu-Pb and Cu-PAl transfer a thin layer on the disc surface and promotes the easy shearing between the layer particles. This also ensures a low friction coefficient in the absence of lubricating oil as well. The formation this layer is a significant characteristic of the Cu-Pb and Cu-PAl material.

These two-layer were clearly visible during the tribological testing of the Cu-Pb and Cu-PAl. Fig. 5 shows these layers on the surface of disc specimens. The Cu-PAl resulted in lowest SWR for starved as well as unlubricated conditions.

The presence of lead and phosphorous particles was also verified by the EDS analysis of the disc. Fig. 6 (a,b,c) presents the EDS results for the disc specimens used for wear and friction testing of Cu-NiAl, Cu-Pb, and Cu-PAl materials. The EDS results were obtained at 10 keV with nearly 1700 counts. Small peaks of Cu with other alloying elements are visible on the EDS pattern clearly. The EDS analysis of the disc samples revealed the

Accepted Manuscript

presence of lead and phosphorous elements on the surface of the disc. These layers helped in reducing the wear from the pin specimens.

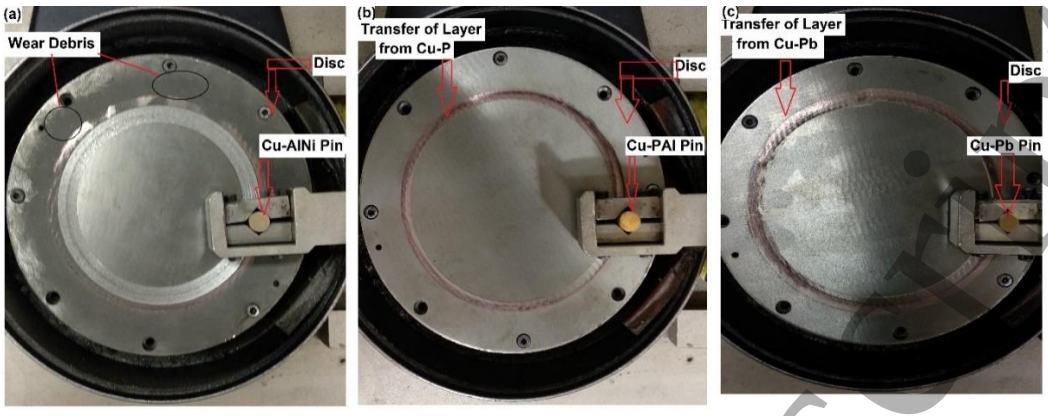


Fig. 5: Presentation of layers on the disc surface (a) for Cu-NiAl (b) Cu-P material (c) Cu-Pb material.

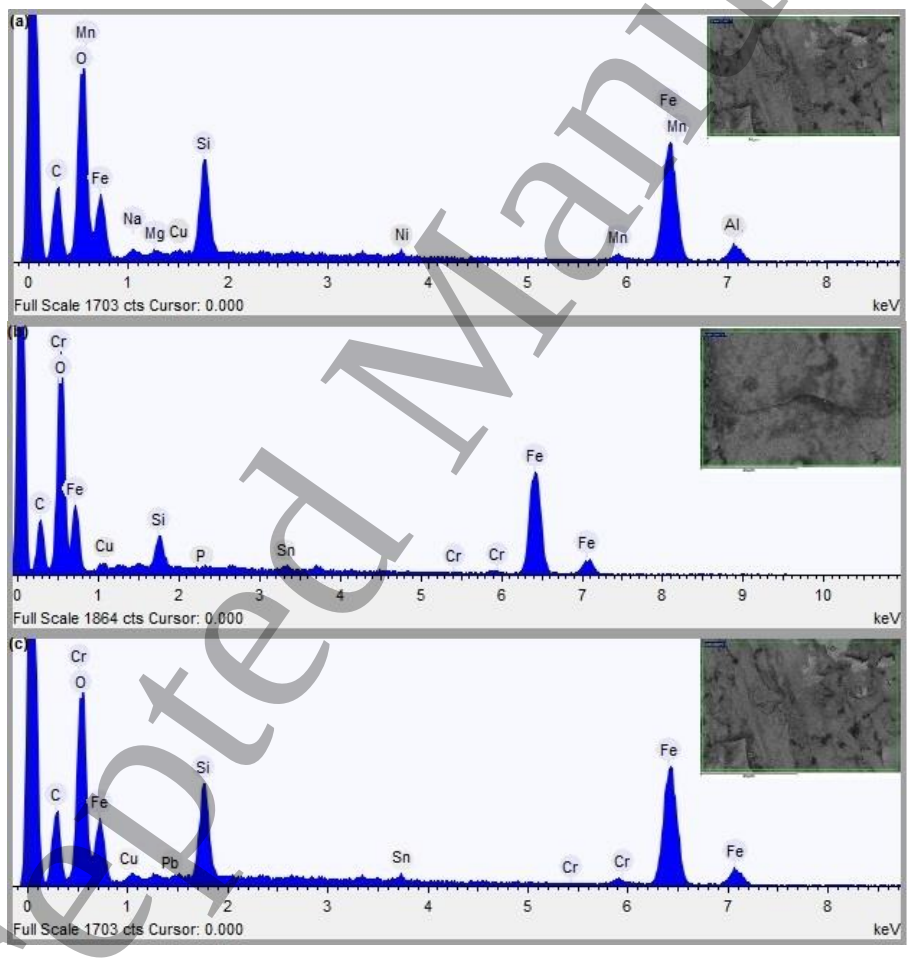
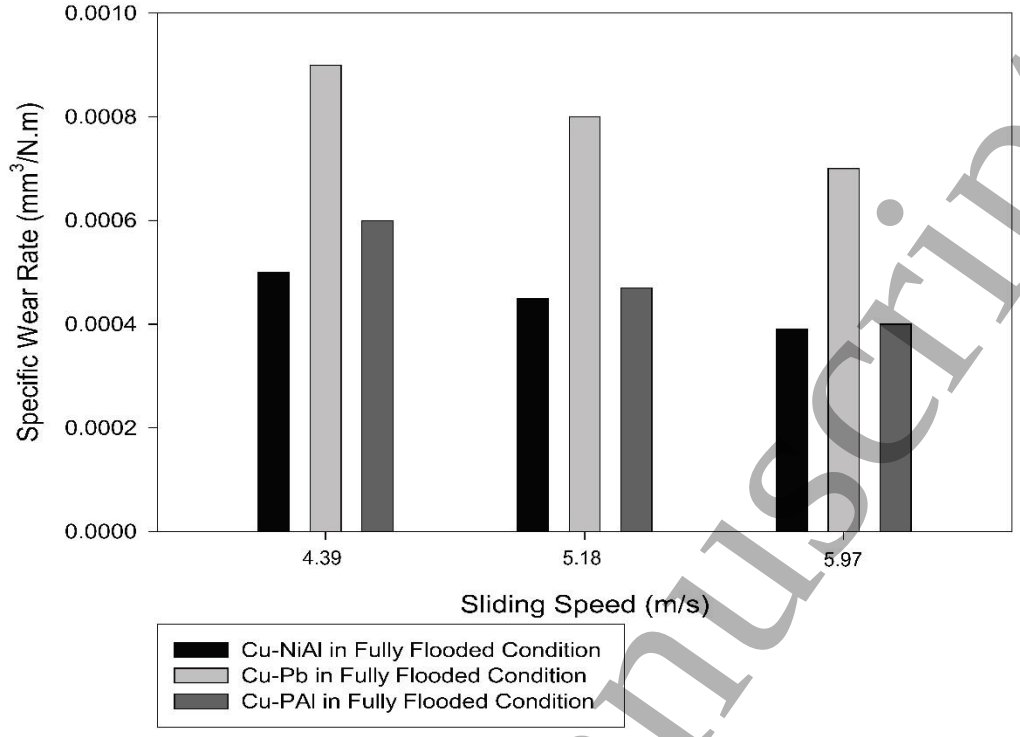


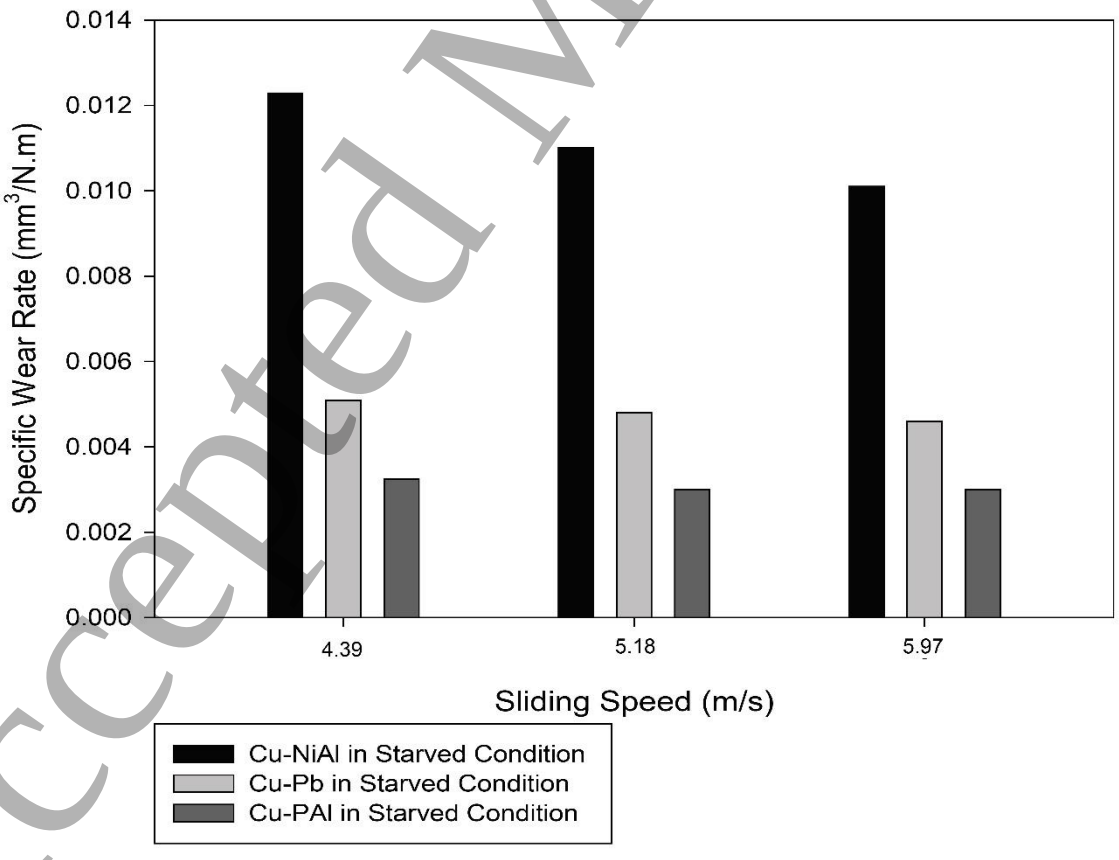
Fig. 6: EDS analysis for the worn disc surface obtained by mating with (a) Cu-NiAl material (b) Cu-PAl material (c) Cu-Pb material.

Accepted Manuscript

(a)



(b)



Accepted Manuscript

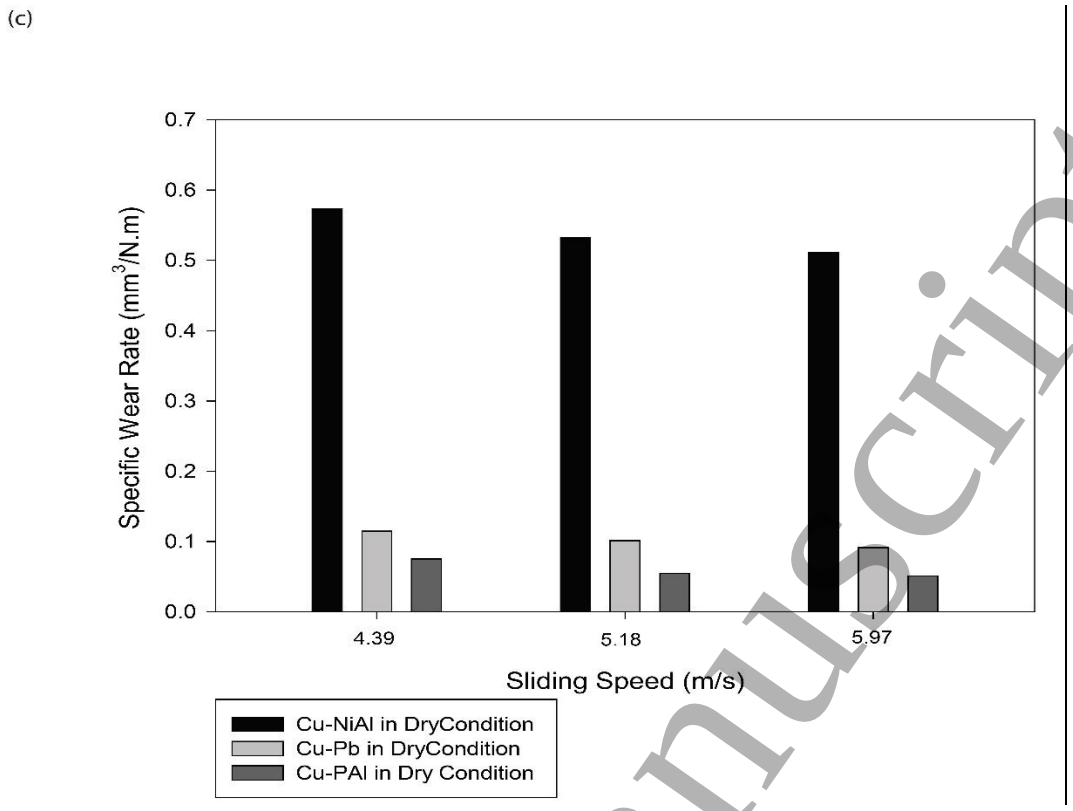


Fig. 7: Variation of specific wear rate for the pin samples in (a) fully flooded lubrication (b) starved lubrication (c) unlubricated condition.

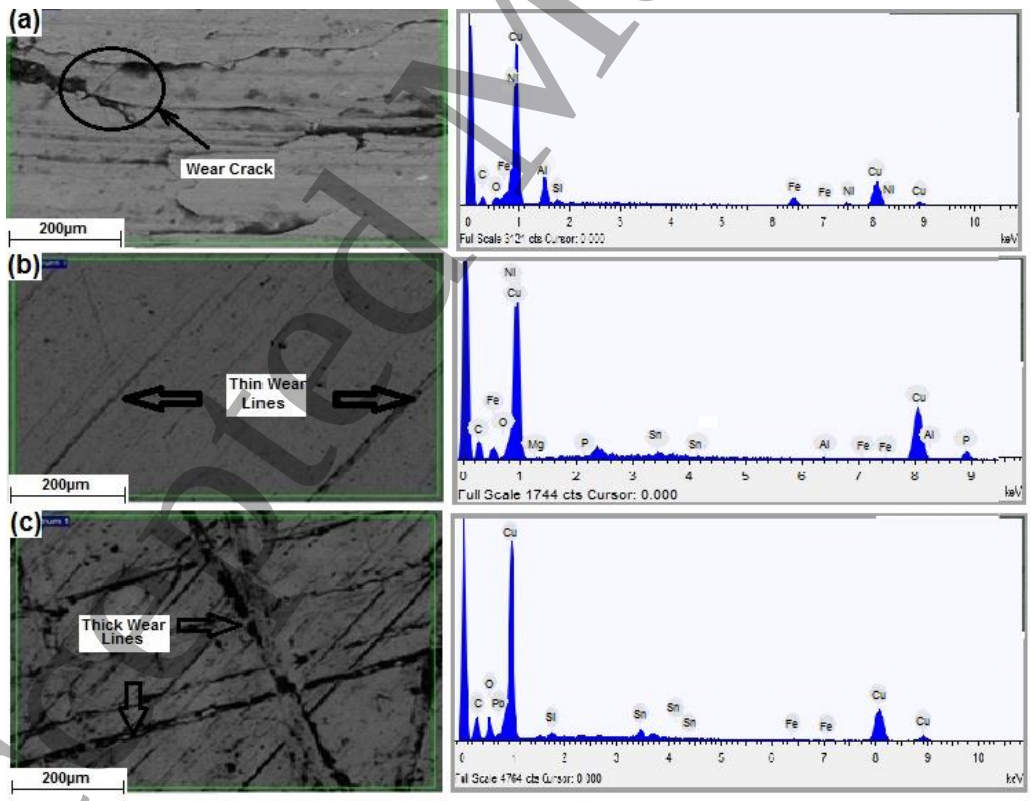


Fig. 8: (a) SEM and EDS analysis image for the worn Cu-NiAl material after unlubricated tests, (b) SEM and EDS analysis image for the worn Cu-PAl material after unlubricated tests, (c) SEM and EDS analysis image for the worn Cu-Pb material after unlubricated tests.

Accepted Manuscript

Fig. 8 (a) presents the scanning electron microscopy (SEM) image of the worn Cu-NiAl pin sample. The SEM images show the deep grooves and wear a wedge section on the worn pin sample. The large friction coefficient on the Cu-NiAl surface promotes the formation of the damaged layer which undergoes plastic deformation. The Cu-NiAl suffered heavy wear in unlubricated condition, which is evidenced by deep grooves on the worn pin surfaces. Fig. 8 (b) presents the SEM image of the worn Cu-PAl pin sample. Flat wear areas were observed on the Cu-PAl worn pin samples. Some thin wear wedges are visible on the surface of the worn sample. Thin wear lines are also visible on the optical micrograph obtains at 10X magnification. The presence of iron particle (Fe) is also visible on the worn surface of the Cu-Pb material. The embed-ability property of the copper material plays a significant role in entrapping the iron particles in the copper matrix. Some amount of The carbon layer is also visible on the wear surfaces of both the materials. Fig. 8 (c) presents the SEM image of the worn Cu-Pb pin sample. Some shallow groves are visible on the surface of the worn sample. These shallow grooves are also visible on the optical micrograph obtains at 10X magnification. The presence of iron particle (Fe) is also visible on the worn surface of the Cu-Pb material. The embed-ability property of the copper material plays a significant role in entrapping the iron particles in the copper matrix.

3.3 Discussion

As explained in the above mentioned experimental results, that the lubrication regimes greatly affects the tribological properties of the materials. During the fully flooded lubrication regime, the amount of specific wear rate and coefficient of friction values were very low. A constant lubricant layer plays a pivotal role and keeps the values low. For the three considered materials, the Cu-NiAl composite presents the maximum wear resistance as compared to Cu-PAl and Cu-Pb. The oxygen in the lubricating oil combines with the aluminium and zinc present in Cu-NiAl and makes a protective oxide layer. This oxide layer prevents the wearing. The more hardness of the Cu-NiAl also helped in improving the wear resistance.
In the case of starved (semi-dry) lubricating condition, a single layer of lubricant oil is used in between the pin and disc. Initially, this layer protects the wearing and after that with time, the soft phases present in Cu-PAl and Cu-Pb plays a significant role in reducing the wear and coefficient of friction. These soft particles of phosphorous (in case of Cu-PAl) and lead (in case of Cu-Pb) mixes with lubricant and act as a third body in between pin and disc. This third body protects the wearing. For unlubricated condition, a visible layer of soft phase particles is present on the surface of the disc in case of Cu-PAl and Cu-Pb material testing (Figure 5). This layer protects the pin material from wearing by preventing the direct contact of the pin from the disc surface. For the unlubricated and starved lubricating conditions, Cu-PAl resulted in a low coefficient of friction and specific wear rate.

4. Conclusions

In this work, Pb free bearing materials were fabricated and tribological studies were conducted under fully flooded, starved and unlubricated conditions using a pin on disc test setup. From this experimental study, the following conclusions could be drawn

- The optical micrographs of Cu-NiAl, Cu-PAl, and Cu-Pb indicates the homogeneous mixing of alloying elements. Stir casting setup was successfully used to fabricate the copper composites.
- In fully flooded tribological studies, all three fabricated materials resulted in very low amounts of specific wear rate and coefficient of friction. The presence of aluminium and nickel contents in Cu-NiAl helped in maintaining low specific wear rate and coefficient of friction values as compared to Cu-PAl and Cu-Pb.
- During the starved and unlubricated condition, Cu-PAl resulted better with low specific wear rate and coefficient of friction as compared to Cu-NiAl and Cu-Pb. A soft layer of copper and phosphorous-rich elements formed on the disc surface, which reduces the coefficient of friction and specific wear rate.
- The scanning electron microscopy examination of the unlubricated pin samples reveals thick wear lines and wear grooves on the surface of Cu-NiAl material. Smaller and thin wear lines were visible for Cu-PAl material which indicates low wearing.
- The EDS analysis of worn disc samples indicates the presence of copper-phosphorous layer for Cu-PAl and copper-lead layer for Cu-Pb, which reduces the wear and coefficient of friction. No such permanent layer was visible for Cu-NiAl material, rather wear debris were seen scattered around the disc surface.

Accepted Manuscript

- The future works shall include the use of bio lubricant or process fluid in place of synthetic lubricant and comparing the tribological characteristics. Apart from this, experiments on the actual journal bearing set up need to be performed for the better understanding of tribological behavior of journal bearing material.

References

[1] Stachowiak Gwidon W., Batchelor Andrew W. Engineering Tribology. 3rd ed. Elsevier Butterworth-Heinemann; 2005.
[2] Thomson J, Zavadil R, Sahoo M, Dadouche A, Dmochowski W, Conlon M. Development of lead-free bearing material for aerospace applications. Int. journal of metalcasting/winter **10**: 19-30 (2010). https://doi.org/10.1007/BF03355483
[3] Bolton W. Materials Technology for Technicians. 3rd vol. Butterworth; 1981.
[4] Schmidt RF. ASM Specialty Handbook Copper and Copper Alloys. ASM Handbook. vol. 15, ASM International; 1992.
[5] Li WS, Wang ZP, Lu Y, Jin YH, Yuan LH, Wang F. Mechanical and tribological properties of a novel aluminum bronze material for drawing dies. Wear 261: 155–163 (2006) https://doi.org/10.1016/j.wear.2005.09.032
[6] Gebretsadik D. W., Hardell J., Prakash Braham, Tribological performance of tin-based overlay plated engine bearing materials, Tribology International. 92, 281 (2015). http://dx.doi.org/10.1016/j.triboint.2015.06.014
[7] Gebretsadik D. W., Hardell J., Prakash Braham, Friction and wear characteristics of different Pb-free bearing materials in mixed and boundary lubrication regimes, Wear. 340-341, 63 (2015). http://dx.doi.org/10.1016/j.wear.2015.06.002
[8] Sharma V. K., Singh R. C., Chaudhary R., An Experimental Study of Tribological Behaviors of Aluminium- and Copper-Based Metal Matrix Composites for Bearing Applications, Int. J. Materials Engineering Innovation. (2018)
[9] Li YY, Leo NT, Xia W. Mechanical, friction and wear behaviors of a novel high-strength wear-resisting aluminum bronze. Wear 197: 130–136 (1996) https://doi.org/10.1016/0043-1648(95)06890-2
[10] Shi Z, Sun Y, Bloyce A, Bell T. Unlubricated rolling–sliding wear mechanisms of complex aluminum bronze against steel. Wear 193: 235–241 (1996) https://doi.org/10.1016/0043-1648(95)06773-6
[11] Blau PJ. Investigation of the nature of micro-indentation hardness gradients below sliding contacts in five copper alloys worn against 52100 steel. J. Mater. Sci. 19: 1957–1968 (1984) https://doi.org/10.1007/BF00550266
[12] Chmura W, Gronostajski Z. Bearing composites made from aluminium and aluminium bronze chips. Journal of Materials Processing Technology 178: 188–193 (2006) doi:10.1016/j.jmatprotec.2006.03.156
[13] Jianfeng YAN, Andrew LINDO, Ruth SCHWAIGER, Andrea M. HODGE. Sliding wear behavior of fully nanotwinned Cu alloys Friction (in Press) (2018) https://doi.org/10.1007/s40544-018-0220-z
[14] Saud S.N., Hamzah E., Abubakar T., Bakhsheshi-rad H.R. Correlation of microstructural and corrosion characteristics of quaternary shape memory alloys Cu-Al-Ni-X (X = Mn or Ti). J. Trans. Nonferrous Met. Soc. China 25: 1158–1170 (2015).
[15] Panagopoulos C.N., Georgiou E.P., Simeonidis K. Lubricated wear behavior of leaded α+β brass. Tribology International 50: 1–5(2012)

[16] Ding Yang, Lv Yuting, Chen Kai, Zhao Bingjie, Han Yuanfei, Wang Liqiang, Lu Weijie. Effects of Microstructure on the Stress Corrosion Cracking Behavior of Nickel-Aluminum Bronze Alloy in 3.5% NaCl Solution. Materials Science & Engineering A https://doi.org/10.1016/j.msea.2018.07.066
[17] Song Q.N., Zheng Y.G., Jiang S.L., Ni D.R., Ma Z.Y. Comparison of corrosion and cavitation erosion behaviors between the as-cast and friction-stir-processed nickel aluminum bronze. Corrosion 69: 1111-1121(2013).
[18] Wu Z., Cheng Y., Liu L., Lv W., Hu W. Effect of heat treatment on microstructure evolution and erosion-corrosion behaviour of a nickel- aluminium bronze in chloride solution. Corrosion Science 98: 260-270 (2015).
[19] Qin Z., Luo Q., Zhang Q., Wu Z., Liu L., Shen B., Hu W. Improving corrosion resistance of nickel-aluminium bronzes by surface modification with chromium ion implantation. Surface and coatings technology 334: 402-409 (2018)
[20] Luo Q., Wu Z., Qin Z., Liu L., Hu W. Surface modification of nickel-aluminium bronze alloy with gradient Ni-Cu solid solution coating via thermal diffusion. Surface and Coatings Technology 309: 106-113 (2017).
[21] Kumar R, Dhiman S. A study of sliding wear behaviors of Al-7075 alloy and Al-7075 hybrid composite by response surface methodology analysis. Mater. Des. 50: 351–359 (2013) doi:10.1016/j.matdes.2013.02.038.
[22] Routa A, Satapathy A. Analysis of dry sliding wear behavior of rice husk filled epoxy composites using the design of experiment and ANN. Procedia Eng. 38: 1218–1232 (2012) doi:10.1016/j.proeng.2012.06.153.
[23] Xu W, Ma X, Tang N, Zhu L, Li W, Ding Y. Effect of post-welding heat treatment on wear resistance of cast-steel die with surfacing layer. Manuf. Rev. 2: 25 (2015) https://doi.org/10.1051/mfreview/2015027

Accepted Manuscript

[24] Zhang P, LeeK H, Lee C H. Reciprocating friction characteristics of magneto- rheological fluid for aluminium under magnetic field. Trans Nonferr Met Soc China 24: 171–6 (2014) https://doi.org/10.1016/S1003-6326(14)63044-2

[25] Tala-Ighil N, Maspeyrot P, Fillon M, Bounif A. Effects of surface texture on journal-bearing characteristics under steady-state operating conditions. J. Engineering Tribology 221: 623-633 (2015) https://doi.org/10.1243/13506501JET287

[26] Kango S, Sharma R, Pandey R. Comparative analysis of textured and grooved hydrodynamic journal bearing. Proceedings of the Institution of Mechanical Engineers, Part J: Journal of Engineering Tribology 228(1):82-95(2013) https://doi.org/10.1177/1350650113499742

[27] Singh R C, Pandey R K, Rooplal, Rangnathan M. S., Tribological performance analysis of textured steel surfaces under lubricating conditions, Surf. Topogr.:Metrol. Prop. 3: 1-9 (2016) doi:10.1088/2051-672X/4/3/034005

[28] Sudeep U., Tandon N., Pandey R. K. Comparisons of Tribological and Vibration Behaviors of Textured Point Contacts of Bearing Steel Lubricated With Oil and Grease Under Starved Conditions. Journal of Tribology 138(3): 0315041-12 (2016) doi: 10.1115/1.4032325

[29] Pramanik A., Effects of reinforcement on wear resistance of aluminum matrix composites, Trans. Nonferrous Met. Soc. China 26, 348−358, (2016).

[30] Marczak R J, Ciach R, Tribological properties of concentrated Al–Zn alloys. Proceedings of the 1st Europe Tribology Congress, London 223–227 (1973).

[31] Jha Pushkar, Gautam Rakesh Kumar, Tyagi Rajnesh. Friction and wear behavior of Cu–4 wt.%Ni–TiC composites under dry sliding conditions. Friction 5(4): 437–446 (2017). DOI 10.1007/s40544-017-0157-7.

[32] Sharma V.K., Singh R. C., Chaudhary R. . Effect of flyash particles with aluminium melt on the wear of aluminium metal matrix composites. Eng. Sci. Tech., Int. J., 20: 1318-1323 (2017). http://dx.doi.org/10.1016/j.jestch.2017.08.004

[33] Dang, W., Ren, S., Zhou, J., Yu, Y. & Wang, L. Tribology International The tribological properties of Ti 3 SiC 2 / Cu / Al / SiC composite at elevated temperatures. Tribiology Int. 104, 294–302 (2016).

[34] Jin, K. et al. Tribology International Synthesis effects of Cr and Ag on the tribological properties of Cu – 9Al – 5Ni – 4Fe – Mn bronze under seawater condition. Tribiology Int. 101, 69–80 (2016).

[35]Atapek, Ş. H., Çelik, G. A., Polat, Ş. & Pisarek, B. Tribological Characterization of Al-bronzes Used as Mold Materials. Archives of Foundry Engineering 17, 7–12 (2017).

[36]Yang, F. et al. The role of nickel in mechanical performance and corrosion behaviour of nickel-aluminium bronze in 3 . 5 wt .% NaCl solution. Corros. Sci. 139, 333–345 (2018).

[37]Zhang, B., Wang, J. & Yan, F. Load-dependent tribocorrosion behaviour of nickel-aluminium bronze in artificial seawater. Corros. Sci. 131, 252–263 (2018).

[38]Wang, Y. et al. Tribology International The tribo-corrosion behavior of Cu-9 wt % Ni-6 wt % Sn alloy. Tribiology Int. 94, 260–268 (2016).

[39] Hassan, A. H., Alrashdan, A. Hayajneh, M. T. & Mayyas, A. T. Tribology International Wear behavior of Al – Mg – Cu – based composites containing SiC particles. Tribiology Int. 42, 1230–1238 (2009).

[40] Wen-sheng, L. I., Zhi-ping, W. & Yang, L. U. Corrosion and wear behaviors of Al-bronzes in 5.0% H2SO4 solution. Trans. Nonferrous Met. Soc. China 19, 311–318 (2008).

[41] Jun, Z. et al. Applied Surface Science Wear performance of the lead free tin bronze matrix composite reinforced by short carbon fibers. Applied Surface Science 255, 6647–6651 (2009).

[42] Tan, Z., Guo, Q., Zhai, W. & Zhao, Z. Tribological characteristics of nickel-aluminium bronze CuAl10Ni5Fe4 against 30CrMnSiA steel after the prior corrosion treatment. Applied Mechanics and Materials 202, 73–77 (2012).

[43] Saarivirta E. Huttunen-, Isotahdon E., Mets¨ajoki J., Salminen T., Carp´en L., Ronkainen H. Tribocorrosion behaviour of aluminium bronze in 3.5 wt.% NaCl solution. Case Studies in Fire Studies. (2018) DOI: https://doi.org/10.1016/j.corsci.2018.08.058

[44] Sláma, P., Dlouhý, J. & Kövér, M. Influence of Heat Treatment On The Microstructure And Mechanical Properties of Aluminium Bronze. MTSEC9 48, 599–604 (2014).

[45] Luo, Q., Qin, Z., Zhang Qi, Wu Zhong, Shen Bin , Liu Lei, Hu et al. The synergistic effect of cavitation erosion and corrosion of nickel-aluminum copper surface layer on nickel-aluminum bronze alloy. J. Alloys Compd. (2018). doi:10.1016/j.jallcom.2018.03.103

[46] Qin, Z., Zhang Qi, Luo Qin, Wu Zhong, Shen Bin , Liu Lei, Hu Wenbin. Microstructure design to improve the corrosion and cavitation corrosion resistance of a nickel-aluminum bronze Eval. Program Plann. (2018). doi:10.1016/j.corsci.2018.04.043

[47] Zhang Jin, Wang Cheng, Zhang Yong, Deng Yunlai. Effects of creep aging upon Al-Cu-Li alloy: Strength, toughness and microstructure. Journal of Alloys and Compounds 764: 452-459(2018)

[48] Namboodiri, V., Pottirayil, A., P, A. K. & Kailas, S. V. Wear Behavior of Friction Stir Processed NAB Alloys in Marine Environment. Tribology Online (2018). doi:10.2474/trol.13.75

Accepted Manuscript

[49] Sundararajan, S. & Rajadurai, J. S. Investigation of microstructure , mechanical , and tribological properties of solid self-lubricating copper hybrid composites processed by solid-state mixing technique. Proc IMechE Part J: J Engineering Tribology 0, 1–17 (2015).
[50] Zhai Wenzheng, Lu Wenlong, Po Zhang, Mingzhuo Zhou, Xiaojun Liu, Liping Zhou. Microstructure, mechanical and tribological properties of nickel-aluminium bronze alloys developed via gas-atomization and spark plasma sintering. Materials Science & Engineering A http://dx.doi.org/10.1016/j.msea.2017.09.047
[51] Lv, Y., Ding, Y., Han, Y., Wang, L. & Lu, W. Strengthening mechanism of friction stir processed and post heat treated NiAl bronze alloy: Effect of rotation rates. Mater. Sci. Eng. A (2016). doi:10.1016/j.msea.2016.12.050
[52] Basumatary, J. & Wood, R. J. K. Synergistic effects of cavitation erosion and corrosion for nickel aluminium bronze with oxide fi lm in 3 . 5 % NaCl solution. Wear 376–377, 1286–1297 (2017).
[53] Ali Mazahery, Mohsen Ostad Shabani. Study on microstructure and abrasive wear behavior of sintered Al matrix composites. Ceramics International 38: 4263–4269 (2012) doi:10.1016/j.ceramint.2012.02.008
[54] Ali Mazahery & Mohsen Ostad Shabani. The performance of pressure assisted casting process to improve the mechanical properties of Al-Si-Mg alloys matrix reinforced with coated B4C particles. Int J Adv Manuf Technol. DOI 10.1007/s00170-014-6266-9
[55] Ali MAZAHERY, Mohsen Ostad SHABANI Microstructural and abrasive wear properties of SiC reinforced aluminum-based composite produced by compocasting Trans. Nonferrous Met. Soc. China 23: 1905−1914(2013) DOI: 10.1016/S1003-6326(13)62676-X
[56] ASTM Standard G99 (2005) 'Standard Test Methods for Wear Testing With A Pin on Disk Apparatus', ASTM International, West Conshohocken, PA, United States
[57] ASTM Standard D445 (1970) 'Standard Method of Test for Viscosity of Transparent and Opaque Liquids (Kinematic and Dynamic Viscosities)' , ASTM International, West Conshohocken, PA, United States.
[58] ASTM Standard D4052 (1984) 'Standard Test Method for Density and Relative Density of Liquids by Digital Density Meter', ASTM International, West Conshohocken, PA, United States.
[59] Prasad B K. Effect of microstructure on the sliding wear performance of a Zn–Al–Ni alloy Wear 240: 100–112 (2000) https://doi.org/10.1016/S0043-1648(00)00369-0
[60] I M Hutchings – 'Tribology: Friction and Wear of Engineering Materials' – Edward Arnold, London, 1992.
[61] Prasad B K. Effects of silicon addition and test parameters on sliding wear characteristics of zinc-based alloys containing 37.5% aluminium. Mater. Trans. JIM 38: 701–706 (1997) http://doi.org/10.2320/matertrans1989.38.701
[62] Torabian H, Pathak J P, Tiwari S N. Wear charactristics of Al–Si alloys. Wear 172: 49–58 (1994). https://doi.org/10.1016/0043-1648(94)90298-4

Accepted Manuscript

Evolutionary Intelligence
https://doi.org/10.1007/s12065-019-00214-9

SPECIAL ISSUE

Fuzzy assessment of the risk factors causing cost overrun in construction industry

Savita Sharma[1] · **Pradeep K. Goyal**[2]

Received: 6 October 2018 / Revised: 22 January 2019 / Accepted: 12 February 2019
© Springer-Verlag GmbH Germany, part of Springer Nature 2019

Abstract
Cost is considered as one of the most important parameters for the success of any construction project. Therefore the risk factors causing cost overrun in the construction industry should be assessed. In this study, 55 important risk factors causing cost overrun in Indian construction projects are identified through intensive literature review and expert opinion. A new fuzzy based model has been proposed to estimate the risk magnitude of these factors, as the theory has the potential to deal with the vagueness, uncertainty and subjective nature of any problems and It is capable of handling the almost same analogous which is found in the complex construction projects. In order to assess the risk factors causing cost overrun, probability index and severity index are considered. A new cost overrun factor index, namely fuzzy index for cost overrun is calculated which indicates the risk magnitude of a certain factor. The applicability of the model has been shown by an example. The risk magnitude for the factor "fluctuation in price material" is determined by collecting the data from the experts of Indian construction industry. On the basis of these risk magnitudes, the importance level the factors are assessed. Top ten factors for causing cost overrun in the Indian construction industry are recognised as fluctuation in price material, lowest bid procurement policy, inflation inappropriate govt. Policy, mistakes and discrepancies in the contract document, inaccurate time and cost estimate, additional work, frequent design change, unrealistic contract duration and financial difficulty faced by contractors.

Keywords Construction · Cost overrun · Fuzzy system · Risk assessment · India

1 Introduction

Cost overrun, which can be defined as an excess of actual cost over budgeted [3, 4] in construction projects, has become a global phenomenon [15]. All project participants are affected by cost overruns. They are the causes of less return-on-investment for the client and additional charges for end-users. Similarly the contractors are not able to earn enough profit [2]. Cost overruns in the Indian construction industry are also very common. The Construction industry in India is the second largest industry of the country after agriculture and accounts for some 6.5% of GDP [10]. It is observed that problem of cost overrun has not been addressed and handled with required attention and due consideration that its impact over the Indian construction industries has been witnessed significantly to the extent that almost 60% project have undergone the time and cost overrun problem. According to the reports published by programme implementation division of the Ministry of Statistics and Programme Implementation (MOSPI) May 2016 [48], total original cost of implementation of 86 projects when sanctioned, was of the order of Rs. 179,120.81 crore but this was subsequently anticipated to Rs. 230,344.92 crore implying a cost overrun of 28.6%. The expenditure incurred on these projects till May, 2016 is Rs. 30,149.3 crore, which is 13.1% of the revised cost of the projects. Hence it is a matter of great concern to assess the causes of cost overrun to alleviate the issue of cost overrun.

During the project cycle cost overrun occurs due to the involvement of various factors. These factors are associated with some form of risk resulting from different sources. Hence,

✉ Savita Sharma
savitasugotra@yahoo.co.in

Pradeep K. Goyal
pk_goyal2003@yahoo.co.in

[1] Department of Civil Engineering, Government Polytechnic College, Ajmer, India

[2] Department of Civil Engineering, Delhi Technological University, Delhi, India

Published online: 11 March 2019

risk assessment of factors causing cost overrun has become a required mission of the construction industry. The can identify the importance of risk factor causing cost overrun so that they can deploy more resources on it to eliminate or mitigate the expected consequences. It is considered a necessary feature in the decision-making process.

The main objective of risk assessment is to estimate risk by identifying the factors causing the risk, the likelihood of occurrence of risk factor, and the severity of such risk. The existing approaches for risk analysis are qualitative, based on the fully subjective judgment of the competent personnel or quantitative such as, Monte-Carlo simulation, sensitive analysis, fault tree analysis, event tree analysis, failure mode effects and criticality analysis, based on precise data. The exact data required for these quantitative methods are very difficult for complex and real situations like construction projects as they involve too many factors with a high level of uncertainty.

A model based on the qualitative approach to assess the risk can be developed by incorporating linguistic variables to address the uncertainties associated with construction activities. The fuzzy set theory (FST) has the potential to deal with incomplete, imprecise and uncertain data. It is better equipped to handle the almost same analogous which is found in the complex construction projects. It can be used for non-accurate inputs also. Baloi and Price [5] compare different theories used for dealing with uncertainty within the construction industry and recommend FST as a vital solution for assessing construction uncertainty. Regarding the uses of fuzzy techniques in cost overrun assessment problems, very limited studies have been found in India during literature survey. This has encouraged for the application of fuzzy techniques in this paper.

Therefore the objective of this study is to propose a model based on fuzzy technique to estimate the magnitude of the risk factors causing cost overrun in the Indian construction industry. On the basis of risk magnitude, the cost overrun factors are prioritized in Indian construction industry. In order to assess the magnitude of the risk factors causing cost overrun, Probability index (PI) and severity index (SI) in the form of fuzzy linguistic variables are considered and the risk magnitude, namely fuzzy index for cost overrun (FIC) for each factor is calculated using the risk matrix originated from PMBOK (version, 2004).

This study will help the participants of Indian construction industry to understand the causes of cost overrun factors associated with construction projects and it will provide a solid overview of the knowledge domain for practitioners.

2 Related work

The fuzzy set theory has been used for decision support tool, evaluation and assessment, forecasting and modelling risks in construction projects. Kangari and Riggs [22] proposed a risk assessment model based on fuzzy set theory (FST) by incorporating natural language computation, a fuzzy set's evaluation of risk, and linguistic approximation modes [41]. The linguistic approximation technique deals with the subjectivity matters in construction risk assessments by determining the nearest natural language expression for the estimated fuzzy set numbers. Paek et al. [35] developed a risk-pricing algorithm, using FST to calculate the bid price of a construction project. Fuzzy arithmetic operations are applied to compute the risk contingency value. Wirba et al. [47] also proposed a fuzzy based risk management system, which recognized risks, checked for dependence amongst them and assessed the risk likelihood of occurrence by using linguistic variables. Tah and Carr [42] also presented a model by incorporating linguistic variables to analyse risk. Kuchta [27] used fuzzy numbers to assess the risks of construction projects. Cho et al. [8] proposed a methodology for risk assessment by combining uncertainty (using fuzzy concepts) and traditional frameworks of risk assessment. Knight and Fayek [25] also made use of fuzzy theory to predict potential cost overruns on engineering design projects. Wang and Liang [44] then proposed the multiple fuzzy goals programming model to minimize project total costs, total completion time, and total crashing costs. Choi et al. [9] presented a risk assessment methodology for underground construction projects. Zheng and Ng [51] analyzed cost and time in the construction projects management, the authors provided methods and tools based on fuzzy sets, to evaluate and manage risks in the underground construction projects. The proposed methodology used a fuzzy risk assessment approach to assess the priority of risks in terms of extra costs over the budget. Shang et al. [39] developed a FST based risk model to assess the risk probability and impact by using linguistic variables in design and conceptual stages. Dikmen and Birgonul [11] presented a methodology to fuzzy risk assessment for international construction projects. The proposed methodology uses effect diagrams to build the risk model and a fuzzy risk assessment approach to estimate priority of risks in terms of extra costs over the budget. Dikmen et al. [12] proposed a fuzzy risk assessment methodology for assessing the risk of cost overrun of international construction projects. Wang and Elhag [45] presented grouped fuzzy decision making approach for assessment of risks in bridge construction project. Lee and Lin [28] presented a new method for fuzzy risk assessment by using fuzzy numbers directly instead of linguistic variables. Chen and Wang [7] have proposed the fuzzy AHP method for evaluation of risks within global construction projects. Karimiazari et al. [23], and Nieto-Morote and Ruz-Vila [33] introduced fuzzy set theory (FST) based risk modelling and analytic methods to deal with ill-defined, vague, imprecise, and complex risk analysis problems.

Yeung et al. [49] adopted fuzzy set theory to measure the performance of relationship-based construction projects in Australia. San Cristobal [38] proposed the use of the PROMETHEE method under fuzzy environments in order to determine the critical path of a network, considering not only time but also cost, quality and safety criteria. Gunduz et al. [18] proposed a fuzzy Assessment Model to Estimate the Probability of delay in Turkish Construction Projects. Shaktawat, and Vadhera [40] presented a fuzzy tool for determination of cost overrun of a river type hydro power plant. Khalek et al. [24] developed the risk models for the global construction market using the analytic hierarchy process (AHP) to evaluate risk factors weights (likelihood) and FUZZY LOGIC approach to evaluate risk factors impact (Risk consequences) using software aids such as EXCEL and MATLAB software. Manoliadis [31] applied the concepts of fuzzy association and fuzzy composition to identify relationships between risks and the consequences on projects performance measures.

3 Proposed approach for developing the model

This section discusses the proposed methodology for developing the model for assessing the risk factors causing cost overrun in detail. The following steps are performed to develop the model.

1. *Cost overrun factor identification* The risk factors causing cost overrun in construction projects are identified through literature review.
2. *Model development* A model is developed to assess the risk factors causing cost overrun using fuzzy inference system.

3.1 Cost overrun factor identification

Risk factors causing cost overrun prevailing in the construction industry are identified through literature review. Due to the seriousness of the problem of cost overrun in construction projects the literature survey reveal a quite number of research studies that discussed and investigated the cost overrun factors in both developed and developing countries. Table 1 illustrates the studies regarding cost overrun factors from different part of the world.

On the basis of the above studies and with the opinion of the experts from Indian construction industry 55 commonly occurred risk factors causing cost overrun in Indian construction projects are considered for assessment. Table 2 shows the commonly occurred risk factors causing cost overrun in Indian construction projects.

3.2 Model development

A model to assess the risk magnitude of the factors causing cost overrun is developed using fuzzy theory. Hence some fundamentals of fuzzy set theory (FST) and fuzzy inference process have been described here.

3.2.1 Basic concept of fuzzy set theory

3.2.1.1 Fuzzy set The fuzzy set theory was first introduced by Zadah [50]. Formally, a fuzzy set A of a universe of discourse X is characterized by a membership function μA (x): X → [0, 1] that takes values in the interval [0 1], can be defined as

$$A = \{(x, \mu_A(x)) / x \in A, \mu_A(x) \in [0, 1]\}$$

where μA(x) is a membership function, which states the degree to which any element x in A is a member of the fuzzy set A. This definition unites each element x in A with μA (x) in the interval [0, 1] which is assigned to x.

3.2.1.2 Membership functions In fuzzy logic a membership function (MF) is represented by a curve that defines the fuzziness value (or degree of membership) of linguistic variables in between 0 and 1. Membership function gives a numerical meaning for each label. There are different shapes of membership functions, viz, triangular, trapezoidal, Gaussian, bell-shaped, piecewise-linear etc. A triangular fuzzy number x (see Fig. 1) with membership function can be expressed by the Eq. (1) given below

$$\mu_{A(x)} = \begin{cases} (x - a_1)/(a_m - a_1) & a_1 \le x \le a_m \\ (a_2 - x)/(a_2 - a_m) & a_m \le x \le a_2 \\ 0 & \text{otherwise} \end{cases} \quad (1)$$

3.2.1.3 Fuzzy operators Important fuzzy operators "AND", "OR" and "NOT" are used to make fuzzy rules. These "fuzzy combination" operators can be explained as follows.

Consider the two fuzzy sets A and B be with membership functions $\mu_A(x)$ and μB(x) respectively.

The intersection operation (corresponds to the logical 'AND') can be defined as:

$$\mu A \cap B(x) = \min \left[\mu A(x), \mu B(x)\right]$$

Union operation (which corresponds to the logical 'OR') can be defined as:

$$\mu AUB(x) = \max \left[\mu A(x), \mu B(x)\right]$$

Table 1 Studies regarding risk factors causing cost overrun from different part of the world

S. no.	Authors	Country	Causes of cost overrun
1	Okpala and Aniekwu [34]	Nigeria	Price fluctuations, additional works, delays, fraudulent practices, shortening of contract period, inaccurate estimates
2	Mansfield et al. [30]	Nigeria	Poor planning, shortage in materials, imported materials, changes in site conditions, design changes were the main causes of construction delays and cost overrun
3	Jackson [21]	UK	Poor project planning and management, unexpected ground condition, design development, lack of information, estimating method, time limit, commercial pressure, procurement route and external factor
4	Frimpong et al. [16]	Ghana	Groundwater planning and scheduling deficiencies, deficiencies the prepared cost estimates, inadequate control procedures, delays in work approval, waiting for information, mistakes during construction, delays in inspection and testing of work and cash flow during construction, frequent breakdowns of construction plant and equipment, shortages of technical personnel, labour shortage, monthly payment difficulties, poor contract management, shortage of materials, plant/equipment parts, contractor's financial difficulties, low bid, material procurement, imported materials, late delivery of materials and equipment, escalation of material prices, slow decision-making, inflation, difficulties in obtaining construction materials at official current price, ground problem, bad weather and unexpected geological conditions
5	Koushki et al. [26]	Kuwait	Contractor-related problems, material-related problems and owners' financial constraints
6	Iyer and Jha [20]	India	Conflict among project participants, ignorance and lack of knowledge, presence of poor project specific attributes and non existence of cooperation, hostile socio-economic and climatic conditions, reluctance in timely decision, aggressive competition at tender stage and short bid preparation time
7	Azhar et al. [4]	Pakistan	Fluctuation in prices of raw materials, unstable cost of manufactured materials, high cost of machineries, lowest bidding procurement procedures, poor project (site) management/poor cost control, delays between design and procurement phases, incorrect/inappropriate methods of cost estimation
8	Enshassi et al. [14]	Gaza	Location of the project, segmentation of the Gaza strip and limitation of movements between areas, political situation, and financial status of the owner
9	Memon et al. [32]	Malaysia	cash flow and financial difficulties faced by contractors, contractor's poor site management, inadequate contractor experience, shortage of site workers and incorrect planning and scheduling by contractors
10	Wakjira [43]	Ethiopian	Incomplete drawings; poor pre planning process; escalating cost of material, lack of timely decision and excessive change order
11	Doloi et al. [13]	Australia	Planning process and scheduling deficiency, method and technique of construction, effective monitoring and feedback, complexity of design and construction, improper control over site resources allocation
12	Ismail et al. [19]	Malaysia	Fluctuation of prices of materials, cash flow and financial difficulties faced by contractors, poor site management and supervision and shortages of materials, shortage of site workers and Financial difficulties of owner
13	Rosenfeld [37]	Universal	Premature tender documents, insufficient information about ground conditions, too small a design budget, force majeure strikes/weather/regulation changes/accidents, etc., too many changes in owners' requirements or definitions, late start of the planning process, and with too low a budget, insufficient, unstandardized owner's brief, shortage in high-quality management personnel, culture of conflicts and lack of trust, unconstructable design, tender-winning prices are unrealistically low (suicide tendering), lack of standard requirements from designers and poorly enforced professional, liability of designers, unclear, ambiguous, and contradicting terms in the tender documents, unbalanced distribution of risk between owner and contractor, unclear division of responsibilities and lack of clear requirements for professional management
14	Wanjari and Dobariya [46]	India	Price escalation of raw material, dispute on bill settlement, delay in planned activity, ambiguous or incomplete tender document, additional work, frequent design changes, lack of co-ordination between construction parties, fraudulent practices and kick backs, mistake during construction, force majeure, high quality expectation from owner, shortening of contract period, wastage on site, relationship between site management and labor, poor financial control on site
15	Al-Hazim et al. [1]	Jordan	Terrain and weather conditions, variation orders, availibility of labour, mistakes in design

Table 2 commonly occurred risk factors causing cost overrun in Indian construction projects

No.	Factors
1	Slow payment of complete work by owner
2	Slow decision making
3	Mode of finance and payment
4	Interference by owner
5	Unrealistic contract duration
6	Poor planning and scheduling
7	Disputes on sites
8	Rework due to error
9	Wastes on site
10	Poor site management
11	Contractor lack of experience
12	Incompetent sub contractor
13	Financial difficulty faced by contractor
14	Obsolete and improper construction technique
15	Inaccurate time and cost estimate
16	Contract management
17	Delay in performing inspection
18	Quality assurance and quality control
19	Inadequate experience of technical consultant
20	Delay in approval of design
21	Improper design and delay in producing design document
22	Frequent design change
23	Change in the scope of the project
24	Lowest bid procurement policy
25	Additional work
26	Cost of material
27	Late material delivery
28	Delay in procurement of material
29	Shortage of construction material
30	Change in material specification
31	Unqualified labour
32	Labour disputes and strikes
33	Low level productivity of labour
34	High cost of labour
35	Shortage of labour
36	Shortage of equipment
37	Equipment availability and failure
38	High cost of machineries
39	Mistakes and discrepancies in contract document
40	Contractual procedure and type of contract
41	Poor coordination between parties
42	Slow information flow in between parties
43	Lack of communication between parties
44	Fluctuation in price materials
45	Inflation
46	Inappropriate govt policy
47	Exchange rate
48	High interest rate charged by bank and loan
49	Fraudulent practices and kickbacks
50	Insurance cost
51	Climatic condition
52	Social and cultural factor
53	Accident during construction
54	Acts of god
55	Differing site condition

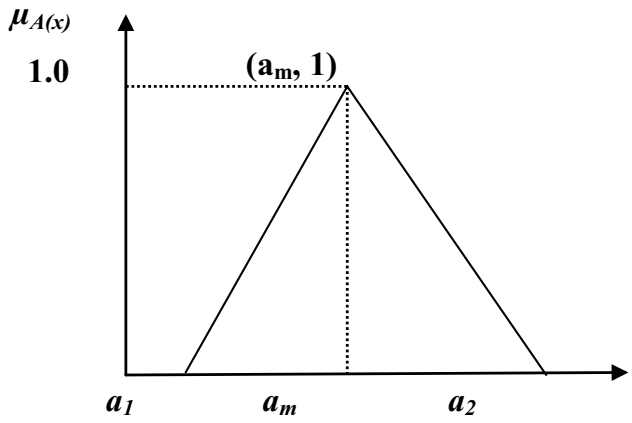


Fig. 1 Triangular membership function

3.2.1.4 IF-THEN rules A fuzzy system is a compilation of IF-THEN rules that connect input linguistic variables to an output value. Each fuzzy rule contains the antecedent and the consequent that includes fuzzy propositions. These propositions in turn are statements and join the linguistic variables with linguistic operators "and", "or" and "not". In the majority of fuzzy modelling, only the linguistic operator "and" is used to join the linguistic labels of the antecedent, whereas the consequent is formed by only one linguistic label. For this reason IF-THEN rules with connective "and" is considered in this study. The general form of a fuzzy rule used in fuzzy logic control system can be explained by relation (2):

$$\text{If } x_1 \text{ is } A_1 \text{ AND } x_2 \text{ is } A_2 \text{ then y is B} \tag{2}$$

where x_1, x_2 are input linguistic variables with A_1, A_2 being their corresponding fuzzy values and y is the output linguistic variable with B as its fuzzy value.

3.2.1.5 Fuzzy inference system Fuzzy inference is the system to map from a given input to an output using fuzzy logic. Mamdani Fuzzy Inference System and Takagi-Sugeno Fuzzy Model (TS Method) are two important methods of FIS. Mamdani Fuzzy Inference System Mamdani and

Assilian [29] is widely used therefore the basic steps of this process are discussed here:

1. Set of fuzzy rules are established first
2. The crisp inputs are fuzzified by defining the membership functions.
3. To establish rule strength fuzzified inputs are combined according to the fuzzy rules.
4. The outcome of the rule are found by combining the rule strength and the output membership function.
5. The outcomes are combined to get an output distribution, and
6. The output distribution is defuzzified to get a crisp output.

Detailed description of this process is shown in Fig. 2.

3.3 Development of model to calculate the risk magnitude of the factors causing cost overrun using Fuzzy Logic Toolbox of the MATLAB Program Software

Based on the above concepts, the following steps are performed to calculate the risk magnitude of the factors causing cost overrun using Fuzzy Logic Toolbox of the MATLAB Program Software [17].

3.4 Define input and output

The risk magnitude usually can be assessed by two main risk parameters, risk probability and risk severity. Therefore the PI, and SI for risk factors causing cost overrun are used as input variables in this model. In order to determine the risk magnitude of the factors causing cost overrun, FIC is measured as the output of this model as shown in Fig. 3. FIC signifies the risk magnitude of a certain factor.

3.4.1 Membership function

Triangular membership function has been used in this study for input and output variable. The triangular fuzzy value of each linguistic variables such as PI, SI and FIC have been shown in Tables 3 and 4. The graphical presentation of membership function for these variables has been shown in Figs. 4, 5 and 6 respectively.

3.4.2 Formation of rules

In the present study probability index and severity index are considered for antecedent part and FIC is considered for consequent part as shown in Fig. 6 to assess the magnitude of the risk factors. The relationship among these parameters is needed to introduce logical rules for the two inputs (probability index and severity index for each factor) and output FIC. For this purpose fuzzy values given in risk matrix, as shown in Table 5, originated from PMBOK (version, 2004) [36] are used here.

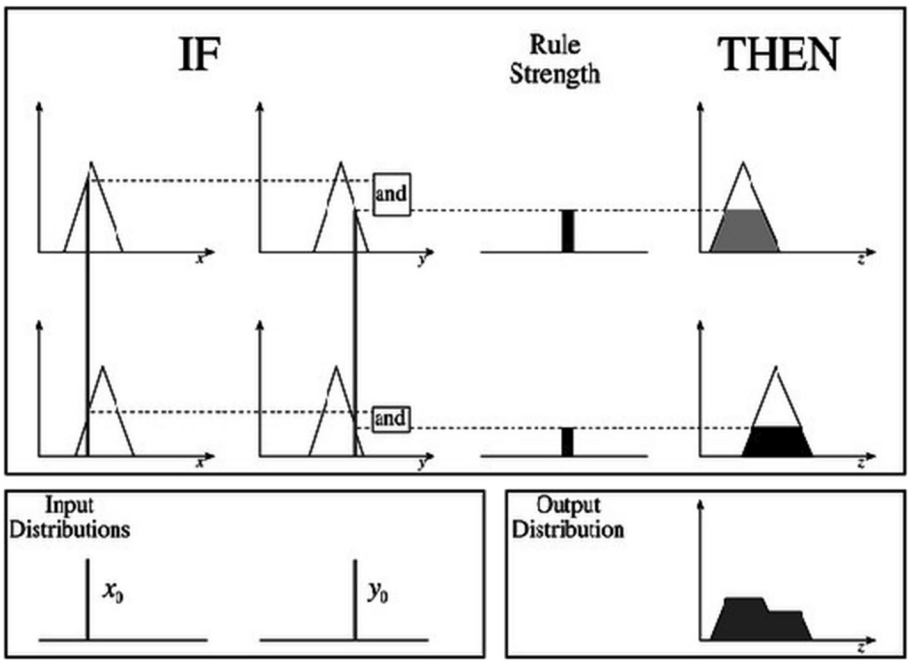


Fig. 2 Mamdani fuzzy inference system

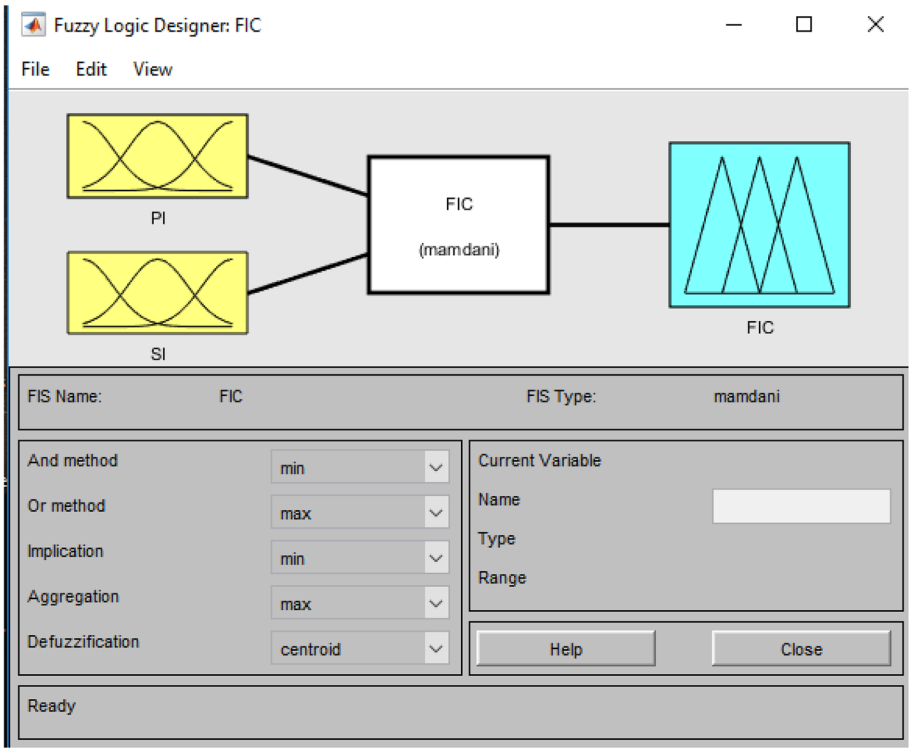


Fig. 3 Input and output of the model

Table 3 Fuzzy value of linguistic variables for input

Fuzzy variable	Fuzzy number
Very low	0, 0, 0.25
Low	0, 0.25, 0.5
Medium	0.25, 0.5, 0.75
High	0.5, 0.75, 1
Very high	0.75, 1, 1

Table 4 Fuzzy value of linguistic variables for output

Fuzzy variable	Fuzzy number
Low	0.3333, 0.3333
Medium	0.3333, 0.6667
High	0.3333, 0.6667, 1
Very high	0.6667, 1, 1

There are two input variables and each input variables consists of five fuzzy sets. in general, if n is the number of fuzzy sets representing one input variable and m is the number of fuzzy sets representing second input variable, then the maximum number of propositions that can be written is m*n. Therefore, there are 25 propositions. Some of the valid propositions are as follow:

1. If probability index is very low and severity index is very low then fuzzy index for cost overrun is low.

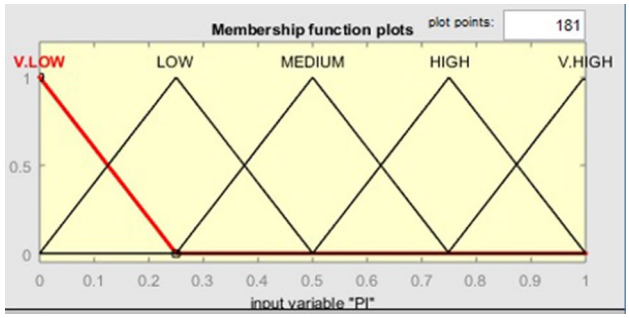


Fig. 4 Graphical presentation of linguistic variables for probability index

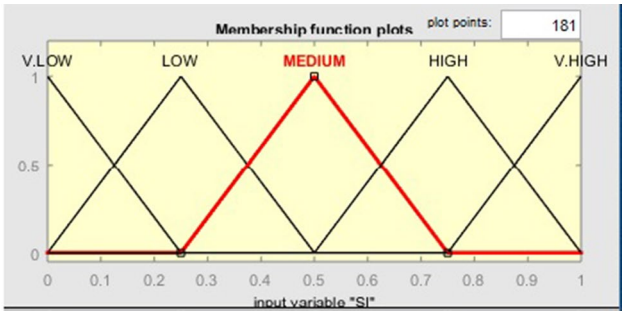


Fig. 5 Graphical presentation of linguistic variables for severity index

2. If probability index is low and severity index is very low then fuzzy index for cost overrun is low.

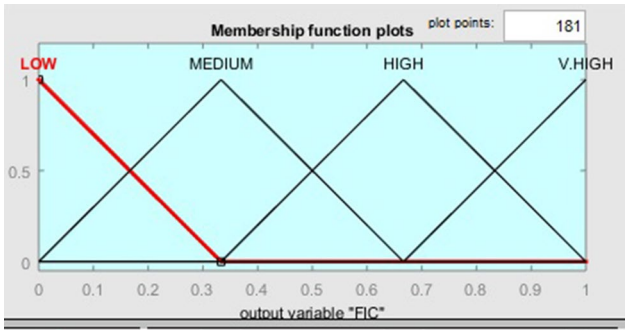


Fig. 6 Graphical presentation of linguistic variables for fuzzy index for cost overrun

Table 5 Risk matrix

Fuzzy index for cost overrun	Probability of occurrence				
	Very low	Low	Medium	High	Very high
Severity level					
Very low	Low	Low	Medium	High	High
Low	Low	Low	Medium	High	Very high
Medium	Low	Medium	High	Very high	Very high
High	Medium	High	High	Very high	Very high
Very high	High	High	Very high	Very high	Very high

3. If probability index is medium and severity index is very low then fuzzy index for cost overrun is medium.
4. If probability index is high and severity index is very low then fuzzy index for cost overrun is high.
5. If probability index is very high and severity index is very low then fuzzy index for cost overrun is high.

The above rules are generated using the rule editor of Fuzzy Logic Toolbox of the MATLAB Program Software as shown in Fig. 7. Based on the descriptions of the input and output variables defined with the FIS Editor, the Rule Editor allows us to construct the rule statements automatically.

3.4.3 Defuzzification

Finally, the model performed defuzzification of the combined fuzzy output to generate crisp output value. The magnitude of the FIC is determined as an exact number in the interval of zero to one. The complete procedure is shown in the *rule viewer window* of Fuzzy Logic Toolbox of the MATLAB Program Software as shown in Fig. 8. The rule viewer displays a roadmap of the whole fuzzy inference process. It allows us to interpret the entire fuzzy inference process at once. The Rule Viewer also shows how the shape of certain membership functions influences the overall result.

Fig. 7 fuzzy rules of the model

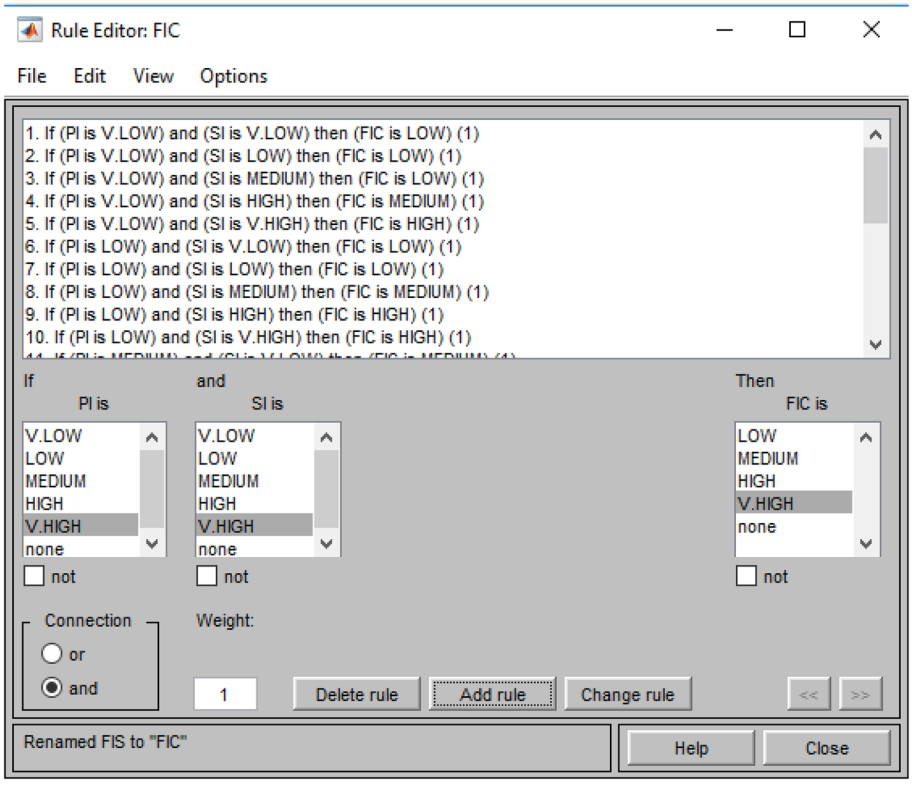


Fig. 8 Defuzzification



Table 6 Experience of the experts

S. no.	Designation of expert	No.	Experience (years)
1	Assistant engineer	3	20
2	Executive engineer	3	10
3	Project manager	4	15

4 Application of developed model

The application of the developed fuzzy risk assessment model is illustrated by means of a practical case study from India. The developed methodology is applied for determining the risk magnitude of factor "Fluctuation in price material". Following steps are performed for determining the FIC of factor "Fluctuation in price material".

4.1 Data collection

The data was collected from the experts of construction industry in India to know the perceptions on the probability index and severity index of the factor "Fluctuation in price material" in Indian construction industry. For this purpose an interview was developed with a panel of ten experts. Experts had a vast experience in construction projects such as water and waste water, roads and railways and public buildings. Table 6 shows the experience of the experts.

A five-point scale of 1–5 was adopted for getting the opinion of the experts for probability and severity index of the factor. These numerical values of the respondents were assigned linguistic values such as '1 = very low; 2 = low; 3 = medium; 4 = high; 5 = very high' for both probability index and severity index. The fuzzy values used in developed model were then assigned to these linguistic variables. Table 7 shows the responses of the experts and their respective fuzzy values.

Table 7 Responses of experts

Expert	PI	SI	Fuzzy value of PI	Fuzzy value of SI
1	4	5	0.5, 0.75, 1	0.75, 1, 1
2	3	4	0.25, 0.5, 0.75	0.5, 0.75, 1
3	2	5	0, 0.25, 0.5	0.75, 1, 1
4	4	4	0.5, 0.75, 1	0.5, 0.75, 1
5	3	5	0.25, 0.5, 0.75	0.75, 1, 1
6	4	5	0.5, 0.75, 1	0.75, 1, 1
7	5	5	0.75, 1, 1	0.75, 1, 1
8	2	4	0, 0.25, 0.5	0.5, 0.75, 1
9	3	4	0.25, 0.5, 0.75	0.5, 0.75, 1
10	3	5	0.25, 0.5, 0.75	0.75, 1, 1

4.2 Average of expert's opinions

To obtain the average of experts opinions, the fuzzy average operation for aggregate method that is known as the ''Triangular Average Formula'' [6] is used.

Triangular average formula for n number of experts.

Consider n experts and fuzzy number $A_i = (a_1^{(i)}, a_m^{(i)}, a_2^{(i)})$, $i = 1, 2, 3 \ldots n$.

The average of two fuzzy numbers A1 and A2 can be calculated as

$$(A_1 + A_2)/2 = ((a_1^{(1)} + a_m^{(1)} + a_2^{(1)}) + (a_1^{(2)} + a_m^{(2)} + a_2^{(2)}))/2$$
$$= ((a_1^{(1)} + a_1^{(2)}), (a_m^{(1)} + a_m^{(2)}), (a_2^{(1)} + a_2^{(2)}))/2$$

The average of n fuzzy number can be calculated as

$$A_{avg} = A_1 + \cdots A_n/n$$
$$A_{avg} = ((a_1^{(1)} + a_m^{(1)} + a_2^{(1)}) + \cdots (a_1^{(n)} + a_m^{(n)} + a_2^{(n)}))/n$$

Using the above formula the fuzzy values for probability and severity index are determined as follows:

Average fuzzy value for probability index (PI) = (0.325, 0.575, 0.8).

Average fuzzy number for severity index (SI) = (0.65, 0.9, 1).

To obtain a crisp value, the fuzzy value (a_1, a_m, a_2) then got converted into best non fuzzy performance (BNP) value using the following formula:

$$\left((a_2 - a_1) + (a_m - a_1)\right)/3 + a_1$$

Best non fuzzy performance (BNP) value for probability index = 0.566.

Best non fuzzy performance (BNP) value for severity index = 0.85.

Using the probability and severity index FIC of risk factor "Fluctuation in price material" is determined as 0.694, which indicates the magnitude of the risk factor.

Similarly the risk magnitude of the other factors is calculated by collecting data regarding the perceptions on the probability index and severity index. The risk magnitude of the other factors causing cost overrun is shown in Table 8.

5 Important factors causing cost overrun in Indian construction industry

On the basis of the perceptions on the probability index and severity index of the factor of experts from Indian construction industry, model calculated the top ten most important causes of cost overruns in construction projects of India included fluctuation in price material, lowest bid procurement policy, inflation, inappropriate govt. policy, inaccurate time and cost estimate, mistakes and discrepancies in contract document, additional work, frequent design change, unrealistic contract duration and financial difficulty faced by the contractor.

6 Conclusion

Cost is one of the fundamental criteria for measuring the success of the project. Therefore the risk factors causing cost overrun in the construction industry should be identified and assessed, for the managers to deploy more resources on critical factors, to eliminate or mitigate the expected consequences due to these factors. It is considered a necessary feature in the decision-making process. The Indian construction industry is also suffering from the problem of cost overrun. Hence in this study 55 important risk factors causing cost overrun in Indian construction projects are identified through intensive literature review and experts opinion. This paper also proposes a new fuzzy based model to assess the risk magnitude of these risk factors, as the theory has the potential to deal with the vagueness, uncertainty and subjective nature of any problems. It is better equipped to handle the almost same analogous which is found in the complex construction projects. In order to assess the risk factors causing cost overrun, PI and SI are considered and cost overrun factor index namely FIC is calculated, which indicates the risk magnitude of a certain factor. An interview was developed with a panel of ten experts from Indian construction industry, to assess the perceptions on the probability index and severity index of the risk factors causing cost overrun and FIC of risk factors are determined. The factors are ranked according to their risk magnitude. The model is useful for project managers to take proper action against these risk factors causing cost overrun.

The top ten factors for causing cost overrun in Indian construction industry are recognised as fluctuation in price material, lowest bid procurement policy, inflation inappropriate govt. Policy, mistakes and discrepancies in contract document, inaccurate time and cost estimate, additional work, frequent design change, unrealistic contract duration and financial difficulty faced by contractor.

6.1 Limitation of approach and future scope

The model is based on fuzzy approach. It cannot be accepted as a universal model. It can be considered as an example of how magnitude of risk factors causing cost overrun may be determined using this model in construction projects. The types of membership function used for developing the fuzzy model can be different. Fuzzy rules are based on matrix. A standard matrix is not available in the literature. Defuzzification method can also be changed. Using the methods based on fuzzy logic subjectivity can be reduced to acceptable level by converting the linguistic values to quantitative

Table 8 Risk magnitude of the factors causing cost overrun

Factors causing cost overrun	Risk magnitude	Rank
Fluctuation in price materials	0.694	1
Lowest bid procurement policy	0.69	2
Inflation	0.687	3
Inappropriate govtpolicy	0.682	4
Inaccurate time and cost estimate	0.68	5
Mistakes and discrepancies in contract document	0.678	6
Additional work	0.675	7
Frequent design change	0.673	8
Unrealistic contract duration	0.669	9
High cost of labour	0.664	10
Financial difficulty faced by contractor	0.661	11
Poor planning and scheduling	0.658	12
Slow decision making	0.652	13
Poor coordination between parties	0.648	14
Exchange rate	0.642	15
Contract management	0.635	16
Cost of material	0.622	17
High interest rate charged by bank and loan	0.618	18
Change in the scope of the project	0.591	19
Disputes on sites	0.576	20
Fraudulent practices and kickbacks	0.572	21
Insurance cost	0.566	22
High cost of machineries	0.562	23
Climatic condition	0.552	24
Rework due to error	0.508	25
Improper design and delay in producing design document	0.505	26
Slow payment of complete work by owner	0.498	27
Quality assurance	0.497	28
Inadequate experience of technical consultant	0.459	29
Lack of communication between parties	0.456	30
Change in material specification	0.452	31
Wastes on site	0.445	32
Delay in approval of design	0.442	33
Slow information flow in between parties	0.440	34
Mode of finance and payment	0.425	35
Social and cultural factor	0.423	36
Slow payment of completed work	0.417	37
Poor site management	0.409	38
Contractual procedure and type of contract	0.382	39
Shortage of labour	0.380	40
Shortage of construction material	0.371	41
Accident during construction	0.37	42
Low level productivity of labour	0.355	43
Interference by owner	0.355	44
Contractor lack of experience	0.352	45
Late material delivery	0.343	46
Incompetent sub contractor	0.340	47
Delay in performing inspection	0.338	48
Unqualified labour	0.332	49
Labour disputes and strikes	0.331	50
Acts of god	0.324	51

Table 8 (continued)

Factors causing cost overrun	Risk magnitude	Rank
Obsolete and improper construction technique	0.322	52
Delay in procurement of material	0.319	53
Shortage of equipment	0.318	54
Equipment availability and failure	0.308	55

values but it is not eliminated completely. Risk factors causing cost overrun in Indian construction industry are based on literature survey result and opinion from the experts of Indian construction industry. Number of respondents selected in the study might have been increased. Numbers of experts included for getting opinion were also very few in comparison to the size of industry. The lack of data and information was one of the main limitations.

The fuzzy inference system used for developing the model can be extended using other fuzzy membership functions and performance of models could have been compared. In addition, the results of fuzzy inference system can be compared with other predictive tools. The developed model may be extended to other industrial sectors for assessing the risks.

References

1. Al-Hazim N, Salem ZA, Ahmad H (2017) Delay and cost overrun in infrastructure projects in Jordan. In: 7th international conference on engineering, project, and production management, Procedia Engineering, vol 182, pp 18–24
2. Ashworth A (2008) Pre-contract studies: development economics, tendering and estimating, 3rd edn. Blackwell Publishing Limited, Oxford
3. Avots I (1983) Cost-relevance analysis for overrun control. Int J Project Manag 1:142–148
4. Azhar N, Farooqui RU, Ahmed SM (2008) Cost overrun factors in construction industry of Pakistan. In: Paper presented at the first international conference on construction in developing countries (ICCIDC-I). Advancing and integrating construction education, research & practice
5. Baloi D, Price ADF (2003) Modeling global risk factors affecting construction cost performance. Int J Proj Manag 21(4):261–269
6. Bojadziev G, Bojadziev M (1997) Fuzzy logic for business, finance, and management. World Scientific, Singapore
7. Chen P, Wang J (2009) Application of fuzzy AHP method to risk assessment of international construction projects. In 2009 international conference on electronic commerce and business intelligence, pp 459–462
8. Cho HN, Choi HH, Kim YB (2002) A risk assessment methodology for incorporating uncertainties using fuzzy concepts. Reliab Eng Syst Saf 78(2):173–183
9. Choi HH, Cho HN, Seo JW (2004) Risk assessment methodology for underground construction projects. J Constr Eng Manag 130:258
10. Das TK (2003) Development of Highways and Airports in India. In: Proceedings of the 6th national conference on construction, CDROM, Technical Session 1, Paper No.7. 10–11 November 2003, New Delhi
11. Dikmen I, Birgonul MT (2006) An analytic hierarchy process based model for risk and opportunity assessment of international construction projects. Can J Civ Eng 33(1):58–68
12. Dikmen I, Birgonul MT, Han S (2007) Using fuzzy risk assessment to rate cost overrun risk in international construction projects. Int J Project Manag 25:494–505
13. Doloi H, Sawhney A, Iyer KC, Rentala S (2012) Analysing factors affecting delays in Indian construction projects. Int J Project Manag 30(4):479–489
14. Enshassi A, Al-Najjar J, Kumaraswamy M (2009) Delays and cost overruns in the construction projects in the Gaza Strip. J Financ Manag Prop Constr 14(2):126–151
15. Flyvbjerg B, Holm MKS, Buhl SL (2002) Underestimating costs in public works projects: error or lie? J Am Plan Assoc 68(3):279–295
16. Frimpong Y, Oluwoye J, Crawford L (2003) Causes of delays and cost overruns in construction of groundwater projects in developing countries; Ghana as a case study. Int J Project Manag 21:321–326
17. Fuzzy Logic Toolbox™ (2015) 2 user's guide, MATLAB. The Math Works, Inc., Natick
18. Gunduz M, Nielsen Y, Ozdemir M (2015) Fuzzy assessment model to estimate the probability of delay in turkish construction projects. J Manag Eng ASCE. https://doi.org/10.1061/(ASCE)ME.1943-5479.0000261
19. Ismail AR, Memon AH, Karim ATA (2013) Significant factors causing cost overruns in large construction projects in Malaysia. J Appl Sci 13:286–293. https://doi.org/10.3923/jas.2013.286.293
20. Iyer KC, Jha KN (2005) Factors affecting cost performance: evidence from Indian construction projects. Int J Project Manag 23:283–295
21. Jackson S (2002) Project cost overrun and risk management in Greenwood. In: Proceedings of association of researchers in construction management, 18th annual ARCOM conference, Newcastle, Northumber University, UK, 2–4 September
22. Kangari R, Riggs LS (1989) Construction risk assessment by linguistics. IEEE Trans Eng Manag 36(2):126–131
23. Karimiazari AR et al (2011) Risk assessment model selection in construction industry. Expert Syst Appl 38:9105–9111
24. Khalek HAE, Aziz RF, Kamel HM (2016) Risk and uncertainty assessment model in construction projects using fuzzy logic. Am J Civ Eng 4(1):24–39
25. Knight K, Fayek AR (2002) Use of fuzzy logic for predicting design cost overruns on building projects. J Constr Eng Manag 128(6):503–512
26. Koushki PA, Al-Rashid K, Kartam N (2005) Delays and cost increases in the construction of private residential projects in Kuwait. Constr Manag Econ 23(3):285–294
27. Kuchta D (2001) Use of fuzzy numbers in project risk (criticality) assessment. Project Manag 19(5):305–310
28. Lee HM, Lin L (2008) A new fuzzy risk assessment approach. Int J Project Manag 1(4):6–7
29. Mamdani EH, Assilian S (1975) An experiment in linguistic synthesis with a fuzzy logic controller. Int J Man Mach Stud 7:1–13

30. Mansfield NR, Ugwu OO, Doran T (1994) Causes of delay and cost overruns in Nigerian construction projects. Int J Project Manag 12(4):254–260
31. Manoliadis O (2018) The assessment of construction project risks with the use of fuzzy Delphi methodology—case study photovoltaic project in Greece. Int J Manag Fuzzy Syst 4(1):7–14. https://doi.org/10.11648/j.ijmfs.20180401.12
32. Memon AH, Rahman IA, Abdullah MR, Azis AAA (2010) Factors affecting construction cost in MARA large construction projects: perspective of project management consultant. Int J Sustain Constr Eng Technol 1:41–54
33. Nieto-Morote A, Ruz-Vila F (2011) A fuzzy approach to construction project risk assessment. Int J Project Manag 29:220–231
34. Okpala DC, Aniekwu AN (1988) Causes of high costs of construction in Nigeria. J Constr Eng Manag 114(2):233–234
35. Paek JH, Lee YW, Ock JH (1993) Pricing construction risks: fuzzy set theory. J Constr Eng Manag 119(4):743–756
36. PMI (2004) A guide to the project management body of knowledge: PMBOKGuide, 3rd edn. Project Management Institute Inc., Newtown Square
37. Rosenfeld Y (2014) Root-cause analysis of construction-cost overruns. J Constr Eng Manag (American Society of Civil Engineers). https://doi.org/10.1061/(ASCE)CO.1943-7862.0000789
38. San Cristobal J (2013) Critical path definition using multi criteria decision making: the PROMETHEE method. J Manag Eng. https://doi.org/10.1061/(ASCE)ME.1943-5479.0000135
39. Shang H, Anumba CJ, Bouchlaghem DM, Miles JC, Cen M, Taylor M (2005) An intelligent risk assessment system for distributed construction teams. Eng Constr Archit Manag 12(4):391–409
40. Shaktawat A, Vadhera S (2016). Fuzzy logic based determination of cost overrun of hydro power plant. In: International conference on electrical power and Systems E (ICEPES), Dec. 14–16, Bhopal, India
41. Taroun A, Yang JB, Lowe D (2011) Construction risk modelling and assessment: insights from a literature review. Built Hum Environ Rev 4(1):87–97
42. Tah JHM, Carr V (2000) A proposal for construction project risk assessment using fuzzy logic. Constr Manag Econ 18:491–500
43. Wakjira T (2011) Risk factors leading to cost overrun in Ethiopian Federal Road Construction projects and its consequences. M. Sc. Thesis, Construction Technology and Management Addis Abab University Ethiopia
44. Wang RC, Liang TF (2004) Project management decisions with multiple fuzzy goals. Constr Manag Econ 22(10):1047–1056
45. Wang YM, Elhag TM (2007) A fuzzy group decision making approach for bridge risks assessment. Comput Ind Eng 53(1):137–148
46. Wanjari SP, Dobariya G (2016) Identifying factors causing cost overrun of the construction projects in India. Sadhana 41(6):679–693. https://doi.org/10.1007/s12046-016-0498-3_IndianAcademyofSciences
47. Wirba EN, Tah JHM, Howes R (1996) Risk interdependencies and natural language computations. J Eng Constr Architect Manag 3(4):251–269
48. http://www.tradingeconomics.com/india/gdp-from-construction. Accessed 27 Jan 2017
49. Yeung J, Chan A, Chan D (2012) Fuzzy set theory approach for measuring the performance of relationship-based construction projects in Australia. J Manag Eng. https://doi.org/10.1061/(ASCE)ME.1943-5479.0000083
50. Zadah LA (1965) Fuzzy sets. Inf Control 8(3):338–353
51. Zheng DXM, Ng T (2005) Stochastic time-cost optimization model incorporating fuzzy sets theory and non-replacement. J Constr Eng Manag 131(2):176–186

Publisher's Note Springer Nature remains neutral with regard to jurisdictional claims in published maps and institutional affiliations.

electronics

MDPI

Article

Green Computing in Sensors-Enabled Internet of Things: Neuro Fuzzy Logic-Based Load Balancing

Pankaj Kumar Kashyap [1], Sushil Kumar [1], Upasana Dohare [1], Vinod Kumar [2] and Rupak Kharel [3,*]

[1] School of Computer and Systems Sciences, Jawaharlal Nehru University, New Delhi-110067, India; pankaj76_scs@jnu.ac.in (P.K.K.); skdohare@mail.jnu.ac.in (S.K.); upasanadohare@yahoo.com (U.D.)
[2] Department of Computer Engineering, Delhi Technological University (DTU), Delhi-110042, India; vinod_k@dtu.ac.in
[3] School of Engineering, Manchester Metropolitan University, Manchester M1 5GD, UK
* Correspondence: r.kharel@mmu.ac.uk

Received: 01 March 2019; Accepted: 25 March 2019; Published: 29 March 2019

Abstract: Energy is a precious resource in the sensors-enabled Internet of Things (IoT). Unequal load on sensors deplete their energy quickly, which may interrupt the operations in the network. Further, a single artificial intelligence technique is not enough to solve the problem of load balancing and minimize energy consumption, because of the integration of ubiquitous smart-sensors-enabled IoT. In this paper, we present an adaptive neuro fuzzy clustering algorithm (ANFCA) to balance the load evenly among sensors. We synthesized fuzzy logic and a neural network to counterbalance the selection of the optimal number of cluster heads and even distribution of load among the sensors. We developed fuzzy rules, sets, and membership functions of an adaptive neuro fuzzy inference system to decide whether a sensor can play the role of a cluster head based on the parameters of residual energy, node distance to the base station, and node density. The proposed ANFCA outperformed the state-of-the-art algorithms in terms of node death rate percentage, number of remaining functioning nodes, average energy consumption, and standard deviation of residual energy.

Keywords: fuzzy logic; neural network; load balancing; supervised learning; back-propagation learning; clustering

1. Introduction

Sensors enabled Internet of Things (IoT) networks have been regarded as reasonable data collection and control applications over various network communication infrastructures through smart sensors called IoT nodes [1–3]. Sensors-enabled IoT networks are comprised of various smart sensor nodes (RFID enabled) that assemble facts (data) from the encompassing conditions and convey the data to the static base station (BS) or overload the data to cloud applications where users download the data for processing [4–6]. Sensors-enabled IoT networks have gained impressive attention in view of their broad application in animal or human tracking and surveillance, medical environments [7], military services, automobile industries [8], stock administration in industrial production [9], environment monitoring, natural hazards and seismic detection, fleet navigation and management, agricultural advancements [10], etc. However, these smart sensor nodes have a limited amount of energy for computation and data communication, and it is troublesome to substitute the power source. In addition, some sensor nodes quickly deplete their energy, which causes network partitions and reduces the lifetime of the network [11]. Reference [12] proposed a model which uses ant colony optimization technique coupled with Huffman coding to deduce the energy consumption in green computing wireless networks. Therefore, the proper use of the energy of the sensors is the

primary challenge. Hence, there is a need to find an approach that schedules the load among the smart sensors, particularly among those that have higher computational power and transmission capabilities.

Clustering is one potential load balancing approach which exists in the literature. Clustering is a technique which divides the entire network into small clusters. The maximum number of cluster heads per cluster is limited to one; each of the cluster heads have the mandatory duty of collecting data from their respective member nodes [13,14]. These member nodes are normally distributed in the same topographical region, so they have correlated data. After obtaining the data from its member nodes, cluster heads apply data aggregation techniques to eliminate any data redundancies, as a result, it effectively truncates the quantity of data to be transferred to the base station. Since only one cluster head per cluster is accountable for routing, to scale down the amount of data transferred, one must make the network scalable and mitigate the load balance problem [15]. There are three major aspects for designing a cluster-based network for data collection and transfer, namely, 1) optimal selection procedure for cluster head, 2) cluster binding, and 3) inter-cluster routing phase for transfer of aggregated data from each cluster head to the base station.

In clustering, cluster head selection procedure is a primary issue. Cluster head selection using traditional mathematical models is not appropriate for complex sensors-enabled Internet of Things. A fuzzy inference system is an appropriate tool to construct a model for cluster head selection since a fuzzy inference system processes the subjective part of human understanding and thinking without using any kind of mathematical tools. Zadeh [16] in 1965 first proposed the theory of fuzzy sets. Later on, Takagi and Sugeno [17] (1985) proposed the fuzzy modeling fuzzy identification or fuzzy modeling to alleviate the problem of various pragmatic applications such as control, inference, prediction, and estimation. As fuzzy modeling provides some great advantages such as the capacity to translate the immanent indecisiveness of human aspects into linguistic variables and effortless understanding of outcomes, as a result of the natural rule portrayal, simple augmentation of rule to the base knowledge is achieved through the expansion of new principles and robustness of system. Although, there are some disadvantages with this approach, there is no proper method defined which can transform human practical knowledge into fuzzy rule databases. Fuzzy modelling is only capable of giving an answer to a question that is written in the rules database. It cannot handle out-of-the-box problems, or in other words, generalization is very difficult. To alleviate this generalization problem, there is the need for a method of tuning or learning the membership function to cut down the error rates and to increase the performance index.

McCulloch and Pitts [18] developed the first artificial neural network model. Both Rosenblatt and Widrow first trained and named the trained variant of the artificial neural network model as the "adaptive liner neuron", later on called the "adaptive linear element algorithm" [19–24]. An artificial neural network is a "connectionist" computation model, which attempts to carve the biological neurons of a human cerebrum. The main advantage of neural networks is learning capacity; this model can learn from training data vectors and input–output pairs of the system. The neural network itself maps the weight functions or membership functions according to the problem up to an acceptable error rate of the system, which makes the system more efficient in terms of performance. Thus, it leads to the idea of augmenting the learning algorithm and generalization capability into the fuzzy system. A neural network receives the clarity of logical interpretation from fuzzy systems to rectify problems. In the early 1990s, Jang and Lin [25], Berenji [26] and Nauck [27] developed a hybrid system called a neuro-fuzzy system. There is diversity in neuro-fuzzy systems, which include fuzzy adaptive learning control networks [25,28], generalized approximate reasoning-based intelligence control [26], neuronal fuzzy controllers [27], fuzzy inference environment software with tuning [29], self-constructing neural fuzzy inference networks [30], fuzzy neural networks [31], evolving/dynamic fuzzy neural networks [32], and adaptive network-based fuzzy inference systems [33].

In this paper, a hybrid system based on two different soft-computing techniques—adaptive neural networks and fuzzy inference systems—is proposed to optimize the number of cluster heads that evenly distribute the load among sensors in a network. We refer to this hybrid system as an

adaptive neuro fuzzy clustering algorithm (ANFCA). The main contribution of the paper is highlighted as follows:

1. Firstly, in the system model, a first-order energy radio model was used to examine the energy consumption throughout the network.
2. Secondly, we designed an adaptive fuzzy logic inference system (AFLIS) with the help of fuzzy rules, sets, and membership functions that were updated (rules of AFLIS were updated) using input–output mapping of the hybrid systems. The output of the AFLIS was used as input for the neural network.
3. Thirdly, in ANFCA, the metrics were input into the fuzzy logic inference system and output was produced, which provided the information about the sensor nodes, whether it was capable or not of playing the role of cluster head. The output of the fuzzy logic inference system was handed to the neuro fuzzy logic inference system to elect the cluster head for the next round. The ANFCA used a supervised learning strategy to adjust the weight of the membership function of the AFLIS.
4. Fourthly, we present an approach to form clusters in which cluster heads aggregate data and send that data to the base station.
5. Finally, the proposed algorithm was simulated and the results were compared with LEACH, CHEF, and LEACH-ERE algorithms to shows the effectiveness of the ANFCA.

This paper is split into well-regulated systematic sections as follow: Section 2 provides a description about related works on green computing without heuristics and fuzzy-centric heuristics. Section 3 presents the proposed adaptive neuro-fuzzy algorithm for green computing in the IoT. Section 4 discusses the simulation and the analysis of the results. Section 5 describes the conclusion of the paper with future perspectives.

2. Related Works

There exist discreet numbers of clustering algorithms in the literature. Here, we reviewed the appropriate papers which were related to the proposed work.

2.1. Green Computing without Heuristics

Low-energy adaptive clustering hierarchy (LEACH) [34] was the first hierarchical clustering algorithm in sensor networks. There are two stages per clustering round in LEACH. The first one is related to cluster head election and formation of clusters within the network and the second one deals with data transmission to the cluster head known as the steady-state stage. A probabilistic model is proposed to choose a cluster head in the cluster setup phase; each sensor node has a certain probability of being assigned as cluster head per round. In general, the probability of a sensor node being elected as a cluster head depends upon a predefined threshold value. Every sensor node generates an arbitrary value between 0 and 1. Generated values of each sensor are compared with the threshold value to become cluster head for an ongoing epoch or round when generated value is below the threshold value. Each elected cluster head broadcasts a message using the carrier-sense multiple-access protocol to avoid inter-cluster interference. The strength of the received signal is used by each sensor node to determine which cluster head they want to join. After that, every cluster head gathers information from their member sensor nodes, and applies data aggregation, and then forwards the aggregated packet to the base station [35]. Thus, LEACH provides equal opportunity for each sensor node to become a cluster head with equal probability. But there are major shortcomings, as it does not take into account the energy consumption of each node, the geographical location of nodes are not included which causes asymmetrical classification of clusters in a network, and it does not use multi-hop nodes for transmission of data. Hybrid energy efficient distributed (HEED) [36] clustering protocol rectifies the shortcomings of LEACH in terms of uneven formation of clusters by including one extra parameter: the residual energy of nodes with nodes density (i.e., the proximity of neighbors' sensor nodes) for selection of cluster heads. Node density plays a major role in reducing the intra-cluster communication. Hybrid energy efficient distributed clustering also uses a probabilistic model

to elect temporary cluster heads, and every sensor node increases the probability of being a cluster head by twice in between rotations. Hybrid energy efficient distributed clustering also suffers from problems where some of the nodes are exempted from the cluster head selection process, and these nodes resolve this problem by pronouncing themselves as cluster head. In addition, several sensors may be exempted from all clusters or be freely available. Power-efficient gathering in sensor information systems (PEGASIS) [37] was introduced to save energy by making a chain of sensor nodes; it uses a greedy approach which means every node accepts delivery of data from its closest neighbors, and these acquired data are then transferred to another closest neighbor node. These assembled data keep on moving subsequently between nodes. Data are fused and then transmitted from specified nodes to the base station. The role of the designated node is replaced by another random node. Therefore, all the nodes deplete their energy proportionally or evenly distribute the load among nodes. Further, average energy spent in each cycle is reduced.

2.2. Green Computing Using Fuzzy-Centric Heuristics

Recently, fuzzy logic systems have been applied to elect cluster heads in sensors-enabled IoT networks. Gupta et al. [38] have proposed to choose a node as cluster head based on energy, density, and centrality of nodes. The main difference between the protocol proposed in Reference [38] and LEACH clustering is that this information is sent by node to the base station (known as a centralized approach). The base station is solely responsible for the selection of the cluster head. The base station processes these data with the help of a Mamdani-type fuzzy inference system, which gives output as a chance to decide the future of the preferred node if that would be suitable as a cluster head or not. The rest of the operations for a steady-state phase of that kind are similar to LEACH clustering. In Reference [39], another cluster head selection mechanism (CHEF) is proposed based on residual energy and local distance. Nodes select a cluster head using local information gathered from neighboring nodes, whereas in Reference [38] the cluster head is elected by the base station. Another improvement over the low-energy adaptive clustering hierarchy (LEACH) protocol is based on fuzzy logic (LEACH-FL) [40]. This protocol is proposed by Reference [37], apart from it, LEACH-FL has three distinct fuzzy variables: node density, energy level, and distance to base station. In this mechanism, the base station gathers information from sensor nodes and applies a Mamdani-type fuzzy inference system to figure out whether a node would be interpreted as a cluster head or not. Lee et al. [41] put forward a clustering head selection algorithm (LEACH-ERE) with the use of energy prediction techniques in accordance with fuzzy logic for homogenous WSNs. All of the above cluster head election mechanisms are based on fuzzy logic, and are intended to equalize the load among sensor nodes, but these are not able to tune the membership function or weight of the fuzzy descriptor to adapt to the environment.

The next one in this series is the cluster head election mechanism using the fuzzy logic (CHEF) protocol [39] that is almost the same as the Gupta fuzzy protocol. In CHEF, the base station is not responsible for selection of the cluster head; it does not gather any information from sensor nodes. The mechanism for selection of the cluster head is localized (a distributed approach) within a cluster. The setup phase is similar to the setup phase of LEACH. The CHEF protocol uses two fuzzy parameters: residual energy and local distance. The CHEF protocol works in rounds; in each round the sensor nodes select random numbers between 0 and 1, much like LEACH. If the chosen value is less than the threshold value, they calculate their chance using the fuzzy inference system. If the chance value of a tentative node is greater than all other chance values of sensor nodes, than it becomes the cluster head for the current round. It does far better than the Gupta protocol in terms of the number of cluster head selections; the Gupta protocol selects only a single cluster head per network (simulation was done under certain circumstances), although it is claimed that it can be increased, the process of creating more clusters is unclear [38].

Another improved version of the LEACH protocol based on fuzzy logic is LEACH-FL [40]. This protocol coupled with the above Gupta protocol (a centralized approach) has three distinct fuzzy variables: node density, energy level, and distance to base station. In this protocol, the base station gathers information from sensor nodes and applies a Mamdani-type fuzzy inference system to

determine whether a node would be interpreted as a cluster head or not. Lee et al. [41] put forward a clustering head selection algorithm (LEACH-ERE) to predict residual energy in accordance with fuzzy logic for homogenous sensors-enabled IoT. The chance value of a cluster head is determined with the aid of two fuzzy norms, expected residual energy, and residual energy of a node. It is similar to the LEACH protocol where each node makes the decision itself to become a cluster head or not, without the help of the base station (called a distributed or localized approach). The sensor node having both extra residual energy as well as expected residual energy, gains additional benefit in becoming a cluster head. However, LEACH-ERE does not consider the distance between the cluster head and base station, or the node density around the sensor node which can lead to uneven energy consumption over the network.

Recently Nayak and Devulpalli [42,43] proposed a new fuzzy-logic-based clustering algorithm where the base station is mobile, and each cluster head does not send aggregated data to the mobile station. There is one super cluster head (SCH) in the network area that gathers the aggregated data from cluster heads and only the SCH dispatches information to the base station. Similar to LEACH, in each round the cluster heads are selected using a probabilistic model. Furthermore, the SCH is elected among cluster heads based on a Mamdani-type fuzzy inference system. According to a distributed approach, each cluster head is determined by its chance value using three fuzzy descriptors: remaining battery power (residual energy), mobility (referring to when the BS changes its position, and then the distance between the SCH and the BS increases or decreases), and centrality (primarily focusing on how central the SCH is to other cluster heads for communication). The chance value is the summation of the centrality mobility and battery power. These fuzzy labels are taken as additives due to the increase or decrease in the mobility and centrality upon the increase or decrease in the mobility of the base station. The chance value that is greater, this cluster head becomes a super cluster head. So, the SCH degrades the transmission taken by nodes, consequently, it reduces the duration of the first node dead over a number of rounds and enhances the network lifetime over LEACH.

In Reference [44], Abidoye et al. present the significance of the IoT in wireless sensor networks. Energy-efficient models are presented for enabling service-oriented applications in IoT-enabled WSN areas in two stages: in the first stage, the clustering-based model is used for service of the application, and in second phase, an energy-aware model is designed. Basically, those approaches are good, but not good enough for IoT networks, and their performances are poor when considering those networks are static. As the IoT provides dynamic networks, there is a need to improve the algorithms, so we emphasize fuzzy-based techniques with adaptive neural networks, which adapt to the dynamic networks of the IoT as well. In Reference [45], Yan li et al. proposed an analytic hierarchy process and fuzzy-based energy management system for industrial equipment management, and showed intensive case studies over IoT networks. In Reference [46], fuzzy-based vehicular physical systems were analyzed in the Internet of Vehicles (IoV), which uses fuzzy frameworks with the Markov chain to optimize location-oriented channel access delay. Signal-to-inference ratios and channel access delays are used as parameters for channel quality measurement. Hu et al. proposed [47] another aspect of the IoV which enables communication at the edge with the help of fuzzy logic. The cluster heads or gateways (smart vehicle) are chosen using fuzzy parameter velocity, vehicle neighboring density, and antenna height. The proposed algorithm provides an optimal number of gateways to bridge the licensed sub 6-GHz communication with millimeter wave to enhance network throughput. In Reference [48], a genetic-based virtualization approach was used to develop a method to overcome the torrent delay and minimize the energy consumption in IoT-enabled sensor networks. In Reference [10], the proposed algorithm was used for proper deployment of sensor nodes for coverage and connectivity for agricultural purposes. There are two methods for deployment of sensor nodes based on seven metrics that quantified the qualities measurement of sensor nodes. Test-bed-based experiment (INDRIYA) is done for simulation purposes to show the effectiveness of the proposed algorithm.

All of the above protocols deal with fuzzy-logic-based algorithms, but none of them are able to tune the membership function or weight of the fuzzy descriptor. To the best of our knowledge, none

of the above are up to the mark for real implementation, where input–output pairs are changing according to the environment. An adaptive artificial neural network is another soft-computing technique where a supervised learning approach is used to adapt to the environment. Therefore, we propose a novel adaptive neuro-fuzzy clustering algorithm (ANFCA) using both fuzzy logic and a neural network to address the problem of leaning rate of membership function, balancing the load, and minimizing the energy consumption to improve the lifetime of the sensor-enabled IoT.

3. Adaptive Neuro-Fuzzy for Green Computing in IoT

In this section, the details of the proposed adaptive neuro fuzzy for green computing in IoT is presented.

3.1. System Model

We consider that there are N sensor nodes deployed randomly in the sensing field in order to sense the surroundings of the environment periodically. These sensor nodes form clusters using the proposed neuro-fuzzy system. Each cluster has one cluster head, which receives data from cluster members. All the sensors are stationary in nature, having equal initial energy and capability for sensing the environment, processing the data, and transmission. The radio link between the nodes is symmetric. It means the nodes require equal energy for transmission in both directions. The base station is outside of the network. Sensor nodes have the capability to adjust their transmission power depending upon the distance between receiving nodes.

We consider the first-order radio model to compute the energy requirement in the proposed work. Let the size of **the** packet be m bits. The total energy consumed in transmitting a packet of m bits across l meter distance between the sender and receiver is given by

$$E_{TNE}(m,l) = \begin{cases} m * E_{elect} + m * \varepsilon_{fsp} * l^2 & if\ l < l_o \\ m * E_{elect} + m * \varepsilon_{mpf} * l^4 & if\ l \geq l_o \end{cases} \quad (1)$$

The energy consumed to receive a packet of m bits from the sender node is given by

$$E_{RCE}(m) = m * E_{elect} \quad (2)$$

where E_{elect} represents information about electronic energy dissipation in the electronic circuit per bit. This is affected by several factors such as digital coding, acceptable bit-rate, modulation, etc. The ε_{fsp} and ε_{mpf} are the energy consumption factor in the free space path and multipath fading, respectively. When the source and receiver nodes are separated within the limit of the threshold value l_o($l_o = \sqrt{\mathcal{E}_{fsp}/\mathcal{E}_{mp}}$), it uses the free space model, otherwise its multipath fading channel will be used to computing the energy consumption for transmitting the message.

3.2. Adaptive Neuro-Fuzzy Clustering Algorithm

In this section, we propose our adaptive neuro-fuzzy clustering algorithm (ANFCA). The proposed algorithm combines the features of the adaptive fuzzy logic algorithm (ALFIS) and the adaptive neural fuzzy feature inference system (ANFIS), described in the following sections. The ALFIS is used to obtain training data for ANFIS. The output of the ANFLIS is used as input for the ANFIS, where the result is tuning, with weight adjustment, of the membership function of the antecedent and consequent of the fuzzy-rule-based system. In the last section, the phase of the proposed algorithm is presented.

3.2.1. Adaptive Fuzzy Logic Inference System

In this section, an adaptive fuzzy logic inference system (AFLIS) is presented to obtain information about a sensor node to become a cluster head. The output of the fuzzy logic inference system is passed as input data set for the next proposed adaptive neuro fuzzy inference system (ANFIS). We employed a Mamdani engine in the adaptive fuzzy logic inference system. Three metrics: residual energy (RE), node density (ND), and node distance to the base station (NDBS) were

considered to compute the observation about a node, whether it can play the role of cluster head or not. As a sensor node has limited power for computation and communication, and these battery powers are almost irreplaceable in nature, residual energy is the most viable parameter for cluster head selection. In addition, these cluster heads are not very far away from base station otherwise data transfer would consume more energy from the nodes. Therefore, node distance to the base station is taken as another factor. Those nodes in the vicinity of the cluster head define the second criterion of node density, as sensor nodes are dispersed in the surrounding area by air support, artificial arrangement or any other method. As a result, each sensor node has a different number of neighbor nodes; if we select nodes with a lower number of neighbors in their communication range and these neighbors are not much closer to each other, these nodes cannot communicate directly to the cluster head and need intermediate nodes for transmission, thus increasing communication cost. Therefore, node density was another parameter taken into account.

The linguistic variables of the three metrics are defined as follows: residual energy (RE) = (below, fair, top); node distance to the base station (NDBS) = (adjacent, midway, distant); and node density (ND) = (deficient, medium, compact). The triangular and trapezoidal fuzzy membership function was used over other membership functions (such as Gaussian, Bell or Sigmoidal) for achieving better performance in real-time scenarios. For below and top values of residual energy, adjacent and distant values of node distance to base station, and deficient and compact values of node density, trapezoidal membership functions were used. The triangular membership function was used for the rest of the values as illustrated in Figures 1–4. The probability (output of adaptive fuzzy inference system) of sensor nodes to be assigned with the responsibility of cluster head was defined by linguistic variable chance (CH) = (weakest, weaker, weak, medium, strong, stronger, strongest). Since we used three metrics in fuzzification, therefore it required a total $3^3 = 27$ rules that are shown in the Table 1. These rules were stored in the knowledge base component of the fuzzy inference system. There were two extreme rules: The first one was related to creating strong chances for assigning the responsibility of cluster head to a sensor node when the value of the residual energy of that sensor node was equal to top, the node density was compact in nature, and the node was adjacent to the base station. The second one was if the value of the residual energy was equal to below, the node was distant from the base station, and the node was deficient in node density, then a node would have a very weak chance to become a cluster head.

Table 1. Fuzzy knowledge database rules.

Rule	IF			THEN	Rule	IF			THEN
	RE	**NDBS**	**ND**	**CH**		**RE**	**NDBS**	**ND**	**CH**
1.	below	adjacent	deficient	weakest	15.	fair	midway	compact	medium
2.	below	adjacent	medium	weaker	16.	fair	distant	deficient	weakest
3.	below	adjacent	compact	weak	17.	fair	distant	medium	weaker
4.	below	midway	deficient	weakest	18.	fair	distant	compact	weaker
5.	below	midway	medium	weakest	19.	top	adjacent	deficient	strong
6.	below	midway	compact	weaker	20.	top	adjacent	Medium	stronger
7.	below	distant	deficient	weaker	21.	top	adjacent	compact	strongest
8.	below	distant	medium	weakest	22.	top	midway	deficient	medium
9.	below	distant	compact	weakest	23.	top	midway	medium	strong
10.	fair	adjacent	deficient	weak	24.	top	midway	compact	stronger
11.	fair	adjacent	medium	medium	25.	top	distant	deficient	strong
12.	fair	adjacent	compact	strong	26.	top	distant	medium	stronger
13.	fair	midway	deficient	weak	27.	top	distant	compact	stronger
14.	fair	midway	medium	weak	-	-	-	-	-

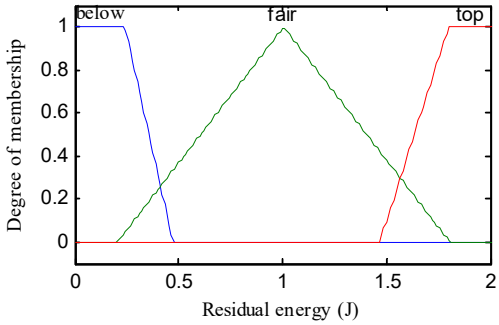


Figure 1. Membership function of RE (residual energy).

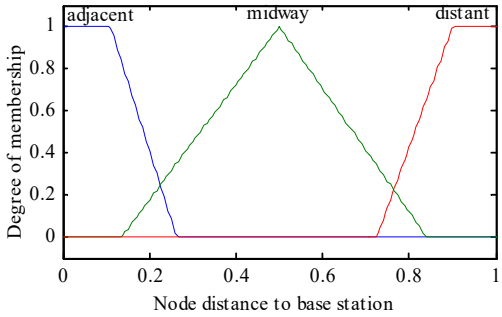


Figure 2. Membership function of NDBS (node distance to the base station).

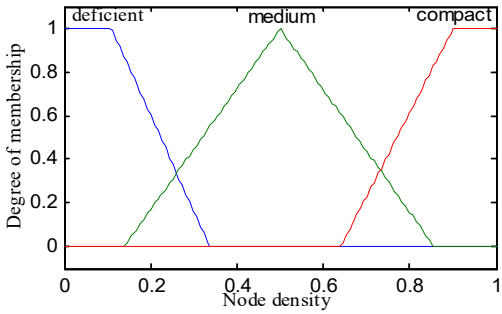


Figure 3. Membership function of ND (node density).

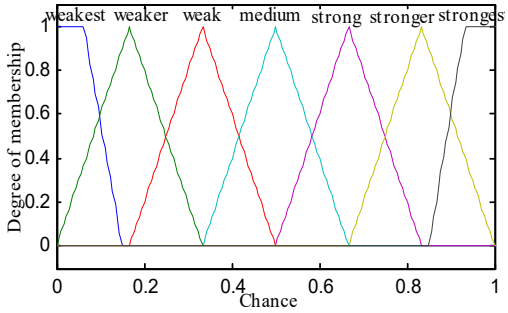


Figure 4. Membership function of CH (chance).

The adaptive fuzzy inference system works in four steps to compute the possibility of a node to evolve into a cluster head.

a. Fuzzification or Input Crisp Value: In this step, we input the three metrics: residual energy, node density, and distance to base station as crisp values in the fuzzy inference system. In

this step, the inference system creates membership functions for each metric that is the intersection points.

b. Knowledge Base or If–Then Rules: The knowledge base consists of all 27 rules, which runs concurrently on inputs and generates output as chance values. There are multiple inputs (three membership values), but selection is done among the minimum membership values which use fuzzy AND operator.
c. Aggregation: There are 27 rules in the fuzzy inference system, which give multiple outputs. In this step, we aggregate all the output to generate a single fuzzy output set using union fuzzy OR operator which choose maximum of rule evaluation.
d. Defuzzification: In this step, whether a sensor node can act as a cluster head or not is computed. For this purpose, we use a centroid method in the defuzzification step under the fuzzy set to get from aggregation, which is given by Equation (3).

$$NODE\ CHANCE\ (CH) = \int \mu_c(z) * zdy / \mu_c(z)dz \quad (3)$$

where $\mu_c(z)$ measures the rate of the membership function of the entity z within fuzzy set C, which is described as follows: $C = \{(z, \mu_P(z))/\ z\ \epsilon\ Z$, where Z denotes the universe of discourse.

3.2.2. Adaptive Neuro-Fuzzy Inference System

Fuzzy logic and artificial neural networks are good candidates for making smart artificial intelligence systems because of their generalization and non-linearity properties. We developed a hybrid system which consists of two different soft-computing techniques: fuzzy logic and artificial neural networks. We named the hybrid system an adaptive neuro fuzzy inference system (ANFIS). Fuzzy logic has expertise in the area of shapes but not on the subjective aspects of human learning into the procedure of exact quantitative analysis. But in any case, it does not have a characterized technique that can be utilized as a guide during the change from human idea into knowledge or rules-based fuzzy inference systems. It is also requires much time to adjust the membership function. Not at all like artificial neural networks, it has a higher ability in the learning procedure to adjust to its condition. Along these lines, the artificial neural network can be used to consequently alter the membership function and lower the rate of error in the assurance of tenets in fluffy rationale. Artificial neural networks are used for weight adjustment of the membership function of the antecedent and consequent of fuzzy-rule-based systems. Jang [49] proposed the ANFIS, which implements the Takagi–Sugeno fuzzy inference system of five layers. The ANFIS technique was intended to permit membership function and if–then rules to be developed in the light of already acquired data of metrics that are input or output data from the previously designed adaptive fuzzy inference system (AFLIS) in Section 4.1. In addition to the ANFIS, the fuzzy rules are tuned automatically, which is already used in adaptive fuzzy inference systems by using supervised learning. The ANFIS uses a trapezoidal membership function for weight adjustment. These membership functions were used with product inference rules in fuzzification level. The model of the proposed ANFIS with three inputs and one output is shown in Figure 5. Each input used the three membership functions following the Takagi–Sugeno type model containing 27 rules, and each of the nodes were governed by the if–then rules shown in Table 1. The antecedent part of the rules depicts a fuzzy subspace, whereas the subsequent part determines the output inside the fuzzy subspace.

-

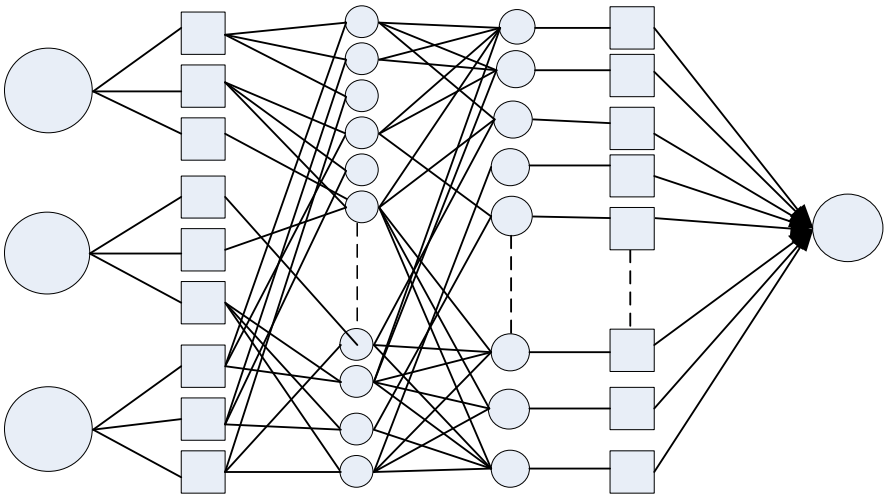


Figure 5. Three input type-3 adaptive neuro fuzzy inference system (ANFIS) with 27 rules and one output.

The ANFIS system is a feed-forward neural network with five layers using a supervised learning algorithm. These layers are denoted as fuzzy layer, T-norm layer, normalized layer, defuzzy layer, and aggregated layer, which represent the first, second, third, fourth, and fifth layers, respectively. The first and fourth layers have adaptive nodes, and the remaining layers have fixed nodes. There are three inputs: residual energy (RE), node distance to base station (NDBS), and node density (ND), and one output: chance (CH). We developed twenty-seven rules of "if–then" for the proposed ANFIS system based on the Takagi–Sugeno fuzzy inference model. These rules are

Rule 1 = If RE is below, NDBS is adjacent and ND is deficient Then F_1= S_1m + T_1n + U_1o + P_1
Rule 2 = If RE is below, NDBS is adjacent and ND is medium Then F_2= S_2m + T_2n + U_2o + P_2
Rule 3 = If RE is below, NDBS is adjacent and ND is compact Then F_3= S_3m + T_3n + U_3o + P_3
...
Rule 25 = If RE is top, NDBS is distant and ND is deficient Then F_{25}= S_{25}m + T_{25}n + U_{25}o + P_{25}
Rule 26 = If RE is top, NDBS is distant and ND is medium Then F_{26}= S_{26}m + T_{26}n + U_{26}o + P_{26}
Rule 27 = If RE is top, NDBS is distant and ND is compact Then F_{27}= S_{27}m + T_{27}n + U_{27}o + P_{27}

Where below, adjacent, and deficient are the membership functions or linguistic variables of inputs RE, NDBS, and ND (part of antecedent), respectively, and S_i, T_j, U_k are linear parameters of then part (consequent) of the Takagi–Sugeno fuzzy inference model. The linguistic variable for residual energy RE (M) = (below, fair, top) is represented as (M_1, M_2, M_3), node distance to base station NDBS (N) = (adjacent, midway, distant) is represented as (N_1, N_2, N_3) and node density ND (O) = (deficient, medium, compact) is represented as (O_1, O_2, O_3).

1. Fuzzy Layer: This section describes the nature of the node which is actually flexible according to backward pass (denoted by square adaptable node) that resembles each input variable relative to membership function. The membership function graph is plotted against each adaptable node to describe their output. Membership function follows Gaussian distribution as shown in Equation (4) or generalized bell-shaped membership function (see Equation (5)) which gives a value in the range of 0 and 1.

$$\mu_{M\alpha}(M) = exp\left[-\left(\frac{m - f_\alpha}{2d_\alpha}\right)^2\right] \quad (4)$$

$$\mu_{M\alpha}(M) = \frac{1}{1 + \left|\frac{m - f_\alpha}{d}\right|^2 e_\alpha} \quad (5)$$

The output of the first layer is given by

$$R_{1,\alpha} = \mu_{M\alpha}(M), \alpha = 1,2,3$$
$$R_{1,\alpha} = \mu_{N\alpha}(N), \alpha = 1,2,3$$
$$R_{1,\alpha} = \mu_{O\alpha}(O), \alpha = 1,2,3$$

where M is the input node to α and μ_{Mi}, μ_{Ni}, μ_{Oi} are the degree of membership function cross-ponding to linguistic variables M_i, N_i, and O_i and $\{d_i, e_i, f_i\}$ are referred to as a parameter set of the membership function or premise parameter. The bell-shaped membership function varies along with the values of the premise parameter set. In this layer, we can also use the triangular and trapezoidal membership function for the input node; they are also valid quantifiers for this node.

2. T-Norm Layer: In this layer, each node is non-adaptive in nature, and called as rule nodes which are depicted by the circle labeled with π (see Figure 5). These nodes represent the firing strength of each rule connected to it. To determine the results of each node, multiply all the signals (membership function) coming to the node. The T-norm operator uses generalized AND to calculate the antecedents/outputs at second layer of the rule.

$$R_{2\alpha} = T_\alpha = \mu_{M\alpha}(M) * \mu_{N\alpha}(N) * \mu_{O\alpha}(O), \alpha = 1,2,3 \quad (6)$$

where T_α is the output of each node which stands for each rule's firing strength.

3. Normalized Layer: Non-adaptive in nature nodes found in the normalized layer, which is known as normalized mode, are depicted by circles labeled as N (see Figure 5). The output of every node is an estimation of the proportion between the αth rule's firing strength to the summation of firing strength of all rules. The result at the third layer or normalized output can be expressed as

$$R_{3\alpha} = T_{\boldsymbol{n}\alpha} = \frac{T_\alpha}{\sum_\alpha T_\alpha}, \alpha = 1,2,3 \quad (7)$$

4. Defuzzy Layer: This layer consists of those nodes which have adaptive essence depicted by a square (see Figure 5). The output of the node is the product of normalized firing strength and individual rule. The output at the fourth layer can be given by

$$R_{4\alpha} = T_{\boldsymbol{n}\alpha} f_\alpha = T_{\boldsymbol{n}\alpha} (s_\alpha m + t_\alpha n + u_\alpha o + p_\alpha) \quad (8)$$

where $T_{\boldsymbol{n}\alpha(s_\alpha m + t_\alpha n + u_\alpha o + p_\alpha)}$ is the normalized firing strength from the normalized layer and $(s_\alpha m + t_\alpha n + u_\alpha o + p_\alpha)$ is a parameter in the node. Defuzzy layer parameters are also known as a consequent parameter.

5. Aggregated Output Layer: This layer consists of a single consolidated node as an output which is specified as non-adaptive in nature. This non-adaptive node gives information about the complete system performance evaluated by adding up all the approaching signals arriving at this layer from the previous node. Summation sign $\sum$ is used inside a circle to represent this aggregated output node. The output of the fifth layer is computed as

$$R_{5\alpha} = \sum_\alpha T_{\boldsymbol{n}\alpha} f_\alpha = \frac{\sum_\alpha W_\alpha f_\alpha}{\sum_\alpha w_\alpha} \quad (9)$$

The ANFIS uses the adaptive neuro fuzzy clustering algorithm (Algorithm 1) to train the premise and consequent parameters. The first layer resembles the adaptive node, which contains the non-linear premise parameter, and the fourth layer consists of the linear consequent parameters. Initially, the gradient descent or back propagation method is used as a learning algorithm. There may be a chance to stick in local minima and slow convergence rates while using back propagation. To rectify these problems Jang [49] uses a hybrid learning algorithm in which two learning strategies—least mean squares and gradient descent—are merged. The convergence rate of the hybrid learning algorithm is much faster than general artificial neural networks that never include local minima. The

working strategy of the ANFCA incorporates two passes: forward pass and backward pass. In the forward pass, input signals (premise metrics) are propagated layer by layer until the fourth layer. These metrics are fixed, and consequent metrics are updated using the least mean squares method. After obtaining the output data at the fourth layer, the data are compared with the actual output and the error is calculated. Now, in the backward pass, the errors which occurred due to the comparison of the output generated in the forward pass and the actual output are sent back to the adaptive node of the first layer. At the same time, the membership functions (premise metrics) are updated using the gradient descent method or back propagation method. During this time, consequent metrics are fixed. Each level of learning is called an epoch. The proposed algorithm works in three phases: selection phase, cluster formation phase, and transfer phase. In the first phase, cluster heads are selected. In the second phase, clusters are formed by calculating their area based upon radius. In the final phase, cluster heads transfer the aggregated data to the base station. The precise description of each phase is presented in the next section.

Algorithm 1- Adaptive Neuro Fuzzy Clustering Algorithm (ANFCA)

1. **Begin**
2. **Input:** Given input training pattern, {RE, NDBS, ND} and maximum number of Epoch to E_{max}. // obtained from first modeling mamdani type fuzzy inference system.
3. **Output** {CH}
4. **Process**
5. **for** E=1 to E_{max}.
6. Input the training data into first layer of Takagi-sugeno inference engine.
7. Membership function $\mu_{M\alpha}(M)$ tuned using Equation (4) and Equation (5).
8. Adjust the firing strength of each node (T_α), using Equation (6) in non-adaptive T-norm layer.
9. Normalize the firing strength of each node (W_{ni}) using Equation (7) in normalized layer.
10. Defuzzification of each node using Equation (8).
11. Aggregated output is produced for each node using Equation (9) in fifth layer.
12. **END**

3.2.3. Phases of the Algorithm

The proposed algorithm of the ANFCA works in three phases as follow.

3.2.3.1. Selection Phase

Initially, the base station starts the operation of clustering; it broadcasts a beacon message (request for IDs, residual energy, distance to base station, and its density) in the network. All the sensor nodes reply an acknowledgment with requested information. Every node estimates the distance between base station and itself using received signal strength indicator. Equation (10) determines the received signal strength.

$$S_r = S_o + 10\,\beta\, log\left(\frac{a_r}{a_o}\right) + \delta \quad (10)$$

$$S_r = S_o 10^{\frac{RSSI-\theta}{10\,\alpha}} \quad (11)$$

Where S_o (in decibel meter) is the reference signal strength at distance a_o, β is used to represent path loss exponent ($2 \le \beta \le 4$), and a_r is the actual distance. Gaussian random variable is represented by δ having mean zero and variance σ^2 (in decibel meter $4 \le \sigma \le 12$). The distance between the base station and a node is calculated using Equation (11). Where θ is the received signal strength in one meter distance from the base station without any obstacles. The base station triggers election procedures for cluster heads choosing some nodes as cluster heads randomly. These temporary cluster head nodes are gone through AFLIS to check the validity of each node whether they can play the role of cluster head or not. Afterwards, output of AFLIS is recorded and trained using ANFIS, and the final

output is recorded. If the nodes have fulfilled the selection criteria for a cluster head, then these nodes are designated as permanent cluster heads for the present round. The selection procedure for a cluster head is rehashed in each cycle so it is potentially able for the sensor to get opportunity to become a part of cluster head group, therefore all nodes exhaust their energy relatively that upgrades the network lifetime.

3.2.3.2. Cluster Formation Phase

The ANFCA forms variable sizes of clusters; the cluster head manages the number of nodes or cluster sizes that eventually balances the load with periodic replacement of cluster heads. Initially, selected cluster heads calculate their radius for formation of cluster phase. The mean radius of each cluster head is obtained by the Equation (12)

$$Cr_{minimum} = \sqrt{\frac{A \times A}{\pi \times n \times k}} \quad (12)$$

Whereas n represents the number of nodes deployed inside the network of area $A \times A$, and k represents the number of clusters. Generally, a cluster has at least a radius equal to Cr. After radius calculation, each cluster head acquires an area according to their radius then sends a join message to each node within the cluster. The nodes make the decision based upon the received signal strength to join which cluster. The sensor node which does not receive any join message declares themselves as cluster head and sends their data directly to the base station. The nodes within the defined radius are called member nodes for their respective clusters. Now, cluster heads schedule a time-division multiple-access approach to gather data from member nodes. This time-division multiple-access schedule reduces intra-cluster collision in addition to cutting down on energy utilization because of the limit on the number of messages exchanged between member nodes. Each cluster head broadcasts time-division multiple-access schedule information in their clusters to their member nodes on when they are able to send messages to their cluster head. The cluster head dictates the time slot for every node, only in their specific time slot can nodes send their message to the cluster head. Therefore, nodes enter the wake-up mode in their time slot, otherwise they go into sleep mode. In this way, nodes conserve their energy. The cluster heads gather messages from their member nodes and apply data aggregation to form single packets of a fixed size.

3.2.3.3. Transfer Phase

According to the time-division multiple-access schedule, the cluster head gathers and aggregates data, and then communicates to the base station directly without using any relay node. The number of messages exchanged is limited to the number of cluster heads which reduces the energy consumption.

4. Simulation

In this section, the performance of the proposed adaptive neuro fuzzy clustering algorithm (ANFCA) was analyzed. The proposed algorithm was simulated by writing a script in MATLAB (R2019a, MathWorks, Natick, MA, USA) and using simulator tools: FIS and ANFIS. The simulator FIS consists of a fuzzy inference model and membership function for each considered metric: residual energy, node density, and node distance to the base station. The ANFIS simulator produced the output that determined the cluster head. The proposed algorithm ANFCA was compared with LEACH, fuzzy-logic-based CHEF, and energy prediction technique using fuzzy-logic-based LEACH-ERE to show its effectiveness.

4.1. Simulation Environment

In this section, the simulation parameters used to conduct simulation of the ANFCA are presented. We considered a 200 × 200 node simulation area of the network, where 200 sensor nodes were distributed randomly. The sensing capabilities of the nodes were limited to 5 m and they were

allowed to transfer data within a 25-meter range in a symmetric way. The simulation cycle time was approximately 60 μs, and it ran until all nodes had died. The size of the packets were 512 bits. The simulation metrics and their values are shown in Table 2.

Table 2. Modeling framework.

Metrics	Specification
Number of nodes	200
Rectangular area	200 × 200 m^2
Node sensing range	5 m
Node transmission range	25 m
Base station location	(200,170)
Packet size m	512 bits
Initial Energy	2 J
E_{TDA}	5 nJ/bit/message
E_{TNE}	50 nJ/bit
$\mathcal{E}_{fsp}$	10 pJ/bit/m^2
$\mathcal{E}_{mpf}$	0.0013 pJ/bit/m^4
Cycle time	60 μs

Evaluation Metrics

- Network Lifetime: Lifetime definition of the network is application dependent, and it may be stated that as the tenure spans from the start, it is the functioning of the network to a moment when a certain percentage of the nodes have died or the network will be disconnected. In this paper, we considered the simulation time until 90% of the nodes were dead.
- (First node death) FND, (Half node death) HND and (Last node death) LND: The round at which the death of the first node occurred was defined as FND. Similarly, the round at which half of the nodes had died was defined as HND. The round at which the last node death has occurred was taken as LND**.**
- Average Residual Energy: Defined as the mean of residual energy of alive nodes in the network with respect to rounds.
- Average Energy Consumption: Defined as the summation of overall energy consumption taken place during the sensing and transmission by each sensor node to the number of sensor nodes with respect to rounds.
- Standard Deviation of Residual Energy: The standard deviation of residual energy is the square root of variance of residual energy of all the sensor nodes. It shows the variation of residual energy around the mean.

4.2. Simulation Results

4.2.1. Network Lifetime Over Rounds

Figure 6 shows the results obtained in the simulation for functioning nodes with respect to each round. It was observed that 90% of all 200 nodes had died by 2000 rounds, and the remaining 10% stretched the lifetime of the network up to another 100 rounds (total: 2100 rounds) for the LEACH algorithm, whereas CHEF showed little improvement over the classical LEACH (20% improvement in network lifetime) which ran up to 2220 rounds smoothly, and there were still 20 nodes alive. The LEACH-ERE initially showed up to 800 rounds with only 20–30 nodes having died, and thereafter the death rate of the nodes increased and almost followed the CHEF curve. The LEACH-ERE showed a 4–5% enhancement over the CHEF and 25% over LEACH. The LEACH-ERE ran up to 2300 rounds. Apart from this proposed algorithm, the ANFCA showed a steady death rate of sensor nodes; at up to 1000 rounds, only 10% of sensor nodes (20 nodes) had died, and thereafter it followed almost a similar curve to the LEACH-ERE up to 1200 rounds. The ANFCA lasted up to 2300 rounds until all

200 sensor nodes (100%) had died. It was clearly observed that the proposed ANFCA runs for a longer time compared with the state-of-the-art algorithms. It is due to the fact that the neuro fuzzy system is employed to rotate the cluster head responsibility among the sensors.

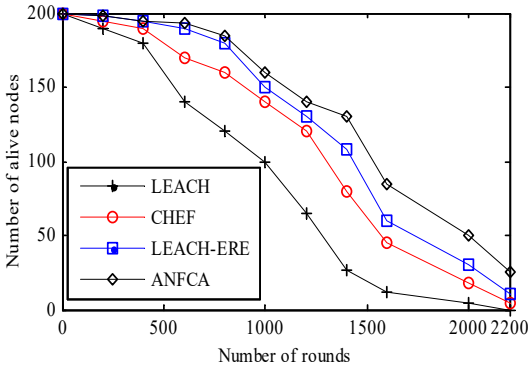


Figure 6. Number of functioning nodes over the rounds.

Figure 7 shows the percentage of nodes that died over the increasing number of rounds. From the simulation results, it was observed that the proposed ANFCA does far better than LEACH and LEACH-ERE. Initially, in the LEACH algorithm, the node death percentage rate slowly increased up to 500 rounds, but thereafter there was a sharp drop from 1400 rounds onwards, and all 200 nodes (100%) died before reaching 2200 rounds. In the case of the ANFCA, about 15% more nodes were still alive compared with the LEACH, and 5% of nodes were still alive compared with the LEACH-ERE after completing 2200 rounds, respectively. The rate of node death for the ANFCA was very slow compared to the state-of-the-art algorithms. It is because the proposed algorithm uses a supervised learning approach for the membership function, which is responsible for updating the membership weight function and lowering the energy consumption rate.

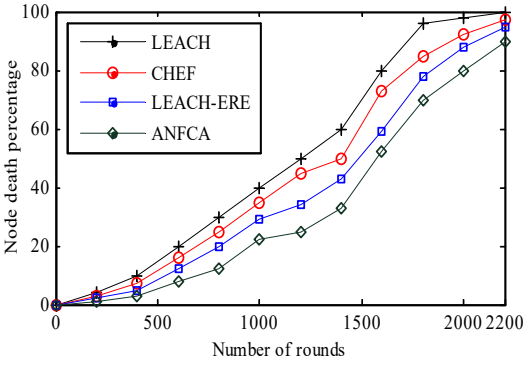


Figure 7. Node death percentages over the rounds.

Table 3 shows the comparative view of the metrics FND, HND, and LND for the proposed algorithm ANFCA and all of the state-of-the-art algorithms with respect to rounds. Figure 8 shows a comparative view of the death percentages' connections with FND, HND, and LND for LEACH, CHEF, LEACH-ERE, and ANFCA. It was observed that FND for LEACH was around the 96th round, FND occurred for ANFCA at the 260th round, which was almost two and half times more than that of LEACH, and the last node died at 1970 rounds for LEACH, whereas LND occurred for ANFCA at the 2310th round. Figure 8 and Table 3 show that the proposed algorithm did far better than the state-of-the-art algorithms, and that the lifetime of the network was enhanced because of the lower death rate of the nodes.

Table 3. Node death rate percentages up to 2500 rounds.

Death percentage (%)	LEACH	CHEF	LEACH-ERE	ANFCA
FND	96	150	205	260
20	600	827	1107	1224
40	934	1223	1536	1707
HND	1167	1400	1665	1810
60	1386	1631	1885	1972
80	1600	1795	1994	2206
LND	1970	2056	2140	2310

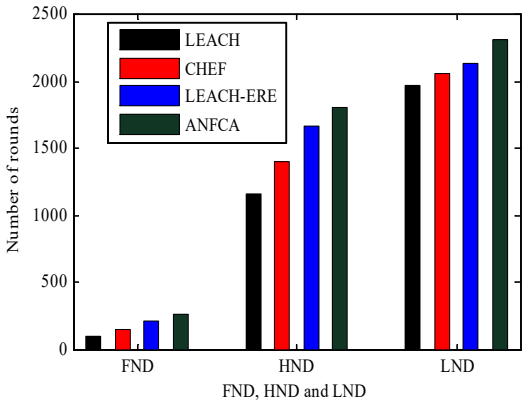


Figure 8. FND, HND, and LND results over the rounds.

4.2.2. Energy Expenditure over Rounds

In this simulation, we show the comparative study of energy expenditure across LEACH, CHEF, LEACH-ERE, and ANFCA. Figure 9 depicts the average residual energy versus the number of rounds for the ANFCA and the state-of-the-art algorithms. Initially, all the sensor nodes had equal energy at 2 joules. The LEACH, CHEF, and LEACH-ERE lost almost equal amounts of energy at 425 rounds, and around 1.72 joule of the average residual energy was remaining out of the initial 2 joules. The energy consumption of the nodes was calculated with the help of Equation (1). The ANFCA outperformed compared to the state-of-the-art algorithms; at the same point (425 rounds), the residual energy of the nodes was approximately 1.86 joule. As the number of rounds increased, LEACH performed the worst among the other algorithms, and all the remaining energy of the nodes was exhausted near 1800 rounds. The CHEF and LEACH-ERE showed better performance than LEACH, in terms of energy usage, with about 11% (up to 2000 rounds) and 20% (up to 2200 rounds), respectively. Overall, in this simulation the proposed algorithm ANFCA did far better than all the other algorithms. The ANFCA ran up to 2480 rounds, and the average remaining residual energy of the nodes was still 0.45 joule.

Figure 10 depicts the average energy consumption versus number of rounds for the ANFCA and the other algorithms. It was observed that, initially, all four algorithms—LEACH, CHEF, LEACH-ERE, and ANFCA—followed the same curvature and consumed almost an equal amount of energy up to 455 rounds, around 0.25 joule. Yet, the ANFCA consumed only 1.67 joule out of 2 joules up to 2200 rounds. In fact, as there was growth in the number of rounds, the LEACH consumed energy much faster than other algorithms because of the probabilistic selection cluster head method and because it does not include the residual energy parameter, whereas CHEF, LEACH-ERE, and ANFCA include fuzzy logic to select a cluster head. The CHEF consumed more energy towards increasing the number of rounds compared with the LEACH-ERE, whereas the proposed algorithm ANFCA

showed that the rate of consuming energy by nodes was uniform until the last node death. The ANFCA consumed 10%, 15%, and 40% less energy than LEACH-ERE, CHEF, and LEACH, respectively. This is because cluster head selection is done initially with the AFLIS model, and thereafter it is refined through the selected cluster head ANFIS model. Thus, overall, the ANFCA appears to be energy-efficient, which ultimately enhances the network's lifetime.

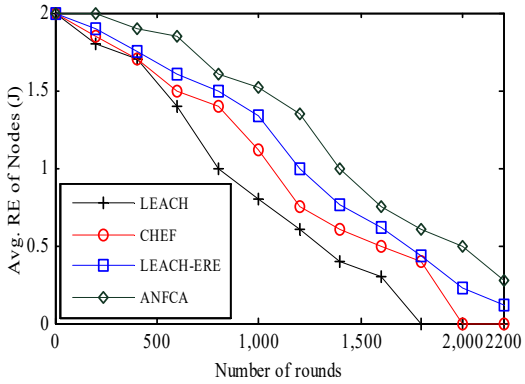


Figure 9. Avgerage residual energy over the rounds.

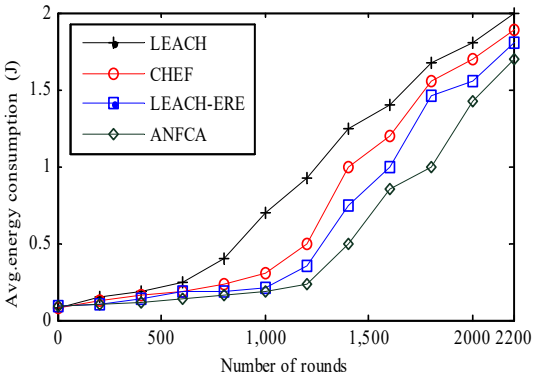


Figure 10. Avgerage energy consumed by nodes over the rounds.

4.2.3. Standard Deviation of Residual Energy

Uniform consumption of energy is highly desirable for load balancing among the sensor nodes which increases the lifetime of the networks. Therefore, we examined the standard deviation of residual energy for all the nodes in the networks and show the variation around the rounds as well as the diaspora from the mean. The energy dissipated by the cluster head and member node per cycle "c" (rounds) was evaluated. The energy consumption by cluster head is expressed as

$$E_{dst}^{c}(h) = \begin{cases} (x_n - 1)mE_{elect} + x_n mE_{da} + mE_{elect} + m\varepsilon_{mpf} l_{h\ to\ BS}^{4}, & h \in CH \\ mE_{elect} + m\varepsilon_{fsp} l_{h\ to\ BS}^{2}, & h \in non - CH \end{cases} \quad (13)$$

where x_n represents the total number of sensor nodes that are actually connected to the cluster head as well as the cluster head node, h is used to represent the nodes, and m is the m-bit data. The average (mean) dissipated energy for a cycle can be computed as

$$\mu(E_{dst}) = \frac{\sum_{h \in N} E_{dst}^{c}(h)}{N} \quad (14)$$

The residual energy for the next cycle (c + 1) is calculated as

$$E_{res}^{c+1}(h) = E_{res}^{c}(h) - E_{dst}^{c}(h) \quad (15)$$

The average (mean) residual energy for next cycle is expressed as

$$\mu\,(E_{res}) = \frac{1}{N}\sum_{i\,\epsilon\,n} E^{c}_{res}(h) \tag{16}$$

The standard deviation of residual energy is the square root of the variance of the residual energy, and is given by

$$\sigma(E_{resdiual}) = \sqrt{\frac{1}{N}\sum_{i\,\epsilon\,n}[\mu(E_{res}) - E_{res}(h)]^2} \tag{17}$$

Figure 11 shows the standard deviation of residual energy versus the rounds for all of the algorithms considered in this simulation. The broader the area of standard deviation, the higher the value of a node's residual energy within one mean (that means that each node dissipates almost equal amounts of energy relatively). The LEACH showed a lower coverage of area among the other algorithms, which means that nodes in the LEACH method have variable amounts of energy dissipation. The CHEF showed much improvement over the LEACH by 27%, as 80% of nodes were within one mean (all 80% had almost equal amounts of residual energy). The LEACH-ERE and the ANFCA were closer to each other on basis of coverage; both the algorithms had coverage of 95% of total nodes. The ANFCA provided a little smoother graph over the LEACH-ERE. For example, as the ANFCA ran up to 2000 rounds, the graph progressed more smoothly. This is because the ANFCA balanced the load using a fuzzy neural system and fairly balanced the energy consumption among the sensor nodes.

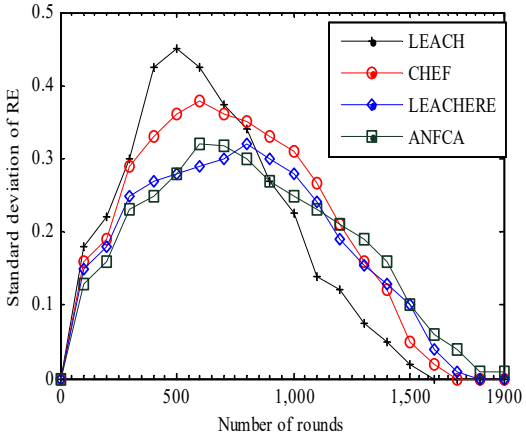


Figure 11. Standard deviation over rounds.

Figure 12 shows the alternative representation of the standard deviation of residual energy of functioning nodes for better visualization. As seen from the bar graph in Figure 12, when the number of functioning nodes was 40, the value of the standard deviation for LEACH was 0.045. This was higher than the other state-of-the-art algorithms, whereas the ANFCA had a standard deviation of residual energy equal to 0.027, which means that the load among the nodes was shared fairly in terms of energy consumption. Lowering the value of the standard deviation means a uniform distribution of the load from the mean. That means energy consumption of the load is evenly distributed among the sensor nodes. When the number of alive nodes was between 80 and 120, the values of the standard deviation for the LEACH-ERE was less than the ANFCA. This shows that for lower numbers of nodes, the LEACH-ERE distributed the load more fairly than the proposed algorithm ANFCA, but when the number of nodes increased between 160 and 200, the ANFCA did better than the state-of-the-art algorithms. Lowering the value of the standard deviation of energy means broadening the coverage area, which includes all the sensors nodes within one mean. This shows that the ANFCA has a better capability to distribute the load evenly among the sensor nodes. This is due to the fact that the

membership function of residual energy is updated as a result of the role of the cluster head being changed every round among the other sensor nodes.

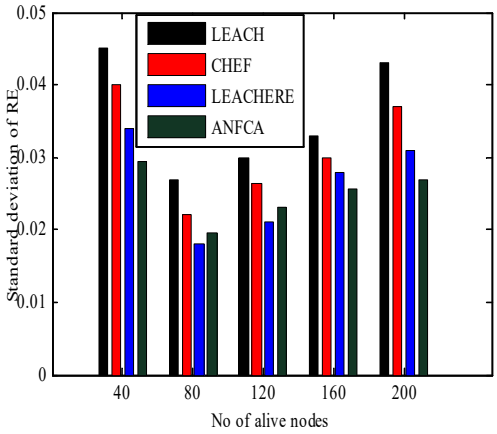


Figure 12. Standard deviation over alive nodes.

5. Conclusion and Future Perspectives

Cluster formation in an evenly and energy-efficient manner is of the utmost priority in a sensors-enabled IoT environment. In this paper, an energy-efficient neuro fuzzy hybrid approach for load balancing was proposed. The key components of the ANFCA are an adaptive neural network and a fuzzy logic inference system, which combined the use of residual energy, node distance to base station, and node density to select a cluster head. With the training data of ANFIS from the fuzzy logic system, the membership function and rules can be legitimately tuned to refine the cluster formation process according to the current situation of the network. The results proved that the proposed algorithm ANFCA formulated the evenly distributed clusters, as well as lowered the energy dissipation in the network, which directly improved the network's lifetime. The simulation results revealed that the proposed algorithm's performance was one step ahead of LEACH and the fuzzy-logic-based CHEF and LEACH-ERE with regards to cluster formation, energy dissipation, and network lifetime, because ANFCA combined the features of an artificial neural network learning strategy into fuzzy logic. The proposed algorithm could be useful in monitoring in the agriculture field. Our proposed work follows a centralized algorithm where all decisions are made by the base station only. In the future, we plan to extend this work to a distributed algorithm rather than a centralized algorithm, which is suitable for a scalable, fault-tolerant, cluster-based network, which considers RFID-enabled smart sensors with multiple gateways for IoT networks. These multiple gateways are loaded with heavy data, thus it must use distributed approaches to balance the load.

Author Contributions: Conceptualization, P.K.K.; Formal analysis, R.K.; Investigation, P.K.K.; Methodology, P.K.K.; Resources, V.K.; Supervision, S.K.; Writing – review and editing, U.D.

Funding: The research was supported by Manchester Metropolitan University, UK and Jawaharlal Nehru University, New Delhi, India, under the grant UPE-II.

Acknowledgments: The research was supported by Manchester Metropolitan University, UK and Jawaharlal Nehru University, New Delhi, India, under the grant UPE-II.

Conflicts of Interest: The authors declare no conflict of interest.

References

1. Farhan, L.; Kharel, R.; Kaiwartya, O.; Hammoudeh, M.; Adebisi, B. Towards green computing for Internet of things: Energy oriented path and message scheduling approach. *Sustain. Cities Soc.* **2018**, *38*, 195–204.
2. Aliyu, A.; Abdullah, A.H.; Kaiwartya, O.; Cao, Y.; Lloret, J.; Aslam, N.; Joda, U.M. Towards video streaming in IoT Environments: Vehicular communication perspective, *Comput. Commun.* **2018**, *118*, 93–119.

3. Kaiwartya, O.; Abdullah, A.H.; Cao, Y.; Altameem, A.; Prasad, M.; Lin, C.T.; Liu, X. Internet of Vehicles: Motivation, Layered Architecture, Network Model, Challenges, and Future Aspects. *IEEE Access* **2016**, *4*, 5356–5373.
4. Kumar K.; Kumar S.; Kaiwartya, O.; Cao, Y.; Lloret, J.; Aslam, N. Cross-Layer Energy Optimization for IoT Environments: Technical Advances and Opportunities. *Energies,* **2017**, *10*, 2073.
5. Verma, J.K.; Kumar, S.; Kaiwartya, O.; Cao, Y.; Lloret, J.; Katti, C.P.; Kharel, R. Enabling green computing in cloud environments: Network virtualization approach toward 5G support. *Trans. Emerg. Telecommun. Technol.* **2014**, *25*, 81–93.
6. Kaiwartya, O.; Kumar, S.; Lobiyal, D.; Abdullah, A.; Hassan, A. Performance improvement in geographic routing for vehicular Ad Hoc networks. *Sensors* **2014**, *14*, 22342–22371.
7. Ullah, F.; Abdullah, A.; Kaiwartya, O.; Arshad, M. Traffic priority-aware adaptive slot allocation for medium access control protocol in wireless body area network. *Computers* **2017**, *6*, 9.
8. Cao, Y.; Yang, S.; Min, G.; Zhang, X.; Song, H.; Kaiwartya, O.; Aslam, N. A Cost-Efficient Communication Framework for Battery-Switch-Based Electric Vehicle Charging. *IEEE Commun. Mag.* **2017**, *55*, 162–169.
9. Kaiwartya, O; Kumar, S; Abdullah, H.A. Analytical model of Deployment Methods for Application of Sensors in non-Hostile Environment. *Wireless Pers. Commun.* **2017**, *97*, 1517–1536.
10. Kaiwartya, O.; Abdullah, A.H.; Cao, Y.; Raw, R.S.; Kumar, S.; Lobiyal, D.K.; Isnin, I.F.; Liu, X.; Shah, R.R. T-MQM: Testbed-Based Multi-Metric Quality Measurement of Sensor Deployment for Precision Agriculture—A Case Study. *IEEE Sensors J.* **2016**, *16*, 8649–8664.
11. Dohare, U.; Lobiyal, D.K.; Kumar, S. Energy balanced model for lifetime maximization in randomly distributed wireless sensor networks. *Wireless Pers. Commun.* **2014**, *78*, 407–428.
12. Aanchal, Kumar, S.; Kaiwartya, O.; Abdullah, A.H. Green computing for wireless sensor networks: Optimization and Huffman coding approach. *Peer-to-Peer Netw. Appl.* **2017**, *10*, 592–609.
13. Liu, A.-F.; Zhang, P.-H.; Chen, Z.-G. Theoretical analysis of the lifetime and energy hole in cluster based wireless sensor networks. Journal of parallel and distributed computing. *J. Parallel Distrib. Comput.* **2011**, *71*, 1327–1355.
14. Khasawneh, A; Latiff, M; Kaiwartya, O; Chizari, H. Next forwarding node selection in underwater wireless sensor networks (UWSNs): Techniques and challenges. *Information* **2016**, *8*, 1–25.
15. Khatri, A.; Kumar, S.; Kaiwartya, O.; Aslam, N.; Meena, N., Abdullah, A.H. Towards green computing in wireless sensor networks: Controlled mobility–aided balanced tree approach. *Int. J. Commun. Syst.* **2017**, *31*, e3463.
16. Zadeh, L.A. Fuzzy sets. *Inf. Control* ***1965,*** *8*, 338–353.
17. Takagi, T.; Sugeno, M. Fuzzy identification of systems and its applications to' modeling and control. *IEEE Trans. Sys. Man. cybern,* **1985**, *15*, 116–132.
18. McCulloch, W.S.; Pitts, W.H. A logical calculus of the ideas immanent in nervous activity. *Bull. Math. Biophys.* **1943**, *5*, 115–133.
19. Rosenblatt, F. The Perceptron: A Probabilistic Model for Information Storage and Organization in the Brain. *Psychol. Rev.* **1958**, *65*, 386–408.
20. Rosenblatt, F. *Principles of Neurodynamics; Perceptrons and the Theory of Brain Mechanisms*. Spartan Books: Washington DC, WA, USA, 1962. Available online: https://catalog.hathitrust.org/Record/000203591 (21, 02, 2019)
21. Rosenblatt, F. *On the Convergence of Reinforcement Procedures in Simple Perceptron.* Cornell Aeronautical Laboratory: Buffalo, NY, USA, 1960.
22. Widrow, B.; Lehr, M.A. 30 years of adaptive neural networks: perceptron, Madaline, and back propagation. *Proc. IEEE*, **1990**, *78*, 1415–1442.
23. Widrow, B.; Winter, R.G.; Baxter, R.A. Layered neural nets for pattern recognition. *IEEE Trans. Acoustics Speech Sig. Process.* **1988**, *36*, 1109–1118.
24. Winter, R.; Widrow, B. MADALINE RULE II: a training algorithm for neural networks. In Proceedings of IEEE 1988 International Conference on Neural Networks, San Diego, CA, USA, 24–27 July 1988. pp. 401–408 ,1988.
25. Lin, C.-T.; Lee, C.S.G. Neural-network-based fuzzy logic control and decision system. *IEEE Trans. Comput.* **1991**, *40*, 1320–1336.
26. Berenji, H.R.; Khedkar, P. Learning and tuning fuzzy logic controllers through reinforcements. *IEEE Trans. Neural Netw.* **1992**, *3*, 724–740.
27. Nauck, D.; Kruse, R. Neuro-Fuzzy Systems for Function Approximation. *Fuzzy Sets Sys.* **1999**, *101*, 261–271.
28. Lin, C.-T. FALCON: a fuzzy adaptive learning control network. In Proceedings of the NAFIPS/IFIS/NASA '94. Proceedings of the First International Joint Conference of The North American Fuzzy Information

Processing Society Biannual Conference. The Industrial Fuzzy Control and Intellige, San Antonio, TX, USA, 18–21 December 1994. pp. 228–232.
29. Tano, S.; Oyama, T.; Arnold, T. Deep Combination of Fuzzy Inference. *Fuzzy Sets Sys.* **1996**, *8*, 338–353.
30. Juang, C.F.; Lin, C.-T. An online self-constructing neural fuzzy inference network and its applications. *IEEE Trans. Fuzzy Sys.* 1998, 6, 12–32.
31. Figueiredo, M.; Gomide, F. Design of fuzzy systems using neuro fuzzy networks. *IEEE Trans. Neural Netw.* **1999**, *10*, 815–827.
32. Nauck, D.; Kalwon, F.; Kruse, R. *Foundation of Neuro-Fuzzy Systems.* John Wiley & Sons, Inc.: New York, NY, USA, 1997.
33. Jang, R. Neuro-Fuzzy Modeling: Architectures, Analysis and Application. PhD Thesis, University of California, Berkley, CA, USA. July 1992.
34. Heinzelman, W.R.; Chandrakasan, A.; Balakrishnan, H. Energy efficient communication protocol for wireless micro sensor networks. In Proceedings of the 33rd Annual Hawaii International Conference on System Sciences, Maui, HI, USA, USA, 7 January 2000, pp. 3005–3014.
35. Heinzelman, W.B.; Chandrakasan, A.P.; Balakrishnan, H. An application-specific protocol architecture for wireless micro sensor networks. *IEEE Trans. Wireless Commun.*, **2002**, *1*, 660–670.
36. Younis, O.; Fahmy, S. HEED: A Hybrid, Energy Efficient, Distributed clustering approach for Ad Hoc sensor networks. *IEEE Trans. Mobile Comp.* **2004**, *3*, 366–379.
37. Lindsey, S.; Raghavendra, C.S.; PEGASIS: Power efficient gathering in sensor information systems. In Proceedings of IEEE Aerospace Conference, Big Sky, MT, USA, 9–16 March 2002. pp. 1125–1130.
38. Sampalli, S; Riordan, D.; . Gupta, I. Cluster-head election using fuzzy logic for wireless sensor networks. In Proceedings of the 3rd Annual Communication Networks and Services Research Conference, Halifax, Canada, May 2005.
39. Kim, J.; Park, S.; Han, Y.; Chung, T. CHEF: Cluster head election mechanism using fuzzy logic in wireless sensor networks. In Proceedings of 2008 10th International Conference on Advanced Communication Technology, Gangwon-Do, South Korea, 17–20 February 2008. pp. 654–659.
40. Ran, G.; Zhang, H.; Gong, S. Improving on LEACH protocol of wireless sensor networks using fuzzy logic. *J. Inf. Comput. Sci.* **2010**, *7*, 767–775.
41. Lee, J.S.; Cheng, W.L. Fuzzy-Logic-Based Clustering Approach for Wireless Sensor Networks Using Energy Predication. *IEEE Sensors J.* **2012**, *12*, 2891–2897.
42. Nayak, P.; Devulapalli, A. A Fuzzy Logic-Based Clustering Algorithm for WSN to Extend the Network Lifetime. *IEEE Sensors J.* **2016**, *16*,137–144.
43. Nayak, P.; Anurag, D. Bhargavi, V.V.N.A. Fuzzy based method super cluster head election for wireless sensor network with mobile base station (FM-SCHM). In Proceeding 2nd International Conference Advance Computational Methodology, 2013. pp. 422–427.
44. Abidoye, A.P.; Obagbuwa, I.C. Models for integrating wireless sensor networks into the Internet of Things. *IET Wireless Sensor Sys.* **2017**, *7*, 65–72.
45. Li, Y.; Sun, Z.; Han, L.; Mei, N. Fuzzy Comprehensive Evaluation Method for Energy Management Systems Based on an Internet of Things. In *IEEE Access* 2017, 5, 21312–21322.
46. Kasana, R.; Kumar, S.; Kaiwartya, O.; Kharel, R.; Lloret, J.; Aslam, N.; Wang, T. Fuzzy-Based Channel Selection for Location Oriented Services in Multichannel VCPS Environments. *IEEE Internet Things J.* 2018, 5, 4642–4651.
47. Hu, Q.; Wu, C.; Zhao, X.; Chen, X.; Ji, Y.; Yoshinaga, T. Vehicular Multi-Access Edge Computing With Licensed Sub-6 GHz, IEEE 802.11p and mmWave. *IEEE Access*, 2018, 6, 1995–2004.
48. Kaiwartya, O.; Abdullah, A.H.; Cao, Y.; Lloret, J.; Kumar, S.; Shah, R.R.; Prasad, M.; Prakash, S. Virtualization in wireless sensor networks: Fault tolerant embedding for internet of things. *IEEE Internet of Things J.* **2018**, *5*, 571–580.
49. Jang, J.S.R. ANFIS: adaptive-network-based fuzzy inference system. *IEEE Trans.Sys. Man Cybernetics* 1993, 23, 665–685.



© 2019 by the authors. Licensee MDPI, Basel, Switzerland. This article is an open access article distributed under the terms and conditions of the Creative Commons Attribution (CC BY) license (http://creativecommons.org/licenses/by/4.0/).

L,M&A: An Algorithm for Music Lyrics Mining and Sentiment Analysis

Vasu Saluja, Minni Jain and Prakarsh Yadav
Delhi Technological University, New Delhi, India
vasusaluja@outlook.com, minnijain91@gmail.com,
prakarshy@gmail.com

Abstract

Here we propose an open source algorithm, L,M&A(Lyrics, Mine and Analyse) to create a dataset of lyrics of the works of various artists. The aim of this approach is to facilitate the generation of a large data set that can be used for improving accuracy of song recommendation algorithms. The limited availability of such datasets has excluded the sentiment analysis of lyrics from music recommendation systems. By using the L,M&A algorithm, it is possible to generate a large dataset which can function as training dataset for future classifier systems. We have used iterative API requests from musixmatch and Genius servers to text mine lyrics data of songs by multiple artists. The data is processed and then analysed for sentiment using lexicons provided in the Tidytext package (BING, AFINN, NRC) and the overall sentiment of artist was determined through modal counts. The occurrence of each sentiments was evaluated and visualized using ggplot2. This representation exhibits the merit of our approach and the applicability of our data. The key feature of our approach is the open source platforms utilized and simplicity of input required from user.

Keywords: Data Mining, Natural Language Processing, Sentiment Analysis, Lyrics Database, Music Recommendation, musicology, Rstudio, musixmatch, Genius

1 Introduction

Music analysis is central to all music recommendation algorithms. Efficient music recommendation algorithms make use of a song's popularity, user's past preference of music and clustering of different types of songs. From the above-mentioned methods, algorithms based on clustering of songs are the most complex. It involves analysis of the elements of song such as lyrics, beats, tempo and a host of other elements. A challenging task for the development of such an algorithm is the presence of accurate classifiers of music sentiment. Considering and analyzing the sentiment behind a music can greatly improve the accuracy of song recommendation algorithms.

The developing music recommendation systems based on lyrics is greatly stymied by the limited availability of open source lyrics datasets. A thorough and comprehensive dataset is necessary for training classifiers that can accurately ascribe sentiment to a song on the basis of its lyrics. Here we

propose an algorithm to mine lyric data for various artists which can be further utilized to generate a sentiment for individual artists.

Classification of artists based on the analysis of lyrical content of their work offers a unique dimension to improve the accuracy of existing song recommendation algorithms. Many music enthusiasts are interested in the lyrics of the songs. At the moment, widely popular genres of music, such as rap, are heavily based on lyrics. Thus, recommendation algorithms that over-look this aspect are often missing out on the accuracy of recommendation such an approach can offer. The employed model is an independent function that requires an artist's name as primary input and through open-source APIs[*†] (Application Programming Interface) gathers the required data regarding that artist's work and then employs our algorithm, L,M&A(Lyrics, Mine and Analyse) to generate a sentiment (based on the different categories of sentiment present in the lexicons used) for that particular artist and is also able to quantitate that sentiment. A wholistic dataset would form the premise of such recommendation systems.

Furthermore, such a dataset can be used to improve the existing sentiment-based lexicons. The sentiment lexicons' scoring is not specific towards lyrics and developing such specific lexicons requires an expansive dataset. This further underscores the need for the availability of music lyrics specific dataset. Herein, our L,M&A algorithm would be the catalyst for generating such datasets. Any user can simply supply a list of artists and the algorithm is able to create a dataset with all the albums of that artist, and subsequently fetch lyrics of all the songs in these albums.

This paper is organized as follows: Section 2 provides the work that has been done to address the lack of musical dataset and its subsequent sentiment analysis. Section 3 provides our proposed work, i.e. how we developed the dataset of lyrics of songs from various artists. Section 4 discusses the salient features of the output of our L,M&A algorithm and a sample of the sentiment analysis done on this dataset. Section 5 provides a glimpse of the future applications of such a dataset, such as music recommendation systems, improving sentiment lexicon accuracy and musicology.

2 Related Work

This sentiment analysis algorithm draws on multiple sources of knowledge [1]–[3]. We greatly rely on the basics of text classification, in form of open-source lexicons. Since the sentiment classifier is based on the text classification method it was necessary to incorporate concepts of negation and advanced pre-processing to ensure that only relevant components of lyrics were extracted and further analysed. It was found that all the works that were referred to had only attempted to ascribe sentiment to individual songs.[4] No attempts were made to correlate the sentiments to artist in regards to the entire discography, i.e. assign a generalized sentiment to an artist rather that individual songs.[5]

The 55,000 songs dataset and million song dataset [6]are open source but they carry certain limitations. Such as, in the million song dataset lyrics are present as a bag of words and lack the structure found in a song. A song is not just collection of words there is an order and structure to how each word is used. Similarly, the 55,000 songs dataset[‡] does not contains the whole work of an artist and is susceptible to noise in the lyrics, in terms of unnecessary words, single characters etc. Apart from these, it needs several pre-processing steps before any analysis can be performed such as removal of contractions, single character & unnecessary words. We also apply these pre-processing steps but in our case the exceptions are quite few and follow a definite pattern, unlike in 55k where web scraping techniques gather several different texts. On the other hand, our method can be used to retrieve lyrics of works of single or multiple artist and at the same time can be scaled to mine data for hundreds of thousands of songs.

[*] https://developer.musixmatch.com
[†] https://docs.genius.com
[‡] https://www.kaggle.com/mousehead/songlyrics#songdata.csv

A thorough literature review had made it apparent that the subject of sentiment analysis through lyrics has previously been done, but in some sense was found to be insufficient to address this complex issue. There are studies where the subject is sentiment determination through analysis of lyrics, but they were found to be limited in the dataset used [7], degree to which the sentiments ascribed were different, for example happy, good, sad, etc.

In the work by Gomez et. al., [1] the methodology for acquisition of data, through data mining, were adequately highlighted. However, after referring it was apparent that the methodology proposed had been applied on a prohibitively small data set of 593 songs. Further works also had a similar short coming in the scope of the data set used to test the model or the algorithm proposed in the paper. Elaborate mathematical models had been proposed, [8] but were not adequately tested to a wholistic degree.

This led to the motivation of our work wherein we employ a direct method of text classification and subsequent sentiment assignment. We attempted to use all the major available open-source lexicons and, compare and contrasted all such lexicons in their ability to accurately determine the sentiment associated to a particular artist. After testing on various data sets of songs it was made apparent that this methodology is highly accurate in ascribing a generalized sentiment to a particular artist. The sentiment ascribed can also be quantitated and incorporated in other functions. This work can also be conveniently applied to other languages simply by changing the lexicon being employed.

3 Proposed Work

Before starting with the actual L,M&A algorithm, we first had to register for the musixmatch & Genius Developer account, from where using the instruction, we acquired the root URL of musixmatch API and Genius API {base_key & genius_baseurl} (API- Used to interact with server database). Along with these, authentication key, for verification was generated on the developer page of both {api_key, access_token}. After all the architecture setup, the necessary packages (jsonlite[§], plyr[**], GeniusR[††], Tidyverse[‡‡], stringdist[§§]) along with the artist dataset is loaded into the R workspace11. Afterwards artist's name was iteratively passed, wherein in each iteration a series of tasks were performed. Represented in Algorithm 1.

At First, we created a request URL to search for xi in the musixmatch database by joining the root URL with the required ARTIST.SEARCH API method of musixmatch (xi as argument) and the api_key {artist_search}. Using jsonlite methods (artist_search as argument) to convert the json response received (json is a data readable format, which is used by several API to parse a request) after connection to the API into a R's data object. Once the response was verified ([art$status_code == 200] – HTTP Code indicating that request was successful) and checked ([art&body !empty] – that the received json response body is not empty), Dataframe was extracted from it wherein the artist name was then tested based on string similarity{stringism()}, if the similarity was above 85% then the ID of the artist was extracted from the dataframe.

Then using the ID another request was created to get the discography of the artist, ARTIST.ALBUMS method {artist_album}. The album dataset was extracted from the JSON response of the request, parsed, checked and verified in the same manner as mentioned above{artist_album}.

[§] https://arxiv.org/abs/1403.2805
[**] http://www.jstatsoft.org/v40/i01
[††] https://github.com/JosiahParry/geniusR
[‡‡] https://www.tidyverse.org/packages/
[§§] https://cran.r-project.org/web/packages/stringdist/index.html

```
if X is a set of all artist name
x_i is the i^th artist name
base_key, api_key, genius_baseurl, access_token
for x_i in X:
        artist_search <- base_key + ARTIST.SEARCH(x_i)+ api_key
        art <- fromJSON(artist_search)
        if (art$status_code == 200 & art$body !empty)
                if (Stringism(x_i ,art$body$artistdata) > 0.85)
                        id <- art$body$artistdata$id
                artist_album <- base_key + ARTIST.ALBUMS(id) + apikey
                  albums <- fromJSON(artist_album)
                if (albums$status_code ==200 & albums$body !empty)
                   album<- select (albums$id, albums$name, albums$trackcount, albums$type)
                   album <- filter (album$type in (Album, EP), album&trackcount >5)
                   data <- dataframe(track_title, lyrics, artist_name)
                   genius_artist <- genius_baseurl + GET_SEARCH (x_i )+ access_token
                   name <- fromJSON(genius_artist)
                   if (name$status_code == 200 & name$body !empty)
                      if (stringsism(name$primary_name, x_i ))
                         name <- filter(name$primary_name_url)
                    for i in album:
                          lyrics <- genius_album(name , i)
                          data <- bind (data, lyrics)
                    data <- summarise(data)
data <- bind_row(data, data)
write_csv(data)

remove contractions & singlechar & lower_casedata
for i in unique(data$artist_name):
        filter (data for same artist name)
        tokens <- unnest_token(data$lyrics)              #tokenization
        antijoin(tokens, stop_words, unnecessary_word)
        bing <- innerjoin(tokens, bing_sentiment)
        nrc <- innerjoin(tokens, nrc_sentiment)
        afinn <- innerjoin(tokens, afinn_sentiment)
        bing_count <- top_n_words(bing)
        nrc_count <- top_n_words(nrc)
        afinn_count <- top_n_words(afinn)

        unnest_token(data$lyric, ngram = 2)     #bigram Tokenization
        words_not <- filter (word1 == "not")
        pair_count <- pairwise_count(tokens)
        pair_corr <- pairwise_correlation(tokens)
        Plot (words_not, pair_count, pair_corr, bing_count, afinn_count, nrc_count, bing, nrc, afinn)
```

Algorithm 1: Lyrics, Mine and Analyse Algorithm (L,M&A)

The data was filtered for album name, ID, track count & release type having type Album or EP and count greater than 5{album}. Reason being an album contains more than 4-5 songs in it. Also, many were listed as albums but were actually compilation of some songs of album. And in case of EP only a few songs are released. Live and singles were neglected, as repetition.

Finally, a query was formed for the genius API to extract and match the name of the artist before providing the information to succeeding function to minimize error. Using genius_baseurl along with GET_SEARCH method of Genius API and access_token, a query was formed{genius_artist}. Data was retrieved (see above) from response and relevant data (artist name present in the variable containing primary URL of an artist, defined on genius server was extracted) based on string similarity between xi and data was filtered accordingly{name}.

The artist name{name} along with all the album names of that artist {album} were used to extract the lyrics of all the songs in a particular album. This was done using GeniusR package genius_album method, where artist name, and album names were passed iteratively to capture the lyrics of all songs of the artist{lyrics}. A dataframe with all the songs in an album were received. Wherein each line of text of a song was as a separate observation in it. All the lines of a song were concatenate into one observation{data}. This was done for all the albums by an artist sequentially, i.e. all the songs.

The whole process was repeated for all the artists in the artist.csv. Finally, all the songs of all the artist were merged to create the final dataset. Represented diagrammatically in Figure 1 A.

After the creation of the data, it was exported as a comma separated file, containing 23,138 observations and 3 variables (track_title, lyric, artist_name). This dataset was then used for sentiment analysis. This was done by first rectifying abbreviated words then removing single character/ digits with no apparent meaning {remove (contraction & singlechar)}, finally converting the lyrics to lower case {lower_casedata}.

The data was iterated artist wise after initial pre-processing. Tokenization [Breaking up a set of texts into individual words] (unigram) of lyrics{unnest_token}, followed by removal of undesirable words (such as “ah”, “uh”, “yo” & many other), stop words and words less than 3 characters{antijoin}.

Once the tokenized dataset was available, Word-clouds are generated to visualize and infer the most used words by an artist (wordcloud2). Sentiment datasets were created for the lexicons (a form of vocabulary, in this case word as key and sentiment associated with that word as value) used, namely AFINN, BING and NRC, provided in Tidytext[***] package, via an inner join (separating out words that are present in both the sentiment dataset and the tokenized, filtered dataset) and then visualized (sentiment vs count). Frequency of words corresponding to different sentiment categories was then evaluated. {bing_count, nrc_count, afinn_count}.

After all the visualization was done for the case of unigrams, tokenization was done for the case of bigrams (set of two consecutive words in test) {ngram = 2}. Polarity of words which were preceded by ‘not’, was checked and plotted {words_not} Afterwards Pair-wise count and Pair-wise correlation (using Widyr[†††] package) of most frequent words with other (pairwise_corr(), pairwise_count()) words were carried out and visualized{ggplot()[‡‡‡]for visualization, Rstudio12 [§§§]as IDE}. Represented diagrammatically in Figure 1 B.

4 Results & Discussion

Through the implementation of the above proposed L,M&A algorithm a dataset of 23138 songs from the set of 265 artists. API requests for various songs of each of the 265 artists were sent to the musixmatch server. A sample of the dataset is shown in Table1. The response was verified and further details of artists’ album name was extracted. The names were then selected, filtered and fed into a dataframe that functions as the basic input of GeniusR package. This ‘Album Dataframe’ is called by the GeniusR package to extract lyrics of the songs in that album.

[***] https://cran.r-project.org/web/packages/tidytext/index.html
[†††] https://cran.r-project.org/web/packages/widyr/index.html
[‡‡‡] http://ggplot2.org
[§§§] http://www.rstudio.com/

Since GeniusR package is highly susceptible for error in input, the Dataframe of artists' name and album names had to be curated appropriately. This was achieved by implementation of multiple "exception handling" conditions.

The main error surrounding this was of the way an artist name was supplied to the function, if there was any variability between the name that we supplied and the artist name stored on Genius API, we got an error. The same was true for the musixmatch API. So in order to resolve this we took string similarity instead of equality between the strings to retrieve artist's name from respective APIs and then use those for further processing, we took a threshold of above 75-85% similarity to proceed further. Another main error that we came across was the case of the albums list of an artist, since we had to supply that as an argument to retrieve lyrics of all the songs in the album, we had to build exception handling (using try-catch blocks) for the cases the album name supplied was not present in the Genius server. We also had to take exception for cases that an artist with already built in platform, but possessed no data on the server, had to be removed accordingly.

This generates a dummy dataset that is used as a feedback into the Album List. Finally, once the algorithm has been completely executed, the dummy dataset is then processed to generate a single array with artists' name, album name and songs' lyrics.

The advantage of our proposed L,M&A algorithm for generation of a dataset is that it requires minimal input form user, in form of artist name, and can provide all the lyrical data that is in that artist's discography. Additionally, we have used a method of string similarity in our API requests, with cut-off of 85% in the name of an artist, this ensures that even if there is variance in spelling or special characters are used the code is still able to accurately determine the artist. This functionality is used twice, once for API requests through the musixmatch server and second time for the GeniusR package. This functionality was necessitated by the difference in musixmatch and GeniusR's method of indexing artist name. The string similarity method ensures that these variances do not lead to a mismatch or return of null value at any point in the algorithm.

The L,M&A algorithm is highly robust and requires an input of .CSV format containing the names of artists. Using such minimal input, it is able to generate highly relevant and accurate results. As an application of the dataset, we further developed an algorithm to perform sentiment analysis on it. We employed various sentiment-based lexicons to quantitate the sentiment for each of the artist. The output data was provided as graphs. The plots shown in this paper, Figure 2, are sufficient for representing the intent of our work. However, the magnitude of data processed is beyond the scope of graphical representation.

The supplied data clearly exhibits the merit in our approach for lyrical analysis with far reaching applications. The most obvious application would be in song recommendation algorithms. The execution of algorithm provided AFFIN count, NRC count and BING count for each of the artist from the collated csv. These plots and generated values formed the basis for further clustering of artist to allow generation of a primitive recommendation system. Considering the case of Beatles, we observed that NRC sentiment of Beatles scored high on positive aspects such as joy and trust. Similarly, in BING count there was a markedly higher frequency of positive words such as love, sweet, free and loving, in comparison to lonely, shame and cry. Finally, in case of AFFIN count the songs scored very high in positive scoring elements like fun, love, happy, sweet, care, etc. Figure 2 On the contrary, Black Sabbath, a band greatly influenced by the era, scored high on elements like fear, sadness and anticipation in NRC count. AFFIN and BING count showed similar results as the band scored high on negative sentiment words like death, cry, pain, etc.

Through our code it is possible to generate a similar data set for any artist. The dataset of lyrics is unique as unlike other data sets that are publicly available, our data set requires very minimal, if any, preprocessing. The structure of lyrics of each song is conserved and can be easily utilized for various forms of analysis. For instance, the sociological analysis or improve accuracy of lexicon or as a basis of music recommendation systems.

Lyrics convey the essence of emotion in a song and can greatly influence the listener's reception of the song. Thus, development of such a classification system is one of the first steps towards improving the existing song recommendation systems. Further pursuit of this classification system is

required to make it highly robust and exploit the intricacies of the vast information provided by lyrics in a song.

5 Conclusion & Future Work

Through the analysis of results presented above it can be concluded that lyrics play a crucial role in the general sentiment of musical works. The quantitated analysis of lyrics in such an algorithmic way allows for betterment of existing music recommendation systems. Many musical connoisseurs greatly appreciate the intricacies of lyrics and such an algorithm directly caters to such needs. The quantitated score obtained from the proposed L,M&A algorithm can be coupled with a weighted function to be seamlessly incorporated into other music comparators, such as tone/tempo analysis.

The limitation to our L,M&A algorithm is centered around the fact that we had to employ quantitated sentiment lexicons. The accuracy of our interpretations and results are directly correlated to the accuracy of used lexicons. Hence, we propose to employ machine learning and fuzzy logic approach to further improve the quantitative accuracy of these lexicons in regards of lyrical words. The training of this algorithm would be carried out on the mined lyrics data. This would curate the lexicons to preform markedly better on atypical data sets, such as music lyrics.

Another application of our data is in the field of music sociological analysis or musicology. Music is greatly representative of the society's mood in that time period. Drastic events like war and communal violence inspire artists to create music that reflects the sentiment of society at that point of time. The quantitated approach offered by our L,M&A algorithm offers a promising new dimension of sociological analysis. The representation of artists' discography in form of graphs and charts allows convenient and accurate assessment of sociological implications of their work.

References

[1] L. M. Gómez and M. N. Cáceres, "Applying Data Mining for Sentiment Analysis in Music," in *Trends in Cyber-Physical Multi-Agent Systems. The PAAMS Collection - 15th International Conference, PAAMS,2017*

[2] S. Howard, C. N. Silla, and C. G. Johnson, "Automatic Lyrics-based Music Genre Classification in a Multilingual Setting," In: *Thirteenth Brazilian Symposium on Computer Music,* 2011.

[3] T. Mullen and N. Collier, "Sentiment analysis using support vector machines with diverse information sources," In *Proceedings of Conference on Empirical Methods in Natural Language Processing,* 2004.

[4] A. Jamdar, J. Abraham, K. Khanna, and R. Dubey, "Emotion Analysis of Songs Based on Lyrical and Audio Features," in *International journal of Artificial Intelligence & Applications,* 2015.

[5] S. Shukla, P. Khanna, and K. K. Agrawal, "Review on sentiment analysis on music," in *2017 International Conference on Infocom Technologies and Unmanned Systems (Trends and Future Directions) (ICTUS)*, 2017.

[6] T. Bertin-Mahieux, D. P. W. Ellis, B. Whitman, and P. Lamere, "The Million Song Dataset," in *Proceedings of the 12th International Conference on Music Information Retrieval (ISMIR 2011)*, 2011.

[7] V. Sharma, A. Agarwal, R Dhir, G. Sikka, "Sentiments mining and classification of music lyrics using SentiWordNet" in *IEEE Xplore*, 2018.

[8] Y. Hu, X. Chen, and D. Yang, "Lyric-based Song Emotion Detection with Affective Lexicon and Fuzzy Clustering Method," in *Proceedings of ISMIR 2009*

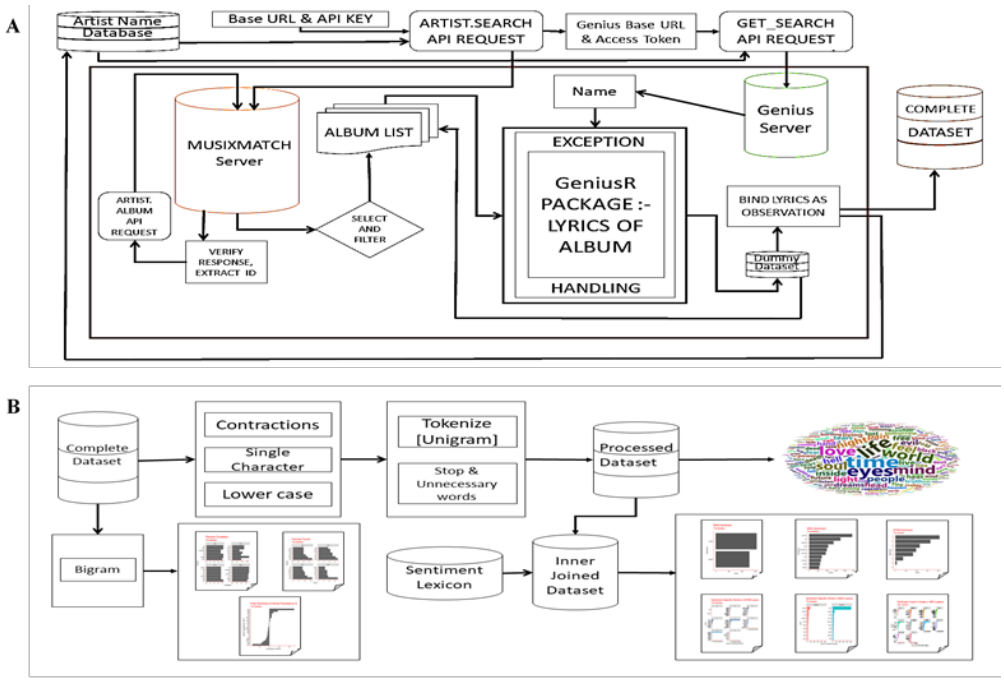


Figure 1: Flow diagram representing the dataset. 1 A represents the data mining aspect of the data (Deep red box represents global loop and deep blue representing local loop), 1 B represents the resultant sentiment analysis

Table 1 : Sample representation of dataset generated

track_title	lyric	artist_name
Baby's in Black	Oh dear, what can I do? Baby's in black and I'm feeling blue	The Beatles
Hey Jude	Hey Jude, don't make it bad Take a sad song and make it	The Beatles
God Is Dead?	Lost in the darkness I fade from the light Faith of my father,	Black Sabbath
Paranoid	Finished with my woman, 'cause she couldn't help me With	Black Sabbath

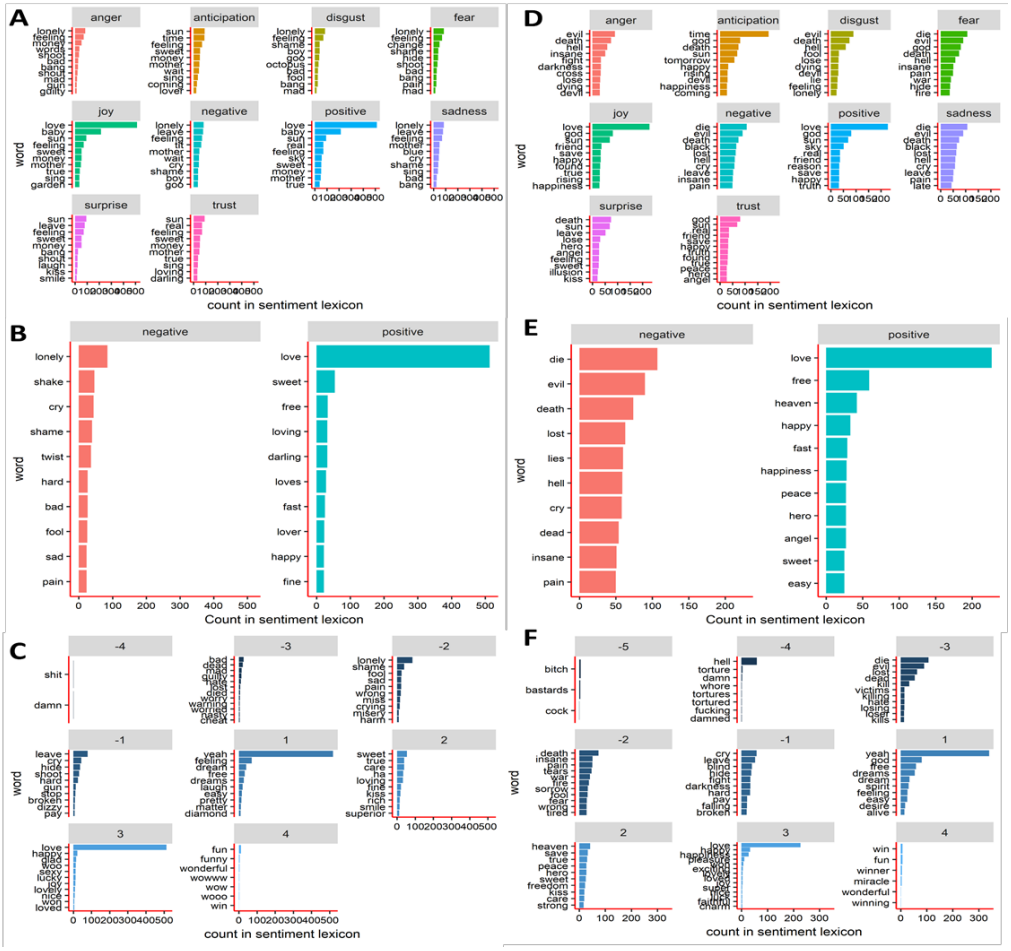


Figure 2: Panel A-C represent the exploratory plots of band 'The Beatles' and panel D-F represent same plots for the band 'Black Sabbath'. Plot A and D represent most used words in different sentiment categories within NRC lexicon, similarly plot B, E, C & F represent for BING and AFINN lexicons.

Mehta and Hasija *Biomedical Dermatology* (2019) 3:3
https://doi.org/10.1186/s41702-019-0041-3

Biomedical Dermatology

RESEARCH Open Access

Meta-analyses of associations of obesity with risk of melanoma and acne based on case-control studies

Avni Mehta and Yasha Hasija*

Abstract

Background: Melanoma and acne are highly prevalent dermatological diseases. A meta-analysis of case-control studies was performed to explore obesity as a risk factor for the same.

Objective: The relationship between increased BMI and melanoma incidence has been investigated in the past. We utilized recent epidemiological evidence to study this association and confirm previous findings. Moreover, to date, no meta-analysis evaluating the relationship between obesity and acne has been performed. We conducted this analysis to cast light on the same.

Methods: PubMed database was searched systematically to identify relevant literature related to the associations of obesity with risk of melanoma and acne respectively. Meta-analyses were performed using Review Manager 5.3, and the resulting risk ratios and 95% confidence intervals (CIs) were analyzed.

Results: A total of 2304 melanoma patients and corresponding 2468 controls, and 983 acne patients and corresponding 1313 controls from 5 and 4 case-control studies respectively were finally enrolled in the meta-analysis. The results showed a weak positive association between increasing BMI ($\geq$ 25 kg/m^2) and melanoma (OR = 1.36; 95% CI = 1.20–1.55), and a null association between increasing BMI ($\geq$ 25 kg/m^2) and acne (OR = 1.27; 95% CI = 0.98–1.65).

Conclusions: The result from the first meta-analysis showed that as BMI increases, there is an increased risk of melanoma incidence. The second meta-analysis revealed the absence of any significant relationship between obesity and acne. However, larger and more high-quality studies are needed to confirm this result.

Keywords: Meta-analysis, Obesity, Melanoma, Acne, Case-control studies

Key points

- There is a need to study the impact of obesity on dermatological diseases like melanoma and acne.
- The meta-analysis revealed that people with BMI $\geq$ 25 kg/m^2 are at a higher risk of melanoma than those with BMI $\leq$ 25 kg/m^2.
- The meta-analysis also showed that an increase in BMI beyond 25 kg/m^2 did not impact acne incidence significantly.

Introduction

Obesity is an escalating global epidemic, and its prevalence has increased dramatically in children by 47% and in adults by 28% between 1980 and 2013 (The GBD 2013 Obesity Collaboration et al. 2014). By 2030, it is estimated that 20% of the world's adult population will be inflicted with obesity and another 38% will be overweight if current trends persist (Kelly et al. 2008).

Affecting at least 300 million people worldwide (Tobin et al. 2013a), this complex disease is now a major health problem. A contributing factor to the aforesaid is the association of this multifactorial disease with numerous comorbidities such as cardiovascular disease (Jokinen, 2015), cancer (Park et al., 2014), diabetes (Garg et al. 2014), hypertension (Becton et al. 2012), osteoarthritis

* Correspondence: yashahasija06@gmail.com
Department of Biotechnology, Delhi Technological University, Delhi 110042, India

© The Author(s). 2019 **Open Access** This article is distributed under the terms of the Creative Commons Attribution 4.0 International License (http://creativecommons.org/licenses/by/4.0/), which permits unrestricted use, distribution, and reproduction in any medium, provided you give appropriate credit to the original author(s) and the source, provide a link to the Creative Commons license, and indicate if changes were made. The Creative Commons Public Domain Dedication waiver (http://creativecommons.org/publicdomain/zero/1.0/) applies to the data made available in this article, unless otherwise stated.

(Berenbaum et al. 2013; Bliddal et al. 2014), and sleep apnea (Tuomilehto et al. 2013).

Obesity also leads to metabolic changes that have dermatological manifestations (Guerra-Segovia and Ocampo-Candiani, 2015), but they have received minimal attention and have not been studied extensively (Yosipovitch et al. 2007). Recently, researchers have developed an interest in studying the role of obesity in psoriasis (Jensen and Skov, 2016; Carrascosa et al. 2014), but obesity is implicated in many other dermatoses as well (Tobin et al. 2013b).

Melanoma is the deadliest form of skin cancer (Ingraffea, 2013) and its incidence continues to increase worldwide at a pace much faster than any other type of solid cancer (Owens, 2014). Acne too, as evidenced by epidemiological data demonstrating a predominance of 9.4%, is one of the most common skin diseases (Stein Gold, 2016) and the eighth most prevalent disease all over the world (Tan and Bhate, 2015).

A previously conducted meta-analysis (Sergentanis et al. 2013) evaluated the association between obesity and melanoma risk. However, it included case-control studies published from 1984 to 2008. We believe that lifestyle factors have changed over the years and hence, it is important to conduct the meta-analysis again utilizing recent reports as they are better indicators of the current scenario. Moreover, no meta-analysis has been conducted so far to study the association between obesity and acne risk.

Hence, the aim of this meta-analysis was to comprehensively examine case-control studies published from 2011 to 2017 that link body mass index (BMI), a marker of obesity, with highly prevalent dermatological diseases like melanoma and acne.

Methods

Search strategy

A comprehensive literature search was performed using PubMed to evaluate the incidence of melanoma and acne in obese and overweight subjects. Our search strategy included terms of "Obesity" (e.g., "body mass index," "body surface area," "BMI," "overweight," "body weight," "obese," "diet," "adiposity," "body size"), "Melanoma" (e.g., "skin cancer," "skin neoplasm," "malignancy"), and "Acne" (e.g., "acne vulgaris," "pimple").

Study selection

All scientific papers published through 2017 were examined. Studies with insufficient data for estimating HR and 95% CI were excluded, as were texts written in languages other than English and those with duplicate data. In case study populations overlapped, only the study of larger size was considered. Scientific papers that did not mention melanoma and acne were eliminated. Other studies that did not use BMI as an obesity index or involve a case-control study were also eliminated. The decision of inclusion or exclusion of each study was made independently by the investigator (A.M).

Data extraction

All candidate articles were evaluated, and data were independently extracted by the investigator (A.M.). For each study, information regarding baseline characteristics (first author's name, year of publication, country, age range, sex, number of cases and controls, sources of cases and controls, adjustment factors) was extracted. The corresponding authors were contacted at least twice in case the data required for the meta-analyses were incomplete, not available, or insufficient in the published study.

Statistical analyses

Statistical analyses were performed using Review Manager 5.3. The odd ratios (ORs) were used as a measure of the association between the particular dermatological disease and obesity. The I^2 statistic was undertaken as an objective measure to quantify the heterogeneity of the included studies. Fixed-effect meta-analysis (Mantel-Haenszel method) was performed on the studies. $P < 0.1$ was indicative of the presence of clear heterogeneity and vice-versa. The condition of being overweight was defined as having BMI $\geq$ 25 and < 30 km/m2 while that of being obese was defined as having BMI $\geq$ 30 kg/m^2.

Results

Study selection

The Preferred Reporting Items for Systematic Reviews and Meta-Analyses (PRISMA) flow diagram is demonstrated in Fig. 1 to show the study selection process. Our PubMed literature search for melanoma yielded 83,083 citations, out of which 32,209 had been published during the preferable time period between 2011 and 2017. Records that were not case-control studies and did not mention the keywords related to melanoma in their title or abstract were excluded to give 114 articles that were eligible for a full-text review. All the studies were published in peer-reviewed journals. Five eligible studies (Antoniadis et al. 2011; Davies et al. 2011; Fortes et al. 2013; De Giorgi et al. 2017; Malagoli et al. 2015) were included in the final meta-analysis after excluding 108 records that had insufficient, incomplete, or irrelevant data. The data from a case-control study by Malagoli et al. (Malagoli et al. 2015) was used in another one (Malavolti et al. 2017) and hence the latter was also excluded from the meta-analysis.

Similarly, for acne, as shown in Fig. 2, a total of 1192 manuscripts were identified from PubMed, out of which 447 had been published between 2011 and 2017. An

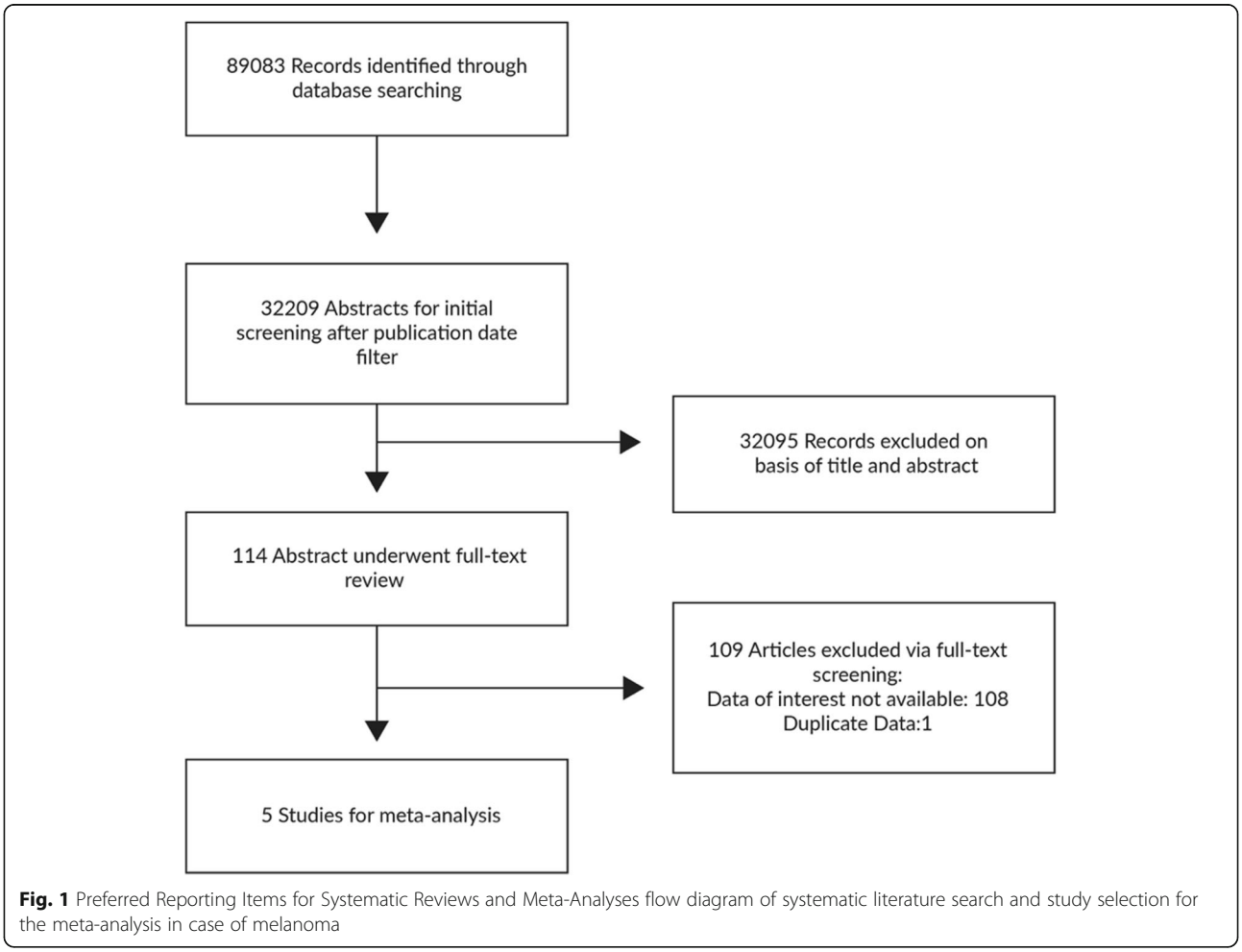


Fig. 1 Preferred Reporting Items for Systematic Reviews and Meta-Analyses flow diagram of systematic literature search and study selection for the meta-analysis in case of melanoma

additional article was identified from other sources. Records that did not mention keywords related to acne in their title or abstract were excluded along with those that did not involve case-control studies. This yielded 26 abstracts for a full-text review. Manuscripts that gave insufficient information on the effect of acne on obesity were rejected. A case-control study by Grossi et al. (Grossi et al. 2016) was also excluded from the meta-analysis since it had the same data as that by Landro et al. (Di Landro et al. 2012). After careful screening, four studies (Di Landro et al. 2012; Di Landro et al. 2016; Lu et al. 2017; Al-Shobaili et al. 2012) were selected for final inclusion in the meta-analysis. This literature search was also conducted according to PRISMA guidelines.

Study characteristics

The main characteristics of the studies included in the meta-analysis for melanoma are listed in Additional file 1. The meta-analysis included 2304 patients with melanoma and 2468 uninfected controls to study the effect of obesity on melanoma. BMI was used as an indicator of obesity. Three studies were performed in Italy, one in Greece, and one in the UK. All the five studies were case-control studies, encompassing participants of all ages, both male and female. The studies were published from 2011 to 2017.

In case of acne, the meta-analysis included a total of 2296 participants of all ages—983 acne patients and 1313 unaffected controls. Two studies were performed in Italy, one in China, and one in Saudi Arabia. These four case-control studies were published between 2012 and 2017 and helped study the association between obesity and acne. BMI was used as an index for obesity. Barring one study that included only female participants, the rest had both male and female participants. The main characteristics of the studies included in the meta-analysis for acne are listed in Additional file 2.

Association between obesity and melanoma

Five studies were included to investigate the relationship between obesity and the risk of melanoma. Two studies reported a higher risk of melanoma in "obese and overweight people" (BMI $\geq$ 25 kg/m^2) while the other three did not show a significant relationship individually. The

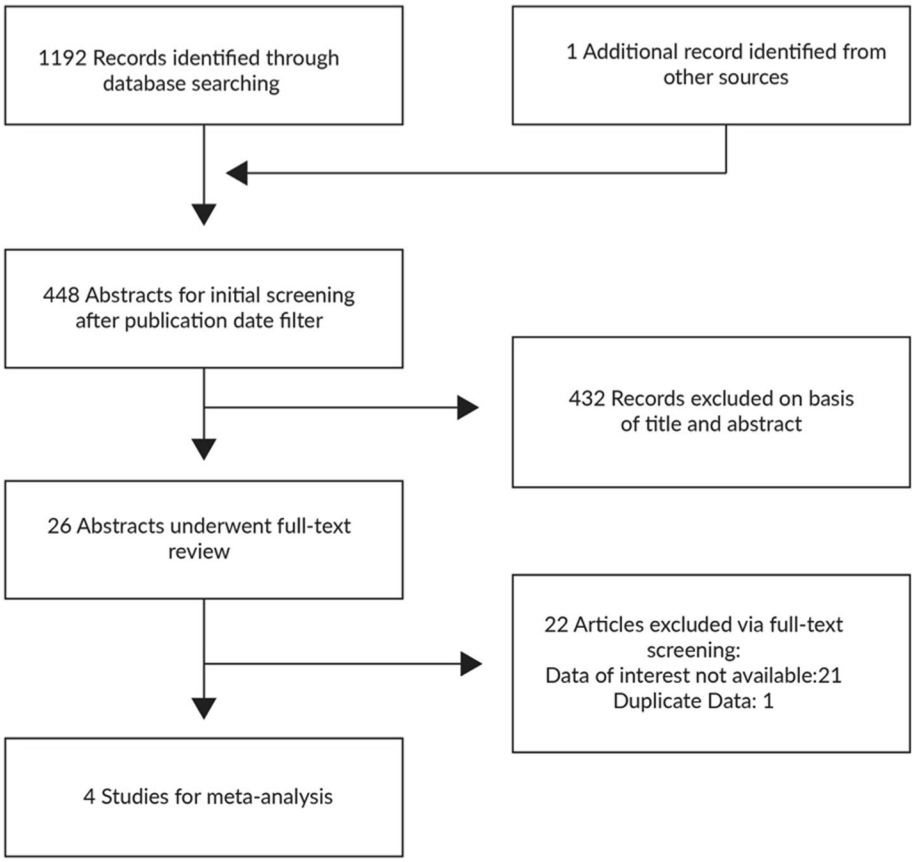


Fig. 2 Preferred Reporting Items for Systematic Reviews and Meta-Analyses flow diagram of systematic literature search and study selection for the meta-analysis in case of acne

pooled estimate was significant (OR = 1.36; 95% CI = 1.20–1.55), with significant heterogeneity (I^2 = 93%; P < 0.00001) (Fig. 3). The analyses for incidence of melanoma in overweight people (25 kg/m^2 ≤ BMI < 30 kg/m^2) (OR = 0.94; 95% CI = 0.8–1.10) and obese people (BMI ≥ 30 kg/m^2) (OR = 1.32; 95% CI = 1.06–1.64) individually have been shown in Additional file 3: Figure S1 and Additional file 4: Figure S2 respectively. The study by Grossi et al. (Grossi et al. 2016) has not been included in these individual analyses since data specific for BMI ranges 25–30 kg/m^2 and ≥ 30 kg/m^2 was unavailable.

Association between obesity and acne

Four studies were included to investigate the relationship between obesity and the risk of acne. One study reported a higher risk of acne in obese and overweight people (BMI ≥ 25 kg/m^2) while the other three did not show a significant relationship individually. No significant association

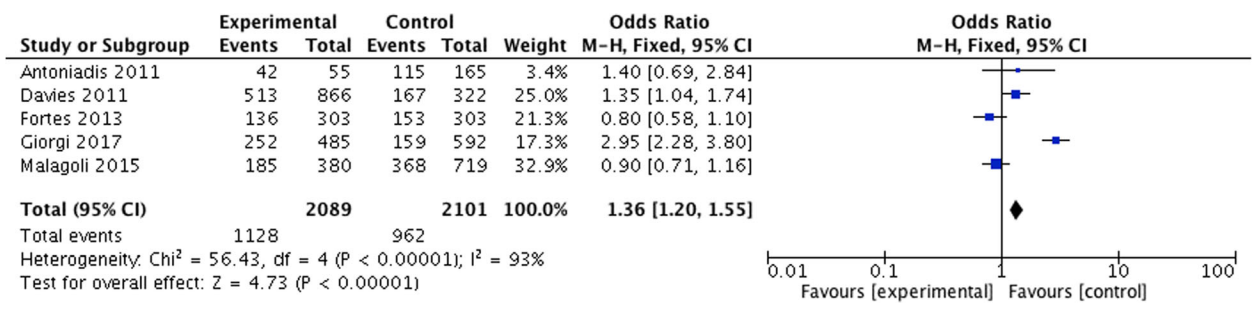


Fig. 3 Forest plot describing effect estimates for melanoma in overweight and obese people pooled together. OR odds ratio CI confidence interval

was documented after a pooled analysis (OR = 1.27; 95% CI = 0.98–1.65; $I^2 = 24\%$) (Fig. 4). Meta-analyses were not conducted for overweight and obese people specifically due to the lack of sufficient data and studies.

Exploration of heterogeneity

Heterogeneity was assessed by visually studying the forest plots. Non-overlapping CIs and P values obtained via the chi-square test were used to make the assessment. $P < 0.1$ denotes statistical significance while $I^2 > 50\%$ indicates substantial heterogeneity.

Publication bias

Since each meta-analysis includes less than 10 studies, publication bias cannot be assessed.

Discussion

This is the first meta-analysis aiming to investigate the relationship between obesity and the risk of acne and also the most recent one to include up-to-date evidence related to the association between obesity and melanoma risk.

Five studies were included to summarize the effect of obesity on the risk of melanoma. The analysis pointed to a weak positive association between increased BMI (≥ 25 kg/m^2) and melanoma (OR = 1.36; 95% CI = 1.20–1.55) with significant heterogeneity between studies. This result is coherent with the result from a meta-analysis conducted in 2008 (Renehan et al. 2008) that involved cohort studies only. It is also concomitant with a meta-analysis conducted in 2011 (Sergentanis et al. 2013) in which 45% of the studies were cohorts and the rest were case-control studies. This meta-analysis also included an unpublished case-control dataset, the numbers of which do not correspond with those in the published version (Antoniadis et al. 2011) that has been included in our meta-analysis.

For the association between obesity, indicated here by BMI ≥ 25 kg/m^2, and the risk of acne, four studies were studied. The meta-analysis showed a null association (OR = 1.27; 95% CI = 0.98–1.65). However, in the future, more prospective, well-designed, and large-scale studies along with basic research need to be conducted to properly explore and validate the relationship between increased BMI and risk of acne.

There are several limitations to our meta-analyses. Most of them hail from the shortcomings of individual studies, but there are other factors that need to be considered as well. Firstly, the pooled studies had varying inclusion or exclusion criteria, geographical locations, sample sizes, etc. Secondly, the confounding factors were not properly adjusted in the individual case-control studies, hence subjecting the associations to confounding bias. Thirdly, the fact that only five studies were included in case of melanoma and four in case of acne point to the high probability of a publication bias. Next, the meta-analyses were constrained to articles published in PubMed, in English, and those that used body mass index as an indicator of obesity. Also, since the enrolled studies were retrospective, the meta-analysis is subject to certain methodical limitations like selection bias and information bias. Lastly, it does not give gender-specific results due to inadequate data availability. The authors of such studies were contacted at least twice for the same.

Our study has several strengths. A comprehensive literature search of PubMed was performed to study the relationship between obesity, as denoted by increased BMI, and dermatological diseases like melanoma and acne. The studies included in the meta-analysis were of high quality. Another merit of this article lies in the fact that it involves the first meta-analysis to evaluate the association between obesity and acne risk.

Conclusions

Our findings from the first meta-analysis support the notion that increased BMI has a weak positive association with incidence of melanoma. This result is congruous with previously conducted meta-analyses that evaluated a different set of studies. The second meta-analysis demonstrated a null association between obesity and acne risk. However, since this is the first meta-analysis to evaluate the relationship between increased BMI and incidence of acne, this result needs to be confirmed by future studies and meta-analyses as more literature accumulates.

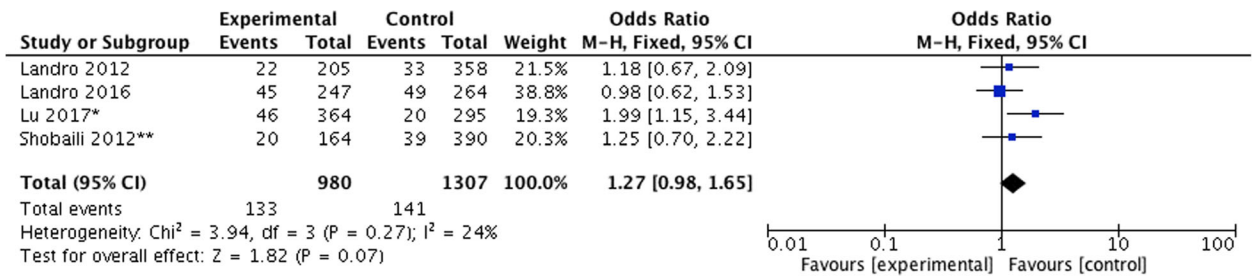


Fig. 4 Forest plot describing effect estimates for acne in overweight and obese people pooled together. *BMI $\geq$ 24 kg/m^2, **BMI $\geq$ 30 kg/m^2; OR odds ratio, CI confidence interval

Additional files

Additional file 1: Baseline characteristics of included studies in melanoma meta-analysis. (DOC 30 kb)

Additional file 2: Baseline characteristics of included studies in acne meta-analysis. (DOC 29 kb)

Additional file 3: Figure S1. Forest plot describing effect estimates for melanoma in overweight people. OR odds ratio CI, confidence interval. (TIFF 641 kb)

Additional file 4: Figure S2. Forest plot describing effect estimates for melanoma in obese people. OR odds ratio, CI confidence interval. (TIFF 641 kb)

Acknowledgements
Not applicable.

Funding
This work has been supported by Department of Biotechnology, Government of India [No.BT/PR5402/BID/7/408/2012].

Availability of data and materials
Not applicable

Authors' contributions
YH conceived the idea of the study. AM designed the study. AM and YH wrote the manuscript. Both the authors approved the final manuscript.

Ethics approval and consent to participate
Not applicable

Consent for publication
Not applicable

Competing interests
The authors declare that they have no competing interests.

Publisher's Note
Springer Nature remains neutral with regard to jurisdictional claims in published maps and institutional affiliations.

Received: 22 November 2018 Accepted: 6 February 2019
Published online: 01 March 2019

References
Al-Shobaili HA, Salem TA, Alzolibani AA, Robaee AA, Settin AA. Tumor necrosis factor-α -308 G/a and interleukin 10 -1082 a/G gene polymorphisms in patients with acne vulgaris. J Dermatol Sci. 2012;68(1):52–5.
Antoniadis AG, Petridou ET, Antonopoulos CN, Dessypris N, Panagopoulou P, Chamberland JP, et al. Insulin resistance in relation to melanoma risk. Melanoma Res. 2011;21(6):541–6.
Becton LJ, Shatat IF, Flynn JT. Hypertension and obesity: epidemiology, mechanisms and clinical approach. Indian J Pediatr. 2012;79(8):1056–61.
Berenbaum F, Eymard F, Houard X. Osteoarthritis, inflammation and obesity. Curr Opin Rheumatol. 2013;25(1):114–8.
Bliddal H, Leeds AR, Christensen R. Osteoarthritis, obesity and weight loss: evidence, hypotheses and horizons - a scoping review. Obes Rev. 2014;15(7):578–86.
Carrascosa JM, Rocamora V, Fernandez-Torres RM, Jimenez-Puya R, Moreno JC, Coll-Puigserver N, et al. Obesity and psoriasis: inflammatory nature of obesity, relationship between psoriasis and obesity, and therapeutic implications. Actas Dermosifiliogr. 2014;105(1):31–44.
Davies JR, Chang YM, Snowden H, Chan M, Leake S, Karpavicius B, et al. The determinants of serum vitamin D levels in participants in a melanoma case-control study living in a temperate climate. Cancer Causes Control. 2011;22(10):1471–82.
De Giorgi V, Gori A, Savarese I, D'Errico A, Scarfì F, Papi F, et al. Role of BMI and hormone therapy in melanoma risk: a case-control study. J Cancer Res Clin Oncol. 2017;143(7):1191–7.
Di Landro A, Cazzaniga S, Cusano F, Bonci A, Carla C, Musumeci ML, et al. Adult female acne and associated risk factors: results of a multicenter case-control study in Italy. J Am Acad Dermatol. 2016;75(6):1134–1141.e1.
Di Landro A, Cazzaniga S, Parazzini F, Ingordo V, Cusano F, Atzori L, et al. Family history, body mass index, selected dietary factors, menstrual history, and risk of moderate to severe acne in adolescents and young adults. J Am Acad Dermatol. 2012;67(6):1129–35.
Fortes C, Mastroeni S, Boffetta P, Antonelli G, Pilla MA, Bottà G, et al. The protective effect of coffee consumption on cutaneous melanoma risk and the role of GSTM1 and GSTT1 polymorphisms. Cancer Causes Control. 2013;24(10):1779–87.
Garg SK, Maurer H, Reed K, Selagamsetty R. Diabetes and cancer: two diseases with obesity as a common risk factor. Diabetes Obes Metab. 2014;16(2):97–110.
Grossi E, Cazzaniga S, Crotti S, Naldi L, Di Landro A, Ingordo V, et al. The constellation of dietary factors in adolescent acne: a semantic connectivity map approach. J Eur Acad Dermatol Venereol. 2016;30(1):96–100.
Guerra-Segovia C, Ocampo-Candiani J. Skin diseases and obesity. Rev Med Inst Mex Seguro Soc. 2015;53(2):180–90.
Ingraffea A. Melanoma. Facial Plast Surg Clin North Am. 2013;21(1):33–42.
Jensen P, Skov L. Psoriasis and obesity. Dermatology. 2016;232(6):633–9.
Jokinen E. Obesity and cardiovascular disease. Minerva Pediatr. 2015;67(1):25–32.
Kelly T, Yang W, Chen CS, Reynolds K, He J. Global burden of obesity in 2005 and projections to 2030. Int J Obes. 2008;32(9):1431–7.
Lu LY, Lai HY, Pan ZY, Wu ZX, Chen WC, Ju Q. Obese/overweight and the risk of acne vulgaris in Chinese adolescents and young adults. 2017;25:5–12.
Malagoli C, Malavolti M, Agnoli C, Crespi CM, Fiorentini C, Farnetani F, et al. Diet quality and risk of melanoma in an Italian population. J Nutr. 2015;145(8):1800–7.
Malavolti M, Malagoli C, Crespi CM, Brighenti F, Agnoli C, Sieri S, et al. Glycaemic index, glycaemic load and risk of cutaneous melanoma in a population-based, case-control study. Br J Nutr. 2017;117(3):432–8.
Owens B. Melanoma. Nature. 2014;515:S109.
Park J, Morley TS, Kim M, Clegg DJ, Scherer PE. Obesity and cancer—mechanisms underlying tumour progression and recurrence. Nat Rev Endocrinol. 2014;10(8):455–65.
Renehan AG, Tyson M, Egger M, Heller RF, Zwahlen M. Body-mass index and incidence of cancer: a systematic review and meta-analysis of prospective observational studies. Lancet. 2008;371(9612):569–78.
Sergentanis TN, Antoniadis AG, Gogas HJ, Antonopoulos CN, Adami HO, Ekbom A, et al. Obesity and risk of malignant melanoma: a meta-analysis of cohort and case-control studies. Eur J Cancer. 2013;49(3):642–57.
Stein Gold LF. Acne: What's new. Semin Cutan Med Surg. 2016;35(6 Suppl):S114–6.
Tan JK, Bhate K. A global perspective on the epidemiology of acne. Br J Dermatol. 2015;172(Suppl 1):3–12.
The GBD 2013 Obesity Collaboration, Ng M, Fleming T, Robinson M, Thomson B, Graetz N, et al. Global, regional and national prevalence of overweight and obesity in children and adults 1980-2013: a systematic analysis. Lancet. 2014;384(9945):766–81.
Tobin AM, Ahern T, Rogers S, Collins P, O'Shea D, Kirby B. The dermatological consequences of obesity. Int J Dermatol. 2013a;52(8):927–32.
Tobin AM, Ahern T, Rogers S, Collins P, O'Shea D, Kirby B. The dermatological consequences of obesity. Int J Dermatol. 2013b;52(8):927–32.
Tuomilehto H, Seppä J, Uusitupa M. Obesity and obstructive sleep apnea—clinical significance of weight loss. Sleep Med Rev. 2013;17(5):321–9.
Yosipovitch G, DeVore A, Dawn A. Obesity and the skin: skin physiology and skin manifestations of obesity. J Am Acad Dermatol. 2007;56(6):901–16.

Ready to submit your research? Choose BMC and benefit from:

- fast, convenient online submission
- thorough peer review by experienced researchers in your field
- rapid publication on acceptance
- support for research data, including large and complex data types
- gold Open Access which fosters wider collaboration and increased citations
- maximum visibility for your research: over 100M website views per year

At BMC, research is always in progress.

Learn more biomedcentral.com/submissions

BMC

Received: 5 July 2018 | Revised: 10 January 2019 | Accepted: 2 February 2019

DOI: 10.1002/cta.2619

RESEARCH ARTICLE

WILEY

New sinusoidal oscillator configurations using operational transresistance amplifier

Gurumurthy Komanapalli | Rajeshwari Pandey | Neeta Pandey

Department of Electronics and Communication Engineering, Delhi Technological University, Delhi, India

Correspondence
Rajeshwari Pandey, Department of Electronics and Communication Engineering, Delhi Technological University, Delhi, India.
Email: rajeshwaripandey@gmail.com

Summary

The objective of this brief is to introduce four new structures of electronically tunable sinusoidal oscillators (SOs) designed using operational transresistance amplifier (OTRA). Each of the proposed SO consists of forward path derived from a generic structure along with one/two OTRA-based resistive gain stages or differentiator in its feedback path. All the proposed SOs enjoy independent tuning of the frequency of oscillation (FO) through resistors without affecting the condition of oscillation (CO). Further, all topologies are found to exhibit low f_o sensitivities at all frequencies with respect to circuit parameters, and the second topology is capable of achieving very low frequencies (VLFs) using less RC component spread and provides linear tuning too. The fourth circuit provides quadrature output. The proposed SOs have been successfully implemented and verified in 180-nm CMOS technology node using ADE (analog design environment) tool Cadence Virtuoso. Both prelayout and postlayout simulation results have been included. To assess the oscillator prefabrication performances, Monte Carlo and process-voltage-temperature (PVT) analyses have been performed. The total harmonic distortion (THD) is observed to be less than 3.5%.

KEYWORDS

frequency stability, layout, operational transresistance amplifier (OTRA), PVT analysis, sensitivity, sinusoidal oscillator

1 | INTRODUCTION

Sinusoidal oscillators (SOs) find many applications in communication, measurement, and instrumentation systems as signal generators or test oscillators (see previous works[1-10] and the references cited therein). A survey of the existing literature on RC oscillators reveals that most of the oscillators have frequency of oscillation (FO) of form $1/2\pi RC$. It should be emphasized that the oscillators that adhere the tuning expression quoted above are suitable to generate frequencies ranging from medium frequencies (MF) to high frequencies (HF) based on the type of active element used. To generate low frequency (LF) oscillations using these SOs would require large passive component values, which ultimately would result in significant area overhead in integrated circuit (IC) implementation.[4-6]

On the other hand, the structures[1,7,11-17] that use FO expression wherein a term like $\sqrt{|1-k|}$ appears in numerator or denominator or both where k is a resistive gain term are capable of generating very low frequency (VLF) without

 © 2019 John Wiley & Sons, Ltd.

using high values of passive components. However, these topologies suffer high FO sensitivity to passive component variations. Another class of SOs[4-6] having FO of the form $\sqrt{k}/2\pi$RC is capable of generating a wide range of frequencies (VLF to HF) and also ensures less FO sensitivities to component variations. The precise motivation of this paper is to present this kind of oscillators.

Traditionally, the operational amplifier (op-amp) has been the most common active element for designing of SOs.[4-6] In recent past, operational transresistance amplifier (OTRA)[18] has gained much consideration from several researchers, due to its inherent pros like bandwidth independent of closed loop gain, higher slew rate, and simplicity in assimilating the effect of parasitic capacitances at the input ports. As a result, OTRA is being used widely for signal processing and generating applications (see previous works[1-3,19-48] and the references cited therein). Consequently, several authors presented different OTRA-based SO topologies[1-3,11,12,19-22,25-48] in which oscillators with FO of form $1/2\pi$RC are presented in previous literatures.[2,3,19-22,25-48] The SO topologies of previous studies[1,11,12] provide with difference term in the numerator in the expression of FO and therefore may be suitably employed as VLF oscillators.

A comparative study of all SO topologies using various analog building blocks (ABBs)[1,4-7,11-17] having scaling factor ($\sqrt{k}$ and/or $\sqrt{|1-k|}$) either in the numerator/denominator or both in the expression of FO has been presented in Table 1. These existing SO configurations have been designed using op-amps,[4-6] current feedback operation amplifier (CFOA),[7,15-17] current differencing buffered amplifier (CDBA),[13] OTRA,[1,11,12] combination of operational transconductance amplifier (OTA), and positive four terminal floating nullor (pFTFN).[14] The inspection of comparative Table 1 divulges that existing structures

- use excessive ABBs[6];
- use more than six resistors[4,6] and more than two capacitors[16] and produce single-phase oscillations;
- use similar ABBs[1,4-7,11-13,15-17] while Kumar et al[14] employ different ABBs;
- are designed using op-amps[4-6] and have restricted performance at higher frequencies due to gain bandwidth dependency and slew limitation of op-amps[2,3];
- provide only single phase (S)[1,4-7,11,12,14-17] output whereas Lahiri[13] gives quadrature (Q) response;
- lack electronic tunability,[4,7,11,12] (circuits C, D, E, G)[15];
- do not support independent control of FO without disturbing CO (circuits C, E, J)[11,12,15];
- have high FO sensitivities to component variations[1,7,11-17];
- use high-value capacitors (order of nF) in attaining VLFs,[4,7,11-14,16,17] which is not favorable from the IC fabrication viewpoint;
- imposes more stringent requirements in achieving variable frequencies as the scaling factor (k) appears in CO.[5,7,11-16]

It is pertinent to mention here that only Lahiri[13] produces quadrature output, however, suffers poor FO sensitivity with respect to component variations. Furthermore, structures of Senani and Bhaskar[4] and Senani[5,6] are less frequency sensitive but have restricted performance at higher frequencies. The SO of Bhaskar and Senani[7] is highly stable but is suitable only for generating VLF oscillations. To sum up, it is apparent that in all structures' features, trade-off is prevalent.

To the best of authors' knowledge, no SO is available in literature that is capable of generating very low to high FOs with the following features available simultaneously: (a) less RC component spread in attaining variable frequencies, (b) minimal FO sensitivity to component variations, (c) electronic tunability, (d) independent FO tuning, (e) excellent frequency stability, and (f) less complex design constraints/equations.

This paper presents four new SO configurations that retain majority/all of the above features. Section 2 provides a brief description of the proposed oscillator circuits. Section 3 examines the effect of nonideality of OTRA on the output of the oscillator. Sensitivity and frequency stability analyses are discussed in Sections 4 and 5, respectively. The analysis such as Monte Carlo and process-voltage-temperature (PVT) are presented in Section 6 along with prelayout and postlayout simulation results. The paper is concluded in Section 7.

2 | PROPOSED OSCILLATOR CONFIGURATIONS

The proposed configurations are designed using OTRA.[18] The circuit symbol of OTRA is shown in Figure 1 where (p, n) and o are low resistance input and output terminals, respectively. The port relations of OTRA are given in the matrix in Equation 1.

TABLE 1 Comparative study of SO topologies pertaining different scaling factors

Reference	No. of Active Elements/Figs	No. of R + C	Output Phase	Electronic Tunability	Independent tuning of FO	Frequency of Oscillation (f_o)
Senani and Bhaskar[4]	1 OPAMP Figure 1 A-D	7 + 2	S	(a,b,d) N (c) N	Y	$\frac{\sqrt{k}}{2\pi\sqrt{C_1C_2R_1R_4}};\ k=\frac{R_e/R_5}{1+R_2/R_3}$
Senani[5]	2 OPAMP	6 + 2	S	Y	Y	$\frac{\sqrt{k}}{2\pi\sqrt{C_1C_2R_1R_4}};\ k=\frac{R_3R_5}{R_4R_6}$
Senani[6]	5 OPAMP	12 + 2	S	Y	Y	$\frac{R_e\sqrt{k}}{2\pi\sqrt{C_1C_2R_1R_2}};\ k=\frac{R_4R_8}{R_3R_7R_9R_{10}}$
Bhaskar and Senani[7]	2CFOA Circuit. (1–3,5)	3 + 2	S	Y N N Y	Y	$\frac{\sqrt{1-k}}{2\pi\sqrt{C_1C_2kR_3R_2}};\ k=\frac{R_1}{R_2}$
Lahiri[13]	2CDBA	5 + 2	Q	Y	Y	$\frac{\sqrt{1-k}}{2\pi\sqrt{C_1C_2kR_1R_4}};k=\frac{R_3}{R_4}$
Kumar et al[14]	1OTA+ 1pFTFN	2 + 2	S	Y	Y	$\frac{\sqrt{(1-k)g_m}}{2\pi\sqrt{C_1C_2kR_2}};k=\frac{R_1}{R_2}$
Abuelma'atti[15]	2CFOA Circuit. (A-H, J,K,M,P)	(H,M) 4 + 2	S	Y	N	$\frac{\sqrt{1-k}}{2\pi\sqrt{C_xC_ykR_zR_y}};\ k=\frac{R_x}{R_y}$
		(G,K,P) 4 + 2	S	N	N	$\frac{\sqrt{1-k_1}}{2\pi\sqrt{C_xC_yk_1(1-k_2)R_bR_d}};\ k_1=\frac{R_a}{R_b};\ k_2=\frac{R_c}{R_d}$
		(D) 4 + 2	S	N	Y	$\frac{1}{2\pi\sqrt{C_xC_y(1-k)R_cR_b\pm R_aR_d}};\ k=\frac{R_a}{R_b}$
		(E) 4 + 2		N	N	
		(F) 4 + 2		Y	Y	
		(J) 4 + 2	S	Y	N	$\frac{1}{2\pi\sqrt{C_xC_y(1-k)R_zR_y}};\ k=\frac{R_x}{R_y}$
		(A) 4 + 2	S	Y	Y	$\frac{\sqrt{C_xC_y(1-k)R_cR_b\pm R_aR_d}}{2\pi\sqrt{C_xC_yR_cR_bR_aR_d}};\ k=\frac{R_a}{R_b}$
		(B) 4 + 2		Y	Y	
		(C) 4 + 2		N	N	
Srivastava et al[16]	1CFOA	4 + 3	S	Y	Y	$\frac{\sqrt{k-1}}{2\pi\sqrt{C_0C_3kR_1R_0}};k=\frac{R_4}{R_0}$
Elwakil[17]	2CFOA	6 + 2	S	Y	Y	$\frac{\sqrt{k}}{2\pi\sqrt{C_1C_2R_1R_2}};k=\frac{1}{\left(1+\frac{R_3R_4}{R(R_3-R_4)}\right)}$
Salama and Soliman[1]	2OTRA Figure 4	4 + 2	S	Y	Y	$\frac{\sqrt{1-k\frac{R_1}{R_3}}}{2\pi\sqrt{kC_1C_2R_1R_4}};\ k=\frac{R_2}{R_4}$
Komanapalli et al[11]	1OTRA	3 + 2	S	N	N	$\frac{\sqrt{1-k}}{2\pi R\sqrt{C_1C_2}};k=\frac{R}{R_1}$
Komanapalli et al[12]	1OTRA	4 + 2	S	N	N	$\frac{\sqrt{\left(1+\frac{R_2}{R}-\frac{R}{R_1}\right)-2k}}{2\pi\sqrt{kRC_1C_2R_1}};\ k=\frac{R_2}{R_1}$
Proposed SO Figure 3A	2OTRA	4 + 2	S	Y	Y	$\frac{\sqrt{k}}{2\pi\sqrt{C_1C_2R_1R_2}};\ k=\frac{R_a}{R_b}$
Proposed SO Figure 3B	3OTRA	6 + 2	S	Y	Y	$\frac{\sqrt{k}}{2\pi\sqrt{C_1C_2R_1R_2}};\ k=\frac{R_aR_c}{R_bR_d}$
Proposed SO Figure 3C	3OTRA	6 + 2	S	Y	Y	$\frac{\sqrt{k}}{2\pi\sqrt{C_1C_2R_1R_2}};\ k=\frac{R_c}{R_d}$
Proposed SO Figure 3D	3 OTRA	6 + 3	Q	Y	Y	$\frac{\sqrt{k}}{2\pi\sqrt{C_2C_3R_1R_3}};\ k=\frac{R_a}{R_b}$

TABLE 1 Comparative study of SO topologies pertaining different scaling factors

Reference	%THD/Sensitivity	CO dependency on k	Lowest/Highest Measured frequency	Component spread (R(Ω)/C(F)	Frequency Stability (S^F)
Senani and Bhaskar[4]	−/0.5	N	38.9 mHz/0.9 Hz	195 Ω to 1 MΩ/0.2 μF	-
Senani[5]	-/-	Y	-	-	-
Senani[6]	0.5% /0.5	N	0.1 Hz/ 1.49 kHz	100 Ω to 10 kΩ/ -	-
Bhaskar and Senani[7]	3.08% /High w.r.t k	Y	1.09 Hz/ ≈24 kHz	≈1 kΩ to 10 kΩ/ 10 nF	$-\sqrt{2n}$ $-\sqrt{2n}$ -1 $-\sqrt{2n}$
Lahiri[13]	-/High w.r.t k	Y	≈650 Hz/ ≈1.6 kHz	10 kΩ to 14 kΩ /5 nF	-
Kumar et al[14]	-/High w.r.t k	Y	42.5 Hz/ 3.3 kHz	1 kΩ to 20 kΩ/10 nF to 11 nF	-
Abuelma'atti[15]	-/High w.r.t k	Y Y Y Y Y Y Y Y Y	-/-	-/-	-
Srivastava et al[16]	-/High w.r.t k	Y	≈0.5 Hz/ 2 Hz	1 MΩ/ 100 nF to 200 nF	-
Elwakil[17]	-/High w.r.t R3,R4	N	51 Hz/ 1.59 kHz	1 kΩ to 100 kΩ /100 nF	-
Salama and Soliman[1]	-/High w.r.t k	Y	-/-	-/-	-
Komanapalli et al[11]	2.2% /High w.r.t k	Y	1 Hz/1.59 MHz	1 kΩ to 10.1 kΩ/ 110 nF	-
Komanapalli et al[12]	2.1% /High w.r.t k	Y	7.9 Hz/ 796 kHz	0.5 kΩ to 100 kΩ/ 100 nF	-
Proposed SO Figure 3A	<2%/0.5	N	0.17 kHz/ 20 MHz	5 kΩ to 0.1 MΩ/5 pF to 300 pF	$-\sqrt{2n}$
Proposed SO Figure 3B	<3.4% /0.5	N	7.5 Hz/37.6 MHz	0.1 kΩ to 0.1 MΩ/2.5 pF to 300 pF	$-\sqrt{2n}$
Proposed SO Figure 3C	<2.5% /0.5	N	0.17 kHz/ 20 MHz	5 kΩ to 0.1 MΩ/5 pF to 300 pF	$-\sqrt{n}$
Proposed SO Figure 3D	2.5%/0.5	N	0.17 kHz/ 20 MHz	5 kΩ to 0.1 MΩ/5 pF to 300 pF	$-\sqrt{2n}$

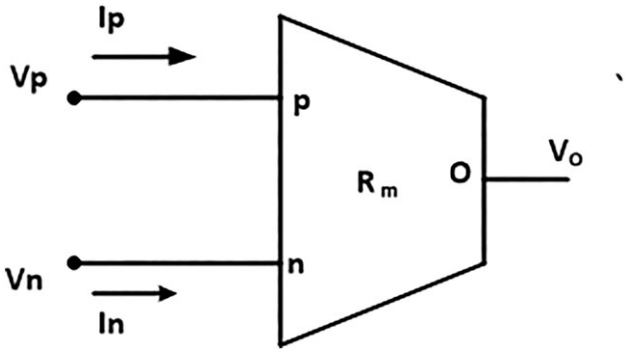


FIGURE 1 Schematic symbol representation of OTRA

$$\begin{bmatrix} V_p \\ V_n \\ V_o \end{bmatrix} = \begin{bmatrix} 0 & 0 & 0 \\ 0 & 0 & 0 \\ R_m & -R_m & 0 \end{bmatrix} \begin{bmatrix} I_p \\ I_n \\ I_o \end{bmatrix}. \tag{1}$$

The R_m is transresistance gain of OTRA, which ideally approaches infinity making two input currents equal. Figure 2 shows the generalized representation of forward path used in the proposed configurations. Considering the node potentials of A, B, D, and E to be V_1, V_2, V_3, and V_x, respectively, and performing routine analysis assuming OTRA to be ideal, the following equations are derived.

$$V_X Y_3 + V_o Y_4 = V_3 Y_6 + V_o Y_5, \tag{2}$$

$$V_1 Y_1 Y_3 + V_2 Y_2 Y_3 + V_o Y_4 (Y_1 + Y_2 + Y_3) = (V_3 Y_6 + V_o Y_5)\,(Y_1 + Y_2 + Y_3), \tag{3}$$

where Y_i represents the admittances of the passive components. By suitable choice of admittances, the following cases are derived.

Case 1. Considering $Y_4 = Y_6 = 0$, $Y_1 = sC_1$, $Y_2 = \frac{1}{R_2}$, $Y_3 = \frac{1}{R_1}$, $Y_5 = sC_2$; $V_1 = V_o$; Equation 3 simplifies to

$$V_o\left(s^2 C_1 C_2 R_1 R_2 + s\{C_2[R_1 + R_2] - C_1 R_2\}\right) - V_2 = 0. \tag{4}$$

Examining Equation 4, it is seen that connecting an OTRA-based inverting resistive gain stage characterized by $\left(-\frac{R_a}{R_b}\right)$ between output of OTRA1 and node B results in new SO configuration as shown in Figure 3A. Its characteristic equation may be expressed as

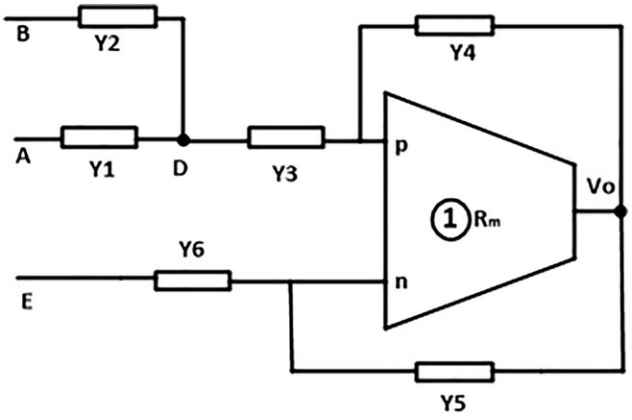


FIGURE 2 Generalized representation forward path used in the proposed configurations

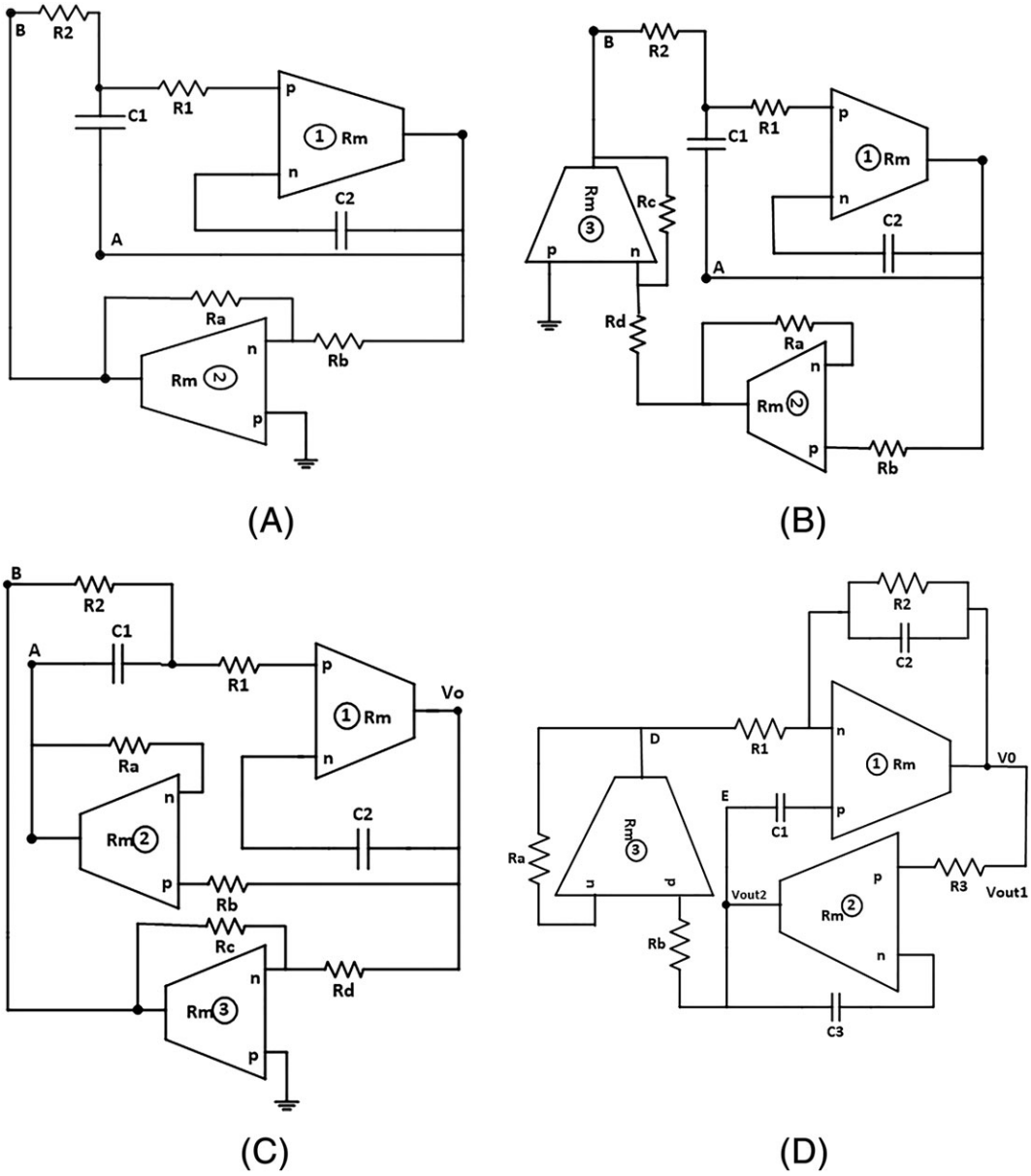


FIGURE 3 Proposed sinusoidal oscillator topologies

$$s^2C_1C_2R_1R_2 + s\{C_2[R_1 + R_2] - C_1R_2\} + \frac{R_a}{R_b} = 0. \tag{5}$$

The corresponding FO and CO are enlisted in Table 2.

Case 2. With component and node settings similar to Case 1 and introducing a cascade connection of inverting and noninverting resistive gain stages (characterized by $-\frac{R_c}{R_d}, \frac{R_a}{R_b}$, respectively) in feedback as shown in Figure 3B, a new SO topology may be obtained, and its characteristic equation is given as

$$\left(s^2C_1C_2R_1R_2 + s\{C_2[R_1 + R_2] - C_1R_2\}\right) + \frac{R_a}{R_b}\frac{R_c}{R_d} = 0. \tag{6}$$

The expressions of FO and CO are shown in Table 2. Judicious choice of these resistive gain values and CO settings not only provides linear tuning but also helps to achieve a wide range of frequencies.

TABLE 2 Frequency of oscillation and condition of oscillation of proposed circuits

Circuit	Frequency of Oscillaton (f_o)		Condition of Oscillation	Error Functions	Passive Compensated Error Functions
Figure 3A	Ideal	$\frac{\sqrt{k}}{2\pi\sqrt{C_1C_2R_1R_2}}$ where $k = \frac{R_a}{R_b}$	$C_2[R_1 + R_2] = C_1R_2$	$\varepsilon_1(s) = 1/1 + sC_pR_a$	$\varepsilon_{1n}(s) = 1/1 + s(C_p - C_X)R_a$
	Nonideal	$\frac{\sqrt{k_n}}{2\pi\sqrt{C_1(C_2 + C_p)R_1R_2}}$; $k_n = \frac{R_a}{R_b}\varepsilon_1(s)$	$(C_2 + C_p)[R_1 + R_2] = C_1R_2$		
Figure 3B	Ideal	$\frac{\sqrt{k}}{2\pi\sqrt{C_1C_2R_1R_2}}$ where $k = \frac{R_aR_c}{R_bR_d}$	$C_2[R_1 + R_2] = C_1R_2$	$\varepsilon_2(s) = 1/1 + sC_pR_c\varepsilon_1(s) = 1/1 + sC_pR_a$	$\varepsilon_{2n}(s) = 1/1 + s(C_p - C_X)$ $R_c\varepsilon_{1n}(s) = 1/1 + s(C_p - C_X)R_a$
	Nonideal	$\frac{\sqrt{k_n}}{2\pi\sqrt{C_1(C_2 + C_p)R_1R_2}}$; $k_n = \frac{R_aR_c}{R_bR_d}\varepsilon_1(s)\varepsilon_2(s)$	$(C_2 + C_p)[R_1 + R_2] = C_1R_2$		
Figure 3C	Ideal	$\frac{\sqrt{k}}{2\pi\sqrt{C_1C_2R_1R_2}}$ where $k = \frac{R_c}{R_d}$	$C_2[R_1 + R_2] = C_1R_2\frac{R_a}{R_b}$	$\varepsilon_2(s) = 1/1 + sC_pR_a\varepsilon_1(s) = 1/1 + sC_pR_c$	$\varepsilon_{2n}(s) = 1/1 + s(C_p - C_X)R_a$
	Nonideal	$\frac{\sqrt{k_n}}{2\pi\sqrt{C_1(C_2 + C_p)R_1R_2}}$; $k_n = \frac{R_c}{R_d}\varepsilon_1(s)$	$(C_2 + C_p)[R_1 + R_2] = C_1R_2\frac{R_a}{R_b}\varepsilon_2(s)$		$\varepsilon_{1n}(s) = 1/1 + s(C_p - C_X)R_c$
Figure 3D	Ideal	$\frac{\sqrt{k}}{2\pi\sqrt{C_2C_3R_1R_3}}$ where $k = \frac{R_a}{R_b}$	$C_3R_3 = C_1R_2$	$\varepsilon_1(s) = 1/1 + sC_pR_a$	$\varepsilon_{1n}(s) = 1/1 + s(C_p - C_X)R_a$
	Nonideal	$\frac{\sqrt{k_n}}{2\pi\sqrt{(C_2 + C_p)(C_3 + C_p)R_1R_3}}$; $k_n = \frac{R_a}{R_b}\varepsilon_1(s)$	$(C_3 + C_p)R_3 = C_1R_2$		

Case 3. Using component and node settings similar to Case 1 and connecting OTRA-based inverting and noninverting resistive gain stages in feedback as shown in Figure 3C, a new SO topology can be obtained, and its characteristic equation is expressed as

$$s^2C_1C_2R_1R_2 + sC_2[R_1 + R_2] - sC_1R_2\frac{R_a}{R_b} + \frac{R_c}{R_d} = 0. \tag{7}$$

From Equation 7, it may be observed from that the topology Figure 3C enjoys completely uncoupled tuning between FO and CO as listed in Table 2.

Case 4. with $Y_1 = Y_2 = Y_4 = 0$, $Y_3 = sC_1$, $Y_4 = \frac{1}{R_3}$, $Y_5 = \frac{1}{R_2} + sC_2$, $Y_6 = \frac{1}{R_1}$; accordingly, Equation 2 minimizes to

$$V_oR_1(1 + sC_2R_2) + V_3R_2 - V_3(sC_1R_1R_2) = 0. \tag{8}$$

New SO, which provides quadrature outputs, can be obtained by connecting OTRA-based noninverting integrator and noninverting gain stage (characterized by $\frac{1}{sC_3R_3}$, $\frac{R_a}{R_b}$, respectively) as shown in Figure 3D, and its characteristic equation is given by

$$s^2C_1C_3R_2R_3 + s\{C_3R_3 - C_1R_2\} + \frac{R_a}{R_b}\frac{R_2}{R_1} = 0. \tag{9}$$

The FO and CO are listed in Table 2. However, this is a noncanonic structure as against the other proposed topologies.

From Table 2, it is clear that all the circuits provide independent tuning of FO by distinct resistors without affecting CO. Therefore, all the circuits enjoy orthogonal tuning. Further, Figure 3C enjoys completely independent tuning between FO and CO without affecting each other.

Furthermore, it is interesting to note that the scaling factors in the numerator of the proposed circuits do not take part in CO unlike topologies in previous works[1,7,11-15] thereby making frequency scaling simpler.

The features of the proposed oscillator configurations may be summarized as follows:

- Topologies A to D of Figure 3 generate very low and/or high single-phase FOs qualifying all the above-listed features. Additionally, Figure 3B provides linear FO tunability whereas Figure 3D provides quadrature outputs.

By considering the above-listed benefits, the proposed circuits add to the present repertoire of OTRA-based oscillators. It is relevant to mention that all the proposed designs have floating passive components. Although grounded capacitors are preferred from fabrication viewpoint, these can be implemented using top-quality IC technology of today, which offers using metal-nsulator-metal (MIM) or metal-oxide-metal (MOM) double poly (poly1-poly2) capacitor processes.[42,49]

2.1 | MOS-C implementation

The current differencing property of the OTRA makes it possible to realize the resistors connected to the input terminals of OTRA, using MOSFETs with complete nonlinearity cancellation.[1] Each resistor needs two matched n-MOSFETs connected in a manner as shown in Figure 4A. Symbols X and Y represent the inverting and noninverting of the OTRA, respectively. The resistor value realized can be stated as

$$R = \frac{1}{(V_a - V_b)\mu_nC_{ox}\frac{W}{L}}, \tag{10}$$

where μ_n = electron mobility, C_{ox} = oxide capacitance per unit area, W/L = effective channel width/effective channel length, and V_a, V_b are the gate voltages.

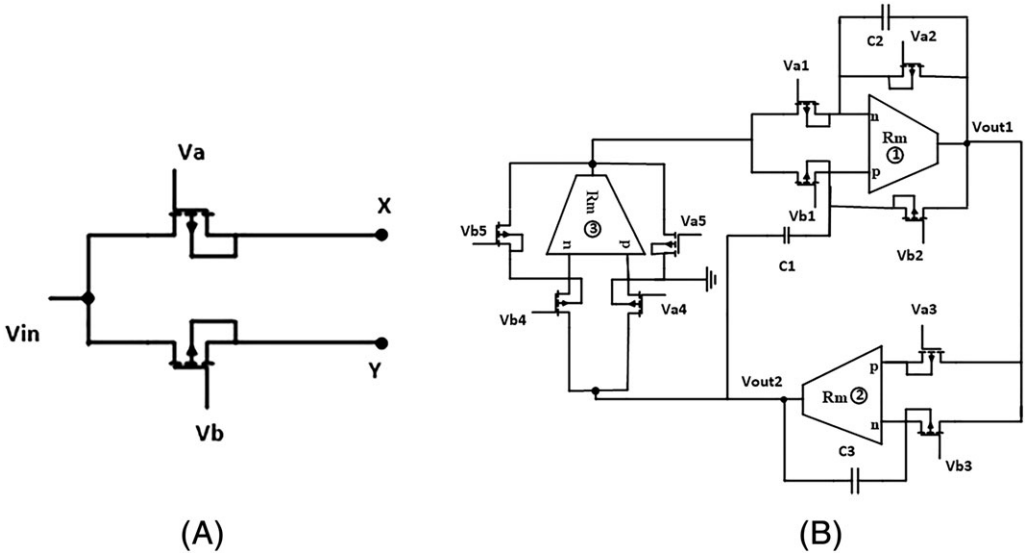


FIGURE 4 A, MOS implementation of resistance.[3] B, Complete MOS-C implementations of Figure 3(d)

A thorough inspection of the circuits of Figure 3 reveals that all the resistors in Figure 3D can be realized using MOSFETs. All resistors except R_2 are MOS realizable in Figure 3A-C. The MOS-C implementation of Figure 3D is depicted in Figure 4B.

3 | NONIDEAL ANALYSIS

For an estimation of the realistic performance of the proposed oscillators, nonideal factors must be included. To analyze to the nonideal effects on oscillations, we consider a single pole model for the transresistance gain (R_m) expressed as

$$R_m(s) = \left(\frac{R_o}{1+\frac{s}{\omega_o}}\right), \tag{11}$$

where R_o represents the dc transresistance gain and ω_o is the transresistance cutoff frequency. For high-frequency applications, $R_m(s)$ reduces to

$$R_m(s) = \frac{1}{sC_p}, \tag{12}$$

where $C_p = {}^1/_{R_o\omega_o}$ denotes parasitic capacitance of OTRA.

Considering this nonideal effect into account, the circuit of Figure 3B is reanalyzed, and the modified characteristic equation may be expressed as

$$s^2C_1(C_2+C_p)R_1R_2 + s\{(C_2+C_p)[R_1+R_2] - C_1R_2\} + \frac{R_c}{R_d}\frac{R_a}{R_b}\varepsilon_1(s)\,\varepsilon_2(s) = 0, \tag{13}$$

where $\varepsilon_1(s) = \dfrac{1}{\{1+sC_pR_c\}}$ and $\varepsilon_2(s) = \dfrac{1}{\{1+sC_pR_a\}}$.

Resulting FO and CO are, respectively, as follows:

$$\text{FO:}\frac{\sqrt{|k_n|}}{2\pi\sqrt{C_1(C_2+C_p)R_1R_2}};\ \text{where}\, k_n = \frac{R_a}{R_b}\frac{R_c}{R_d}\varepsilon_1(s)\varepsilon_2(s), \tag{14}$$

$$\text{CO: } (C_2 + C_p)[R_1 + R_2] = C_1 R_2. \tag{15}$$

It is clear from (14) and (15) that FO and CO are altered in the presence of nonidealities. Therefore, the compensation method must be applied for high-frequency applications to account for the errors $\varepsilon_1(s)$,$\varepsilon_2(s)$ introduced in FOs. The complete passive compensation may be achieved by simply connecting single capacitor C_X between V_1 and p terminal of the second OTRA and V_2 and n terminal of the third OTRA as shown in Figure 5. The characteristic equation of Figure 6 may be written as

$$s^2 C_1 (C_2 + C_p) R_1 R_2 + s\{(C_2 + C_p)[R_1 + R_2] - C_1 R_2\} + \frac{R_c}{R_d}\frac{R_a}{R_b}\varepsilon_{1n}(s)\,\varepsilon_{2n}(s) = 0, \tag{16}$$

where $\varepsilon_{1n}(s) = \dfrac{1}{\{1 + s(C_p - C_X)R_a\}}$, $\varepsilon_{2n}(s) = \dfrac{1}{\{1 + s(C_p - C_X)R_c\}}$.

Equation 16 signifies that by choosing the capacitor C_X equal to parasitic capacitance C_p, the effect of C_p can be nullified. Further, the effect of C_p can be eliminated by preadjusting the value of capacitor C_2 thus achieving self-compensation. By extending the nonideal analysis to other proposed topologies, it is noted that the ideal FO and CO of these configurations also get modified, and the corresponding expressions are listed in Table 2. Furthermore, the passive compensated error functions ($\varepsilon_{1n}(s)$, $\varepsilon_{2n}(s)$) for all topologies are recorded in Table 2. However, for brevity, the procedure for determining $\varepsilon_{1n}(s)\varepsilon_{2n}(s)$ is not shown for all structures explicitly except for Figure 3B.

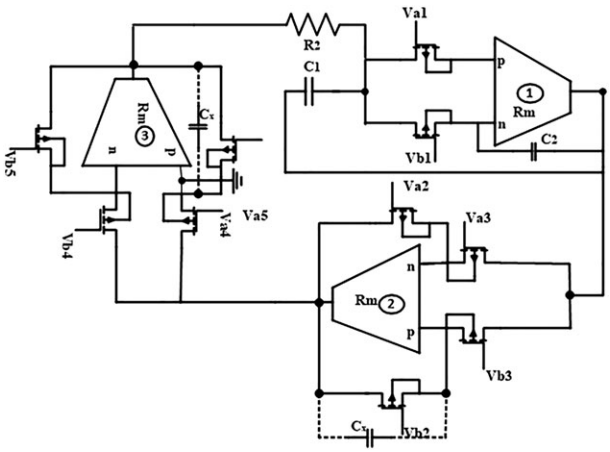


FIGURE 5 Passive compensated proposed SO (Figure 3B)

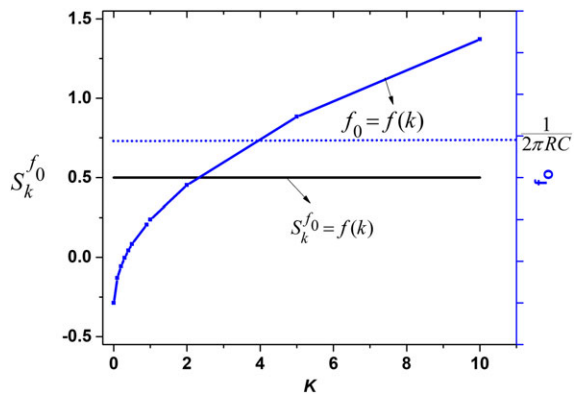


FIGURE 6 f_0 and $S_k^{f_0}$ as a function of k for proposed topologies [Colour figure can be viewed at wileyonlinelibrary.com]

TABLE 3 Sensitivity calculations for proposed circuits

Ckt. No	$S_Y^{f_o}$
Figure 3A	$\left\|S_{R_1}^{f_o}\right\| = \left\|S_{R_2}^{f_o}\right\| = \left\|S_{C_1}^{f_o}\right\| = \left\|S_{C_2}^{f_o}\right\| = \left\|S_k^{f_o}\right\| = \frac{1}{2};\ \left\|S_{C_p}^{f_o}\right\| = \frac{C_p}{2(C_2+C_p)}$
Figure 3B	$\left\|S_{R_1}^{f_o}\right\| = \left\|S_{R_2}^{f_o}\right\| = \left\|S_{C_1}^{f_o}\right\| = \left\|S_{C_2}^{f_o}\right\| = \left\|S_k^{f_o}\right\| = \frac{1}{2};\ \left\|S_{C_p}^{f_o}\right\| = \frac{C_p}{2(C_2+C_p)}$
Figure 3C	$\left\|S_{R_1}^{f_o}\right\| = \left\|S_{R_2}^{f_o}\right\| = \left\|S_{C_1}^{f_o}\right\| = \left\|S_{C_2}^{f_o}\right\| = \left\|S_k^{f_o}\right\| = \frac{1}{2};\ S_{R_a}^{f_o} = S_{R_b}^{f_o} = 0;\ \left\|S_{C_p}^{f_o}\right\| = \frac{C_p}{2(C_2+C_p)}$
Figure 3D	$\left\|S_{R_1}^{f_o}\right\| = \left\|S_{R_3}^{f_o}\right\| = \left\|S_{C_2}^{f_o}\right\| = \left\|S_{C_3}^{f_o}\right\| = \left\|S_k^{f_o}\right\| = \frac{1}{2};\ S_{R_2}^{f_o} = S_{C_1}^{f_o} = 0;\ \left\|S_{C_p}^{f_o}\right\| = \frac{C_p}{2(C_2+C_p)(C_3+C_p)}$

TABLE 4 Frequency stability factors for proposed topologies

Circuit	Condition	S_F
Figure 3A	$C_1 = 2C$, $C_2 = C$ and $R_1 = R_2 = R_a = R$, $R_b = R/n$	$-\sqrt{2n}$
Figure 3B	$C_1 = 2C$, $C_2 = C$ and $R_1 = R_2 = R_b = R_c = R_a = R$, $R_d = R/n$	$-\sqrt{2n}$
Figure 3C	$C_1 = C_2 = C$ and $R_1 = R_2 = R_b = R_c = R$, $R_a = 2R$, $R_d = R/n$	$-\sqrt{n}$
Figure 3D	$C_1 = C_2 = C_3 = C$ and $R_1 = R_2 = R_3 = R_a = R$, $R_b = R/n$	$-\sqrt{2n}$

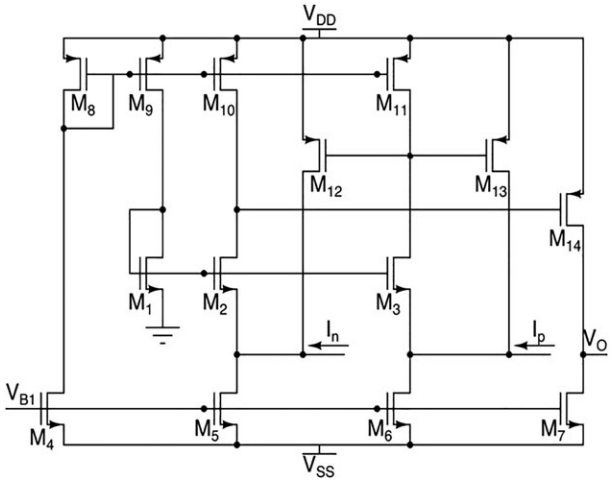
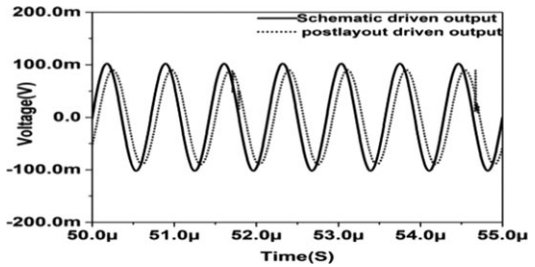
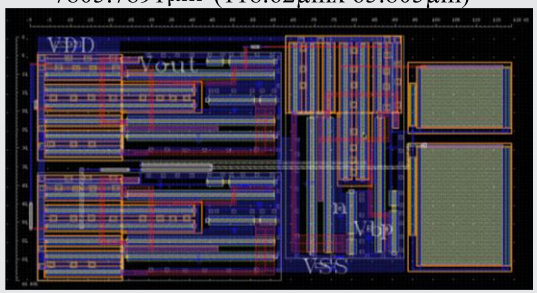
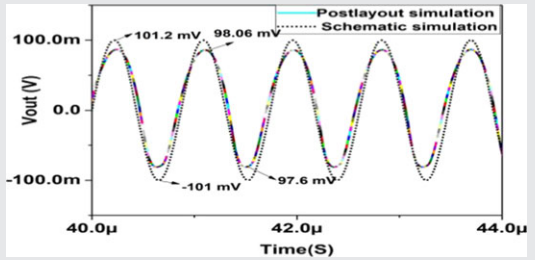
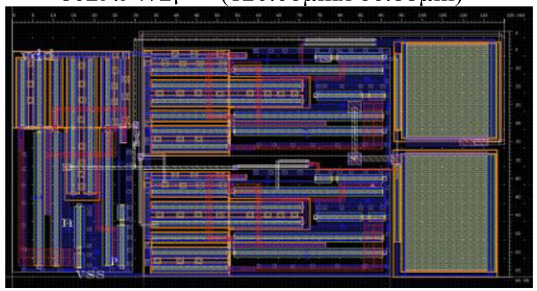
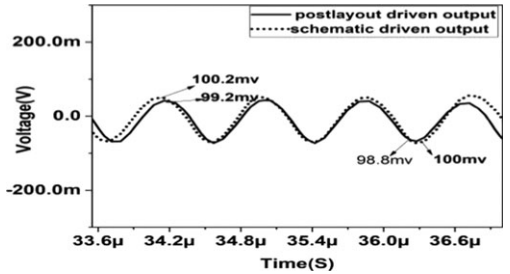


FIGURE 7 CMOS OTRA[18]

TABLE 5 Aspect ratios of transistors

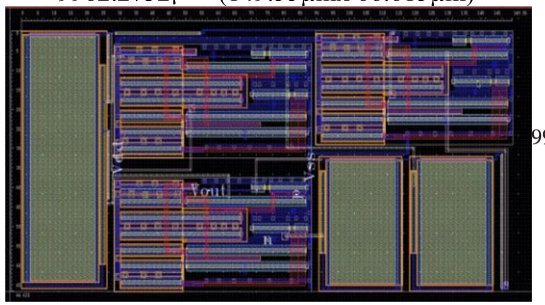
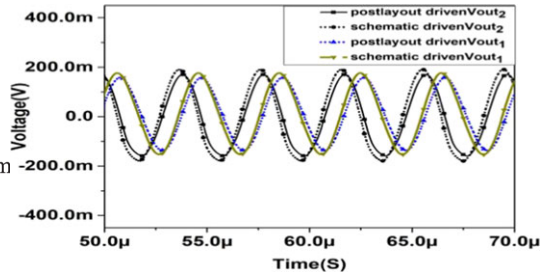
Transistor	W (μm)/L (μm)
M1-M3	36/0.9
M4	3.6/0.9
M5, M6	10.8/0.9
M7	3.6/0.9
M8-M11	18/0.9
M12, M13	36/0.9
M14	18/0.18

TABLE 6 Prelayout and postlayout results

Figure 3A	$R_1 = R_2 = R_b = 10$ kΩ, $R_a = 1$ kΩ, $C_1 = 5$ pF, $C_2 = 2.5$ pF/ FO:1.42 MHz	5253.4218μm^2(87.45μmx 60.07μm). 	
Figure 3B	$R_1 = R_2 = 10$ kΩ, $R_a = R_c = 1$ kΩ, $R_b = R_d = 4$ kΩ, $C_1 = 5$ pF, $C_2 = 2.5$ pF/ FO:1.12 MHz.	7805.7891μm^2(118.62μmx 65.805μm) 	
Figure 3C	$C_1 = 5$ pF, $C_2 = 4$ pF, $R_1 = R_2 = 10$ kΩ, $R_c = 1$ kΩ, $R_d = 10$ kΩ/FO:1.12 MHz	8029.9472μm^2(120.06μmx 66.88μm) 	

(Continues)

TABLE 6 (Continued)

Figure 3D	$C_2 = C_3 = 5$ pF, $C_1 = 10$ pF, $R_1 = 15$ kΩ, $R_2 = 5$ kΩ,$R_3 = 10$ kΩ, $R_b = 20$ kΩ, $R_a = 0.4$ kΩ/FO:260 kHz	9962.2732μm^2(149.55μmx 66.615μm)  9962.2732 μm	

4 | SENSITIVITY ANALYSIS

The sensitivity[42] of parameter X with respect to circuit parameters, say Y, is given as

$$S_Y^X = \frac{\partial X}{\partial Y}.\frac{Y}{X}. \tag{17}$$

Thus, sensitivity is an important performance criterion for any circuit[5-7,42] that enables analog IC designer to choose which elements should be carefully designed to maintain high circuit performance. Therefore, sensitivity analysis for the proposed circuits is carried out, and sensitivities of f_o for all configurations with respect to various circuit parameters are listed in Table 3. The frequency and f_o sensitivity ($S_k^{f_0}$) variation with respect to k for topologies of Figure 3 has been depicted in Figure 6. The sensitivity $\left|S_k^{f_0}\right|$ is fixed and is equal to 1/2, for the entire frequency range for all configurations.

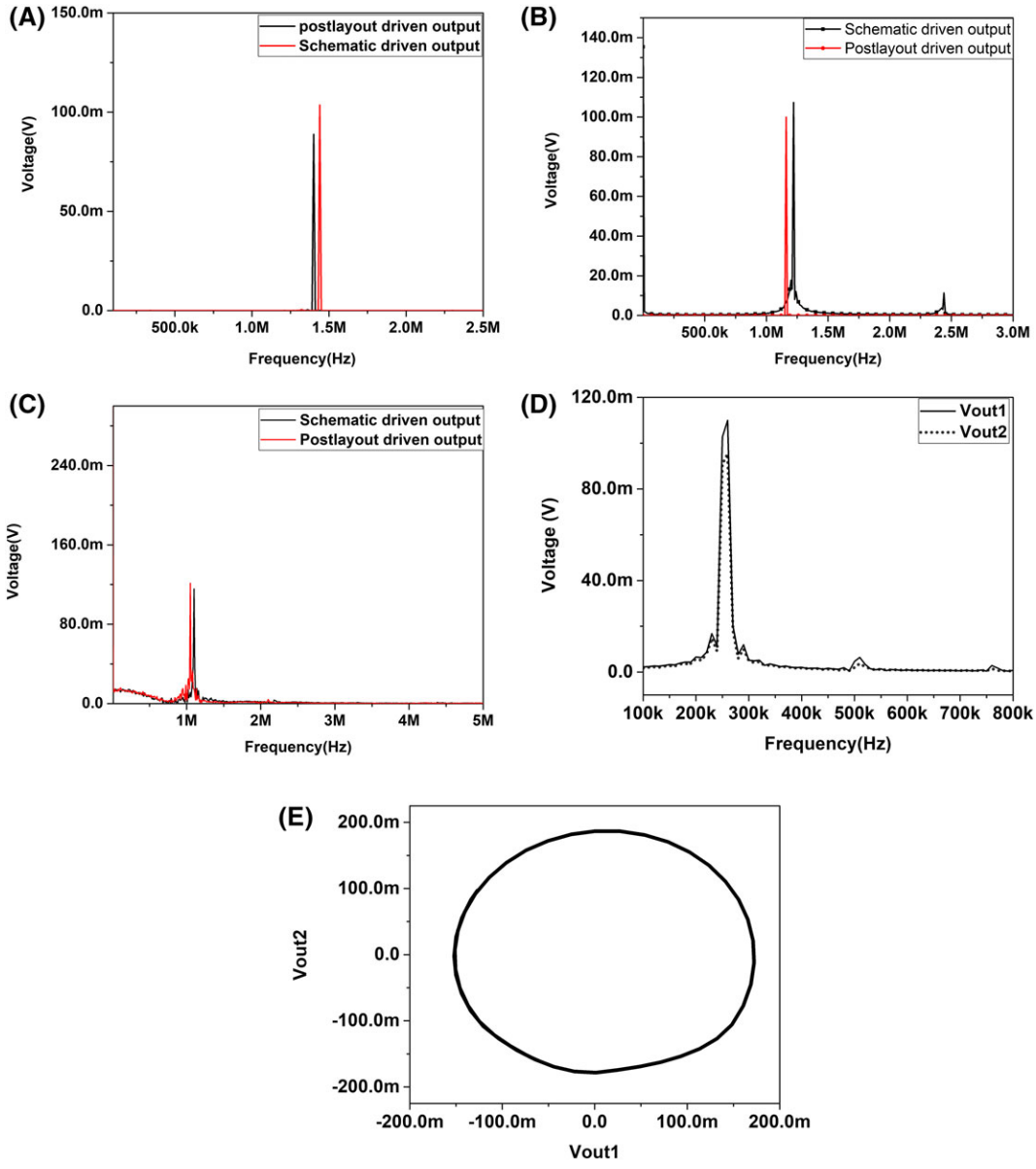


FIGURE 8 (A)-(D) FFT spectrums of Figure 3A-D and (E) Vout1 versus Vout2 graph for proposed QO (Figure 3D) [Colour figure can be viewed at wileyonlinelibrary.com]

5 | FREQUENCY STABILITY

The frequency stability is yet another significant performance measure for sinusoidal oscillators.[7] The frequency stability (S_F) is defined as $S_F = \frac{d\varphi(\alpha)}{d\alpha}\Big|_{\alpha=1}$, where $\alpha = \frac{\omega}{\omega_o}$ is the normalized frequency and $\varphi(\alpha)$ characterizes the phase function of the open loop transfer function of the oscillator.

The frequency stability factors are derived for all proposed topologies for chosen condition setting as shown in Table 4. Inspection of Table 4 suggests that the high S_F values can be achieved by selecting a larger value of n for all the circuits in Figure 3. Therefore, the proposed oscillators offer excellent frequency stability.

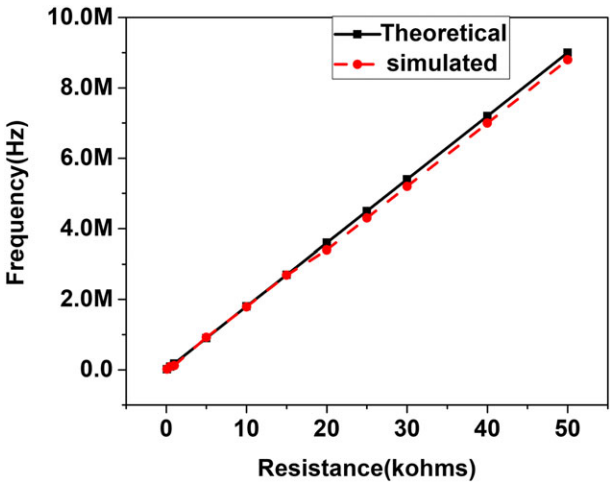


FIGURE 9 Variation of FO with R for Figure 3B [Colour figure can be viewed at wileyonlinelibrary.com]

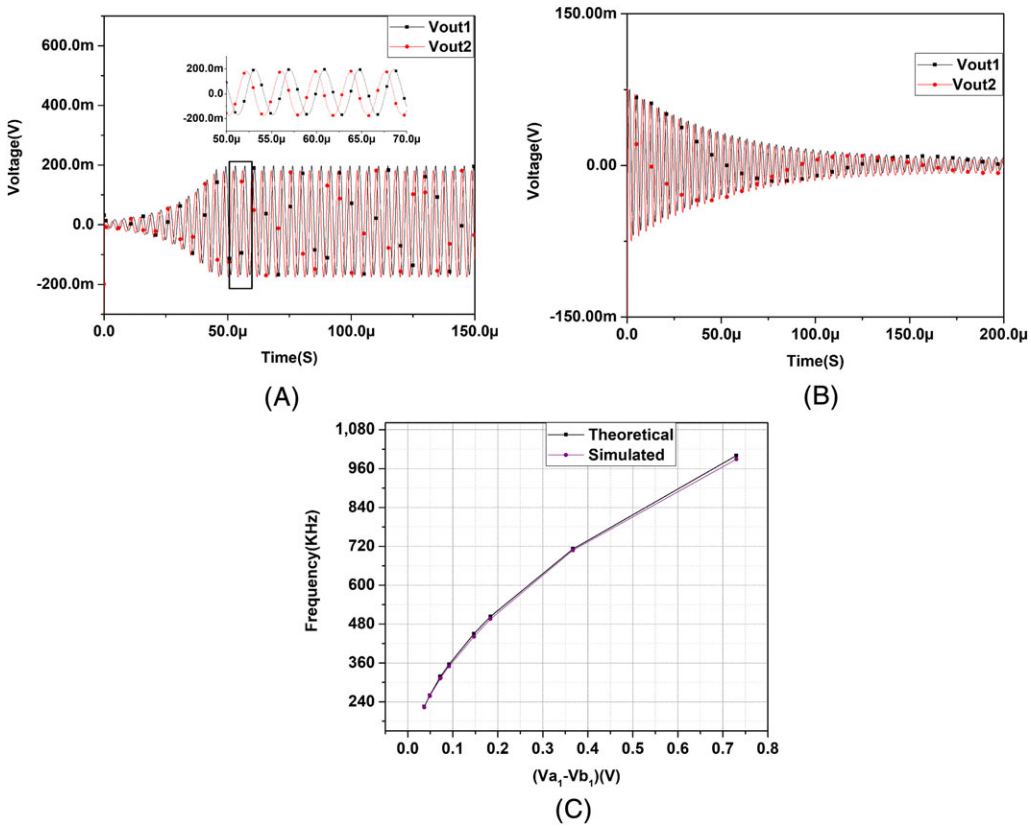


FIGURE 10 Simulated output waveforms at 260 kHz for proposed SO (Figure 4B): A, growing oscillations; B, decay of oscillations; C, variation of FO with R_1 by changing $(Va_1 - Vb_1)$ [Colour figure can be viewed at wileyonlinelibrary.com]

6 | SIMULATION AND LAYOUT RESULTS

To validate the theoretical analysis, the proposed topologies are simulated using the CMOS implementation of the OTRA[18] shown in Figure 7. The simulations are performed using cadence virtuoso ADE spectre tool at 180-nm technology node. Supply voltages are taken as ±0.9 V and bias voltage as −0.3 V. The sizes of the transistors used are listed in Table 5.

For the proposed configurations of Figure 3, the layouts and corresponding prelayout and postlayout transient outputs for chosen passive component values are shown in Table 6. The postlayout simulation results validate the layout implemented by physical verification checks[20,42,49] such as design rule check (DRC), layout vs schematic check (LVS), and RC parasitic extraction. Due to the inclusion of parasitics, the postlayout simulated frequencies are slightly decreased compared with simulated frequencies. The discrepancies between presimulation and postsimulation for all oscillators are found to be less than 5.1%. Therefore, all the topologies have been found to work in corroboration with theoretical propositions.

The percentage of total harmonic distortions (THDs) of the proposed configurations are observed to be less than 3.5%. The frequency spectrums of Figure 3 are shown in Figure 8A-D, and graph between Vout1 versus Vout2 for a simple limit cycle of period one for proposed QO (Figure 3D) is shown in Figure 8E.

To validate the linear variability of FO with R for Figure 3B, R is varied from 0.1 to 50 kΩ while the remaining resistance and capacitance values are chosen as $R_1 = R_2 = 10$ kΩ, $R_a = R_c = R$, $R_b = R_d = 25$ kΩ, and $C_1 = 5$ pF, $C_2 = 2.5$ pF. The corresponding graph is depicted in Figure 9, which confirms the linear relation between FO and R. The maximum %THD was observed to be 2.4%.

Further, to demonstrate the electronic tunability of the proposed SOs, the topology of Figure 3D was chosen wherein the resistors R_a, R_b, R_1, R_2, R_3, and R_4 are realized using MOS transistors. The corresponding MOS-C–based implementation is shown in Figure 4B. According to the technology node used for simulation, the parameter values are follows: $\mu_n = 327.37$ cm^2/V·s; gate oxide thickness $T_{ox} = 4 \times 10^{-9}$ m, channel width offset (WINT) and channel length offset

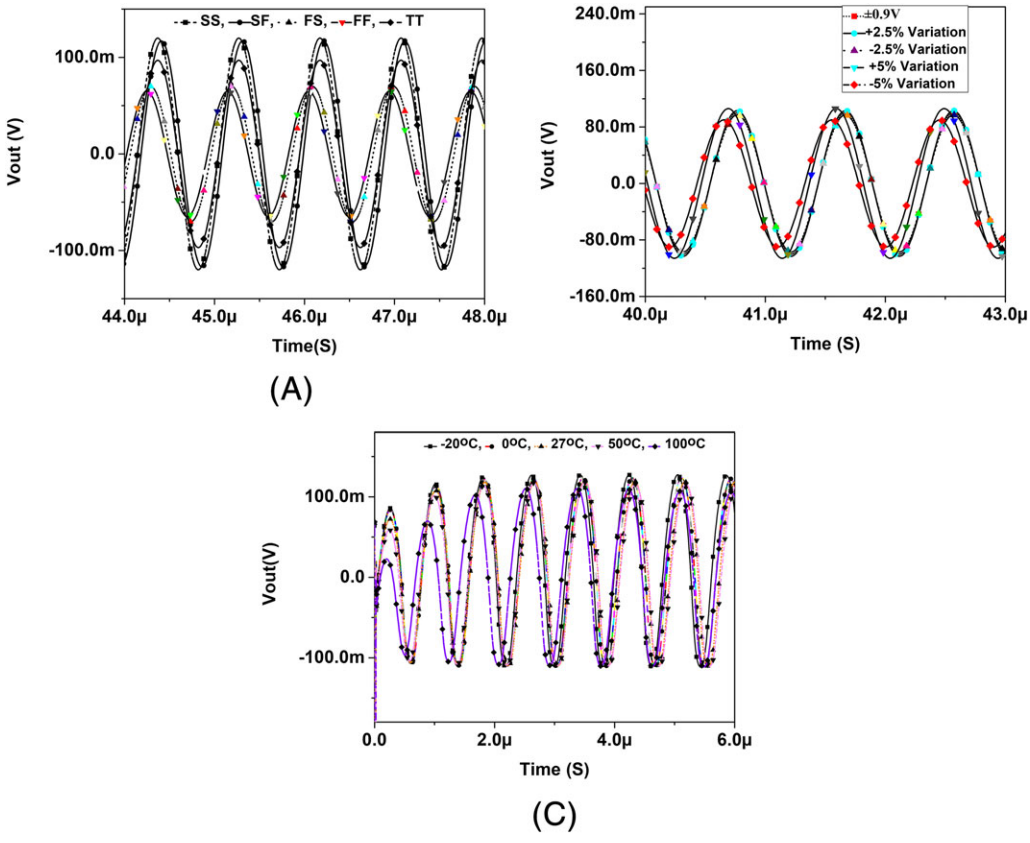


FIGURE 11 Output waveforms of PVT analysis corresponding to (A) process variations, (B) supply voltage variations, and (C) variations in temperature [Colour figure can be viewed at wileyonlinelibrary.com]

(LINT) = 0.01 μm. Therefore, the C_{ox} is calculated as 8.65×10^{-3} F. In simulations; we assumed W_{drawn} as 3.6 μm and L_{drawn} as 0.72 μm. To realize R ≈ 10 kΩ, (≈1 kΩ) the gate controlling voltages V_{ai}, V_{bi} (where i = 1-4) are adjusted, so that $V_{ai} - V_{bi}$ is equal to 0.073 V (0.73 V).

The growth and sustained oscillations of Figure 4B at 260 kHz is illustrated in Figure 10A, and the decaying oscillations are depicted in Figure 10B. Further, Figure 10C depicts the plot of variation of FO by tuning resistor R_1 (by altering gate controlling voltages Va_1 and Vb_1).

To assess the oscillator prefabrication performances PVT, Monte Carlo analysis is carried out for all the topologies. To conserve space, only the results obtained for Figure 3B are shown. Figure 11A shows the effect of different process corners (SS, SF, TT, FS, FF) on the output waveform, whereas Figure 11B,C represent output sinusoidal waveforms in the presence of supply voltage variations (±2.5%, ±5%) and temperature variations, respectively. It may be seen from Figure 11 that no abrupt change in the output in the presence of PVT variations is observed. Similar PVT results have been accomplished for remaining proposed topologies, and good quality of sine waves has been acquired in all of them.

The robustness of the proposed circuits (Figure 3C,D) is tested by performing Monte Carlo simulations by considering Gaussian distribution for hundred runs with a nominal tolerance of 3% in R_a/R_b and R_2, respectively, which in turn would affect the CO of the configurations. Figure 12 shows the histogram of the Monte Carlo runs, and it signifies that the circuits generate stable output in all iterations despite a change introduced in CO.

To operate the proposed circuit (Figure 3B) in VLF mode, the passive component values are chosen as C_1 = 300 pF, C_2 = 150 pF, and $R_1 = R_2 = 0.1$ MΩ, $R_a = R_c = 0.1$ kΩ, $R_b = R_d = 0.1$ MΩ. The frequency of the generated waveform is 7.31 Hz as against the calculated value of 7.5 Hz. The resultant transient response and frequency spectrum are shown in Figure 13A,B. The total harmonic distortion (THD) is found to be less than 2.5%.

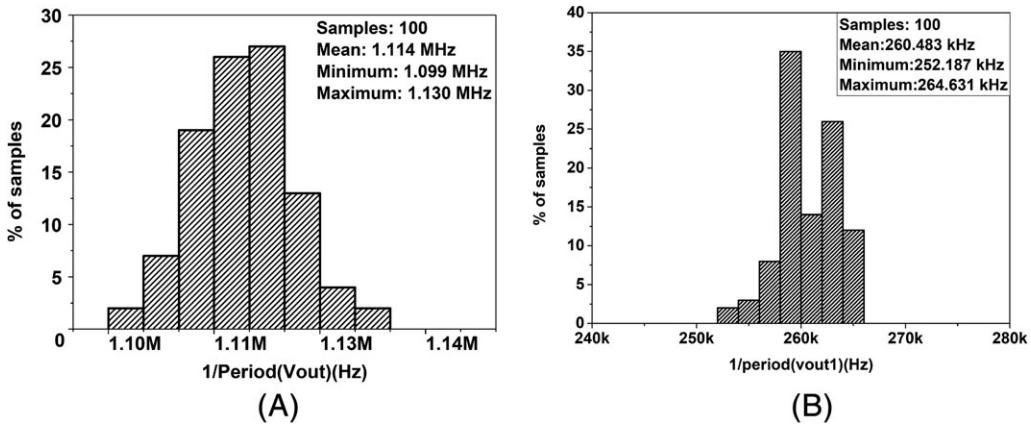


FIGURE 12 Histogram of the proposed circuits for (A) Figure 3C; (B) Figure 3D

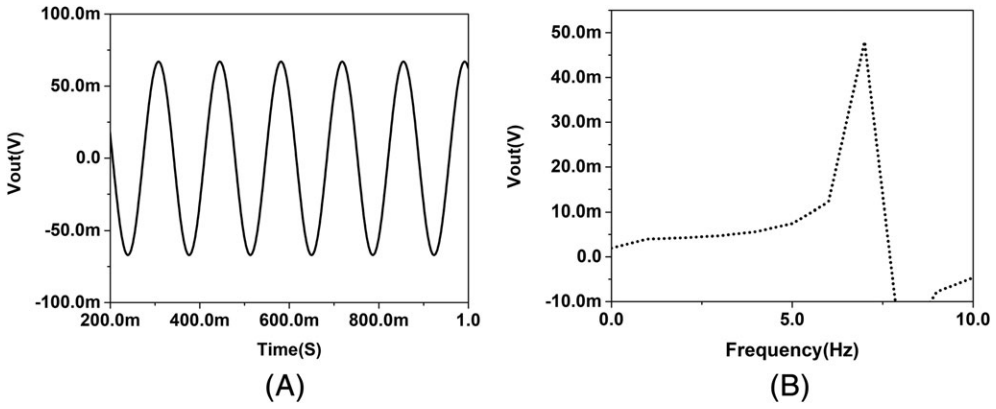


FIGURE 13 A, Simulated transient waveform. B, FFT spectrum

7 | CONCLUSION

Four new OTRA-based sinusoidal oscillators are reported in this paper, out of which one circuit provides quadrature output too. All the discussed topologies provide electronic tuning, independent control of FO without disturbing CO. One of the configurations in the proposed topologies provides linear tuning that is suitable for measurement and instrument applications. Active and passive sensitivities of FO are calculated and are found to be low. Monte Carlo analysis and PVT analysis have been presented to estimate the mismatch, after the fabrication process. The simulation and layout designs are executed by analog design environment (ADE) spectre tool by cadence virtuoso using 180-nm parameters.

ORCID

Rajeshwari Pandey https://orcid.org/0000-0002-7539-7888

REFERENCES

1. Salama KN, Soliman AM. Novel oscillators using the operational transresistance amplifier. *Microelectron J*. 2000;31(1):39-47. https://doi.org/10.1016/S0026-2692(99)00087-7
2. Çam U. A novel single-resistance-controlled sinusoidal oscillator employing single operational transresistance amplifier. *Analog Integr Circuits Signal Process*. 2002;32(2):183-186. https://doi.org/10.1023/A:1019586328253
3. Chien H. Third-order sinusoidal oscillator using a single CMOS operational transresistance amplifier. *J Appl Sci Eng*. 2016;19(2):187-196. https://doi.org/10.6180/jase.2016.19.2.09
4. Senani R, Bhaskar DR. Single op-amp sinusoidal oscillators suitable for generation of very low frequencies. *IEEE Trans Instrum Meas*. 1991;40(4):777-779. https://doi.org/10.1109/19.85353
5. Senani R. Novel sinusoidal oscillator employing grounded capacitors. *Electron Lett*. 1980;16(2):62-63.
6. Senani R. New types of sinewave oscillators. *IEEE Trans Instrum Meas*. 1985;34(3):461-463. https://doi.org/10.1109/TIM.1985.4315370
7. Bhaskar DR, Senani R. New CFOA-based single-element-controlled sinusoidal oscillators. *IEEE Trans Instrum Meas*. 2006;55(6):2014-2021. https://doi.org/10.1109/TIM.2006.884139
8. Manickam A, Chevalier A, McDermott M, Ellington AD, Hassibi A. A CMOS electrochemical impedance spectroscopy (EIS) biosensor array. *IEEE Trans Biomed Circuits Syst*. 2010;4(6 PART 1):379-390. https://doi.org/10.1109/TBCAS.2010.2081669
9. Revanna N, Viswanathan TR. Low frequency CMOS sinusoidal oscillator for impedance spectroscopy. *2014 IEEE Dallas Circuits and Systems Conference: Enabling an Internet of Things - From Sensors to Servers, DCAS 2014* 2014; 1–4. https://doi.org/10.1109/DCAS.2014.6965342.
10. Senani R, Bhaskar DR. New active-R sinusoidal vcos with linear tuning laws. *Int J Electron*. 1996;80(1):57-61. https://doi.org/10.1080/002072196137598
11. Komanapalli G, Pandey R, Pandey N. Minimum component count low frequency sinusoidal oscillator based on single OTRA. *IJCTA*. 2016;9(22):181-187.
12. Komanapalli G, Pandey N, Pandey R. Single OTRA based low frequency sinusoidal oscillator realization. *IOP Conf Ser: Mater Sci Eng*. 2017;225:12151. https://doi.org/10.1088/1757-899X/225/1/012151
13. Lahiri A. Low-frequency quadrature sinusoidal oscillators using current differencing buffered amplifiers. *Indian J Pure Appl Phys*. 2011;49(6):423-428.
14. Kumar V, Pal K, Gupta GK. Novel single resistance controlled sinusoidal oscillator using FTFN and OTA. *Indian J Pure Appl Phys*. 2006;44(8):625-627.
15. Abuelma'atti MT. Identification of a class of two CFOA-based sinusoidal RC oscillators. *Analog Integr Circuits Signal Process*. 2012;71(1):155-157. https://doi.org/10.1007/s10470-011-9778-3
16. Srivastava DK, Singh VK, Senani R. New very low frequency oscillator using only a single CFOA. *Am J Electr Electron Eng*. 2015;3(1):1-3. https://doi.org/10.12691/ajeee-3-1-1
17. Elwakil AS. Systematic realization of low-frequency oscillators using composite passive-active resistors. *IEEE Trans Instrum Meas*. 1998;47(2):584-586. https://doi.org/10.1109/19.744209
18. Mostafa BH, Soliman AM. A modified CMOS realization of the operational transresistance amplifier (OTRA). *Frequenz*. 2006;60:3-4.
19. Senani R, Singh AK, Gupta A, Bhaskar DR. Simple simulated inductor, low-pass/band-pass filter and sinusoidal oscillator using OTRA. *Circuits Syst*. 2016;7(3):83-99. https://doi.org/10.4236/cs.2016.73009

20. Nagar BC, Paul SK. Lossless grounded FDNR simulator and its applications using OTRA. *Analog Integr Circuits Signal Process*. 2017;92(3):507-517. https://doi.org/10.1007/s10470-017-1021-4
21. Cakir C, Cam U, Cicekoglu O. Novel allpass filter configuration employing single OTRA. *IEEE Trans Circuits Syst Express Briefs*. 2005;52(3):122-125. https://doi.org/10.1109/TCSII.2004.842055
22. Salama KN, Soliman AM. CMOS operational transresistance amplifier for analog signal processing. *Microelectron J*. 1999;30(3):235-245. https://doi.org/10.1016/S0026-2692(98)00112-8
23. Çam U, Kaçar F, Cicekoglu O, Kuntman H, Kuntman A. Novel two OTRA-based grounded immitance simulator topologies. *Analog Integr Circuits Signal Process*. 2004;39(2):169-175. https://doi.org/10.1023/B:ALOG.0000024064.73784.58
24. Nagar BC, Paul SK. Single OTRA based two quadrant analog voltage divider. *Analog Integr Circuits Signal Process*. 2018;94(1):161-169. https://doi.org/10.1007/s10470-017-1085-1
25. Soliman AM. Two integrator loop quadrature oscillators: a review. *J Adv Res*. 2013;4(1):1-11. https://doi.org/10.1016/j.jare.2012.03.001
26. Pittala CS, Srinivasulu A. A sinusoidal oscillator using single operational transresistance amplifier. *2013 5th International Conference on Advanced Computing, ICoAC 2013* 2014; 508–511. https://doi.org/10.1109/ICoAC.2013.6922003.
27. Pandey R, Pandey N, Komanapalli G, Anurag R. OTRA based voltage mode third order quadrature oscillator. *ISRN Electronics*, Hindawi Publishing Corporation. 2014;2014:5.
28. Pandey R, Pandey N, Paul SK. MOS-C third order quadrature oscillator using OTRA. *2012 Third International Conference on Computer and Communication Technology* 2012; (1):77–80. https://doi.org/10.1109/ICCCT.2012.24.
29. Chien HC. New realizations of single OTRA-based sinusoidal oscillators. *Act Passive Electron Compon*. 2014;2014:1-12. https://doi.org/10.1155/2014/938987
30. Nagar BC, Paul SK. Voltage mode third order quadrature oscillators using OTRAs. *Analog Integr Circuits Signal Process*. 2016;88(3):517-530. https://doi.org/10.1007/s10470-016-0781-6
31. Avireni S, Pittala CS. Grounded resistance/capacitance-controlled sinusoidal oscillators using operational transresistance amplifier. *WSEAS Trans Circuits Syst*. 2014;13:145-152.
32. Pittala CS, Srinivasulu A. Two simple sinusoidal oscillators using single operational transresistance amplifier. In: 3r rd Two International Conference on Signal Processing, Processing, Communication and Networking (ICSCN) 3 rd Two. 2015; 247–263.
33. Pandey R, Pandey N, Kumar R, Solanki G. A novel OTRA based oscillator with non interactive control. In: *2010 International Conference on Computer and Communication Technology, ICCCT-2010*. 2010; 658–660.
34. Gupta A, Senani R, Bhaskar DR, Singh AK. OTRA-based grounded-FDNR and grounded-inductance simulators and their applications. *Circuits, Systems, Signal Process*. 2012;31(2):489-499. https://doi.org/10.1007/s00034-011-9345-2
35. Kumngern M, Kansiri I. Single-element control third-order quadrature oscillator using OTRAs. In: International Conference on ICT and Knowledge Engineering. 2015; 24–27.
36. Pandey R, Pandey N, Komanapalli G, Singh AK, Anurag R. New realizations of OTRA based sinusoidal oscillator. In: 2015 2nd International Conference on Signal Processing and Integrated Networks (SPIN) New 2015; 913–916.
37. Komanapalli G, Pandey N, Pandey R. OTRA based second and third order sinusoidal oscillators and their phase noise performance. In: *AIP Conference Proceedings*. Vol.1859. https://doi.org/10.1063/1.4990170. Eluru, India: AIP Publishing; 2017.
38. Nagar BC, Paul SK. Realization of OTRA-based quadrature oscillator using third-order topology. In: Konkani A, Bera R, Paul S, eds. *Advances in Systems, Control and Automation. Lecture Notes in Electrical Engineering*. Singapore: Springer Nature Singapore Pte Ltd.; 2018:375-386.
39. Komanaplli G, Pandey N, Pandey R. New realization of quadrature oscillator using OTRA. *Int J Electr Comput Eng (IJECE)*. 2017;7(4):1815-1823. https://doi.org/10.11591/ijece.v7i3.pp1815-1823
40. Kilinc S, Cam U. Operational transresistance amplifier based first-order allpass filter with an application example. *2004 47th Midwest Symp Circuits Syst, 2004 MWSCAS'04*. 2004;1:65-1:68. https://doi.org/10.1109/MWSCAS.2004.1353898
41. Shaker PC, Srinivasulu A. Four new oscillators using operational transresistance amplifier. *Radioelectron Commun Syst*. 2017;60(5):206-214. https://doi.org/10.3103/S0735272717050028
42. Komanapalli G, Pandey N, Pandey R. New realization of third order sinusoidal oscillator using single OTRA. *Int J Electron Commun (AEÜ)*. 2018;93(June):182-190. https://doi.org/10.1016/j.aeue.2018.06.005
43. Pittala CS, Srinivasulu A. Quadrature oscillator using operational transresistance amplifier. In: Int Conf on Applied Electronics 2014; 117–120.
44. Salama KN, Soliman AM. Active RC applications of the operational transresistance amplifier. *Frequenz*. 2000;54(7–8):171-176. https://doi.org/10.1515/FREQ.2000.54.7-8.171
45. Hou C, Huang C, Horng J. A criterion of a multiloop oscillator circuit. *J Circuits, Syst Comput*. 2007;16(1):105-111.
46. Hou CL, Chang CW, Horng JW. A quadrature oscillator employing the dominant poles of the OTRAs. *J Adv Eng*. 2007;2(3):185-187.
47. Pandey R, Pandey N, Bothra M, Paul SK. Operational transresistance amplifier-based multiphase sinusoidal oscillators. *J Elect Comput Eng*. 2011;2011:4. https://doi.org/10.1155/2011/586853

48. Pandey R, Pandey N, Mullick R, Yadav S, Anurag R. All pass network based MSO using OTRA. *Adv Electron*. 2015;2015:1-7. https://doi.org/10.1155/2015/382360

49. Baker RJ. *CMOS Circuit Design, Layout, and Simulation*. 3rd ed. New York: Wiley; 2010.

How to cite this article: Komanapalli G, Pandey R, Pandey N. New sinusoidal oscillator configurations using operational transresistance amplifier. *Int J Circ Theor Appl*. 2019;1–20. https://doi.org/10.1002/cta.2619

Received: 31 August 2018 | Revised and accepted: 3 November 2018

DOI: 10.1002/mmce.21701

WILEY INTERNATIONAL JOURNAL OF RF AND MICROWAVE COMPUTER-AIDED ENGINEERING

REVIEW ARTICLE

Recent developments in bandwidth improvement of dielectric resonator antennas

Sounik Kiran Kumar Dash[1] | Taimoor Khan[2]

[1]Department of Electronics and Communication Engineering, CHRIST (Deemed-to-be University), Bengaluru, India

[2]Department of Electronics and Communication Engineering, National Institute of Technology Silchar, Assam, India

Correspondence
Department of Electronics and Communication Engineering, National Institute of Technology, Silchar, Assam, 788010, India.
Email: ktaimoor@ieee.org

Abstract

This article shows a compressed chronological overview of dielectric resonator antennas (DRAs) emphasizing the developments targeting to bandwidth performance characteristics in last three and half decades. The research articles available in open literature give strong information about the innovation and rapid developments of DRAs since 1980s. The sole intention of this review article is to, (a) highlight the novel researchers and to analyze their effective and innovative research carried out on DRA for the furtherance of its performance in terms of only bandwidth and bandwidth with other characteristics, (b) give a practical prediction of future of DRA as per the past and current state-of-art condition, and (c) provide a conceptual support to the antenna modelers for further innovations as well as miniaturization of the existing ones. In addition some of the significant observations made during the review can be noted as follows; (a) hybrid shape DRAs with Sierpinski and Minkowski fractal DRAs seems comfortable in obtaining wideband as well as multiband, (b) combination of multiple resonant modes (preferably lower modes) can lead to wider impedance bandwidth, (c) at proper matching wider patch with slotted dielectric resonator can exhibit better bandwidth.

KEYWORDS

antenna performance, antenna review, bandwidth, dielectric resonator antenna

1 | INTRODUCTION

Dielectric resonator antenna, known as DRA or sometime DR-antenna, has been brought remarkable attention around the globe in last three and half decades. Though, the concept of the dielectric resonator (DR) as a high Q-factor material has been brought by Richtmyer[1] in 1939 but it was used as an effective electromagnetic radiator in 1983.[2] Since then, it has grown up rapidly with various improvements. The potential reasons behind its techno-popularity can be considered as follows: (a) DRAs made of dielectric material and has three dimensional design flexibility (Figure 1). Here the permittivity, physical dimension of DR controls its resonant frequency as well as Q-factor. Like radius for hemispherical shape, height-to-radius ratio for cylindrical shape and width-to-length ratio for rectangular shapes, affects the resonant frequency. The presence of nonconducting material minimizes the conductor losses, even at millimeter wave frequencies and achieves >95% efficiency, which is quite challenging for other antennas.[3–5] (b) it supports wide range of coupling techniques which enables excitation of several modes guaranteeing improved radiation pattern with more coverage. This kind of flexibility is rarely available with other conventional antennas.[3,4] These techniques can be improved further with integration of array concept, (c) the size of the DRA depends on free space wavelength (λ_0) as well as relative permittivity (ε_r), whereas other antenna size depends upon only λ_0, means the DRAs are characterized by comparatively smaller form factor than other antennas.[3,4] By each passing years investigations on different modeling techniques and performance improvements have been carried out by the researchers in order to meet the demand of modern wireless applications.

The several modeling techniques and applications have already been well discussed by the authors in two review articles,[4,5], respectively. Few other limited review articles[6–10] have also been published in the open lierature. The available

 © 2019 Wiley Periodicals, Inc.

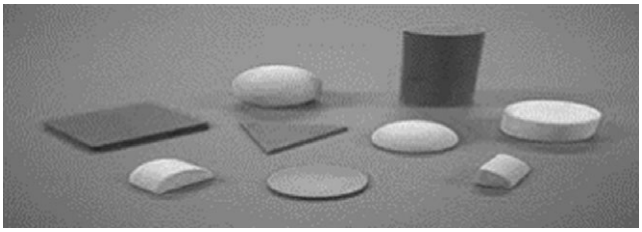


FIGURE 1 Different shapes of dielectric resonators

book[3] and review articles[6,7] mainly highlights different performances (such as gain, circular polarization, and mutual coupling reduction) in DRAs as well as in hybrid shape DRAs. Some authors have highlighted the recent advances say bandwidth, compactness, reconfigurability, array, and so on.[8,9] The recent advances pointing toward broadband, ultra-wideband, and multiband have been reported in Reference.[10]

However, to the best of authors' knowledge no such review is available in References [6,7] covering all the developing technologies and mechanisms dedicated to DRA bandwidth improvement. And this type of review article seems to be equally important among the researchers working on DRA. Hence, the sole intention of this review article is to bring out the notable research carried out on DRA targeting to performance characteristics like; bandwidth, gain, directivity, circular polarization, and mutual coupling reduction, by the means of physical parameters optimizations. For a fruitful technical understanding, based on research and development trends, the sections are chronologically arranged and well discussed. This review article is abridged as follow: The basics of DRA and its major parts are briefed in Section 2. Section 3 describes research carried out on DRA for bandwidth. To bring the attention of readers a well-organized summery of this whole review process is kept in Section 4 followed by the conclusion in Section 5. For ease of understanding, the overall flow of this review process is tabulated in Table 8.

2 | DR AS AN ANTENNA AND ITS MAJOR PARTS

Initially, the DRs were used in filter and oscillator applications intending for storing of energy. Because of its inherent high Q-factor, it led the resonator to store more energy by checking the radiation.[1] In 1983, a research group headed by Long,[2] explored that, when the Q-factor is lowered, placed on a metal plate, and excited, the radio waves bounce back and forth in-between the resonator boundary and creates standing radio-wave. And this standing radio waves can penetrate out from the resonator boundary by means of radiation once it is excited at proper resonating mode. Briefly, the DR antenna needs three basic parts, that is, DR, ground plane, and coupling mechanism.

In case of DR, hemispherical, cylindrical, and rectangular shapes are considered as the most common shapes.[1,2] In addition to these regular shapes, some other modified shapes like, hemispherical, hybrid DR by stacking, variation of permittivity, fractal, electromagnetic band gap (EBG), superstrate, horn, and so on have also been well analyzed for performance regulation[2,3] as per the application requirement. Moreover, different coupling mechanism say, aperture coupling, probe coupling, microstrip line coupling, coplanar coupling, dielectric image guide coupling, and so on, also plays an important role in regulating the performance.[2,3] It can be noted that, DRA can be placed above thick metallic ground plane or above dielectric substrate backed by thin ground plane.

3 | DRA RESEARCH ON BANDWIDTH

DRA deals with many advanced features, among which wide bandwidth is considered to the prominent one.[1] By each passing years, different advanced approaches are being reported either for further enhancement of default bandwidth or creation of dual-/multi-band operation using resonator shape. Broadly, these approaches can be divided into four categories; firstly, according to the antenna geometry (DR shape/fractal/EBG/metamaterial), secondly, the coupling mechanism (feeding type/aperture shape), thirdly, the DR permittivity, and lastly, according to the excitation of specific mode. From ease of readers' point of view, these techniques are discussed separately for single-band,[11–169] dual-band,[170–180] and multi-band,[181–186], respectively. Moreover, some other characteristics say radiation/notch[187–191] are also discussed in the preceding part of this section. The organization of this section is summarized in Figure 2.

3.1 | Bandwidth improvement in single band operation

The literature on research of single bandwidth based DRA[11–169] is broadly divided into by means of antenna geometry, coupling scheme, DR permittivity, and mode of operation. The discussion flow is summarized in Figure 3.

3.1.1 | Bandwidth improvement using different antenna geometry

During this reviewing process, it has been noticed that, the researchers have reported bandwidth improvement by

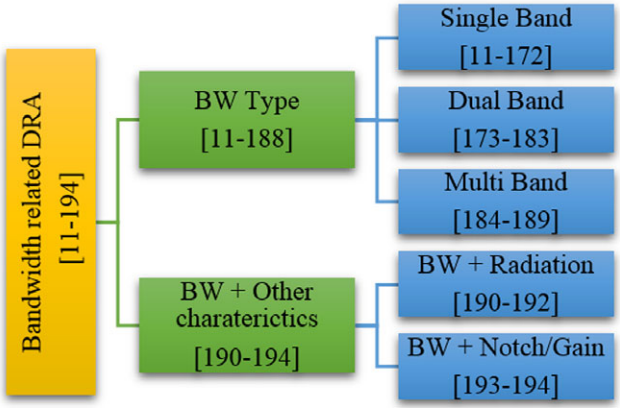


FIGURE 2 Shows the flow of bandwidth related DRA analysis

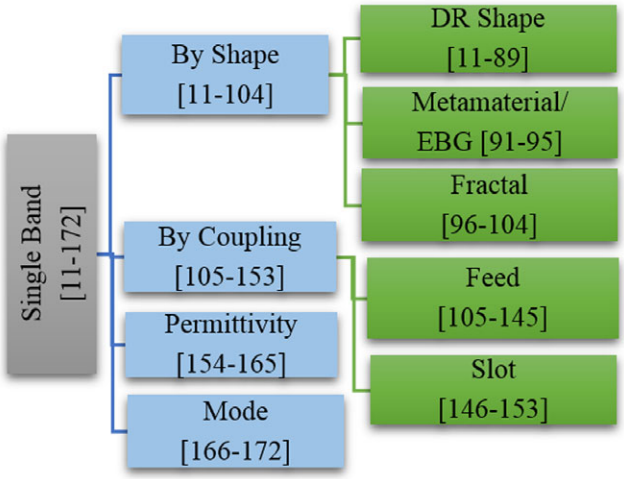


FIGURE 3 Shows categorization of analysis flow of single band DRAs

means of DR shape modification,[11–89] incorporation of EBG/metamaterial,[91–95] or fractal.[96–104]

Different shapes of DR for bandwidth improvement

As it is known that, DR is 3D object its dimension plays an important role in controlling the operation range. The very familiar concept, that is, stacking (one DR upon another DR) was first introduced by Kishk[11] in 1989. In this case, two DRs have two resonant frequencies, and when they are stacked dual resonance concept works out for broadening the antenna bandwidth. This technique can be extended for triple/multiple stacking in-order to further enhance the bandwidth. Apart from this, the concept of parasitic coupling[3] and multiple DR with single feed[3] are also being used by placing a DR near to a parent DR. These techniques ultimately require an extra DR which can be considered as a drawback. Hence, the approaches with single DRA element for the same purpose, are quite interesting. The most popular/tradition technique is lowering the inherent Q-factor. As Q-factor is directly related to dielectric constant (permittivity), then by decreasing the dielectric constant the Q-factor can be lowered resulting wider bandwidth.[2]

$$BW = \frac{s-1}{Q\sqrt{s}} \times 100\% \quad (1)$$

Where, s-desired VSWR at the input port of the DRA.

Hence, different approaches have been reported targeting lower Q-factor for bandwidth widening. This involves, intrusion of any sort of air gap inside the DR or in-between the DR and ground plane. This is supplemented by a shift in resonant frequency and increase in volume.[3] Some researchers have also introduced spilt DR,[21] segmented DRs[39] for the same purpose. Briefly, it can be said that, the alteration of aspect ratio of DR mostly plays a crucial role in controlling the bandwidth. The concept of hybrid DR (ie, combination two or more DR shapes) has also been reported for obtaining wide band and ultra-wideband.[58] In this regard some super shaped DRs, say EYE-shape,[30] A-shape,[61] Z-shape,[66] pentagon shape,[84] dumbbell shape,[86] as shown in Figure 4 have also been proposed. The complete compressive literature is discussed here.

Kishk et al.[11] have explored the concept of wide band DRA with 25% impedance bandwidth in a co-axial probe fed cylindrical shaped DRA placed on a conducting ground plane. Lee and Simons,[12] have reported a novel Substantial bandwidth improvement technique, that is, placing parasitic resonator directly above (stacked form) and on both sides of the main resonator which gave comparatively more impedance bandwidth than that of single element DRA. Wong and Chen[13] have explored that, a dielectric coating can act as a transition between inner wave of the DR and free space wave and lead for a wider impedance, which has been proved in case of a hemispherical DRA. Shum and Luk[14] have explored the stacking and air gap intrusion concept for bandwidth enhancement purpose in a DR antenna while

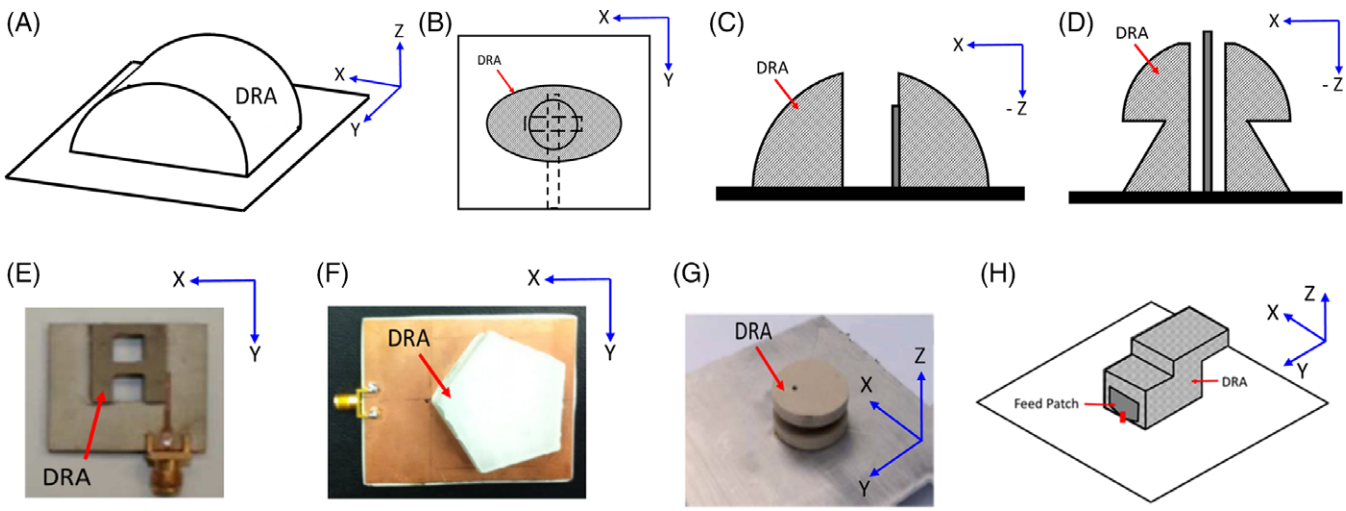


FIGURE 4 Different shapes of DRA developed for wide bandwidth purpose: (A) Split CDRA,[21] (B) EYE Shape DRA,[30] (C) Half HDRA,[39] (D) Pawn shape DRA,[58] (E) A-shape DRA,[61] (F) Pentagon shape DRA,[84] (G) Dumbbell shpae DRA,[86] (H) Z-shape DRA[66]

experimenting a probe fed DRA (5% for single element DRA while 20% for stacked with air gap). Chen et al.,[15] have reported that a dielectric coated DR antenna doubles the impedance bandwidth than that of without coating. Luk et al.[16] have investigated theoretically a hemispherical DR antenna with concentric conductor for wide impedance bandwidth (19% VSWR <2), by using Greens' function and MoM method. After this, a two/three element slot coupled DR antenna was investigated by Fan and Antar[17] for obtaining better bandwidth as compared to single element which can further be utilized for dual band purpose also.

Sangiovanni et al.[18] have demonstrated a coaxial probe fed cylindrical DRA offering >30% impedance bandwidth by taking another annular dielectric ring inside of same height and of different permittivity. Mongia[19] has studied the effect of antenna size on bandwidth and frequency. Drossos et al.[20] have studied the effect air-gap intrusion between the DR and microstrip feed for wider bandwidth. Kishk et al. [21] have studied a coaxial probe fed split cylindrical DRA on a conducting ground plane using MoM operating in HEM_{11} or HEM_{12} modes to achieve wideband of 35% as well as dual-band by inserting a resonator of a different dielectric material inside another resonator. Kishk et al.[22] have studied the effect of conical DR orientation on bandwidth and concluded that inverted cone has much wider bandwidth than noninverted one, but however the split cone achieved the highest, that is, 50% impedance BW which supports more modes. Ong et al. ,[23] have investigated a disc ring resonator and found 47% BW when inner DR permittivity is taken higher than the outer one and 30% when inner dielectric is lower than the outer one.

Kishk[24] has explored the triangle-cylinder (special case of truncated tetrahedron) fed by a coaxial probe operating over a wide range of 40% bandwidth. Gupta et al.,[25] experimented the bandwidth of individual circular and rectangular patch suspended on a dielectric material of $\varepsilon_r = 3.05$ for 18% and 13% impedance bandwidth, respectively. Lapierre et al.,[26] have achieved 74% impedance bandwidth by exciting an annular ring DR with a monopole antenna in $TM_{01\delta}$. Nannini et al.,[27] have observed that stacking and air intrusion improved the bandwidth of a slot fed CDRA. Guo et al.,[28] have reported something more for the bandwidth enhancement and found stacked annular CDRA operating for 42% impedance BW while 18% for only stacked one. Denidni et al.,[29] have reported a coaxial probe fed two equiangular-triangle across sections to give broad side radiation pattern operating between 1.71 and 2.51 GHz, that is, 38% impedance bandwidth. Chair et al.,[30] have designed an EYE shaped DRA excited through a narrow slot for X-band application with 27% BW.

After that, wideband cylindrical and rectangular DRA were proposed by Young et al.[31] They attained an impedance bandwidth of 30%, by considering radius-to-height and length-to-width ratio for cylindrical and rectangular DRA, respectively. Coulibaly et al.,[32] have studied the effect of intermediate substrate for bandwidth enhancement in a microstrip stepped patch DRA by 43%. A co-axial fed T-shaped compact DRA having two equilateral-triangle cross sections has been studied by Rao et al. [33] for a wideband width of 60% covering several application oriented bands like; DCS, PCS, UMTS, WLANS. Chair et al.,[34] have found perforated DRA as a substitute of having annular ring DRA with lower permittivity outside the cylindrical disk, which resulted with enhanced 26.7% impedance bandwidth.

Rezaei et al.,[35] have analyzed a two segment rectangular DRA separated by a metal plate for 76.8% impedance bandwidth and also informed that, high permittivity gives better coupling while lower ones give wide bandwidth. Ruan et al.,[36] have achieved 67% impedance bandwidth in a 2-layer stacked resonator by considering the material combination and probe length with feed position. Ge et al.,[37] have suggested to insert relatively low dielectric permittivity segment between the DR of high permittivity and the ground plane in order to have a wideband and also achieved a BW (6.7-20) GHz with a notch (16.5-17) GHz. Guha and Antar[38] have investigated a four-element DRA combination for monopole like radiation pattern over 29% impedance bandwidth and 4 dBi gain with $HEM_{11\delta}$, which is double than that of the normal bandwidth of monopole having height two times of the proposed DRA. Again Guha et al. ,[39] have demonstrated a 99.08% efficient two element half-hemispherical DR-antenna operating over 35% with monopole like radiation pattern and 5 dBi peak gain and in[40] Guha et al. have suggested some novel guidelines in view of ultra-wideband (5-13 GHz) monopole DRA.

Ruan et al.,[41] have reported a UWB double annular-ring DR-antenna covering 3 to 11.2 GHz range where radius and heights played an important role for bandwidth enhancement. Chair et al.,[42] have analyzed stacked DRA with both co-axial and aperture feeding mechanism for getting BW > 40% while >30% for one step with 5 dBi gain. Chang and Kiang,[43] have designed a CPW-fed three side metal coated rectangular DR-antenna of 4.2 to 6.8 GHz operating range (47% BW) for WLAN application by modeling the dielectric-air interface as perfect magnetic conductor. Huang and Kishk,[44] have modeled a stacked DRA for wide band of 66% for co-axial probe feed while 32% for aperture coupling mechanism. Kumar et al. ,[45] have designed a microstrip along with vertical strip feeding mechanism for a low radiation Q-value novel cylindrical DR-antenna operated over 35% BW centered at 3 GHz. Ghosh et al.,[46] have designed a wide band transreceive monopole fed DRA with wide band (4.8-11.0 GHz) characteristics for Bluetooth technology. Again, a 110% impedance bandwidth T-shaped monopole fed DRA was designed by Ghosh et al.[47] Chang et al.,[48] have found 20% impedance bandwidth (4.76-5.86 GHz) with broadside radiation pattern in a DRA. Rocha et al. ,[49] have improved the bandwidth up to 13.2% of a probe fed vertically stacked two cylindrical disks of dielectrics Cr0.75Fe1.25O3 (CRFO) and

Fe0.5Cu0.75Ti0.75O3 (FCTO) by exciting in $HEM_{11\delta}$ mode. A skirt monopole fed conical ring DR-antenna operating in higher order modes (TM_{012+6} and TM_{016}) has been giving a bandwidth ranging 1.8-6.9 GHz was proposed by Jazi et al.[50] Li et al.,[51] have developed conformal patch fed hemispherical DRA covered a wide band of 40% centered at 3.1 GHz and which could be shifted to 3.5 GHz adjusting the length and width of the feeding patch. Denidni and Weng,[52] have proposed a rectangular-DRA with bevel-shaped patch feed and an air-gap inserting technique for obtaining 120% bandwidth ranging 2.6 to 11 GHz. Rashidian and Klymyshyn[53] have developed a 5.2:1 aspect ratio DRA of $\varepsilon_r = 25$ with dual mode and wideband (>16%) characteristics. Chang and Feng[54] have modeled a L-shaped microstrip monopole type feed for achieving 25% impedance bandwidth centered at 5.5 GHz. Apart from this, an annular slot excited two layered hemispherical DRA with wide band characteristics (reduced from 55% to 31%) has been experimented using Green's function and MoM approach by Leung and So.[55]

Rashidian and Klymyshyn,[56] have explored that dual mode operation with high aspect ratio DR structure that leads to bandwidth improvement by adopting two segment DRA techniques for bandwidth better than 11%. Ryu and Kishk,[57] have got 81% impedance bandwidth in a simple and compact DRA using partial ground plane in vertical direction. Guha et al.[58] have investigated a quarter wave monopole fed novel pawn shaped hybrid DR-antenna operating over a wide range of 122% bandwidth (5.5-23 GHz) and 4-6 dBi gain. In 2009, an extremely compact co-axial fed DR-antenna achieving 109.5% (3.1-10.6 GHz) has been reported by Ge and Esselle.[59] Rashidian and Klymyshyn,[60] have designed a microstrip-fed miniaturized antenna for obtaining broadband (16%) with stable radiation pattern and low cross-polarization. Ryu and Kishk,[61] have reported an A-shaped UWB DR-antenna for achieving more than 93% and 95% impedance bandwidth and antenna efficiency, respectively. Again, Ryu and Kishk[62] have designed a CPW fed UWB (115%) DRA followed by a triangularly notched cylindrical DRAs placed laterally on the ground plane offering UW bandwidth of 76.7% (4.5-10.1 GHz). Jazi et al.,[64] have reported a 10 GHz bandwidth DR-antenna with monopole like radiation. Guha et al.,[65] have modeled and realized a 120% impedance bandwidth in a monopole fed hybrid dielectric ring resonator with monopole like radiation over the entire operating bandwidth. Denidni et al. ,[66] have investigated rigorously a novel Z-shaped DRA with air-gap and bevel shaped patch to achieve a wide bandwidth of 120%. Ge et al.,[67] have suggested to adopt standard conducting mirror wall technique to reduce the volume of the UWB DRA. Ahmed et al.,[68] have demonstrated a microstrip type printed monopole fed DR-antenna for wideband applications, where inner grove inside the DR helped in enhancing the bandwidth as well as controlling the slot width. Two split ring resonator ($\varepsilon_r = 7.4$) fed by a T-junction ended type coaxial line has been developed to achieve a wide impedance bandwidth of 43.2% and 31.4% radiation bandwidth by Wang et al.[69]

Chaudhary et al.,[70] have stacked ZST and Epoxy composite system for getting wide impedance bandwidth of ~58.7% with peak gain of 6.3 dB for X-band applications. Guha et al.,[71] have developed an UWB DRA using conical and hemispherical DRA for achieving of 126% bandwidth (4:1) and 4 to 5 dBi gain. Rashidian et al.,[72] have proposed a parallel fed standing strips rectangular DRA for achieving more than 60% impedance bandwidth with 5.5 to 9.5 dBi gain. Ge,[73] has used a rectangular DRA with a thin dielectric segment for enhancing the bandwidth up to 67% ranging between 0.8 and 1.6 GHz and used a shorting plate to reduce the volume. Abedian et al.,[74] have proposed a compact two-segments DRA using a U-shaped feed for achieving UWB band ranging 3.14 to 10.9 GHz, that is, 110% BW apart from this the U-shaped slot helped in achieving a strong field distribution and symmetry radiation pattern.

Ge[75] has demonstrated and suggested that by cutting a groove on the bottom of the DR and using metallic patch connected to a coaxial probe for excitation purpose can increase the band and also achieved himself a bandwidth of 109.5% with a measured gain of 6 dBi. Oliveira et al.,[76] have used CaTiO3 ($\varepsilon_r = 20$) for designing of a low profile DRA for achieving 7.42% bandwidth. Chaudhary et al.,[77] have proposed wideband multilayer multi permittivity half-split coaxial probe fed CDRA excited at $TM_{21\delta}$ ($0 < d < 1$) mode for covering 63.7% impedance bandwidth ranging 4.05 to 6.9 GHz with an average gain of 5.79 dB. Ge et al.,[78] have used bottom side cutting groove and square patch with probe feed technique in a rectangular DRA for UWB operation. Alja'afreh et al.,[79] have proposed a comparatively small sized U-shaped DRA covering 2.4 to 3.0 GHz range (ie, about 22%), while Batcha et al.,[80] have reviewed and suggested some technique for bandwidth enhancement along with the improvement of other characteristics. A planer coplanar wave guide excited monopole antenna integrated with narrow band cylinder shaped DRA has been developed by Wang et al.[81] which provided a 2:1 voltage standing wave ratio (VSWR) bandwidth for 3.05 to 13.5 GHz and 5.1 to 5.8 GHz, respectively, by exciting $HEM_{11\delta}$ mode and apart from this a triple band could be attained instead of a NB antenna by moving the DR toward to Port 1 or Port 2, which is achieved by exciting other two modes.

Pahadsingh and Sahu[82] have reported multiple modified feeding mechanism in a cylindrical DRA for ultra wideband (UWB) operation over 3 to 12 GHz targeting to cognitive radio application. Wang and Wei,[83] have proposed a compact ultra-wideband (2.5-11 GHz) rectangular shaped DRA while excited by a planar monopole and narrow band (5.1-5.5 GHz) while excited by a slot. Sharma and Brar,[84] have designed regular and irregular pentagon shaped DRA

for covering BW of 42% (from 2.55 to 3.9 GHz) and 45.8% (from 2.57 to 4.1 GHz), respectively. Mukherjee et al.,[85] have proposed a half hemispherical shaped DRA where array of slot were realized for obtaining a wide impedance bandwidth of 1.3 GHz, that is, . >29%. Chaudhary et al.,[86] have proposed a dumb-bell shaped DRA for enhancement of bandwidth and achieved to be of 57.59% ranging between 4.11 and 6.69 GHz with an average gain of 4.88 dB. Fang and Leung,[87] have excited a two layered hemispherical DRA at TM_{101} mode using a coaxial probe which gave 31.9% impedance bandwidth that to 14.2% while in a single layer. This improved bandwidth has been achieved with 20% expense of antenna diameter.

Haraz et al.[88] have achieved 90% impedance bandwidth over 4.5 to 11.8 GHz in a microstrip-line fed (printed monopole) loaded with a half-cylindrical DRA. Recently Guha et al.,[89] have proposed a hybrid mushroom shaped DRA to achieve 137% bandwidth, which seems to be the widest in its category. Laribi and Hakem[90] have used lens technique with DRA to improve the bandwidth up to 9.5 GHz with gain ~19 dB. Fakhte and Oraizi[91] have excited uniaxial stacked DRs using probe and finite conducting sheet to get wideband of 19.4% and 8.1 dB peak gain. Recently, Ranjan and Gangwar[92] have been used a probe coupled half split cylindrical DRA rectangular DRA to reach 51% impedance bandwidth with 5.94 dBi gain. From all these available literatures it can be concluded that the shape of the DRA has a significant role on controlling the bandwidth. Apart from standard geometrical shapes the effect of hybrid shapes as well as perforated shapes and stacking concepts seem more effective in enhancing the bandwidth by way of increasing radiation. Different bandwidth ranges covered by different shapes of DRAs are summarized in Table 1.

TABLE 1 Percentage bandwidth of DRAs related to different DR shapes

Bandwidth	Shaped DR and Refs.
0%-9%	Cylindrical parasitic,[12] cylindrical,[27] rectangular[76]
10%-19%	Rectangular,[25] (cylindrical),[27] stacked-cylindrical,[49] High aspect ratio rectangular,[53] two segmented-high aspect ratio rectangular[56]
20%-29%	Stacked cylindrical,[11] stacked ring resonator,[14] eye-shaped,[30] perforated-cylindrical,[34] Four-element cylindrical,[38] rectangular with tunnel,[48] ring-resonator,[54] U-shaped[79]
30%-39%	Cylindrical-embedded,[18] split-cylindrical,[21] L-shaped,[29] cylindrical + rectangular,[31] half-hemispherical,[39] cylindrical,[45] two-layered hemispherical,[55] half-hemispherical with array of slots,[85] two-layer transparent hemispherical[87]
40%-49%	Disc-ring,[23] tetrahedron and triangular,[24] stacked double annular-ring,[28] rectangular,[32] stair-shaped,[42] meal coated rectangular,[43] half-hemispherical,[51] split-ring resonator,[69] pentagon shape[84]
50%-59%	Conical,[22] two-layer rectangular,[70] dumbbell-shape,[86] conical[22] stacked-rectangular,[75] dumbbell-shaped[86]
60%-69%	T-shaped DRA,[33,36] multi-layer cylindrical,[44] rectangular,[72] rectangular,[73] half-split cylindrical,[77] cylindrical[82]
70%-79%	Cylindrical,[26] two-segment rectangular[35]
80%-89%	Rectangular[57]
90%-99%	Edge mounted rectangular,[61] half-cylindrical[88]
≥100%	Cylindrical,[47] rectangular,[52] pawn-shaped,[58,59] rectangular inserted[62] conical and hemispherical,[65] Z-shaped,[66] conical and hemispherical ring,[71] two-segment rectangular,[74] rectangular stacked,[75] hybrid shapes[89]

Fractal loaded/planar DRA for bandwidth improvement

Fractal concept defines the increase of electrical length with decrease in volume by the occurrence of similar pattern in a reduced manner.[93] The incorporation of this concept in DRA has been reported firstly by Hajihashemi and Abiri.[94] This concept is quite popular as it exploits compactness and multiband characteristics. It can be noted that, the increase in number of iteration lowers the Q-factor and improved bandwidth. However, proper attention is needed in finding the critical iteration point for optimum result. Different types of fractals namely Sierpinski,[95] Minkowski,[97] Apollonian Gasket,[99] and so on have been reported in literature[95–104] in context of DRA as shown in Figure 5.

In 2009, Karmakar et al. ,[95] have implemented the Sierpinski fractal concept in a cylindrical DRA for achieving 50% (covering X-band) impedance bandwidth. Again, the same fractal concept has been used by Soren et al.[96] on a rectangular DRA to achieve 87.86% impedance bandwidth with 4.6 dBi gain. Dhar et al. ,[97] have done Minkowski boundary fractal along with CPW-feeding loop slot to improve the impedance bandwidth up to 64% with 2.5 to 4.9 dBi gain. Azari et al.,[98] have proposed a unique super wideband fractal compact DRA covering 2 to 40 GHz, which is one of the highest bandwidth for DRA with acceptable gain and radiation pattern. Mukherjee et al.,[99] have designed a hemispherical DRA with Apollonian Gasket of circles type fractal concept for achieving 47% impedance bandwidth with resonant frequency of 3.6 GHz. A co-axial probe fed a novel Sierpinski carpet fractal based photonic band gap (PBG) structure has been developed by Mukherjee et al.,[100] for bandwidth enhancement from 10.4% to 21% with 6.4 dBi gain and 90% efficiency while excited for TE_{111} mode. Dhar et al.,[101] have investigated a CPW-fed slot antenna with Minkowski fractal for confirming bandwidth and gain enhancement with exhibiting a hepta-band performance with 3.1 dBi gain. Fan et al.,[102] have shown that, using offset distance of each DR in a parasitic coplanar three-element DRA makes a threefold increase in the bandwidth, that is, 10.3%. Mukherjee et al.,[103] have used EBG structure to enable broadband and high gain in a hemispherical DRA. Kiran et al.[104] have combined the Sierpinski and Minkowski fractal to obtain wideband of 66%.

Though all the fractal concept has been popular since their inception in DRA, however, Sierpinski fractal has been used extensively by many researchers for wideband purpose with an average 36% impedance bandwidth, while Minkowaki fractal technique has been used for wideband as well as multi/heptaband applications. Moreover, the use of combined Sierpinski and Minkowski technique, and planar

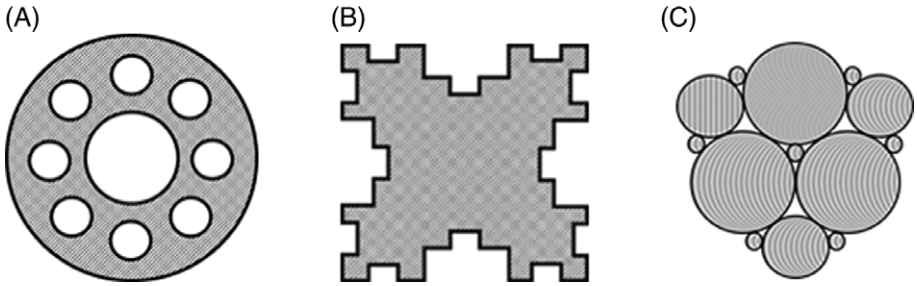


FIGURE 5 Different fractal geometries (top view) used for wide bandwidth purpose: (A) Sierpinski,[95] (B) Minkowski,[97] (C) Apollonian Gasket[99]

concept have been contributed somewhat toward wideband purpose. A comparative study of different fractal loaded DRA are reported in Table 2.

3.1.2 | Bandwidth improvement using coupling mechanism

Next to DRA shape,[11–104] the coupling mechanism plays an important role in controlling performance characteristics of DRA. This technique is also known as bandwidth improvement by means of impedance matching and this can be established either by modification in feeding line[45,105–144] or slot types.[145–152]

Bandwidth improvement via different feed lines

In this approach, primary concern is given to transfer maximum input energy into the DR. It is common fact that, the feed line need to be not only perfectly coupled with the resonator body, but also transfer maximum power/energy up to the coupling point to avoid unnecessary reflection. Hence, instead of traditional feeding line,[105–111] some advanced types say, aperture,[112] parasitic strip,[114] L-shaped probe,[117] elliptical patch,[121] trapezoid patch,[122] bevel shape patch,[126] have been proposed in literature as shown in Figure 6. The complete literature[45,105–144] is discussed here.

Mongia et al.[105] have obtained a 10% frequency bandwidth in a half-split microstrip line-slot fed CDRA with excitation in its dipole mode. Ittipiboon et al.,[106] have suggested that the bandwidth of rectangular ring DRA could be enhanced to 28%. Leung and To,[107] have investigated an aperture coupled DR-antenna with perpendicular feed to operate over 14%. Luk et al.[108] have informed that a vertical strip at the end of the microstrip line can increase the impedance matching in a CDRA up to 19% wide impedance bandwidth, whereas only 7% to 12% in conventional aperture-coupled DRA. Kishk et al.[109] have compared the impedance bandwidth of two different conical structure fed with coaxial probe and concluded that the cone inserted in the ground plane archived the wide band. Kishk et al.[110] have presented a coaxial probe fed DRA to archive 25% impedance and radiation bandwidth. Agrawal et al.[111] have proposed inverted T-shaped feed line coupling with a rectangular DRA to reach 120% impedance bandwidth with peak gain of 8.7 dBi. Chair et al.,[112] have designed an aperture coupled flipped stair structure with rectangular and circular cross section to achieve a bandwidth of 49.3% for square-shape and 32.8% for the square cross-sectional shape.

Deng et al.,[113] have designed a co-axial fed dual ceramic DRs and tuned the distance between the DRs for obtaining a wide bandwidth of 33.4% (1160 MHz) with good radiation pattern as that of single DRA. Li and Sun,[114] have analyzed and adjusted the feed line (parasitic strip) to achieve wide impedance bandwidth of 12% (270 MHz) in a DRA. Guha et al.[115] have achieved 3.2% impedance bandwidth in a quarter wave monopole fed DRA with monopole like radiation pattern. Gao et al.,[116] have proposed a rectangular DRA and a conductor backed CPW fed through slot achieved 23.5% (4.86-6.15 GHz). Kishk et al.,[117] have proposed L-shaped probe feed at the air filled groove DRA of $\varepsilon_r = 10.2$ giving 32% bandwidth whereas 39% bandwidth for $\varepsilon_r = 4.1$. Kumar et al.,[118] have experimentally analyzed a parasitic conducting strip cylindrical DRA with microstrip feed for achieving a bandwidth of 17.33%. The effect of coupling between the DR and feed-line as well as additional layer on bandwidth enhancement up to 28% has been studied by Rezaei et al.[119] Thirakoune et al.,[120] have analyzed the effect of directors and reflector on the DRA loaded monopole that covers 3 to 8 GHz frequency range with an 11.5 dB peak directivity. Kumar et al.,[45] have proposed a microstrip fed cylindrical shaped DR-antenna ($\varepsilon_r = 20.8$) offering 35% impedance bandwidth whereas 16.5% bandwidth with better matched vertical feed with conical radiation pattern. Zhang et al.,[121] have used a new conformal elliptical patch feeding mechanism to a compact U-shaped DR operating over 72% impedance bandwidth with 4.3 to 7.6 dBi gain for military as well as civilian communications.

An enhanced wide bandwidth of 73.0% has been achieved in a vertical trapezoid patch fed inverted L-shaped DRA by

TABLE 2 Details of fractal/planer DRAs

Bandwidth	Specific geometry	Refs.
50%	Sierpinski fractal on cylindrical DRA	Karmakar et al.[95]
87.86%	Sierpinski fractal on a rectangular DRA	Soren et al.[96]
64%	Minkowski boundary fractal	Dhar et al. ,[97]
2-40 GHz	Koch fractal like monopole	Azari et al.[98]
47%	Hemispherical DRA with Apollonian Gasket of circles type fractal	Mukherjee et al.[99]
21%	Sierpinski carpet fractal based photonic band gap (PBG)	Mukherjee et al.[100]
Heptaband	Minkowski fractal	Dhar et al.[101]
10.3%	Parasitic coplanar 3-element DRA	Fan et al.[102]
~30%	CDRA arrays	Drossos et al.[103]
66%	Combination of Sierpinski and Minkowski fractal	Kiran et al.[104]

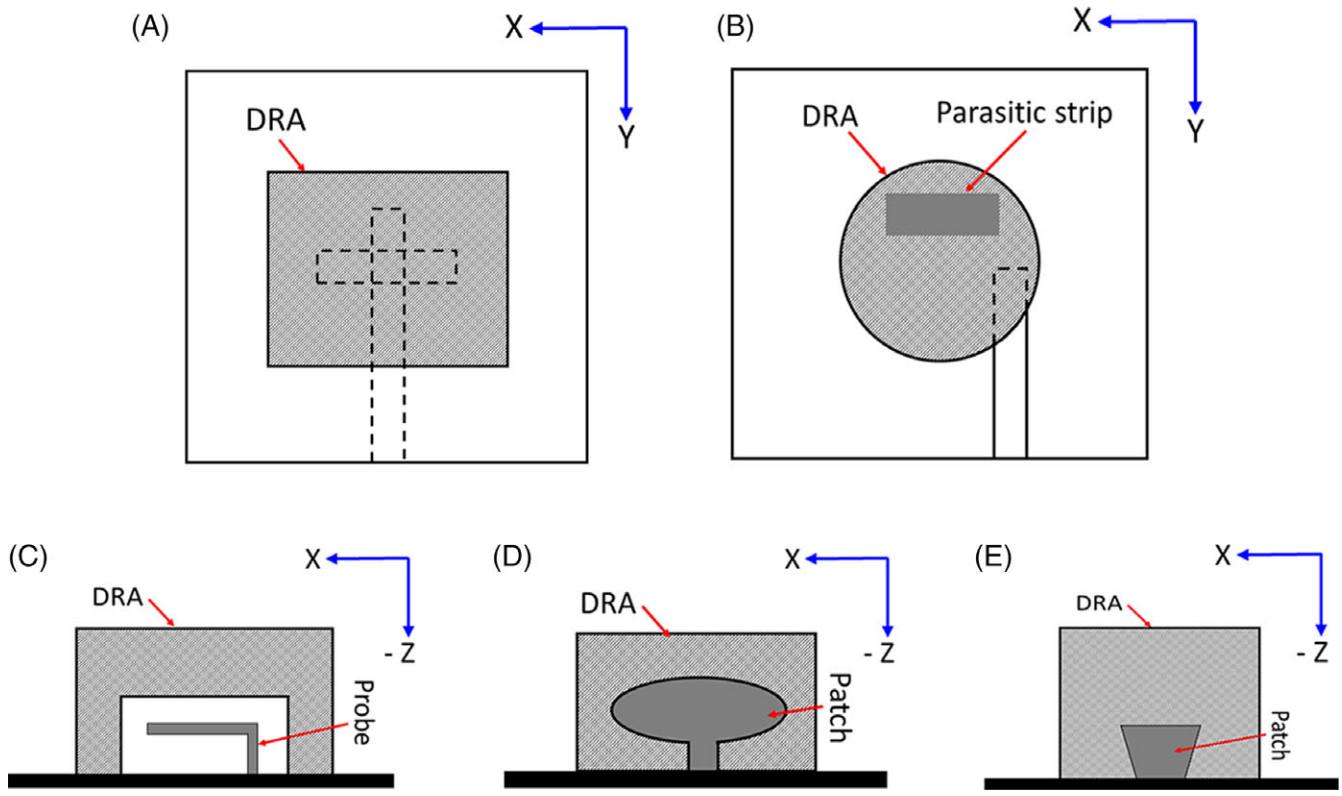


FIGURE 6 Different feeding mechanism used for wide bandwidth purpose: (A) Aperture,[112] (B) Parasitic strip,[114] (C) L-shape probe,[117] (D) Elliptical patch,[121] (E) Trapezoid patch[122]

Liang and Denidni.[122] Ghosh and Chakraborty,[123] have investigated a low mutually coupled two identical DRA loaded with T-shaped monopole antenna for UWB applications. Singh and Sharma,[124] have proposed single probe feed and anti-probe feed for a cylindrical DRA of $\varepsilon_r = 10.2$ operating at 82% (for single probe) and 68% (for anti-probe) with improved radiation pattern gain and cross-polarization. Al-Zoubi and Kishk,[125] have modeled a Mongia et al.[105] have obtained a 10% frequency bandwidth in a half-split microstrip line-slot vertical strip along with a coaxial probe for the feeding of a rectangular DRA where the measured return loss was found to be 65% (7.5 GHz bandwidth) with 8.3 dBi gain. A bevel shaped patch excited with CPW feed line was applied to a rectangular DRA ($\varepsilon_r = 10$) for obtaining a UWB band by Denidni and Weng.[126] Liang and Denidni[127] have used a co-axial probe fed rectangular DRA placed in a concave ground plane for obtaining 55% bandwidth (3.28-5.77 GHz) with 3.7 to 6.2 dBi gain. Liang et al.,[128] have designed an L-shaped DR-antenna fed by a conformal inverted-trapezoidal patch connected to a microstrip line which achieved 71.4% impedance bandwidth ranging 3.87 to 8.17 with 5 to 8.5 dBi gain. Ge and Esselle,[129] have found a $S_{11} < -10$ dB return loss over 3.1 to 10.7 GHz while a coaxial probe was used a feed. Gopakumar et al.[130] have investigated a half split circular, cylindrical profile DR antenna fed by a microstrip feed line offering 36.7% impedance bandwidth. A compact circular shaped-DR coupled by a crescent patch and CPW feed line has been designed for achieving UW band over 1.6 to 15 GHz by Weng et al.[131] Thame and Wu[132] have designed coaxial probe fed Bowtie shaped DRA for 49% bandwidth. Zheng et al.[133] have investigated a UWB monopole excited DRA for giving 110% impedance bandwidth ranging. A microstrip-line-fed Isosceles trapezoidal DRA has been designed by Gopakumar and Mathew[134] to offer the Kakade and Ghosh[135] have found wideband in a rectangular waveguide fed hemispherical DRA. Huynh et al.,[136] have developed a probe fed cylindrical DRA for achieving 46% impedance bandwidth by adjusting the aspect ratio and permittivity. An E-shaped patch with shorting wall technique has been adopted by Gao et al.[137] to achieve a bandwidth of 58% between 4.38 and 7.96 GHz with a rectangular DRA. Chaudhary and Rajni,[138] have excited a ring DRA with annular shaped microstrip feed covering 66.72% impedance bandwidth (3.49-7.2 GHz) with 4.31 dB gain. Rashidian et al.,[139] have investigated the matching of microstrip fed DRA for achieving a bandwidth of 35% by using a tapered microstrip feed. After this, 163.6% impedance bandwidth ranging 2 to 20 GHz with average gain of 5.64 dB using bevel shaped patch and coplanar wave guide excited cylindrical DRA has been proposed by Prachin et al.[140] Ozzaim et al.,[141] have designed a hybrid monopole DRA covering 138% impedance bandwidth. After this, Guha et al.,[142] have examined a UWB hybrid DRA of 137% (5:1) impedance bandwidth with monopole type feeding mechanism. Sunab et al.,[143] have realized a quadrature fed CP DRA for bandwidth of 43.3%, the AR bandwidth of 42.8% axial ratio bandwidth and 40.8% gain bandwidth. Prachi et al.,[144] have proposed a rounded bevel

TABLE 3 Bandwidth of DRAs based on feed line mechanism

Bandwidth	0%-9%	10%-19%
Ref.	NA	105,107,108,114,118
Bandwidth	20%-29%	30%-39%
Ref.	106,110,116,119,134	45,112,113,117,130,139
Bandwidth	40%-49%	70%-79%
Ref.	112,132,136,143	121,122,128
Bandwidth	80%-89%	≥100%
Ref.	124	111,133,140–142,144

shaped fed cylindrical DRA for achieving 124.4% impedance bandwidth covering 4.4 to 18.9 GHz.

Further, the achieved bandwidth using different feed lines are differentiated in terms bandwidth ranges in Table 3. This clearly surmise that, the feeding network put substantial impact on controlling the bandwidth ranges from 10% to more than 100%. However, at the same time the effect of shape of the DR cannot be avoided.

3.1.3 | Bandwidth improvement via different coupling slots

In case of DRA, coupling slot plays a key role in reducing input reflection by transferring maximum energy to the radiator. So, choice of specific shape of coupling-slot as per frequency range, DR shape, and feed line is quite tricky. Of course, depending upon the shape and number of slot(s), the bandwidth varies. All the bandwidth related literatures[145–152] emphasizing slot types are discussed here.

Leung et al.,[145] have reported annular-slot for coupling the DRA to offer better bandwidth of 18% as compared to 8 to 12% than those conventional DRA. Hui and Yung,[146] have analyzed a rectangular-slot coupled antenna loaded by a dielectric hemisphere with double dielectric coatings and also observed that the second dielectric coating layer significantly increased the bandwidth up to 8.5%. So and Leung[147] have studied the effect of slot on impedance bandwidth and utilized parasitic patch to increase the bandwidth frequency (3.75-4.35 GHz) tuning purpose. Buerkle et al.,[148] have merged the slot resonance and dielectric structure itself to achieve 25% impedance bandwidth with 4 dBi gain. Kishk[149] have designed a slot-fed mechanically more rigid structured DRA for achieving 50% impedance bandwidth.

Weng et al.,[150] have used the air dielectric between the rectangular DR and the ground plane for enhancing the bandwidth up to 61%. Deng et al.,[151] have introduced a pair of symmetrical edge resonators to antenna, where each resonator is composed of a T-shaped slot etched on the edge of the radiator and a strip printed on the opposite side of the substrate along with U-slot DFS concept to achieve dual band of 2.4 to 2.48 GHz for Bluetooth and 3.1 to 10.6 GHz for UWB frequency bands. Rahimian et al.,[152] have used branch line coupler to excite a rectangular DRA for operating over more than 90% impedance bandwidth. Moreover, different bandwidth ranges covered by means of slot mechanisms are briefed in Table 4. From this it is confirmed that, different slot types have significant effect on bandwidth range covering up to ~70% impedance bandwidth.

3.1.4 | Bandwidth improvement via high permittivity

During this review process it has been also found some papers related to bandwidth by highlighting permittivity in their title. Mainly the effect of high permittivity on impedance bandwidth is discussed here.[153–164] Mongia et al.,[153] have reported a high permittivity rectangular DRA ($\varepsilon_r = 100$) to achieve 3% impedance bandwidth. Leung et al.,[154] have investigated high permittivity dual disk DRA for getting 4.6 times wider impedance bandwidth than that of single element. Leung et al.,[155] have proposed a low profile DRA disk of high permittivity to achieve a bandwidth of 25%. Guo and Luk[156] have designed a coplanar waveguide fed low permittivity DR-antenna with an extra added vertical strip for improving coupling attained impedance bandwidth of 22% and 5.5 dBi gain. Bijumon et al.,[157] have used high permittivity DRA loaded over a patch to achieve 14% impedance bandwidth centered at 2.32 GHz. Zu[158] has demonstrated some techniques for obtaining broadband DRA. Rashidian et al.,[159] have used strip excitation technique to very low permittivity resonator ($\varepsilon_r = 6$) to get 18% bandwidth whereas 11% for $\varepsilon_r = 10$ and reached to 42% when the strip acted like radiator when mixed with dielectric constant of 4. Rotaru et al.,[160] have found a wide impedance band between 2.4 and 2.5 GHz in a "C" shaped high permittivity DRA.

Huynh et al.,[161] have informed that, the impedance bandwidth could be maximized for a small relative permittivity that is greater than unity while radiation pattern degraded if the permittivity decreases. Wide band of 81.7% has been achieved by Madhuri et al.,[162] in a rectangular ring slot coupled high permittivity rectangular DR-antenna. Avadanei et al.,[163] have proposed to excite high permittivity DR material in superior modes to obtain wide impedance bandwidth, which has been experimented in a rectangular slot fed cylindrical DRA. Liu et al.,[164] have developed low profile multilayered DR with the combination of two high permittivity DR and low permittivity layer in-between them which gave an impedance bandwidth of 10.49% and gain >6 dBi. A compressive details of bandwidth ranges are shown in Table 5.

3.1.5 | Bandwidth improvement via exciting different mode

Though, the physical parameters of any antenna affects the bandwidth performances, still one hypothetical parameter known as mode also affects the same. The behavior of the antenna improves by means of better radiation characteristics by exciting certain radiating modes of the resonator and for this purpose feed type plays an important role. The compressive discussion of some novel ideas of certain mode excitation[85,150,165–169] for bandwidth control is discussed here. The field distribution of some of the common radiating mode of DRA (here only Cylindrical shape) are shown in Figure 7.

Li and Leung,[165] have developed a strip fed DR-antenna for achieving 43% impedance bandwidth by exciting TE_Y

TABLE 4 Bandwidth of DRAs based on slot mechanism

Bandwidth	0%-9%	10%-19%	20%-29%
Ref.	146	145	148
Bandwidth	50%-59%	60%-69%	90%-99%
Ref.	149	150	152

mode and the higher order TE_{Y3}. Chang and Kiang,[166] have proposed a rectangular-slot fed offset well type DRA to attain a bandwidth of 18% with more than 4 dBi gain by exciting TE^{y}_{111} mode. Chang and Kiang,[167] have designed to achieve a 29% wide impedance band by merging three resonant bands of different modes. Again, Chang and Kiang,[168] have merged three resonant modes (ie, TE^{y}_{111}, TE^{y}_{112}, TE^{y}_{113}) to achieve 33% impedance bandwidth (4.89-6.86 GHz), with broadside ration pattern. Weng et al.,[150] have proposed a slot fed DRA with merged resonant modes of the isolated DRs and equivalent DR to achieve wide impedance bandwidth of 62%. Ge et al.,[169] have analyzed a rectangular DRA with sorting conducting wall where the low Q-modes of the overlapping bands were exploited to achieve wide continuous band of more than 109.5%. Mukherjee et al.,[85] have excited a half hemi-spherical DRA in TM_{101} mode by SMA connectors and probe along with the array of slots and achieved ~17.74% bandwidth and when the probe length was increased it enhanced to >29%. Further, different specific modes and their respective bandwidth ranges are highlighted in Table 6. It clears that, single mode gives an average ~25% impedance bandwidth while the merge of modes gives an average >35% impedance bandwidth. However, in every case, the reduction of volume (weight) of the DR is a superior advantage.

3.2 | Bandwidth improvement in dual-band/multi-band operation

The dual-band/multi-band operation of DRA is also quite important from application point of view.[4] Hence, for the same purpose, different techniques have been proposed in context to DRA. For easy and smooth classification, literature based on dual-band[170–180] and on multi-band[181–186] is discussed in this section, respectively.

A microstrip fed ring DRA for dual frequency operation has been proposed by Sung et al.,[170] which can applicable for satellite and wireless applications. Kumar et al.,[171] have designed a microstrip fed cylindrical sector DRA with VSWR bandwidth of 12.35% and 17.82%. Kumar et al. ,[172] have designed microstrip fed cylindrical shaped DR-antenna for operating impedance bandwidth of 2.46% for band 1 (1.684-1.726 GHz) and 1.15% for band 2 (2.426-2.454 GHz). Lim and Leung,[173] have studied

TABLE 5 DRAs details related to permittivity/shape

Bandwidth	0%-9%	10%-19%
Ref.	153,158	157–159,164
Bandwidth	20%-29%	80%-89%
Ref.	155,156	162

dual wide band aperture coupled DRA ($\varepsilon_r = 6$) for operating in (2.21-2.855) GHz and (4.385-5.455) GHz for WLAN applications. Gao et al.[174] have developed dual band rectangular CPW fed hybrid DRA resonating at 2.4 and 5.3 GHz.

Adz et al.,[175] have proposed a E-shaped aperture fed cylindrical DRA for dual band operation at 5 GHz (with conducting strip under DRA) and 2.45 GHz (with metallic top loaded DRA). Kumar et al.[176] have reported a laminated wave-guide fed cylindrical DRA to operate at 9.76, 10.53, and 11.8 GHz with bandwidth 56, 160, and 250 MHz, respectively. Sharma et al.,[177] have excited three different modes ($HEM_{11\delta}$, $TM_{01\delta}$, and $HEM_{12\delta}$) in a cylindrical DRA by means of different feeding techniques resulting multi band operation over 2.5 to 3.02 GHz, 3.76 to 3.86 GHz, and 4.38 to 4.72 GHz. A dual band and wide band microstrip feed excited ring DRA has been developed by Khalily et al.,[178] which covers 73% (2.78-5.95 GHz; wide band) and dual bands of 8% (2.4-2.6 GHz) and 56% (3.3-5.85 GHz). Mehmood et al.,[179] have designed dual band transparent glass DRA fed by a microstrip feed line with perpendicular strip covers 18% (5.15-5.95 GHz), where the modified feed created dual resonance. Zou and Pan,[180] have introduced annular circular slot with two rectangular slot opposite (135° and 45°), to a rectangular DRA ($\varepsilon_r = 12$) for creating dual bands of 3.7%, 9.1% for the lower band and 3.7%, 14.4% for the upper band, respectively. Moreover, the dual band DRA operating frequency details are summarized in Table 7.

Hamsakutty et al.,[181] have modeled a single coaxial fed Hexagonal DRA resonating at 2.215, 2.784, 3.445, and 3.955 GHz. Sangiovanni et al. ,[182] have proposed multi-frequency stacked DRA with 4.9% impedance bandwidth and 1.75 maximum higher to lower frequency ratio. Hamsakutty et al.,[183] have investigated a coaxial probe fed metal-coated DR-antenna for 3 VSWR bands operating at 1.46, 2.41, and 3.23 GHz. Fang and Leung,[184] have designed a rectangular DRA for single-band, dual-band where different excitation sources have used for dual band, wide band designs. Paul et al.,[185] have proposed two identical high permittivity DRA kept 7.5 mm apart from each other for multiband operation resonating at 1.9 and 2.4 GHz. After this, a high permittivity compact DRA of ($\varepsilon_r = 140$), has been proposed by Bit-Babik et al.[186] for multimode operation with enhanced bandwidth of 25%.

3.3 | Bandwidth Improvement with other characteristics

In literature, in-addition to only-bandwidth analysis some researchers have also pointed out some other important characteristics (far-field characteristics)[187–189] and notch.[190,191] These are discussed here. Singh and Sharma[187] have designed a dual co-axial fed cylindrical DRA for 68% impedance bandwidth with broad side radiation pattern and 82% BW with omnidirectional and directional ration pattern as well as high cross polarizations for single probe feed. Ryu

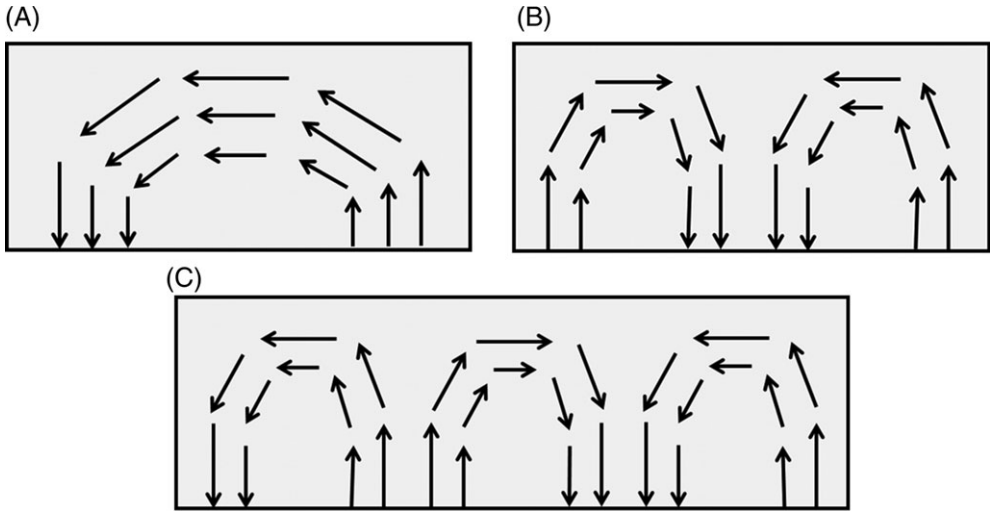


FIGURE 7 E-field distribution (side view) of rectangular DRA: (A) TE^{y}_{111}, (B) TE^{y}_{112}, (C) TE^{y}_{113}

et al.,[188] have proposed a compact coplanar wave guide fed monopole type DRA for UWB operation over 3.1 to 10.6 GHz with omnidirectional radiation pattern and very low cross polarization. Khalily et al.[189] have developed a rectangular DR-antenna with tapered strip excitation on one side while narrow strip on the opposite side to enhance the bandwidth up to 96% (ie, 2.13-6.08 GHz) with improved radiation pattern compared to 66% in convectional one. A circular patch with monopole like radiation, have inserted in to the DR structure by Niroo-Jazi et al.,[190] for controlling of the stop band in between a UWB ranging 2 to 10.7 GHz with stopband response between 5.15 and 5.825 GHz. Shao et al.,[191] have designed probe fed UWB rectangular stacked DRA operating over 3.1 to 10.6 GHz with a band notch generated by a thin printed dipole near the feeding probe.

4 | SUMMARY

In this survey article, the bandwidth related literatures covering more than 180 articles have been discussed. From readers' point of view the bandwidth related articles have been analyzed from different aspects as shown in Table 8. On summarizing this review process, several observations have been stated. The research on DRA for single band is much more

TABLE 6 Bandwidth and mode details of DRAs

BW details	Effects of mode(s)	Refs.
43%	Exciting TE^{Y} mode + higher order TE^{y}_{3}	Li and Leung[165]
18% (5-6 GHz)	Exciting TE^{y}_{111} mode	Chang and Kiang[166]
29%	By merging three resonant bands of different modes	Chang and Kiang[167]
33% (4.89-6.86 GHz)	Merging three resonant modes (ie, TE^{y}_{111}, TE^{y}_{112}, TE^{y}_{113})	Chang and Kiang[168]
62% (2.4-4.5 GHz)	Resonant modes of the isolated DRs and equivalent merged DR	Weng et al.[150]
109.5%	Low Q-modes of the overlapping bands were exploited	Ge et al.[169]
>29%.	TM_{101} mode excited	Mukherjee et al.[85]

TABLE 7 Details of DRAs related to dual band

Dual/multi band details	Refs.
Dual frequency operation	Sung et al.[170]
Dual VSWR bandwidth of 12.35% and 17.82%	Kumar et al.[171]
2.46% for band 1 (1.684-1.726 GHz) and 1.15% for band 2 (2.426-2.454 GHz)	Kumar et al.[172]
(2.21-2.855) GHz and (4.385-5.455) GHz	Lim and Leung[173]
Dual band resonating at 2.4 GHz and 5.3 GHz	Gao et al.[174]
Dual band operation at 2.45 GHz and 5 GHz	Adz et al.[175]
Operating at 9.76, 10.53, and 11.8 GHz	Kumar et al.[176]
Covering (2.5-3.02) GHz, (3.76-3.86) GHz, and (4.38-4.72) GHz	Sharma et al.[177]
73% (2.78-5.95 GHz) (wide band) and dual bands of 8% (2.4-2.6 GHz) and 56% (3.3-5.85 GHz)	Khalily et al.[178]
18% (5.15-5.95) GHz	Mehmood et al.[179]
3.7%, 9.1% for the lower band and 3.7%, 14.4% for the upper band	Zou and Pan[180]

TABLE 8 Summary of bandwidth based DRAs

Stage 1	Stage 2	Stage 3	Refs.
Bandwidth	Single band	By shape	11–104
		By coupling	45,105–152
		By permittivity	153–164
		By mode	85,150,165–169
	Dual band	–	170–180
	Multi band	By shape	181,182
		By coupling	183,184
		By permittivity	185,186
	Bandwidth with other characteristics	BW + radiation	187–189
		BW+ notch/gain	190,191

than dual/multiband research. Among these, the DR shape has been found to be a major key factor in controlling operation range than the coupling mechanism, permittivity, and mode of operation. At the same time the research on radiation characteristics and notch along with bandwidth is very less. The outcome of this review article can be summarized as, (a) highlights the research based on single band, dual band, and multi band separately, (b) differentiate the techniques by means of shape, coupling, permittivity, and mode of operation, and (c) shows some research based on bandwidth along with other characteristics. The different configurations of DRAs for different features are summarized in Table 8.

5 | CONCLUSION

This review article has highlighted chronologically the advancement of DRA from bandwidth point of view. The open intention of this review work is to show an encouraging path to the antenna modelers for the performance advancement of DRA in terms of bandwidth with miniaturization of the existing ones.

The review article reveals that, DRA has the capability for almost all types of bandwidth characteristics in an improved manner than those convectional antennas. The number of referenced paper gives an idea of tremendous investigation on bandwidth, which indicates a wide control of modern wireless communication covering all bands in near future. From a qualitative point of view, it can be noted that, (a) the shape of the DRA mainly fractal and hybrid shape has much impact on improving bandwidth by means of increasing the radiation, (b) use of extra conducting sheet seems to be more effective in enhancing bandwidth by enabling strong coupling to the DRA, (c) excitation of certain modes enables the energy to come out easily from the DR to the free space resulting enhanced bandwidth.

From a prospective point of view, this article may be helpful in, (a) getting an idea for designing DRA for any specific range of operation or specific band, (b) design of some hybrid shape DR with favorable coupling mechanism, which has not yet been so far, (c) introduction of some hybrid fractal DRA. However, authors recommendations are as follows: (a) from shape point of view hybrid DRA with Sierpinski and Minkowski could be a superior alternative for wideband as well as multiband, (b) from mode point of view combination of multiple modes preferably lower modes can be combined for wider impedance bandwidth, (c) from coupling point of view wider patch with slotted DR could achieve better bandwidth provided perfect matching network.

No doubt the authors have tried at their level best to frame out all novel and important contribution of bandwidth related DRA research starting from innovation to advancement around the globe, still the authors apologize to the great researcher community if any important and novel contribution is skipped unknowingly and unintentionally during this review process.

ORCID

Sounik Kiran Kumar Dash https://orcid.org/0000-0003-2635-4213
Taimoor Khan https://orcid.org/0000-0002-3960-1423

REFERENCES

1. Richtmyer RD. Dielectric resonators. *J Appl Phys*. 1939;10:391-398.
2. Long SA, Mcallister MW, Shen LC. The resonant cylindrical dielectric cavity antenna. *IEEE Trans Antennas Propag*. 1983;31(3):406-412.
3. Petosa A. *Dielectric Resonator Antenna Handbook*. Norwood, MA: Artech Publication House; 2007.
4. Dash SKK, Khan T, De A. Modelling of dielectric resonator antennas using numerical methods: a review. *J Microw Power Electromagn Energy*. 2016; 50(4):269-293.
5. Dash SKK, Khan T, De A. Dielectric resonator antennas: an application oriented survey. *Int J RF Microw Comp Aided Eng*. 2017;27(3).
6. Dash SKK, Khan T, Antar YMM. A state-of-art review on performance improvement of dielectric resonator antennas. *Int J RF Microw Comp Aided Eng*. 2018;28(6).
7. Petosa A, Ittipiboon A. Dielectric resonator antennas: a historical review and the current state of the art. *IEEE Antennas Propag Mag*. 2010;52(5): 91-116.
8. Leung KW, Lim EH, Fang XS. Dielectric resonator antennas: from the basic to the aesthetic. *Proc IEEE*. 2012;100(7):2181-2193.
9. Soren D, Ghatak R, Mishra RK, Poddar DR. Dielectric resonator antennas: designs and advances. *Prog Electromagn Res B*. 2014;60:195-213.
10. Keyrouz S, Caratelli D. Dielectric resonator antennas: basic concepts, design guidelines, and recent developments at millimeter-wave frequencies. *Int J Antennas Propag*. 2016;2016, Article ID 6075680, 20 pages.
11. Kishk A, Ahn B, Kajfez D. Broadband stacked dielectric resonator antennas. *IEE Electron Letters*. 1989;25(18):1232-1233.
12. R. Q. Lee and R. N. Simons. Bandwidth enhancement of dielectric resonator antennas. Proceedings of the IEEE Antennas and Propagation Society International Symposium Digest; 1993; Ann Arbor, MI. Vol 3, pp. 1500-1503.
13. Wong K-L, Chen N-C. Analysis of a broadband hemispherical dielectric resonator antenna with dielectric coating. *Microw Opt Technol Lett*. 1994;7 (2):73-76.
14. S. M. Shum, and K. M. Luk. Bandwidth enhancement of probe-fed dielectric ring resonator antenna with parasitic element. Proceedings of the IEEE Antennas and Propagation Society International Symposium Digest; 1994; Seattle, WA. Vol. 2, pp. 768-771.
15. Chen NC, Su HC, Wong KL. Analysis of a broadband slot coupled dielectric-coated hemispherical dielectric resonator antenna. *Microw Opt Technol Lett*. 1995;8(1):13-16.
16. K. M. Luk, K. W. Hung, and E. K.N. Yung. Hemispherical dielectric resonator antenna with a concentric conductor. Proceedings of the IEEE Antennas and Propagation Society International Symposium Digest; 1995; Newport Beach, CA. pp. 730-733.
17. Z. Fan, and Y. M. M. Antar. Experimental investigation of multi-element dielectric resonator antennas. Proceedings of the IEEE Antennas and Propagation Society International Symposium Digest; 1996; Baltimore, MD. Vol. 3. pp. 2034-2037.
18. Sangiovanni A, Dauvignac JY, Pichot C. Embedded dielectric resonator antenna for bandwidth enhancement. *IET Electron Lett*. 1997;33(25):2090-2091.
19. R. K. Mongia. Reduced size metallized dielectric resonator antennas. Proceedings of the IEEE Antennas and Propagation Society International Symposium Digest; 1997; Montreal, Quebec. Vol. 4, pp. 2202-2205.
20. Drossos G, Wu Z, Davis LE. The air gap effect on a microstrip-coupled cylindrical dielectric resonator antenna. *Microw Opt Technol Lett*. 1999;20 (1):36-40.
21. Kishk A, Glisson AW, Junker GP. Band width enhancement for split cylindrical dielectic resonator antenna. *Prog Electromagn Res*. 2001;33:97-118.

22. Kishk AA, Yin Y, Glisson AW. Conical dielectric resonator antennas for wide-band applications. *IEEE Trans Antennas Propag*. 2002;50(4): 469-474.
23. Ong SH, Kishk AA, Glisson AW. Wideband disc-ring dielectric resonator antenna. *Microw Opt Technol Lett*. 2002;35(6):425-428.
24. A. A. Kishk. Tetrahedron and triangular dielectric resonator antenna with wideband performance. Proceedings of the IEEE Antennas and Propagation Society International Symposium; 2002; San Antonio, Texas. Vol. 4, pp. 462-465.
25. Gupta V, Sinha S, Koul SK, Bhat B. Wideband dielectric resonator loaded suspended microstrip patch antennas. *Microw Opt Technol Lett*. 2003;37 (4):300-302.
26. M. Lapierre, Y. M. M. Antar, A. Ittipiboon, and A. Petosa. A wideband monopole antenna using dielectric resonator loading. Proceedings of the IEEE Antennas and Propagation Society International Symposium; 2003; Columbus, OH. Vol. 3, pp. 16-19.
27. Nannini C, Ribero JM, Dauvignac JY, Pichot C. Bi-frequency behaviour and bandwidth enhancement of a dielectric resonator antenna. *Microw Opt Technol Lett*. 2004;42(5):432-434.
28. Guo YX, Ruan YF, Shi XQ. Wide-band stacked double annular-ring dielectric resonator antenna at the end-fire mode operation. *IEEE Trans Antennas Propag*. 2005;53(10):3394-3397.
29. Denidni TA, Rao Q, Sebak AR. Broadband L-shaped dielectric resonator antenna. *IEEE Antennas Wirel Propag Lett*. 2005;4:453-454.
30. R. Chair, A. A. Kishk, and K. F. Lee. Wideband low profile eye shaped dielectric resonator antennas. Proceedings of the IEEE Antennas and Propagation Society International Symposium; 2005; Vol. 3A, pp. 582-585. (DOI: 10.1109/APS.2005.1552319)
31. Young CSD, Long SA. Wideband cylindrical and rectangular dielectric resonator antennas. *IEEE Antennas Wirel Propag Lett*. 2006;5(1):426-429.
32. Y. Coulibaly, T. A. Denidni, H. BouT, L. Talbi. Design of a new broadband dielectric resonator antenna. Proceedings of the 1st European Conference on Antennas and Propagation; 2006; Nice. pp. 1-4.
33. Rao Q, Denidni TA, Sebak AR. Broadband compact stacked T-shaped DRA with equilateral-triangle cross sections. *IEEE Microw Wirel Compon Lett*. 2006;16(1):7-9.
34. Chair R, Kishk AA, Lee KF. Experimental investigation for wideband perforated dielectric resonator antenna. *IET Electron Lett*. 2006;42(3): 137-139.
35. Rezaei P, Hakkak M, Forooraghi K. Design of wide-band dielectric resonator antenna with a two-segment structure. *Prog Electromagn Res*. 2006;66: 111-124.
36. Ruan YF, Guo YX, Shi XQ. Wideband dielectric resonator antenna. *Microw Opt Technol Lett*. 2006;48(2):222-226.
37. Ge Y, Esselle KP, Bird TS. A wideband probe-fed stacked dielectric resonator antenna. *Microw Opt Technol Lett*. 2006;48(8).
38. Guha D, Antar YMM. Four-element cylindrical dielectric resonator antenna for wideband monopole-like radiation. *IEEE Trans Antennas Propag*. 2006;54(9):2657-2662.
39. Guha D, Antar YMM. New half-hemispherical dielectric resonator antenna for broadband monopole-type radiation. *IEEE Trans Antennas Propag*. 2006;54(12):3621-3626.
40. Guha D, Antar YMM, Ittipiboon A, Petosa A, Lee D. Improved design guidelines for the ultra-wideband monopole-dielectric resonator antenna. *IEEE Antennas Wirel Propag Lett*. 2006;5:373-376.
41. Ruan YF, Guo YX, Shi XQ. Double annular-ring dielectric resonator antenna for ultra-wideband application. *Microw Opt Technol Lett*. 2007;49 (2):362-366.
42. Chair R, Kishk AA, Lee KF. Wideband stair-shaped dielectric resonator antennas. *IET Microw Antennas Propag*. 2007;1(2):299-305.
43. Chang TH, Kiang JF. Broadband dielectric resonator antenna with metal coating. *IEEE Trans Antennas Propag*. 2007;55(5):1254-1259.
44. Huang W, Kishk AA. Compact wideband multi-layer cylindrical dielectric resonator antennas. *IET Microw Antennas Propag*. 2007;1(5):998-1005.
45. Kumar AVP, Hamsakutty V, Yohannan J, Mathew KT. A wideband conical beam cylindrical dielectric resonator antenna. *IEEE Antennas Wirel Propag Lett*. 2007;6:15-17.
46. S. Ghosh, A. Roy, and A. Chakrabarty. Ultra wideband characterization of dielectric loaded monopole transreceive antenna system considering mutual coupling. Proceedings of the IEEE International Conference Signal Processing, Communications and Networking; 2008; Chennai. pp. 20-24.
47. Ghosh S, Chakraborty A. Ultrawideband performance of dielectric loaded t-shaped monopole transmit and receive antenna/emi sensor. *IEEE Antennas Wirel Propag Lett*. 2008;7:358-361.
48. Chang T-H, Huang Y-C, Su W-F, Ki J-F. Wideband dielectric resonator antenna with a tunnel. *IEEE Antennas Wirel Propag Lett*. 2008;7:275-278.
49. Rocha HHB, Freire FNA, Sohn RSTM, et al. Bandwidth enhancement of stacked dielectric resonator antennas excited by a coaxial probe: an experimental and numerical investigation. *IET Microw Antennas Propag*. 2008;2 (6):580-587.
50. Jazi MN, Denidni TA. Design and implementation of an ultrawideband hybrid skirt monopole dielectric resonator antenna. *IEEE Antennas Wirel Propag Lett*. 2008;7:493-496.
51. Li Y, Yang H, Ruan C. A novel wideband dielectric resonator antenna. *J Electromagn Waves and Appl*. 2008;22:1499-1507.
52. Denidni TA, Weng Z. Rectangular dielectric resonator antenna for ultra-wideband applications. *IET Electron Lett*. 2009;45(24):1210-1212.
53. Rashidian A, Klymyshyn DM. Microstrip-fed high aspect ratio dielectric resonator antenna with dual-resonance broadband characteristics. *IET Electron Lett*. 2009;45(2):94-95.
54. Chang W, Feng Z. Investigation of a novel wideband feeding technique for dielectric ring resonator antennas. *IEEE Antennas Wirel Propag Lett*. 2009; 8:348-351.
55. Leung KW, So KK. Theory and experiment of the wideband two-layer hemispherical dielectric resonator antenna. *IEEE Trans Antennas Propag*. 2009;57(4):1280-1284.
56. Rashidian A, Klymyshyn DM. On the two segmented and high aspect ratio rectangular dielectric resonator antennas for bandwidth enhancement and miniaturization. *IEEE Trans Antennas Propag*. 2009;57(9):2775-2780.
57. K. S. Ryu, and A. A. Kishk. UWB dielectric resonator antenna mounted on a vertical ground plane edge. Proceedings of the IEEE Antennas and Propagation Society International Symposium; 2009; Charleston, SC. pp. 1-4.
58. Guha D, Gupta B, Antar YMM. New pawn-shaped dielectric ring resonator loaded hybrid monopole antenna for improved ultrawide bandwidth. *IEEE Antennas Wirel Propag Lett*. 2009;8:1178-1181.
59. Y. Ge and K. P. Esselle. An extremely compact dielectric resonator antenna for space-limited UWB wireless communication devices. Proceedings of the European Radar Conference; 2009; Rome. pp. 393-396.
60. A. Rashidian, and D. M. Klymyshyn. A novel approach to enhance the bandwidth of miniaturized microstrip-fed dielectric resonator antennas. Proceedings of the 3rd European Conference on Antennas and Propagation; 2009; Berlin. pp. 397-399.
61. Seungwoo Ryu K, Kishk AA. Ultrawideband dielectric resonator antenna with broadside patterns mounted on a vertical ground plane edge. *IEEE Trans Antennas Propag*. 2010;58(4):1047-1053.
62. K. S. Ryu, and A. A. Kishk. UWB dielectric resonator antenna with low cross-polarization. Proceedings of the IEEE Radio and Wireless Symposium; 2010; New Orleans, LA. pp. 551-554.
63. Sankaranarayanan D, Kiran DV, Mukherjee B. Laterally placed CDRA with triangular notches for ultra-wideband applications. *Freq J RF-Eng Telecommun*. 2017;72(1-2):1-6.
64. M. N. Jazi, T. A. Denidni, and A. R. Sebak. Ultra-wideband dielectric-resonator antenna based on hybrid techniques. Proceedings of the IEEE 14th International Symposium on Antenna Technology and Applied Electromagnetics & the American Electromagnetics Conference; 2010; Ottawa, ON. pp. 1-4.
65. D. Guha, B. Gupta, and Y. M. M. Antar. Hybrid monopole-DRA: new geometries for improved ultra-wideband operation. Proceedings of the IEEE Antennas and Propagation Society International Symposium; 2010; Toronto, ON. pp. 1-4.
66. Denidni TA, Weng Z, Jazi MN. Z-shaped dielectric resonator antenna for ultra-wideband applications. *IEEE Trans Antennas Propag*. 2010;58(12): 4059-4062.
67. Y. Ge, K. P. Esselle, and T. S. Bird. Compact broadband dielectric resonator antennas. Proceedings of the IEEE International Conference on Electromagnetics in Advanced Applications; 2010; Sydney, NSW. pp. 213-215.
68. Ahmed OMH, Sebak AR, Denidni TA. Compact UWB printed monopole loaded with dielectric resonator antenna. *IET Electron Lett*. 2011;47(1):7-8.
69. H. W.ng, and V. V. Varadan. Low profile wideband hybrid dielectric resonator and split ring resonator antenna. Proceedings of the IEEE International Symposium on Antennas and Propagation; 2011; Spokane, WA. pp. 1685-1687.

70. R. K. Chaudhary, Himangshu Bhusan Baskey, K. V. Srivastava, A. BisW. s. Wideband two-layer rectangular dielectric resonator antenna with (Zr0.8sn0.2)Tio4-epoxy composite system. Proceedings of the IEEE Indian Antenna Week; 2011; Kolkata. pp. 1-4.

71. Guha D, Gupta B, Antar AYMM. Hybrid monopole-DRAs using hemispherical/ conical-shaped dielectric ring resonators: Improved ultrawideband designs. *IEEE Trans Antennas Propag*. 2012;60(1):303-398.

72. Rashidian A, Shafai L, Klymyshyn DM. Compact wideband multimode dielectric resonator antennas fed with parallel standing strips. *IEEE Trans Antennas Propag*. 2012;60(11):5021-5031.

73. Y. Ge. Size-reduced dielectric resonator antenna for UWB applications. Proceedings of the IEEE Asia-Pacific conference on antennas and propagation; 2012; Singapore. pp. 45–46.

74. Abedian M, Rahim SKA, Khalily M. Two-segments compact dielectric resonator antenna for UWB application. *IEEE Antennas Wirel Propag Lett*. 2012;11.

75. Ge Y. Methods to improve the bandwidth performance for compact dielectric resonator antennas. *Microw Opt Technol Lett*. 2012;54(10).

76. Oliveira EEC, D'assunc AG, Oliveira AOJBL, Cabral AM. Small size dual-band rectangular dielectric resonator antenna based on calcium titanate (Catio3). *Microw Opt Technol Lett*. 2012;54(4).

77. Chaudhary RK, Srivastava KV, Biswas A. Wideband multilayer multi-permittivity half-split cylindrical dielectric resonator antenna. *Microw Opt Technol Lett*. 2012;54(11):2587-2590.

78. Y. Ge, T. Wei, and Z. Hai. Design of compact UWB dielectric resonator antennas. Proceedings of the IEEE International Symposium on Antennas and Propagation; 2012; Chicago, IL. pp. 1-2.

79. S. S. Alja'afreh, Y. Huang, and L. Xing. A small wideband U-shaped dielectric resonator antenna. Proceedings of the Antennas and Propagation Conference; 2012; Loughborough. pp. 1-4.

80. A. S. Batcha, L. C. Kwang, and G. Vetharatnam. Bandwidth enhancement of dielectric resonator antenna (DRA). Proceedings of the IEEE International Conference on RFID Technologies and Applications; 2013; Johor Bahru, Malaysia. pp. 1-4.

81. Y. Wang, and G. Wei, T. A. Denidni, and Q. Zeng. Ultra-wideband planar monopole integrated with cylindrical dielectric resonator antenna. Proceedings of the IEEE Antennas and Propagation Society International Symposium; 2013; Orlando, FL; pp. 1696-1697.

82. Pahadsingh S, Sahu S. Planar UWB integrated with multi narrowband cylindrical dielectric resonator antenna for cognitive radio application. *AEU Int J Electron C*. 2017;74:150-157.

83. Y. Wang, G. Wei, Q. Zeng, and T. A. Denidni. Integrated ultra-wideband/-narrow band dielectric resonator antenna. Proceedings of the IEEE Antennas and Propagation Society International Symposium; 2013; Orlando, FL; pp. 1692–1693.

84. Sharma SK, Brar MK. Aperture-coupled pentagon shape dielectric resonator antennas providing wideband and multiband performance. *Microw Opt Technol Lett*. 2013;55(2):395-400.

85. Mukherjee B, Patel P, Reddy GS, Mukherjee J. A novel half hemispherical dielectric resonator antenna with array of slots for wideband applications. *Prog Electromagn Res C*. 2013;36:207-221.

86. Chaudhary RK, Srivastava KV, Biswas A. A broadband dumbbell-shaped dielectric resonator antenna. *Microw Opt Technol Lett*. 2014;56(12):2944-2947.

87. Fang XS, Leung KW. Design of wideband omnidirectional two-layer transparent hemispherical dielectric resonator antenna. *IEEE Trans Antennas Propag*. 2014;62(10):5353-5357.

88. Haraz OM, Sebak AR, Denidni TA. A hybrid printed monopole antenna loaded with dielectric resonator for wideband and circular polarization applications. *Int J RF Microw Comp Aided Eng*. 2012;22(5).

89. Guha D, Ganguly D, George S, Kumar C, Sebastian MT, Antar YMM. A new design approach for a hybrid monopole to achieve increased ultrawide bandwidth. *IEEE Antennas Propagat Mag*. 2017;59(1):139-144.

90. Fakhte S, Oraizi H. Compact uniaxial anisotropic dielectric resonator antenna operating at higher order radiating mode. *IET Electron Lett*. 2016;52(19):1579-1580.

91. Gupta RD, Parihar MS. Differentially fed wideband rectangular dra with high gain using short horn. *IEEE Antennas Wirel Propag Lett*. 2017.

92. Ranjan P, Gangwar RK. Probe feed half split cylindrical dielectric resonator antenna for wideband application. *AEU Int J Electron C*. 2015;69:1709-1714.

93. Falconer K. *Fractal Geometry: Mathematical Foundations and Applications*. John Wiley & Sons, Ltd; 2003.

94. Hajihashemi MR, Abiri H. Parametric study of novel types of dielectric resonator antennas based on fractal geometry. *Int J RF Microw Comp Aided Eng*. 2007;17(5):416-424.

95. D. P. Karmakar, D. Soren, R. Ghatak, D. R. Poddar, and R. K. Mishra. A wideband sierpinski carpet fractal cylindrical dielectric resonator antenna for X-band application. Proceedings of the IEEE Applied Electromagnetics Conference; 2009; Kolkata, India. pp. 1-3.

96. D. Soren, R. K. Mishra, R. Ghatak, and D. R. Poddar. A monopole type Sierpinski carpet fractal patterned rectangular dielectric resonator antenna for UWB application. Proceedings of the IEEE Indian Antenna Week; 2011; pp. 1-5. (DOI: 10.1109/IndianAW.2011.6264919)

97. Dhar S, Ghatak R, Gupta B, Poddar DR. A wideband minkowski fractal dielectric resonator antenna. *IEEE Trans Antennas Propag*. 2013;61(6):2895-2903.

98. Azari A, Ismail A, Sali A, Hashim F. A new super wideband fractal monopole-dielectric resonator antenna. *IEEE Antennas Wirel Propag Lett*. 2013;12:1014-1016.

99. Mukherjee B, Patel P, Mukherjee J. Hemispherical dielectric resonator antenna based on apollonian gasket of circles-a fractal approach. *IEEE Trans Antennas Propag*. 2014;62(1):40-47.

100. B. Mukherjee, P. Patel, and J. Mukherjee. Hemispherical dielectric resonator antenna embedded in a novel Sierpinski carpet fractal based photonic band gap structure for wideband systems. Proceedings of the IEEE 3rd Asia-Pacific Conference, on Antennas and Propagation; 2014; pp. 147-150.

101. Dhar S, Patra K, Ghatak R, Gupta B, Poddar DR. A dielectric resonator-loaded minkowski fractal-shaped slot loop heptaband antenna. *IEEE Trans Antennas Propag*. 2015;63(4):1521-1529.

102. Fan Z, Antar YMM, Ittipiboon A, Petosa A. Parasitic coplanar three-element dielectric resonator antenna subarray. *IET Electron Lett*. 1996;32(9):789-790.

103. Mukherjee B, Kumar VD, Gupta M. A novel hemispherical dielectric resonator antenna on an electromagnetic band gap substrate for broadband and high gain systems. *AEU Int J Electron C*. 2014;68(12):1185-1190.

104. Kiran DV, Sankaranarayanan D, Mukherjee B. Compact embedded dual-element rectangular dielectric resonator antenna combining Sierpinski and minkowski fractals. *IEEE Trans Comp Pack Manufact Technol*. 2017;7(5):786-791.

105. Mongia RK, Ittipiboon A, Antar YMM, Bhartia P, Cuhaci M. A half-split cylindrical dielectric resonator antenna using slot-coupling. *IEEE Microw Guided Wave Lett*. 1993;3(2):38-39.

106. A. Ittipiboon, A. Petosa, D. Roscoe, and M. Cuhaci. An investigation of a novel broadband dielectric resonator antenna. Proceedings of the IEEE Antennas and Propagation Society International Symposium, Digest; 1996; Vol. 3, pp. 2038-2041.

107. Leung KW, M. W. To. Aperture-coupled dielectric resonator antenna with a perpendicular feed. *IET Electron Lett*. 1997;33(12):1000-1001.

108. Luk KM, Lee MT, Leung KW, Yung EKN. Technique for improving coupling between microstripline and dielectric resonator antenna. *IET Electron Lett*. 1999;35(35):357-358.

109. Kishk AA, Glisson AW, Yin Y. Conical dielectric resonator antennas excited by a coaxial probe. *Microw Opt Technol Lett*. 2001;29(3):160-161.

110. A. A. Kishk, A. W. Glisson, and X. Zhang. Analysis of dielectric resonator antennas excited by a coaxial probe with wideband enhancement. Proceedings of the IEEE Antennas and Propagation Society International Symposium; 2002; San Antonio, TX. Vol. 1, pp. 568–571.

111. Agrawal S, Gupta RD, Parihar MS, Kondekar PN. A wideband high gain dielectric resonator antenna for RF energy harvesting application. *AEU Int J Electron C*. 2017;78:24-31.

112. Chair R, Kishk AA, Lee KF, Smith CE. Broadband aperture coupled flipped staired pyramid and conical dielectric resonator antennas. *Proc IEEE*. 2004;1375-1378.

113. Deng SM, Tsai CL, Chang SF, Bor SS. Coaxial-fed monopole antenna coupled by dual rectangular ceramic dielectric resonators for wideband operation. *Microw Opt Technol Lett*. 2005;46(5):500-503.

114. T. W. Li, and J. S. Sun. Wideband dielectric resonator antenna with parasitic strip. Proceedings of the IEEE International Conference on Wireless Communications and Applied Computational Electromagnetics; 2005; Honolulu, Hawaii. pp. 376-379.

115. D. Guha, Y. M. M. Antar, A. Ittipiboon, A. Petosa, and D. Lee. in search of ultra wideband performance of the monopole-dielectric resonator antenna. Proceedings of the IEEE European Conference on Antenna and Propagation; 2006; Nice, France. pp. 1–4.

116. Gao Y, Popov AP, Ooi BL, Leong MS. Experimental study of wideband hybrid dielectric resonator antenna on small ground plane. *IET Electron Lett*. 2006;42(13):731-733.

117. Kishk AA, Chair R, Lee KF. Broadband dielectric resonator antennas excited by L-shaped probe. *IEEE Trans Antennas Propag*. 2006;54(8): 2182-2189.

118. Kumar AVP, Hamsakutty V, Yohannan J, Mathew KT. Microstripline fed cylindrical dielectric resonator antenna with a coplanar parasitic strip. *Prog Electromagn Res*. 2006;60:143-152.

119. Rezaei P, Hakkak M, Forooraghi K. Effect of magnetic layer on the microstrip-excited rectangular dielectric resonator antennas bandwidth. *J Electromagn Waves Appl*. 2007;21(7):915-927.

120. S. Thirakoune, A. Petosa, and A. Ittipiboon. Yagi-like Dra-loaded monopole. Proceedings of the IEEE International Conference on Electromagnetics in Advanced Applications; 2007; Torino, Italy. pp. 891–894.

121. Zhang LN, Zhong SS, Xu SQ. Broadband U-shaped dielectric resonator antenna with elliptical patch feed. *IET Electron Lett*. 2008;44(16):947-949.

122. X. L. Liang, and T. A. Denidni. Wideband dielectric resonator antenna using a trapezoid-patch feeding technique. Proceedings of the IEEE Antennas and Propagation Society International Symposium; 2008; San Diego. pp. 1-4.

123. S. Ghosh, A. Chakrabarty. Mutual coupling between ultra wideband dielectric loaded T-shaped monopole antennas. Proceedings of the IEEE Region 10 Colloq. and the 3rd International Conference on Industrial and Information Systems; 2008; Kharagpur, India. pp. 1-4.

124. A. Singh, and S. K. Sharma. Wideband cylindrical dielectric resonator antenna fed-in using anti-probes providing directional patterns with low cross-polarization. Proceedings of the IEEE Antennas and Propagation Society International Symposium; 2009; pp. 1–4.

125. A. S. Al-Zoubi, and A. A. Kishk. Wide band strip-fed rectangular dielectric resonator antenna. Proceedings of the IEEE Antennas and Propagation Society International Symposium; 2009, pp. 2379-2382.

126. Denidni TA, Weng Z. Hybrid ultra-wideband dielectric resonator antenna and band-notched designs. *IET Microw Antennas Propag*. 2011;5(4): 450-458.

127. Liang X-L, Denidni TA. Wideband rectangular dielectric resonator antenna with a concave ground plane. *IEEE Antennas Wirel Propag Lett*. 2009;8: 367-370.

128. Liang X-L, Denidni TA, Zhang L-N. Wideband L-shaped dielectric resonator antenna with a conformal inverted-trapezoidal patch feed. *IEEE Trans Antennas Propag*. 2009;57(1).

129. Ge Y, Esselle KP. A UWB probe-fed dielectric resonator antenna. *Proc IEEE*. 2009.

130. Gopakumar C, Yohannan J, Kalappura UG, Mathe KT. An investigation of wideband circular cylindrical sector dielectric resonator antenna with microstripline feed. *Microw Opt Technol Lett*. 2009;51(12):2861-2865.

131. Weng ZB, Weng XM, Jiao YC, Zhang FS. CPW-fed dielectric resonator antenna for ultra-wideband applications. *Microw Opt Technol Lett*. 2010; 52(12):2709-2712.

132. Thamae LZ, Wu Z. Broadband bowtie dielectric resonator antenna. *IEEE Trans Antennas Propag*. 2010;58(11):3707-3710.

133. K. H. Zheng, H. O. Chua, and L. -W. Li. Analysis and design of UWB monopole-dielectric resonator antenna. Proceedings of the IEEE International Conference on Ultra-Wideband; 2010; Nanjing, China. Vol.1, pp. 1-4.

134. Gopakumar C, Mathew KT. A wideband microstrip-line-fed isosceles trapezoidal dielectric resonator antenna with modified ground plane. *Prog Electromagn Res C*. 2010;16:127-136.

135. Kakade AB, Ghosh B. Analysis of the rectangular w.Veguide slot coupled multilayer hemispherical dielectric resonator antenna. *IET Microw Antennas Propag*. 2012;6(3):338-347.

136. Huynh AP, Jackson DR, Long SA, Wilton DR. A study of the impedance and pattern bandwidths of probe-fed cylindrical dielectric resonator antennas. *IEEE Antennas Wirel Propag Lett*. 2011;10:1313-1316.

137. Gao Y, Feng Z, Zhang L. Compact dielectric-resonator-patch antenna with bandwidth enhancement. *Microw Opt Technol Lett*. 2012;54.

138. Chaudhary RK, Rajni. Wideband ring dielectric resonator antenna with annular-shaped microstrip feed. *IEEE Antennas Wirel Propag Lett*. 2013; 12:595-498.

139. Rashidian A, Aligodarz MT, Shafai L, Klymyshyn DM. On the matching of microstrip-fed dielectric resonator antennas. *IEEE Trans Antennas Propag*. 2013;61(10):5291-5296.

140. Prachi, R. K. Chaudhary, and K. V. Srivastava. Wideband cylindrical dielectric resonator antenna excited by a rounded bevel shaped patch. Proceedings of the IEEE Antennas and Propagation Society International Symposium; 2013; Orlando, FL. pp. 1910-1911.

141. Ozzaim C, Üstuner F, Tarim N. Stacked conical ring dielectric resonator antenna excited by a monopole for improved ultra wide bandwidth. *IEEE Trans Antennas Propag*. 2013;61(3):1435-1438.

142. D. Guha, D. Ganguly, S. George, Y. M. M. Antar. Monopole-type dielectric resonator antenna with improved bandwidth characteristics. Proceedings of the IEEE Antennas and Propagation Society International Symposium; 2014; Memphis, Tennessee. pp. 1988-1989.

143. Sunab RY, Chenb QH. Quadrature feed wideband circularly polarized cylindrical dielectric resonator antenna. *J Electromagn Waves Appl*. 2014; 28(8):1011-1017.

144. Prachi C, Chaudhary RK, Srivastava KV. Rounded bevel shaped fed cylindrical dielectric resonator antenna for wideband applications. *Microw Opt Technol Lett*. 2015;57(10):2364-2368.

145. Leung KW, Wong WC, Luk KM, Yung EKN. Annular slot-coupled antenna. *IET Electron Lett*. 1998;34(13):1275-1277.

146. Hui HT, Yung EKN. Analysis of a rectangular slot antenna loaded by a dielectric hemisphere with double dielectric coatings. *J Electromagn Waves Appl*. 2000;14:857-872.

147. So KK, Leung KW. Bandwidth enhancement and frequency tuning of the dielectric resonator antenna using a parasitic slot in the ground plane. *IEEE Trans Antennas Propag*. 2005;53(12):4169-4172.

148. Buerkle A, Sarabandi K, Mosallaei H. Compact slot and dielectric resonator antenna with dual-resonance, broadband characteristics. *IEEE Trans Antennas Propag*. 2005;53(3):1020-1027.

149. Kishk AA. Experimental study of broadband embedded dielectric resonator antennas excited by a narrow slot. *IEEE Antennas Wirel Propag Lett*. 2005;4:79-81.

150. Weng Z, Weng X, Jiao Y, Zhang F. Wideband rectangular dielectric resonator antenna (DRA) with slot-fed design. *Prog Electromagn Res Lett*. 2010;16:181-190.

151. Deng JY, Guo LX, Liu ZY, Wu RR. Dual-band antenna with inserted edge resonators and U-slot DGS. *J Electromagn Waves Appl*. 2012;26(10):1292-1299.

152. Rahimian Z, Nikmehr S, Pourziad A. Circularly polarized rectangular dielectric resonator antennas with branch-line coupler for wideband applications. *AEU Int J Electron C*. 2015;69:169-175.

153. Mongia RK, Ittibipoon A, Cuhaci M. Low profile dielectric resonator antennas using a very high permittivity material. *IET Electron Lett*. 1994; 30(17):1362-1363.

154. Leung KW, Chow KY, Luk KM, Yung EKN. Off set duai-disk dielectric resonator antenna of very high permittivity. *IET Electron Lett*. 1996;32 (22):3028-3029.

155. Leung KW, Luk KM, Chow KY, Yung EKN. Bandwidth enhancement of dielectric resonator antenna by loading a low-profile dielectric disk of very high permittivity. *IET Electron Lett*. 1997;33(9):725-726.

156. Guo Y-X, Luk K-M. On the improving coupling between coplanar waveguide and low-permittivity dielectric resonator antenna. *IEEE Trans Antennas Propag*. 2003;51(8):2144-2146.

157. Bijumon PV, Menon SK, Sebastian MT, Mohanan P. Enhanced bandwidth microstrip patch antennas loaded with high permittivity dielectric resonators. *Microw Opt Technol Lett*. 2002;35(4).

158. Z. Wu. Broadband miniaturized dielectric resonator antennas. Proceedings of the IEEE International Conference on Electromagnetics in Advanced Applications; 2007; pp. 883-886. (DOI: 10.1109/ICEAA.2007.4387446)

159. A. Rashidian, and D. M. Klymyshyn. Strip-fed excitation of very low permittivity dielectric resonator antennas. Proceedings of the IEEE Asia Pacific Microwave Conference; 2008; Macau, China. pp. 1-4.

160. Rotaru M, Sykulski JK. Numerical investigation on compact multimode dielectric resonator antennas of very high permittivity. *IET Science, Measurement Technol*. 2009;3(3):217-228.

161. A. P. Huynh, S. A. Long, and D. R. Jackson. Effects of permittivity on bandwidth and radiation patterns of cylindrical dielectric resonator antennas. Proceedings of the IEEE Antennas and Propagation Society International Symposium; 2010; pp. 1-4.

162. Madhuri RG, Hadalgi PM, Hunagund PV. Design of high-permittivity rectangular dielectric resonator antenna. *Microw Opt Technol Lett*. 2011;53(5): 1077-1079.

163. Avadanei OG, Banciu MG, Nicolaescu L, Nedelcu L. Superior modes in high permittivity cylindrical dielectric resonator antenna excited by a central rectangular slot. *IEEE Trans Antennas Propag*. 2012;60(11):5032-5038.

164. Liu Y, Liu H, Wei M, Gong S. A low-profile and high-permittivity dielectric resonator antenna with enhanced bandwidth. *IEEE Antennas Wirel Propag Lett*. 2015;14:791-794.

165. B. Li, and K. W. Leung. A wideband strip-fed rectangular dielectric resonator antenna. Proceedings of the IEEE Antennas and Propagation Society International Symposium; 2005; Washington, DC. Vol. 2A, pp. 172-175.

166. Chang TH, Kiang JF. Broadband dielectric resonator antenna with an offset well. *IEEE Antennas Wirel Propag Lett*. 2007;6:564-567.

167. T. Chang, and J. F. Kiang. Bandwidth enhancement by merging resonant modes of dielectric resonator antenna. Proceedings of the IEEE Antennas and Propagation Society International Symposium; 2007; pp. 2733-2736.

168. Chang TH, Kiang JF. Bandwidth broadening of dielectric resonator antenna by merging adjacent bands. *IEEE Trans Antennas Propag*. 2009;57(10): 3316-3320.

169. Ge Y, Esselle KP, Bird TS. Compact dielectric resonator antennas with ultrawide 60%–110% bandwidth. *IEEE Trans Antennas Propag*. 2011;59 (9):3445-3448.

170. Sung Y, Ahn CS, Kim Y-S. Microstrip line fed dual frequency dielectric resonator antenna. *Microw Opt Technol Lett*. 2004;42(5):388-390.

171. Kumar AVP, Hamsakutty V, Yohannan J, Mathew KT. Microstripline fed cylindrical sector dielectric resonator antenna. *Proc IEEE Asia-Pacific Microwave Conference*. 2005;4.

172. Kumar AVP, Yohannan J, Anandan CK, Mathew KT. Microstrip line fed cylindrical dielectric resonator antenna for dual-band operation. *Microw Opt Technol Lett*. 2005;47(2):150-153.

173. Lim EH, Leung KW. Dual-wideband rectangular dielectric resonator antenna for WLAN communications. *Microw Opt Technol Lett*. 2006;48 (2):378-380.

174. Gao Y, Ooi BL, Popov AP. Dual-band hybrid dielectric resonator antenna with CPW-fed slot. *Microw Opt Technol Lett*. 2006;48(1):170-172.

175. J. J. Adz, M. H. M. Khir, M. A. Zakariya, Z. Baharudin, and Et al. A compact dual band directional cylindrical dielectric resonator antenna. Proceedings of the IEEE 4th International Conference on Intelligent and Advanced Systems; 2012; Kuala Lumpur. Vol. 1, pp. 265-268.

176. P. Kumar, S. Dwari, S. Singh, and N. K. Agrawal. Design investigation of a laminated waveguide fed multi-band Dra for military applications. Frequenz J RF-Eng Telecommun. 2017;72(1-2): (7-14). (DOI: https://doi.org/10.1515/freq-2016-0295).

177. Sharma A, Das G, Ranjan P, Sahu NK, Gangwar RK. Novel feeding mechanism to stimulate triple radiating modes in cylindrical dielectric resonator antenna. *IEEE Access*. 2016;4:9987-9992.

178. Khalily M, Rahim MKA, Murad NA, Samsuri NA, Kishk AA. Rectangular ring-shaped dielectric resonator antenna for dual and wideband frequency. *Microw Opt Technol Lett*. 2013;55(5):1077-1081.

179. A. Mehmood, Y. Zheng, H. Braun, M. Hovhannisyan, M. Letz, and R. Jakoby. Dual band dielectric resonator antenna for hiperlan based on transparent glass material. Proceedings of the IEEE German Microwave Conference; 2014; Aachen, Germany. pp. 1–4.

180. Zou M, Pan J. A simple dual-band circularly polarized rectangular dielectric resonator antenna. *Prog Electromagn Res Lett*. 2015;53:57-63.

181. Hamsakutty V, Kumar AVP, Yohannan J, Bindu G, Mathew KT. Coaxial fed hexagonal dielectric resonator antenna for multifrequency operation. *Microw Opt Technol Lett*. 2006;48(5):878-880.

182. Sangiovanni A, Pichot JYDC. Stacked dielectric resonator antenna for multifrequency operation. *Microw Opt Technol Lett*. 1998;18(4):303-306.

183. Hamsakutty V, Kumar AVP, Bindu G, et al. A multifrequency coaxial-fed metal coated dielectric resonator antenna. *Microw Opt Technol Lett*. 2005; 47(6):573-575.

184. Fang XS, Leung KW. Designs of single-, dual-, wide-band rectangular dielectric resonator antennas. *IEEE Trans Antennas Propag*. 2011;59(6): 2409-2414.

185. Paul B, Mridula S, Mohanan P, Bijumon PV, Sebastian MT. A compact very-high-permittivity dielectric-eye resonator antenna for multiband wireless applications. *Microw Opt Technol Lett*. 2004;43(2):118-121.

186. G. B. Babik, C. D. Nallo, and A. Faraone. Multimode dielectric resonator antenna of very high permittivity. Proceedings of the IEEE Antennas and Propagation Society International Symposium; 2004; Vol. 2, pp. 1383-1386.

187. Singh A, Sharma SK. Investigations on wideband cylindrical dielectric resonator antenna with directive radiation patterns and low cross polarization. *IEEE Trans Antennas Propag*. 2010;58(5):1779-1783.

188. Ryu KS, Kishk AA. UWB dielectric resonator antenna having consistent omnidirectional pattern and low cross-polarization characteristics. *IEEE Trans Antennas Propag*. 2011;59(4):1403-1408.

189. Khalily M, Rahim MKA, Kishk AA. Bandwidth enhancement and radiation characteristics improvement of rectangular dielectric resonator antenna. *IEEE Antennas Wirel Propag Lett*. 2011;10:393-395.

190. Jazi MN, Denidni TA. Experimental investigations of a novel ultra-wideband dielectric resonator antenna with rejection band using hybrid techniques. *IEEE Antennas Wirel Propag Lett*. 2012;11:492-495.

191. Shao Y, Ge Y, Chen Y, Zhang H. Compact band-notched UWB dielectric resonator antennas. *Prog Electromagn Res Lett*. 2015;52:87-92.

AUTHOR BIOGRAPHIES



Sounik Kiran Kumar Dash is presently working as an Assistant Professor in the Department of Electronics and Communication Engineering at CHRIST (Deemed to be University), Bengaluru, India. He received his BTech degree in the stream of Electronics & Communication Engineering from Centurion University of Technology and Management, Bhubaneswar, India in 2013, MTech degree with specialization of Communication System Engineering from KIIT University, Bhubaneswar, India in 2015, and PhD from National Institute of Technology (NIT) Silchar, Assam, India in 2018. His current research interests include Dielectric Resonator Antennas (DRAs), RF Energy Harvesting, UWB Antennas, MIMO Antennas, Reconfigurable Antennas, Numerical Methods in Electromagnetics, and Neural Networks. He has authored or coauthored over twenty research articles in referred journals (like IEEE, IET, Wiley, Taylor & Francis, Cambridge University Press, and so on) and international conference/symposium proceedings (like URSI-GASS, EuMW, AEMC, and so on) of repute. He is an active reviewer of several referred journals of international repute, that is, AEU-International Journal of Electronics and Communications (Elsevier), International Journal of RF and Microwave Computer-Aided Engineering (Wiley), Journal of Electromagnetic Waves and Applications (Taylor & Francis), Journal of Microwave Power and Electromagnetic Energy (Taylor & Francis), Journal of RF-Engineering and Telecommunications (Frequenz), and International Journal of Antennas and Propagation (Hindawi), and so on. He has received several grants like; Special Student Grant from European Microwave

Association (EuMA), Belgium, Foreign Travel Grant from Council of Scientific & Industrial Research (CSIR), Govt. of India for attending various international events. He is an active member IEEE APS/SPS/EDS (USA), URSI (Bengium), and IAENG (China).



TAIMOOR KHAN is presently an Assistant Professor in the Department of Electronics and Communication Engineering at National Institute of Technology Silchar, India where he serves as a full time faculty member since 2014. During September to December 2016, he worked as a Visiting Assistant Professor in Telecommunication Field of Study at Asian Institute of Technology, Bangkok, Thailand under Short-term Deputation Programme of Ministry of HRD, Govt. of India. Prior to joining NIT Silchar, he served several organizations like: Delhi Technological University (Formerly Delhi College of Engineering), Govt. of NCT of Delhi, Delhi, India as an Assistant Professor for more than 2 years; Netaji Subhas Institute of Technology Patna, India as an Associate Professor and Head of the Department for one and half year and Shobhit Institute of Engineering and Technology, Meerut, Uttar Pradesh, India as a Lab Instructor, Lecturer and Assistant Professor for more than 9 years. Dr. Khan awarded his Ph.D. Degree in Electronics and Communication Engineering from National Institute of Technology (NIT) Patna, India in the year 2014. He obtained his Master Degree in Communication Engineering from Shobhit Institute of Engineering and Technology (A Deemed University), Meerut, Uttar Pradesh, India in 2009; Bachelor Degree in Electronics and Communication Engineering from The Institution of Engineers (India), Kolkata, India in the year 2005 and Polytechnic Diploma in Electronics Engineering from Government Polytechnic Saharanpur, Uttar Pradesh, India in 2001. His active research interest includes Communication Engineering, Printed Microwave and Millimeter Wave Circuits, Electromagnetic Bandgap Structures, Computational Electromagnetics and Artificial Intelligence Paradigms in Electromagnetics. He has published over 65 research papers in international journals of repute like; IEEE, IET, Wiley, Taylor and Frances, Cambridge University, Progress in Electromagnetic research, and so on as well as in international/national conference proceedings including URSI GASS, European Microwave Week, AEMC, APACE, ISMOT, and so on. Dr. Khan is also executing two funded research projects, Govt. of India. He is an active senior member IEEE, fellow, IETE (India), life member, IAENG (China), member URSI (Belgium), and life member, ISTE (India).

How to cite this article: Dash SKK, Khan T. Recent developments in bandwidth improvement of dielectric resonator antennas. *Int J RF Microw Comput Aided Eng*. 2019;e21701. https://doi.org/10.1002/mmce.21701

ResearchGate

See discussions, stats, and author profiles for this publication at: https://www.researchgate.net/publication/331077735

Sarcasm Detection Using Soft Attention-Based Bidirectional Long Short-Term Memory Model with Convolution Network

Article *in* IEEE Access · February 2019

DOI: 10.1109/ACCESS.2019.2899260

CITATIONS
0

READS
96

6 authors, including:



Le Son
Vietnam National University, Hanoi
144 PUBLICATIONS **1,630** CITATIONS

SEE PROFILE



Anand Nayyar
Duy Tan University
74 PUBLICATIONS **155** CITATIONS

SEE PROFILE

Some of the authors of this publication are also working on these related projects:

Books Published View project

Published View project

All content following this page was uploaded by Anand Nayyar on 06 March 2019.

The user has requested enhancement of the downloaded file.

SPECIAL SECTION ON EMERGING TRENDS, ISSUES AND CHALLENGES IN UNDERWATER ACOUSTIC SENSOR NETWORKS

IEEE Access
Multidisciplinary | Rapid Review | Open Access Journal

Received January 30, 2019, accepted February 11, 2019, date of publication February 13, 2019, date of current version March 5, 2019.

Digital Object Identifier 10.1109/ACCESS.2019.2899260

Sarcasm Detection Using Soft Attention-Based Bidirectional Long Short-Term Memory Model With Convolution Network

LE HOANG SON[1,2], AKSHI KUMAR[3], SAURABH RAJ SANGWAN[3], ANSHIKA ARORA[3], ANAND NAYYAR[4], AND MOHAMED ABDEL-BASSET[5]

[1]Division of Data Science, Ton Duc Thang University, Ho Chi Minh 700000, Vietnam
[2]Faculty of Information Technology, Ton Duc Thang University, Ho Chi Minh 700000, Vietnam
[3]Department of Computer Science & Engineering, Delhi Technological University, Delhi 110042, India
[4]Graduate School, Duy Tan University, Da Nang 550000, Vietnam
[5]Department of Operations Research, Faculty of Computers and Informatics, Zagazig University, Zagazig 44519, Egypt

Corresponding author: Mohamed Abdel-Basset (analyst_mohamed@zu.edu.eg)

ABSTRACT A large community of research has been developed in recent years to analyze social media and social networks, with the aim of understanding, discovering insights, and exploiting the available information. The focus has shifted from conventional polarity classification to contemporary application-oriented fine-grained aspects such as, emotions, sarcasm, stance, rumor, and hate speech detection in the user-generated content. Detecting a sarcastic tone in natural language hinders the performance of sentiment analysis tasks. The majority of the studies on automatic sarcasm detection emphasize on the use of lexical, syntactic, or pragmatic features that are often unequivocally expressed through figurative literary devices such as words, emoticons, and exclamation marks. In this paper, we propose a deep learning model called sAtt-BLSTM convNet that is based on the hybrid of soft attention-based bidirectional long short-term memory (sAtt-BLSTM) and convolution neural network (convNet) applying global vectors for word representation (GLoVe) for building semantic word embeddings. In addition to the feature maps generated by the sAtt-BLSTM, punctuation-based auxiliary features are also merged into the convNet. The robustness of the proposed model is investigated using balanced (tweets from benchmark SemEval 2015 Task 11) and unbalanced (approximately 40000 random tweets using the Sarcasm Detector tool with 15000 sarcastic and 25000 non-sarcastic messages) datasets. An experimental study using the training- and test-set accuracy metrics is performed to compare the proposed deep neural model with convNet, LSTM, and bidirectional LSTM with/without attention and it is observed that the novel sAtt-BLSTM convNet model outperforms others with a superior sarcasm-classification accuracy of 97.87% for the Twitter dataset and 93.71% for the random-tweet dataset.

INDEX TERMS Sarcasm, deep learning, attention, social data.

I. INTRODUCTION

The biggest challenge in sentiment analysis tasks is to accurately determine the veracity of the statement in literal sense so as to classify text on the basis of polarity (positive or negative). Sentiment analysis achieves decent results in the case of literal language as it conveys the expected interpretation. However, the use of figurative language that is inherently emblematic represents something other than the concrete meaning, thereby making sentiment analysis a non-trivial problem. ''Sarcasm is defined as a specific type of sentiment where people express their negative feelings using positive or intensified positive words in the text'' [1]. It is a rhetoric narrative that presents a communicatively significant discord between the actual situation and the utterance content. For example, a tweet/post, ''*It is wonderful feeling to waste hours in traffic jams!*'' clearly indicates this discord between the actual situation of ''being stuck in traffic jam'' and the utterance content ''wonderful.'' This contrast and shift of sentiments in sarcastic expressions validates sarcasm as a special instance of sentiment analysis. Therefore, the detection of sarcastic expressions will enhance

The associate editor coordinating the review of this manuscript and approving it for publication was Muhammad Imran.

2169-3536 © 2019 IEEE. Translations and content mining are permitted for academic research only.
Personal use is also permitted, but republication/redistribution requires IEEE permission.
See http://www.ieee.org/publications_standards/publications/rights/index.html for more information.

the automatic sentiment analysis of huge and diverse social web data.

Automatic sarcasm detection is typically a text-classification problem, which relies on a variety of feature-extraction and learning techniques. In general, the Twitter post size characterizes short text with a character limit of 280, which is insufficient in providing the desired word co-occurrence data. This data sparseness is challenging for conventional learning models based on statistical features, such as term frequency–inverse document frequency (TF-IDF) or co-occurrence. Deep learning architectures have proven capabilities when dealing with natural language, as they can learn by example, offer a flexible set of modeling alternatives while curtailing feature engineering, scale up to big data, exploit unlabeled data to detect trends and identify patterns too complex for humans to notice, and be used for multitask learning [2]. The **primary contribution** of this work includes:

- Improving the performance of the sentiment analysis task by building, training and evaluating a deep learning model, *s*Att-BLSTM convNet, a hybrid of *soft* attention-based bidirectional long short-term memory (*s*Att-BLSTM) and convolution neural network (convNet)
- Feature engineering for automatic sarcasm detection using figurative literary devices such as words, emoticons, and exclamation marks.
- Performance benchmarking by testing different kinds of models and datasets for sarcastic tone classification in real-time.

The proposed deep learning model, *s*Att-BLSTM convNet, has eight layers:

- *Input Layer:* The input tweet to the model.
- *Embedding Layer:* Each word within tweet is mapped into a low dimension vector using GloVe. This look-up encodes the input into real-valued vectors called embedding vectors.
- *BLSTM layer:* The output of the word-embedding layer is fed into the BLSTM layer. The purpose of this layer is to learn high-level features from the previous step.
- *Attention Layer:* A*soft* attention mechanism (based on *softmax*) is used, which generates semantic context vectors. These are merged with the BLSTM output features and auxiliary features to train the convNet.
- *Convolution Layer:* The convolution operation is performed to obtain a convolved feature vector.
- *Activation Layer:* A **Re**ctified **L**inear **U**nit (ReLU) activation function is applied on the feature vectors (output of convNet layer).
- *Down-sampling Layer:* The max-pooling operation is used as a down-sampling strategy in convNets.
- *Representation Layer:* A fully connected layer that consists of a linear transformation layer and *softmax* activation function to generate the output predictions.

To build word embeddings, GloVe [3], which generates a word vector table, is used. GloVe is a count-based model of representing words by feature vectors. This model maps all the tokenized words in each tweet to its respective word vector table. Proper padding is performed to unify the feature vector matrix. This matrix is given as an input to the bidirectional long-short-term-memory (BLSTM) layer. The BLSTM networks set up an additional layer to the unidirectional LSTM networks, where the hidden-to-hidden connections flow in opposite temporal order. The network thus exploits information from the past and the future. The output vector representation from the BLSTM is transformed into an attention-weighted sum of these output vectors. This word-level attention hypothesis relies on valuable words within text that contribute to the meaning in context, and thus computes attention probabilities over the input stimuli from the BLSTM. Consequently, the output feature representations from BLSTM are concatenated together as the output of the attention layer, which, combined with auxiliary features, is provided as input to the convNet. The convNet consists of multiple filters with a variable-size window connected to a small part of the input to generate a convolved feature map.

Several filters are used to extract features in a convolution layer and each filter gives an activation map. The next layer is the activation layer, or the ReLU layer, which introduces non-linearity to the network and generates a rectified feature map. This rectified feature map is fed to the pooling layer to reduce the dimensionality of the feature map. A *k-max* pooling operation is employed, which selects the top k features with respect to the various hidden layers and generates a pooled feature map. This pooled feature map is input to the fully connected *softmax* layer, which calculates the probability of any output word and classifies the tweet as sarcastic or non-sarcastic.

- Basic sentiment analysis tools have difficulty distinguishing between positive and negative statements, especially when sarcasm, irony, and mixed feelings are included discretely or in combination. Practical models to predict sarcastic text are thus imperative, and the proposed model combines semantics from the attention-based bidirectional LSTM network with auxiliary pragmatic features to a deep convolution network for enhanced prediction performance.
- The multiple layers involve nonlinearity that aids learning complex representations.

The rest of the paper is structured as follows. Section 2 briefly discusses the pertinent work within the domain of sentiment analysis and deep learning based automatic sarcasm detection followed by Section 3, which illustrates the proposed *s*Att-BLSTM convNet model and its working details. Section 4 explicates the results and provides an analysis of the same. The final section, Section 5, concludes the study and expounds upon the scope of future work.

II. RELATED WORK

The growing pursuit of Internet users in all forms of social media has intensified researchers' interest to intelligently mine the content available, both quantitatively and qualitatively. Twitter, currently the most famous micro-blog,

connects people across the globe and has a high level of user involvement. It has gradually emerged as a huge source of sentiment-rich data [4]. The keyword ''sentiment analysis'' was initially witnessed in the published work [5] in 2003, and since then, both primary [4], [6], [7] and secondary studies have been reported across pertinent literature [8]–[11]. Furthermore, the literature is well-equipped with studies pertaining to sentiment analysis using machine learning paradigms on specifically textual user-generated online content on social media. Aloufi and El Saddik [12] proposed a model for sentiment analysis of football specific tweets using three classifiers, namely, support vector machine, multinomial Navies Bayes and random forest. Pai and Liu [13] put forward a model for prediction of vehicle sales by sentiment analysis of twitter data and stock market values using least squares support vector regression. Research using deep learning models for sentiment analysis has also been reported. Tseng *et al.* [14] analyzed textual opinions found in teaching evaluation questionnaires and applied the analysis results to assisting the selection of outstanding teaching faculty members using attention-based LSTM. Wu and Chi [15] proposed a model having quadratic connections of LSTM capable of capturing complex semantic representations of natural language texts and evaluated on the benchmark dataset, the Stanford Sentiment Treebank. Bouazizi and Ohtsuki [6] extended the concept of binary or ternary classification and proposed an approach to classify text collected from Twitter into seven sentiment classes. The authors further proposed [16] multi-class sentiment analysis which addresses the identification of the exact sentiment conveyed by the user using the task of quantification that identifies all the existing sentiments within a tweet instead of attributing a single sentiment label to it. Zhang *et al.* [17] proposed a model combining convolution neural network and bidirectional gated recurrent unit for sentence semantic classification. Han *et al.* [18] used CNN and BLSTM to design four kinds of memory network models for text sentiment classification. Fu *et al.* [19] proposed a lexicon-enhanced LSTM model that uses sentiment lexicon as extra information pre-training a word sentiment classifier. Wang *et al.* [20] proposed a sophisticated algorithm based on deep learning and information geometry for sentiment classification.

Significant studies exemplify sarcasm as a contradiction in polarity [21], [22]. Sarcasm detection has been reported as a non-trivial challenge for sentiment analysis across literature studies. There have been expansive efforts by researchers to investigate sarcasm-detection techniques on various social media channels as a sub-task of sentiment analysis [23]. Bouazizi and Ohtsuki [24] propose a pattern-based approach to detect sarcasm on Twitter considering four sets of features that cover the different types of sarcasms.

Architectures based on deep learning techniques have gained popularity in natural language programming applications as they are capable of handling data sparseness in unbalanced datasets. Studies on bullying and verbal aggression have been reported deep neural network for short-text sentiment analysis [25]. A few such approaches have been reported for automatic sarcasm detection as well. Felbo *et al.* [26] proposed a DeepMoji model, which is based on the occurrences of emoji, for detecting the emotional content on Twitter. It uses a variant of LSTM, a 6-layer model that is a hybrid of BLSTM and the attention mechanism for the detection of sarcastic tweets. A new convolution network-based architecture is presented in [27] that learn user embeddings in addition to utterance-based embeddings, which allows the authors to learn user-specific context. The similarity between word embeddings is used by Joshi *et al.* [28] as features for sarcasm detection. The authors have concatenated features from previous works to these word embedding-based features. Ghosh and Veale [29] have built a model combining a convNet with a recurrent neural network (RNN, long short-term memory) followed by a deep neural network. It is observed that this approach shows an improvement for the deep learning architecture when compared with recursive SVM. In [30], models based on a pre-trained convNet have been developed that are used to extract emotion, sentiment, and even personality features for sarcasm detection. In another study, [31], bidirectional LSTM is used to capture syntactic and semantic information over tweets, along with a pooling neural network to extract contextual features automatically from history tweets. Performance using neural features is compared with discrete manual features and an improvement is observed. Attention mechanism has been previously used by researchers in the domain of natural language understanding as it selectively focuses on information-rich phrases within the sequence of sentence. Recently, authors Seo *et al.* [32] and Wang *et al.* [33] demonstrated the effective use of attention for compression and question-answering.

III. AUTOMATED SARCASM DETECTION

The proposed framework for automatic sarcasm detection has four key components, namely, (*A*) data acquisition, (*B*) preprocessing, (*C*) implementation of the *s*Att-BLSTM convNet model, and (*D*) evaluation using performance measures. These are explained in detail in the following subsections.

A. DATASET ACQUISITION

To evaluate the performance of the proposed model, the following datasets have been used for empirical analysis. The purpose of using two varied datasets was to further validate the results achieved and determine the robustness of the selected features and the model trained on these features.

1) BALANCED DATASET: SEMEVAL 2015 TASK 11

The original SemEval dataset consists of 20000 hashtag-annotated tweets, which were created for the Twitter sentiment analysis task. SemEval 2015 task 11 [34] defined the challenge as a ''dataset for sentiment analysis of figurative language on Twitter.'' The objective of the task is specifically to evaluate the use of figurative language, where the word or phrase described as ''figurative'' meant that it is being used in a way that was symbolic and represented something

other than its concrete meaning. Although figurative language encompasses an extensive variety of literary tools and techniques, such as similes, emoticons, metaphor, personification, idiom, and hyperbole, this benchmark dataset contains tweets with specific figurative types, namely, sarcasm, irony, and metaphor. The sarcasm corpus is thus constructed by collecting self-annotated tweets with the hashtags #irony, #sarcasm, and #not. Although there is a subtle difference between the three, we consider all of them in the same category for performing this empirical analysis. Thus, this study is also indicative of how this generalization influences the obtained results. The experiments used the SemEval 2013 task 2 dataset as the negative class data [35]. Manual perusal of the two datasets revealed that both contain tweets from general topics, thus avoiding any bias in our experimentation. To collect data for the experiments, we tried to retrieve 15961 tweets using a list of the dataset's tweet ids provided, out of which 7994 are sarcastic and 7324 are non-sarcastic.

2) IMBLANCED DATASET: RANDOM TWEETS

In real time, the presence of sarcasm in tweets is less frequent. A randomly sampled dataset containing 15,000 sarcastic and 25,000 non-sarcastic tweets is built using the Sarcasm Detector tool.[1]

B. PRE-PROCESSING

After the data acquisition, to intelligently mine the text, the tweets are pre-processed to clean and transform the data for feature extraction [36]. These include the following processes.

- URLs, mentions, hashtags, and numbers in the tweets are replaced with placeholders
- All tweets are tokenized by the Natural Language Toolkit (NLTK) [37]
- All tokens are sampled in lowercase
- All tweets are stemmed to the root word using Porter's Stemmer [38]
- All non-ASCII-English characters were removed, to limit the domain of data to the English language
- All words are replaced by pre-trained GloVe word vectors. Words that do not exist in the pre-trained embeddings are set to a zero vector

Several auxiliary features are used to enhance the classification model. These are primarily pragmatic markers concerned with language use. We consider the following five punctuation-based features that help understand the subtleties of sarcasm in text, as these indicate figurative text and symbolic clues within the text:

- Number of exclamation marks (!) in the tweet
- Number of question marks (?) in the tweet
- Number of periods (.) in the tweet
- Number of capital letters in the tweet
- Number of uses of "or" in the tweet

[1] www.thesarcasmdetector.com

C. THE PROPOSED sATT-BLSTM CONVNET MODEL

The proposed deep learning model uses 8 layers: the input layer, embedding layer, BLSTM layer, attention layer, convolution layer, activation and ReLU layer, max pooling layer, and representation layer. Fig. 1 depicts the architecture of the proposed multi-layer model. The details of each layer are provided in the subsequent subsections.

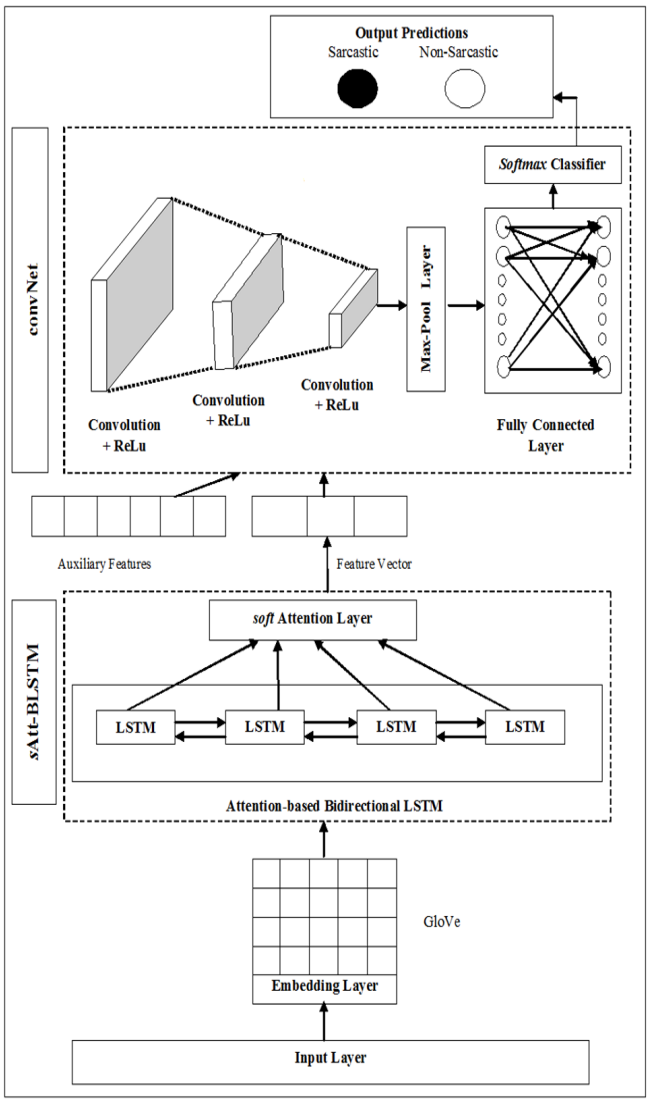


FIGURE 1. System architecture of the proposed sAtt-BLSTM ConvNet.

1) INPUT LAYER

The tweets after pre-processing are fed to the input layer. The input layer is connected to the embedding layer, which builds word embeddings using GloVe.

2) EMBEDDING LAYER

The embedding layer maps the input into real-valued vectors using encoding from look-up tables. Word embeddings facilitate learned word representations. The benefits of extracting features based on word embedding to detect sarcasm have been recently reported [28]. In this study, to build word embeddings, GloVe, which generates a word vector table,

is used. GloVe is a count-based model of representing words by feature vectors. This log-bilinear model studies the relationship of words by counting the number of times they co-occur. Thus, this model aids in mapping all the tokenized words in each tweet to their respective word vector tables. Proper padding is performed to unify the feature vector matrix. That is, if the total number of given tweets is Z and there is a tweet X with t tokens, generation of a word vector Table 5 with dimension d of the word vectors is completed using GloVe. Thus, for all Z, each t in X is mapped to its respective V. After this mapping, each X is expressed as a vector of the word embeddings concatenation (E). Thus, the feature vector matrix is obtained as shown in (1).

$$\mathrm{F} = \mathrm{U} + \mathrm{B} + \mathrm{T} + \mathrm{P} + \mathrm{E}, \tag{1}$$

where + is the concatenation operator of the vector. The tweets are of varying length, so to unify the feature vector matrix representation of tweets, the tweets with the maximum length in the given corpus are used as a threshold value. This is done basically to fix the length of the tweet matrix. Hence, for all the tweets that were shorter than this threshold, zero padding was performed. This matrix was finally fed as input (i.e., F) to the BLSTM layer.

3) BLSTM LAYER

LSTM is an RNN that contains special units in the recurrent hidden layer called memory blocks [39]. Self-connections exist within the memory cells. There is an input, output, and forget gate for each memory cell. The hidden layer of LSTM is also called the LSTM cell. LSTM has the capability to plot long-term dependencies by defining each memory cell with a set of gates $\Re^d$, where d is the memory dimension of the hidden state of LSTM [28]. At each iteration t, the LSTM cell has the layer input x_t and the layer output h_t. LSTM contains three gates, which are functions of the current input $\mathrm{x_t}$ and hidden state $\mathrm{h_{t-1}}$: input gate $\mathrm{i_t}$, forget gate $\mathrm{f_t}$, and output gate $\mathrm{o_t}$. The cell also takes the cell input state s_t, the cell output state c_t, and the previous cell output state c_{t-1} into account while training and updating parameters.

The input gate, forget gate, output gate, and input cell state can be calculated using equations (2)–(7).

$$i_t = \sigma(w_{i_x} x_t + w_{i_h} h_{t-1} + b_i) \tag{2}$$
$$f_t = \sigma(w_{f_x} x_t + w_{f_h} h_{t-1} + b_f) \tag{3}$$
$$o_t = \sigma(w_{o_x} x_t + w_{o_h} h_{t-1} + b_o) \tag{4}$$
$$s_t = tanh\left(w_{s_x} x_t + w_{s_h} h_{t-1} + b_s\right) \tag{5}$$
$$c_t = f_t \odot c_{t-1} + i_t \odot s_t \tag{6}$$
$$h_t = tanh\,(c_t) \odot o_t \tag{7}$$

In equations (2)–(7),

- $\odot$ is the element-wise product;
- $w_i\, w_f\, w_o\, w_s$ are weighing factors used for mapping the hidden layer input to the three gates and the input cell state;
- $b_i\, b_f\, b_o\, b_s$ are bias vectors;
- σ is the gate activation function, which is normally the sigmoid function;
- tanh is the hyperbolic tangent function.

The final output of the LSTM layer is a vector of all the outputs, represented by (8).

$$Y_t = [h_{t-n}, ..., h_{t-1}] \tag{8}$$

The bidirectional LSTM connects two hidden layers to a single output layer. The forward-layer output sequence $h^{\rightarrow}$ is iteratively calculated using inputs in a positive sequence from time t-n to time t-1, while the backward-layer output sequence, $h^{\leftrightarrow}$ is calculated using the reversed inputs from time t-n to t-1 [40]. Both the forward- and backward-layer outputs are calculated by using the standard LSTM updating equations. This creates two copies of the hidden layer, one fit in the input sequences as is and one as a reversed copy of the input sequence [40]. These representations are concatenated together using the attention mechanism. That is, the BLSTM layer generates an output vector in which each element is calculated by using (9).

$$y_t = \sigma\,(h^{\rightarrow} t, h^{\leftrightarrow} t) \tag{9}$$

where σ is a soft attention function to combine the two output sequences. By this means, our model can capture as many salient words from both directions as possible. Thus, similar to that of the LSTM layer, the final output of the BLSTM layer can be represented by a vector (10).

$$\mathrm{Y_t} = [\mathrm{y_{t-n}}, ..., \mathrm{y_{t-1}}] \tag{10}$$

4) ATTENTION LAYER

The idea of attention [41] has originated by the observation that each word contributes to the meaning of tweet (sentence) differently that is; all words do not contribute equally to the representation of the sentence meaning. The users reading text can intuitively identify important, meaningful parts of the sentence. The attention mechanism adds an additional structure to the network, which is learned as part of the standard model training via back-propagation. A deterministic, differentiable attention mechanism, known as soft attention [42], is used, where the weights on each location are usually given by a *softmax*, and the output of the attention module is a weighted sum of representations at each location. This whole process can be described by a differentiable function, so that training can be performed jointly with the rest of the network using back-propagation.

We use a word-level attention mechanism to focus on the words that have a closer semantic relationship to the sentence meaning. That is, the word-level attention is applied to the feature representations of BLSTM. The output is thus a weighted combination of all the input states, not just the last state. The attention mechanism gives an attention score $e_{i,t}$ to each word t in the sentence i, as given by (11).

$$e_{i,t} = g(Wh_t c), \tag{11}$$

where g is an activation function.

Then the weight probability $a_{i,t}$ of each h_t is computed by (12).

$$a_{i,t} = \frac{\exp(e_{i,t})}{\sum_{k=1}^{T} \exp(e_{i,k})} \tag{12}$$

- Auxilary Features

Pragmatic features, such as punctuation or repetition of words, aid in understanding the subtleties of sarcasm in text, as these indicate figurative text and symbolic clues within the text. Punctuation is considered ideal for the representation of syntactic features, as the punctuation features contribute to a substantial boost in classification quality [42]. These can be exemplified by the use of exclamation points/marks, repeated letters (especially vowels), or uppercase letters (ALL CAPS) in textual messages such as tweets/posts. A few examples where these punctuation features impact the emotion quotient in text are given below:

- ➢ An exclamation point or exclamation mark (!) intensifies the emotional content preserving the semantic orientation [43]. For example: *"The location is great!!!!"* is more intense than *"The location is great."*
- ➢ Repeated letters (especially vowels) added to elongate the spelling of a word (e.g., ''haaaaaapppyyy'') is used to emphasize the word or to express enthusiasm in computer-mediated communication [44].
- ➢ Capitalization, such as explicitly using ALL CAPS to emphasize a sentiment-relevant word with other non-capitalized words in the document, increases the intensity of the sentiment preserving semantic orientation [45]. For example, ''Simply LOVED the place!'' is more intense than ''Simply loved the place!''

Thus, sarcasm detection can be made easy by observing the syntactic pattern of tweet to identify punctuation such as:

- ➢ Number of contiguous question marks, exclamation points, and combinations thereof
- ➢ Whether the last token contains a question mark or exclamation point
- ➢ Occurrence of punctuation sequences such as ''!!!'' and ''?!''

In this study, the set of punctuation-based features shown in Table1 are extracted for each tweet.

TABLE 1. Punctuation-based features used.

excl	No. of exclamation marks in the post/tweet
ques	No. of question marks in the post/ tweet
dots	No. of periods in the post/tweet
caps	No. of capital letters in the post/tweet
quotes	No. of quotation marks (‘’ or “”) in the post/tweet

5) CONVOLUTION LAYER

ConvNet has two primary parts, namely, feature learning (Conv, ReLU, and Pool) and classification (fully connected and softmax). The output features of the sAtt BLSTM are combined with auxiliary features and provided as input to the convNet. Each convolving filter has a variable window size (s), height, and width. This window slides over to the input matrix and calculates localized feature vector (v_j) for each possible word (window size) using a nonlinear activation function (f) and a bias (b_a).

A transition matrix (T) is generated for each filter. This filter comprises of a layer of weights (weight matrix, W) that are applied to parts of the input matrix to obtain a single unit as the output. This is performed for the bias and weight during the network-learning adjustment, as illustrated in (13).

$$v_j = f\left(T.F_{j:j+s-1} + b_a\right) \tag{13}$$

Here, $F_{j:j+s-1}$shows the local vector from position j to $j + s - 1$ in F. Hence, formation of this v_j together with the completion of the convolution operation generates a new vector, n, as in (14).

$$n = [v_1, v_2, v_3, \ldots, v_{d-s+1}] \tag{14}$$

After the sliding operation, the output from each part is then combined in order to obtain the resultant output, called the transformed feature map, that serves as the input to the next layer: the ReLU Layer.

6) RELU LAYER

The activation or ReLU Layer [46] is applied for dealing with the nonlinearity in the convNet model. It generates a rectified feature map, which is fed to the pooling layer to reduce the dimensionality of the feature map.

7) POOLING LAYER

In this work, max pooling [47] is used, which takes the largest element from the rectified feature map. It reduces the dimensionality of the feature map and helps retain the most significant features. The k-max pooling operation (p) is performed for feature selection that chooses the top k features conforming to various hidden layers, where p is expressed as (15).

$$p = \max\{v_1, v_2, v_3, \ldots, v_{d-s+1}\} \tag{15}$$

8) REPRESNTATION LAYER

The output layer is a fully connected layer that consists of the softmax activation function. The pooled feature map is input to the *fully connected* softmax layer, which calculates the probability of any output word and classifies the tweet as sarcastic or non-sarcastic as an output. The output vector of the *softmax* layer ($O^{(z)}$) is as (16).

$$O^{(z)} = T^{(z)} O^{(z-1)} + b_a^{(z)}, \tag{16}$$

where

$O^{(z-1)}$ denotes the output vector the pooling layer
$T^{(z)}$ is the transition matrix
$b_a^{(z)}$ represents the bias factor of softmax layer.

Thus, using a fully connected *softmax* layer yields the probability-distribution [48] of the sarcasm detection (P_d), which is denoted using (17).

$$P_d\ (j \mid X, \theta) = \frac{[\exp\ (O_{j[Z]})]}{[\sum_{k=1}^{n} \exp\ (O_{j[Z]})]}, \tag{17}$$

where θ is the parameter of the model and j is the class label.

D. RESULTS AND ANALYSIS

For discussing the results, the empirical analysis has been broadly divided into two parts: (i) parameter setting for the proposed model and (ii) comparison with multiple baselines on the basis of classification accuracy.

1) PARAMETER SETTING

Optimal selection of parameters is imperative to achieve superlative performance results. We use the validation data to tune the hyper-parameters so as to obtain the best results. Table 2 lists the values used in this work.

TABLE 2. Hyperparameter values.

Hyperparameter	Value
Dimension of GloVe vectors	200
Hidden units of LSTMs (Forward, Backward)	500 each
Mini-batch size	10
Number of convNet layers	3
Number of convolution filters	100
Window size	(3,3)
Activation function of convNet	ReLU
Regularization	Dropout Operation
Drop-out rate	0.5: word embedding; 0.2: BLSTM; 0.4: convNet
Learning rate	0.2

The weights of the network are randomly initialized from a Gaussian distribution with variance scaled to 0.01, and the biases are initialized to zero except the forget-gate bias, which is initialized to 1.

2) PERFORMANCE RESULT

The proposed model is evaluated to predict sarcasm in tweets using two datasets, namely SemEval 2015 task 11 and random tweets containing a total of 40,000 tweets. The results have been assessed using key performance indicators (accuracy, recall, precision, and F-measure [49, 50]). Table 3 lists the results of the proposed *s*Att-BLSTM convNet model implemented on the two datasets and Fig. 2 depicts the results graphically.

3) COMPARISON WITH BASELINE DEEP LEARNING MODELS RESULT

We compare the results of the proposed model with three other deep learning architectures, namely, LSTM, BLSTM without attention, and convNet. The word embedding was performed using GloVe for each baseline model and the evaluation was made for both datasets using the four key performance indicators. The results obtained for LSTM, BLSTM without attention, BLSTM with attention and convNet are shown in Tables 4, 5, 6 and 7, respectively.

TABLE 3. Performance of the proposed *S*Att-BLSTM convNet model.

*s*Att-BLSTM convNet	SemEval Dataset	Random Tweets
Accuracy	97.87	93.71
Recall	96.83	92.67
Precision	92.14	90.49
F-measure	93.57	88.29

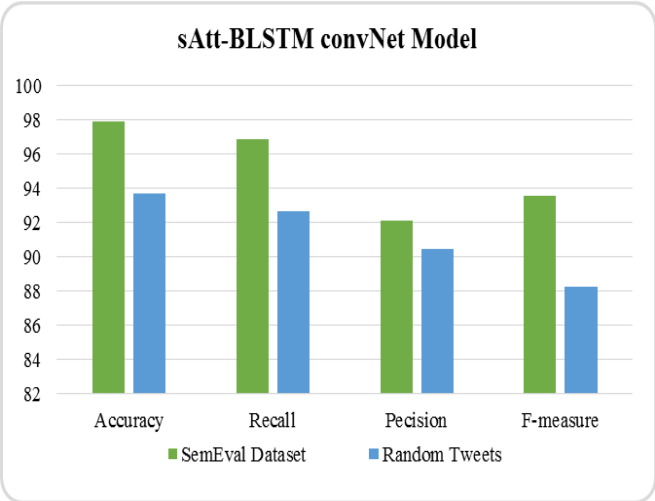


FIGURE 2. sAtt-BLSTM convNet Model Performance on two Datasets.

TABLE 4. Performance OF LSTM.

LSTM model	SemEval Dataset	Random Tweets
Accuracy	84.89	79.75
Recall	83.51	78.01
Precision	86.78	74.98
F-measure	80.39	76.91

TABLE 5. Performance of BLSTM without attention.

BLSTM without Attention	SemEval Dataset	Random Tweets
Accuracy	86.32	81.03
Recall	84.39	80.27
Precision	81.61	78.76
F-measure	85.25	79.45

TABLE 6. Performance of BLSTM with attention.

BLSTM without Attention	SemEval Dataset	Random Tweets
Accuracy	89.03	85.65
Recall	85.51	82.34
Precision	87.76	85.55
F-measure	87.25	84.04

TABLE 7. Performance of convNet.

ConvNet model	SemEval Dataset	Random Tweets
Accuracy	91.60	88.28
Recall	90.53	87.61
Precision	90.19	86.01
F-measure	88.57	84.72

It can be clearly observed that the proposed *s*Att- BLSTM convNet outperforms the other models with an accuracy of 91.60% achieved for the SemEval dataset and 88.28% for random tweets. LSTM shows the least accuracy of 84.89% and 79.75% for the SemEval and random tweet datasets, respectively. The models, in order from lowest to highest accuracy, are LSTM < BLSTM without Attention < BLSTM with Attention < convNet < *s*Att-BLSTM convNet. The best recall is also observed for the proposed *s*Att-BLSTM convNet for both the datasets. However, the convNet model demonstrates the best precision value of 92.19% for the SemEval dataset, whereas the proposed sAtt-BLSTM convNet model shows the best precision for the random tweets. Table 8 summarizes the comparison of the accuracy results obtained by the above five models. Fig. 3 graphically illustrates these comparative results.

TABLE 8. Accuracy comparison of models.

Dataset → / Models ↓	SemEval Dataset	Random Tweets
LSTM	84.89	79.75
BLSTM without Attention	86.32	81.03
BLSTM with Attention	89.03	85.65
convNet	91.60	88.28
*s*Att-BLSTM convNet	97.87	93.71

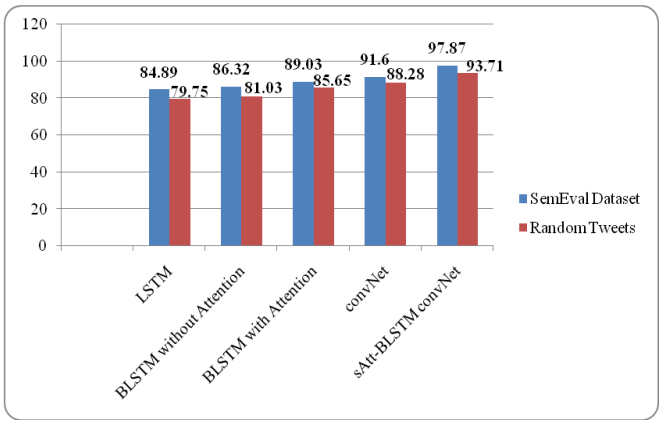


FIGURE 3. Accuracy Comparison of the Proposed Model with Baseline Models.

IV. CONCLUSION

Social media is an informal means of communication that includes considerable use of slang, malformed words, short forms, colloquial expressions, mash-up words, etc. All these amplify the ambiguity, vagueness, and imprecision in the available social web content and makes the task of analyzing generic and specific sentiment computationally difficult. Sarcasm is a specific type of sentiment and its automatic detection is a dynamic area of research. In this work, we proposed *s*Att-BLSTM convNet, a hybrid of *soft* attention-based bidirectional long short-term memory (*s*Att-BLSTM) and convolution neural network (convNet), to detect sarcasm in short text (tweets). Semantic word embeddings and pragmatic auxiliary features were used to train the network. The proposed model demonstrates the highest classification accuracy for both the datasets as compared to the baseline models. The use of mash-up languages and novelty in vocabulary with advanced architectures [51]–[81] add to the challenges of automated detection of sarcasm and characterize some open problems for future research within the domain.

REFERENCES

[1] S. K. Bharti, B. Vachha, R. K. Pradhan, K. S. Babu, and S. K. Jena, "Sarcastic sentiment detection in tweets streamed in real time: A big data approach," *Digit. Commun. Netw.*, vol. 2, no. 3, pp. 108–121, 2016.
[2] S. N. Sivanandam and S. N. Deepa, *Principles of Soft Computing (With CD)*. Hoboken, NJ, USA: Wiley, 2007.
[3] J. Pennington, R. Socher, and C. Manning, "Glove: Global vectors for word representation," in *Proc. Conf. Empirical Methods Natural Lang. Process. (EMNLP)*, 2014, pp. 1532–1543.
[4] A. Kumar and A. Jaiswal, "Empirical study of Twitter and Tumblr for sentiment analysis using soft computing techniques," in *Proc. World Congr. Eng. Comput. Sci.*, 2017, pp. 1–5.
[5] K. Dave, S. Lawrence, and D. M. Pennock, "Mining the peanut gallery: Opinion extraction and semantic classification of product reviews," in *Proc. 12th Int. Conf. World Wide Web*, 2003, pp. 519–528.
[6] M. Bouazizi and T. Ohtsuki, "A pattern-based approach for multi-class sentiment analysis in Twitter," *IEEE Access*, vol. 5, pp. 20617–20639, 2017.
[7] S. Shayaa *et al.*, "Sentiment analysis of big data: Methods, applications, and open challenges," *IEEE Access*, vol. 6, pp. 37807–37827, 2018.
[8] A. Kumar and T. M. Sebastian, "Sentiment analysis: A perspective on its past, present and future," *Int. J. Intell. Syst. Appl.*, vol. 4, no. 10, pp. 1–14, 2012.
[9] A. Kumar and T. M. Sebastian, "Sentiment analysis on Twitter," *Int. J. Comput. Sci. Issues*, vol. 9, no. 3, pp. 372–378, 2012.
[10] T. Al-Moslmi, N. Omar, S. Abdullah, and M. Albared, "Approaches to cross-domain sentiment analysis: A systematic literature review," *IEEE Access*, vol. 5, pp. 16173–16192, 2017.
[11] A. Kumar and A. Jaiswal, "Systematic literature review of sentiment analysis on Twitter using soft computing techniques," *Concurrency Comput., Pract. Exper.*, p. e5107, 2019. doi: 10.1002/cpe.5107.
[12] S. Aloufi and A. El Saddik, "Sentiment identification in football-specific tweets," *IEEE Access*, vol. 6, pp. 78609–78621, 2018.
[13] P. F. Pai and C. H. Liu, "Predicting vehicle sales by sentiment analysis of Twitter data and stock market values," *IEEE Access*, vol. 6, pp. 57655–57662, 2018.
[14] C. W. Tseng, J. J. Chou, and Y. C. Tsai, "Text mining analysis of teaching evaluation questionnaires for the selection of outstanding teaching faculty members," *IEEE Access*, vol. 6, pp. 72870–72879, 2018.
[15] D. Wu and M. Chi, "Long short-term memory with quadratic connections in recursive neural networks for representing compositional semantics," *IEEE Access*, vol. 5, pp. 16077–16083, 2017.
[16] M. Bouazizi and T. Ohtsuki, "Multi-class sentiment analysis in Twitter: What if classification is not the answer," *IEEE Access*, vol. 6, pp. 64486–64502, 2018.
[17] D. Zhang, L. Tian, M. Hong, F. Han, Y. Ren, and Y. Chen, "Combining convolution neural network and bidirectional gated recurrent unit for sentence semantic classification," *IEEE Access*, vol. 6, pp. 73750–73759, 2018.
[18] H. Han, J. Liu, and G. Liu, "Attention-based memory network for text sentiment classification," *IEEE Access*, vol. 6, pp. 68302–68310, 2018.
[19] X. Fu, J. Yang, J. Li, M. Fang, and H. Wang, "Lexicon-enhanced LSTM with attention for general sentiment analysis," *IEEE Access*, vol. 6, pp. 71884–71891, 2018.

[20] M. Wang, Z. H. Ning, C. Xiao, and T. Li, "Sentiment classification based on information geometry and deep belief networks," *IEEE Access*, vol. 6, pp. 35206–35213, 2018.

[21] E. Camp, "Sarcasm, pretense, and the semantics/pragmatics distinction," *Noûs*, vol. 46, no. 4, pp. 587–634, Dec. 2012.

[22] E. Riloff, A. Qadir, P. Surve, L. D. Silva, N. Gilbert, and R. Huang, "Sarcasm as contrast between a positive sentiment and negative situation," in *Proc. EMNLP*, vol. 13, 2013, pp. 704–714.

[23] E. Cambria, S. Poria, F. Bisio, R. Bajpai, and I. Chaturvedi, "The CLSA model: A novel framework for concept-level sentiment analysis," in *Proc. Int. Conf. Intell. Text Process. Comput. Linguistics*. London, U.K.: Springer, 2015, pp. 3–22.

[24] M. Bouazizi and T. O. Ohtsuki, "A pattern-based approach for sarcasm detection on Twitter," *IEEE Access*, vol. 4, pp. 5477–5488, 2016.

[25] C. Junyi, S. Yan, and K.-C. Wong, "Verbal aggression detection on Twitter comments: Convolutional neural network for short-text sentiment analysis," *Neural Comput. Appl.*, pp. 1–10, Mar. 2018. doi: 10.1007/s00521-018-3442-0.

[26] B. Felbo, A. Mislove, A. Søgaard, I. Rahwan, and S. Lehmann. (2017). "Using millions of emoji occurrences to learn any-domain representations for detecting sentiment, emotion and sarcasm." [Online]. Available: https://arxiv.org/abs/1708.00524.

[27] S. Amir, B. C. Wallace, H. Lyu, and P. C. M. J. Silva. (2016). "Modelling context with user embeddings for sarcasm detection in social media." [Online]. Available: https://arxiv.org/abs/1607.00976

[28] A. Joshi, P. Bhattacharyya, M. Carman, J. Saraswati, and R. Shukla, "How do cultural differences impact the quality of sarcasm annotation?: A case study of indian annotators and american text," in *Proc. 10th SIGHUM Workshop Lang. Technol. Cultural Heritage, Social Sci., Hum.*, 2016, pp. 95–99.

[29] A. Ghosh and T. Veale, "Fracking sarcasm using neural network," in *Proc. 7th Workshop Comput. Approaches Subjectivity, Sentiment Social Media Anal.*, 2016, pp. 161–169.

[30] F. A. Gers, J. Schmidhuber, and F. Cummins, "Learning to forget: Continual prediction with LSTM," in *Proc. 9th Int. Conf. Artif. Neural Netw. (ICANN)*, 1999, pp. 1–20.

[31] M. Zhang, Y. Zhang, and G. Fu, "Tweet sarcasm detection using deep neural network," in *Proc. 26th Int. Conf. Comput. Linguistics, Tech. Papers (COLING)*, 2016, pp. 2449–2460.

[32] M. Seo, A. Kembhavi, A. Farhadi, and H. Hajishirzi. (2016). "Bidirectional attention flow for machine comprehension." [Online]. Available: https://arxiv.org/abs/1611.01603

[33] W. Wang, N. Yang, F. Wei, B. Chang, and M. Zhou, "R-NET: Machine reading comprehension with self-matching networks," Natural Lang. Comput. Group, Microsoft Res. Asia, Beijing, China, Tech. Rep. 05, 2017.

[34] A. Ghosh *et al.*, "Semeval-2015 task 11: Sentiment analysis of figurative language in twitte," in *Proc. 9th Int. Workshop Semantic Eval. (SemEval)*, 2015, pp. 470–478.

[35] J. Hltcoe, "Semeval-2013 task 2: Sentiment analysis in Twitter," Assoc. Comput. Linguistics, Atlanta, GA, USA, Tech. Rep. 2, 2013, p. 312.

[36] I. Guyon and A. Elisseeff, "An introduction to feature extraction," in *Feature Extraction*. Berlin, Germany: Springer, 2006, pp. 1–25.

[37] E. Loper and S. Bird, "NLTK: The natural language toolkit," in *Proc. ACL Workshop Effective Tools Methodol. Teach. Natural Lang. Process. Comput. Linguistics, Assoc. Comput. Linguistics*, vol. 1, 2002, pp. 63–70.

[38] M. F. Porter, "An algorithm for suffix stripping," *Program*, vol. 14, no. 3, pp. 130–137, 1980. [Online]. Available: https://tartarus.org/martin/PorterStemmer/

[39] H. Salehinejad, J. Baarbe, S. Sankar, J. Barfett, E. Colak, and S. Valaee. (2017). "Recent advances in recurrent neural networks." [Online]. Available: https://arxiv.org/abs/1801.01078

[40] A. Graves, N. Jaitly, and A.-R. Mohamed, "Hybrid speech recognition with deep bidirectional LSTM," in *Proc. IEEE Workshop Autom. Speech Recognit. Understand. (ASRU)*, Dec. 2013, pp. 273–278.

[41] M. T. Luong, H. Pham, and C. D. Manning. (2015). "Effective approaches to attention-based neural machine translation." [Online]. Available: https://arxiv.org/abs/1508.04025

[42] K. Xu *et al.*, "Show, attend and tell: Neural image caption generation with visual attention," in *Proc. Int. Conf. Mach. Learn.*, Jun. 2015, pp. 2048–2057.

[43] D. Davidov, O. Tsur, and A. Rappoport, "Enhanced sentiment learning using Twitter hashtags and smileys," in *Proc. 23rd Int. Conf. Comput. Linguistics, Posters, Assoc. Comput. Linguistics*, 2010, pp. 241–249.

[44] M. Thelwall and K. Buckley, "Topic-based sentiment analysis for the social Web: The role of mood and issue-related words," *J. Amer. Soc. Inf. Sci. Technol.*, vol. 64, no. 8, pp. 1608–1617, 2013.

[45] C. H. E. Gilbert and A. Vader, "VADER: A parsimonious rule-based model for sentiment analysis of social media text," in *Proc. 8th Int. Conf. Weblogs Social Media (ICWSM)*, 2014, pp. 1–10.

[46] Y. Li and Y. Yuan, "Convergence analysis of two-layer neural networks with relu activation," in *Proc. Adv. Neural Inf. Process. Syst.*, 2017, pp. 597–607.

[47] Y. Kim. (2014). "Convolutional neural networks for sentence classification." [Online]. Available: https://arxiv.org/abs/1408.5882.

[48] Z. Jianqiang, G. Xiaolin, and Z. Xuejun, "Deep convolution neural networks for Twitter sentiment analysis," *IEEE Access*, vol. 6, pp. 23253–23260, 2018.

[49] D. M. Powers, "Evaluation: From precision, recall and F-measure to ROC, informedness, markedness and correlation," *J. Mach. Learn. Technol.*, vol. 2, no. 1, pp. 37–63, 2011. [Online]. Available: http://hdl.handle.net/2328/27165

[50] M. P. S. Bhatia and A. Kumar, "A primer on the Web information retrieval paradigm," *J. Theor. Appl. Inf. Technol.*, vol. 4, no. 7, pp. 657–662, 2008.

[51] D. J. Hemanth, J. Anitha, A. Naaji, O. Geman, D. E. Popescu, and L. H. Son, "A modified deep convolutional neural network for abnormal brain image classification," *IEEE Access*, vol. 7, pp. 4275–4283, 2018.

[52] L. H. Son and H. Fujita, "Neural-fuzzy with representative sets for prediction of student performance," *Appl. Intell.*, vol. 49, no. 1, pp. 172–187, 2019.

[53] D. J. Hemanth, J. Anitha, L. H. Son, and M. Mittal, "Diabetic retinopathy diagnosis from retinal images using modified hopfield neural network," *J. Med. Syst.*, vol. 42, no. 12, p. 247, 2018.

[54] D. J. Hemanth, J. Anitha, and L. H. Son, "Brain signal based human emotion analysis by circular back propagation and deep Kohonen neural networks," *Comput. Elect. Eng.*, vol. 68, pp. 170–180, May 2018.

[55] C. N. Giap, L. H. Son, and F. Chiclana, "Dynamic structural neural network," *J. Intell. Fuzzy Syst.*, vol. 34, pp. 2479–2490, Jan. 2018.

[56] S. Doss *et al.*, "APD-JFAD: Accurate prevention and detection of Jelly Fish attack in MANET," *IEEE Access*, vol. 6, pp. 56954–56965, 2018.

[57] D. T. Hai, L. H. Son, and T. Le Vinh, "Novel fuzzy clustering scheme for 3D wireless sensor networks," *Appl. Soft Comput.*, vol. 54, pp. 141–149, May 2017.

[58] R. Kapoor, R. Gupta, R. Kumar, L. H. Son, and S. Jha, "New scheme for underwater acoustically wireless transmission using direct sequence code division multiple access in MIMO systems," *Wireless Netw.*, pp. 1–13, May 2018. doi: 10.1007/s11276-018-1750-z.

[59] R. Kapoor, R. Gupta, L. H. Son, S. Jha, and R. Kumar, "Detection of power quality event using histogram of oriented gradients and support vector machine," *Measurement*, vol. 120, pp. 52–75, May 2018.

[60] R. Kapoor, R. Gupta, L. H. Son, S. Jha, and R. Kumar, "Boosting performance of power quality event identification with KL divergence measure and standard deviation," *Measurement*, vol. 126, pp. 134–142, Oct. 2018.

[61] H. V. Long, M. Ali, L. H. Son, M. Khan, and D. N. Tu, "A novel approach for fuzzy clustering based on neutrosophic association matrix," *Comput. Ind. Eng.*, to be published. doi: 10.1016/j.cie.2018.11.007.

[62] P. T. M. Phuong, P. H. Thong, and L. H. Son, "Theoretical analysis of picture fuzzy clustering: Convergence and property," *J. Comput. Sci. Cybern.*, vol. 34, no. 1, pp. 17–32, 2018.

[63] Y. H. Robinson, E. G. Julie, K. Saravanan, R. Kumar, and L. H. Son, "FD-AOMDV: Fault-tolerant disjoint ad-hoc on-demand multipath distance vector routing algorithm in mobile ad-hoc networks," *J. Ambient Intell. Hum. Comput.*, pp. 1–18, Nov. 2019. doi: 10.1007/s12652-018-1126-3.

[64] K. Saravanan, E. Anusuya, R. Kumar, and L. H. Son, "Real-time water quality monitoring using Internet of Things in SCADA," *Environ. Monitor. Assessment*, vol. 190, no. 9, p. 556, 2018.

[65] K. Saravanan, S. Aswini, R. Kumar, and L. H. Son, "How to prevent maritime border collision for Fisheries?—A design of real-time automatic identification system," *Earth Sci. Inform.*, pp. 1–12, Nov. 2019. doi: 10.1007/s12145-018-0371-5.

[66] K. Singh, K. Singh, L. H. Son, and A. Aziz, "Congestion control in wireless sensor networks by hybrid multi-objective optimization algorithm," *Comput. Netw.*, vol. 138, pp. 90–107, Jun. 2018.

[67] N. Singh, L. H. Son, F. Chiclana, and J.-P. Magnot, "A new fusion of salp swarm with sine cosine for optimization of non-linear functions," *Eng. Comput.*, pp. 1–28, Jan. 2019. doi: 10.1007/s00366-018-00696-8.

[68] L. H. Son, "A novel kernel fuzzy clustering algorithm for geo-demographic analysis," *Inf. Sci.-Inform. Comput. Sci., Intell. Syst., Appl., Int. J.*, vol. 317, pp. 202–223, Oct. 2015.
[69] L. H. Son, "Generalized picture distance measure and applications to picture fuzzy clustering," *Appl. Soft Comput.*, vol. 46, pp. 284–295, Sep. 2016.
[70] L. H. Son and P. V. Hai, "A novel multiple fuzzy clustering method based on internal clustering validation measures with gradient descent," *Int. J. Fuzzy Syst.*, vol. 18, no. 5, pp. 894–903, 2016.
[71] S. Jha, R. Kumar, J. M. Chatterjee, and M. Khari, "Collaborative handshaking approaches between Internet of computing and Internet of Things towards a smart world: A review from 2009–2017," *Telecommun. Syst.*, pp. 1–18, Jun. 2018. doi: 10.1007/s11235-018-0481-x.
[72] L. H. Son and N. D. Tien, "Tune up fuzzy C-means for big data: Some novel hybrid clustering algorithms based on initial selection and incremental clustering," *Int. J. Fuzzy Syst.*, vol. 19, no. 5, pp. 1585–1602, 2017.
[73] L. H. Son and T. M. Tuan, "A cooperative semi-supervised fuzzy clustering framework for dental X-ray image segmentation," *Expert Syst. Appl.*, vol. 46, pp. 380–393, Mar. 2016.
[74] L. H. Son and P. H. Thong, "Some novel hybrid forecast methods based on picture fuzzy clustering for weather nowcasting from satellite image sequences," *Appl. Intell.*, vol. 46, no. 1, pp. 1–15, 2017.
[75] L. H. Son and T. M. Tuan, "Dental segmentation from X-ray images using semi-supervised fuzzy clustering with spatial constraints," *Eng. Appl. Artif. Intell.*, vol. 59, pp. 186–195, Mar. 2017.
[76] N. T. Tam, D. T. Hai, L. H. Son, and L. T. Vinh, "Improving lifetime and network connections of 3D wireless sensor networks based on fuzzy clustering and particle swarm optimization," *Wireless Netw.*, vol. 24, no. 5, pp. 1477–1490, 2018.
[77] N. D. Thanh, M. Ali, and L. H. Son, "A novel clustering algorithm in a neutrosophic recommender system for medical diagnosis," *Cogn. Comput.*, vol. 9, no. 4, pp. 526–544, 2017.
[78] P. H. Thong and L. H. Son, "Picture fuzzy clustering: A new computational intelligence method," *Soft Comput.*, vol. 20, no. 9, pp. 3549–3562, 2016.
[79] P. H. Thong and L. H. Son, "A novel automatic picture fuzzy clustering method based on particle swarm optimization and picture composite cardinality," *Knowl.-Based Syst.*, vol. 109, pp. 48–60, Oct. 2016.
[80] P. H. Thong and L. H. Son, "Picture fuzzy clustering for complex data," *Eng. Appl. Artif. Intell.*, vol. 56, pp. 121–130, Nov. 2016.
[81] T. M. Tuan, T. T. Ngan, and L. H. Son, "A novel semi-supervised fuzzy clustering method based on interactive fuzzy satisficing for dental X-ray image segmentation," *Appl. Intell.*, vol. 45, no. 2, pp. 402–428, 2016.



LE HOANG SON received the Ph.D. degree in mathematics–informatics from the VNU University of Science, Vietnam National University (VNU), in 2013. He was a Senior Researcher and the Vice Director with the Center for High Performance Computing, VNU University of Science, Vietnam National University, from 2007 to 2018. He has been promoted to an Associate Professor in information technology, since 2017. Since 2018, he has been the Head of the Department of Multimedia and Virtual Reality, VNU Information Technology Institute, VNU. He is also Visiting Professor with Ton Duc Thang University, Vietnam. His current research interests include artificial intelligence, data mining, soft computing, fuzzy computing, fuzzy recommender systems, and geographic information systems.



AKSHI KUMAR received the B.E. degree (Hons.) in computer science and engineering from Maharishi Dayanand University, Rohtak, in 2003, the M.Tech. (Hons.) in computer science and engineering from Guru Gobind Singh Indraprastha University, Delhi, in 2005, and the Ph.D. degree in computer engineering (Web mining) from the Faculty of Technology, University of Delhi, in 2011. She has been with the university for the past ten years. She is currently an Assistant Professor with the Department of Computer Science & Engineering, Delhi Technological University (formerly Delhi College of Engineering). Her research interests include intelligent systems, user-generated big-data, social media analytics, and soft computing.



SAURABH RAJ SANGWAN received the bachelor's degree in computer science and engineering from DCRUST, Murthal, India, and the M.Tech. degree in software engineering from the Department of Computer Science & Engineering, Delhi Technological University, Delhi, India, in 2018. He is currently a Research Scholar with the Web Research Group, Department of Computer Science & Engineering, Delhi Technological University. His research interests include intelligent systems, text mining, and social Web.



ANSHIKA ARORA received the B.Tech. degree in computer science and engineering from the University of Delhi, New Delhi, India, in 2017. She is currently pursuing the M.Tech. degree in software engineering with Delhi Technological University, Delhi, India. Her research interests include social Web, sentiment analysis, and machine learning.



ANAND NAYYAR received the M.C.A. degree (Hons.) from Punjabi University, Patiala, in 2008, the M.Phil. degree in computer science with the 1st Division from Vinayaka Missions University, in 2009, the M.Tech. degree (Hons.) in information technology in 2011, the M.B.A. degree in information systems from Sikkim Manipal University with 1st Division, and the Ph.D. degree in computer science from Desh Bhagat University, Mandi Gobindgarh, in 2017. He is currently a Professor, a Researcher, and a Scientist with the Graduate School, Duy Tan University, Da Nang, Vietnam. He has more than 300 Publications in various National, International Conferences cum International Journals (Scopus/ISI/SCI/SCIe) of high repute. He is currently in WSN, MANET, swarm intelligence, cloud computing, big data, network security, the Internet of Things (IoT), machine learning, deep learning, network simulation, and 5G communications.



MOHAMED ABDEL-BASSET received the B.Sc., M.Sc., and Ph.D. degrees in information systems and technology from the Faculty of Computers and Informatics, Zagazig University, Egypt. He is working on the application of multi-objective and robust meta-heuristic optimization techniques. He has published more than 150 articles in international journals and conference proceedings. His current research interests include optimization, operations research, data mining, computational intelligence, applied statistics, decision support systems, robust optimization, engineering optimization, multi-objective optimization, swarm intelligence, evolutionary algorithms, and artificial neural networks. He holds the program chair in many conferences in the fields of decision making analysis, big data, optimization, complexity and the Internet of Things, and editorial collaboration in some journals of high impact. He is also an/a Editor/Reviewer in different international journals and conferences.

View publication stats

Multimedia Tools and Applications
https://doi.org/10.1007/s11042-019-7390-1

Sentiment analysis of multimodal twitter data

Akshi Kumar [1] · Geetanjali Garg [1]

Received: 8 October 2018 / Revised: 28 January 2019 / Accepted: 19 February 2019
Published online: 12 March 2019
© Springer Science+Business Media, LLC, part of Springer Nature 2019

Abstract

Text-driven sentiment analysis has been widely studied in the past decade, on both random and benchmark textual Twitter datasets. Few pertinent studies have also reported visual analysis of images to predict sentiment, but much of the work has analyzed a single modality data, that is either text or image or GIF video. More recently, as the images, memes and GIFs dominate the social feeds; typographic/infographic visual content has become a non-trivial element of social media. This multimodal text combines both text and image defining a novel visual language which needs to be analyzed as it has the potential to modify, confirm or grade the polarity of the sentiment. We propose a multimodal sentiment analysis model to determine the sentiment polarity and score for any incoming tweet, i.e., textual, image or info-graphic and typographic. Image sentiment scoring is done using SentiBank and SentiStrength scoring for Regions with convolution neural network (R-CNN). Text sentiment scoring is done using a novel context-aware hybrid (lexicon and machine learning) technique. Multimodal sentiment scoring is done by separating text from image using an optical character recognizer and then aggregating the independently processed image and text sentiment scores. High performance accuracy of 91.32% is observed for the random multimodal tweet dataset used to evaluate the proposed model. The research further demonstrates that combining both textual and image features outperforms separate models that rely exclusively on either images or text analysis.

Keywords Multimodal text · Twitter · Sentiment · Context-aware · Optical character recognition

1 Introduction

The current affordable and ubiquitous generation of Web provides substantial amount of opinionated social big data which facilitates decision making. Sentiment Analysis has gained

✉ Akshi Kumar
akshikumar@dce.ac.in

Geetanjali Garg
geetanjali.garg@dtu.ac.in

[1] Department of Computer Science & Engineering, Delhi Technological University, Delhi, India

importance as quick as a wink for tracking the mood/view of people by analyzing this unstructured, multimodal, informal, high-dimensional and noisy social data. It helps in gaining insights for a particular subject, topic, event or a matter within various domains such as market, business or government intelligence [30]. Formally, sentiment analysis is defined as the computational study of people's opinions, attitudes and emotions towards an entity [27]. It is a specialized type of Natural Language Processing (NLP) problem that relies on the analysis of the huge amount of user-generated online web content produced daily in social networks, blogs, e-commerce sites, and other user-editable web forums. Pertinent literature within the area report the use of various techniques such as machine learning, lexicon-based, hybrid techniques and concept-based techniques (contextual and ontology based) etc. to mine the opinion [31]. Out of these, the use of machine learning techniques to mine opinion especially on Twitter text data has been demonstrated the most [13, 20, 22, 39, 40]. Recently, visual communication using images to express views, opinions, feelings, emotions and sentiments has increased tremendously on social platforms like Flickr, Instagram, Twitter, Tumblr, etc. [11, 19, 22, 23].

Images are particularly powerful as they have cognition associated and visual experiences convey sentiments and emotions better. Consequently visual sentiment analysis has been of interest to researchers and it has been observed that deep learning techniques have outperformed the conventional machine learning techniques in analyzing the visual sentiment. Multimodal capabilities offered by popular social networking websites such as Facebook, Twitter, and Tumblr have further enabled mix of text and images in a variety of ways for better social engagement. The ascendant use of info-graphics, typographic-images, memes and GIFs in social feeds is a testimony to this. Visual content is interesting, engaging and effective. Visual content has both typographic as well infographic content. Typography deals with arranging size, style and weight of the right typoface to provide a visually pleasing format of the text and helps in holding reader's attention. Infography deals with graphic representation of the data to make it easier to perceive.

As discussed, text-driven sentiment analysis has been widely studied [3, 14, 27, 28] and few pertinent studies which report visual sentiment analysis of images are available in literature [5, 7, 19, 49, 54–56]. But, much of the reported work has analyzed a single modality data whereas multiple modalities of text and image remain unexplored. Moreover, human expressions are extremely complicated as statements, images and their mix can convey a wide range of emotions, and often require context to fully understand. Thus, the study to comprehend this text-image relationship is imperative as this combination can modify or enhance the semantics and consequently the sentiment. For example, consider the multimodal text given in the Fig. 1. Here the image of a growling lion depicts a negative, beastly behavior (negative sentiment polarity) which is *modified* by the textual content "*Go Hunt Your dream*" which is a motivational, positive statement (positive sentiment polarity).

Now, consider another example of multimodal tweet given in Fig. 2. Here the rainbow colored key- house depicts a happy home with positive vibes and the text "*Love has just checked in*" strengthens this happiness emotion and thus the positive polarity of the sentiment.

Motivated by this polarity shifts and depths due to content modality, we propose a model to analyze sentiments from multimodal Twitter data which will facilitate visual listening for social media analytics. The model analyzes the incoming tweet for its modality (text, image or image with text) and based on it forwards it to the respective processing module. The model has five modules:

- *Data Acquisition Module:* Input tweet to the model



Fig. 1 Example Multimodal Text with sentiment modification

- *Image Module:* SentiBank and Regions with Convolution neural network (R-CNN) along with Senti-Strength based on the model given by Mandhyani et al. [37]
- *Text Module:* A hybrid of Lexicon and Machine Learning techniques (Gradient Boosting and SentiCircle [44])
- *Multimodal Module:* Image sent to Image Module for sentiment analysis and text is retrieved using Computer Vision API for Optical Character Recognition (CV/OCR) and then sent to the Text module for sentiment analysis;
- *Aggregation Module:* Resultant scores from Text and Image modules are combined to produce aggregate sentiment score for the multimodal tweet.

The novelty of the research is twofold. Firstly, the model is able to analyze sentiment for any incoming tweet, i.e., textual, visual or info-graphic and typographic. Secondly, it proposes a hybrid technique (Machine learning and lexicon) for context-aware textual sentiment analysis. The robustness of the individual modules is evaluated using benchmark datasets (STS-Gold for Text module [43]; Flickr 8k for Image module [17]) and the proposed model is evaluated



Fig. 2 Example Multimodal Text with sentiment strengthening

using random multimodal tweets collected on the recent topic related LGBT verdict of Indian Penal Court (IPC) section 377 in India (#section377). The results have been evaluated using accuracy as the performance metric.

The rest of the paper is structured as follows: Section 2 briefly discusses the pertinent work within the domain of textual, image and multimodal sentiment analysis followed by Section 3, which illustrates the proposed multimodal sentiment analysis model and its working details. Section 4 explicates the results and provides an analysis of the same. The final section, Section 5, concludes the study and expounds upon the scope of future work.

2 Related work

The term 'Sentiment Analysis' was initially witnessed in the published work [9] in 2003 and since then both primary [11, 13, 19–23, 25, 27–29, 31, 32, 39, 40] and secondary studies [24, 26, 30] have been reported across pertinent literature. Twitter, currently the most famous micro- blog connects people across the globe and has high level of user involvement. It has gradually emerged as a huge source of sentiment-rich data. Kumar and Jaiswal [22], have compared two social media (Twitter and Tumbler) for sentiment analysis and analyzed the performance using soft computing techniques. Also, literature is well-equipped with studies pertaining to sentiment analysis using machine learning paradigms on specifically textual user generated online content on social media [40] showed that emoticons could be used to collect a labeled dataset for sentiment analysis. Golder and Macy [14] investigated temporal patterns in emotion using tweets, and Bollen et al. [3] investigated the impact of collective mood states on the stock market.

Explosive growth of using images to express opinions in Microblog makes only text-based sentiment analysis an obsolete technique to understand the sentiments of users. Soleymani et al. [47] discusses the current work, challenges and opportunities in the field of multimodal sentiment analysis in detailed manner. There are many images in social networks that have similar emotional but different usual contents and opinion mining on these images is a challenging task. Besides the text based sentiment analysis, the image based sentiment analysis becomes important. The research in this field fall under three areas which are: aesthetics [8, 18, 38], emotion detection [33–36, 48, 51, 52, 54–56] and sentiment ontology [5]. Low level features of image are used in Emotion detection to detect the emotion in an image. J. Yanulevskaya et al. [51, 52] proposed a system to categorize emotion using low-level features. Machajdik and Hanbury [36] represented emotional content of an image by extracting low level features. Lu et al. [35] explored the relationship between emotions and shapes. Zhao et al. [54–56] proposed a principles-of-art-based emotion features (PAEF) which attained good performance in affective image classification and affective image retrieval. However, low-level image features are limited in the large-scale image sentiment detection. Visual Sentiment Ontology (VSO) was proposed by Borth et al. [5] which is based on such visual concepts which are strongly related to sentiments. They used high-level Adjective Noun Pairs (ANPs) which are strongly relevant with sentiment instead of the low-level features. Then they proposed SentiBank, which is used to detect the presence of ANPs in an image. Experiments are done on image tweets which demonstrate significant improvement in accuracy. Yang et al. [50] proposed an image discovery framework considering textual, visual and social features. They have proposed the Visual-Social-Textual Rank (VSTRank) algorithm to calculate the importance score for each image to identify images that have emotional content. Siersdorfer et al. [46] analyzed the relation between the sentiment of the metadata content to images and

their visual content in social environment. For sentiment analysis of images authors' have extracted numerical values based on their textual metadata. Authors have used Support Vector Machine (SVM) to build machine learning model for sentiment analysis of images. It is concluded that the visual features of images can support in predicting the polarity of sentiments. Girshick et al. [12] have built a model "R-CNN: Regions with CNN features". Color histogram and SIFT-based features of images are used to train a sentiment polarity classifier. Gajarla and Gupta [11] used deep learning to predict the emotion depicted by an image. They have classified the Image categories as Love, Happiness, Violence, Fear and Sadness. They have collected data set from Flickr API. They have used three techniques which are SVM on high level features of VGG-ImageNet, fine-tuning on pre-trained models like RESNET, Places205 VGG16 and VGG-Image Net. Kumar et al. [23] proposed a visual sentiment framework using a convolutional neural network. They have used Flickr images for training the model and Twitter images for testing the proposed model.

Successful results in multimodal sentiment analysis have been achieved using non-negative matrix factorization [49] and latent correlations [19]. Chen et al. [7] investigated the image posting behavior of social media users and found in their study that two thirds of the participants added an image to their tweets to enhance the emotion of the text. You and Luo [53] have analyzed the online sentiment changes of Twitter users considering both the textual and visual content. They also show the correlation between textual content and visual content. Poria et al. [41] gave a novel methodology for multimodal sentiment analysis, which consists in harvesting sentiments from Web videos by demonstrating a model that uses audio, visual and textual modalities as sources of information. Katsurai and Satoh [19], exploit correlations among multiple views: visual and textual views and a sentiment view the correlations being constructed using SentiWordNet. Dataset for this correlation is collected from Flickr and Instagram images. A novel Unsupervised Sentiment Analysis (USEA) framework for social media images has been proposed in a work [49] which uses relations between visual content and relevant contextual information. Authors found out both textual information and visual content for sentiment based image clustering in a non-negative matrix factorization framework. Cai and Xia [6] have used convolution neural networks (CNN) for sentiment analysis of multimodal tweets which consist of text and image. Two individual CNN architectures are used for learning textual features and visual features, which are combined as input of CNN architecture for exploiting the internal relation between text and image. Hare et al. [16] developed a system to analyze streams of image data. They explored trends in visual artefacts in the image tweets.

To the best of our knowledge, till date no work has been done on multimodal text tweets where the text is embedded in the image as a typographic or infographic visual content. This research proffers a model-based solution to this open problem of research within the sentiment analysis domain. The proposed multimodal sentiment analysis model is illustrated in the following section.

3 The proposed model for multimodal sentiment analysis

Multimedia involves multiple modalities of text, audio, images, videos, drawings etc. Twitter has transformed from a text based micro-blogging (very micro) platform to a visual one gradually. Recent studies also claim that the tweets with image links get 2x the engagement rate of those without [7, 19].

The proposed model takes into account both the modalities, text and image independently and their combination to analyze the sentiment in tweets. The incoming tweet is firstly examined for its modality type, that is, whether it is an image, a text or a multimodal text (image + text = typographic or info-graphic). The further processing is done on the basis of the identified modality type. For an image only tweet, the image module is implemented which uses an existing model of SentiBank [4] and R-CNN to determine the sentiment polarity and sentiment score of the image. For a text only tweet, the text module after pre-processing employs a machine learning based ensemble method (Gradient boosting) to classify the tweet in to one of the three polarity categories, namely, positive, negative or neutral. Post this; a lexicon based approach (SentiCircles), which captures contextual semantics, is used to determine the sentiment polarity and strength of the tweet. This polarity and strength obtained separately from the machine learning and lexicon based techniques is combined to do a scoring of sentiment which has the range [−3, 3]. Subsequently, for an image with text, the text is detected and extracted using a computer vision API and recognized using optical character

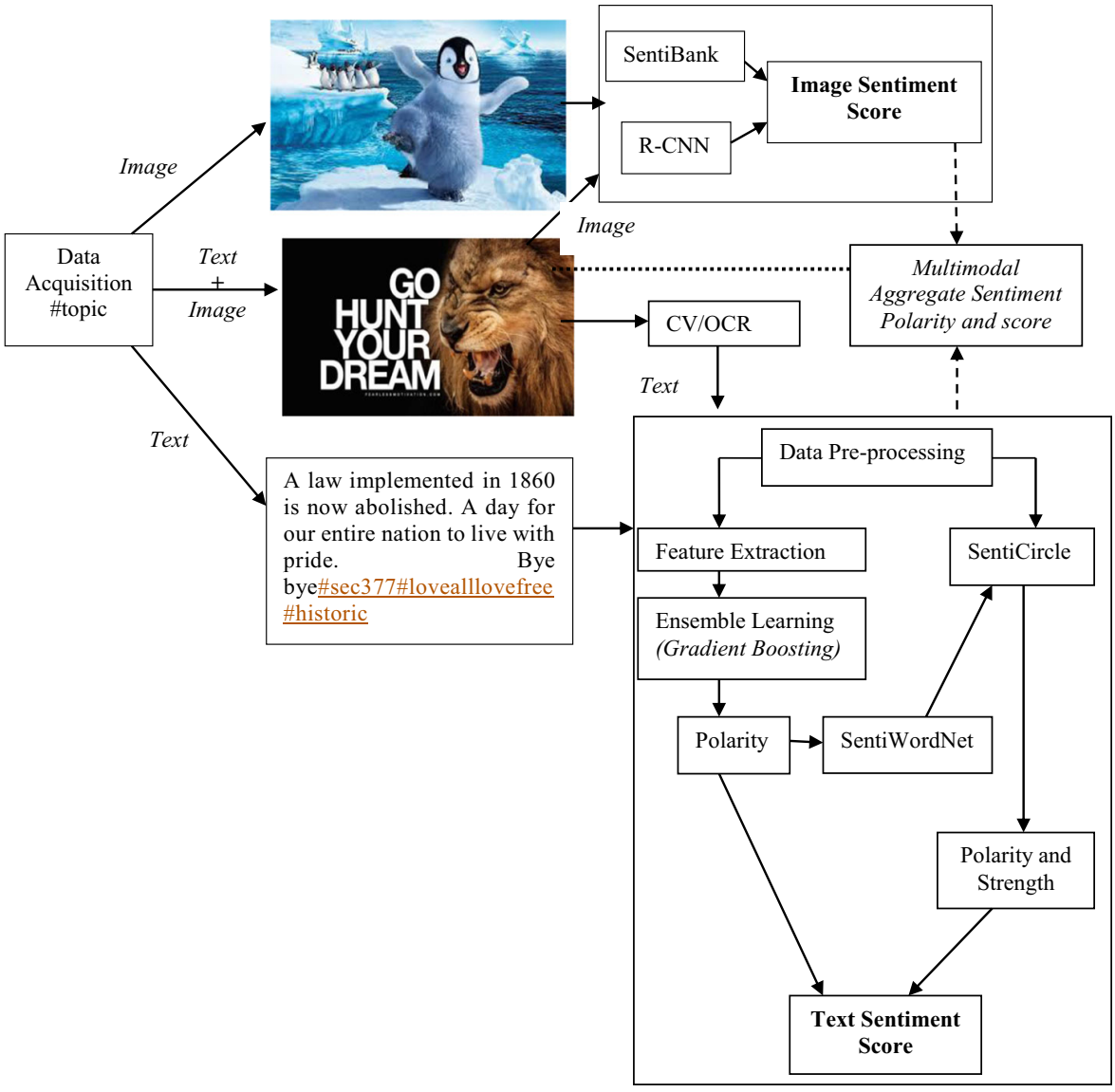


Fig. 3 Systematic flow of the proposed model

recognition approach. The recognized text is then processed in the text module whereas the image is sent to the image module for processing. The resultant scores from both these modules are combined to give an aggregate sentiment polarity and score. Figure 3 illustrates the systematic flow of the proposed model.

The following sub-sections expound the details:

3.1 Data acquisition

To evaluate the system using the aforesaid classification techniques tweets pertaining to a topic (#topic) are extracted from the publically available Twitter datasets using its API. 8000 multimodal tweets were collected on the recent topic related LGBT verdict of Indian Penal Court (IPC) section 377 in India using hashtag #section377.

3.2 Image Sentiment Analysis

The image only content is processed using the SentiBank, Regions with Convolution neural network (R-CNN) and SentiStrength to obtain a sentiment score within the range [−2, 2]. This analytic model to determine sentiment in images was given by Mandhyani et al. [37] in the year 2017.

- *SentiBank:* It a large-scale visual sentiment ontology which includes 1200 semantic concepts and corresponding automatic classifiers. Each concept is defined as an Adjective Noun Pair (ANP), where adjective depicts the emotion for a specific object/scene described by a noun [4].
- *R-CNN:* R-CNN is one of the popular and efficient object detection models. R-CNN uses selective search for reducing the number of bounding boxes that are fed to the classifier. Selective search uses local cues like texture, intensity, color etc. to generate all the possible locations of the object. After this, these boxes are fed to CNN based classifier. In R-CNN the convolution neural network is forced to focus on a single region at a time because that way interference is minimized as it is expected that only a single object of interest will dominate in a given region. The regions are fed to a CNN for object detection.
- *SentiStrength:* SentiStrength is a sentiment analysis program which estimates the strength of positive and negative sentiment in short web texts, even for informal language. Words are classified and rated based on positive and negative strength, i.e., −1 (not negative) to −5 (extremely negative) and 1 (not positive) to 5 (extremely positive).

The pseudo-code to compute the image sentiment score is given in Fig. 4:

1. Nouns from 1200 ANPs are separated
2. Objects from 200 RCNN classes are taken
3. Compute the distance between the noun and objects of 200 RCNN classes by using Radial basis function(RBF)
4. New ANP weights are multiplied with SentiStrength of adjectives for each ANP.
5. Sum-up all ANPs to get the sentiment score within the range [-2,2]

Fig. 4 Pseudo-code for image sentiment scoring

3.3 Textual sentiment analysis

The textual sentiment analysis is a multi-step process which consists of the following:

- *Data Pre-processing:* Data pre-processing is done for cleaning and transforming the data for relevant feature extraction. The HTML entities in the tweet are decoded (Eg. &amp is changed to &), URLs were removed, expressions corresponding to retweet (RT) at the beginning of the tweet are removed, contractions present in the tweet are replaced by their extended words (Eg, "I'll" is replaced with 'I will), punctuations present including hast-tag '#'etc., are removed. Further, three or more repetitive occurrences of a character are replaced with a single character. For example, *'happppy'* is changed to *'hapy'*. Terms in the tweet which contains only digits are removed. Extra spaces in the tweet are removed and finally, all the characters of the tweet were changed to lowercase. Additionally, all non-ASCII-English characters were removed, to keep the domain of the data specific to the English language. Part of Speech tagging is also done to extract common structural patterns such as verb, adverb, adjective and noun.
- *Feature Extraction:* This step identifies the characteristics of the datasets that are specifically useful in detecting sentiments. The classical bag-of-features framework is utilized. We form a list of tweet words from the tweets in the corpus, which are tagged as a noun, verb, adjective, adverb or pronoun using the Part-of-speech (POS) tagger provided by NLTK [2]. Now the frequency distribution of each tweet word in this list is obtained and the top 5000 most common words are considered. These words constitute the bag-of-words which are to be used as feature words to find the unigrams. Next, we form a feature vector corresponding to each tweet. The features used are:
    - Unigrams: presence/absence of feature words
    - Part-of-Speech(POS)features: count of nouns, verbs, adjectives, adverbs, interjections and pronouns
    - Negation: count of occurrences of negation word 'not'
    - Count of Emoticon features: Various combinations of punctuation marks have been mapped into six classes of emoticons:-Smiley(:),:-), (:), laugh(: D, xD), love(<3,:*), wink(;),;-D), frown(: -(,:(), and cry(:'() and their count is taken as feature
    - Count of elongated words(e.g. yummmy)
    - Count of capitalized words
    - Length of message.
- *Ensemble Learning:* An iterative learning model, gradient boosting is then used to train the textual sentiment analysis module. The gradient boosting is meta-model which consists of multiple weak models whose output is added together to get an overall prediction. The evaluated polarity is input the SentiWordNet [10] to obtain the respective sentiment score. SentiWordNet contains sentiment scores for all WordNet entries.
- *SentiCircle:* Each cleaned tweet is firstly tokenized, and each token is POS tagged using NLTK. Each token is lemmatized using WordNet Lemmatizer [15] and then stemmed to its root form using Porter Stemmer [42]. Based on the POS tag assigned to each token, it is scored using SentiWordNet. SentiWorNet offers a fixed, context-independent, word-sentiment orientations and strengths. SentiCircles considers the contextual co-occurrence patterns to capture conceptual information and update strength and polarity in sentiment lexicons accordingly.
    - Scoring from SentiWordNet

- If the POS tag matches one of the tags in SentiWordNet for that term, then all positive and negative scores for that word corresponding to that tag are weighted average inversely according to their sense number separately. Else all positive and negative scores corresponding to that word are averaged.
- If positive and negative scores are unequal, then higher of them is returned with appropriate sign, else machine learning output polarity is considered in deciding. If polarity is positive, then positive score is returned and if the polarity is negative, then negative score is returned. For neutral output of machine learning, positive score is returned.

- Negation handling terms that are preceded by any of the negative words listed in General Inquirer[1] under the NOTLW category1, have the sign of their score reversed. For example, in the tweet "*Uber Premier is not amazing!*", the term "*amazing*" is preceded by a negation. Therefore, instead of using its original sentiment score (0.75 in the SentiWordNet lexicon for example, this score negated (−0.75)
- Term-Context vector is then created, that is for each word, and a vector of words that appear in context of the given word is formed. If the given word appears in any other tweet and that tweet matches the current tweet in having at-least one common user, topic etc., then all the words in that tweet is considered as part of the context-vector of the given word.
- After forming term-context vector for each term in the tweet corpus, corresponding values of TDOC, θ, x and y are determined for each of the context terms in the context-vector of the term [44]
- For each term, its sentiment polarity and strength is calculated by finding geometric median of all its context-terms using Weiszfeld's algorithm [1].
- For each tweet, its sentiment polarity and strength is calculated by finding geometric median of all its terms using Weiszfeld's algorithm.

- Once the polarity from the ensemble learning algorithm and polarity & strength from SentiCircles is determined, these values are combined to determine the text sentiment score which has the range [−3, 3].

3.4 Multimodal text: text in image

For typographic or infographic multimodal text, we have used the Computer Vision API to extract text using OCR from the image. This process of text retrieval from image comprises of three sub-components viz. text detection, text extraction and text recognition. Text extraction is a crucial step in improving the accuracy and quality of the concluding recognition output. It aims at segmenting text from background that is to isolate text pixels from those of background. An effective text extraction method facilitates the use of commercial OCR without any amendments. For this we have used Open CV version3.4.2**,** EAST text detector proposed by Zhou et al. [57] which is a deep learning model, based on a novel architecture and training pattern. It is capable of running at near real-time at 13 FPS on 720p images and obtains state-of-the-art text detection accuracy. The extracted text is passed through an OCR for recognition.

[1] www.wjh.harvard.edu/~inquirer

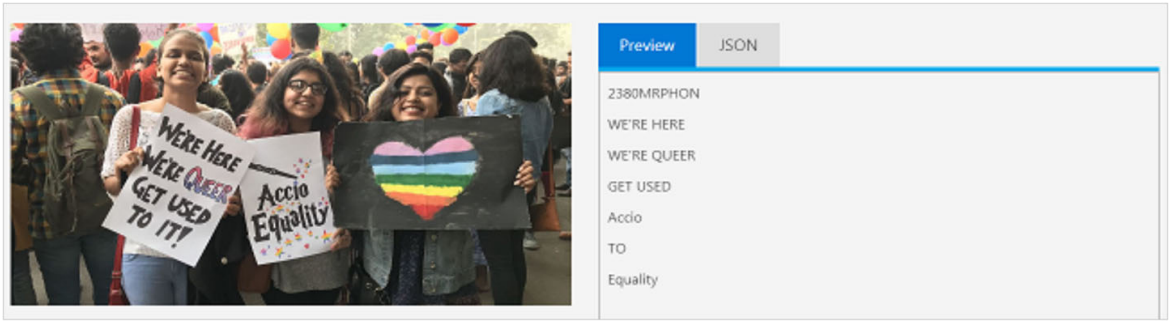


Fig. 5 Sample text extraction using the Computer Vision API

OCR is conversion of images of typed, handwritten or printed text into machine-encoded text. OCR first preprocess images by techniques like de-skewing, line & word detection, layout analysis, character segmentation etc. to improve recognition accuracy. The character recognition is generally done in two passes. The output of the first pass is transferred to second pass which is a kind of adaptive recognition. Second pass of recognition uses letter shapes recognized with high confidence on the first pass to recognize better the remaining letters on the second pass. OCR sometimes uses a post processing step which makes use of dictionary to improve upon accuracy. Figure 5 shows the sample text extraction using the API.

The text thus recognized is then sent to textual sentiment analysis module for determining the text sentiment score whereas the image is sent to the visual sentiment analysis module for finding the image sentiment score. These individual scores are combined to produce the aggregate sentiment score for the multimodal tweet. Figure 6 depicts the concept of multimodal sentiment analysis using optical character recognition.

4 Results and analysis

To investigate the robustness of the proposed model, the individual text and image modules are validated using benchmark datasets and the model is evaluated for random multimodal tweets. The empirical analysis is thus broadly divided into three parts; (i) Image sentiment analysis on benchmark Flickr 8 k dataset, (ii) Text sentiment analysis on benchmark STS-Gold dataset, and (iii) Multimodal text (text + image) sentiment analysis using randomly collected tweets on the selected topic.



Fig. 6 OCR and multimodal sentiment analysis

Table 1 Performance accuracy of image sentiment analysis techniques

Technique	Accuracy
SentiBank	71%
SentiBank+RCNN	76.04%

4.1 Image sentiment analysis

Image Sentiment is determined using a hybrid of SentiBank and RCNN. Flickr 8 k, a publically available dataset which comprises of images from flicker website is used to train and test the performance of RCNN for object detection. SentiBank consists of 1200 trained visual concept detectors providing a mid-level representation of sentiment. The results were evaluated initially by only using SentiBank technique and then using a combinational technique of SentiBank with RCNN. Table 1 depicts the performance accuracy.

Figure 7 shows the results graphically.

4.2 Text Sentiment Analysis

For textual analysis step we used STS-Gold, a standard dataset for Twitter sentiment analysis created by Saif et al. [45]. It contains a total of 2206 tweets, out of which 1402 are negative, 632 are positive and 77 are neutral. The performance of the text sentiment analysis module is evaluated using three approaches, the lexicon-only (SentiWordNet) technique, machine learning approach (Gaussian Naïve Bayesian, Decision Tree, Random Forest and Gradient Boosting) and hybrid approach. Table 2 depicts the accuracy results.

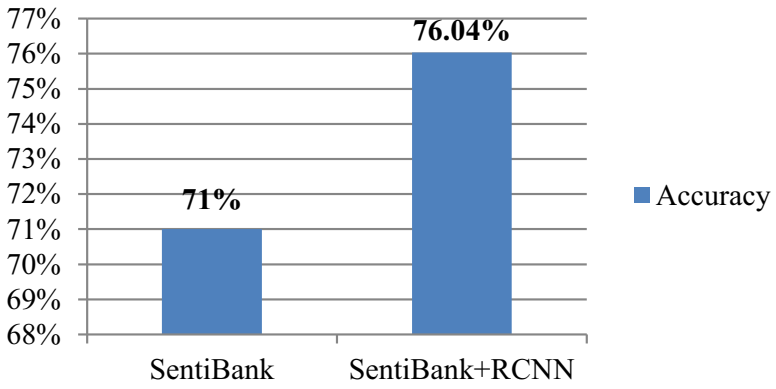


Fig. 7 Accuracy of image sentiment analysis techniques

Table 2 Performance accuracy of text sentiment analysis techniques

Approach	Technique	Accuracy
Lexicon Based	SentiWordNet (SWN)	59.43%
Machine Learning Based	Gradient Boosting (GB)	78.01%
	Decision Tree (DT)	71.35
	Random Forest (RF)	74%
	Gaussian Naïve Bayesian (NB)	64.45%
Hybrid	SentiWordNet +Gradient Boosting (SWN + GB)	82.21%

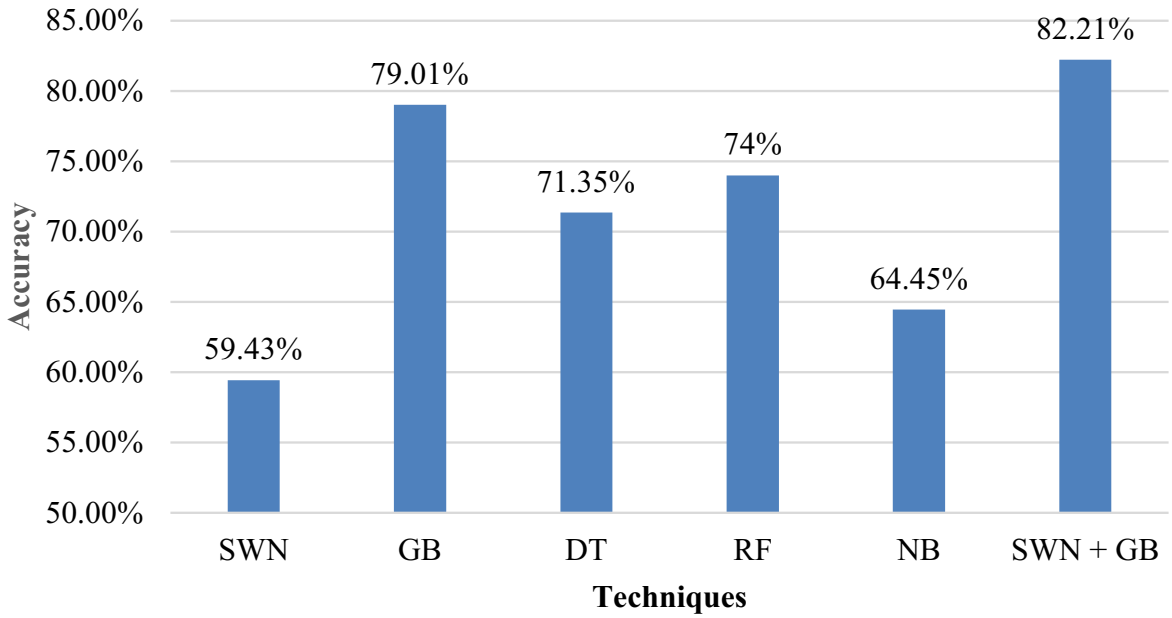


Fig. 8 Accuracy of text sentiment analysis techniques

Figure 8 shows these results graphically.

4.3 Multimodal Sentiment Analysis

Table 3 depicts the generic characteristics of text and image tweets:

8000 random multimodal tweets on the recent topic related LGBT verdict of Indian Penal Court (IPC) section 377 in India (#section377) were extracted. The distribution of modalities in these tweets is shown in the Fig. 9.

Table 3 Twitter text and image generic characteristics

Text Characteristics	Tweet length	• 280 characters • This limit is Not for Japanese, Korean, Chinese tweets
	Retweet	• No limit on number of times a tweet can be retweeted. • Only recent 100 people who retweeted a tweet will be shown.
	Tweet Limit	1000 tweets/day/Person
	Number of Language supported	40
Image Characteristics	GIF support	• Animated GIFs cannot be included in tweet with multiple images • We can send only 1 GIF per tweet • GIF in full is attached • Photos and GIFs attachment do not count towards character limit • Supports looping GIF
	Image limit	• We can select up to 4 photos to tweet at once • Up to 25 stickers can be attached to a photo
	Format of image tweet	• It accepts GIF,JPEG,PNG • Does not accept Bmp, TIFF
	Size of image tweet	• 5 Mb photo • 5 Mb GIF on mobile • Up to 15 Mb on web

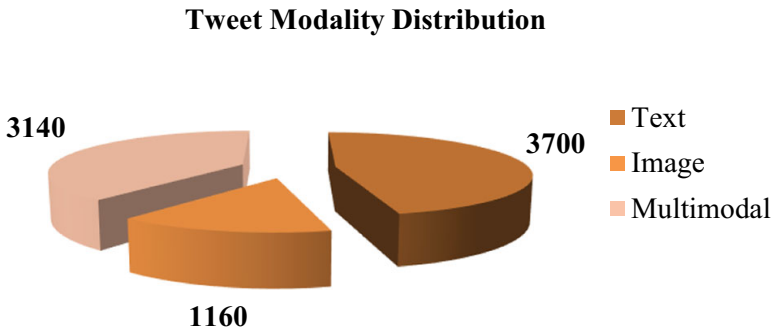


Fig. 9 Distribution of tweet modality types

The performance of the proposed model is evaluated for these multimodal tweets and the accuracy results for the same are shown in Table 4:

Figure 10 shows these results graphically.

5 Conclusion and future scope

Images are more expressive than text and at the same time text embedded or represented as an image further defines this power of expressiveness. This research proposed a model for sentiment analysis to capture this expressiveness for text in an image, both typographic or infographic, as sentiment polarity and strength. The multimodal sentiment analysis model for Twitter offered novelty in two ways. Firstly, it was able to handle multi-modalities in tweets, that is, text and image individually and text in an image to analyze the sentiment and secondly, the textual sentiment analysis was based on a hybrid of context-aware lexicon and ensemble learning. The model will serve as a visual listening tool for enhanced social media monitoring and analytics. The performance results were motivating and improve the generic sentiment

Table 4 Performance accuracy of proposed model

Module	Accuracy
Image module	77.63%
Text module	84.62%
Multimodal (proposed)	91.32%

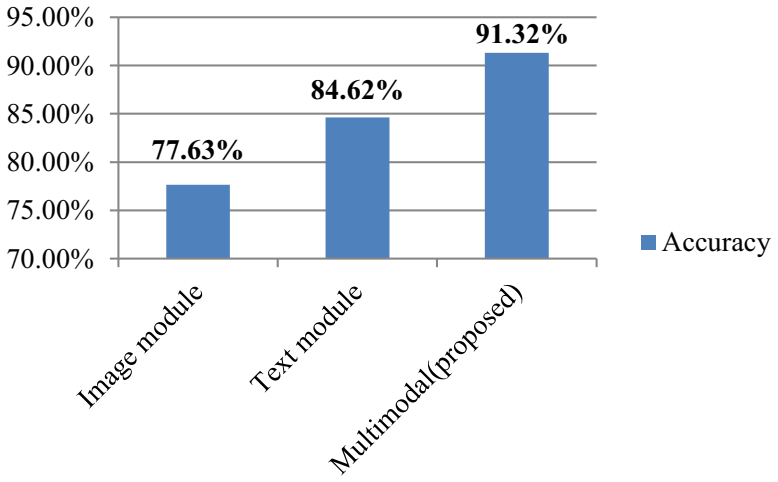


Fig. 10 Accuracy of proposed model

analysis task. The primary limitation of the model is that the text recognition is restricted by the capability of the Computer Vision API. Moreover, as social media is an informal way of communication, multilinguity (code-mix and code-switch languages, for example a mix of English and Hindi, a native Indian language) is widely seen, but such content (text or text in image) could not be processed. Also, the OCR has a limited capability for handwritten text recognition and suffers from reduced accuracy with 'lack of contrast' images where the text color and the background color are almost similar. In this research, only the text and image modality type had been considered whereas other modalities such as animated GIFs and memes define an open problem within the research domain. Also, the use of word embeddings and deep learning for context-aware sentiment analysis of text can be explored.

References

1. Aftab, K., Hartley, R. and Trumpf, J., 2015. Generalized weiszfeld algorithms for lq optimization
2. Bird S, Loper E (2004) NLTK: the natural language toolkit. In: Proceedings of the ACL 2004 on Interactive poster and demonstration sessions (p. 31). Association for Computational Linguistics
3. Bollen J, Mao H, Zeng X-J (2011) Twitter mood predicts the stock market. J Comput Sci 2(2011):1–8
4. Borth D, Chen T, Ji R, Chang SF (2013) Sentibank: large-scale ontology and classifiers for detecting sentiment and emotions in visual content. In: Proceedings of the 21st ACM international conference on Multimedia (pp. 459–460). ACM
5. Borth D, Ji R, Chen T, Breuel T, Chang S-F (2013) Large-scale visual sentiment ontology and detectors using adjective noun pairs. In: Proceedings of the 21st ACM international conference on Multimedia, pp. 223–232. ACM
6. Cai G, Xia B (2015) Convolutional neural networks for multimedia sentiment analysis. In Natural Language Processing and Chinese Computing (pp. 159–167). Springer, Cham
7. Chen T, Salah Eldeen HM, He X, Kan MY, Lu D (2017) VELDA: Relating an Image Tweet's Text and Images. In AAAI 2015 Jan 25 (pp. 30–36)
8. Datta R, Joshi D, Li J, Wang JZ (2006) Studying aesthetics in photographic images using a computational approach. In: European Conference on Computer Vision (pp. 288–301). Springer, Berlin
9. Dave K, Lawrence S, Pennock DM (2003) Mining the peanut gallery: Opinion extraction and semantic classification of product reviews. Proceedings of the 12th international conference on World Wide Web. ACM. 519–528
10. Esuli A, Sebastiani F (2007) SentiWordNet: a high-coverage lexical resource for opinion mining. Evaluation. 17:1–26
11. Gajarla V, Gupta A (2015) Emotion detection and sentiment analysis of images. Georgia Institute of Technology, Atlanta
12. Girshick R, Donahue J, Darrell T, Malik J (2014) Rich feature hierarchies for accurate object detection and semantic segmentation. In Proceedings of the IEEE conference on computer vision and pattern recognition, pp. 580–587
13. Go A, Bhayani R, Huang L (2009) Twitter sentiment classification using distant supervision. CS224N Project Report, Stanford 1(12)
14. Golder SA, Macy MW (2011) Diurnal and seasonal mood vary with work, sleep, and day length across diverse cultures. Science 333(6051):1878–1881
15. Hao T, Rusanov A, Boland MR, Weng C (2014) Clustering clinical trials with similar eligibility criteria features. J Biomed Inform 52:112–120
16. Hare JS, Samangooei S, Dupplaw DP, Lewis PH (2013) Twitter's visual pulse. In: Proceedings of the 3rd ACM conference on International conference on multimedia retrieval (pp. 297–298). ACM
17. Hodosh M, Young P, Hockenmaier J (2013) Framing image description as a ranking task: Data, models and evaluation metrics. J Artif Intell Res 47:853–899
18. Jia J, Wu S, Wang X, Hu P, Cai L, Tang J (2012) Can we understand van gogh's mood?: learning to infer affects from images in social networks. In: Proceedings of the 20th ACM international conference on Multimedia. ACM, pp. 857–860
19. Katsurai M, Satoh SI (2016) Image sentiment analysis using latent correlations among visual, textual, and sentiment views. In: Acoustics, Speech and Signal Processing (ICASSP), 2016 IEEE International Conference on (pp. 2837–2841). IEEE

20. Kouloumpis E, Wilson T, Moore JD (2011) Twitter sentiment analysis: The good the bad and the omg! ICWSM 11(538–541):164
21. Kumar A, Dogra P, Dabas V (2015) Emotion analysis of Twitter using opinion mining. In: Contemporary Computing (IC3), 2015 Eighth International Conference on, IEEE, pp. 285–290
22. Kumar A, Jaiswal A (2017) Empirical study of twitter and tumblr for sentiment analysis using soft computing techniques. Proceedings of the World Congress on Engineering and Computer Science 1:1–5
23. Kumar A, Jaiswal A (2017) Image sentiment analysis using convolutional neural network. In: International Conference on Intelligent Systems Design and Applications (pp. 464–473). Springer, Cham
24. Kumar A, Jaiswal A (2019) Systematic literature review of sentiment analysis on Twitter using soft computing techniques. Concurrency and Computation: Practice and Experience: e5107
25. Kumar A, Jaiswal A, Garg S, Verma S, Kumar S (2019) Sentiment Analysis Using Cuckoo Search for Optimized Feature Selection on Kaggle Tweets. International Journal of Information Retrieval Research (IJIRR) 9(1):1–15
26. Kumar, Akshi, Renu Khorwal, and Shweta Chaudhary (2016) A survey on sentiment analysis using swarm intelligence." Indian Journal of Science and Technology 9, no. 39
27. Kumar A, Sebastian TM (2012) Sentiment analysis: A perspective on its past, present and future. International Journal of Intelligent Systems and Applications 4(10):1–4
28. Kumar A, Sebastian TM (2012) Sentiment analysis on Twitter. IJCSI International Journal of Computer Science Issues 9(3):372–378
29. Kumar A, Sebastian TM (2012) Machine learning assisted sentiment analysis. In: Proceedings of International Conference on Computer Science & Engineering (ICCSE'2012), pp. 123–130
30. Kumar A, Sharma A (2017) Systematic literature review on opinion mining of big data for government intelligence. Webology 14(2)
31. Kumar A, Sharma A (2018) Socio-sentic framework for sustainable agricultural governance. Sustainable Computing: Informatics and Systems
32. Kumar A, Sharma A (2019) Opinion mining of Saubhagya Yojna for Digital India. In: International Conference on Innovative Computing and Communications, pp. 375–386. Springer, Singapore
33. Li B, Feng S, Xiong W, Hu W (2012) Scaring or pleasing: exploit emotional impact of an image. In: Proceedings of the 20th ACM international conference on Multimedia. ACM, pp. 1365–1366
34. Li B, Xiong W, Hu W, Ding X (2012) Context-aware affective images classification based on bilayer sparse representation. In: Proceedings of the 20th ACM international conference on Multimedia. ACM, pp. 721–724
35. Lu X, Suryanarayan P, Adams Jr RB, Li J, Newman MG, Wang JZ (2012) On shape and the computability of emotions. In Proceedings of the 20th ACM international conference on Multimedia (pp. 229–238). ACM
36. Machajdik J, Hanbury A (2010) Affective image classification using features inspired by psychology and art theory. In: Proceedings of the 18th ACM international conference on Multimedia. ACM, pp. 83-92
37. Mandhyani J, Khatri L, Ludhrani V, Nagdev R, Sahu S (2017) Image Sentiment Analysis. International Journal of Engineering Science 4566
38. Marchesotti L, Perronnin F, Larlus D, Csurka G (2011) Assessing the aesthetic quality of photographs using generic image descriptors. In: Computer Vision (ICCV), 2011 IEEE International Conference on. IEEE, pp. 1784–1791
39. Neethu MS, Rajasree R (2013) Sentiment analysis in twitter using machine learning techniques. In: Computing, Communications and Networking Technologies (ICCCNT), 2013 Fourth International Conference on, (pp. 1–5). IEEE
40. Pak A, Paroubek P (2010) Twitter as a corpus for sentiment analysis and opinion mining. In: LREC, vol. 10, pp. 1320–1326
41. Poria S, Cambria E, Howard N, Huang GB, Hussain A (2016) Fusing audio, visual and textual clues for sentiment analysis from multimodal content. Neurocomputing 174:50–59
42. Porter MF (1980) An algorithm for suffix stripping. Program. 14(3):130–137
43. Saif H, Fernandez M, He Y, Alani H (2013) Evaluation datasets for Twitter sentiment analysis: a survey and a new dataset, the STS-Gold
44. Saif H, Fernandez M, He Y, Alani H (2014) Senticircles for contextual and conceptual semantic sentiment analysis of twitter. In: European Semantic Web Conference (pp. 83–98). Springer, Cham
45. Saif H, He Y, Fernandez M, Alani H (2016) Contextual semantics for sentiment analysis of Twitter. Inf Process Manag 52(1):5–19
46. Siersdorfer S, Minack E, Deng F, Hare J (2010) Analyzing and predicting sentiment of images on the social web. In: Proceedings of the 18th ACM international conference on Multimedia. ACM, pp. 715–718
47. Soleymani M, Garcia D, Jou B, Schuller B, Chang SF, Pantic M (2017) A survey of multimodal sentiment analysis. Image Vis Comput 65:3–14
48. Vonikakis V, Winkler S (2012) Emotion-based sequence of family photos. In: Proceedings of the 20th ACM international conference on Multimedia. ACM, pp. 1371–1372

49. Wang Y, Wang S, Tang J, Liu H, Li B (2015) Unsupervised sentiment analysis for social media images. In: IJCAI. pp. 2378–2379
50. Yang Y, Cui P, Zhu W, Zhao HV, Shi Y, Yang S (2014) Emotionally representative image discovery for social events. In: Proceedings of International Conference on Multimedia Retrieval. ACM, p. 177
51. Yanulevskaya V, Uijlings J, Bruni E, Sartori A, Zamboni E, Bacci F, Melcher D, Sebe N (2012) In the eye of the beholder: employing statistical analysis and eye tracking for analyzing abstract paintings. In: Proceedings of the 20th ACM international conference on Multimedia. ACM, pp. 349–358
52. Yanulevskaya V, van Gemert JC, Roth K, Herbold AK, Sebe N, Geusebroek JM (2008) Emotional valence categorization using holistic image features. In: ICIP. pp. 101–104
53. You Q, Luo J (2013) Towards social imagematics: sentiment analysis in social multimedia. In: Proceedings of the Thirteenth International Workshop on Multimedia Data Mining, ACM, p. 3
54. Zhao S, Gao Y, Jiang X, Yao H, Chua TS, Sun X (2014) Exploring principles-of-art features for image emotion recognition. In: Proceedings of the 22nd ACM international conference on Multimedia (pp. 47–56). ACM
55. Zhao S, Yao H, Wang F, Jiang X, Zhang W (2014) Emotion based image musicalization. In: Multimedia and Expo Workshops (ICMEW), 2014 IEEE International Conference on (pp. 1–6). IEEE
56. Zhao S, Yao H, Yang Y, Zhang Y (2014) Affective image retrieval via multi-graph learning. In: Proceedings of the 22nd ACM international conference on Multimedia (pp. 1025–1028). ACM
57. Zhou X, Yao C, Wen H, Wang Y, Zhou S, He W, Liang J (2017) EAST: an efficient and accurate scene text detector. In Proc. CVPR, pp. 2642–2651



Akshi Kumar is an Assistant Professor in the Department of Computer Science & Engineering at Delhi Technological University (formerly Delhi College of Engineering). She has received her doctorate degree in Computer Engineering from the University of Delhi. She has received her M.Tech (Master of Technology) and BE (Bachelor of Engineering) degrees in Computer Engineering. She has many publications to her credit in various International Journals with high impact factor and International Conferences with best paper awards. Her research interests include Intelligent Systems, Text Mining, Sentiment Analysis, Social media analytics and soft computing. She has authored books & co-authored book-chapters within her domain of interest. She is a member of IEEE, IEEE (WIE) and ACM and a life member of IACSIT, IAENG, ISTE and CSI.



Geetanjali Garg is an Assistant Professor and research scholar in the Department of Computer Science & Engineering at Delhi Technological University (formerly Delhi College of Engineering). She has received her M.Tech (Master of Technology) degree in Computer Technology & Applications from the University of Delhi. She has received her B.Tech (Bachelor of Technology) degree in Computer Science & Engineering. Her research interests include Social media mining, Sentiment analysis,Semantic Web and Intelligent systems.

Publisher's note Springer Nature remains neutral with regard to jurisdictional claims in published maps and institutional affiliations.

Evolving Systems
https://doi.org/10.1007/s12530-019-09275-8

ORIGINAL PAPER

Spatial shape feature descriptors in classification of engineered objects using high spatial resolution remote sensing data

Rubeena Vohra[1,2] · **K. C. Tiwari**[2]

Received: 8 September 2018 / Accepted: 14 February 2019
© Springer-Verlag GmbH Germany, part of Springer Nature 2019

Abstract
Spatial and spectral features are two important attributes that form the knowledge based database, useful in classification of engineered objects, using remote sensing data. Spectral features alone may be insufficient to identify buildings and roads in urban areas due to spectral homogeneity and similarity exhibited by them. This has led researchers to explore the spatial features described in terms of shape descriptors to improve accuracy of classification of engineered objects. This paper discusses the parameters of spatial shape features and the method for implementing these features for improving the extraction of engineered objects, using the support vector machine (SVM). SVM classified results obtained using spatial shape features is compared with gray level co-occurrence statistical features in which the former has shown better classification accuracy for buildings and roads. The classification accuracy is also calculated using spectral features of buildings and roads by classifiers such as spectral angle mapper and spectral information divergence. The analysis shows that spatial shape features improve the classification results of buildings and roads in urban areas.

Keywords Spatial shape features · Support vector machine · Spectral angle mapper · Spectral information divergence · Connected component analysis · Spatial and spectral resolution

1 Introduction

Research in analysing geographical regions of Earth's surface with the availability of spatial, spectral, temporal and radiometric resolution remote sensing data has increased manifolds. The resolution of remote sensing data defines the resolving power which not only includes the capability of identifying the various objects but also, provides the information for analyzing the properties of those objects. Spectral resolution statistics is the medium of remotely sensed image for land cover classification applications (Gu et al. 2018; Weng 2012). Temporal resolution helps in generating land cover maps for environmental planning, land use change detection and transportation planning (Usman et al. 2015). Spatial resolution influences the accuracy of the ground objects in urban land cover applications (Small 2016).

Urban land cover is one of the major regions of the Earth's surface that leads to various physical, socio-economical and environmental phenomenon's; therefore, high resolution remote sensing data plays a vital role in classifying diverse and complex urban landscape which is a mosaic of engineered and non engineered objects (Bumairiyemu Maimaiti et al. 2017). The engineered objects are the urban impervious surfaces used to describe the road intersections, building corners and other well defined objects (Ll et al. 2018). Engineered objects are constituted from composite materials that show similar physical and chemical properties, (Luca et al. 2014; Herold et al. 2004) therefore, their spectral information may not be sufficient to classify the objects with high accuracy. Evidently, the classification of such objects needs to be addressed by spatial information in terms of their structure and shape (Im et al. 2012). In the literature various adaptive and automatic classifiers have been reported for computing the statistical properties of the data (Zhou and Angeloc 2006; Angelov et al. 2010).

It is well known from the literature that the spatial information can improve the classification accuracy of urban

✉ Rubeena Vohra
rubeena.vohra@gmail.com; r_rubeena81@yahoo.co.in

K. C. Tiwari
kcchtphd@gmail.com

[1] Electronics andCommunication, Bharatividyapeeth's College of Engineering, Paschim Vihar, New Delhi 110063, India

[2] Civil Engineering, Delhi Technological University, Shahbad Daulatpur, New Delhi 110042, India

Published online: 27 February 2019

objects from high resolution remote multispectral data. Many effective models for obtaining the spatial features such as gray level co-occurrence matrix (GLCM) have been interpreted for spectral classification (Ouma et al. 2008; Zhang 1999). Segmentation techniques are employed which automatically group the neighbouring pixels into contiguous regions that exhibit similar spatial arrangement (Van Der Linden et al. 2007; Sargana et al. 2017). Another representative technique for extracting spatial information is Markov Random Field (MRF) model (Dong et al. 2009, 2001). Wavelet transform (WT) techniques are used to extract textural features at different approximation scales (Myint et al. 2004; Zhu and Yang 1998). Differential Morphological Profiles are used to extract spatial features for multi-scale geometry analysis (Pesaresi et al. 2001; Benediktsson et al. 2003). Notably, length–width extraction algorithm (LWEA) (Shackelford and Davis 2003) has been developed which measures the spatial features within spectrally similar neighbourhood pixels. In addition to LWEA, pixel shape index (PSI) (Zhang et al. 2006) has been developed that forms another spatial feature extraction algorithm to extract the spectrally similar objects. All these techniques deal with spatial analytical approach for extracting the statistical/geometrical/shape features for studying the homogeneity and heterogeneity of the neighbouring pixels.

Well-defined computation of spatial arrangement of pixels is an important factor for consideration in calculating the features for delineation of objects in the data (Nithya and Ramakrsishnan 2018). However, the classical shape features approach is based on extracting features by extending and measuring the length of each direction line. Consequently, this method does not provide sufficient contextual information around the central pixel of curved structures, and pixels in the shape features can be allocated to different values (Han et al. 2012). Another approach, of using morphological profiles (Lv et al. 2014) has been conducted but with limited accuracy. Although the integration of shape features by incorporating spatial information (Shi et al. 2014) shows good performance in the extraction of roads, it is difficult to obtain universal shape feature extraction method for all situations, and therefore, further study is necessary.

Based upon the above discussions, the paper investigates the parameters of spatial shape features for improving the classification accuracy of buildings and roads in urban landscape with two objectives as given below.

(i) First objective pertains to delineation of buildings and roads using spatial shape features such as length, width and PSI. The paper implements the established mathematical formula of spatial structure features; however, it presents an improved way of calculating the directional lines. The novelty is in the methodology of computing local spatial structure feature for a window box on the bounding box, then extending it as an object and finally passing it to SVM classifier. To obtain this, first of all the bounding box of the buildings and roads are extracted from the dataset. Then, the features as direction line histograms are extracted from bounding boxes around the objects. These features are calculated at each box or window level. The features of each window box are concatenated and extended at object level. The inference of high resolution images requires appropriate classifier for identifying the correct classes. SVM classifier which is fast and effective learning algorithm is used to interpret multiple spatial shape features.

(ii) The other objective is to show the comparative assessment of classification accuracy of engineered objects using other spatial and spectral features. This is accomplished by performing a comparative analysis for classification of buildings and roads using proposed parameters for calculating spatial shape features with classical textural features. Further, the comparative analysis using only spectral features is also shown for delineating buildings and roads. Multispectral classifiers such as Spectral Information Divergence (SID) and Spectral Angle Mapper (SAM) are used to achieve the purpose.

The rest of the paper is organised as follows. Section 2 describes the dataset. Section 3 describes the theoretical background of the spatial attributes. Section 4 discusses the flowchart and the methodology of the experiments conducted. Section 5 discusses the step by step outcome of the experiment and explores the benefit of spatial, textural and spectral attributes on different classifiers. Finally, Sect. 6 concludes the paper.

2 Data set

The data set (IEEE GRSS 2014) acquired over Black Lake area of Thetford Mines, province of Québec, Canada (46.047927N, 71.366893W) has been used in this study. The region in the mosaic consists of a variety of natural and man-made objects such as trees, vegetation, soil, roads and buildings. The data has been acquired using a digital color camera (2 Megapixels). The airborne visible imagery shown in Fig. 1 consists of uncalibrated, high spatial resolution, digital data with sparse ground coverage. The average spatial resolution of visible imagery is approximately 0.1 m.

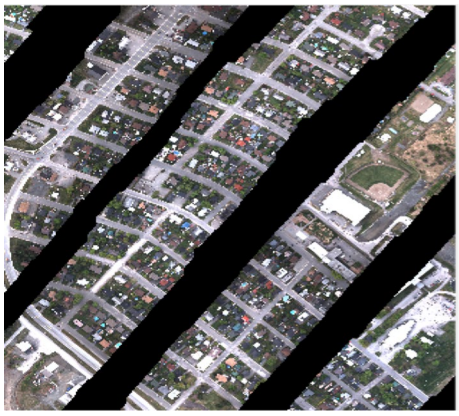


Fig. 1 High spatial resolution multispectral aerial imagery

3 Overview of spatial feature analysis

For supervised classification of engineered objects the accurate knowledge of features is highly important. The features aid in thematic feature extraction as they form the relevant and discriminative database necessary for separating one object/class from the other. Features are extracted by grouping similar characteristics of pixels in terms of their spatial and spectral domain.

3.1 Homogeneity analysis in spatial domain

Homogeneity analysis is the study of clusters of pixels in binary images that determines the connected regions (Aksoy et al. 2005). For each connected region, it provides the pixel properties or important features in the spatial domain such as color, area, perimeter, centroid and bounding box (Chang et al. 2004). Connected components are those clusters of pixels in a binary image that hold the same intensity values which are connected to each other by 4-pixel or 8-pixel connectivity (Celebi 2012).

3.2 Spatial shape feature set analysis

Shape features are indispensable if examining the context of each pixel in a spatial domain where the dominant shape of objects is rectangular. Therefore, in order to measure the spatial dimensions of spectrally similar connected pixels, the length and width direction line values for connected pixels are calculated. To discriminate objects such as buildings and roads, their size characteristics are of vital importance. These size features such as length and width direction line values are used to examine the contextual feature along the horizontal and vertical directions around the central pixel. Direction line (DL) histograms (Huang et al. 2007) are computed to evaluate the values of length and width of the spatially connected objects. Mathematically, these features are defined as (Hasani and Samadzadegan 2015):

$$\text{For length spatial feature:} L = \max\left(d_i(c)\right), \tag{1}$$

$$\text{For width spatial feature: } W = \min\left(d_i(c)\right). \tag{2}$$

where d_i is the direction line and c is the central pixel.

Along with the length and width direction line features, the pixel shape index (PSI) also contributes in extracting the shape features of spectrally similar connected pixels (Huang et al. 2008). PSI is a feature which measures the gray similarity distance in every direction with respect to the central pixel. It is the mean or sum of all the direction lines from the central pixel. The algorithm for computing the direction lines is as follows:

Mathematically, pixel homogeneity for a direction line is defined as:

$$PH_i = \left| p_{s(cen)} - p_{s(surr)} \right| \tag{3}$$

where PH_i represents the spectral homogeneity of the i_{th} direction between the central pixel and its surrounding pixel, *n* denotes the number of spectral bands, $p_{s(cen)}$ is the spectral value of the central pixel and $p_{s(surr)}$ denotes the spectral value of the surrounding pixel, which is on the direction line. After determining all direction lines D, the length of each direction line d_i is calculated. The shape index of the central pixel is the total length of all direction lines, which is defined as (Zhang et al. 2006):

$$PSI_{m,n} = \sum_{i=1}^{D} d_i, \tag{4}$$

where $PSI_{m,n}$ represents the shape index of the central pixel (m, n).

The shape index of the complete object is defined as:

$$PSI = \sum_{i=1}^{D} d_i / D. \tag{5}$$

There are three parameters of PSI: the total number of directions D, the extension of the direction line and the threshold T for pixel shape homogeneity which is required to be evaluated for better extraction of engineered objects in urban land surface. These parameters are discussed in detail under experiment section.

3.3 Gray level co-occurrence matrix

Gray level co-occurrence matrix (GLCM) is the most common second order statistical spatial feature technique (Bayram et al. 2011). GLCM reveals statistical properties

about the spatial distribution of the gray levels in the image. GLCM matrix calculates the frequency of occurrence of pixels 'i' with gray-level intensity or a tone either horizontally, vertically, or diagonally to adjacent pixels with the value 'j'. Once the matrix of GLCMs is created then several statistics listed in Table 1 can be deduced to obtain the information about the texture of an image (Borchani and Stamon 1997). The statistical features are calculated by considering the pixels in pairs in a predefined neighbourhood around the current pixel. Each element of GLCM describes the relative occurrence of two pixels within a predefined window size. The window size and the statistics used in this study are discussed under experiment section. These features are widely used in classification of images as high resolution imagery can describe the ground texture in detail.

Table 1 Textural features

Textural features	Formulae
Homogeneity	$\sum_{i=0}^{N-1}\sum_{j=0}^{N-1}\frac{g(i,j)}{1+\lvert i-j\rvert}$
Contrast	$\sum_{i=0}^{N-1}\sum_{j=0}^{N-1} g(i,j)\lvert i-j\rvert$
Energy	$\sum_{i=0}^{N-1}\sum_{j=0}^{N-1} g(i,j)^2$
Entropy	$\sum_{i=0}^{N-1}\sum_{j=0}^{N-1} g(i,j)\log g(i,j)$

where (i,j) are the coordinates in the co-occurrence matrix space; g(i,j) is the co-occurrence matrix value at that coordinate; *N* is the dimension of the co-occurrence matrix

4 Experiments

This study shows the impact of various features on classification of the engineered objects in an urban landscape from high spatial resolution remote sensing data. It also emphasises the classification accuracy of the engineered objects by comparing various classifiers in terms of spatial and spectral features. The following flowchart in Fig. 2 gives the pipeline of the process carried out in this study.

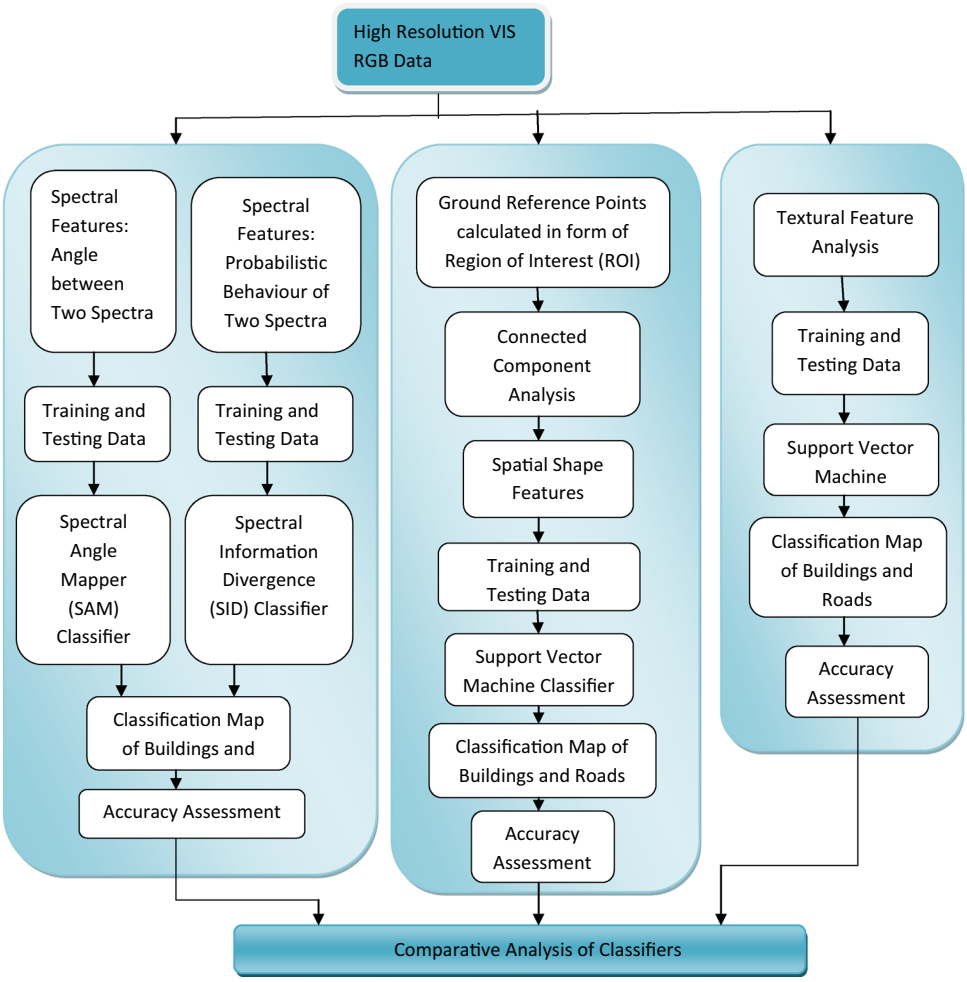


Fig. 2 Flowchart of the experiment

Two experiments are performed to test the effectiveness of the proposed methodology. The first experiment is designed to detect the influence of shape and size features on the extracted bounding box on connected regions. The features are used for classification of buildings and roads through a supervised classification algorithm. The second experiment is to compare the classification output using different spatial and spectral features. Both the experiments are carried on the dataset of Black Lake area of Thetford Mines, province of Québec, Canada.

4.1 Experiment I—influence of parameters of spatial shape features (SSF) on bounding box of connected regions

In this experiment the focus is on the extraction of two Engineered objects i.e., buildings and roads using SSF in urban areas. Although, these objects usually present analogous spectral features but have different shape and size characteristics, therefore these objects can be well identified by computing the spatial features.

4.1.1 Generation of bounding box

The following flowchart in Fig. 3 describes the pre-processing steps involved in generating the connected regions from VIS RGB data in carrying out this experiment.

Generally, the roads have smaller width and larger lengths, so the length–width ratio will be greater, whereas, in contrast the buildings have smaller length–width ratio and diverse shape characteristics. In the dataset available, the buildings have multifarious rectangular polygon shape structures, therefore, in this experiment 8- pixel connectivity is used to exploit the pixel properties which are connected horizontally, vertically and diagonally so that neighbour to every pixel is able to touch one of their edges or corners of multifarious structure. If CC_i be the i_{th} connected component of the binary image and CC_s be the set that includes all CC_i, then the bounding box feature of the connected component is defined as $B(CC_i)$ which is exploited to obtain the coordinates of the connected region. Bounding Box is an important and relevant pixel feature of connected component which builds the multifarious structure of roads and buildings to a object region in rectangular shaped polygon, where (Xl_i, Yl_i) is the top left coordinate and (Xr_i, Yr_i) is the bottom right coordinate of the polygon. Bounding box property helps in segmenting objects with homogenous pixel properties from the background. For this, labelled components of a rectangular bounding box polygon are automatically cropped and the image is displayed, which is shown in results section.

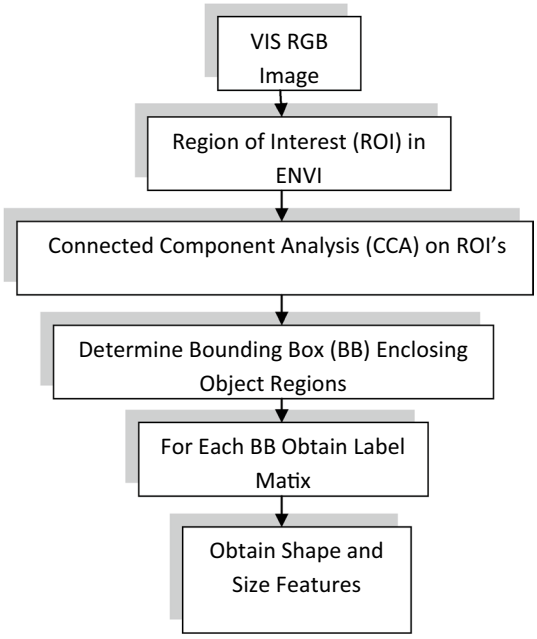


Fig. 3 Flowchart for depicting connected regions

4.1.2 Generation of spatial shape features

Shape and size spatial features are obtained from the bounding boxes of connected components. These spatial features are the length, width and PSI features. The features such as length and width are computed only in two directions around the central pixel which is inadequate to provide the essential information along the other directions. In this experiment, four directional lines for length and width measurements are proposed around the central pixel. The optimal choice of directional lines is highly important for describing the contextual structure around the central pixel. Two directions seem to be inadequate and more directions would unnecessarily add up spatial feature space generation leading to higher computations. Thus, the optimal feature sets of the central pixel in this experiment is formulated as d1: length and width values in horizontal direction, d2: length and width values in vertical direction, d3: length and width values diagonally at 45° to the horizontal direction and d4: length and width values diagonally at 135° to the horizontal direction around the central pixel. The following Fig. 4 shows the proposed direction lines throughout the central pixel.

The value of D is kept fixed in this experiment. Since, our problem is classification of buildings and roads that has diverse structural patterns in urban landscape, therefore, it is necessary to keep the feature length same. Next, the parameter is the length of each and every direction line. The total number of pixels for each and every direction line is determined by size of sliding window applied on the bounding box. Therefore, different sized sliding windows are experimented in respect to view the effect of spatial shape

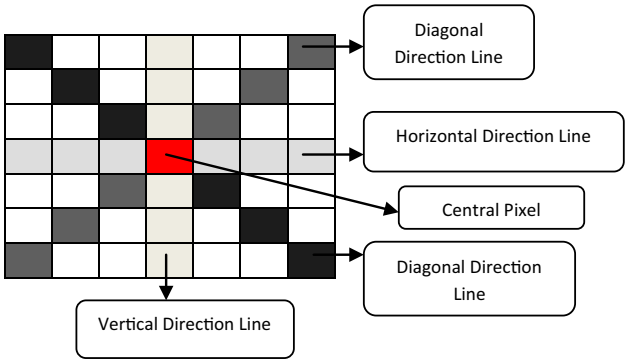


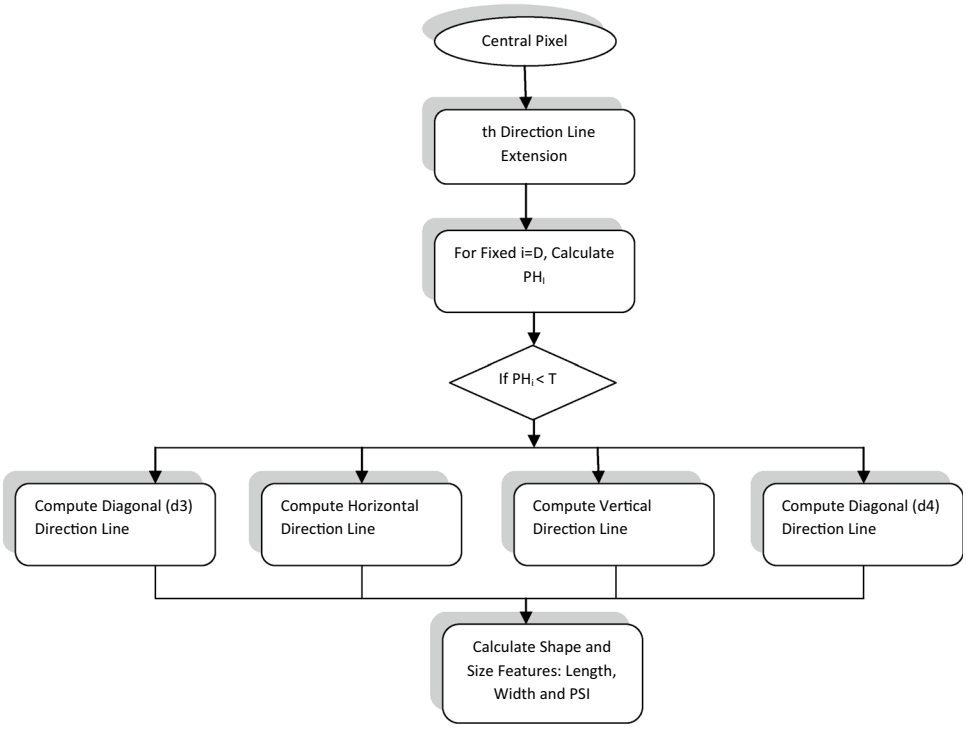
Fig. 4 Direction lines

features in every direction. The outcome of this experiment is discussed in the results section. The pixel homogeneity is calculated along horizontal, vertical and diagonal direction lines around the central pixel if the threshold condition is satisfied. The histogram sum is calculated for pixel homogeneity values. The maximum value of the histogram gives the length feature and the minimum value of the histogram gives the width feature. PSI is calculated by summing up all the length and width values for a fixed value of number of directions. The following Fig. 5 shows the step wise flow line of the parameters computed for proposed PSI shape feature.

These calculated features are extracted from the bounding box of the connected regions in order to extract the shape and spatial arrangement of the objects in the image. The influence of the calculated features on the bounding box was determined through experiments. The shape and size features were calculated on the each and every bounded box of the extracted number of the objects. It is seen that if the features are extracted once over the complete bounding box then the spatial arrangement and shape features are unable to provide sufficient contextual information of the objects. Therefore, in order to calculate the overall neighbourhood information within the bounding box the spatial shape features of an object are computed in a unique way. The bounding box of an object is divided in non-overlapping boxes in horizontal and vertical direction and then the local SSF features are computed for each box. The features of each box are concatenated and passed to SVM classifier for classification. This concept has been explained using Fig. 6. The feature computation of each box is explained in Fig. 7.

Figure 7 explains the SSF features computed considering the distribution of gray channel intensity in horizontal, vertical, 45° diagonal and 135° diagonal. To reduce the computational complexity, in SSF calculations directional lines are not chosen explicitly, rather it assumes four directions of directional lines and these directions are horizontal, vertical, 45° and 135°. In each direction, only the pixels whose intensity is less than a threshold from central pixel is considered in the histogram vector, and then this histogram vectors are used to further calculate features of SSF.

Fig. 5 Flowchart of shape and size features calculation



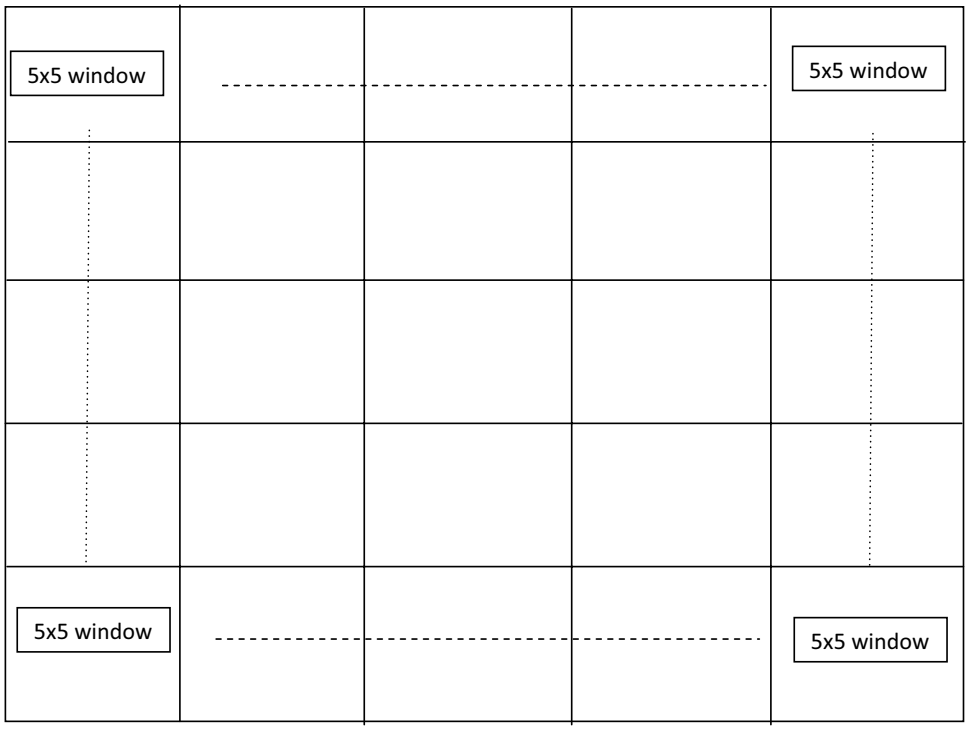


Fig. 6 Dividing 25 × 25 bounding box in 5 × 5 boxes/windows

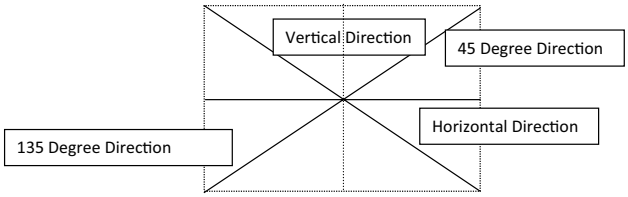


Fig. 7 Direction line in each window

4.1.3 SVM classification

The extracted features are divided into training and testing parameters which are fed to Support Vector Machine (SVM) classifier. To evaluate the classification performance of SVM, true positives of the concerned engineered objects are evaluated and the results are shown in next section. The following flowchart in Fig. 8 shows the steps involved in classifying the engineered objects on the basis of the proposed parameters used for computing shape and size features.

In this experiment, the features calculated on each window box in four directions around the central pixel for assessing the shape index for complete object are calculated which are shown in results section. These parameters forms the pixel shape features which are incorporated on bounding box in different windowing styles. The features are calculated on four different window sizes of bounding box and the effect of the shape features on each window style is shown in results section.

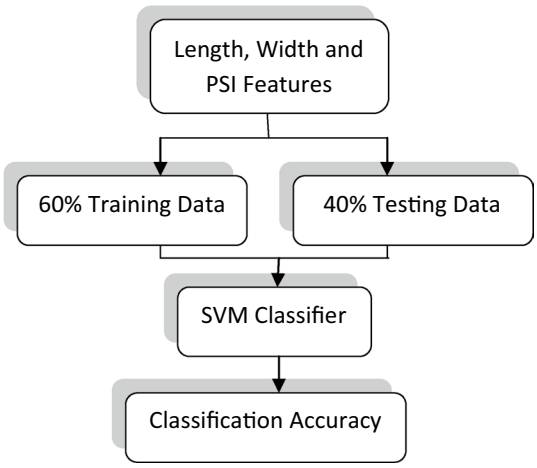


Fig. 8 Flowchart for classification

4.2 Experiment II—compare the classification effect from Spatial and spectral features

Another experiment is done to study the influence of spatial and spectral features on different classifiers. This experiment is carried out to study the potential use of dataset for different features and classifiers. For this, the effect of three classifiers is studied. Supervised learning algorithm i.e., Support Vector Machine (SVM) is trained and tested for textural and spatial shape features, whereas spectral features of the dataset are well explored for Spectral Angle Mapper (SAM) and

Spectral Information Divergence (SID) Algorithm. The classification assessment is carried out in terms of overall accuracy (OA), producer's accuracy (PA) and kappa co-efficient K_c. Further, the overall comparison of all the three classifiers is shown in terms of PA for buildings and roads. The steps required to perform this experiment is shown in Fig. 2.

4.2.1 Support vector machine classifier

Support Vector Machine (SVM) is a popular method of supervised classification. In this study, SVM approach of single classifier with multiple features as an input is used because of its fast and effective processing (Halldorsson et al. 2004). SVM classifiers (Melgani and Bruzzone 2004) of the form $f(x) = w\,\Phi(x) + b$ are made to learn from the data $\{x_i, y_i\}$, where x_i is an n- dimensional input feature vector, f(x) denotes the hyper-plane that separates the class labels on the basis of the support vectors on the hyper-plane $y_i = \pm 1$ on each side, w and b are the parameters i.e., weights and bias of the hyper-plane. The hyper-plane calculation can be optimized as follows (Camps-Valls and Bruzzone 2005):

$$\min_{w,b,\varepsilon} \frac{1}{2} w^2 + C \sum_{i=0}^{N} \varepsilon_i, \tag{6}$$

where C is a regularization parameter and ε_i is slack variable. The design parameters of SVM used in the experiment are tabulated in Table 3 in results section.

4.2.2 Spectral angle mapper

Spectral Angle Mapper (SAM) is a supervised spectral pixel based classification method. It performs classification based on spectral similarity between image spectra and reference spectra (Petropoulos et al. 2015). This algorithm determines the spectral similarity between the two spectra using angle measuring approach in n-D space to match target pixels with reference spectra (E.U.S. Guide 2008). Small angles between the two spectra determine high similarity and large angles between the two spectra determines the low similarity. The angles between the spectra are represented as vectors in a space with dimensionality equal to the number of bands. The angle α between the spectrum vector to be classified and the reference spectrum vector b is computed as:

$$\alpha = \cos^{-1}\left(\frac{\vec{a}.\vec{b}}{\| \vec{a} \| \| \vec{b} \|}\right), \tag{7}$$

The main advantage of using SAM classifier is that it is based only on the angular information and not affected by the solar illumination factors (Kruse et al. 1993).The design parameters of SAM classifier used in the experiment are explained under results section.

4.2.3 Spectral information divergence

Spectral information divergence (SID) is a supervised spectral based classifier that measures the discrepancy of probabilistic behaviours between the spectral signatures of the two pixels (Zhang et al. 2014). As this algorithm uses an information measure on the basis of divergence to match pixels to the reference spectra, therefore, it may be useful in preserving the spectral properties. The criterion for classification of the pixels for a particular class is that for more likely pixels the divergence will be smaller.

4.2.4 Accuracy assessment

Accuracy assessment of the thematic classification maps generated from SVM, SAM and SID is generated on the basis of confusion matrix analysis which is shown in results section. The parameters calculated are producer's accuracy (PA), overall accuracy (OA) and kappa statistical coefficient (K_c) (Congalton 2001). OA is the number of validated pixels that have been correctly classified to the total number of validated pixels used for all the classes. PA estimates the probability that the classifier has correctly labelled an image pixel. K_c is the proportion of correctly classified validated pixels after random agreements are removed.

5 Results and discussions

This section focuses on step by step analysis of the experiments conducted. Both experiments were conducted on aerial high resolution VIS RGB data of size 3769 × 4386 with 0.2 m spatial resolution which is shown in Fig. 1.

5.1 Experiment I—SVM classification of engineered objects using spatial shape features (SSF) on bounding box of connected regions

5.1.1 Generation of bounding box

First, the region of interest (ROI) in the form of polygon is obtained for two objects i.e., buildings and roads from VIS RGB data using ENVI software. This region of interest has objects in irregular shape, therefore, in order to extract the similar spatial properties it is required to study the pixel properties of irregular polygons by connected component analysis. From the connected component analysis, bounding box is extracted for both the objects which provide the information of coordinates of the polygons. The total number of

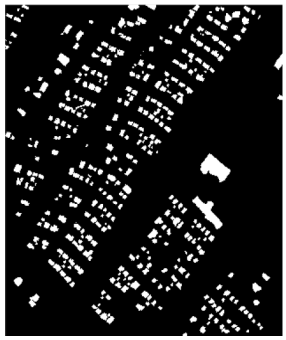


Fig. 9 Binary ROI of buildings



Fig. 10 Binary ROI of roads

bounding box generated for building is of size 456 × 4 and for roads it is of size 363 × 4. The binary image of the connected objects with similar pixel properties is segmented from the background and is displayed in Figs. 9 and 10. Since, the size of bounding boxes of the connected objects is dissimilar, therefore, it is necessary to resize them into same size. Hence for computational purpose, the bounding box of all the connected objects is resized to 25 × 25.

5.1.2 Generation of spatial shape features

In order to compute pixel shape homogeneity by PSI, the influence of three parameters i.e., directionality, total number of directions D and threshold T is studied in the algorithm. The directionality of the neighbouring pixels encountered from the central pixel is taken in four directions i.e. at 0°, 45°, 90° and 135°. The directionality of the direction lines are so chosen such that the similar pixel intensity object can be detected over all contours around the central pixel. Since, the spatial shape descriptors are used for computing the classification problem, therefore, the number of directions D is kept same i.e, 4 so that the entire feature length remains the same and does not lead to the computational burden.

Next, the extension of the direction line in all these four directions from the central pixel is calculated. For this, two styles of applying direction lines on bounding box are presented. In the first style, the shape homogeneity parameters are applied on the entire area of each bounding box of size 25 × 25 as explained in Fig. 3. The length of direction lines around the central pixel is the pixel elements in the current row till the length of the edge of the bounding box. For each direction line, from the central pixel, the absolute values of shape homogeneity are evaluated. Hence, the spatial shape feature in terms of length, width and PSI are evaluated which is explained in Eqs. 1–5. In the second style, window box of size 5 × 5, 1 × 5 and 1 × 1 is chosen which is moved over the original bounding box of size 25 × 25. For this movement, the window box is shifted both in rows and in columns as explained in Fig. 6. For 25 × 25 bounding box and the 5 × 5 window, a total of 25 non-overlapping window boxes are considered in horizontal and vertical direction by dividing the image in five equal parts in horizontal direction and five equal parts in vertical direction. The features are computed from each 5 × 5 window box. Since, each window is a small window of size 5 × 5, the four assumed directions for considering pixel distributions and then computing SSF feature should be good enough without losing any information. In each direction, only the pixels whose intensity is less than a threshold from central pixel is considered in the histogram vector, and then this histogram vectors are used to further calculate features of SSF.

Next, the parameter T which indicates the maximum spatial distance between the central pixel and its neighbouring pixel in the gray channel representation of image is to be chosen. It is a scaling factor in the algorithm and is pertinent to the spatial resolution of the data and the size of the region of interest of the bounding box on which the statistical features are evaluated. It is noted that as the parameter T increases from 10 to 120 the true positives for discriminating buildings and roads escalates. At T = 100 it reaches the maximum, then after T = 100 the true positive observation of the object "road" suddenly declines. Table 2 shows the calculation of correctly predicted objects i.e., buildings

Table 2 Calculation of correctly predicted objects *wrt* threshold

True Positive	Threshold											
	T = 10	T = 20	T = 30	T = 40	T = 50	T = 60	T = 70	T = 80	T = 90	T = 100	T = 110	T = 120
Buildings	62	68	100	100	100	56	100	100	100	100	98	96
Roads	64	58	60	0	68	0	69	0	66	73	0	0

and roads for various values of the threshold. The value of threshold ought to be determined through experiments as this parameter is related with the shape and spatial arrangement of objects in the data.

5.1.3 SVM classification

Table 3 shows the total number of training and testing bounding box of buildings and roads. The set of three spatial shape features i.e., length, width, PSI direction line histograms are obtained from bounding box areas of buildings and roads by the proposed windowing technique. The size of feature space is a vector of size 75 × 456 for buildings and 75 × 363 for roads. Computational complexity is of order n, O (n), where n is number of pixel, since the feature depends on the histogram at the core of computation. The total compute time for calculating spatial shape features is 20.27 ms and the average time for computing spatial shape features is 0.81 ms. The calculated features are divided into training and testing samples. Table 4 shows the number of training and testing spatial shape features obtained by moving non overlapping window of size 5 × 5 on bounding box of connected components of buildings and roads. These spatial shape features are the input features for training SVM classifier.

The design of SVM for this specific application involves computing of class labels for each pixel in training and testing spatial shape features. The class labels are trained and establish the parameters for the classifier which is shown in Table 5.

The linear SVM trained classifier is applied to testing spatial shape feature class labels to distinguish the two classes i.e., buildings and roads on the basis of the optimized hyperplane generated from the parameters listed in Table 5. The classification map is generated from SVM classified results which is shown in Fig. 11.

Table 3 Training and Testing Samples

Class	Samples		
	Training bounding box	Testing bounding box	Total number of bounding box
Buildings (60% of total number of bounding box)	274	182	456
Roads (40% of total number of bounding box)	218	145	363
Total	492	327	819

Table 4 Training and Testing SSF Features

Feature training and testing samples for classes	SSF _training features	SSF _testing features
Buildings	75 × 274	75 × 182
Roads	75 × 218	75 × 145

5.1.4 Accuracy assessment

The classification accuracy of buildings and roads are calculated in terms of PA. The classification accuracy of buildings and roads by the influence of spatial shape features on various windowing techniques by SVM classifier is shown in Table 6.

The accuracy statistics in Table 6 shows that the SVM classifier results on spatial shape features calculated by the proposed parameters by moving non overlapping window of size 5 × 5 on the bounding box of connected components shows better results for extraction of buildings and roads. The high accuracy of classifying roads indicates that the stack of spatial shape descriptors may enhance and exploit the structural characteristics of elongated engineered objects in urban landscape.

5.2 Experiment II—compare the classification effect from spatial and spectral features

5.2.1 Features extraction

5.2.1.1 Spatial features: textural features The textural features are calculated on the connected regions using GLCM approach. The parameters are calculated by applying window of size 3 × 3 onto the bounding box coordinates. Two spatial statistical parameters are calculated i.e., contrast and homogeneity for each visible band. In total 486 features are obtained, in which textural feature space of 81 GLCM contrast and homogeneity values on each visible band of the data is obtained.

The range of the contrast between a pixel and its neighbor the whole image is given as:

$$\text{Range} = [0 \left(\text{size}\,(\text{GLCM}, 1) - 1^2\right]. \tag{8}$$

Table 5 Design parameters of SVM for spatial shape features

Design parameters of SVM	Support vector	Alpha	Bias	Kernel function
Buildings	291 × 75	291 × 1	3.2196	Linear
Roads	311 × 75	311 × 1	−0.0161	Linear

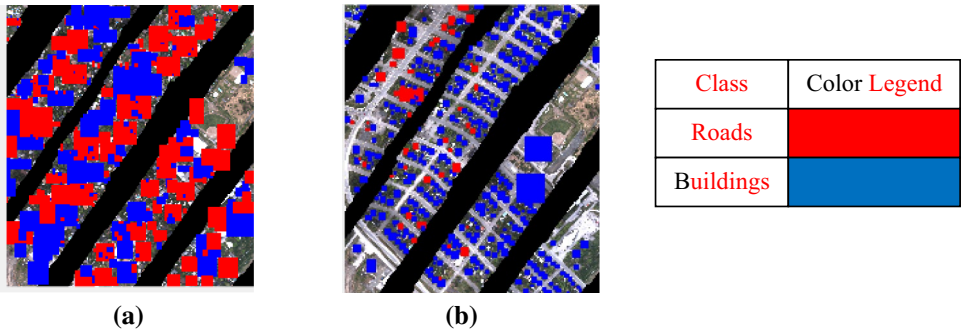


Fig. 11 Classification map of using spatial shape features: **a** Roads and **b** buildings

Table 6 Accuracy assessment for spatial shape features

Accuracy assessment (%)	Input features			
	Shape features extracted from bounding box of size 25×25	Shape features extracted from proposed window (5×5) on bounding box	Shape features extracted from proposed window (1×5) on bounding box	Shape features extracted from proposed window (1×1) on bounding box
	SVM classification			
Producer's accuracy for object building (%)	100	100	100	100
Producer's accuracy for object road (%)	0	97.3	51	0

Shape features are calculated by keeping the parameter D = 4, direction lines at 0°, 45°, 90° and 135°, T = 100

In our experiment, the minimum value of contrast is 0 where the constant intensity values of the objects are seen. The maximum value of contrast is 0.667 which defines the difference in brightness of the bldings and roads within the same field of view.

The range of homogeneity statistical parameter lies in the range of [0 1]. In our experiment, the minimum value of this statistics is 0.667 and the maximum value observed is 1. Homogeneity statistics is 1 for a diagonal GLCM which defines the closeness of the distribution of the pixel elements for buildings and roads.

5.2.1.2 Spectral features: mean spectra The mean spectra of the training spectra for both the objects i.e., buildings and roads is obtained from the ENVI software. This training spectra is used in SAM and SID classifiers to obtain the angle and information measure for classifying the objects.

5.3 Classifiers

5.3.1 Spectral angle mapper

On the basis of the mean spectral signature generated for the objects buildings and roads in this experiment, for SAM classification, a single value of 0.3 radians is used as the maximum classification threshold value. This is selected after the careful consideration of different threshold angle values between the reference and testing spectrum on the basis of the classification accuracy assessment. The classified image is shown in Fig. 12. The color legend chosen for object road is "red", for object building is "green".

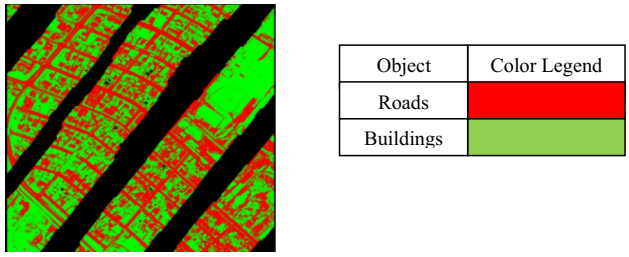


Fig. 12 Classification map of buildings and roads by SAM classifier

5.3.2 Spectral information divergence

In this experiment, for SID classification the similarity measure between the reference spectra and testing spectra the threshold value of cross entropy is chosen to be 0.050. If the cross entropy of reference and testing pixels is less than 0.050 then the spectra has similar probabilistic

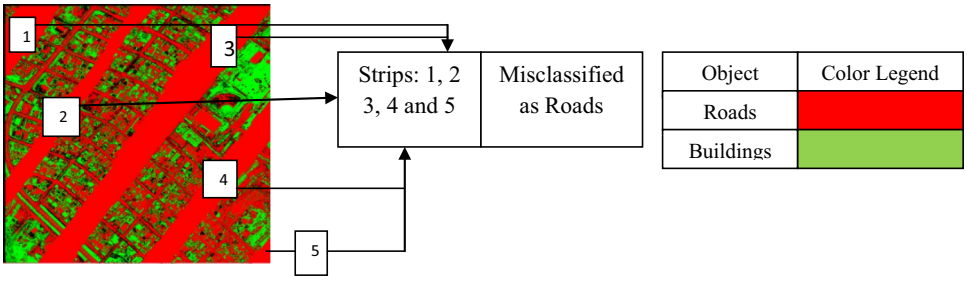


Fig. 13 Classification map of buildings and roads by SID classifier

Table 7 Training and testing textural features

Feature training and testing samples for classes	Textural training features	Textural testing features
Buildings	486×274	486×182
Roads	486×218	486×145

Table 8 Design Parameters of SVM for Textural Features

Design parameters of SVM	Support vector	Alpha	Bias	Kernel function
Buildings	701×486	701×1	−0.3839	Linear
Roads	701×486	701×1	−0.3839	Linear

measure and the testing pixels is classified to the reference pixel otherwise it is considered to be misclassified. If the probabilistic measure between the two pixels is more than 0.050, then lesser is the possibility of the matching of testing pixel with the reference pixel. The classification map for buildings and roads on the basis of spectral features is shown in Fig. 13. The color legend chosen for object road is "red" and for object building is "green".

5.3.3 Support vector machine

Textural features obtained from bounding box areas of buildings and roads form training and testing datasets. Table 7 shows the number of training and testing spatial textural features obtained. These spatial textural features are the input features for training linear SVM classifier.

The class labels are trained and establish the support vector and bias parameters for the classifier which is shown in Table 8. The linear SVM trained classifier is applied to testing textural feature class labels and on the basis of the optimized hyper-plane generated from SVM classifier the engineered objects are distinguished.

The classification map generated from SVM classified results on the basis of textural features is shown in Fig. 14.

5.4 Assessment of classification

The assessment of classification by spectral classifiers show that SAM classifier performs better than SID for classifying the engineered objects particularly buildings and roads. The overall accuracy and K_c parameters are high for SAM classification as this algorithm is based on the angular similarity between the reference and testing spectra's of buildings and roads which may be different due to their structural dissimilarity. The following Table 9 shows the OA and K_c statistical assessment for both the classifiers. The classification map generated from SID classifier in Fig. 12 clearly shows that

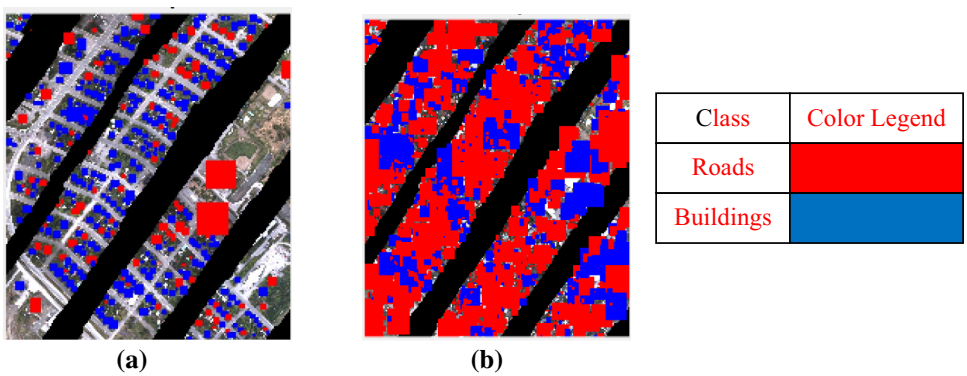


Fig. 14 Classification map using textural features by SVM: **a** Buildings and **b** Roads

Table 9 Accuracy Assessment of Spectral Classifiers

Accuracy assessment	SAM	SID
K_c	0.6123	0.437
OA (%)	80.09	66.52

Table 10 SVM classified training and testing true positive percentage

True positives of engineered objects	Training percent (%)	Testing percent (%)
Buildings	100	100
Roads	74	73

Table 11 Classification accuracy of spatial and spectral features

Producers' accuracy	Shape features SVM	Spectral features SID	Spectral features SAM	Textural features SVM
Buildings	100	51.04	96.70	77.0
Roads	97.3	86.22	66.83[a]	58.2

[a]High producers' accuracy of roads is due to misclassification of non-informative area in the data as roads, which can be seen in Fig. 12. The overall accuracy of SID is low due to this factor which is shown in Table 9

the roads are highly misclassified for the strips in the data that has no information.

Further, in Table 10 the classification effect of spatial shape features using SVM algorithm is shown. It is clear from the table that for buildings 100% true positives are obtained from the labelled supervised training data and for roads the achieved true positives are 73% from the 74% of labelled supervised learning data. The classification accuracy of engineered objects from spatial shape features can be seen from Table 11. It shows the comparative analysis of the achieved classified results with respect to other conventionally existing spectral feature classifiers i.e., SAM and SID. Also, the comparison is performed with SVM based classification using textural features. It can be seen that the classification accuracy of buildings and roads has been improved by the proposed parameters of the spatial shape features (Table 11).

The higher performance of SVMs can be attributed to the higher capability of finding the optimal hyper-plane for separating the similar characterised classes. The higher classification accuracy of SVM shows that it is the best class separation classifier than SAM and SID classifiers though SAM and SID classifiers are easy and rapid in implementation.

6 Conclusion

Spatial shape descriptor based classification for objects exhibiting similar spectral characteristics in high resolution remote sensing imagery is the main aim of this objective. This has been achieved by exploring the parameters of pixel shape descriptors. The proposed methodology of applying the shape descriptors on the connected components using SVM classifier has improved the classification accuracy of the engineered objects. Further, the classification accuracy of different classifiers on the basis of textural and spectral features is also studied. The results confirm that only spectral features may not be sufficient in high spatial resolution remote sensing imageries for classifying engineered objects. SVMs have outperformed in identifying buildings by shape features in comparison to SAM and SID classifiers using spectral features. Although the classification accuracy of roads seems better in SID classifiers but the lower values of kappa coefficient and overall accuracy has helped in determining that the higher producers' accuracy of roads is due to misclassification of road pixels in this class. The erroneous judgement of roads may be due to spectrally similar angle and information measures in reference and testing spectra's. This verification has embarked the usefulness of spatial shape descriptors in identifying the engineered objects in urban landscape.

The findings in this study are relevant for urban planners as it may aid them in understanding and planning infrastructure development. Further, the results of this objective show significant contribution in extraction of buildings and roads with the help of spatial shape descriptors.

References

Aksoy S et al (2005) Multi-resolution segmentation and shape analysis for remote sensing image classification. In: IEEE international conference on recent advances in space technology

Angelov P, Sadeghi-Tehran P, Ramezani R (2010) An approach to automatic real-time novelty detection, object identification, and tracking in video streams based on recursive density estimation and evolving Takagi–Sugeno fuzzy systems. Int J Intell Syst 26(3):189–205

Bayram U, Can G, Duzgun S, Yalabik N (2011) Evaluation of textural features for multispectral images. In: XVII Proceedings on image and signal processing for remote sensing. SPIE, p 8180

Benediktsson JA, Pesaresi M, Arnason K (2003) Classification and feature extraction for remote sensing images from urban areas based on morphological transformations. IEEE Trans Geosc Remote Sens 41(9):1940–1949

Borchani M, Stamon G (1997) Texture features for image classification and retrieval. In: Proceedings on multimedia storage and archiving systems II, SPIE **3229**

Camps-Valls G, Bruzzone L (2005) Kernal-based methods for hyperspectral image classification. IEEE Trans Geosci Remote Sens 43(6):1351–1362

Celebi ME (2012) A simple and efficient algorithm for connected component labeling in color images. Image Process Algorithms Syst X Parallel Process Imaging Appl II 8295(1)
Chang F, Chen C-J, Lu C-J (2004) A linear time component labelling algorithm using contour tracing technique. Comput Vis Image Underst 93(2):206–220
Congalton RG (2001) Accuracy assessment and validation of remotely sensed and other spatial information. Int J Wildland Fire 10(4):321–328
Dong Y, Milne AK, Forster BC (2001) Segmentation and classification of vegetated areas using polarimetric SAR image data. IEEE Trans Geosci Remote Sens 39(2):321–329
Dong Y, Forster BC, Milne AK (2009) Segmentation of radar imagery using Gaussian Markov random field model. Int J Remote Sens 20(8):1617–1639
Gu X, Angelov PP, Zhang C, Atkinson PM (2018) A massively parallel deep rule-based ensemble classifier for remote sensing scenes. IEEE Geosci Remote Sens Lett 15(3):345–349
Guide EUS (2008) ENVI On-line software user's manual. ITT Visual Information Solutions
Halldorsson GH, Benediktsson JA, JR Sveinsson (2004), Source based feature extraction for support vector machines in hyperspectral classification. Proc IEEE Int Geosci Remote Sens Symp 536–539
Han Y, Kim H, Choi J, Kim Y et al (2012) A shape–size index extraction for classification of high resolution multispectral satellite images. Int J Remote Sens 33(6):1682–1700. https://doi.org/10.1080/01431161.2011.599348
Hasani H, Samadzadegan F (2015) 3D Object classification based on thermal and visible imagery in urban area. Int Arch Photogramm Remote Sens Spat Inform Sci XL-1/W5
Herold M, Roberts DA, Gardner ME et al (2004) Spectrometry for urban area remote sensing—development and analysis of a spectral library from 350 to 2400 nm. Remote Sens Environ 91:304–319
Huang X, Zhang L, Li P (2007) Classification and extraction of spatial features in urban areas using high-resolution multispectral imagery. IEEE Geosci Remote Sens Lett 4(2):260–264
Huang X, Zhang L, LI P (2008) Classification of very high spatial resolution imagery based on the fusion of edge and multispectral information. Photogramm Eng Remote Sens 74:1585–1596
IEEE GRSS (2014) Data fusion contest, presented to image analysis and data fusion technical committee. IEEE Geoscience and Remote Sensing Society (GRSS)
Im J, Lu Z, Rhee J, Quackenbush LJ (2012) Impervious surface quantification using a synthesis of artificial immune networks and decision/regression trees from multi-sensor data. Remote Sens Environ 117:102–113
Kruse F et al (1993) The spectral image processing system (SIPS)—interactive visualization and analysis of imaging spectrometer data. Remote Sens Environ 44(2):145–163
Ll M, Zang S et al (2018) Spatial and temporal variation of the urban impervious surface and its driving forces in the central city of Harbin. J Geography Sci 28(3):323–336
Luca D et al (2014) Assessing the performance of two unsupervised dimensionality reduction techniques on hyperspectral APEX data for high resolution urban land-cover mapping. ISPRS J Photogramm Remote Sens 87:166–179
Lv ZY et al (2014) Morphological profiles based on differently shaped structuring elements for classification of images with very high spatial resolution. IEEE J Sel Topics Appl Earth Obs Remote Sens 7(12):4644–4652
Maimaiti B, Ding J, Simayi Z, Kasimu A (2017) Characterizing urban expansion of Korla city and its spatial-temporal patterns using remote sensing and GIS methods. J Arid Land 9(3):458–470
Melgani F, Bruzzone L (2004) Classification of hyperspectral remote sensing images with support vector machines. IEEE Trans Geosci Remote Sens 42(8):1778–1790
Myint SW, Lam NSN, Taylor JM (2004) Wavelets for urban spatial feature discrimination: comparisons with fractal, spatial autocorrelation, and spatial co-occurence approaches. Photogramm Eng Remote Sens 70(7):803–812
Nithya S, Ramakrsishnan S (2018) Local line directional neighbourhood pattern for texture classification. EURASIP J Image Video Process. https://doi.org/10.1186/s13640-018-0347-x
Ouma YO, Tetuko J, Tateishi R (2008) Analysis of co-occurrence and discrete wavelet transform textures for differentiation of forest and non-forest vegetation in very-high resolution optical-sensor imagery. Int J Remote Sens 29:3417–3456
Pesaresi M, Benediktsson JA (2001) A new approach for the morphological segmentation of high-resolution satellite imagery. IEEE Trans Geosci Remote Sens 39(2):309–320
Petropoulos GP, Kalivas DP et al (2015) Urban vegetation cover extraction from hyperspectral imagery and geographic information system spatial analysis techniques: case of Athens, Greece. J Appl Remote Sens 9(1):096088
Sargana AB et al (2017) A comprehensive review on handcrafted and learning-based action representation approaches for human activity recognition. Appl Sci 7(1):110
Shackelford AK, Davis CH (2003) A combined fuzzy pixel-based and object-based approach for classification of high-resolution multispectral data over urban areas. IEEE Trans Geosci Remote Sens 41:2354–2363
Shi W, Miao Z, Wang Q, Zhang H (2014) Spectral–spatial classification and shape features for urban road centerline extraction. IEEE Geosci Remote Sens Lett 11(4):788–792
Small C (2003) High spatial resolution spectral mixture analysis of urban reflectance. Remote Sens Environ 88:170–186
Small C (2016) Projecting the urban future: contributions from remote sensing. Spat Demogr 4(1):17–37
Usman M, Liedl R, Shahid MA, Abbas A (2015) Land use/land cover classification and its change detection using multi-temporal MODIS NDVI data. J Geogr Sci 25(12):1479–1506
Van der Linden S, Janz A, Waske B et al (2007) Classifying segmented hyperspectral data from a heterogeneous urban environment using support vector machines. J Appl Remote Sens 1(1):013543
Weng Q (2012) Remote sensing of impervious surfaces in the urban areas: requirements, methods, and trends. Remote Sens Environ 117:34–49
Zhang Y (1999) Optimisation of building detection in satellite images by combining multispectral classification and texture filtering. ISPRS J Photogramm Remote Sens 54:50–60
Zhang L, Huang X, Huang B, Li P (2006) A pixel shape index with spectral information for classification of high spatial resolution remotely sensed imagery. IEEE Trans Geosci Remote Sens 44(10):2950–2961
Zhang E, Zhang X, Yang S, Wang S (2014) Improving hyperspectral image classification using spectral information divergence. IEEE Geosci Remote Sens Lett 11(1):249–253
Zhou X, Angelov P (2006) Real-time joint landmark recognition and classifier generation by an evolving fuzzy system. In: IEEE international conference on fuzzy system, pp 1205–1212
Zhou X, Angelov P (2007) Autonomous visual self-localization in completely unknown environment using evolving fuzzy rule-based classifier. In: IEEE Conference on computational intelligence in security and defence applications 131–138
Zhu C, Yang X (1998) Study of remote sensing image texture analysis and classification using wavelet. Int J Remote Sens 19(16):3197–3203

Publisher's Note Springer Nature remains neutral with regard to jurisdictional claims in published maps and institutional affiliations.

emeraldinsight

VINE Journal of Information and Knowledge Management Systems

The impact of knowledge management system on student performance: A case study of the University of Delhi

Namita Jain, Vikas Gupta,

Article information:

To cite this document:
Namita Jain, Vikas Gupta, (2019) "The impact of knowledge management system on student performance: A case study of the University of Delhi", VINE Journal of Information and Knowledge Management Systems, Vol. 49 Issue: 1, pp.115-135, https://doi.org/10.1108/VJIKMS-07-2018-0065
Permanent link to this document:
https://doi.org/10.1108/VJIKMS-07-2018-0065

Downloaded on: 05 March 2019, At: 20:25 (PT)
References: this document contains references to 102 other documents.
To copy this document: permissions@emeraldinsight.com
The fulltext of this document has been downloaded 14 times since 2019*
Access to this document was granted through an Emerald subscription provided by emerald-srm:544911 []

For Authors

If you would like to write for this, or any other Emerald publication, then please use our Emerald for Authors service information about how to choose which publication to write for and submission guidelines are available for all. Please visit www.emeraldinsight.com/authors for more information.

About Emerald www.emeraldinsight.com

Emerald is a global publisher linking research and practice to the benefit of society. The company manages a portfolio of more than 290 journals and over 2,350 books and book series volumes, as well as providing an extensive range of online products and additional customer resources and services.

Emerald is both COUNTER 4 and TRANSFER compliant. The organization is a partner of the Committee on Publication Ethics (COPE) and also works with Portico and the LOCKSS initiative for digital archive preservation.

*Related content and download information correct at time of download.

Downloaded by Delhi Technological University At 20:25 05 March 2019 (PT)

The current issue and full text archive of this journal is available on Emerald Insight at:
www.emeraldinsight.com/2059-5891.htm

The impact of knowledge management system on student performance

A case study of the University of Delhi

Namita Jain
Delhi School of Management, Delhi Technological University, Delhi, India and Shri Ram College of Commerce, Delhi, India, and

Vikas Gupta
Delhi School of Management, Delhi Technological University, Delhi, India

Received 28 August 2018
Revised 9 December 2018
Accepted 31 December 2018

Downloaded by Delhi Technological University At 20:25 05 March 2019 (PT)

Abstract

Purpose – The purpose of this paper is to empirically test the role of knowledge management system (KMS) on the performance of students in higher educational institutions (HEIs).

Design/methodology/approach – Building on the extensive review of literature, the authors explored the factors of KMS to arrive at the conceptual model which was then validated using structural equation modeling. For the quantitative analysis, data were collected from undergraduate students using questionnaires distributed both through online and offline modes.

Findings – Empirical evidence supports the view that KMS have a direct and significant impact on the student performance (SP) in HEIs.

Research limitations/implications – The data are limited to 311 undergraduate students from the University of Delhi, India.

Practical implications – With the onset of national rankings framework like NAAC (National Assessment and Accreditation Council), NIRF (National Institutional Ranking Framework) and the attempt to achieve global recognition in THE (Times Higher Education), Quacquarelli Symonds and other world university rankings, the HEIs are trying hard to improve their performance comprehensively. In such a scenario, this paper provides insights into how HEIs can enhance performance of its students by harnessing KMS.

Originality/value – The current paper empirically validates the effect of KMS on the performance of students in an educational institution. While the impact of KMS on performance is measured empirically in corporations, such studies are scanty in academic centers. Moreover, while measuring the performance in HEIs using KM, the focus on ranking parameters has never been there. Such an orientation is essential as the rankings are getting wide acceptance from a global audience.

Keywords Technology, Knowledge management system, Rankings, Higher educational institutions, Student performance

Paper type Research paper

1. Introduction

The progress of a nation largely depends on its education system, which in turn has the potential to do justice to its clients (students) if it can make available the right knowledge at the right time to enable one to take the right decision.

The above statement calls for an appropriate knowledge management system (KMS) in education. With the advent of globalization and cross-border movement of students, institutes want to obtain top ranks in global ranking systems to increase their visibility and

VINE Journal of Information and Knowledge Management Systems
Vol. 49 No. 1, 2019
pp. 115-135
© Emerald Publishing Limited
2059-5891
DOI 10.1108/VJIKMS-07-2018-0065

Downloaded by Delhi Technological University At 20:25 05 March 2019 (PT)

attract international students (Shastry, 2017). To attain this objective, there must be a portrayal of excellent graduation outcomes, success in innovation projects, good placements and internships. The students world over demand greater exposure, rewarding skillsets and learning opportunities. Similarly, industry demands skills that are readily transferable to industry (Murthy, 2010). Given such rising expectations from all potential stakeholders and challenging goals, proper management of the education system is imperative to maximize the potential and productivity of available resources, limited in nature.

The paper proposes that such demands can be met by an effective KMS application in the institutes. If done efficiently, KMS can lead to improved teaching, better research, innovation, additional sources of income, exposure to overseas opportunities and skill development (Kidwell *et al.*, 2001). In this endeavor, information and communications technology (ICT) can act as a catalyst by reducing spatial and temporal barriers and improving access to knowledge (Hendriks, 1999). In fact, if latest ICTs are used to their full potential, it can revolutionize the teaching-learning process. Nowadays information technology is used extensively to facilitate knowledge management which is also referred to as KMS (Alavi and Leidner, 2001). According to Rah *et al.* (2010) KMS refers to "a (generally IT based) system for managing knowledge in organizations, supporting creation, capture, storage and dissemination of information."

The objective of this paper is to test the role of KMS on the performance of students in Indian higher educational institutions (HEIs). India is a developing nation characterized by low per capita income and high density of young population. About 50 per cent of its population is under the age of 25 years and this demographic dividend is expected to peak by 2020 as per the economic survey 2017 (Sethi, 2017). As the nation progresses in a knowledge-driven society, Indian students will become the largest consumer of higher educational services in the world. As per UNESCO report 2016, 2.5 lac Indian student migrate to other countries for higher studies and spend about $3.7bn toward their maintenance (Krishnan, 2017). This situation may be because of the dearth of globally recognized institutes in India and growing competition for limited seats in them. As per THES and Quacquarelli Symonds (QS) ranking 2018, only six HEIs in India could make it to the top 400 and none could make it to the top 100. The study by NASSCOM also reveals that only a fourth of Indian graduates are readily employable (Choudhari and Arya, 2011). Under such circumstances, the present study investigates the role of KMS in shaping the skills and improving the performance of students in HEIs in India. For this purpose, data were collected from the University of Delhi which is a renowned Central university in the capital and attracts students from all over the country. The main campus colleges being the hub of educational activity were directly approached with the structured questionnaire. Besides online circulation was also done via applications like WhatsApp, e-mail and so on.

2. Literature review and research synthesis

2.1 Knowledge and knowledge management

Knowledge starts with data (raw facts), figures and numbers. Information is data put into context after appropriate processing. Knowledge is information which can be acted upon. It incorporates experience and judgment which enables efficient decision-making (Laal, 2011).

KM is a discipline that promotes an integrated approach to identifying, capturing, evaluating, retrieving, and sharing all of an enterprise's information assets. These assets may include databases, documents, policies, procedures, and previously un-captured expertise and experience in individual workers" (Duhon, 1998). According to Gates (2000), "KM is a very clever term to describe a very simple subject. Many of us simply do not think in terms of managing knowledge, but we all do it. Each of us is a personal store of

Downloaded by Delhi Technological University At 20:25 05 March 2019 (PT)

knowledge with training, experiences, and informal networks of friends and colleagues, whom we seek out when we want to solve a problem or explore an opportunity". The concept of KM exists for decades, but most organizations accept it only as theory and have not put it into practice correctly. Educational institutions do engage in knowledge transfer from teacher to students, but only some of them contribute to knowledge creation, knowledge acquisition, and knowledge documentation. No attempt is made to capture the tacit knowledge (knowledge that resides in mind) of the educators who retire or resign and the students completing their respective courses. Even if the information is captured, it may not be well documented, leading to knowledge loss. Many institutions lack the open knowledge sharing culture. Literature supports the view that knowledge is a valuable resource that requires proper holistic management.

2.2 Research synthesis

Several papers studied the concept of KM in education, but limited studies validated the impact of KM on organizational performance, though they have been undertaken in the corporate world. The Table I below abstracts the research in not only the education sector but the corporate sector too. This is so because the empirical studies of corporate can be replicated in HEIs with some variations.

From Table I, it can be inferred that most studies established a significant positive relationship between KM and performance (Nasser H. Zaied *et al.*, 2012; Rasula *et al.*, 2012; Gholami *et al.*, 2013; Lee and Choi, 2003) while some other studies could not establish a significant direct relation between KM and organization performance (Masa'deh *et al.*, 2017; Mills and Smith, 2011; Ferraresi *et al.*, 2012; Abualoush *et al.*, 2018). The analysis revealed that KM can improve business performance only if it is applied in true spirit taking care of the other organizational characteristics. Organizations must strategically implement KM to achieve the desired outcome (Ho, 2008).

3. Research gap

As can be seen from Table I, most papers studied the relationship between KMS and corporate performance, but limited research has been carried out in the educational sector whose parameters are different. Even the concept of "KM in education" is not well understood. Very few HEIs, especially in developing countries, actively research or produce new knowledge (Bratianu, 2011; Gill, 2009). In addition, seemingly no attempt is made to capture the tacit knowledge (knowledge that resides in mind) of the educators who retire or resign and the students completing their respective courses. Many institutions even lack the culture that promotes knowledge sharing and innovation. Thus, there arises a need to measure KMS in HEIs and its likely influence on performance.

3.1 Objective

The objective is to find the relationship between KMS and student performance (SP) in HEIs. To achieve this objective, data were collected through a structured questionnaire and structural equation modeling was applied to find the effect of independent variable KMS on dependent variable SP.

4. Background and construct development

Nonaka (1991) in his article "Knowledge Creating Company" popularized the notion of types of knowledge which is tacit (personal and embedded in the minds of individual) and explicit (expressed and captured). According to Siakas *et al.* (2010), in an organization, working

Downloaded by Delhi Technological University At 20:25 05 March 2019 (PT)

Table I.
Empirical studies in KM

Sr No.	Independent variable	Dependent variable	Sample	Technique	Findings	Author and year
1	KM process	Job performance	Lecturers at Jordan University	SEM	KM processes positively affect KM performances which further affect job performance. Though there is limited influence of KM on job performance	Masa'deh *et al.* (2017)
2	KM measured through knowledge transfer, acquisition, documentation, creation and application	Organizational learning	Mixed methodology approach was adopted. Data were collected from 270 respondents of 6 HEIs in Uganda. 13 interviews were conducted	Correlation, regression and canonical correlation was performed	There exists interdependent relationship between KM and organizational learning	Turyasingura (2011)
3	Organizational culture	KM	Teaching staff of two public faculties in Central Europe	Correlation	There is statistically significant correlation between different types of organizational culture and KM processes	Omerzel *et al.* (2011)
4	Entrepreneurship	KM	Employees of Islamic Azad University	Path analysis using LISREL	Entrepreneurship has a direct effect on KM	Nazem (2015)
5	KM	Academic performance	41 colleges in Iraqi HEIs	Correlation and regression	Iraqi HEIs can benefit from KM processes	Zwain *et al.* (2012)
6	KM	Quality education	University leaders in Nepal	Conceptual model	KM tools are useful to quality education	Raj Adhikari (2010)
7	Factors related to KM in education have been explored Public and private HEIs in Malaysia		Public and private HEIs in Malaysia	Factor analysis, T-test	There are significant differences in KM processes with respect to public and private HEIs	Ramachandran *et al.* (2009)
8	Culture, attitude, motivation, opportunities and nature of knowledge	Knowledge sharing	Teaching staff of public and private HEIs in Malaysia	Cross-sectional survey. ANOVA, regression was applied	Positive relation between the IDV and DV for both public and private HEIs	Sadiq Sohail and Daud (2009)
9	KM capability in KM processes	KM effectiveness	Experts in Thailand	Qualitative analysis including Literature Review	Indicators of Knowledge acquisition, creation, storage and application were identified	Aujirapongpan *et al.* (2010)

(*continued*)

Downloaded by Delhi Technological University At 20:25 05 March 2019 (PT)

Sr No.	Independent variable	Dependent variable	Sample	Technique	Findings	Author and year
10	KM measured through knowledge acquisition, conversion, use and protection	Business Performance	Web based survey of 241 Brazilian companies	Structural equation modeling (SEM)	KM affects business performance through strategic orientation and innovativeness. This strategic bent enables companies to foresee and counter market changes	Ferraresi *et al.* (2012)
11	KM infrastructure and processes	Organizational performance	Egyptian organizations	Correlation, regression in SPSS	If quality of knowledge is good, management performance improves significantly	Nasser H. Zaied *et al.* (2012)
12	KM practices measured through IT, organization and knowledge elements	Organizational performance	Data from 329 companies of Slovenia and Croatia	SEM Lisrel 8.51.	KM heavily relies on technology, but there should be presence of trust and other supportive organization elements	Rasula *et al.* (2012)
13	KM practices	Organizational performance measured through productivity, innovation and customer satisfaction.	282 Senior managers in a Small and medium enterprise	SEM Lisrel 8.3	To improve company's performance, information should be collected from customers, suppliers and stakeholders. ICT can be employed for organization and dissemination of this vital information	Gholami *et al.* (2013)
14	Knowledge resources	Organizational performance	189 managers working in company	SEM	Organization structure and knowledge application have direct effect on performance, while technology and knowledge conversion do not	Mills and Smith (2011)

(*continued*)

Table I.

Downloaded by Delhi Technological University At 20:25 05 March 2019 (PT)

Table I.

Sr No.	Independent variable	Dependent variable	Sample	Technique	Findings	Author and year
15	KM enablers and processes	Performance measured in terms of learning and efficiency	Data were collected from 58 firms	Factor analysis was performed	There exists positive relationship between IDVs and DVs. Knowledge creation is essential, organization should not undermine ideas	Lee and Choi (2003)
16	Knowledge circulation processes (KCP)	Knowledge management performance indicators (KMPI)	Firms listed on KOSDAQ (Korea)	Correlation	When KCP efficiency increases, then KMPI (measured through Price earnings ratio, stock price and R&D expenditure) also increases	Lee *et al.* (2005)
17	KM enablers and factors	Firm performance	An empirical research was conducted in Greek medium and large firms	SEM	Culture and technology effect KM effectiveness which in turn positively affect firm performance	Theriou *et al.* (2011)
18	KM processes and IT competency	Firm performance	162 managers of companies were surveyed	SEM	KM processes mediate the relationship between IT competency and firm performance	Pérez-López and Alegre (2012)
19	KM and IT capability	Business performance	395 higher level managers of emerging economy firms	SEM	KM and IT capability positively affect business performance	(Turulja and Bajgoric, 2018)
20	KM and IS (Information System)	Employee performance	287 employees of pharma industries in Jordan	SEM	KM and IS affect employee performance through employee empowerment but not directly	(Abualoush *et al.*, 2018)

Source: Compiled by the authors

knowledge is initially tacit which becomes explicit when shared or stored through a process of socialization or codification respectively in a physical or cyber space. The explicit knowledge again transforms to implicit through a process of learning, simulated application or practice. This continuous transformation from one form to another creates a spiral of learning and relearning which stimulates knowledge creation (Nonaka *et al.*, 2000). The bottom line of the above phenomenon is that if any conversion flow is blocked, then the organization will lose its ability to create and derive benefit from knowledge produced. Therefore, proper management of knowledge is essential.

Using the highly cited models and concepts, the paper explored the indicators of KMS, which is an independent variable in this study. The indicators of SP, which is a dependent variable, are derived from the national and international ranking framework.

4.1 Independent variable

4.1.1 Knowledge creation. KC refers to adding or building new components to the existing knowledge domain (Pentland, 1995). Knowledge can result into being as user's process data and information based on their understanding and experiences. The modes of KC are higher order thinking, group interaction, research and development and learning by doing. KC is critical to any organizations' success as innovations are rewarding both in monetary and non-monetary terms. Innovative organizations not only earn goodwill by making a positive difference in the lives of people across the globe but also cash in on valuable patents. In this era of intensive competition, innovation is the only cutting-edge mechanism which promises of turning a stagnant knowledge pool into an ever-growing flow of knowledge (Fan and Lee, 2016). Having a huge potential, KC is accepted as a significant construct of KMS in many studies (Table AI).

4.1.2 Knowledge transfer. Knowledge transfer (KT) refers to the exchange of ideas, facts, experiences and learnings from one person to another within and outside the organization(s) (Bartol and Srivastava, 2002). Information can flow face to face in a meeting or via online technological tools. KT is more than communication, as it requires not only a medium but also a will to share and an intent to mutually benefit through increased understanding. KT is important, as unshared knowledge will remain hidden and fail to create surplus value. KT is recognized as a vital constituent of KMS in a number of studies (Table AI).

4.1.3 Knowledge storage. Knowledge storage (KS) refers to the establishment and maintenance of knowledge repository which can very well be drawn upon in case of need (Tan and Goh, 1999; Rowley, 2000). In an organization, knowledge is typically stored in documents, reports, manuals and databases. Databases increase the shelf life of data as records are saved in a soft format largely immune to wear and tear. Online storage not only enhances usability as a feature of query processing and search but also helps in organizing and presentation of seemingly unmanageable data. Stored and captured knowledge is the cornerstone of KMS, as without it all generated information like the valuable knowledge of experts is prone to getting lost. The importance of KS is acknowledged in various prominent papers (refer Table AI).

4.1.4 Knowledge culture. Knowledge culture (KCul) refers to the norms, values, and shared understanding among people working in an organization (Schein, 2006). Bock (1999) has defined knowledge culture as "organizational lifestyle which enables and initiates people to create, share and use knowledge on behalf of organization and continuous success". Culture though invisible is reflected by the practices an organization adopts, aspires and appreciates (Gold *et al.*, 2001). Applying KM practices create successful routines that help organizations remain up to date (Chai-Arayalert and Nakata, 2013). Culture can be instilled through continuous reinforcement, members' involvement, training, recognition

Downloaded by Delhi Technological University At 20:25 05 March 2019 (PT)

Downloaded by Delhi Technological University At 20:25 05 March 2019 (PT)

and rewards. The role of knowledge culture has been appreciated by a number of researchers worldwide (Table AI).

4.1.5 Information and communication technology. With the advent of ICT in education, the ways of teaching and learning are revolutionized. Now textbooks are replaced by e-books, encyclopedia by Wikipedia and chalk-boards by smart-boards to name a few (Omona *et al.*, 2010; Gupta and Jain, 2017). Slowly but gradually, we are moving towards Education 4.0 where the barriers between man and machine would blur and latest technological tools like robots, virtual reality and artificial intelligence would find their way in education (Fisk, 2017). This dynamic environment though thrills but raises concerns at the same time regarding technological adaptability given limited human capability. The benefits and dangers of technology are still being scanned and explored. ICT is accepted as an important construct of KMS in many studies (Table AI).

4.2 Dependent variable

4.2.1 Student performance. The dependent variable of the study – SP – is the outcome of the teaching-learning process. Educational institutions provide skills which are measured mainly through academic results of students. The course curriculum is designed to test communication skills, creative thinking, logical reasoning, and data crunching ability of students. Apart from exams, there also exists learning by doing via innovation projects wherein students are given an opportunity to apply their knowledge to solve problems, improve performance and bring a difference in the lives of people on the ground level. After completion of the course, students usually look for employment. Today, learning and working are no longer separate. Education becomes a currency to get employed or self-employed in earning a living (Iftf.org, 2015). Graduates may also choose higher studies rather than jobs. They do so to further enhance their skills and gain specialization in specific fields. Getting admissions in top-class institutions is not easy and the student must have a thorough knowledge of the content apart from other soft and hard skills. The dependent variable SP is an important construct and is widely recognized in the literature. It is vital to tap the immense energy, potential and skills that lay underneath in a student. If this hidden talent is not developed or utilized, education loses its purpose (Cheng *et al.*, 2001). The construct SP is very relevant to the theme of the paper and have been picked from national and international ranking framework NAAC, NIRF, THES and QS World University Ranking Appendix 1.

4.3 Hypotheses and conceptual model

After a thorough review of literature in the previous sections, the authors identified the determinants of KMS as KC, KT, KS, KCuL and ICT. The paper further proceeds to investigate the effects of these KMS constructs on the performance of students in higher educational institutes. Thus, we hypothesize the following:

H1. KMS significantly and positively affect SP in HEIs.

H1.1 KC significantly and positively affect SP in HEIs.

H1.2 KT significantly and positively affect SP in HEIs.

H1.3 KCul significantly and positively affect SP in HEIs.

H1.4 KS significantly and positively affect SP in HEIs.

H1.5 ICT significantly and positively affect SP in HEIs.

5. Research methodology

To pursue research, a questionnaire was made on a five point Likert scale with statements ranging from strongly disagree (1) to strongly agree (5). The constructs were identified through an extensive review of the literature and the questions were adapted according to the research objectives and the area of study. Experts in this field were approached to check content validity of the questionnaire. First, a pilot study was conducted and reliability was checked on a sample of 50 respondents. As the reliability was above 0.6 for all the constructs, the final data were collected. The responses collected were close to 362 in number, but after cleaning only 311 could be used for final analysis.

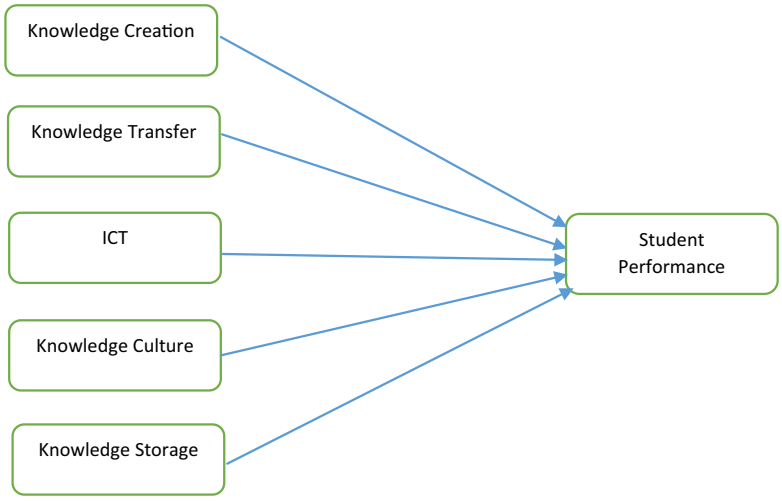
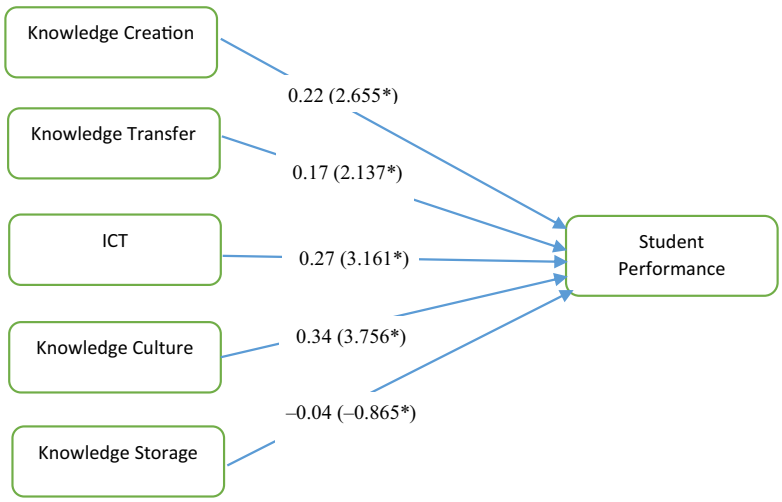


Figure 1.
Conceptual model compiled by the authors



Note: *Critical ratio

Figure 2.
Structural model with path coefficients analyzed from data

Downloaded by Delhi Technological University At 20:25 05 March 2019 (PT)

Downloaded by Delhi Technological University At 20:25 05 March 2019 (PT)

5.1 Exploratory factor analysis

To derive a small number of common factors from a large number of variables, exploratory factor analysis was performed in SPSS. This is in line with achieving parsimony in the model (Malhotra and Dash, 2012). Principal factors were extracted using Varimax rotation. In this case six factors were derived which are KCuL, ICT, KT, KC, KS and SP. With a view to determine reliability, Cronbach alpha was calculated. Reliability of all the factors is above 0.6 (Bagozzi and Yi, 1988) as can be seen from Table AII (Appendix 2).

To determine sample adequacy, KMO and Bartlett test is performed. In this case, the KMO value is 0.891, which depicts great sample adequacy (Hutcheson and Sofroniou, 1999). Bartlett's test is significant which shows that the correlation matrix is significantly different from an identity matrix (Field, 2009).

5.2 Measurement model

Structural equation modeling using Amos was performed. Confirmatory factor analysis (CFA) is used to confirm if the variables load as predicted on the expected number of factors (Malhotra and Dash, 2012). First, a measurement model was constructed to check reliability and validity. Thereafter, both (AVE) and composite reliability (CR) were calculated to measure convergent validity which shows how well the observed variables in a construct correlate with each other (Hair *et al.*, 2010). In the analysis, all values were acceptable, i.e. CR $>$ 0.7, AVE $>$ 0.5 and CR $>$ AVE, thus depicting convergent validity. Discriminant validity is used to measure if a construct is distinct from other constructs and makes a unique contribution. The values of maximum shared variance (MSV) is less than AVE in the analysis confirming discriminant validity (Hair *et al.*, 2010) (Appendix 3).

5.3 Structural model

After testing the measurement model, the structural model was constructed to test the dependence relationship between the constructs (Hair *et al.*, 2006; Anderson and Gerbing, 1988). Research hypotheses were tested by estimating the significance of the path coefficient, which is a standardized regression coefficient (beta). In AMOS, Critical Ratio (CR) for regression weights is used instead of *t*-values. If CR is $>$1.96 for a regression weight, that path is significant at 0.05 level confirming a given hypothesis (Kang *et al.*, 2008; Gao *et al.*, 2008).

The model fit indices are as follows. The cmin/df value or chi-square is calculated to verify the model fit that is how the expected values differ from observed values. A smaller difference is considered better. In this case, the value is 1.703 which is interpreted as excellent by the tool. The goodness of fit measure CFI is above 0.955 and the badness of fit measure RMSEA is less than 0.06 again identified as excellent (Appendix 4).

6. Discussion and conclusion

In this paper, we tried to infer whether the components of KMS, i.e. KC, KS, KT, KCul and ICT, have a positive and significant effect on SP in HEIs. To determine this, structural equation modeling in Amos was performed which gave the following results (Appendix 5).

From the estimates, it can be inferred that KMS significantly and positively affects SP in HEIs. The R^2 of the study was 67 per cent. Such positive and significant results between KM and organizational performance were obtained in some studies (Lee *et al.*, 2005; Rasula *et al.*, 2012; Pérez-López and Alegre, 2012; Theriou *et al.*, 2011) while weak influence was found in some other studies (Mills and Smith, 2011; Masa'deh *et al.*, 2017).

As hypothesized, KC is found to have a significant positive impact on the performance of students ($p < 0.05$, beta 0.22). The results are similar to the ones as concluded by other

researchers (Lee *et al.*, 2005; Mills and Smith, 2011; Choi *et al.*, 2010; Pérez-López and Alegre, 2012). Research and development, group discussions and interaction with experts unlock the creativity of any person including students in a higher educational institution. Students being young carry fresh perspective and generate new and multiple ways of solving a problem through perseverance, hard work and trial and error. These traits help them improve their performance in exams, interviews and innovation projects.

As postulated, KT is found to have a significant positive effect on SP ($p < 0.05$, beta 0.17) as concluded by other studies (Lee *et al.*, 2005; Wang and Wang, 2012; Kang *et al.*, 2008). The presence of supportive relationships along with individual's own positive attitude promotes knowledge sharing (Liu and Cho, 2011). The current study validated that KT broadens mental horizon of members, which mutually benefits them through improved performance in multifaceted ways.

The use of ICT is beneficial as it saves time, effort and money. It has made information accessible at the click of a button in even far-flung areas conveniently. Students with special needs have also immensely benefitted from technology. The study revealed that young generation is quickly adapting to technology and is excited to learn with new technological tools. ICT has increased student engagement and thereby their performance ($p < 0.05$, beta 0.27). These results are consistent with other studies (Andreeva and Kianto, 2012; Rasula *et al.*, 2012; Pérez-López and Alegre, 2012; Choi *et al.*, 2010) while in contrast with Mills and Smith (2011).

KCul emerged as the strongest factor influencing performance ($p < 0.001$, beta 0.34). The results are in line with Lee *et al.* (2005) and Rasula *et al.* (2012) who stated that culture is a major driver of performance. A strong positive culture marked by involvement, continuous learning, application of best practices increases productivity, potential and morale of members. Culture facilitates and supports organizations in achieving their goals. However, the results are contrary to Mills and Smith (2011).

KS is the only factor which is not having a significant effect on the SP ($p > 0.05$, beta −0.04). The findings suggest that undergraduate students prefer hardbound textbooks to e-books and other e-databases. This is because the textbooks are customized to the examination pattern of the university. While interacting with students it was found that there is a continuous transference of tacit knowledge between them, rather than their depending upon or using already stored or documented information (Chou, 2005). The results are in contrast with Donate and de Pablo (2015) who found an indirect effect of KS on performance and Lee *et al.* (2005) who found a positive significant effect.

In this study, SP is measured by academic results, success in innovation projects, placements and selection in top institutes for higher studies. These factors measure the outcomes of KMS and are derived from the various national and international rankings. The data analysis supports the fact that knowledge empowers and therefore its proper management is an utmost priority, more so in this information age. KMS will immensely benefit both the students and the institutes by enriching their knowledge and providing them a better understanding as reflected by the R^2 value of 0.67.

6.1 Knowledge practices among students in the university

It has been observed that students in the university share knowledge via both offline and online discussion forums, networking, storytelling and group project activities. They have also formed communities of practice or societal groups to share their views on topics of common interest. Students participate in different competitions and take a keen interest in academic festivals. Students across disciplines come together to solve problems at hand through collective brainstorming and teamwork. Besides, informal sharing of knowledge

Downloaded by Delhi Technological University At 20:25 05 March 2019 (PT)

Downloaded by Delhi Technological University At 20:25 05 March 2019 (PT)

can take place in canteens, corridors and while commuting. As regards knowledge storage, though magazines, journals and annual reports are released, much knowledge exists in tacit form and not documented because of time constraint, lack of interest and motivation to do the same. To transform student learning into application, an innovation-oriented center of learning called Cluster Innovation Centre is established within the University of Delhi. The Centre harnesses the potential of bright young minds to incubate enterprising ideas through its research and development programs (University of Delhi, 2018). However, given the size of population in India, many more such initiatives are required.

7. Implications for practice

The current paper presents an empirical proof that KMS significantly affect SP. The study establishes that to achieve excellent performance, the culture that promotes knowledge creation and sharing must be imbibed. Though KM initiatives have begun in India at the policy level, they need to be applied honestly, used effectively and extended further to percolate the entire educational ecosystem. Some of these initiatives are the formulation of indigenous benchmarking mechanisms such as NAAC and NIRF. Other initiatives are creating Institutes of Eminence, GIAN (Global Initiative of Academic Networks) and IMPRINT to impact research, innovation and technology. Besides this, SWAYAM – an Indian massive open online course and National Digital Library have been established. In addition, the development of model curriculum is in the pipeline which will keep pace with the changing requirements worldwide and provide quality learning to the students (Devi, 2017). In this endeavor India can also learn from its Asian counterparts like Singapore and China who made to the list of top 30 universities through active research, benchmarking and best practices (OECD 2011; Lane, 2017; THES 2018). Moreover, lessons could be learnt from first world countries like American and British Universities which have harnessed technology, teaching-learning and research capabilities to make an impressive foothold (MIT, 2018; Oxford, 2018).

8. Recommendations

The present paper presents an empirical proof that KMS significantly affect SP and therefore knowledge assets need to be developed and managed. To achieve the goal of knowledge creation, the institutions must have research and development cells and innovation centers. Similarly, to promote knowledge transfer, the academic events such as conferences, workshops and seminars be organized and experts from industry be called to share their viewpoints. In KMS, the role of ICT cannot be ignored. The institutions must make available key academic and collaborative technologies to facilitate the further enhancement of knowledge. KS, though an important aspect of KMS could not come up as a significant factor. This finding suggests that having databases and repositories are not enough, the organizational members must be aware of them and of their utility. While interacting with respondents, it was found that though the databases and manuals were available, it was not used because of lack of awareness and training to use them. By this research entourage, the authors propose that knowledge culture must be present in the institution as an enabler. There should be tolerance for mistakes to encourage risk-taking and innovation. There should be trust and collaboration to facilitate greater KT. Moreover, there should be individual and group rewards for knowledge sharing. Last but not the least, feedback collected must be taken into account. Valuable knowledge accumulated must be applied for decision-making and solving upcoming challenges proactively.

9. Future scope

The current paper is limited in scope and studied the effect of KMS on the performance of educational institutions by collecting data from Indian undergraduates. In future, the impact of other factors like politico-legal and socio-economic environment, competition, internationalization, infrastructure, funding, fairness and equity on the performance of educational institutions could also be explored. The scope of this study may also be broadened to take into account other important stakeholders like teachers and non-teaching staff and also by doing a comparative analysis between different countries to understand the similarities and dissimilarities in their KM practices and learn from realized outcomes.

References

Abualoush, S.H., Obeidat, A.M., Tarhini, A., Masa'deh, R.E. and Al-Badi, A. (2018), "The role of employees' empowerment as an intermediary variable between knowledge management and information systems on employees' performance", *VINE Journal of Information and Knowledge Management Systems*, Vol. 48 No. 2, pp. 217-237.

Ahmad, T. (2015), "Preparing for the future of higher education", *On the Horizon*, Vol. 23 No. 4, pp. 323-330, doi: 10.1108/oth-06-2015-0029.

Alavi, M. and Leidner, D.E. (2001), "KM and KM systems: conceptual foundations and research issues", *MIS Quarterly*, Vol. 25 No. 1, pp. 107-136.

Anderson, J.C. and Gerbing, D.W. (1988), "Structural equation modeling in practice: a review and recommended two-step approach", *Psychological Bulletin*, Vol. 103 No. 3, p. 411.

Andreeva, T. and Kianto, A. (2012), "Does knowledge management really matter? Linking knowledge management practices, competitiveness and economic performance", *Journal of Knowledge Management*, Vol. 16 No. 4, pp. 617-636.

Aujirapongpan, S., Vadhanasindhu, P., Chandrachai, A. and Cooparat, P. (2010), "Indicators of knowledge management capability for KM effectiveness", *Vine*, Vol. 40 No. 2, pp. 183-203.

Bagozzi, R.P. and Yi, Y. (1988), "On the evaluation of structural equation models", *Journal of the Academy of Marketing Science*, Vol. 16 No. 1, pp. 74-94.

Bartol, K.M. and Srivastava, A. (2002), "Encouraging knowledge sharing: the role of organizational reward systems", *Journal of Leadership and Organizational Studies*, Vol. 9 No. 1, pp. 64-76.

Bock, F. (1999), "The intelligent approach to knowledge management: viewing KM in terms of content, culture, process, and infrastructure", *Knowledge Management Review*, Vol. 7 Nos March/April, pp. 22-25.

Bratianu, C. (2011), *Universities as Knowledge-Intensive Learning Organizations in Innovative Knowledge Management: Concepts for Organizational Creativity and Collaborative Design IGI Global*, pp. 1-17.

Chai-Arayalert, S. and Nakata, K. (2013), "Semiotic approach to a practice-oriented knowledge transfer".

Cheng, Y.C., Chow, K.W. and Tsui, K.T. (Eds) (2001), "New teacher education for the future: international perspectives", Springer Science and Business Media.

Choi, S.Y., Lee, H. and Yoo, Y. (2010), "The impact of information technology and transactive memory systems on knowledge sharing, application, and team performance: a field study", *MIS Quarterly*, pp. 855-870.

Chou, S. (2005), "Knowledge creation: absorptive capacity, organizational mechanisms, and knowledge storage/retrieval capabilities", *Journal of Information Science*, Vol. 31 No. 6, pp. 453-465.

Choudhari, A. and Arya, S. (2011), "Only 25% graduates employable: nasscom", [online] available at: https://timesofindia.indiatimes.com/toireporter/author-Abhishek-Choudhari-&-Shishir-Arya-479218541.cms, (accessed 24 June 2018), The Times of India.

Downloaded by Delhi Technological University At 20:25 05 March 2019 (PT)

Downloaded by Delhi Technological University At 20:25 05 March 2019 (PT)

Chow, W. and Chan, L. (2008), "Social network, social trust and shared goals in organizational knowledge sharing", *Information and Management*, Vol. 45 No. 7, pp. 458-465.

Crauise O′ Brien, R. (1995), "Employee involvement in performance improvement: a consideration of tacit knowledge, commitment and trust", *Employee Relations*, Vol. 17 No. 3, pp. 110-120.

Davenport, T.H., De Long, D.W. and Beers, M.C. (1998), "Successful knowledge management projects", *Sloan Management Review*, Vol. 39 No. 2, pp. 43-57.

Davis, F.D. (1989), "Perceived usefulness, perceived ease of use, and user acceptance of information technology", *MIS Quarterly*, Vol. 13 No. 3, pp. 319-340.

Devi, B. (2017), "Vision must be revised every 10 years. Outlook", [online] available at: www.outlookindia.com/magazine/story/vision-must-be-revised-every-10-years/299164 (accessed 4 July 2018).

Donate, M.J. and de Pablo, J.D.S. (2015), "The role of knowledge-oriented leadership in knowledge management practices and innovation", *Journal of Business Research*, Vol. 68 No. 2, pp. 360-370.

Drew, S.A. (1997), "From knowledge to action: the impact of benchmarking on organizational performance", *Long Range Planning*, Vol. 30 No. 3, pp. 427-441.

Duhon, B. (1998), "It's all in our heads", *Inform, September*, Vol. 12 No. 8, pp. 8-13.

Fan, I.Y. and Lee, R.W. (2016), "Intellectual Capital-based innovation planning: empirical studies using wiNK model", *Journal of Intellectual Capital*, Vol. 17 No. 3, pp. 553-569.

Ferraresi, A., Quandt, C., Santos, S. and Frega, J. (2012), "KM and strategic orientation: leveraging innovativeness and performance", *Journal of Knowledge Management*, Vol. 16 No. 5, pp. 688-701.

Field, A. (2009), *Discovering Statistics Using SPSS*, Sage publications.

Fisk, P. (2017), "Education 4.0 ... the future of learning will be dramatically different, in school and throughout life. - Peter fisk", [online], available at: www.thegeniusworks.com/2017/01/future-education-young-everyone-taught-together/ Geniusworks, (accessed 16 June 2018).

Gao, S., Mokhtarian, P. and Johnston, R. (2008), "Nonnormality of data in structural equation models. transportation research record", *Transportation Research Record: Journal of the Transportation Research Board*, Vol. 2082 No. 1, pp. 116-124.

Gaskin, J. and Lim, J. (2016a), "Master validity tool", AMOS Plugin, Gaskination's StatWiki.

Gaskin, J. and Lim, J. (2016b), "Model fit measures", AMOS Plugin, Gaskination's StatWiki.

Gates, B. (2000), *Remarks by Bill Gates*, Intel Exchange e-Business Conference San Francisco, Calif. available at: www.microsoft.com/presspass/exec/billg/speeches/2000/10-12intelexchange.aspx, October 12.

Gholami, M.H., Asli, M.N., Nazari-Shirkouhi, S. and Noruzy, A. (2013), "Investigating the influence of KM practices on organizational performance: an empirical study", *Acta Polytechnica Hungarica*, Vol. 10 No. 2, pp. 205-216.

Gill, A. (2009), "Knowledge management initiatives at a small university", *International Journal of Educational Management*, Vol. 23 No. 7, pp. 604-616.

Gold, A.H., Malhotra, A. and Segars, A.H. (2001), "KM an organizational capabilities perspective", *Journal of Management Information Systems*, Vol. 18 No. 1, pp. 185-214.

Gupta, V. and Jain, N. (2017), "Harnessing information and communication technologies for effective knowledge creation: shaping the future of education", *Journal of Enterprise Information Management*, Vol. 30 No. 5, pp. 831-855, available at: https://doi.org/10.1108/JEIM-10-2016-0173

Hair, J.F., Black, W.C., Babin, B.J. and Anderson, R.E. (2010), *MultivariateDataAnalysis*, 7th Ed., Prentice-Hall, Upper Saddle River, NJ.

Hair, J.F., Black, W.C., Babin, B.J. and Tatham, R.L. (2006), "Multivariate data analysis", 6th Ed., Pearson/Prentice Hall, Upper Saddle River, NJ.

Han, B.M. and Anantatmula, V.S. (2007), "Knowledge sharing in large IT organizations: a case study", *Vine*, Vol. 37 No. 4, pp. 421-439.

He, W., Qiao, Q. and Wei, K. (2009), "Social relationship and its role in KM systems usage", *Information and Management*, Vol. 46 No. 3, pp. 175-180.

Hendriks, P. (1999), "Why share knowledge? The influence of ICT on the motivation for knowledge sharing", *Knowledge and Process Management*, Vol. 6 No. 2, p. 91.

Ho, L.A. (2008), "What affects organizational performance? The linking of learning and knowledge management", *Industrial Management and Data Systems*, Vol. 108 No. 9, pp. 1234-1254.

Hu, L. and Bentler, P.M. (1999), "Cutoff criteria for fit indexes in covariance structure analysis: conventional criteria versus new alternatives", *SEM*, Vol. 6 No. 1, pp. 1-55.

Hutcheson, G.D. and Sofroniou, N. (1999), *The Multivariate Social Scientist: Introductory Statistics Using Generalized Linear Models*, Sage.

Iftf.org (2015), "Learning is earning in the national learning economy", [online] available at: www.iftf.org/fileadmin/user_upload/downloads/learning/IFTF_ACT_LearningIsEarning_ResearchMap.pdf (accessed 15 June 2018).

Jolaee, A., Md Nor, K., Khani, N. and Md Yusoff, R. (2014), "Factors affecting knowledge sharing intention among academic staff", *International Journal of Educational Management*, Vol. 28 No. 4, pp. 413-431.

Kang, Y.J., Kim, S.E. and Chang, G.W. (2008), "The impact of knowledge sharing on work performance: an empirical analysis of the public employees' perceptions in South korea", *intl. Journal of Public Administration*, Vol. 31 No. 14, pp. 1548-1568.

Kidwell, J.J. Vander Linde, K.M. and Johnson, S.L. (2001), Knowledge Management Practices.

Krishnan, A. (2017), "What india's student exodus means", (online) available at: www.thehindu.com/business/Economy/what-indias-student-exodus-means/article21827549.ece The Hindu, (accessed 24 June 2018).

Laal, M. (2011), "Knowledge management in higher education", *Procedia Computer Science*, Vol. 3, pp. 544-549.

Lane, B. (2017), Theaustralian.com.au. available at: ww.theaustralian.com.au/higher-education/china-strategy-for-world-rankings-takes-off/news-story/2e8c03070893681809891a437e3e2d74 (accessed 4 July 2018).

Lee, H. and Choi, B. (2003), "KM enablers, processes, and organizational performance: an integrative view and empirical examination", *Journal of Management Information Systems*, Vol. 20 No. 1, pp. 179-228.

Lee, K.C., Sangjae, L. and In Won, K. (2005), "KMPI: measuring KM performance", *Information and Management*, Vol. 42 No. 3, pp. 469-482.

Lin, T. and Huang, C. (2008), "Understanding KM system usage antecedents: an integration of social cognitive theory and task technology fit", *Information and Management*, Vol. 45 No. 6, pp. 410-417.

Liu, J. and Cho, S. (2011), "Examining the relationship between knowledge sharing and performance rewards in the hospitality industry", Citeseer.

Malhotra, N.K. and Dash, S. (2012), (2013), *Marketing Research, an Applied Orientation*,

Masa'deh, R., Shannak, R., Maqableh, M. and Tarhini, A. (2017), "The impact of KM on job performance in higher education", *Journal of Enterprise Information Management*, Vol. 30 No. 2, pp. 244-262.

Mills, A.M. and Smith, T.A. (2011), "KM and organizational performance: a decomposed view", *Journal of Knowledge Management*, Vol. 15 No. 1, pp. 156-171.

MIT (2018), "MIT – mission", [online] available at: http://web.mit.edu/mission.html (accessed 4 July 2018).

Downloaded by Delhi Technological University At 20:25 05 March 2019 (PT)

Murthy, K.V.B. (2010), "Reengineering higher education: The seamless knowledge management system for the university", *Strategic Pervasive Computing Applications Emerging Trends IGI Global*, pp. 250-268.

NAAC (2017), "National assessment and accreditation council", [online] available at: http://NationalAssessmentAndAccreditationCouncil,Bengaluru (accessed 5 October 2017).

Nasser H. Zaied, A., Soliman Hussein, G. and M. Hassan, M. (2012), "The role of KM in enhancing organizational performance", *International Journal of Information Engineering and Electronic Business*, Vol. 4 No. 5, p. 27.

Nazem, F. (2015), "The structural model of knowledge management in universities".

Nirfindia.org (2017), "MHRD, National institute ranking framework (NIRF)", [online] available at: www.nirfindia.org/Home (accessed 5 October 2017).

Nonaka, I. (1991), "The knowledge creating company", *Harvard Business Review*, Vol. 69 No. 6, pp. 96-104.

Nonaka, I., Toyama, R. and Konno, N. (2000), "SECI, Ba and leadership: a unified model of dynamic knowledge creation", *Long Range Planning*, Vol. 33 No. 1, pp. 5-34.

OECD (2003), *Conclusions from the Results of the Survey of Knowledge Management Practices for Ministries/Departments/Agencies of Central Government in OECD Member Countries*, Paris.

Omerzel, D.G., Biloslavo, R., Trnavčevič, A. and Trnavčevič, A. (2011), "KM and organisational culture in higher education institutions", *Journal of East European Management Studies*, Vol. 16 No. 2, pp. 111-139.

Omona, W., VanderWeide, T. and Lubega, J. (2010), "Using ICT to enhance knowledge management in higher education: a conceptual framework and research agenda", *International Journal of Education and Development Using Information and Communication Technology*, Vol. 6 No. 4, pp. 83-101.

Organization for Economic Co-operation and Development OECD (2011), "Singapore: rapid improvement followed by strong performance", *Lessons from PISA for the United States*, pp. 159-176.

Oxford (2018), "Reputation and quality | University of oxford", [online] available at: www.ox.ac.uk/admissions/graduate/why-oxford/reputation-and-quality?wssl=1 (accessed 4 July 2018).

Paulin, D. and Suneson, K. (2012), "Knowledge transfer, knowledge sharing and knowledge barriers–three blurry terms in KM", *The Electronic Journal of KM*, Vol. 10 No. 1, pp. 81-91.

Pentland, B.T. (1995), "Information systems and organizational learning: the social epistemology of organizational knowledge systems", *Accounting, Management and Information Technologies*, Vol. 5 No. 1, pp. 1-21.

Pérez-López, S. and Alegre, J. (2012), "Information technology competency, knowledge processes and firm performance", *Industrial Management and Data Systems*, Vol. 112 No. 4, pp. 644-662.

QS World University Rankings – Methodology (2017), "Top universities", [online] available at: www.topuniversities.com/qs-world-university-rankings/methodology (accessed 5 October 2017).

Rah, J.A., Gul, S. and Ashraf Wani, Z. (2010), "University libraries: step towards a web based knowledge management system", *Vine*, Vol. 40 No. 1, pp. 24-38.

Raj Adhikari, D. (2010), "Knowledge management in academic institutions", *International Journal of Educational Management*, Vol. 24 No. 2, pp. 94-104.

Ramachandran, S.D., Chong, S.C. and Ismail, H. (2009), "The practice of knowledge management processes: a comparative study of public and private higher education institutions in Malaysia", *Vine*, Vol. 39 No. 3, pp. 203-222.

Rasula, J., Vuksic, V.B. and Stemberger, M.I. (2012), "The impact of knowledge management on organisational performance", *Economic and Business Review for Central and South-Eastern Europe*, Vol. 14 No. 2, p. 147.

Downloaded by Delhi Technological University At 20:25 05 March 2019 (PT)

Rowley, J. (2000), "Is higher education ready for knowledge management?", *International Journal of Educational Management*, Vol. 14 No. 7, pp. 325-333.

Sadiq Sohail, M. and Daud, S. (2009), "Knowledge sharing in higher education institutions: perspectives from Malaysia", *VINE*, Vol. 39 No. 2, pp. 125-142.

Schein, E.H. (2006), *Organizational Culture and Leadership*, John Wiley and Sons, Vol. 356.

Sethi, N. (2017), "India's demographic dividend to peak by 2020: economic Survey. Business Standard", [online] available at: www.business-standard.com/budget/article/india-s-demographic-dividend-to-peak-by-2020-economic-survey-117013101013_1.html (accessed 24 June 2018).

Shastry, V. (2017), "Inside the global university rankings game", [online] available at: www.livemint.com/, www.livemint.com/Sundayapp/SxzP28yPCeSyNUCDpfSYiJ/Inside-the-global-university-rankings-game.html (accessed 16 June 2018).

Shim, J. (2010), "The relationship between workplace incivility and the intention to share knowledge: the moderating effects of collaborative climate and personality traits", Doctoral dissertation, University of Minnesota.

Siakas, K.V., Georgiadou, E. and Balstrup, B. (2010), "Cultural impacts on knowledge sharing: empirical data from EU project collaboration", *Vine*, Vol. 40 Nos 3/4, pp. 376-389.

Sinha, N., Kakkar, N.K. and Gupta, V. (2015), "Harnessing the power of knowledge management for innovation", *International Journal of Knowledge and Learning*, Vol. 10 No. 2, pp. 124-146.

Tan, C.W. and Goh, A. (1999), "Implementing ECA rules in an active database", *Knowledge-Based Systems*, Vol. 12 No. 4, pp. 137-144.

Theriou, N., Maditinos, D. and Theriou, G. (2011), "Knowledge management enabler factors and firm performance: an empirical research of the greek medium and large firms", *European Research Studies*, Vol. 14 No. 2, p. 97.

Times Higher Education (THE) (2017), "World university rankings 2018 methodology", [online] available at: www.timeshighereducation.com/world-university-rankings/methodology-world-university-rankings-2018 (accessed 5 October 2017).

Turulja, L. and Bajgoric, N. (2018), "Information technology, knowledge management and human resource management: investigating mutual interactions towards better organizational performance", *VINE Journal of Information and Knowledge Management Systems*, Vol. 48 No. 2, pp. 255-276.

Turyasingura, W. (2011), "Interdependency of KM and learning: the case of higher education institutions in Uganda", Diss.

University of Delhi (2018), [online] available at: www.du.ac.in/du/ (accessed 9 December 2018).

Wang, Z. and Wang, N. (2012), "Knowledge sharing, innovation and firm performance", *Expert Systems with Applications*, Vol. 39 No. 10, pp. 8899-8908.

Yew, W.K. and Aspinwall, E. (2005), "An empirical study of the important factors for knowledge-management adoption in the SME sector", *Journal of Knowledge Management*, Vol. 9 No. 3, pp. 64-82.

Zwain, A.A.A., Teong, L.K. and Othman, S.N. (2012), "Knowledge management processes and academic performance in iraqi HEIs: an empirical investigation", *International Journal of Academic Research in Business and Social Sciences*, Vol. 2 No. 6, p. 273.

Further reading

Donate, M. and Canales, J. (2012), "A new approach to the concept of knowledge strategy", *Journal of Knowledge Management*, Vol. 16 No. 1, pp. 22-44.

Fornell, C. and Larcker, D.F. (1981), "Evaluating structural equation models with unobservable variables and measurement error", *Journal of Marketing Research*, pp. 39-50.

Downloaded by Delhi Technological University At 20:25 05 March 2019 (PT)

García-Sánchez, E., García-Morales, V.J. and Bolívar-Ramos, M.T. (2017), "The influence of top management support for ICTs on organisational performance through knowledge acquisition, transfer, and utilization", *Review of Managerial Science*, Vol. 11 No. 1, pp. 19-51.

Hair, J.F., Anderson, R.E., Tatham, R.L. and William, C.B. (1995), "Multivariate data analysis with readings", No.4.

Masa'deh, R., Gharaibeh, A., Maqableh, M. and Karajeh, H. (2013), "An empirical study of antecedents and outcomes of knowledge sharing capability in jordanian telecommunication firms: a structural equation modeling approach", *Life Science Journal*, Vol. 10 No. 4, pp. 2284-2296.

Newkirk, H. and Lederer, A. (2006), "The effectiveness of strategic information systems planning under environmental uncertainty", *Information and Management*, Vol. 43, pp. 481-501.

Stevens, J.P. (2002), *Applied Multivariate Statistics for the Social Sciences*, (4th Ed.), Erlbaum, Hillsdale NJ.

Downloaded by Delhi Technological University At 20:25 05 March 2019 (PT)

Downloaded by Delhi Technological University At 20:25 05 March 2019 (PT)

Appendix 1

Type of variable	Construct	Indicators	Source
IDV (Independent variable)	*KC*	*KC1*: Research and development is facilitated in our institute *KC2*: Cross-functional teamwork is used for problem-solving *KC3*: There is adequate corporate-academia interface	Pentland (1995); Lee and Choi (2003); Lee *et al.* (2005); Lin and Huang (2008); Shim, (2010); Omerzel *et al.* (2011); Alavi and Leidner (2001)
IDV	*KT*	*KT1*: Peers are willing to share knowledge possessed by them *KT2*: I am willing to share my knowledge with other peers *KT3*: I feel that sharing knowledge broadens my horizon	Yew and Aspinwall (2005); Chou (2005); Chow and Chan (2008); Shim (2010); Masa'deh *et al.* (2017); Turyasingura (2011); Paulin and Suneson (2012); Jolaee *et al.* (2014)
IDV	*KS*	*KS1*: I make use of the online database like emerald, Ebsco- host, etc. *KS2*: I refer e-books and e-documents. *KS3*: Experience and know-how of intellectuals is documented	Tan and Goh (1999); Yew and Aspinwall, (2005); Kang *et al.* (2008); He *et al.* (2009); Turyasingura (2011)
IDV	*KCuL*	*KCuL1*: Training: Our teachers try new ways of teaching and learning *KCuL2*: Motivation: My institution recognizes and rewards students who create and share knowledge *KCuL3*: Involvement: Our feedback is considered *KCuL4*: Benchmarking: Best practices are applied in our institution *KCuL5*: Practice: Our curriculum is regularly updated based on recent developments	Yew and Aspinwall, (2005); Lee *et al.* (2005); Davenport *et al.* (1998); Rasula *et al.* (2012); OECD (2003); Andreeva and Kianto, (2012); Drew (1997); Crauise O′ Brien (1995); Sinha *et al.* (2015)
IDV	*ICT*	*ICT1*: I feel comfortable and easily adapt to new software and technological tools *ICT2*: Integrating technology with traditional teaching methods is beneficial. *ICT3*: New ICT tools like virtual reality, artificial intelligence, robots can make learning effective in the future	Davis (1989); Gupta and Jain (2017); Ahmad (2015) Han and Anantatmula, (2007)
DV (Dependent variable)	*SP*	*SP1*: Academic results of our institution are better than other colleges *SP2*: Students achieve success in innovation projects *SP3*: Students are selected in top institutes of higher learning *SP4*: Average placements of our institution are better than other colleges	NAAC (2017); NIRF (2017); THE, (2017); QS, (2017)

Source: Compiled by the authors

Table AI. Survey items construct development

Downloaded by Delhi Technological University At 20:25 05 March 2019 (PT)

Appendix 2

Table AII.
Rotated component matrix

	Component					
	KCUL	SP	ICT	KT	KC	KS
KCUL1	0.598					
KCUL2	0.610					
KCUL3	0.698					
KCUL4	0.721					
KCUL5	0.782					
SP1		0.601				
SP2		0.720				
SP3		0.671				
SP4		0.751				
ICT1			0.727			
ICT2			0.682			
ICT3			0.814			
KT1				0.816		
KT2				0.810		
KT3				0.583		
KC1					0.798	
KC2					0.758	
KC3					0.514	
KS1						0.679
KS2						0.739
KS3						0.891
Cronbach's alpha	0.868	0.808	0.748	0.755	0.778	0.699

Appendix 3

Table AIII.
Model validity measures

	CR	AVE	MSV	MaxR(H)	1	2	3	4	5	6
1	0.812	0.521	0.504	0.825	*0.722*					
2	0.813	0.522	0.504	0.820	0.710***	*0.723*				
3	0.753	0.506	0.464	0.763	0.544***	0.682***	*0.711*			
4	0.801	0.573	0.413	0.806	0.535***	0.631***	0.642***	*0.757*		
5	0.789	0.556	0.491	0.804	0.701***	0.681***	0.549***	0.488***	*0.746*	
6	0.790	0.557	0.110	0.800	0.332***	0.179**	0.150*	0.039	0.297***	*0.747*

Notes: Significance of correlations: †$p < 0.100$; *$p < 0.050$; **$p < 0.010$; ***$p < 0.001$
Source: Hu and Bentler (1999); Gaskin and Lim, (2016a, b)

Appendix 4

Measure	Estimate	Threshold	Interpretation
CMIN	260.582	–	–
DF	153	–	–
CMIN/DF	1.703	Between 1 and 3	Excellent
CFI	0.955	>0.95	Excellent
SRMR	0.051	<0.08	Excellent
RMSEA	0.048	<0.06	Excellent
PClose	0.643	>0.05	Excellent

Source: Hu and Bentler (1999); Gaskin and Lim, (2016a, b)

Table AIV.
Model fit measures

Appendix 5

	Estimate	S.E.	C.R.	P	Decision
SP <— KCUL	0.332	0.088	3.756	***	Supported
SP <— ICT	0.242	0.077	3.161	0.002	Supported
SP <— KT	0.157	0.073	2.137	0.033	Supported
SP <— KC	0.182	0.069	2.655	0.008	Supported
SP <— KS	−0.036	0.042	−0.865	0.387	Not supported

Note: Maximum likelihood estimates

Table AV.
Regression weights

Corresponding author
Namita Jain can be contacted at: namitajain105@gmail.com

For instructions on how to order reprints of this article, please visit our website:
www.emeraldgrouppublishing.com/licensing/reprints.htm
Or contact us for further details: **permissions@emeraldinsight.com**

Downloaded by Delhi Technological University At 20:25 05 March 2019 (PT)

International Journal of Research in Engineering and Innovation (IJREI)
journal home page: http://www.ijrei.com
ISSN (Online): 2456-6934

Thermodynamic performances using energy-exergy analysis of NH_3H_2O vapor absorption refrigeration system cascaded with vapor compression refrigeration systems using ecofriendly refrigerants

R.S. Mishra

Department of Mechanical and Production Industrial and Automobiles Engineering, Delhi Technological University, Delhi, India

Abstract

The main aim of the study is to locate for components in the system for maximum irreversibility and to find ways to improve the system. The overall objective is to accomplish the thermodynamic analysis of the refrigeration systems and study their thermodynamic viability. Fourth generation refrigerants i.e. R-1234yf and R1234ze) are needed because the high GWP of the R134A that are used in existing refrigeration and air conditioning systems. The hydro fluoro olefins (HFOs) known as fourth generation refrigerants are available in limited quantities and also their thermodynamic performance on cascaded vapor absorption- compression refrigeration systems are not completely tested in different applications by the various investigators. . The thermodynamic performance of fourth generation refrigerants in terms of their first low efficiency termed as coefficient of performance (COP, second law efficiency termed as exergetic efficiency and exergy destruction ratio for a specified cooling load and compared with the third generation HFC-134a refrigerant. It is found that fourth generation HFO-1234yf refrigerant have slightly low(around 1.477% first law efficiency (COP) and exergetic efficiency and reduction in exergy destruction ratio of at -53^{o}C of low temperature evaporator. However, HFO1234ze can replace R134a as its thermodynamic performance is almost similar to R134a for -30^{o}C of low temperature evaporator temperature due to low GWP (around. The effect of performance parameters such as temperature over lapping (approach), generator temperature, high pressure absorber temperature, low pressure absorber temperature, condenser temperature of vapor absorption on thermodynamic performances (such as first and second law efficiencies , exergy destruction ratio have been presented.
© 2019 ijrei.com. All rights reserved

Keywords: Thermodynamic performances, cascaded vapor compression-absorption refrigeration systems, ecofriendly refrigerants

1. Introduction

A refrigeration system utilized high grade energy in terms of work supplied by an electric motor to transfer heat from a space to be cooled. Low temperature boiling fluids called refrigerants which absorbed thermal energy to get vaporized in the evaporator causing a cooling effect in the region being to be cooled. Even though comparing the advantages and disadvantages of various refrigeration systems, two most important parameters i.e. the operating temperature and refrigerating capacity are of vital importance in these systems. These systems can be evaluated using energy and exergy analyses which are based on first and second law of thermodynamics to compute and the coefficient of performance, exergy destruction ratio and exergetic efficiency respectively.

An extensive review of the literature has been done on different refrigeration and air conditioning systems by the various investigators which has been classified as

(i) Vapor Absorption Refrigeration Systems.
(ii) Vapor Compression Refrigeration Systems.
(iii) Vapor-compression-absorption refrigeration systems.

Vapor Absorption system is an attractive method for utilizing low grade energy directly for cooling. This is an important advantage as against the conventional vapor compression system which operates on high grade energy. Another important feature of these systems is that it does not use any

Corresponding author: Prof. R.S. Mishra
Email Address: hod.mechanical.rsm@dtu.ac.in

moving component except a very small liquid pump. Vapor absorption system consists of four basic components viz. an evaporator, an absorber (located on low pressure side), a generator and a compressor (located on high pressure side). A refrigerant flows from the condenser to the evaporator, then via absorber to the generator and back to condenser, while the absorbent passes from absorber to the generator and back to absorber. For maximum efficiency, the pressure difference between the low pressure side and high pressure side is maintained as small as possible. Although, the initial cost of these systems is at present higher but their operating expenses are often appreciably lower, which can further be reduced if efficient absorption and distillation can be achieved. Since, the efficiency of these processes is determined largely by thermodynamic properties of the refrigerant absorbent combination, an extensive study of these properties is of utmost importance in the development of an efficient absorption refrigeration cycle. A large number of researchers have carried out research in the field of vapor absorption refrigeration using different working pairs and the most common working pairs are LiBr-H2O and NH3-H2O. Alizadeh et al [1] carried out theoretical study on design and optimization of water – lithium bromide refrigeration cycle and determined that for a given refrigerating capacity higher generator temperature causes high cooling ratio with smaller heat exchange surface at a low cost. In vapor compression system there are four major components: evaporator, compressor, condenser and expansion device. Power is supplied to the compressor and heat is added to the system in the evaporator, whereas in the condenser heat rejection occurs. Heat rejection and heat addition are dissimilar to different refrigerants. A standard vapor compression cycle consists of four processes viz. a 28 reversible adiabatic compression from the saturated vapor to the compressor pressure followed by a reversible heat rejection at constant pressure causing de-superheating and condensation. This is further extended to an irreversible expansion at constant enthalpy from saturated liquid to evaporator pressure and there after a reversible heat addition at constant pressure causing evaporation to saturated vapor. Keshwani and Rastogi [2] studied a two stage VCR system for refrigerant CFC12 and determined the optimum inter-stage pressure in in two stage VCRS for minimization of overall compressor work. Zubair et al [3-4] showed that the optimum inter stage pressure for a two stage refrigeration system and found that optimum inter stage pressure for refrigerant R-134a for maximum COP of the system which was closed to the saturation pressure corresponding to the arithmetic mean of the refrigerant condensation and evaporation temperatures. And found that the system irreversible losses are lowest at an intermediate saturation temperature near to arithmetic mean of the condensation and evaporation temperatures. Aprea et al [5] studied that vapor compression refrigeration systems using refrigerant R-502 which is an azeotropic mixture of refrigerants R-22 and R-115. are widely used for cold storage refrigeration. Doring et al [6] carried out an experimental study of R-507 and developed mathematical correlations using measured thermodynamic data and found that the compressor discharge temperature for R-507 was approximately 8K below in comparison to R-402. Sami and Desjardins [7] carried out performance evaluation of R-407B, R-507, R-408A and R-404A as substitutes to R-502. And found that the R408A blend has a higher performance than R-502. Nikolaidis and Probert [8] used exergy analysis to investigate the behaviour of two stage compound compression cycle with flash intercooling using R-22 as refrigerant by varying the condenser saturation temperature and evaporator saturation temperature from 298 to 308 K and 238 to 228 K respectively. They determined the effect of temperature change in condenser and evaporator on plants irreversibility rate. They concluded that the changes in the temperatures of condenser and evaporator significantly effecting the overall irreversibility of the plants and concluded that the two stage compound compression system with flash intercooling using R-22 as refrigerant needs optimization.

Dopazo et al [9] analyzed performance parameters of a CO_2/NH_3 cascade cooling system and their effect on system COP and exergetic efficiency using general mathematical model which was validated using experimental results and concluded that the isentropic efficiency for each compressor in cascade system should be determined for the optimum CO2 condensing temperature and maximum COP.

Miguel Padilla et. al. [10] developed analysis model by carried out energy-exergy analysis of the impact of direct replacement of R-12 by zeotropic mixture R-413A on the performance of a domestic vapor compression refrigeration system and concluded that the overall energy and exergy performance of system working with R-413A is better than R-12. Qureshi and Zubair [11] developed first and second law analysis for investigating thermodynamic performance degradation due to fouling in a vapor compression cycle for various applications. Using refrigerants R-134a, R-410A and R-407C. The first law analysis indicates that R-134a always performs better unless only the evaporator is being fouled. However, the second law shows that R-134a performs the best in all cases. The second-law efficiency indicates that R-717 performs the best in all cases. Volumetric efficiency of R-410A and R-717 remained the highest under the respective conditions studied. Furthermore, performance degradation of the evaporator often has a larger effect on compressor power requirement while that of the condenser has an overall larger effect on the COP.

2. Cascade Refrigeration System

A cascade system consists of two independently operated single-stage refrigeration systems: a lower system that maintains a lower evaporating temperature and produces a refrigeration effect and a higher system that operates at a higher evaporating temperature. These two separate systems are connected by a cascade condenser in which the heat released by the condenser in the lower system is extracted by the evaporator in the higher system. Reduces irreversibility during heat exchange process between working fluids and results in improved system performance. Cascade vapor refrigeration system comprises two separate single stage

NH_3H_2O absorption refrigeration cycle and cascaded vapor compression cycle with a different refrigerants, best suited for the working conditions. It is necessary to use a cascade vapor compression system when the difference between the temperature at which heat is rejected and the temperature at which refrigeration is required is so large that a single refrigerant with suitable properties cannot be found. In low-temperature applications, including rapid freezing and the storage of frozen food, the required evaporating temperature of the refrigeration system ranges from –40°C to –55°C, therefore, single-stage vapor-compression refrigeration system is insufficient, while two-stage or cascade refrigeration systems are used for low-temperature applications. The high- and low-pressure sides of a two-stage refrigeration system are charged with the same refrigerant, whereas the high and low-temperature circuits in a cascade system are filled separately with appropriate refrigerants. Therefore, using HFO refrigerants in both two-stage and cascade refrigeration system helps to meet the requirements of environmental regulations [12-13] Mishra [13] described. Cascade refrigeration systems which are where the evaporating temperature of frozen-food cabinets ranges from –30°C to –50°C. In these units, two single-stage systems are thermally coupled through a cascade condenser. The high-temperature stage of a cascade refrigeration system usually uses HFO -1234ze, whereas the low-temperature circuit of the refrigeration system can be charged with HFO-1234yf and HFC-134a and carbon dioxide (R744).

2.1 Vapor Compression-Absorption System

Vapor Compression-absorption heat pump/refrigeration cycle represents a cycle in which vapor is mechanically compressed, absorbed and then desorbed using a liquid solution cycle. These systems may be considered as hybrid systems between conventional vapor compression and vapor absorption systems. The hybrid vapor compression/absorption heat pump cycle combines two well-known heat pump concepts, the compression heat pump and the absorption heat pump. It uses a mixture of refrigerants as the working fluid, one as the absorbent and the other as the desorbent. A key advantage of the hybrid heat pump is the extended range of temperatures available for a mixture compared to pure refrigerants. This is the effect of the reduced vapor pressure obtained for a refrigerant in a mixture with less volatile component. Another advantage is the gliding temperature obtained in the absorber and desorbed. Fernandez-Seara et al [14] investigated a compression absorption cascade refrigeration system. The results were computed for refrigerants carbon-dioxide and ammonia in the compression stage and ammonia water in absorption stage. It is shown that the intermediate temperature level is an important design parameter that causes an opposite effect on the COP of the compression and absorption systems. Kairouani and Nahdi [15] developed a novel combined refrigeration system using geothermal energy for hybrid system and carried out thermodynamic analysis of the cycle. The possibility of selected three working fluids R-717, R-22 and R-134a for the conventional and ammonia–water Pair for the absorption system at the geothermal temperature source is in the range of 343-349K and the results show that the COP of a combined system is significantly higher than that of a single stage refrigeration system to reduce the continuously increasing electrical energy consumption. Garimella et al [16] analyzed a novel cascaded absorption/vapor-compression cycle with a high temperature lift for a naval ship application. A single-effect LiBr–H2O absorption cycle and a subcritical CO_2 vapor-compression cycle were coupled together to provide low-temperature refrigerant −40°C and developed a thermodynamic model to analyze the performance of the cascaded system, and parametric analyses were conducted to estimate the performance of the system over a range of operating conditions. The performance of the cascaded system was also compared with an equivalent two-stage vapor-compression cycle and found to exhibit very high COPs over a wide range of operating conditions and when compared to an equivalent vapor-compression system, was found to avoid up to 31% electricity demand. Yari et al [17] studied and compared the GAX and GAX hybrid absorption refrigeration cycles using first and second law of thermodynamics. They performed the exergy analyses in order to calculate the total exergy destruction rate within the cycles and also reveal the contribution of different components to the destructions and concluded that in both cycles the generator temperature (Tgen) has more influence on the second law efficiency whereas, the coefficient of performance (COP) of the cycles are comparatively less affected by this temperature. An increase of about 75% in the second law efficiency of the GAX cycle was found as the generator temperature was varied from 400 to 440 K. With this variation of the generator temperature, the increase in the corresponding COP was around 5%.

Zheng and Meng [18] studied the thermodynamic performances of the hybrid refrigeration cycle and proposed the fundamental concept in terms of ultimate refrigerating temperature and investigated the impact of compressor pressure increasing on the thermodynamic performances and also observed that the refrigeration cycle performance varies with the change of compressor outlet pressure and depends on the absorption sub-system or the compression sub-system. Mishra and Ankit Dewedi [19] also described methods for improving thermal performances of vapor absorption system using heat pipes. Comprehensive review of the literature on Vapor Absorption Systems, Compression-Absorption System and Vapor Compression System has been carried out on various aspects of energy-exergy analysis and the type of cycles analyzed, working pairs used and using entropy generation principle. With regards to vapor absorption cycles, it is found that mostly the studies are carried out on large capacity systems and the investigation had been carried out with in a limited range of system design parameters. The literature on small vapor absorption systems is limited and very few studies have been done on smaller systems. The above studies are simulation studies. About compression absorption systems studies have been carried out by many investigators mostly analytically and experimentally. The investigations

have been done on wet compression cycles which eliminated the need of the solution pump. However the literature on exergy analysis of such systems is limited and NH3-H_2O is the most suitable working fluid due to its high latent heat and excellent heat and mass transfer properties. Literature review revealed that thermodynamic optimization on compressor-absorption system was carried out to find optimum working condition for a given external condition. The temperature gradient in the absorber is optimized. The literature reveals that cost optimization of the system is essential to minimize the cost as this system is more capital intensive than the conventional compression refrigeration system and cascaded absorption-compression refrigeration system. With respect to vapor compression systems, literature review revealed that natural refrigerants such as ammonia, propane, propylene are halogen free and are safe for the environment. Many investigators have carried out theoretical and experimental investigations on alternative refrigerants. Considerable talked about the replacement of R-134a by using HFO refrigerants of low GWP less than 7. In view of the increase in the cost of our existing resources, the advantage of minimizing losses in the use of this energy is very important and essential. Exergy analysis is a prime area for effective improvement of the systems. In the present work energy and exergy analysis of the refrigeration systems is done in order to improve the system thermodynamically. The main idea was to have possible future direction of research is to search the HFO refrigerants (such as low GWP of R1234yf and R1234ze) to replace HFC refrigerant (i.e. R134a).

3. Results and Discussions

Following two cascade system have been chosen for numerical computation and input data is also given below of each system.

System1: NH_3H_2O vapor absorption refrigeration system cascaded with vapor compression refrigeration system using HFC-134a ecofriendly refrigerant.

- Temperature of Absorber=35ºC.
- Temperature of Condenser=35ºC
- Temperature of Generator=80ºC to 115ºC
- Evaporator temperature of vapor compression refrigeration system= 5 ºC
- Evaporator temperature of vapor compression refrigeration system= -53 ºC
- Compressor efficiency=0.8
- Heat exchanger effectiveness =0.5
- Refrigeration effect =29.09"kW"
- Temperature overlapping(Approach) =10 ºC

System2: NH_3H_2O vapor absorption refrigeration system cascaded with vapor compression refrigeration system using HFO-1234yf ecofriendly refrigerant.

- Temperature of Absorber=35ºC.
- Temperature of Condenser=35ºC
- Temperature of Generator=80ºC to 115ºC
- Evaporator temperature of vapor compression refrigeration system= 5 ºC
- Evaporator temperature of vapor compression refrigeration system= -53 ºC
- Compressor efficiency=0.8
- Heat exchanger effectiveness =0.5
- Refrigeration effect =29.09"kW"
- Temperature overlapping(Approach) =10 ºC

Input variables used in the for numerical computation of NH_3H_2O vapor absorption refrigeration system cascaded with vapor compression refrigeration systems using HFC-134a (system-1) and HFO-1234yf (system-2) refrigerants following ranges

- Effect of temperature overlapping (Approach= Temperature of cascade condenser vapor compression refrigeration cycle- cascade evaporator temperature of vapor absorption refrigeration cycle) variation from 0 to 20 using HFC-134a and HFO-1234yf refrigerants
- Generator temperature variation NH_3H_2O vapor absorption refrigeration from 65 ºC to 115 ºC,
- Evaporator temperature vapor compression refrigeration system from $T_{_EVA_VCRS}$ = -30 to - 53ºC.
- Evaporator temperature vapor absorption refrigeration system $T_{_EVA_VARS}$= 30 ºC to 45ºC,
- Absorber temperature vapor absorption refrigeration system $T_{_EVA_VARS}$= 30 ºC to 45ºC.

3.1 Effect of of low temperature evaporator temperature of vapor compression refrigeration cycle on thermal performances of NH_3H_2O vapor absorption refrigeration cascaded with vapor compression refrigeration system

Table-1 (a) shows the variation of low temperature evaporator circuit temperature with variation of thermal performances such as first law efficiency (coefficient of performance (COP) of cascaded vapor absorption system) & second law efficiency in terms of exergetic efficiency and exergy destruction ratio based on exergy of fuel of NH_3H_2O vapor absorption refrigeration system cascaded with vapor compression refrigeration using HFC-134a refrigerant and it is found that when low temperature evaporator circuit temperature of vapor absorption refrigeration system is increasing, the thermodynamic performances in terms of ($COP_{_Cascad}$,) is decreasing and exergetic efficiency $_{Cascade\ System}$ is also decreasing and EDR is increasing . Similarly exergy destruction ratio based on the exergy of product ($EDR_{_Cascade}$) is also decreasing and exergetic efficiency is increasing. The optimum values of single effect vapor absorption refrigeration cycle cascaded with vapor compression cycle for generator temperature of 80ºC and condenser temperature and absorber temperature of 35ºC by using HFO-1234yf refrigerant (system-2) has 1.477% lower COP than System-1 using HFC-134a

Table-1(a): Effect of evaporator temperature on thermal performances of NH_3H_2O vapor absorption refrigeration cascaded with vapor compression refrigeration system using R134a ecofriendly refrigerant ($COP_NH_3H_2O$= 0.322, Rational EDR_{VARS}=0.8683, EDR_{VARS}=6.594, Exergetic Efficiency$_{NH3H2O}$=0.1317) for ,T_{EVA}=-1ºC, Absorber temperature=35ºC, generator temperature=80ºC, Condenser temperature$_{VARS}$=35ºC, Collector Area= 31.65 m^2), Compressor efficiency=0.80, T_{EVA}=-53ºC and Approach (temperature overlapping) =10, {SYSTEM-1}

T_EVA (ºC)	$COP_{Cascade}$	$EDR_{Cascade}$	$Exergetic\ Efficiency_{cascade}$
-53	0.5339	1.549	0.3924
-52	0.5364	1.553	0.3917
-51	0.5390	1.558	0.3910
-50	0.5416	1.583	0.3902
- 45	0.5545	1.593	0.3856
- 40	0.5673	1.633	0.3798
-35	0.5802	1.683	0.3727
-30	0.5931	1.745	0.3643

Table-1(b): Effect of evaporator temperature on thermal performances of NH_3H_2O vapor absorption refrigeration cascaded with vapor compression refrigeration system using R1234yf ecofriendly refrigerant ($COP_NH_3H_2O$= 0.322, Rational EDR_{VARS}=0.8683, EDR_{VARS}=6.594, Exergetic Efficiency$_{NH3H2O}$=0.1317) for ,T_{EVA}=-1ºC, Absorber temperature=35ºC, generator temperature=80ºC, Condenser temperature$_{VARS}$=35ºC, Collector Area= 31.65 m^2), Compressor efficiency=0.80, T_{EVA}=-53ºC and Approach (temperature overlapping) =10, {SYSTEM-2}

T_EVA (ºC)	$COP_{Cascade}$	$EDR_{Cascade}$	$Exergetic\ Efficiency_{cascade}$
-53	0.5336	1.552	0.3918
-52	0.5361	1.556	0.3912
-51	0.5387	1.561	0.3904
-50	0.5413	1.566	0.3897
--45	0.5541	1.597	0.3851
-40	0.5670	1.637	0.3793
-35	0.5799	1.687	0.3722
-30	0.5928	1.748	0.3638

The variation of thermal performances such as coefficient of performance (COP) of cascaded vapor absorption system & second law efficiency in terms of exergetic efficiency and exergy destruction ratio based on exergy of fuel of NH_3H_2O vapor absorption refrigeration system cascaded with vapor compression refrigeration using HFO-1234yf refrigerant in table-1-(b) because HFO has GWP is four as compared to HFC-134a which has GWP of 1360 it is found that when low temperature evaporator circuit temperature of vapor absorption refrigeration system is increasing**,** the thermodynamic performances in terms of (COP_{Cascad},) is decreasing and exergetic efficiency$_{Cascade\ System}$ is also decreasing and $EDR_{Rational}$ is increasing . Similarly exergy destruction ratio based on the exergy of product ($EDR_{Cascade}$) is also decreasing and exergetic efficiency is increasing. The optimum values of single effect vapor absorption refrigeration cycle cascaded with vapor compression cycle for generator temperature of 80ºC and condenser temperature and absorber temperature of 35ºC by using HFO-1234yf refrigerant (system-2) has lower COP & lower exergetic efficiency and higher EDR than System-1 using HFC-134a

Table-1(c): Effect of evaporator temperature on thermal performances of NH_3H_2O vapor absorption refrigeration cascaded with vapor compression refrigeration system using R134a ecofriendly refrigerant ($COP_NH_3H_2O$= 0.322, Rational EDR_{VARS}=0.8683, EDR_{VARS}=6.594, Exergetic Efficiency$_{NH3H2O}$=0.1317) for ,T_{EVA}=-1ºC, Absorber temperature=35ºC, generator temperature=80ºC, Condenser temperature$_{VARS}$=35ºC, Collector Area= 31.65 m^2), Compressor efficiency=0.80, T_{EVA}=-53ºC and Approach (temperature overlapping) =10, {SYSTEM-1}

T_EVA (ºC)	$COP_{Cascade}$	Rational $EDR_{Cascade}$	$Exergetic\ Efficiency_{cascade}$
-53	0.5339	0.6076	0.3924
-52	0.5364	0.6083	0.3917
-51	0.5390	0.6090	0.3910
-50	0.5416	0.6098	0.3902
- 45	0.5545	0.6144	0.3856
- 40	0.5673	0.6202	0.3798
-35	0.5802	0.6273	0.3727
-30	0.5931	0.6347	0.3643

Table-1 (c) shows the variation of low temperature evaporator circuit temperature with variation of thermal performances such as first law efficiency in terms of coefficient of performance (COP) of cascaded vapor absorption system & second law efficiency in terms of exergetic efficiency and exergy destruction ratio based on exergy of fuel of NH_3H_2O

vapor absorption refrigeration system cascaded with vapor compression refrigeration using HFC-134a refrigerant (system-1) and it is found that when low temperature evaporator circuit temperature of vapor absorption refrigeration system is increasing , the rational EDR based on exergy of fuel is increasing .

Table-1(d): Effect of evaporator temperature on thermal performances of NH_3H_2O vapor absorption refrigeration cascaded with vapor compression refrigeration system using R1234yf ecofriendly refrigerant ($COP_NH_3H_2O$= 0.322, Rational EDR_{VARS}=0.8683, EDR_{VARS}=6.594, Exergetic $Efficiency_{NH3H2O}$=0.1317) for ,T_{EVA}=-1ºC, Absorber temperature=35ºC, generator temperature=80ºC, Condenser $temperature_{VARS}$=35ºC, Collector Area= 31.65 m^2), Compressor efficiency=0.80, T_{EVA}=-53ºC and Approach (temperature overlapping) =10, {SYSTEM-2}

T_EVA (ºC)	$COP_{Cascade}$	Rational $EDR_{Cascade}$	Exergetic $Efficiency_{cascade}$
-53	0.5336	0.6082	0.3918
-52	0.5361	0.6088	0.3912
-51	0.5387	0.6096	0.3904
-50	0.5413	0.6103	0.3897
--45	0.5541	0.6149	0.3851
-40	0.5670	0.6207	0.3793
-35	0.5799	0.6278	0.3722
-30	0.5928	0.6362	0.3638

Table-1 (d) The variation of thermal performances s coefficient of performance (COP) of cascaded vapor absorption system & second law efficiency in terms of exergetic efficiency and exergy destruction ratio based on exergy of fuel of NH_3H_2O vapor absorption refrigeration system cascaded with vapor compression refrigeration using HFO-1234yf refrigerant (System-2) shown in Table-1(d) with the the variation of low temperature evaporator circuit temperature of cascade vapour absorption refrigeration systems and it is found that when low temperature evaporator circuit temperature of vapor absorption refrigeration system is increasing , the rational EDR based on exergy of fuel is increasing. Table-1 (e) & Table-1 (f) show the variation of low temperature evaporator circuit temperature with variation of thermal performances such as first law efficiency in terms of coefficient of performance (COP) of cascaded vapor absorption system & second law efficiency in terms of exergetic efficiency and exergy destruction ratio based on exergy of fuel of NH_3H_2O vapor absorption refrigeration system cascaded with vapor compression refrigeration using HFC-134a refrigerant (System-1) and it is found that when low temperature evaporator circuit temperature of vapor absorption refrigeration system is increasing , coefficient of performance (COP_{VCRS}) is increasing & the rational EDR based on exergy of fuel of cascaded vapor compression refrigeration system is decreasing. Also second law efficiency (exergetic $efficiency_{VCRS}$) of cascaded vapor compression system is also increasing

Table-1(e): Effect of evaporator temperature on thermal performances of NH_3H_2O vapor absorption refrigeration cascaded with vapor compression refrigeration system using R1234yf ecofriendly refrigerant ($COP_NH_3H_2O$= 0.322, Rational EDR_{VARS}=0.8683, EDR_{VARS}=6.594, Exergetic $Efficiency_{NH3H2O}$=0.1317) for ,T_{EVA}=-1ºC, Absorber temperature=35ºC, generator temperature=80ºC, Condenser $temperature_{VARS}$=35ºC, Collector Area= 31.65 m^2), Compressor efficiency=0.80, T_{EVA}=-53ºC and Approach (temperature overlapping) =10, {SYSTEM-1}

T_EVA (ºC)	$COP_{Cascade}$	Rational $EDR_{Cascade}$	Exergetic $Efficiency_{cascade}$
-53	3.486	2.427	0.2918
-52	3.601	2.442	0.2905
-51	3.721	2.458	0.2892
-50	3.848	2.475	0.2878
- 45	4.592	2.571	0.2801
-40	5.587	2.69	0.2710
-35	6.986	0.2839	0.2605
-30	9.093	3.023	0.2485

Table-1(f): Effect of evaporator temperature on thermal performances of NH_3H_2O vapor absorption refrigeration cascaded with vapor compression refrigeration system using R1234yf ecofriendly refrigerant ($COP_NH_3H_2O$= 0.322, Rational EDR_{VARS}=0.8683, EDR_{VARS}=6.594, Exergetic $Efficiency_{NH3H2O}$=0.1317) for ,T_{EVA}=-1ºC, Absorber temperature=35ºC, generator temperature=80ºC, Condenser $temperature_{VARS}$=35ºC, Collector Area= 31.65 m^2), Compressor efficiency=0.80, T_{EVA}=-53ºC and Approach (temperature overlapping) =10, {SYSTEM-2}

T_EVA (ºC)	$COP_{Cascade}$	Rational $EDR_{Cascade}$	Exergetic $Efficiency_{cascade}$
-53	3.486	0.6082	0.2918
-52	3.601	0.6195	0.2905
-51	3.721	0.6108	0.2892
-50	3.848	0.6122	0.2878
- 45	4.592	0.6199	0.2801

-40	5.587	0.6290	0.2710
-35	6.986	0.6395	0.2605
-30	9.093	0.6515	0.2485

Table-1 (g) The variation of low temperature evaporator circuit temperature with variation of thermal performances such as first law efficiency in terms of exergy destruction ratio based on exergy of fuel of NH_3H_2O vapor absorption refrigeration system cascaded with vapor compression refrigeration using HFO-1234yf refrigerant (System-1) is shown in Table-1(g) and it is found that when low temperature evaporator circuit temperature of vapor absorption refrigeration system is increasing , coefficient of performance (COP_VCRS) is increasing

Table-1(g): Effect of evaporator temperature on thermal performances of NH_3H_2O vapor absorption refrigeration cascaded with vapor compression refrigeration system using R1234yf ecofriendly refrigerant (COP_NH_3H_2O= 0.322, Rational EDR_$_{VARS}$=0.8683, EDR_$_{VARS}$=6.594, Exergetic Efficiency_$_{NH3H2O}$=0.1317) for ,T_$_{EVA}$=-1°C, Absorber temperature=35°C, generator temperature=80°C, Condenser temperature_$_{VARS}$=35°C, Collector Area= 31.65 m^2), Compressor efficiency=0.80, T_$_{EVA}$=-53°C and Approach (temperature overlapping) =10, {SYSTEM-2}

T_EVA (°C)	COP_$_{Cascade}$	Rational EDR_$_{Cascade}$	Exergetic Efficiency$_{cascade}$
-53	3.473	2.433	0.2913
-52	3.587	2.448	0.290
-51	3.707	2.464	0.2887
-50	3.832	2.480	0.2873
- 45	4.571	2.576	0.2796
-40	5.558	2.696	0.2706
-35	6.943	2.845	0.2601
-30	9.025	3.030	0.2482

3.2 Effect of ecofriendly refrigerants in low temperature evaporator t of vapor compression refrigeration cycle on thermal performances of NH_3H_2O vapor absorption refrigeration cascaded with vapor compression refrigeration system

Table-2(a-b) show, the effect of ecofriendly refrigerants in low temperature circuit with variation of thermal performances such as first law efficiency in terms of coefficient of performance (COP) of cascaded vapor absorption system & second law efficiency in terms of exergetic efficiency and exergy destruction ratio based on exergy of fuel of single effect Li/Br-H_2O vapor absorption refrigeration system cascaded with vapor compression refrigeration at 5°c and at 8°C of cascaded vapor absorption refrigeration system evaporator temperature and vapor compression evaporator temperature of -30°C and it is found that the performance of HFC-134a. Similarly Table-2(c). It was also observed that by changing evaporator temperature from 1°C to 6°C the thermodynamic performances enhanced significantly

Table-2(a): performance comparison of thermal performances of NH_3H_2O vapor absorption refrigeration cascaded with vapor compression refrigeration system using ecofriendly refrigerants (COP_NH_3H_2O= 0.322, Rational EDR_$_{VARS}$=0.8683, EDR_$_{VARS}$=6.594, Exergetic Efficiency_$_{NH3H2O}$=0.1317) for ,T_$_{EVA}$=-1°C, Absorber temperature=35°C, generator temperature=80°C, Condenser temperature_$_{VARS}$=35°C, Collector Area= 31.65 m^2), Compressor efficiency=0.80, T_$_{EVA}$=-53°C and Approach (temperature overlapping) =10,

Refrigerant	COP_$_{Cascade}$	EDR_$_{Cascade}$	Exergetic Efficiency$_{cascade}$
R134a	0.5335	1.552	0.3918
R1234yf	0.5323	1.597	0.3892
R152a	0.5346	1.541	0.3936
R290	0.5336	1.552	0.3919
R600a	0.5344	1.543	0.3933
R600	0.5349	1.537	0.3942

Table2 (b): performance comparison of thermal performances of NH_3H_2O vapor absorption refrigeration cascaded with vapor compression refrigeration system using ecofriendly refrigerants (COP_NH_3H_2O= 0.322, Rational EDR_$_{VARS}$=0.8683, EDR_$_{VARS}$ =6.594, ExergeticEfficiency_$_{NH3H2O}$=0.1317) for T_$_{EVA}$=-1°C, Absorber temperature=35°C,generator temperature=80°C, Condenser temperature_$_{VARS}$=35°C, Compressor efficiency =0.80, T_$_{EVA}$=-53°C and Approach (temperature overlapping) =10,

Refrigerant	COP_$_{VCRS}$	EDR_$_{VCRS}$	Exergetic Efficiency_$_{VCRS}$
R134a	3.472	2.433	0.2913
R1234yf	3.406	2.460	0.2890
R152a	3.516	2.415	0.2928
R290	3.475	2.432	0.2914
R600a	3.509	2.418	0.2925
R600	3.533	2.408	0.2933

Table-2(c): performance comparison of thermal performances of NH_3H_2O vapor absorption refrigeration cascaded with vapor compression refrigeration system using ecofriendly refrigerants (COP_NH_3H_2O= 0.322, Rational EDR_$_{VARS}$=0.8683, EDR_$_{VARS}$=6.594, Exergetic Efficiency_$_{NH3H2O}$=0.1317) for ,T_$_{EVA}$=-1°C, Absorber temperature=35°C, generator temperature=80°C, Condenser temperature_$_{VARS}$=35°C, Collector Area= 31.65 m^2), Compressor efficiency=0.80, T_$_{EVA}$=-53°C and Approach (temperature overlapping) =10,

Refrigerant	COP_$_{Cascade}$	EDR_$_{Cascade}$	Exergetic Efficiency$_{cascade}$
R134a	0.5335	1.552	0.3918
R1234yf	0.5323	1.597	0.3892
R152a	0.5346	1.541	0.3936
R290	0.5336	1.552	0.3919
R600a	0.5344	1.543	0.3933
R600	0.5349	1.537	0.3942

Table2 (d): performance comparison of thermal performances of NH_3H_2O vapor absorption refrigeration cascaded with vapor compression refrigeration system using ecofriendly refrigerants (COP_NH_3H_2O= 0.322, Rational EDR_$_{VARS}$=0.8683, EDR_$_{VARS}$ =6.594, ExergeticEfficiency_$_{NH3H2O}$=0.1317) for T_$_{EVA}$=-1°C, Absorber temperature=35°C, generator temperature=80°C, Condenser temperature_$_{VARS}$=35°C, Compressor efficiency =0.80, T_$_{EVA}$=-53°C and Approach (temperature overlapping) =10,

Refrigerant	COP_$_{Cascade}$	EDR_$_{Cascade}$	Exergetic Efficiency$_{cascade}$
R134a	3.472	2.433	0.2913
R1234yf	3.406	2.460	0.2890
R152a	3.516	2.415	0.2928
R290	3.475	2.432	0.2914
R600a	3.509	2.418	0.2925
R600	3.533	2.408	0.2933

Table-2(a) shows, the effect of ecofriendly refrigerants in low temperature circuit with variation of thermal performances such as first law efficiency in terms of coefficient of performance (COP) of cascaded vapor absorption system & second law efficiency in terms of exergetic efficiency and exergy destruction ratio based on exergy of fuel of NH_3H_2O vapor absorption refrigeration system cascaded with vapor compression refrigeration at 5°C of cascaded vapor absorption refrigeration system evaporator temperature and vapor compression evaporator temperature of -30°C and it is found that the performance of HFC-134a.is higher than R1234yf. Similarly Table-2(b) shows, the effect of ecofriendly refrigerants in low temperature circuit with variation of thermal performances such as first law efficiency in terms of coefficient of performance (COP) of cascaded vapor absorption system & second law efficiency in terms of exergetic efficiency and exergy destruction ratio based on exergy of fuel of NH_3H_2O vapor absorption refrigeration system cascaded with vapor compression refrigeration at 8°c of cascaded vapor absorption refrigeration system evaporator temperature and vapor compression evaporator temperature of -30°C and it is found that the performance of HFO-1234yf . It was also observed that by changing evaporator temperature from 5°C to 10°C the thermodynamic performances enhanced.

3.3 Variation of temperature overlapping of NH_3H_2O vapor absorption system with thermal performances of cascaded vapor absorption compression refrigeration system

Table-3 (a) and (d) shows the variation of approach with variation of thermal performances such as first law efficiency in terms of coefficient of performance (COP) of cascaded vapor absorption system & second law efficiency in terms of exergetic efficiency and exergy destruction ratio based on exergy of fuel of NH_3H_2O vapor absorption refrigeration system cascaded with vapor compression refrigeration using HFC-134a refrigerant and it is found that when temperature overlapping in terms of approach (means condenser temperature of vapor compression refrigeration minus evaporator temperature of vapor absorption refrigeration system) is increasing , the thermodynamic performances in terms of COP_$_{Cascade}$, exergetic efficiency_$_{Cascade\ System}$ is decreasing and EDR_ is increasing

Table-3(a) Thermal performances comparison of thermal performances of NH_3H_2O vapor absorption refrigeration cascaded with vapor compression refrigeration system using R134a ecofriendly refrigerant (COP_NH_3H_2O= 0.322, Rational EDR_$_{VARS}$=0.8683, EDR_$_{VARS}$ =6.594, ExergeticEfficiency_$_{NH3H2O}$=0.1317) for T_$_{EVA}$=-1°C, Absorber temperature=35°C, generator temperature=80°C, Condenser temperature_$_{VARS}$=35°C, Compressor efficiency =0.80, T_$_{EVA}$=-53°C and Approach (temperature overlapping) =10, ***(Approach =T_$_{Cond_VCRS}$ -T_$_{Eva_VARS}$)*** using R134a

Approach (°C)	COP_$_{Cascade}$	EDR_$_{Cascade}$	Exergetic Efficiency$_{cascade}$
0	0.5569	1.307	0.4334
2	0.5522	1.354	0.4248
4	0.5475	1.402	0.4164
5	0.5452	1.426	0.4122
6	0.5429	1.450	0.4082

8	0.5384	1.499	0.4002
10	0.5339	1.549	0.3924
12	0.5294	1.599	0.3848
14	0.5250	1.650	0.3773
15	0.5228	1.676	0.3737
16	0.5206	1.702	0.3701
18	0.5162	1.755	0.3629
20	0.5119	1.809	0.3560

Table-3(b) *Thermal performances comparison of thermal performances of NH_3H_2O vapor absorption refrigeration cascaded with vapor compression refrigeration system using* R1234yf *ecofriendly refrigerant ($COP_NH_3H_2O$= 0.322, Rational $EDR_{_VARS}$=0.8683, $EDR_{_VARS}$ =6.594, $ExergeticEfficiency_{_NH3H2O}$=0.1317) for $T_{_EVA}$=-1ºC, Absorber temperature=35ºC, generator temperature=80ºC, Condenser temperature$_{_VARS}$=35ºC, Compressor efficiency =0.80, $T_{_EVA}$=-53ºC and Approach (temperature overlapping) =10,*

Approach (ºC)	$COP_{_Cascade}$	$EDR_{_Cascade}$	$Exergetic\ Efficiency_{cascade}$
0	0.5563	1.313	0.4324
2	0.5515	1.361	0.4236
4	0.5468	1.410	0.4150
5	0.5444	1.435	0.4107
6	0.5420	1.460	0.4066
8	0.5373	1.511	0.3983
10	0.5326	1.562	0.3903
12	0.5280	1.615	0.3824
14	0.5233	1.669	0.3746
15	0.5210	1.697	0.3708
16	0.5187	1.725	0.3670
18	0.5141	1.781	0.3595
20	0.5095	1.839	0.3522

Similarly exergy destruction ratio based on the exergy of product (EDR_Cascade) is also decreasing, Table-3 (b) shows the variation of approach with variation of thermal performances such as first law efficiency in terms of coefficient of performance (COP) of cascaded single effect vapor absorption system & second law efficiency in terms of exergetic efficiency and exergy destruction ratio based on exergy of fuel of NH_3H_2O vapor absorption refrigeration system cascaded with vapor compression refrigeration using HFO-1234yf refrigerant and it is found that when temperature overlapping in terms of approach (means condenser temperature of vapor compression refrigeration minus evaporator temperature of vapor absorption refrigeration system) is increasing , the thermodynamic performances in terms of ($COP_{_Cascade}$, Exergetic $efficiency_{_Cascade\ System}$) is decreasing and $EDR_{_Rational}$ is increasing. Similarly exergy destruction ratio based on the exergy of product ($EDR_{_Cascade}$) is also decreasing. The performance of NH_3H_2O vapor absorption system cascaded with vapor compression system using HFC-134a and HFO-1234yf for low temperature circuit evaporator at -53ºC and generator temperature at 80ºC have been compared and also shown in Tables-1(a) & Tables-1(b) respectively and it is found that thermodynamic performances using HFO-1234yf in NH_3H_2O cascaded vapor absorption system (system-2) in terms of COP is 1.354% lower and exergetic efficiency is 3.5543% lower than using HFC-134a For increment in EDR is 6.1144% as temperature overlapping approach at 10ºC.

Table-3(c) Thermal performances comparison of thermal performances of NH_3H_2O vapor absorption refrigeration cascaded with vapor compression refrigeration system using R134a ecofriendly refrigerant ($COP_NH_3H_2O$= 0.322, Rational $EDR_{_VARS}$=0.8683, $EDR_{_VARS}$ =6.594, $ExergeticEfficiency_{_NH3H2O}$=0.1317) for $T_{_EVA}$=-1ºC, Absorber temperature=35ºC,generator temperature=80ºC, Condenser temperature$_{_VARS}$=35ºC, Compressor efficiency =0.80, $T_{_EVA}$=-53ºC and Approach (temperature overlapping) =10, (Approach =$T_{_Cond_VCRS}$ -$T_{_Eva_VARS}$) using R134a

Approach (ºC)	$COP_{_Cascade}$	Rational $EDR_{_Cascade}$	$Exergetic\ Efficiency_{cascade}$
0	0.5569	0.5666	0.4334
2	0.5522	0.5752	0.4248
4	0.5475	0.5836	0.4164
5	0.5452	0.5878	0.4122
6	0.5429	0.5918	0.4082
8	0.5384	0.5998	0.4002
10	0.5339	0.6076	0.3924
12	0.5294	0.6152	0.3848
14	0.5250	0.6227	0.3773
15	0.5228	0.6263	0.3737

16	0.5206	0.6299	0.3701
18	0.5162	0.6471	0.3629
20	0.5119	0.6440	0.3560

Table-3 (c) shows the variation of approach with variation of thermal performances such as first law efficiency in terms of coefficient of performance (COP) of NH_3H_2Ocascaded vapor absorption system & second law efficiency in terms of exergetic efficiency and exergy destruction ratio based on exergy of fuel of NH_3H_2O vapor absorption refrigeration system cascaded with vapor compression refrigeration using HFC-134a refrigerant and it is found that when temperature overlapping in terms of approach (means condenser temperature of vapor compression refrigeration minus evaporator temperature of vapor absorption refrigeration system) is increasing, the EDR_ is increasing. Similarly rational exergy destruction ratio based on the exergy of fuel ($EDR_{_Cascade}$) is increasing.

Table-3(d) *Thermal performances comparison of thermal performances of NH_3H_2O vapor absorption refrigeration cascaded with vapor compression refrigeration system using* R134a *ecofriendly refrigerant (COP_NH_3H_2O= 0.322, Rational $EDR_{_VARS}$=0.8683, $EDR_{_VARS}$ =6.594, $ExergeticEfficiency_{_NH3H2O}$=0.1317) for $T_{_EVA}$=-1°C, Absorber temperature=35°C,generator temperature=80°C, Condenser $temperature_{_VARS}$=35°C, Compressor efficiency =0.80, $T_{_EVA}$=-53°C and Approach (temperature overlapping) =10 (System-1)*

Approach (°C)	$COP_{_Cascade}$	Rational $EDR_{_Cascade}$	Exergetic $Efficiency_{cascade}$
0	0.5563	0.5676	0.4324
2	0.5515	0.5766	0.4236
4	0.5468	0.5850	0.4150
5	0.5444	0.5893	0.4107
6	0.5420	0.5934	0.4066
8	0.5373	0.6017	0.3983
10	0.5326	0.6097	0.3903
12	0.5280	0.6176	0.3824
14	0.5233	0.6254	0.3746
15	0.5210	0.6302	0.3708
16	0.5187	0.6330	0.3670
18	0.5141	0.6405	0.3595
20	0.5095	0.6478	0.3522

Table-3(e) *Thermal performances comparison of thermal performances of NH_3H_2O vapor absorption refrigeration cascaded with vapor compression refrigeration system using* R1234yf *ecofriendly refrigerant (COP_NH_3H_2O= 0.322, Rational $EDR_{_VARS}$=0.8683, $EDR_{_VARS}$ =6.594, $ExergeticEfficiency_{_NH3H2O}$=0.1317) for $T_{_EVA}$=-1°C, Absorber temperature=35°C,generator temperature=80°C, Condenser $temperature_{_VARS}$=35°C, Compressor efficiency =0.80, $T_{_EVA}$=-53°C and Approach (temperature overlapping) =10, (System-1)*

Approach (°C)	$COP_{_VCRS}$	$EDR_{_VCRS}$	$ExergeticEfficiency_{_VCRS}$
0	4.756	2.055	0.3273
2	4.445	2.127	0.3198
4	4.167	2.20	0.3125
5	4.039	2.237	0.3090
6	3.917	2.274	0.3054
8	3.691	2.350	0.2985
10	3.486	2.427	0.2918
12	3.299	2.506	0.2852
14	3.127	2.587	0.2788
15	3.046	2.629	0.2756
16	2.968	2.670	0.2725
18	2.822	2.755	0.2663
20	2.686	2.842	0.2603

Table-3(f) Thermal performances comparison of thermal performances of NH_3H_2O vapor absorption refrigeration cascaded with vapor compression refrigeration system using R1234yf *ecofriendly refrigerant (COP_NH_3H_2O= 0.322, Rational EDR_$_{VARS}$=0.8683, EDR_$_{VARS}$ =6.594, ExergeticEfficiency_$_{NH3H2O}$=0.1317) for T_$_{EVA}$=-1°C, Absorber temperature=35°C,generator temperature=80°C, Condenser temperature_$_{VARS}$=35°C, Compressor efficiency =0.80, T_$_{EVA}$=-53°C and Approach (temperature overlapping) =10, (System-1)*

Approach (°C)	COP_$_{VCRS}$	Rational EDR_$_{VCRS}$	Exergetic Efficiency_$_{VCRS}$
0	4.756	0.6727	0.3273
2	4.445	0.6802	0.3198
4	4.167	0.6875	0.3125
5	4.039	0.6910	0.3090
6	3.917	0.6946	0.3054
8	3.691	0.7015	0.2985
10	3.486	0.7082	0.2918
12	3.299	0.7148	0.2852
14	3.127	0.7212	0.2788
15	3.046	0.7244	0.2756
16	2.968	0.7275	0.2725
18	2.822	0.7337	0.2663
20	2.686	0.7397	0.2603

Table-3(g) Thermal performances comparison of thermal performances of NH_3H_2O vapor absorption refrigeration cascaded with vapor compression refrigeration system using R1234yf *ecofriendly refrigerant (COP_NH_3H_2O= 0.322, Rational EDR_$_{VARS}$=0.8683, EDR_$_{VARS}$ =6.594, ExergeticEfficiency_$_{NH3H2O}$=0.1317) for T_$_{EVA}$=-1°C, Absorber temperature=35°C,generator temperature=80°C, Condenser temperature_$_{VARS}$=35°C, Compressor efficiency =0.80, T_$_{EVA}$=-53°C and Approach (temperature overlapping) =10,*

Approach (°C)	COP_$_{VCRS}$	EDR_$_{VCRS}$	Exergetic Efficiency_$_{VCRS}$
0	4.719	2.063	0.3264
2	4.404	2.137	0.3188
4	4.123	2.212	0.3113
5	3.994	2.250	0.3077
6	3.870	2.289	0.3041
8	3.641	2.368	0.2969
10	3.433	2.449	0.2899
12	3.242	2.532	0.2831
14	3.067	2.618	0.2764
15	2.984	2.662	0.2731
16	2.905	2.706	0.2698
18	2.755	2.797	0.2634
20	2.615	2.891	0.2570

Table-3(h) *Thermal performances comparison of thermal performances of NH_3H_2O vapor absorption refrigeration cascaded with vapor compression refrigeration system using* R1234yf *ecofriendly refrigerant (COP_NH_3H_2O= 0.322, Rational EDR_$_{VARS}$=0.8683, EDR_$_{VARS}$ =6.594, ExergeticEfficiency_$_{NH3H2O}$=0.1317) for T_$_{EVA}$=-1°C, Absorber temperature=35°C, generator temperature=80°C, Condenser temperature_$_{VARS}$=35°C, Compressor efficiency =0.80, T_$_{EVA}$=-53°C and Approach (temperature overlapping) =10,*

Approach (°C)	COP_$_{VCRS}$	Rational EDR_$_{VCRS}$	Exergetic Efficiency_$_{VCRS}$
0	4.719	0.6136	0.3264
2	4.404	0.6812	0.3188
4	4.123	0.6887	0.3113
5	3.994	0.6923	0.3077
6	3.870	0.6959	0.3041
8	3.641	0.7031	0.2969
10	3.433	0.7111	0.2899
12	3.242	0.7169	0.2831
14	3.067	0.7236	0.2764
15	2.984	0.7269	0.2731
16	2.905	0.7302	0.2698
18	2.755	0.7366	0.2634
20	2.615	0.7530	0.2570

Table-3 (g) & Table-3(h) show the variation of approach with variation of thermal performances such as first law efficiency in terms of coefficient of performance (COP) of cascaded vapor absorption system & second law efficiency in terms of exergetic efficiency and exergy destruction ratio based on exergy of fuel of NH_3H_2O vapor absorption refrigeration

system cascaded with vapor compression refrigeration using HFC-1234yf refrigerant and it is found that when temperature overlapping in terms of approach (means condenser temperature of vapor compression refrigeration minus evaporator temperature of vapor absorption refrigeration system) is increasing, first law efficiency ($COP_{_VCRS}$) and second law efficiency of cascaded vapor compression system are decreasing.. Similarly Exergy destruction Ratio based on exergy of product and Rational exergy destruction ratio based on the exergy of fuel ($EDR_{_VCRS}$) are also increasing

4. Conclusions

The following conclusions were drawn from present investigations.

(i) The thermal performance of single NH_3H_2O vapour absorption refrigeration system cascaded with vapour compression system using HFO -1234yf refrigerant is always than the NH_3 H_2O vapour absorption refrigeration system cascaded with vapour compression system (system-1)using HFC -134a refrigerants. The thermodynamic performances using HFO-1234yf (system-2) in cascaded vapour absorption system in terms of COP is 1.477% % lower and exergetic efficiency is slightly lower than using HFC-134a in the vapour compression refrigeration system.

(ii) In the NH_3H_2O vapour absorption refrigeration system cascaded with vapour compression refrigeration using HFC-134a refrigerant and it is found that absorber temperature of NH_3H_2O vapour absorption refrigeration system is increasing , the thermodynamic performances in terms of ($COP_{_Cascade}$,) is decreasing and Exergetic efficiency$_{_Cascade\ System}$ is increasing and $EDR_{_}$ is decreasing.

(iii) In the NH_3H_2O vapour absorption refrigeration system cascaded with vapour compression refrigeration using HFC-134a refrigerant and it is found that when condenser temperature of vapour absorption refrigeration system is increasing, the thermodynamic performances in terms of ($COP_{_Cascad}$,) and Exergetic efficiency$_{_Cascade\ System}$ both are decreasing and $EDR_{_Rational}$ is increasing.

(iv) In the NH_3H_2O vapour absorption refrigeration system cascaded with vapour compression refrigeration using HFC-134a refrigerant and it is found that when generator temperature of vapour absorption refrigeration system is increasing , the thermodynamic performances in terms of ($COP_{_Cascad}$,) is decreasing and Exergetic efficiency$_{_Cascade\ System}$ is increasing and $EDR_{_Rational}$ is decreasing

(v) In the NH_3H_2O vapour absorption refrigeration system cascaded with vapour compression refrigeration using HFC-134a refrigerant and it is found that when Vapour absorption system evaporator temperature ($T_{_evaporator}$)of NH_3-H_2O vapour absorption refrigeration system is increasing , the thermodynamic performances in terms of ($COP_{_Cascad}$,) is decreasing and Exergetic efficiency$_{_Cascade\ System}$ is increasing and $EDR_{_Rational}$ is decreasing . Similarly exergy destruction ratio based on the exergy of product ($EDR_{_Cascade}$) is also decreasing and exergetic efficiency is increasing.

(vi) In the NH_3H_2O vapour absorption refrigeration system cascaded with vapour compression refrigeration using HFC-134a refrigerant and it is found that when heat exchanger effectiveness of vapour absorption refrigeration system) is increasing, the thermodynamic performances in terms of ($COP_{_Cascade}$) & exergetic efficiency$_{_Cascade\ System}$) is increasing and $EDR_{_cascade}$ is decreasing when heat exchanger effectiveness is increasing.

(vii) In the NH_3H_2O vapour absorption refrigeration system cascaded with vapour compression refrigeration using HFC-134a refrigerant and it is found that when temperature overlapping in terms of approach (means condenser temperature of vapour compression refrigeration minus evaporator temperature of vapour absorption refrigeration system) is increasing, the thermodynamic performances in terms of ($COP_{_Cascade}$, Exergetic efficiency$_{_Cascade\ System}$) is decreasing and $EDR_{_Rational}$ is increasing.

References

[1] Alizadeh, S., Bahar, F., Geoola, F., Design and optimization of an absorption refrigeration system operated by solar energy, Solar Energy, Vol. 22, (1997), pp. 149-154 .

[2] Keshwani, H.B. and Rastogi, K.V., Optimum inter-cooler pressure in multistage compression of refrigerants, All India Symposium on Refrigeration, AirConditioning and Environmental Control in Cold Storage Industry, (1968), pp. E 6.1-13.

[3] Zubair, S.M. and Khan, S.H., On optimum interstage pressure for two stage and mechanical subcooling vapour compression refrigeration cycles, Journal of Solar Energy Engineering, Vol. 117(1), (1995), pp. 64-66

[4] Zubair, S.M., Yaqub, M. and Khan, S.H., Second law based thermodynamic analysis of two stage and mechanical sub-cooling refrigeration cycles, International Journal of Refigeration, Vol. 19(8), (1996), pp. 506-516

[5] Aprea, C., Mastrullo, R. and Rossi, F.D., Behaviour and performances of R502 alternative working fluids in refrigerating plants, International Journal of Refrigeration, Vol. 19(4), (1996), pp. 257-263

[6] Doring, R., Buchwald,H. and Hellman, J., Results of experimental and theoretical studies of the azeotropic refrigerant R507,International Journal of Refrigeration, Vol. 20(2), (1997), pp. 78-84.

[7] Sami, S.M. and Desjardins, D.E., Performance enhancement of some alternatives to R502, International Journal of Energy Research, Vol. 24(4), (2000), pp. 279-289.

[8] Nikolaidis, C. and Probert, D., Exergy method analysis of a two stage vapour compression refrigeration plants performance, Applied Energy, Vol. 60, (1998), pp. 241-256

[9] Alberto Dopazo, J., Fernandez-Seara, J., Sieres, J. and Uhia, F.J., Theoretical analysis of a CO2-NH3 cascade refrigeration system for cooling applications at low temperatures, Applied Thermal Engineering, Vol. 29, (2009), pp. 1577-1583

[10] Padilla, M., Revellin, R. and Bonjour, J., Exergy analysis of R413A as replacement of R12 in a domestic refrigeration system, Energy Conversion and Management, Vol.51, (2010), pp. 2195-2201 60 60.

[11] Qureshi, B.A., Zubair, S.M., Performance degradation of a vapor compression refrigeration system under fouled conditions, International Journal of Refrigeration, Vol. 34(4), (2011), pp. 1016-1027

[12] R.S. Mishra (2018) Comparison of thermal performances of single effect, double effect and triple effect LiBr-H2O absorption system cascaded with vapour compression refrigeration systems using ecofriendly refrigerants, International Journal of Research in Engineering and Innovation Vol-2, Issue-6 , 610-621
[13] R.S. Mishra (2018) Comparison of thermal performances of single effect, double effect and triple effect LiBr-H2O absorption system cascaded with vapour compression refrigeration systems using ecofriendly refrigerants, International Journal of Research in Engineering and Innovation Vol-2, Issue-6 , 610-621
[14] Fernandez-Seara et al . Compression-absorption cascade refrigeration system, Applied Thermal Engineering, Vol. 26, (2006), pp. 502-512
[15] Kairouani, L. and Nehdi, E., Cooling performance and energy saving of a compression-absorption refrigeration system assisted by geothermal energy, Applied Thermal Engineering, Vol. 26, (2006), pp. 288-294
[16] Garimella, S., Brown, A., Nagavarapu, A.K., Waste heat driven absorption/vapor-compression cascade refrigeration system for megawatt scale, high-flux, low-temperature cooling, International Journal of Refrigeration, Vol. 34(8), (2011), pp. 1776-1785
[17] Yari, M., Zarin, A., Mahmoudi, S.M.S., Energy and exergy analyses of GAX and GAX hybrid absorption refrigeration cycle, Renewable Energy, Vol. 36(7), (2011), pp. 2011-2020
[18] Zheng, D., Meng, X., Ultimate refrigerating conditions, behavior turning and a thermodynamic analysis for absorption-compression hybrid refrigeration cycle, Energy Conversion and Management, Vol. 56, (2012), pp. 166-174
[19] R.S. Mishra Ankit Dewedi [2017] Methods for improving thermal performances of vapour absorption system using heat pipes International Journal of Research in Engineering and Innovation (IJREI), Vol-1, Issue-3), 118-125.

Cite this article as: R.S. Mishra, Thermodynamic performances using energy-exergy analysis of NH_3H_2O vapor absorption refrigeration system cascaded with vapor compression refrigeration systems using ecofriendly refrigerants, International Journal of Research in Engineering and Innovation Vol-3, Issue-2 (2019), 144-156.

ResearchGate

See discussions, stats, and author profiles for this publication at: https://www.researchgate.net/publication/330781623

Strength Enhancement of the Subgrade Soil of Unpaved Road with Geosynthetic Reinforcement Layers

Article *in* Transportation Geotechnics · January 2019

DOI: 10.1016/j.trgeo.2019.01.007

CITATIONS
0

READS
31

3 authors, including:



Meenakshi Singh
Delhi Technological University
1 PUBLICATION **0** CITATIONS

SEE PROFILE

All content following this page was uploaded by Meenakshi Singh on 06 March 2019.

The user has requested enhancement of the downloaded file.

Transportation Geotechnics 19 (2019) 54–60

Contents lists available at ScienceDirect

Transportation Geotechnics

journal homepage: www.elsevier.com/locate/trgeo

Strength enhancement of the subgrade soil of unpaved road with geosynthetic reinforcement layers

Meenakshi Singh[a,*], Ashutosh Trivedi[a], Sanjay Kumar Shukla[b,c]

[a] Department of Civil Engineering, Delhi Technological University, Delhi, India
[b] Discipline of Civil and Environmental Engineering, School of Engineering, Edith Cowan University, Australia
[c] School of Building and Civil Engineering, Fiji National University, Fiji

ARTICLE INFO

Keywords:
Subgrade
CBR value
Geogrids
Geomat
Reinforcement

ABSTRACT

Geosynthetic reinforcement layers are often used to improve the performance of pavement structures. The performance of an unpaved road is routinely measured in terms of the California bearing ratio (*CBR*), which is an index of strength of subgrade soil of unpaved road. In the present study, an experimental investigation was carried out to evaluate the performance of the subgrade soil by placing a single layer and double layers of geosynthetic reinforcements (Glasgrid, Tenax 3D grid and Tenax multimat) horizontally at varying depths from the top surface of subgrade soil. Through a series of *CBR* tests in the laboratory, an attempt was made to determine the optimum depth of the reinforcement layer. The single layer of reinforcement has been placed at the middle, one-third and one-fourth of the height of the *CBR* specimen from the top surface of the soil in the CBR mould. The double layers of reinforcement were placed at one-fourth of the specimen height from the top surface and the bottom surface. The results show the significant contribution in terms of increased *CBR* value of the soil, resulting in reduced design thickness of the pavement layers above the subgrade soil. It has been observed that for a single layer reinforcement the Tenax 3D grid performs better than other geosynthetics used in this study while the Tenax multimat performs best for double layers. The results indicate that for the maximum benefit, the Tenax 3D grid reinforcement should be placed in between 0.3*H* and 0.36*H* where *H* is the height of the soil specimen. For Glasgrid and Tenax multimat reinforcements, the maximum effect of reinforcement is obtained when they are placed between 0.41*H* and 0.62*H*.

Introduction

In the current construction practice, the geosynthetic layers are often utilized for improving the weak/unsuitable soil subgrade for paved and unpaved roads. The geosynthetic layer as a reinforcement can be used effectively to reinforce the unpaved road built on soft soil subgrades, resulting in increased life of the road. The benefits obtained from the use of geosynthetic layers in unpaved roads can be observed not only with respect to performance and durability but also with respect to construction and economy [23]. The concept of using geosynthetic as reinforcement in paved/unpaved road construction started in the 1970s. Since then, many experimental and numerical studies have been reported in the literature to evaluate the benefits of using the geosynthetics in road construction [5,25]. Due to the successful application of geosynthetics in roads, different types of geosynthetics have been developed worldwide and their market is steadily growing [22].

Several researchers have shown the benefits of geosynthetic reinforcement in unpaved roads over weak subgrades to improve their performance [9,8,18,11]. The position of the reinforcement layer in the subgrade also influences the performance of the road [19,21,24]. Several field trials and full-scale laboratory investigations have illustrated that the geosynthetics used to reinforce the unpaved roads on soft ground facilitate confinement, reduce the depth of ruts, improve load-bearing capacity, extend the service life and reduce the necessary fill thickness [1,2,11,10]. Relatively thicker pavement sections and base-course layers indicate that more material is required for construction, and therefore it increases the cost. Geosynthetics have been used as an alternative to reduce the cost of these materials and improve the performance of reinforced road sections. Some studies have been carried out to quantify the benefit of using the geogrid base reinforcement [3]. Initial cost and maintenance cost of reinforced road section has been an important factor which should be considered for evaluating the benefits of geosynthetic reinforcement. Palmeira and Antunes [17] have shown that the presence of geosynthetic reinforcement in unpaved road

* Corresponding author.
E-mail addresses: meenakshi_2k14@dtu.ac.in (M. Singh), atrivedi@dce.ac.in (A. Trivedi), s.shukla@ecu.edu.au (S.K. Shukla).

https://doi.org/10.1016/j.trgeo.2019.01.007
Received 19 November 2018; Received in revised form 25 January 2019; Accepted 30 January 2019
Available online 31 January 2019
2214-3912/ © 2019 Published by Elsevier Ltd.

reduces the maintenance cost which yields to the important savings in the overall cost of the road construction.

The behavior of the road surface depends on the strength of the fill material and the subgrade of the pavement. The strength of the subgrade is most often expressed in terms of the California Bearing Ratio (*CBR*), which is the ratio of test load to standard load at a specific penetration, by a standard plunger [12]. Many functions of geosynthetics have been reported such as separation, reinforcement, filtration, drainage, fluid barrier and protection [22]. One of the important applications of geosynthetics is reinforcement which is used to improve the strength of weak soil, that is to increase in *CBR* of soils [4,6,15,20]. The soils with low *CBR* value have higher benefits of geosynthetic reinforcement in terms of improved strength than those soils with higher *CBR* values [7]. The improvement in subgrade performance can facilitate compaction, reduces the aggregate layer thickness, delay rut formation and extend the service life of unpaved roads, particularly in cases of very soft subgrades with *CBR* value less than three [11]. In the literature very conflicting results have appeared for the position of geosynthetic as a reinforcement layer. Some researchers believe that the maximum effect of reinforcement layer is obtained when geosynthetic is placed near the load or at bottom half of the height of specimen in the CBR mould, while others have found that placing the geosynthetic reinforcement at the centre of the CBR mould is most beneficial [13].

This work presents a study on the use of three different types of geosynthetics as the reinforcement at different depths within the subgrade soil for improvement of its *CBR* value. The main objective of research is to investigate the optimum position of geosynthetic reinforcement layer within the subgrade soil thickness, which has not been given due attention in the past.

Materials used

Subgrade soil

The soil used in the present research was locally available soil obtained from the campus of Delhi Technological University, Delhi. The soil is classified as silty sand (SM) using the particle-size analysis and Atterberg limit tests as per Indian Soil Classification System (IS: 2720). The particle-size distribution curve of the soil is shown in Fig. 1. The basic properties of the soil are also determined in the laboratory and they are given in Table 1.

Reinforcement

Two types of geogrids (Glasgrid, Tenax 3D grid) and one geomat (Tenax multimat) were used as the geosynthetic reinforcement in this study. The geosynthetic samples are shown in Fig. 2. The properties of geogrids and geomat as provided by the manufacturer are given in Table 2. Glasgrid is a high strength, open fiberglass grid custom knitted in a stable construction and coated with a patent-pending elastomeric polymer and self-adhesive glue. Every component of the matrix shall be stabilized against ultraviolet degradation and inert to chemicals normally found in a natural soil environment. Tenax 3D grid is manufactured from a unique extrusion technique resulting in a perforated sheet that is specifically shaped in three directions (3D). This unique extrusion technique produces a structure with vertical longitudinal ribs capable to guarantee the best possible interaction mechanism between geogrids and granular soils by restricting the horizontal movement of soil particles and preventing further displacements. This increase in interaction from the 3D Grids enables consistent reductions in aggregate layer thickness. Tenax multimat is a three dimensional mat composed by extruded and bi-oriented polypropylene grids, laid one upon each another and tied up by means of a black polypropylene yarn.

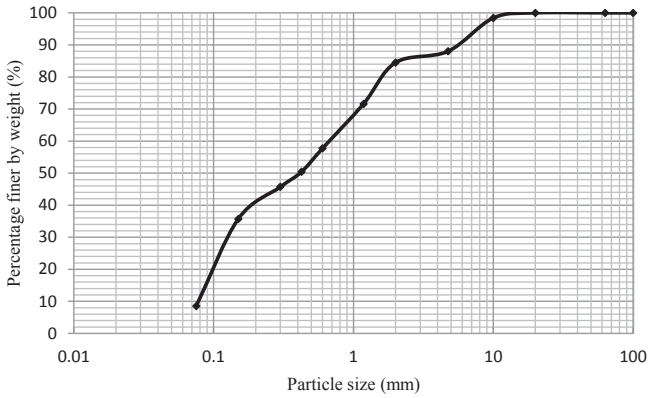


Fig. 1. Particle-size distribution of subgrade soil.

Table 1
Engineering properties of subgrade soil.

S. no.	Particulars	Subgrade soil
1	Specific gravity	2.55
2	Liquid limit (%)	29
3	Plastic limit (%)	20
4	Plasticity index (%)	9
5	IS Classification	SM
6	Optimum moisture content (%)	13.91
7	Maximum dry unit weight (kN/m^3)	18.74
8	California bearing ratio (*CBR*) (%)	1.66

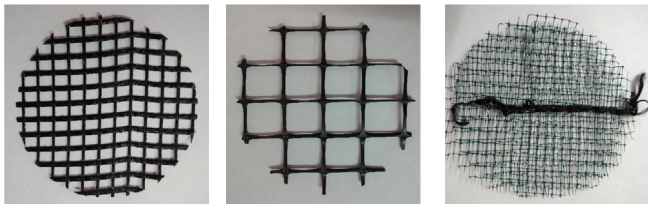


Fig. 2. Geogrids and geomat used in the study: (a) Glasgrid, (b) Tenax 3D grid, (c) Tenax multimat.

Geosynthetics are available with a variety of geometric and polymer compositions to meet a wide range of functions and applications. Selection of geosynthetic may have specific requirement depending on the type of application. Geogrids are used mainly for reinforcement and separation could be a function served by geogrids when soils are having very large particle sizes. Therefore, two types of geogrids were selected for the present study and the performance of the geogrid for reinforcement relies on its rigidity, strength, stiffness and aperture size, which accounts for its high capacity for interlocking with soil particles. The selection of a geosynthetic for a particular application is governed by several other factors, such as specification, durability, availability and cost [23,22].

Experimental investigation

The standard Proctor compaction test was carried out as per IS: 2720 (Part VII-1980) to determine the maximum dry unit weight (MDU) and optimum moisture content (OMC) for the soil. The MDU and OMC of soil were found to be 18.74 kN/m^3 and 13.91% respectively.

The design method that determines the required layer thickness of the aggregate with the reinforcement in the subgrade has been based on the *CBR* of the subgrade soil [9]. If the *CBR* of the subgrade is improved by providing the reinforcement, then the required thickness of the granular subbase/base layer can be reduced for a given traffic volume or, alternatively, the traffic volume can be increased for a given

Table 2
Properties of geogrids and geomat (Courtesy of H. M. B. S Textile Private Limited, New Delhi).

Geosynthetics	Description	Value	Unit	Test method
Glasgrid	Mass per unit area	405	g/m^2	ASTM D5261
	Grid size	12.5 × 12.5	mm	
	Material	Fiberglass reinforcement with modified polymer coating and pressure sensitive adhesive backing	–	–
	Tensile strength (Ultimate)	115 × 115 ± 15 (MD × TD)	kN/m	ASTM D6637 EN-ISO 10319:2008
	Tensile elongation (Ultimate)	2.5 ± 0.5%	–	ASTM D6637 EN-ISO 10319:2008
	Tensile resistance@2% strain	95 × 95 ± 20	kN/m	ASTM D6637 EN-ISO 10319:2008
	Secant stiffness EA@1% strain	4600 × 4600 ± 600 (MD × TD)	N/mm	ASTM D6637 EN-ISO 10319:2008
	Damage during installation	< 5%	–	Internal test method
Tenax 3D grid	Structure	Bi-oriented geogrids	–	–
	Mesh type	Quadrangular apertures	–	–
	Polymer type	Polypropylene	–	–
	Aperture size[c,d]	30 × 30 (MD × TD)	mm	–
	Transversal rib width[c]	2.6	mm	–
	Longitudinal rib thickness[e]	3.8	mm	–
	Junction thickness[c]	6	mm	–
	Stiffness at 0.5% strain[a,b,c]	550 × 350 (MD × TD)	kN/m	ISO 10319
	Installation damage factor	1	–	ASTM D5818
Tenax multimat	Structure	Three dimensional geomat composed by 3 layers	–	–
	Mesh type	Rectangular apertures	–	–
	Polymer type	Polypropylene	–	–
	Peak tensile strength[c,f]	3.8 × 13 (MD × TD)	kN/m	ISO 10319
	Yield point elongation[a,c]	23 × 23 (MD × TD)	%	ISO 10319
	Mass per unit area[a]	180	g/m^2	ISO 9864
	Thickness[a]	8	mm	ASTM D6525
	Aperture size[a,c]	7 × 9 (MD × TD)	mm	–

[a] Typical values.
[b] Tests performed using extensometers.
[c] MD: machine direction (longitudinal to the roll) – TD: transverse direction (across roll width).
[d] Aperture tolerance: ± 5 mm.
[e] Thickness/width tolerance: −5%.
[f] 95% lower confidence limit values, ISO 2602.

thickness of granular subbase/base layer. It is not always possible to get good quality granular material as per the design specifications either because of unavailability or increase in cost because of long haulage distance. Hence there is a need of subgrade soil stabilization with geosynthetic reinforcement to increase the strength and reduce the granular layer thickness over the subgrade soil. Therefore, the unsoaked CBR tests were conducted on the subgrade soil without reinforcement and with a single layer and double layer of different types of geosynthetic reinforcement as described in IS: 2720 (Part 16) – 1979. To evaluate the effect of geosynthetic reinforcement on subgrade strength, the single layer of reinforcement was placed at different positions, namely $H/2$, $H/3$, $H/4$ where H is the height of the soil specimen of the CBR mould from the top surface and double layer of reinforcement was placed at $H/4$ from top and bottom surface of the soil specimen.

The location of single and double layers of reinforcement within the subgrade were selected based on the literature because most of the researchers believe that maximum benefit of reinforcement is obtained when the reinforcement layer is placed in the upper half portion of the CBR mould. Half of the height of CBR mould was taken to place the reinforcement layers to get the maximum benefit of reinforcement. Therefore, three positions for single layers of reinforcement and one position for double layer of reinforcement were selected.

The geosynthetic reinforcement was cut in the form of a circular disk of diameter slightly less than the diameter of CBR mould. The dry weight required for filling the mould was calculated based upon the maximum dry unit weight (MDU) and the water corresponding to OMC was added in the soil and then the soil was mixed thoroughly. The mould is filled with this soil by placing geosynthetic reinforcement at predetermined depth as shown in Fig. 3. The cross section of the model



Fig. 3. Orientation of reinforcement layer placed at predetermined depth in CBR mould.

along with the position of geosynthetic reinforcement is shown in Fig. 4. The surcharge weights were placed on the specimen to stimulate the effect of the thickness of road construction overlying the layer being tested. Load is applied to the plunger into the soil at the rate of 1.25 mm/min. Readings of the load were taken at penetration of 0.5 mm to until a total penetration of 12.5 mm. The standard *CBR* tests were performed in the laboratory to compare the performance of various geosynthetics under the same subgrade soil condition. The soil specimen height in the *CBR* mould was taken as an equivalent to the thickness of the prepared subgrade soil in the field. Laboratory tests can

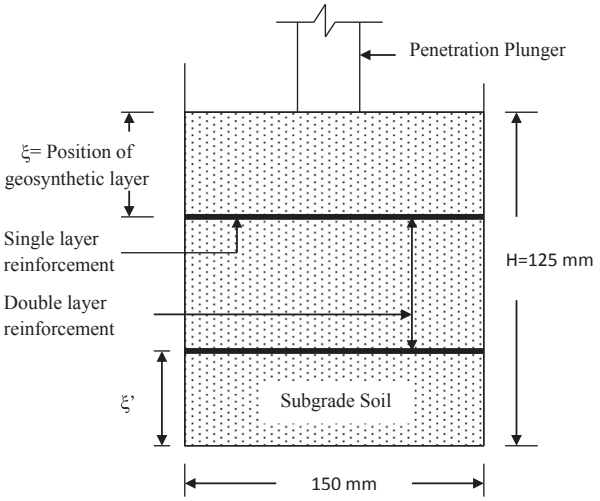


Fig. 4. Schematic representation of the specimen in *CBR* test model, position of geosynthetic is, $\xi = H/2$, $H/3$ and $H/4$ for single layer of reinforcement and $\xi = \xi' = H/4$, for double layers of reinforcement.

be conducted more quickly and usually have more alternatives but they are only able to simulate field conditions. Further, the scaling and boundary effect can have influence on the final results, but any change in specimen size will create difficulty for comparative analysis. Thus the measured values can be treated as relative measurements.

The improvement in *CBR* value of subgrade soil with reinforcement is measured in terms of the reinforcement ratio η, which is defined as a ratio of *CBR* value of soil with reinforcement (CBR_R) to that of original soil (*CBR*),[14,22].

$$\eta = \frac{CBR_R}{CBR}$$

This ratio indicates the contribution of geosynthetic reinforcement towards increasing the *CBR* value of a soil and compares the performance of geogrids and geomat reinforcement on the same soil. To quantify the role of reinforcement in increasing the strength, the reinforcement ratio is calculated for various cases (as shown in Table 3) and compared to distinguish the role of geosynthetic layer in improvement.

Table 3
Results of *CBR* tests for different positions of geosynthetics.

Type of geosynthetic	Position of geosynthetic reinforcement	*CBR* (%)	Increase in *CBR* with respect to unreinforced section (%)	Reinforcement ratio (η)
Glasgrid	*H*/2	2.21	33.13	1.33
	H/3	1.76	6.02	1.06
	H/4	2.04	22.89	1.23
	Double layers	3.52	112.05	2.12
Tenax 3D grid	*H*/2	1.76	6.02	1.06
	H/3	2.08	25.30	1.25
	H/4	2.04	22.89	1.23
	Double layers	6.25	276.51	3.77
Tenax multimat	*H*/2	2.63	58.43	1.58
	H/3	1.74	4.82	1.05
	H/4	1.94	16.87	1.17
	Double layers	7.05	324.70	4.25

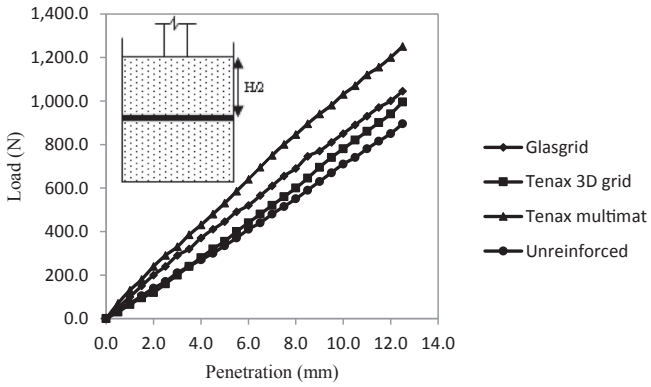


Fig. 5. Load penetration curve with geosynthetic placed at, $\xi = H/2$.

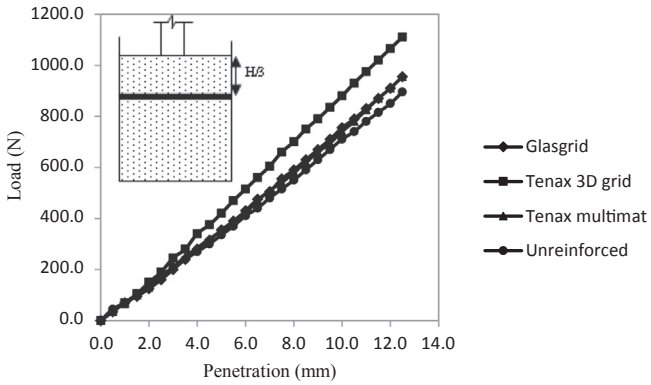


Fig. 6. Load penetration curve with geosynthetic placed at, $\xi = H/3$.

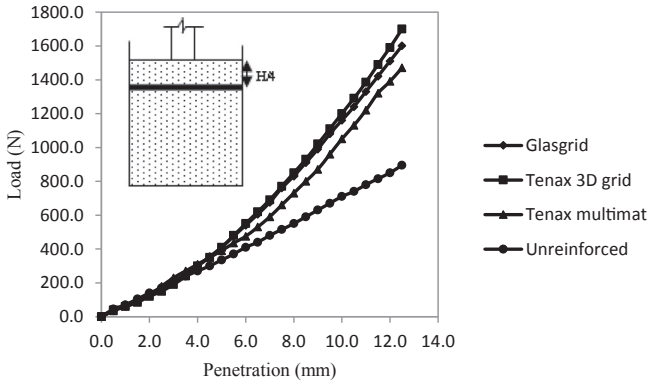


Fig. 7. Load penetration curve with geosynthetic placed at, $\xi = H/4$.

Results and discussion

CBR value

Figs. 5–7 present the variation of the load-penetration curves obtained from the *CBR* tests for unreinforced and reinforced sections with a single layer of reinforcement. It can be observed that placing the geosynthetic reinforcement at varying depths increases the *CBR* value significantly. The amount of increase in the *CBR* value depends on the position of geosynthetic reinforcement (ξ) and type of reinforcement. The *CBR* value of the unreinforced soil specimen corresponding to 2.5 mm and 5.0 mm penetrations were found to be 1.26% and 1.66% respectively as shown in Fig. 5, which were increased to 1.79% and 2.21% respectively, when Glasgrid reinforcement was placed at depth $H/2$. Further placing Tenax multimat reinforcement at same depth $H/2$, enhanced the *CBR* value to 2.16% and 2.63% respectively

corresponding to 2.5 mm and 5.0 mm penetrations. When Tenax 3D grid reinforcement layer was placed at the same depth $H/2$, it decreased the *CBR* value at 2.5 mm penetration to 1.19% but increased the *CBR* at 5.0 mm penetration to 1.76%. The maximum value of *CBR* obtained at 5.0 mm penetration is 2.63% when Tenax multimat reinforcement layer was placed at depth $H/2$. Similar results have been observed for other geosynthetic reinforcements placed at depth $H/3$ and $H/4$ as shown in Figs. 6 and 7.

Fig. 6 presents the variation of load-penetration curve for the soil specimen without reinforcement and soil specimen reinforced with different types of geosynthetic reinforcement layer at depth $H/3$. The increase in the *CBR* value of the Tenax 3D grid reinforced soil specimen corresponding to 2.5 mm and 5.0 mm penetrations were found to be 1.41% and 2.08% respectively. In case of Tenax multimat reinforcement it increased to 1.30% and 1.74% respectively corresponding to 2.5 mm and 5.0 mm penetrations. Only in case of Glasgrid reinforced specimen the *CBR* value decreased at 2.5 mm penetration to 1.19% and increased at 5.0 mm penetration to 1.76% as compared to the unreinforced specimen. The maximum value of *CBR* obtained at 5.0 mm penetration is 2.08% when Tenax 3D grid reinforcement was placed at depth $H/3$.

Fig. 7 represents the influence of the position of the reinforcing layer on the load-penetration curve for both unreinforced and reinforced specimens obtained from the *CBR* tests when the reinforcement was placed at depth $H/4$. The *CBR* value of the Tenax multimat reinforced soil corresponding to 2.5 mm and 5.0 mm penetrations were found to be 1.34% and 1.94% respectively. For Glasgrid and Tenax 3D grid reinforced soil specimen, the same *CBR* value was obtained at 5.0 mm penetration is 2.03% but it decreased to 1.19% and 1.12% at 2.5 mm penetration corresponding to Glasgrid and Tenax3D grid reinforcement respectively. The results are in good agreement with data presented by Williams [7] on effect of geosynthetic reinforcement on *CBR* strength of soil that leads to improve the strength of soil, resulting in a decrease in the surface penetration and deformation with stress distribution over a wider area. This means that the inclusion of single layer of geosynthetic reinforcement increases soil resistance against loading.

Fig. 8 shows the variation of the load-penetration curves obtained from the *CBR* tests for unreinforced and reinforced sections with double layers of reinforcement. The *CBR* value of the soil increased to 1.86% and 3.52% corresponding to 2.5 mm and 5.0 mm penetrations respectively when the subgrade is reinforced with double layers of Glasgrid reinforcement. The strength of the soil increased further by placing double layers of Tenax 3D grid reinforcement and Tenax multimat reinforcements. The *CBR* value of soil reinforced with double layers of Tenax 3D grid reinforcement corresponding to 2.5 mm and 5.0 mm penetrations were found to be 3.72% and 6.25% respectively as shown in Fig. 8, which were increased to 4.16% and 7.05% when the soil was reinforced with double layers of Tenax multimat reinforcement. It is clearly observed that Tenax multimat performs far better in terms of increase in *CBR* and load carrying capacity for double layers of reinforcement. The highest increase in *CBR* value was achieved when the subgrade soil was reinforced with double layers of reinforcement as compared to the unreinforced section and the section reinforced with a single layer of reinforcement.

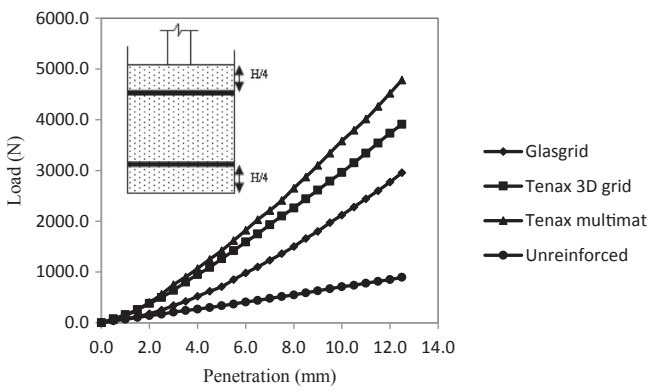


Fig. 8. Load penetration curve with double geosynthetic layer placed at $\xi = \xi' = H/4$.

The reason for the improvement in the strength of the subgrade soil reinforced with single and double layers of reinforcement is that, the geosynthetics used in the study has good interlocking and frictional capability which can provide tensile resistance to any lateral movements. Thus it improves the strength of the soil with low *CBR*. Another reason for the improvement in the strength of the subgrade with low *CBR* is that, through the inclusion of geosynthetic reinforcement layers the maximum vertical stress on the subgrade is reduced. The vertical stress on the subgrade is more uniformly distributed than on the absence of a geosynthetic. Therefore, reinforcement helps to improve the bearing capacity of the soil with low *CBR*. Also, the combining action of geosynthetic tension and geosynthetic improved load distribution results in vertical restraint of the subgrade.

Effect of multiple layer reinforcements

Table 3 shows the results of the *CBR* tests on soil reinforced with three different types of geosynthetics and presents the reinforcement ratio for these three types of geosynthetic reinforcement placed at depth $H/2$, $H/3$ and $H/4$ and double layers. It is clear that there is a considerable amount of increase in the *CBR* value of a soil reinforced with different types of geosynthetics at various depths. As the reinforcement ratio exceeds unity ($\eta > 1$) throughout the tests for different types of geosynthetic reinforcement used in the tests as shown in Table 3, which indicates the beneficial effect of reinforcement at varying depth to increase the subgrade strength of geosynthetic reinforced unpaved road. The location of the geosynthetic reinforcement within the subgrade is an important factor for the performance of unpaved road. The reinforcement ratio varies from 1.05 to 1.58 for a single layer of geosynthetic reinforcement and 2.12 to 4.25 for double layers of geosynthetic reinforcement respectively. Out of three types of geosynthetic reinforcement used in the study, geogrids perform better than geomat for soil reinforced with a single layer of reinforcement. Only in one case geomat reinforcement yields the maximum strength when it is placed at $\xi = H/2$ from the top, when compared to the other two geogrids. Geomat performs best among the three types of geosynthetic when soil is reinforced with double layers of reinforcement. An increase in the number of reinforcement layers led to the further increase in strength and load carrying capacity of soil. The reinforcement ratio lies between 2 and 5 which indicates that an introduction of geosynthetic as double layers of reinforcement offers a good resistance against the penetration.

Comparison of different types of geosynthetic reinforcement

Fig. 9 shows the relative influence of geosynthetic reinforcement at different positions on the reinforcement ratio. Three different types of geosynthetic were used in the test and properties of these geosynthetic material were presented earlier in Table 2. The comparison of the ability of different types of geosynthetic used in this study to reinforce the weak subgrade soil can only be accomplished if the conditions between each of the individual tests are identical. The comparison between the different types of geosynthetic reinforcement, in terms of reinforcement ratio is described in Fig. 9 for the section with a single layer of reinforcement placed at $H/2$, $H/3$, $H/4$ and double layers of reinforcement. It can be observed that the reinforced section with double layers of reinforcement has higher strength than the section reinforced with a single layer of reinforcement. Comparing the performance of different types of geosynthetic reinforcement is difficult because all three geosynthetics used are individually different from

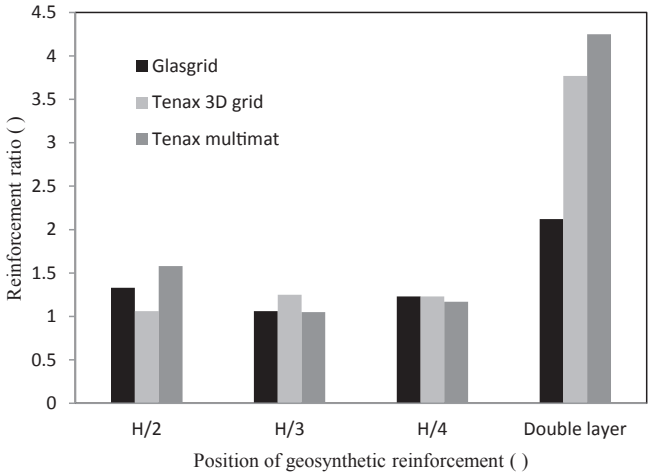


Fig. 9. Variation in reinforcement ratio for the various positions of geosynthetic reinforcement.

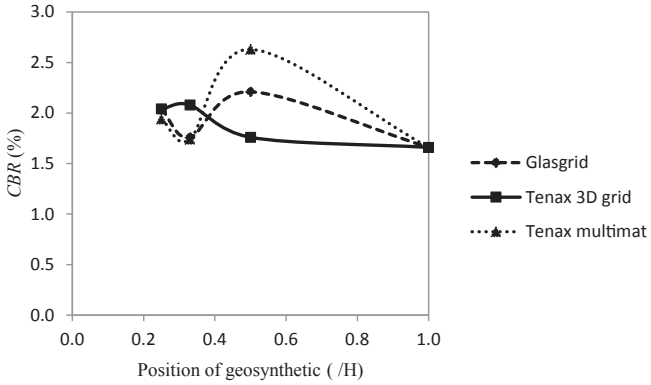


Fig. 10. Optimum position of geosynthetic based on *CBR* value of soil reinforced with different types of geosynthetics.

each other based on the properties given in Table 2. Important parameters which are responsible for comparing the performance of various geosynthetics to increase the subgrade strength are (1) type of geosynthetic used, (2) properties of geosynthetic, such as strength, stiffness, aperture size etc., (3) number of geosynthetic layers, and (4) depth of geosynthetic reinforcement. It is hard to identify which parameter has more important effect on the enhancement of subgrade strength reinforced with different types of geosynthetic. Therefore, it is better to investigate and quantify the mechanism that is responsible for the improved strength when different types of geosynthetics are used for comparison. The performance of the subgrade soil of an unpaved road is improved through three mechanisms: (1) impact of load distribution on subgrade soil resilient modulus, (2) subgrade soil vertical restraint, and (3) load transfer by the tensioned membrane effect [22]. The presence of geosynthetic in the subgrade soil reduces the maximum vertical stress on it and also more uniformly distributes the vertical stress on the subgrade soil than in the absence of a geosynthetic. Tensioned membrane effect becomes important only when large deformations occur in subgrade soil, when it is weak/soft.

Out of three types of geosynthetics used to reinforce subgrade with a single layer of reinforcement at varying depths, both geogrid reinforcements perform better than the geomat reinforcement except one case when geomat reinforcement it is placed at $\xi = H/2$ which yields the maximum strength when compared to the other two geogrids. Both geogrid reinforcements behaved similarly and gain the similar strength when placed at $\xi = H/4$. The same order was obtained for achieving the improvement when reinforcement layer was placed at $\xi = H/3$ and $\xi = H/4$ where Tenax 3D grid yields the maximum improvement. The results show that the behaviour of reinforced subgrade was better than that of the unreinforced subgrade and improvement with reinforcement is more pronounced when reinforcement layer is placed near to the load. The overall preference of choosing reinforcement type should be given to Tenax 3D grid which performs better than other geosynthetics because of the higher tensile strength and has relatively higher stiffness. Even handling of Tenax 3D grid over Glasgrid was easier because of the pressure sensitive adhesive provided at the back creates little inconvenience. Aperture size is different for all types of geosynthetic which governs the lateral confinement effect and justifies the selection of geogrid over geomat for subgrade reinforcement. To ensure effective interlocking between geosynthetic and soil, aperture size is a factor to be considered. The results of subgrade soil reinforced with double layers of reinforcement shows that Tenax multimat reinforcement type performs best because they offer good interlocking and frictional resistance. Increasing the number of reinforcement layers leads to enhance the strength significantly, as compared to the single layer of reinforcement and the extent of improvement is independent of type of geosynthetic. Tenax multimat is composed of tieing three layers of extruded and bi-oriented polypropylene grids. The non uniform texture of top and bottom layers of Tenax multimat offers good tensile resistance to the lateral movement. The relative cost of reinforcement type is also a factor which should be considered before the final selection is made.

Optimum position of the geosynthetic

Fig. 10 shows the effect of placement of a single layer of geosynthetic reinforcement along the height of the specimen on *CBR*. A set of experiments were carried out to determine the optimum position of placing the geosynthetic reinforcement along the depth of the subgrade in order to produce a maximum gain in the strength. The results of CBR tests indicates that for the maximum benefit, the geosynthetic reinforcement layer should be placed either at the middle of the height of specimen or between the upper one-third layer and middle layer which yields the higher strength as compared to the other locations. The tests were conducted at three different positions of geosynthetic and the maximum value of all strength parameters was obtained in the case when Tenax multimat reinforcement layer was placed at middle half of the specimen. Based on the properties of these geosynthetics, an increase in the strength of subgrade depends on the value of ξ i.e the depth of placement of reinforcement. Placing the geosynthetic at base of the specimen is just as good as having no reinforcement in the sample. The beneficial position of the geosynthetic reinforcement was obtained by plotting the graph between *CBR* of the soil and depth of the geosynthetic placement from top as shown in Fig. 8. The optimum position of the geosynthetic reinforcement layer should be taken as $0.3H$ to $0.36H$ for Tenax 3D grid reinforcement and $0.41H$ to $0.62H$ for Glasgrid reinforcement and Tenax multimat reinforcement where H is the height of the soil specimen. Naeini and Moayed [16] have also shown that the best location of geosynthetic reinforcement layer is at 30% of the thickness measured from the top of CBR mould. Reinforcement inclusion can be less effective if it is not placed at the proper location. Thus reinforcement layer should be located at the optimal depth to improve contribution of the geosynthetic reinforcement. For field applications, the finding of optimal location of geosynthetic reinforcement for maximum enhancement in *CBR* is essential.

Conclusions

In the present study, reinforcement benefits of different types of geosynthetics in unpaved road have been evaluated in terms of their *CBR* value. The performance of several geosynthetics in terms of increase in CBR value of soil with reinforcement can be compared with each other because all the tests are performed under the same

condition, that is, with the same subgrade soil. All these experiments can be related to an unpaved road as to whether the geosynthetic reinforcement can really improve the subgrade soil strength where the specimen height is considered as the depth of compacted subgrade soil in field. The findings indicate that there is a considerable amount of increase in strength of subgrade soil reinforced with geosynthetics and the amount of increase depends on the properties and type of geosynthetics, depth and number of reinforcement layers, and mechanisms involved. It is important to mention here that these findings are based on the laboratory investigations carried out in this study. It is possible that these findings may vary if conducted in the field. Therefore, actual field trials must be made to have more confidence in these results.

The important findings of this research are summarized below:

1. The inclusion of a single layer and double layers of geosynthetic reinforcements at varying depths in soil enhances the strength of the subgrade soil in terms of *CBR* value
2. The *CBR* value of the soil increases by 5–60% when a single layer of reinforcement is placed within the subgrade soil and strength increases by 112–325% when it is reinforced with double layers of reinforcement. The amount of improvement depends upon the position of reinforcement layer and type of reinforcement.
3. Placing the geosynthetic reinforcement in the double layers yields the largest improvement regardless of the type of geosynthetic.
4. The optimum benefit of reinforcement is evident if it is placed at middle height of the CBR mould and for better improvement in strength the reinforcement layer should be placed between the upper one-third layer and middle layer.
5. Of the three geosynthetics used in the study, Tenax 3D grid performed better than other two geosynthetics for soil reinforced with a single layer of reinforcement at $\xi = H/3 = H/4$ and Tenax multimat performed better than other two geosynthetics for soil reinforced with double layers of reinforcement and single layer of reinforcement at $\xi = H/2$.
6. Optimum location of reinforcement was found as $0.3H$ to $0.36H$ for Tenax 3D grid reinforcement layer and $0.41H$ to $0.62H$ for both Glasgrid reinforcement layer and Tenax multimat reinforcement layer.

Appendix A. Supplementary material

Supplementary data to this article can be found online at https://doi.org/10.1016/j.trgeo.2019.01.007.

References

[1] Abu-Farsakh MY, Akond I, Chen Q. Evaluating the performance of geosynthetic-reinforced unpaved roads using plate load tests. Int J Pavement Eng 2016;17:901–12. https://doi.org/10.1080/10298436.2015.1031131.

[2] Abu-Farsakh M, Hanandeh S, Mohammad L, Chen Q. Performance of geosynthetic reinforced/stabilized paved roads built over soft soil under cyclic plate loads. Geotext Geomembr 2016;44:845–53. https://doi.org/10.1016/j.geotexmem.2016.06.009.

[3] Abu-Farsakh M, Souci G, Voyiadjis GZ, Chen Q. Evaluation of factors affecting the performance of geogrid-reinforced granular base material using repeated load triaxial tests. J Mater Civ Eng 2012;24:72–83. https://doi.org/10.1061/(ASCE)MT.1943-5533.0000349.

[4] Adams CA, Apraku E, Opoku-boahen R. Effect of triaxial geogrid reinforcement on CBR strength of natural gravel soil for road pavements. J Civ Eng Res 2015;5:45–51. https://doi.org/10.5923/j.jce.20150502.05.

[5] Al-Qadi IL, Brandon TL, Valentine RJ, Lacina BA, Smith TE. Laboratory evaluation of geosynthetic-reinforced pavement sections. Transp Res Rec 1994:25–31.

[6] Choudhary A, Gill K, Jha J, Shukla S. Improvement in CBR of the expansive soil subgrades with a single reinforcement layer. Proc Indian Geotech Conf. 2012. p. 289–92.

[7] Duncan-Williams E, Attoh-Okine NO. Effect of geogrid in granular base strength – an experimental investigation. Constr Build Mater 2008;22:2180–4. https://doi.org/10.1016/j.conbuildmat.2007.08.008.

[8] Fannin RJ, Sigurdsson O. Field observations on stabilization of unpaved roads with geosynthetics. J Geotech Eng 1996;122:544–53. https://doi.org/10.1061/(ASCE)0733-9410(1996) 122:7(544).

[9] Giroud JP, Noiray L. Geotextile-reinforced unpaved road design. J Geotech Eng 1981;107(9):1233–54.

[10] Góngora IAG, Palmeira EM. Influence of fill and geogrid characteristics on the performance of unpaved roads on weak subgrades. Geosynth Int 2012;19:191–9. https://doi.org/10.1680/gein.2012.19.2.191.

[11] Hufenus R, Rueegger R, Banjac R, Mayor P, Springman SM, Brönnimann R. Full-scale field tests on geosynthetic reinforced unpaved roads on soft subgrade. Geotext Geomembr 2006;24:21–37. https://doi.org/10.1016/j.geotexmem.2005.06.002.

[12] IS : 2720 (Part VII-1980). IS : 2720 (Part VII-1980), Methods of Test for Soils, Determination of Water Content-Dry Density Relation using Light Compaction, Bureau of Indian Standards, New Delhi (Reaffirmed 2011). Indian Stand; 2011.

[13] Kamel MA, Chandra S, Kumar P. Behaviour of subgrade soil reinforced with geogrid. Int J Pavement Eng 2004;5:201–9. https://doi.org/10.1080/1029843042000327122.

[14] Koerner RM. Desigining with geosynthetics. 6th ed. New York: Xlibris PublishingCo.; 2012.

[15] Kuity A, Roy TK. Utilization of geogrid mesh for improving the soft subgrade layer with waste material mix compositions. Procedia – Soc Behav Sci 2013;104:255–63. https://doi.org/10.1016/j.sbspro.2013.11.118.

[16] Naeini SA, Ziaie-Moayed R. Effect of plasticity index and reinforcement on the CBR value of soft clay. Int J Civ Eng 2009;7:124–30.

[17] Palmeira EM, Antunes LGS. Large scale tests on geosynthetic reinforced unpaved roads subjected to surface maintenance. Geotext Geomembr 2010;28:547–58. https://doi.org/10.1016/j.geotexmem.2010.03.002.

[18] Paper T, Of A, As OAD, Of U. Technical Paper by Som N, Sahu RB. Bearing capacity of a geotextile-reinforced unpaved road as a function of deformation: a model study n.d.;6:1–17.

[19] Perkins SW, Ismeik M. A Synthesis and Evaluation of Geosynthetic-Reinforced Base Layers in Flexible Pavements: Part I. Geosynth Int 1997;4(6):549–604.

[20] Rajesh U, Sajja S, Chakravarthi VK. Studies on engineering performance of geogrid reinforced soft subgrade. Transp Res Procedia 2016;17:164–73. https://doi.org/10.1016/j.trpro.2016.11.072.

[21] Raymond G, Ismail I. The effects of geogrid reinforcement on unbound aggregates. Geotext Geomembr 2003;21:355–80. https://doi.org/10.1016/S0266-1144(03)00044-X.

[22] Shukla SK. An introduction to geosynthetic engineering. London: CRC Press; 2016.

[23] Shukla SK. Geosynthetics and their applications. London: Thomas Telford Publishing; 2002.

[24] Subaida EA, Chandrakaran S, Sankar N. Laboratory performance of unpaved roads reinforced with woven coir geotextiles. Geotext Geomembr 2009;27:204–10. https://doi.org/10.1016/j.geotexmem.2008.11.009.

[25] Vinod P, Minu M. Use of coir geotextiles in unpaved road construction. Geosynth Int 2010;17:220–7. https://doi.org/10.1680/gein.2010.17.4.220.

View publication stats

AIP Advances

Zero-index metamaterial based all-dielectric nanoantenna

Cite as: AIP Advances **9**, 035115 (2019); https://doi.org/10.1063/1.5086234
Submitted: 19 December 2018 . Accepted: 28 February 2019 . Published Online: 12 March 2019

Nishant Shankhwar, Yogita Kalra, Qiang Li, and Ravindra Kumar Sinha

View Online Export Citation CrossMark

Don't let your writing keep you from getting published!

AIP Author Services

Learn more today!

© 2019 Author(s).

AIP Advances ARTICLE scitation.org/journal/adv

Zero-index metamaterial based all-dielectric nanoantenna

Cite as: AIP Advances 9, 035115 (2019); doi: 10.1063/1.5086234
Submitted: 19 December 2018 • Accepted: 28 February 2019 •
Published Online: 12 March 2019

View Online Export Citation CrossMark

Nishant Shankhwar,[1] Yogita Kalra,[1] Qiang Li,[2] and Ravindra Kumar Sinha[1,3,a)]

AFFILIATIONS

[1]TIFAC-Centre of Relevance and Excellence in Fiber Optics and Optical Communication, Department of Applied Physics, Delhi Technological University, Bawana Road, Delhi 110042, India

[2]State Key Laboratory of Modern Optical Instrumentation, College of Optical Science and Engineering, Zhejiang University, Hangzhou 310027, China

[3]CSIR-Central Scientific Instruments Organisation (CSIO), Chandigarh 160030, India

[a)]**Electronic mail:** dr_rk_sinha@yahoo.com

ABSTRACT

In this article, a highly directive all-dielectric zero-index metamaterial (ZIM) based nanoantenna has been proposed which has the ability to directionally transmit the radiation from an isotropic quantum emitter. The zero-index metamaterial (ZIM) used here, is basically a rods-in-air type photonic crystal, which exhibits zero-index behaviour owing to the existence of a Dirac-cone at the Gamma (Γ) point in its photonic band structure. The emitter is embedded inside the ZIM and the radiation pattern can be controlled by varying the shape and size of the array.

© 2019 Author(s). All article content, except where otherwise noted, is licensed under a Creative Commons Attribution (CC BY) license (http://creativecommons.org/licenses/by/4.0/). https://doi.org/10.1063/1.5086234

I. INTRODUCTION

A zero refractive index medium is the one in which electromagnetic waves do not undergo any change in phase.[1–4] In other words, phase of the wave at the boundary of emergence is same as that at boundary of incidence. Several different types of metamaterials have been developed so far which exhibit near-zero material parameters and are accordingly referred to as epsilon-near-zero (ENZ) or mu-near-zero (MNZ) metamaterials. In addition to this, a few special structures which have both - ENZ and MNZ properties simultaneously are called zero-index metamaterials (ZIM). These metamaterials have a large number of application including wavefront engineering,[2] directivity and gain enhancement of antennas,[5,6] electromagnetic cloaking,[3,7] phase matching for nonlinear application[8] such as four-wave mixing,[9] second harmonic generation,[10] unidirectional transmission,[11] defect waveguides,[12] ZIM cavities,[13] PT symmetry,[14,15] etc.

In this article, directivity enhancement capability has been investigated at nanoscale. Temelkuran et al., in 2000, reported a highly directive photonic crystal based resonant antenna.[16] They used a combination of a monopole source and a layer-by-layer photonic crystal. Enoch et al., in 2002, reported an entirely different structure which had a monopole antenna embedded inside a metamaterial.[17] Metamaterial was made up of multiple layers of copper grids separated from each other by foam. The monopole operated near the plasma frequency of the metamaterial and ENZ behaviour resulted in directivity enhancement. This was followed by several other works which employed ENZ or ZIM structures to enhance directivity and gain of different types of gigahertz antennas.[5,6,18–24] All these structures were basically made up of metallic resonators and hence had intrinsic ohmic losses. For nanoscale application, all-dielectric ZIMs are more suitable option, as they are free from ohmic losses. Dielectric ZIMs are basically photonic crystals having Dirac like dispersion at Γ point.[3,25–27] Beside effectively zero refractive index, Dirac dispersion has many other interesting applications as well.[28,29]

Aim of this paper is to propose a ZIM based all-dielectric nanoantenna to directionally radiate emissions from isotropic nanoscale emitter. In the following sections, the ZIM has been discussed in detail along with the condition of zero index behaviour including the principle and operation of the proposed nanoantenna.

© Author(s) 2019

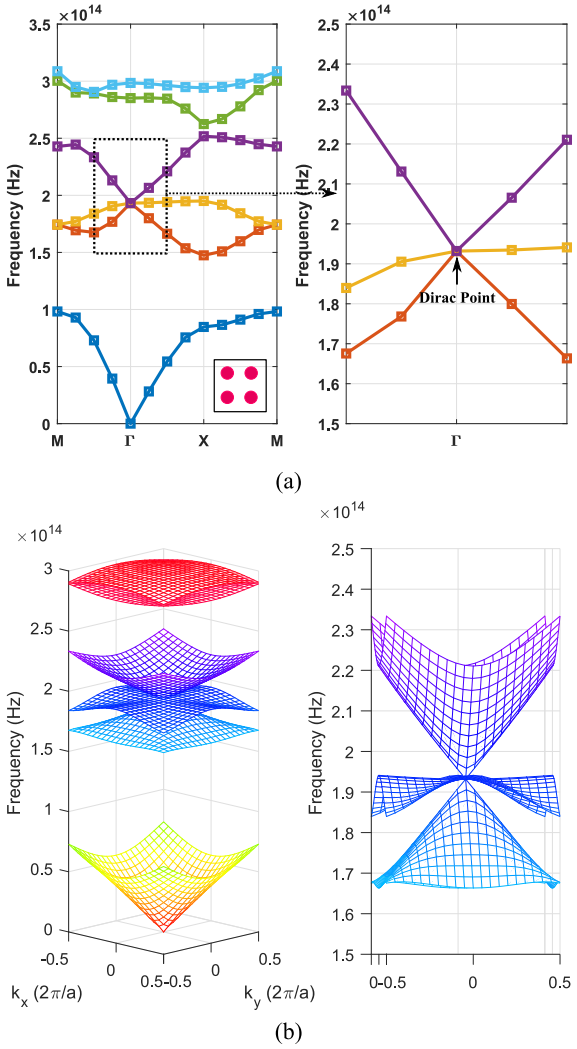


FIG. 1. (a) Photonic band structure of the ZIM. The inset shows the square shape of the array. The region around the Dirac point has been zoomed to show the linear dispersion in its neighbourhood. (b) 3D dispersion surfaces displaying the formation of Dirac cones.

II. ZERO REFRACTIVE INDEX METAMATERIAL

A. Design of ZIM

The ZIM used here is a photonic crystal (PhC) made up of Silicon (ε = 12.5) rods in air. Such a structure can be tailored to achieve Dirac like dispersion at the center of Brillouin zone.[3] Dirac like dispersion means that the dispersion curves should be linear in the vicinity of the point of intersection, referred to as Dirac point. Figure 1(a) shows the photonic band structure of ZIM in which the location of Dirac point and the linear nature of dispersion is displayed. Linear dispersion manifests itself in the conically shaped dispersion surfaces, referred to as Dirac cones, touching each other at the Dirac point (see Figure 1(b)). The frequency corresponding to Dirac point is 193 THz which translates to 1550 nm wavelength. The periodicity (a = 840 nm) of the array and radius (r = 0.2a) of each rod have been suitably chosen to achieve Dirac point at 1550 nm.

B. Condition for effectively zero refractive index

The necessary condition for zero refractive index is the existence of Dirac cone at Γ point, hence linear nature of dispersion.[27] For better comprehension, let us write the wave vector k as a function of angular frequency ω in Taylor series form about the Dirac point as,

$$k(\omega) = k(\omega_D) + \frac{k'(\omega_D)}{1!}(\omega - \omega_D) + \frac{k''(\omega_D)}{2!}(\omega - \omega_D)^2 + \dots \quad (1)$$

where ω_D is the frequency corresponding to Dirac point. If $k(\omega_D)$ = 0 and the dispersion curve is almost linear (as shown in Figure 1), higher order terms can be neglected and equation 1 reduces to

$$k(\omega) = \frac{\omega - \omega_D}{v_D} \quad (2)$$

where $v_D = (d\omega/dk)|_{\omega=\omega_D} = 1/k'(\omega_D)$ is the group velocity at Dirac point. It is clearly visible in equation 2 that with respect to frequency, the value of $k(\omega)$ varies from negative, through zero, to positive. The refractive index follows the same trend with zero value at ω_D. This condition is hard to achieve in case of PhCs because wave vector is generally a quadratic function of frequency at the center of Brillouin zone. However, a PhC having a particularly chosen r/a ratio (0.2 in this case, but may have a different value for a different dielectric) can fulfill the condition of linear dispersion. For any other value, the

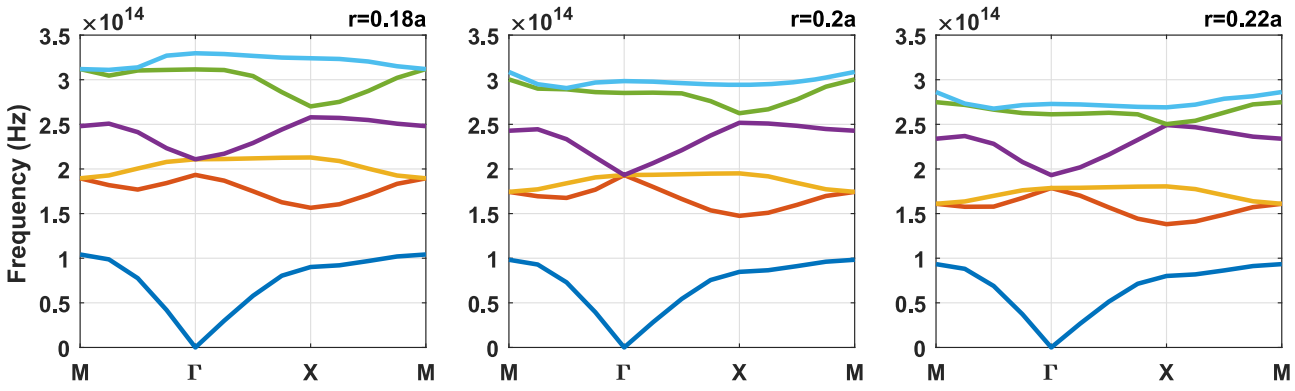


FIG. 2. Illustration of how critical the r/a ratio is for Dirac like dispersion.

© Author(s) 2019

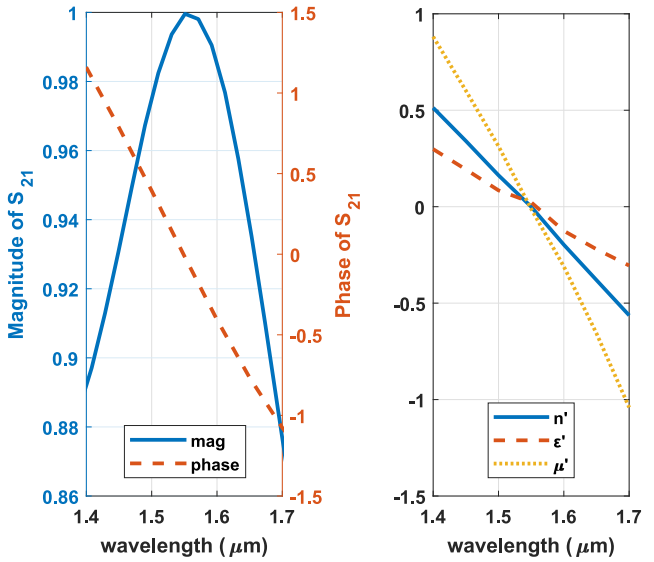


FIG. 3. (Left) Magnitude and phase of scattering parameter S_{21}. (Right) Effective material parameters retrieved s-parameter inversion.

condition fails and Dirac cones are lost. This has been demonstrated in Figure 2. It can be observed that even a slight change from the appropriate value of r/a disturbs the Dirac cone. It should be noted that the structure can be tuned to different wavelength if one varies the periodicity without disturbing the r/a ratio.

C. Calculation of effective material parameters

To confirm this, an s-parameter inversion based parameter retrieval technique has been implemented to calculate the effective permittivity, effective permeability and effective refractive index.[30] The calculated material parameters have been plotted with respect to wavelength and are shown in Figure 3. Figure 3(a) shows that, the phase of the S_{21} parameter is zero at 1.55 μm and in Figure 3(b) it is shown that, the refractive index curve passes through zero at 1.55 μm It should be noted that, as the wave vector and effective index tend to zero inside a ZIM, the effective wavelength tends to infinity. Hence effective medium theory still holds good and the above-mentioned parameter retrieval technique is absolutely applicable.

III. Nanoantenna

A. Fundamental principle

Inside a ZIM, a wave experiences zero change in phase, i.e. all the points on the boundary and in the bulk of a ZIM vibrate in the same phase. This property can be exploited to generate highly directive radiation.[2,4] If an infinitely long ZIM slab is provided with a current line source embedded inside, highly directive beams can be obtained, as illustrated in Figure 4. In Figure 4(a), cross-section of ZIM with an embedded current line source (acting as a point source in 2D) is shown. It is can be observed in Figure 4(c) that, a substantially larger amount of radiation emerges out of the longer edge of the ZIM slab compared to the shorter one. It is attributed the fact that every point in ZIM which vibrates in phase with the embedded point source, acts as a source itself. Hence it seems logical that the longer boundary of the slab, which has a greater number of points, gives out a larger amount of radiation compared to the shorter boundary. In this way, the ZIM slab plays the role of a highly directive antenna for an omnidirectional source.

B. Design and operation of the proposed nanoantenna

Based on the above principle one can think of ZIM based directive nanoantenna which comprises a 2D array of silicon rods in air operating in TM mode (as discussed in section II). While calculating the band structure, the rods are assumed to be infinite in length which seems impractical. Upon fabrication on a substrate, rods will obviously have a finite height hence their behaviour is bound to deviate from the ideal case. However, Li et al. successfully developed

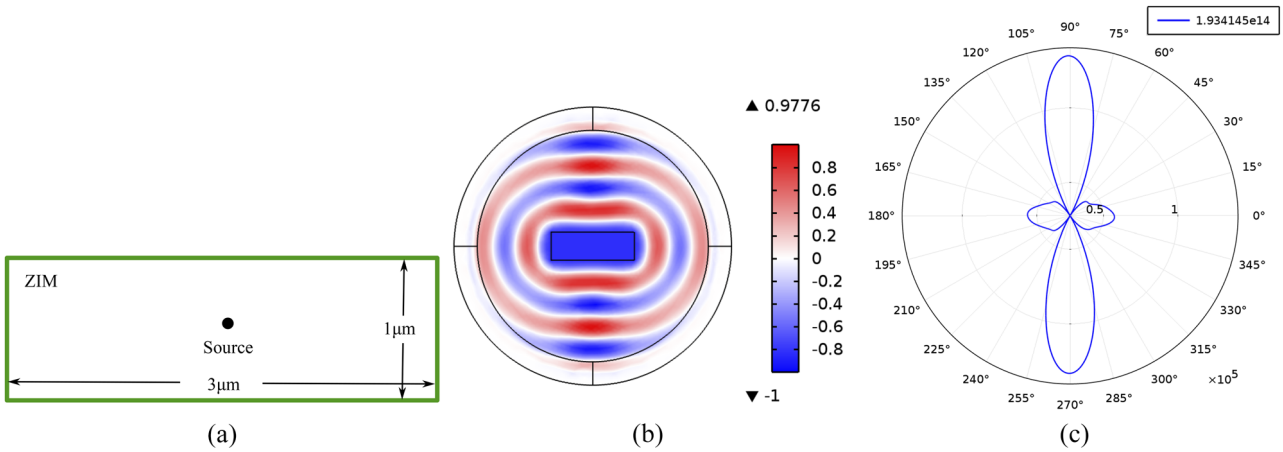


FIG. 4. Demonstration of the capability of a homogeneous ZIM slab to generate highly directional beams of light. (a) Geometry of the slab with an embedded current line source, (b) Electric field distribution around it, and (c) farfield plot to display the amount power flow w.r.t. the azimuthal coordinate at 193.4 THz (1550 nm).

© Author(s) 2019

an on-chip compatible ZIM in which silicon rods of finite height were made to behave like infinite ones by purposely enclosing them between parallel sheets of a conductor (gold).[31] In this way the electric field remains along the axis of the rods and TM mode is enforced. Such an arrangement can be used to directionally radiate light generated by nanoscale emitters like quantum dots. Figure 5(a) shows the design of the proposed nanoantenna with quantum emitter embedded in it. The nanoantenna contains ZIM to provide high directivity, and Bragg reflector to reduce backward radiation. The ZIM is made up of a 3 × 7 periodic array of silicon rods whose periodicity a = 840 nm, radius $r = 0.2a$ and height $h = 4r$. The central rod has been removed and the quantum emitter sits in its place. A point dipole source was used to represent the emitter during computation. Bragg mirror is made up of periodically placed silicon slabs of quarter-wave thickness. The thickness of each slab is t_1 = 109 nm and the air gap between them is t_2 = 387 nm. Figure 5(b) illustrates the original radiation pattern of the emitter alone in which the power is seen flowing isotropically in H plane. But when the emitter is embedded inside the ZIM, most of the power flows towards the positive x direction, as shown in Figure 5(c). One can easily notice the large frontal lobe, small back lobe and insignificant side lobes.

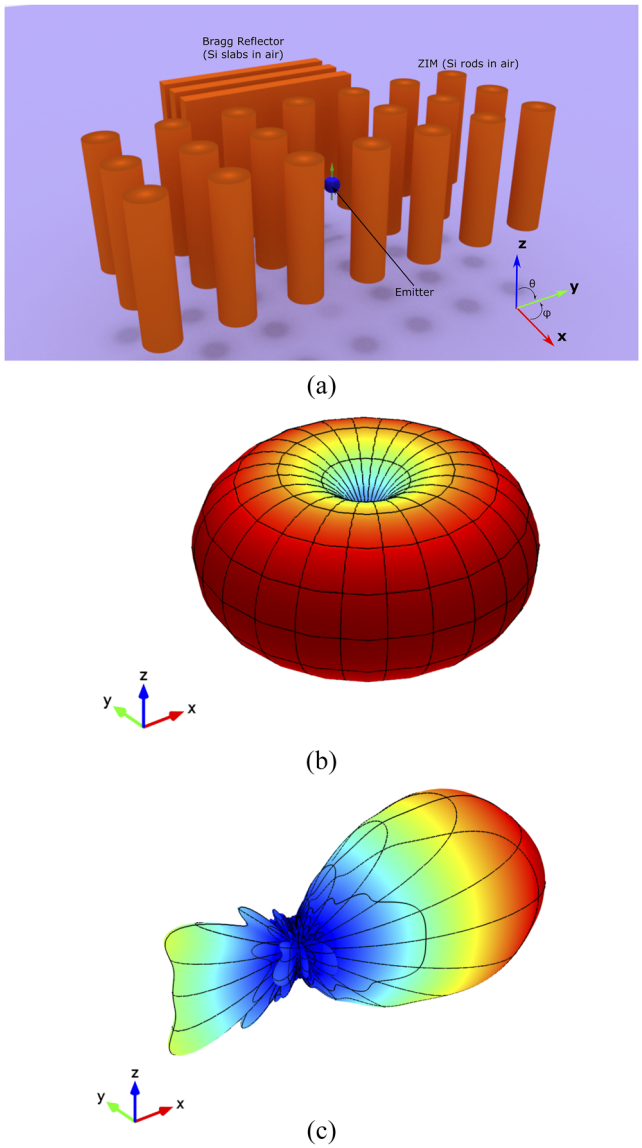


FIG. 5. (a) Design of ZIM based nanoantenna. (b) Radiation pattern of the emitter alone, and (c) radiation patter of the emitter with nanoantenna.

From the radiation pattern, other useful parameters such as directivity and beamwidth have also been calculated. The directivity D has been calculated using the formula[32]

$$D(\theta, \phi) = \frac{4\pi p(\theta, \phi)}{P_{rad}} \tag{3}$$

where θ and ϕ respectively represent the polar and azimuthal coordinate of a spherical coordinate system, $p(\theta, \phi)$ is the power radiated in a particular direction and P_{rad} is the total power radiated. Plots for directivity D as a function of ϕ in H plane and as a function of θ in E plane respectively are shown in Figure 6. Maximum directivity in H plane comes out to be 8.28 dB at $\phi = 0^\circ$ and in E plane it is 6.04 dB at $\theta = 90^\circ$. It should be noted that directivity has been expressed in decibels (dB) in Figures 6(a) and (c) to easily calculate the 3 dB beamwidth. 3 dB beamwidth is 45° in H plane and 63° E plane.

IV. EFFECT OF THE SURROUNDING MATERIAL

Though air has been taken as the surrounding medium for the sake of simplicity, it is obvious that during on-chip fabrication the rods shall be embedded in some matrix such as SU-8,[31] poly(methyl methacrylate) (PMMA),[33] etc. Hence it is necessary to study how the design parameters need to be modified according to the choice of the surrounding medium, in order to achieve a proper Dirac Cone. Figure 7(a) shows the variation of the required r/a ratio with respect to refractive index, n_s, of the surrounding medium, for the formation of Dirac cone. It also shows the decreasing trend in the normalized frequency (a/λ) corresponding to Dirac point with increase in refractive index. If one intends to keep radius, a constant, the periodicity needs to be decreased with respect to increase in surrounding material's refractive index, as shown in Figure 7(b), so that Dirac point and hence zero-index is achieved at 1550.

V. EFFECT OF THE GAP BETWEEN ZIM AND BRAGG MIRROR

It is understandable that since the reflected wave renters the ZIM, interference effects are bound to influence that output power. Hence it becomes necessary to study the effect of gap between ZIM and the Bragg mirror, on the output power received. On contemplating Figure 8, it is noticed that before re-entering the ZIM, wave has undergone path difference of $2g + \lambda/2$. The factor of $\lambda/2$ has been incorporated to include the phase reversal occured on being reflected by an optically denser medium. Basic understanding of interference phenomenon leads us to the following conditions:

For constructive interference,

$$2g + \lambda/2 = n\lambda \tag{4}$$

© Author(s) 2019

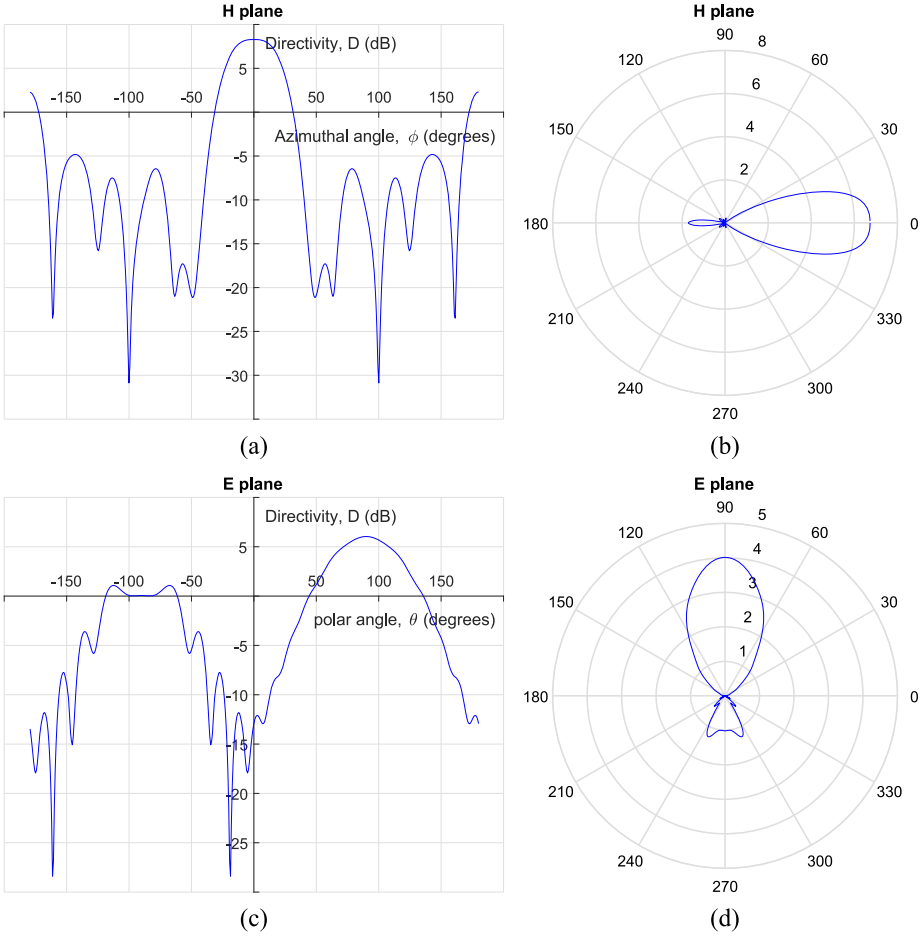


FIG. 6. Directivity D in H plane - (a) Cartesian plot and (b) Polar plot. Directivity in E plane - (c) Cartesian plot and (d) Polar plot.

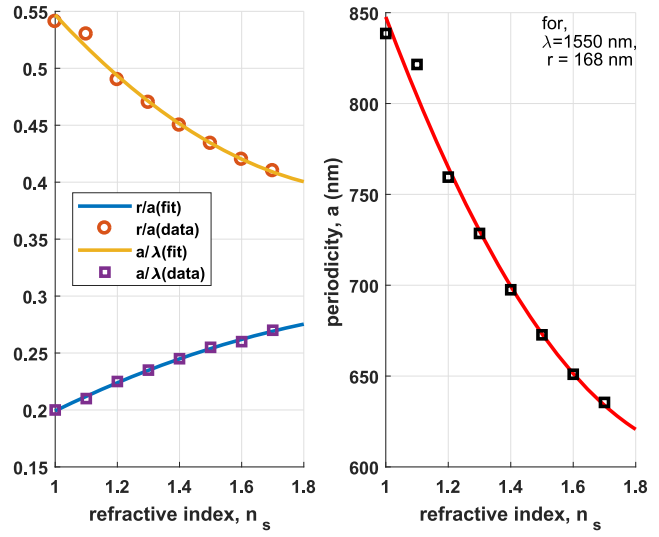


FIG. 7. (Left) Dependence of required *r*/*a* ration and normalized frequency (a/λ) on the refractive index of the chosen surrounding medium, (Right) Variation of periodicity of the rods with respect to the refractive index of the chosen surrounding medium.

or

$$g = (2n-1)\lambda/4 \tag{5}$$

For destructive interference,

$$2g + \lambda/2 = (2n+1)\lambda/2 \tag{6}$$

or

$$g = n\lambda/2 \tag{7}$$

Constructive interference results in high output power in the farfield zone. Hence the value of gap parameter g should be set accordingly. To determine the most suitable value, the gap parameter was varied from 100 nm to 1500 nm upon which two maxima were observed at 340 nm and 1085 nm. Figure 9 shows the variation of electric field intensity in the farfield zone with respect to the variation of the gap parameter. The periodic nature observed is intrinsic property of interference phenomenon. However the values of g corresponding to local maxima in intensity profile are not exactly equal to those predicted by equation 5 on assuming $n = 1$ and $n = 2$ repectively.

Table I shows the comparision between the values of g according to equation 5 and values obtained by numerical analysis shown in Figure 9. It can be observed that numerically obtained positions of maxima are deviated by 47.5 nm and 77.5 nm respectively, from

© Author(s) 2019

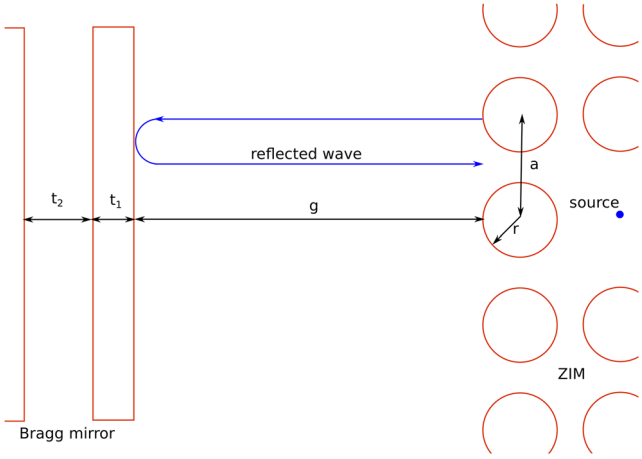


FIG. 8. Schematic illustration of the design of the nanoantenna showing various geometrical parameters.

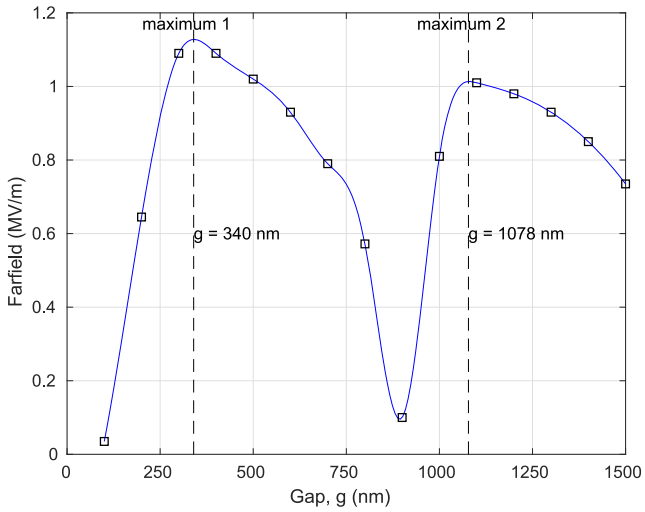


FIG. 9. Variation of output field with respect to the gap parameter *g*.

those precited by equation 5. The reason for this deviation is the fact the reflector is made up of pure dielectric slabs which cannot offer a perfectly reflecting boundary to the incoming radiation and a small amount of light is always able to slightly penetrate into the first layer. This imperfection leads to the discrepancy that actual gap value comes out to be slightly smaller than that in the ideal case.

TABLE I. Values of gap parameter *g* corresponding to maximum output in the farfield zone.

	maximum 1	maximum 2
Present case (Fig. 9)	340 nm	1085 nm
Ideal case (Eq. 5)	387.5 nm ($n = 1$)	1162.5 nm ($n = 2$)
Deviation	47.5 nm	77.5 nm

VI. CONCLUSION

Zero-index metamaterial based nanoantenna has been successfully designed and analyzed. It has been demonstrated that the proposed ZIM nanoantenna can unidirectionally radiate the electromagnetic radiation from an isotropic quantum emitter embedded in it. The proposed structure is simple and compatible with on-chip fabrication techniques. Although the nanoantenna is free from ohmic losses for being made up of dielectric, there will surely be some power dissipation in the parallel conductors. But on the bright side, this is more of an advantage than a limitation, because radiation losses along the z-direction are checked this way.

ACKNOWLEDGMENTS

The authors from India gratefully acknowledge (i) Initiatives and support for the establishment of TIFAC-Centre of Relevance and Excellence in Fiber Optics and Optical Communication at Delhi Technological University (Formerly Delhi College of Engineering) Delhi, through the Mission REACH program of TechnologyVision-2020 of the Government of India and (ii) Support from "DST, Govt. of India for BRICS multilateral project" All Dielectric and Hybrid Nano Antennas for Multifunctional Sensors. Qiang Li acknowledge the supports of National Key Research and Development Program of China (2017YFE0100200). Nishant Shankhwar acknowledges the support through Junior Research Fellowship awarded by University Grants Commission (India) under UGC-NET-JRF scheme.

REFERENCES

[1] N. Engheta and R. W. Ziolkowski, *Metamaterials: physics and engineering explorations* (John Wiley & Sons, 2006).
[2] A. Alu, M. G. Silveirinha, A. Salandrino, and N. Engheta, "Epsilon-near-zero metamaterials and electromagnetic sources: Tailoring the radiation phase pattern," Physical Review B **75**, 155410 (2007).
[3] X. Huang, Y. Lai, Z. H. Hang, H. Zheng, and C. Chan, "Dirac cones induced by accidental degeneracy in photonic crystals and zero-refractive-index materials," Nature Materials **10**, 582 (2011).
[4] I. Liberal and N. Engheta, "Near-zero refractive index photonics," Nature Photonics **11**, 149 (2017).
[5] Z. H. Jiang, Q. Wu, D. E. Brocker, P. E. Sieber, and D. H. Werner, "A low-profile high-gain substrate-integrated waveguide slot antenna enabled by an ultrathin anisotropic zero-index metamaterial coating," IEEE Transactions on Antennas and Propagation **62**, 1173–1184 (2014).
[6] J. P. Turpin, Q. Wu, D. H. Werner, B. Martin, M. Bray, and E. Lier, "Near-zero-index metamaterial lens combined with AMC metasurface for high-directivity low-profile antennas," IEEE Transactions on Antennas and Propagation **62**, 1928–1936 (2014).
[7] J. Hao, W. Yan, and M. Qiu, "Super-reflection and cloaking based on zero index metamaterial," Applied Physics Letters **96**, 101109 (2010).
[8] R. W. Boyd, *Nonlinear optics* (Academic press, 2003).
[9] H. Suchowski, K. O'Brien, Z. J. Wong, A. Salandrino, X. Yin, and X. Zhang, "Phase mismatch–free nonlinear propagation in optical zero-index materials," Science **342**, 1223–1226 (2013).
[10] N. Mattiucci, M. J. Bloemer, and G. D'Aguanno, "Phase-matched second harmonic generation at the dirac point of a 2-D photonic crystal," Optics Express **22**, 6381–6390 (2014).
[11] Y. Fu, L. Xu, Z. Hong Hang, and H. Chen, "Unidirectional transmission using array of zero-refractive-index metamaterials," Applied Physics Letters **104**, 193509 (2014).
[12] Y. Fu, Y. Xu, and H. Chen, "Additional modes in a waveguide system of zero-index-metamaterials with defects," Scientific Reports **4**, 6428 (2014).

© Author(s) 2019

[13]Y. Fu, Y. Xu, and H. Chen, "Inhomogeneous field in cavities of zero index metamaterials," Scientific Reports **5**, 11217 (2015).
[14]Y. Fu, Y. Xu, and H. Chen, "Zero index metamaterials with PT symmetry in a waveguide system," Optics Express **24**, 1648–1657 (2016).
[15]Y. Fu, X. Zhang, Y. Xu, and H. Chen, "Design of zero index metamaterials with PT symmetry using epsilon-near-zero media with defects," Journal of Applied Physics **121**, 094503 (2017).
[16]B. Temelkuran, M. Bayindir, E. Ozbay, R. Biswas, M. Sigalas, G. Tuttle, and K.-M. Ho, "Photonic crystal-based resonant antenna with a very high directivity," Journal of Applied Physics **87**, 603–605 (2000).
[17]S. Enoch, G. Tayeb, P. Sabouroux, N. Guérin, and P. Vincent, "A metamaterial for directive emission," Physical Review Letters **89**, 213902 (2002).
[18]C. Saleh, D. Bensafieddine, E. Laamari, and M. Bouzouad, "A zero-index metamaterial single layer superstrate for patch antenna gain enhancement," Acta Physica Polonica A **128** (2015).
[19]H. Zhou, Z. Pei, S. Qu, S. Zhang, J. Wang, Z. Duan, H. Ma, and Z. Xu, "A novel high-directivity microstrip patch antenna based on zero-index metamaterial," IEEE Antennas and Wireless Propagation Letters **8**, 538–541 (2009).
[20]M. Sun, Z. N. Chen, and X. Qing, "Gain enhancement of 60-GHz antipodal tapered slot antenna using zero-index metamaterial," IEEE Transactions on Antennas and Propagation **61**, 1741–1746 (2013).
[21]Y. Liu, X. Guo, S. Gu, and X. Zhao, "Zero index metamaterial for designing high-gain patch antenna," International Journal of Antennas and Propagation **2013**.
[22]M. H. Ullah, M. T. Islam, and M. R. I. Faruque, "A near-zero refractive index meta-surface structure for antenna performance improvement," Materials **6**, 5058–5068 (2013).
[23]J. Zhu, G. Lu, J. Zhang, and B. Li, "Gain enhancement for planar quasi-yagi antenna with zero-index metamaterial," in *2016 IEEE International Conference on Microwave and Millimeter Wave Technology (ICMMT)*, Vol. 2 (IEEE, 2016) pp. 549–551.
[24]B. Zhou and T. J. Cui, "Directivity enhancement to Vivaldi antennas using compactly anisotropic zero-index metamaterials," IEEE Antennas and Wireless Propagation Letters **10**, 326–329 (2011).
[25]A. K. Geim and K. S. Novoselov, "The rise of graphene," Nature Materials **6**, 183 (2007).
[26]R. Sepkhanov, Y. B. Bazaliy, and C. Beenakker, "Extremal transmission at the dirac point of a photonic band structure," Physical Review A **75**, 063813 (2007).
[27]L.-G. Wang, Z.-G. Wang, J.-X. Zhang, and S.-Y. Zhu, "Realization of dirac point with double cones in optics," Optics Letters **34**, 1510–1512 (2009).
[28]O. Peleg, G. Bartal, B. Freedman, O. Manela, M. Segev, and D. N. Christodoulides, "Conical diffraction and gap solitons in honeycomb photonic lattices," Physical Review Letters **98**, 103901 (2007).
[29]M. Katsnelson, "Zitterbewegung, chirality, and minimal conductivity in graphene," The European Physical Journal B-Condensed Matter and Complex Systems **51**, 157–160 (2006).
[30]D. Smith, D. Vier, T. Koschny, and C. Soukoulis, "Electromagnetic parameter retrieval from inhomogeneous metamaterials," Physical Review E **71**, 036617 (2005).
[31]Y. Li, S. Kita, P. Muñoz, O. Reshef, D. I. Vulis, M. Yin, M. Lončar, and E. Mazur, "On-chip zero-index metamaterials," Nature Photonics **9**, 738 (2015).
[32]A. E. Krasnok, I. S. Maksymov, A. I. Denisyuk, P. A. Belov, A. E. Miroshnichenko, C. R. Simovski, and Y. S. Kivshar, "Optical nanoantennas," Physics-Uspekhi **56**, 539 (2013).
[33]P. Moitra, Y. Yang, Z. Anderson, I. I. Kravchenko, D. P. Briggs, and J. Valentine, "Realization of an all-dielectric zero-index optical metamaterial," Nature Photonics **7**, 791 (2013).

© Author(s) 2019